I.R.Iran

ISSN:2423-5547
e-ISSN:2423-7469

Journal of Renewable Energy and Environment

Volume 10, Number 4, Autumn 2023

Materials and Energy Research Center

Iranian Association of Chemical Engineers

In the Name of God

Journal of Renewable Energy and Environment

DISCLAIMER

Journal of Renewable Energy and Environment: (ISSN: 2423-5547) (e-ISSN: 2423-7469)

Website: www.jree.ir, E-mail: jree@merc.ac.ir

Tel: (+9826)36280040-49 (Ext. 381), Fax: (+9826)36201888

Journal of Renewable Energy and Environment, P. O. Box: 13145-1659, Tehran, Islamic Republic of Iran

Materials and Energy Research Center (MERC); Iranian Association of Chemical Engineers (IAChE)

ISSN: 2423-5547; e-ISSN: 2423-7469

Journal of Renewable Energy and Environment (JREE): Vol. 10, No. 4, (Summer 2023), 1-162

CONTENTS

ISSN: 2423-5547; e-ISSN: 2423-7469

Journal of Renewable Energy and Environment (JREE): Vol. 10, No. 4, (Summer 2023), 1-162

AIMS AND SCOPE

Journal of Renewable Energy and Environment (JREE) publishes original papers, review articles, short communications and technical notes in the field of science and technology of renewable energies and environmental-related issues including:

- Generation
- Storage
- Conversion
- Distribution
- Management (economics, policies and planning)
- Environmental Sustainability

INSTRUCTIONS FOR AUTHORS

Submission of manuscript represents that it had neither been published nor submitted for publication elsewhere and is result of research carried out by author(s). Only the extended and upgraded articles presented in a conference and/or appeared in a symposium proceedings could be evaluated for publication.

Authors are required to include a list describing all the symbols and abbreviations in the paper. Use of the international system of measurement units is mandatory.

- On-line submission of manuscripts results in faster publication process and is recommended. Instructions are given in the JREE web sites: www.jree.ir
- References should be numbered in brackets and appear in sequence through the text. List of references should be given at the end of the paper. All journal articles listed in the References section must follow with article doi.
- Figure captions are to be indicated under the illustrations. They should sufficiently explain the figures.
- Illustrations should appear in their appropriate places in the text.
- Tables and diagrams should be submitted in a form suitable for reproduction.
- Photographs should be of high quality saved as jpg files.
- Tables' illustrations, figures and diagrams will be normally printed in single column width (8 cm). Exceptionally large ones may be printed across two columns (17 cm).

JREE: Vol. 10, No. 4, (Autumn 2023) 1-13

Journal of Renewable Energy and Environment

Journal Homepage: www.jree.ir

Materials and Energy Research Center

MERC

Research Article

Analysis and Evaluation of Effective Environmental Indicators in the Heat Island of District 1 of Tehran using (RS)

Ali Sayyadi, Mohammad Javad Amiri *

Faculty of Environment, College of Engineering, University of Tehran, Tehran, Iran.

PAPER INFO

Paper History:
Received: 30 August 2022
Revised: 10 November 2022
Accepted: 30 November 2022

Keywords:
Heat Island,
NDVI,
LST,
SPSS

ABSTRACT

One of the environmental problems today is the rising land surface temperature and the formation of heat islands in metropolitan areas, which have arisen due to the unplanned expansion of these cities. Satellite imagery is widely used in urban environmental studies to provide an integrated view and reduce costs and time. In this study, Landsat satellite imagery in TM, ETM+, and OLI sensors from 1984 to 2020, remote sensing techniques, and GIS is used to analyze the data, and SPSS software is employed to examine the correlation between the data. The results indicate that the land surface temperature in District 1 of Tehran has increased during the last 38 years. Moreover, land use in District 1 has changed significantly over this period, and urban land use increased from 16 % (1984) to 35 % (2020) while vegetation declined from 32 % to 14 %. The results of linear regression analysis show a significant correlation between satellite images and weather station data. The significance coefficient (Sig) in all stations is less than 0.05 with a 95 % confidence interval. Besides, the coefficient of variation (R) for all stations is above 80 %, and the coefficient R2 has a desirable value. The findings suggest that the trend of rising temperatures in District 1 of Tehran has become an environmental problem and the changes in land use such as declining vegetation and increasing the acceleration of urbanization are among the factors that affect it.

https://doi.org/10.30501/jree.2022.355387.1438

1. INTRODUCTION

The acceleration of urbanization in the world is increasing. To be specific, 55.3 % of the world population lived in cities in 2015. The population may increase to 68.4 % by 2050 (United Nations Department of Economic and Social Affairs, 2019). The acceleration of urbanization leads to climate change and greenhouse gas emission. Urbanization dramatically reduces vegetation and changes radiance, heat, humidity, roughness, and urban surface diffusion (Al-Hatab et al., 2018). Urbanization continuously increases artificial surfaces, including roads and buildings, changes radiative fluxes and climates, intensifies urban warming, and forms urban hotspots (Lia et al., 2020; Tepanosyan et al., 2021). The spread of this phenomenon creates an urban heat island (El-Hadidy, 2021).

Urban heat island is formed in cities or metropolises due to human-induced changes to land surfaces when urban areas experience higher temperatures than the rural ones. Natural land surfaces are replaced by urban materials such as buildings, roads, and other asphalt areas and then, heat islands come into being (Mendez-Astudillo et al., 2020; Macintyre, 2021; Kabano et al., 2021). This increase in temperature starts at 2 °C and can increase to several °C (Harun et al., 2020).

Heat island causes irreparable damage to humans and the environment. Urban heat island is a principal factor affecting urban climatology, including urban vegetation and air pollution (Li et al., 2021), environmental and human health, including vulnerable groups (Wang et al., 2021), and public health (Sekertekin & Zadbagher, 2021; Vasenev et al., 2021), include an increasing mortality rate (Koopmans et al., 2020). Therefore, the heat island must be controlled. One approach to controlling and monitoring the heat island is the combined use of RS and GIS. Many researchers have merged RS and GIS (Liu et al., 2021). RS satellites provide a simple way to investigate thermal differences between urban and rural areas, LST recovery, and urban heat islands (Ahmed, 2018). A review of the relevant lectures and records shows that the term heat island was first proposed by Howard about a century ago, in 1833. Further research indicates that urbanization has caused significant changes in the meteorological parameters and features of the earth's surface and, as a result, has given rise to many changes in the local weather and climate. Guo et al (2020) and Galdies & Lau (2020) investigated the effect of urban heat islands, extreme temperatures, and long-term climate change in Hong Kong. This study showed that despite the severe heat island effects between urban and suburban areas, urban parks could

*Corresponding Author's Email: mjamiri@ut.ac.ir (M.J. Amiri)
URL: https://www.jree.ir/article_163301.html

Please cite this article as: Sayyadi, A., & Amiri, M.J., (2023). Analysis and evaluation of effective environmental indicators in the heat island of district 1 of Tehran using (RS). *Journal of Renewable Energy and Environment (JREE), 10*(4), *01-13 https://doi.org/10.30501/jree.2022.355387.1438*.

minimize the effect of heat islands. They recommend several adaptation measures related to urban spatial planning concerning climate change. Galdies & Lau (2020) and Portela et al (2020) investigated the effect of urban and industrial characteristics on the earth's surface temperature. The results showed that high LST values were concentrated in urban and industrial areas with buildings, impermeable pavements, and scattered vegetation. Urban areas with weak vegetation form intense heat islands (Portela et al., 2020). Lemus-Canovas et al. (2019) estimated the hot and cold poles of Barcelona metropolis by calculating the Earth's surface temperature from Landsat 1. The results illustrated that the heat poles were primarily concentrated in industrial and urban areas. Cold poles are found in urban green areas as well as forest areas. The maximum temperature range between land surface covers was observed in spring and summer, while this difference was insignificant in winter. This study showed that the air temperature in green areas reached up to 2.5 degrees Celsius lower than in urban areas (Lemus-Canovas, 2019). Recent studies exploring the city of Tehran demonstrate that the minimum temperatures in Tehran have increased compared to the Varamin station, which indicates the release of more thermal energy in Tehran than that in its suburbs (Akbari, 2000). Studies related to Tehran's thermal island show that the effect of Tehran's thermal island has become more apparent, and along with the growth and development of the metropolis of Tehran, the spatial and temporal characteristics of the thermal island have changed. The spatial structure of the ground surface temperature, the effects of Tehran's thermal island, and the methods of obtaining temperature in hot and polluted areas are of particular importance (Sadeghinia et al., 2013).

According to the findings of (Galdies & Lau, 2020; Guo, 2020; Portela et al., 2020), the influencing factors in the formation of heat islands include the amount of vegetation and changes in the residential context as well as the type of materials, which in this thesis has also been examined firstly by examining the changes in the residential context and the vegetation status of the area with the NDVI index. Galdies & Lau (2020) and Portela et al (2020) Both investigated the thermal island utilizing LST. In this study, LST was also used to investigate the condition of the thermal islands. In this research, in addition to examining the thermal island, an exaggerated digital elevation model map of the first region of Tehran was also prepared and Has been studied. In addition to the studies mentioned above, the correlation between the data has been investigated, and due to the relative nature of the data, Pearson and Spearman tests have been used. Another advantage of this research is the regional survey (past research is generally carried out in the country (Galdies & Lau, 2020) or carried out in the city (Portela et al., 2020)). This study aimed to investigate the state of heat islands and the factors affecting them in District 1 of Tehran using RS technology, Landsat satellite images, and thermal bands from 1984 to 2020 with emphasis on LST, land use, vegetation, and changes in height and geometry shape is done.

2. METHOD

2.1. The location of the study area

Tehran metropolis consists of 22 districts. District 1 is one of the urban areas of Tehran located at the northeastern tip and the northernmost point of Tehran, along the longitudes of 534272.5 east and 5446670.5 west and the latitudes of 3964923.5 north and 3964923.5 south. The district is limited to Alborz Mountains from the north, the Evin region from the west, Parkway and Sadr Highway from the south, and Lavasanat from the east. District 1 of Tehran is a part of Shemiranat city. The district is also known as Shemiran. According to the 2016 census of Iran, the population of this district is 487,508 people (166,881 households) and an area of about 8944/3604 hectares. The location of District 1 and the divisions of the districts are shown in Figure 1.

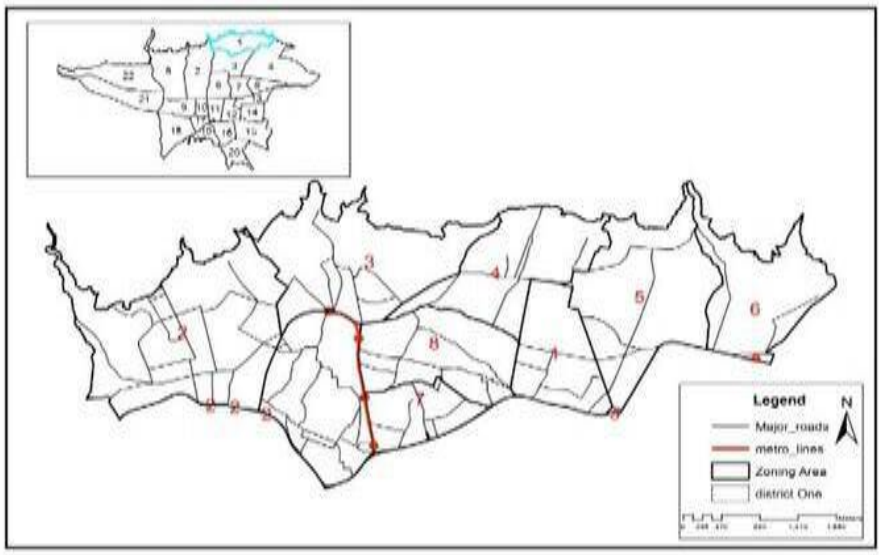

Figure 1. Location of study area

2.2. Methodology

This is a descriptive-analytical and applied study in terms of purpose. This study uses Landsat satellite images for environmental and spatial analyses of District 1. To this end, Landsat satellite images in TM-ETM-OLI sensors for the years 1984, 1994, 2004, 2014, and 2020 are available on the United States Geological Survey (USGS) website and NASA. This study uses thermal RS techniques (including 10 Landsat satellite images) and GIS that have been effectively and efficiently combined to investigate the factors affecting LST and the formation of a heat island in District 1 due to its special

topographic conditions. One of the most important factors is the increase in LST, which, as mentioned, is measured using thermal RS in the summer and winter. Another factor is the study of vegetation in the study area from 1984 to 2020 using the Normalized Difference Vegetation Index (NDVI) and the three-dimensional shape and elevation of the area. Another factor is land use, which refers to the characteristics of homogeneous and repetitive components and features of the land surface, which can be distinguished from other features with a clear boundary. The basis of the land study is the land cover map information that must be extracted from raw RS data and then classified before entering the GIS. The classification of satellite images is the most crucial part of satellite data interpretation. In this study, the images prepared from 1984 to 2020 are analyzed and classified to examine changes in land use in District 1. RS data collected from the land surface by various sensors may be subject to shortcomings and errors. Thus, deficiencies must be compensated and errors eliminated using satellite imagery. ARC GIS 10.8, Envi5.2, and SPSS are used to output, process, and analyze Landsat images.

Table 1. Landsat satellite imagery specifications

Date of taking the image	Satellite	Sensor	PATH	ROW	Thermal band
1984-04-25	LANDSAT_5"	"TM"	164	035	6
1984-11-19	LANDSAT_5"	"TM"	164	035	6
1987-07-07	LANDSAT_5"	"TM"	164	035	6
1987-01-12	LANDSAT_5"	"TM"	164	035	6
1990-07-31	LANDSAT_5"	"TM"	164	035	6
1990-12-22	LANDSAT_5"	"TM"	164	035	6
1992-01-26	LANDSAT_5"	"TM"	164	035	6
1992-08-05	LANDSAT_5"	"TM"	164	035	6
1994-01-15	LANDSAT_5"	"TM"	164	035	6
1994-08-27	LANDSAT_5"	"TM"	164	035	6
1996-08-23	LANDSAT_5"	"TM"	164	035	6
1996-10-10	LANDSAT_5"	"TM"	164	035	6
1998-01-26	LANDSAT_5"	"TM"	164	035	6
1998-08-06	LANDSAT_5"	"TM"	164	035	6
2000-01-16	"LANDSAT_7"	"ETM"	164	035	6
2000-08-11	"LANDSAT_7"	"ETM"	164	035	6
2002-01-13	"LANDSAT_7"	"ETM"	164	035	6
2002-08-09	"LANDSAT_7"	"ETM"	164	035	6
2004-01-19	"LANDSAT_7"	"ETM"	164	035	6
2004-08-14	"LANDSAT_7"	"ETM"	164	035	6
2006-02-25	"LANDSAT_7"	"ETM"	164	035	6
2006-08-04	"LANDSAT_7"	"ETM"	164	035	6
2008-01-14	"LANDSAT_7"	"ETM"	164	035	6
2008-08-09	"LANDSAT_7"	"ETM"	164	035	6
2010-01-03	"LANDSAT_7"	"ETM"	164	035	6
2010-08-15	"LANDSAT_7"	"ETM"	164	035	6
2012-01-25	"LANDSAT_7"	"ETM"	164	035	6
2012-08-04	"LANDSAT_7"	"ETM"	164	035	6
2014-01-14	"LANDSAT_7"	"ETM"	164	035	6
2014-08-10	"LANDSAT_7"	"ETM"	164	035	6
2016-02-03	"LANDSAT_8"	"OLI_TIRS"	164	035	10-11
2016-08-15	"LANDSAT_8"	"OLI_TIRS"	164	035	10-11
2018-01-25	"LANDSAT_8"	"OLI_TIRS"	164	035	10-11
2018-08-05	"LANDSAT_8"	"OLI_TIRS"	164	035	10-11
2020-01-15	"LANDSAT_8"	"OLI_TIRS"	164	035	10-11
2020-08-10	"LANDSAT_8"	"OLI_TIRS"	164	035	10-11

2.3. Land use

One of the factors affecting the increase in temperature in District 1 is land use because this district, like other districts of Tehran, has experienced its fair share of spatial changes in different years, which have significantly increased the city's temperature at different times. Remote sensing, which aims to identify and separate land phenomena and classify them, and Landsat satellite imagery from 1984 to 2020 were used to study these changes. Band composition in Landsat images is one of the methods used to obtain a land-use map before classification. This study uses the 2-3-4 band combination for TM, ETM+, and OLI sensors. In this combination, band 4 is the infrared band, with the vegetation having the highest reflectance. Band compositions for preparing land-use maps for District 1 of Tehran from 1984 to 2020 can be seen in Figure 2. As seen in the figure, the study area is divided into five classes: green space and vegetation in green, urban land use in pink, barren and abandoned lands in white, poor lands or mountains in purple, and roads in black.

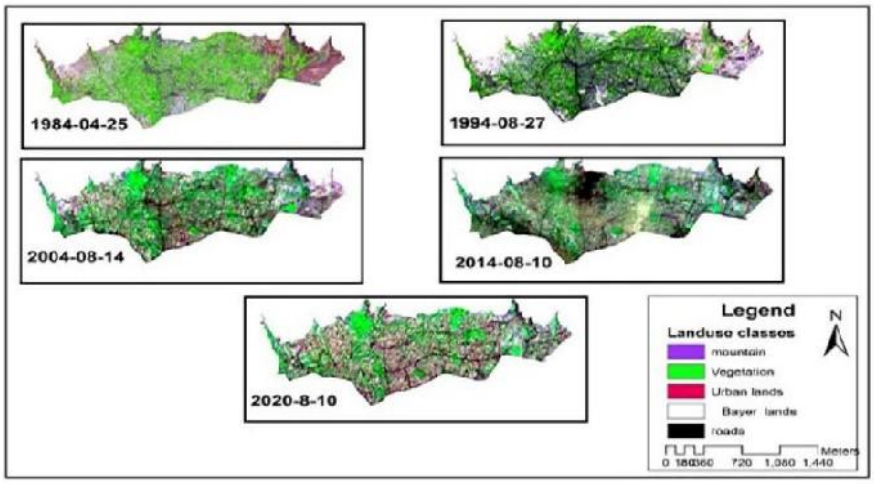

Figure 2. Land-use map

After color composition, also called visual interpretation, digital processing is used to classify the images of the study area so that some areas are first selected as a sample or class, and the classification is performed using the maximum likelihood estimation, which has been mentioned as the most accurate and widely used method of classifying images. After classification, its accuracy, considered a criterion for classification valuation, is checked. The overall accuracy of the classification is calculated using Equation (1) as follows (Makhdoom et al., 2004):

$$\text{Overall accuracy} = \frac{\text{The sum of the pixels that are correctly classified}}{\text{The whole pixels of the image}} \quad \ldots(1)$$

The generated accuracy is a measure of the correct classification of the pixels of a class relative to the same class in the ground truth. It is expressed in Equation (2) (Makhdoom et al., 2004):

$$\text{the accuracy of the producer of class x} = \frac{\text{Total correctly classified pixels of class X}}{\text{The desired pixels in the ground truth}} \quad (2)$$

Besides, user accuracy indicates the probability that a pixel in a classified map belongs to the same class. User accuracy, which is the knowledge of the degree of confidence in the generated map, is calculated via Equation (3) as follows (Makhdoom et al., 2004):

$$\text{Class x user accuracy} = \frac{\text{Total correctly classified pixels of class X}}{\text{Class x pixels on the map}} \quad (3)$$

Finally, the *k* coefficient, which represents the agreement between the classification and the ground truth data, has a range between 0 and 1, in which 1 indicates the complete agreement between the classified map and the ground truth data (Makhdoom et al., 2004). The *k* coefficient is calculated via Equation (4):

$$k = \frac{\theta 2 - \theta 1}{\theta 2 - 1} \quad (4)$$

where θ1 is the overall accuracy and θ2 is the contingent agreement, which is calculated as follows (Makhdoom et al., 2004):

$$\theta 2 = \blacksquare \quad Xi + \blacksquare \quad x + \frac{i}{N} \quad (5)$$

There are several models and methods for classification using RS. This study uses the maximum likelihood estimation due to its high classification accuracy and reliability.

2.4. Land Surface Temperature (LST)

One of the most critical factors affecting the increase in temperature of District 1 is LST, which is obtained by the thermal bands of Landsat satellites in TM, ETM+, and OLI sensors. The pixels of the images must first be processed to obtain correct information to prepare a thermal map of the city. All of these are called image pre-processing or image correction. One of the most critical corrections applied to image pixels is radiometric. One part of radiometric corrections of images is spectral correction performed on Digital Numbers (DNs) or the pixel so that when the image is taken, it has DNs. These DNs contain information about land surface phenomena. However, the initial data contains basic information (uncorrected) and cannot represent the land surface parameters such as temperature, humidity, vegetation, etc. The DNs of the satellite imagery must be corrected to apply the values of the ground surface parameters to the desired satellite imagery. The DNs of each image must be converted into radiance and reflectance. This form of correction is referred to as spectral correction. Several models and methods for converting the DNS of satellite images into radiance and reflectance are referred to below. Equation (6) converts raw image values into radiance for Landsat TM and ETM images (Chander et al., 2009).

$$L\lambda = \left(\frac{\text{LMAX}-\text{LMIN}}{\text{Qcalmax}-\text{Qcalmin}}\right)(\text{Qcal} - \text{Qcalmin}) + \text{LMIN} \quad (6)$$

where Lλ is the spectral radiance in the sensor, Qcal is the pixel value (DN) in the desired band, Qcalmin is the minimum pixel value (DN), Qcalmax is the maximum pixel value (DN), and LMIN and LMAX are minimum and maximum spectral radiances in the sensor. This file is available and can be downloaded in the metadata file of every satellite image. Moreover, the reflectance coefficient for the Landsat TM5.ETM7 sensor is calculated based on Equation (7) (Chander et al., 2009):

$$p\lambda = \frac{\pi \times L\lambda \times d^2}{\text{ESUN}\,\lambda \times COS\,\theta S}) \quad (7)$$

where pλ is the reflectance coefficient, π = 3.1459, Lλ is the spectral radiance in the sensor, d is the distance between the

earth and the sun (astronomical unit), ESUN is the average of the sun's rays, and θ is the angle of the sun's rays (degrees).

Equation (8) is used to obtain the spectral radiance in the OLI sensor (Chander et al., 2009):

$$L\lambda = ML * Qcal + AL \quad (8)$$

where Lλ is the radiance above the atmosphere (watts/m^2*srad*μm), ML is the multiplicative conversion factor, Qcal is the pixel values (DNs) 10 and 11, and AL is the aggregate conversion factor.

2.5. Obtain the brightness temperature

Thermal band data can be converted from spectral radiance in the sensor into brightness temperature, assuming that the earth is a black body and includes the effects of the atmosphere (absorption and radiance). The brightness temperature for Landsat satellite sensors is calculated from Equation (9) (Rajeshwari & Mani, 2014).

$$T = \frac{K2}{Ln(\frac{K1}{L\lambda}+1)} \quad (9)$$

where T is the temperature affecting the brightness in the sensor in Kelvin; L is the spectral radiance of the meter in terms of ($Wm^{-2}sr^{-1}um^{-1}$). The values of K1 and K2 are the first and second calibration constants (Wm^{-2}), respectively, and the coefficients of K1 and K2 are calculated in Table (2).

Table 2. Coefficients K1 and K2 for Landsat satellite

Sensor coefficient (band)	Calibration coefficient (K1)	Calibration coefficient (K2)
L5-TM B6	607.76	1260.56
L7-ETM+B6	666.09	1282.71
L8-OLI B10	777.89	1321.08
L8-OLI B11	480.89	1201.14

2.6. Vegetation

One of the other factors affecting the temperature increase in District 1 is its vegetation density, which is obtained using Landsat satellite images and NDVI. NDVI is calculated based on Equation (10) (VAN de Griend & Owe,1993):

$$NDVI = \frac{NIR-RED}{NIR+RED} \quad (10)$$

where NIR is the reflectance in the infrared band, and RED is the reflectance in the red band. Although the value of this index is in the range of -1 and 1 theoretically, in practice, it is less than (1) and more than -1. The values of this index for dense vegetation tend to be 1, but negative values characterize clouds, snow, and water, and rocks and barren soils with similar spectral reactions used in the two bands are seen with values close to zero. In this index, typical soil is considered equal to 1. The higher the pixel distance from the soil size, the denser the vegetation. In this regard, NDVI is applied to Landsat images. The vegetation map of District 1 of Tehran has been complied and prepared from 1984 to 2020 in five classes: very light red, relatively light orange, medium-density yellow, relatively high light green, and very high-density dark green.

2.7. Changes in elevation

Another factor affecting climate, environmental, and thermal changes in District 1 is the changes in elevation and geometric and three-dimensional shape of this district so that most of the areas and neighborhoods of the district are located at high altitudes (for example, Punak, Islamic Azad University, Science and Research Branch, Hesarak, etc.). As shown in Figure 3 (digital elevation model map of District 1 with an accuracy of 5 m), most areas and neighborhoods of this district are located at altitudes between 1400 and 1835.

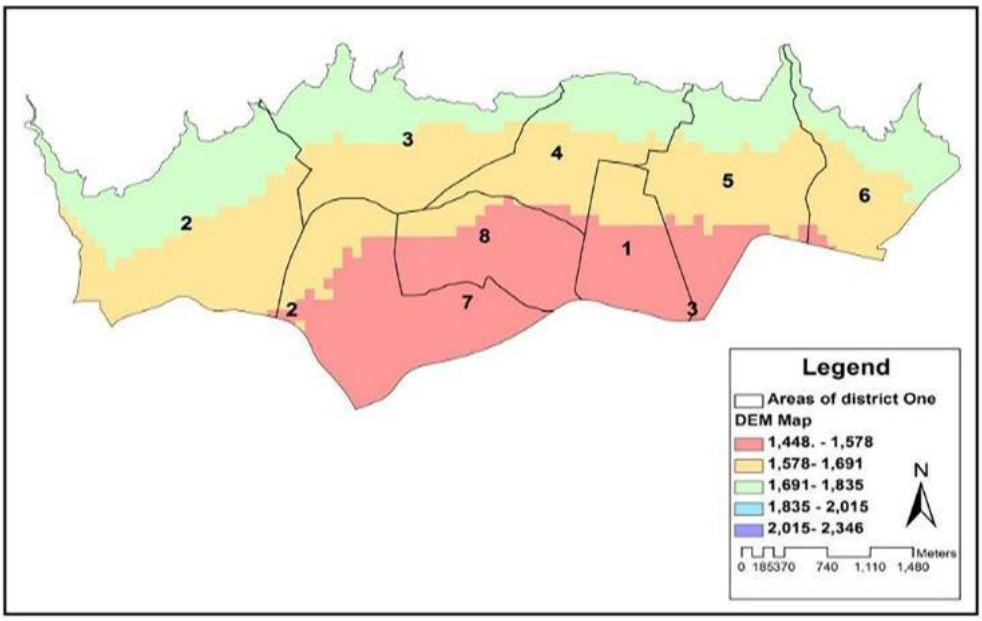

Figure 3. Digital elevation model map

Figure (4) is slightly exaggerated and shows the mountains, poor terrain, and high altitudes of most of the neighborhoods and residential areas of District 1 of Tehran. These areas are located like a hole around these mountains. Like a barrier, these mountains and poor terrain prevent winds and cyclones from entering the district and, consequently, increase the temperature in the district.

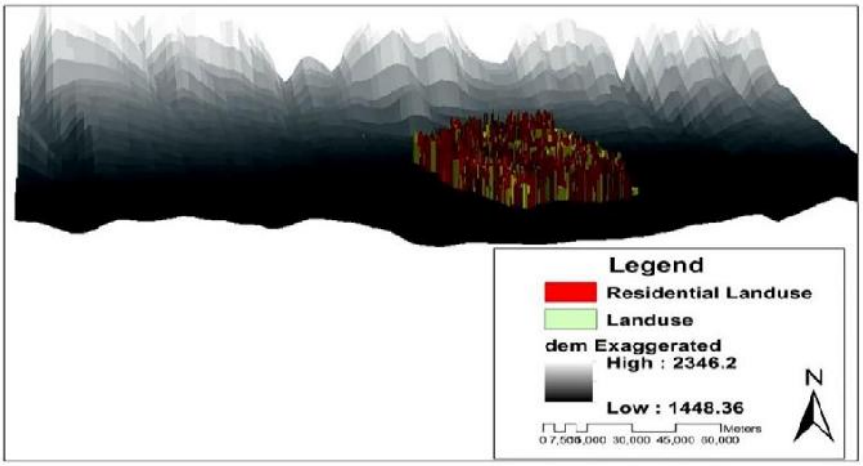

Figure 4. Exaggerated map of digital elevation model

2.8. The correlation between LST and weather stations

Data in the studied years were received from reputable centers (Table 3), and the correlation between the surface temperature of stations and Landsat images was obtained using SPSS software and the linear regression method to examine the correlation between satellite images and weather stations.

Table 3. Weather stations in Tehran

Year	Tehran station	Shemiran station	Chitgar station	Geophysics station
1984-04-25	17.7	13.7	15.4	3.5
1984-11-19	11.4	9.4	11.6	12.3
1994-08-27	31.2	28.9	33.1	31.5
1994-01-15	-6	4.1	6.7	5.7
2004-08-14	31.4	27.9	31.9	31.1
2014-01-14	5.3	3.7	7.3	5.5
2020-08-20	36.9	36.5	38.3	35.6
2020-01-15	8.2	7.6	9.2	6.6

The linear regression model assumes a linear relationship (or a straight line) between the dependent variable and each predictor, as described in Equation (11).

$$yi = b0 + b1xi1 + ... + bpxip + ei \quad (11)$$

where:
y_i is the value of item i of the quantitative dependent variable.
p is the number of predictors.
b_j is the value of coefficient j, j = 0, …, p
X_{ij} is the value of item i of predictor j.
e_i is the error in the observed value for item i.

The model is linear because increasing the predictor j by 1 unit increases the dependent value of the units bi. It should be noted that b0 is the intercept. b0 will be the value of the dependent variable predictor model when the value of each predictor is zero. The initial condition for linear regression is the normal distribution of data. Therefore, the normal distribution of data is first checked using the Smirnov test (Tables 4 and 5).

Table 4. Smirnov test to check the normal distribution of data for satellite images

One-sample Kolmogorov-Smirnov test		Blue class	Green class	Yellow class	Orange class
N		10	10	10	10
Normal parameters [a,b]	Mean	4.050	8.250	12.850	1486080.0000
	Std. deviation	19.0299	19.1184	20.3880	1840520.55245
Most extreme differences	Absolute	.173	.164	.182	.186
	Positive	.173	.164	.167	.140
	Negative	-.171	-.155	-.182	-.186
Test statistic		.173	.164	.182	.186
Asymp. Sig. (2-tailed) test distribution is normal.		.200 [c,d]	.200 [c,d]	.200 [c,d]	.200 [c,d]

a: Test distribution is normal.
b: Calculated from data.
c: Liliefors Significance Correction.
d: This is a lower bound of the true significance.

Table 5. Smirnov test to check the normality of data distribution for weather stations

One-sample Kolmogorov-Smirnov test		Tehran station	Shemiran station	Chitgar station	Geophysics station
N		10	10	10	10
Normal parameters [a,b]	Mean	17.40	16.49	19.18	16.73
	Std. deviation	14.535	12.688	13.124	13.429
Most extreme differences	Absolute	.229	.216	.234	.275
	Positive	.160	.212	.218	.275
	Negative	-.229	-.216	-.234	-.237
Test statistic		.229	.216	.234	.275
Asymp. Sig. (2-tailed) test distribution is normal.		.147[c]	.200 [c,d]	.129 [c]	.031 [c]

a: Test distribution is normal.
b: Calculated from data.
c: Liliefors Significance Correction.
d: This is a lower bound of the true significance.

According to the above tables, the data are distributed normally. The correlation between the data is then examined. Pearson and Spearman's tests are used because the data are relative (Tables 6 and 7).

Table 6. Pearson test for satellite images and weather stations

Pearson correlation		Blue class	Green class	Yellow class	Orange class	Red class	Tehran station	Shemiran station	Chitgar station	Geophysics station
Blue class		1	.990**	.983**	.968**	.958**	.832**	.871**	.885**	.787**
	Sig. (2-tailed)		.000	.000	.000	.000	.003	.001	.001	.007
	N	10	10	10	10	10	10	10	10	10
Green class	Pearson correlation	.990**	1	.994**	.986**	.976**	.852**	.881**	.896**	.815**
	Sig. (2-tailed)	.000		.000	.000	.000	.002	.001	.000	.004
	N	10	10	10	10	10	10	10	10	10
Yellow class	Pearson correlation	.983**	.994**	1	.997**	.985**	.846**	.856**	.870**	.766**
	Sig. (2-tailed)	.000	.000		.000	.000	.002	.002	.001	.010
	N	10	10	10	10	10	10	10	10	10
Orange class	Pearson correlation	.968**	.986**	.997**	1	.989**	.846**	.845**	.857**	.751*
	Sig. (2-tailed)	.000	.000	.000		.000	.002	.002	.002	.012
	N	10	10	10	10	10	10	10	10	10
Red class	Pearson correlation	.958**	.976**	.985**	.989**	1	.877**	.876**	.886**	.779**
	Sig. (2-tailed)	.000	.000	.000	.000		.001	.001	.001	.008
	N	10	10	10	10	10	10	10	10	10
Tehran station	Pearson correlation	.832**	.852**	.846**	.846**	.877**	1	.965**	.962**	.906**
	Sig. (2-tailed)	.003	.002	.002	.002	.001		.000	.000	.000
	N	10	10	10	10	10	10	10	10	10
Shemiran station	Pearson correlation	.871**	.881**	.856**	.845**	.876**	.965**	1	.997**	.956**
	Sig. (2-tailed)	.001	.001	.002	.002	.001	.000		.000	.000
	N	10	10	10	10	10	10	10	10	10
Chitgar station	Pearson correlation	.885**	.896**	.870**	.857**	.886**	.962**	.997**	1	.965**
	Sig. (2-tailed)	.001	.000	.001	.002	.001	.000	.000		.000
	N	10	10	10	10	10	10	10	10	10
Geophysics station	Pearson correlation	.787**	.815**	.766**	.751*	.779**	.906**	.956**	.965**	1
	Sig. (2-tailed)	.007	.004	.010	.012	.008	.000	.000	.000	
	N	10	10	10	10	10	10	10	10	10

*. Correlation is significant at a level of 0.05 (2-tailed). / **. Correlation is significant at a level of 0.01 (2-tailed).

Table 7. Spearman test for satellite images and weather stations

Spearman's rho correlations			Blue class	Green class	Yellow class	Orange class	Red class	Tehran station	Shemiran station	Chitgar station	Geophysics station
Spearman's rho	Blue class	Correlation coefficient	1.000	.982**	.976**	.960**	.973**	.693*	.689*	.796**	.565
		Sig. (2-tailed)	.	.000	.000	.000	.000	.026	.028	.006	.089
		N	10	10	10	10	10	10	10	10	10
	Green class	Correlation coefficient	.982**	1.000	.994**	.988**	.997**	.705*	.686*	.772**	.571
		Sig. (2-tailed)	.000	.	.000	.000	.000	.023	.029	.009	.084
		N	10	10	10	10	10	10	10	10	10
	Yellow class	Correlation coefficient	.976**	.994**	1.000	.997**	.997**	.705*	.677*	.772**	.541
		Sig. (2-tailed)	.000	.000	.	.000	.000	.023	.032	.009	.106
		N	10	10	10	10	10	10	10	10	10
	Orange class	Correlation coefficient	.960**	.988**	.997**	1.000	.994**	.720*	.679*	.768**	.537
		Sig. (2-tailed)	.000	.000	.000	.	.000	.019	.031	.009	.110
		N	10	10	10	10	10	10	10	10	10
	Red class	Correlation coefficient	.973**	.997**	.997**	.994**	1.000	.721*	.693*	.782**	.576
		Sig. (2-tailed)	.000	.000	.000	.000	.	.019	.026	.008	.082
		N	10	10	10	10	10	10	10	10	10
	Tehran station	Correlation coefficient	.693*	.705*	.705*	.720*	.721*	1.000	.967**	.927**	.733*
		Sig. (2-tailed)	.026	.023	.023	.019	.019	.	.000	.000	.016
		N	10	10	10	10	10	10	10	10	10
	Shemiran station	Correlation coefficient	.689*	.686*	.677*	.679*	.693*	.967**	1.000	.948**	.778**
		Sig. (2-tailed)	.028	.029	.032	.031	.026	.000	.	.000	.008
		N	10	10	10	10	10	10	10	10	10
	Chitgar station	Correlation coefficient	.796**	.772**	.772**	.768**	.782**	.927**	.948**	1.000	.770**
		Sig. (2-tailed)	.006	.009	.009	.009	.008	.000	.000	.	.009
		N	10	10	10	10	10	10	10	10	10
	Geophysics station	Correlation coefficient	.565	.571	.541	.537	.576	.733*	.778**	.770**	1.000
		Sig. (2-tailed)	.089	.084	.106	.110	.082	.016	.008	.009	.
		N	10	10	10	10	10	10	10	10	10

*. Correlation is significant at a level of 0.05 (2-tailed).

**. Correlation is significant at a level of 0.01 (2-tailed).

Since the significant coefficients of the Pearson and Spearman models are less than the confidence level of 0.05, it can be argued that there is a significant relationship between the data of weather stations in Tehran and Landsat satellite images. Thus, the linear regression model can be used between them, as described in Equation (11).

3. RESULTS AND DISCUSSION

One of the most critical factors affecting the increase in temperature in District 1 of Tehran is LST. This study prepared a thermal zoning map using Landsat thermal images in ETM and TM sensors in Band (6) and Oli sensors in Bands (10) and (11) in the winter and summer from 1984 to 2020 (Figure 5). The study area was then classified into five classes: blue, green, yellow, orange, and red, each class containing the corresponding temperature in degrees Celsius (Table 8). According to Figure 5 and Table 8, the trend of temperature is ascending in District 1 in both summer and winter, indicating climate change, rising LST in District 1, and the formation of a heat island in the district.

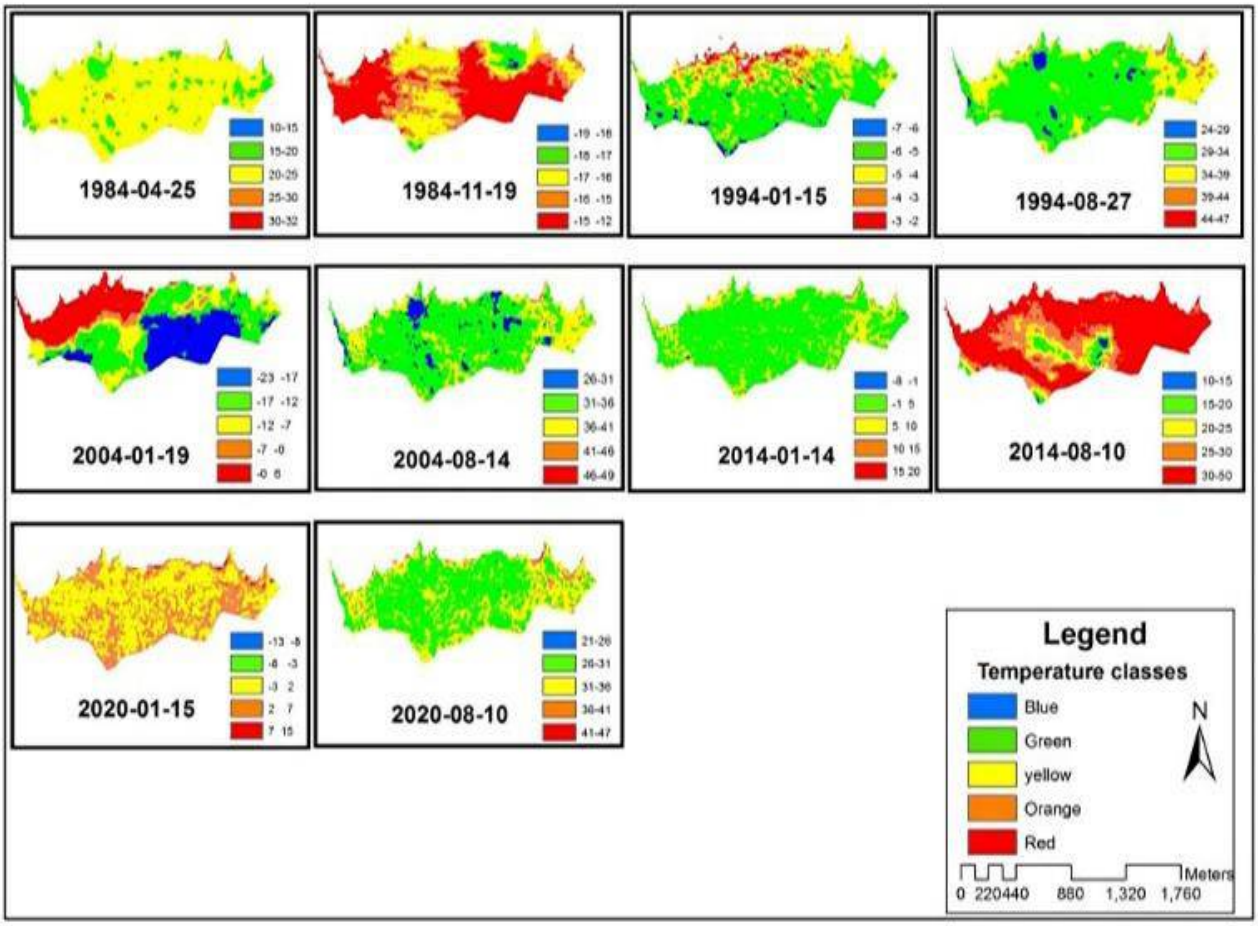

Figure 5. LST map

Table 8. LST classification using Landsat thermal images

Year	Classes				
	Blue	**Green**	**Yellow**	**Orange**	**Red**
1984_04_25	10_15	15_20	20_25	25_30	30_35
1984_11_19	-18_-19	-17_-18	-16_-17	-15_-16	-15_-12
1994_08_27	24_29	29_34	34_39	39_44	44_47
1994_01_15	-6_-7	-6_-5	-5_-4	-4_-3	-3_-2
2004_08_14	26_31	31_36	36_41	41_46	46_49
2004_01_19	-23_-17	-17_-12	-12_-7	-7_0	0_6
2014_08_10	10_15	15_20	20_25	25_30	30_50
2014_01_14	-8_-1	-1_5	5_10	10_15	15_20
2020_08_10	21_26	26_31	31_36	36_41	41_47
2020_01_15	-13_-8	-8_-3	-3_2	2_7	7-15

According to Table 8, the trend of temperature increases in District 1 has been increasing in both summer and winter; thus, the blue class in the summer (1984) was between 10 and 15 °C and changed to 21 to 26 °C in 2020. Moreover, the red class with the highest density had a temperature between 30 and 32 °C in 1984, which reached 50 °C in 2014 and 47 °C in 2020. It rose from -18 °C in winter to 15 °C in 2020.

Land use is another factor that affects LST changes in District 1 of Tehran. Land-use change map of District 1 of Tehran was prepared using Landsat satellite imagery, supervised classification, and maximum likelihood estimation from 1984 to 2020 in five classes: vegetation, urban land use, barren lands, poor lands, and mountains and roads (Figure 6).

Following the preparation of the land-use change map, the area percentage for each land-use class and the accuracy of classes with ground truth data (k) were obtained (Table 9).

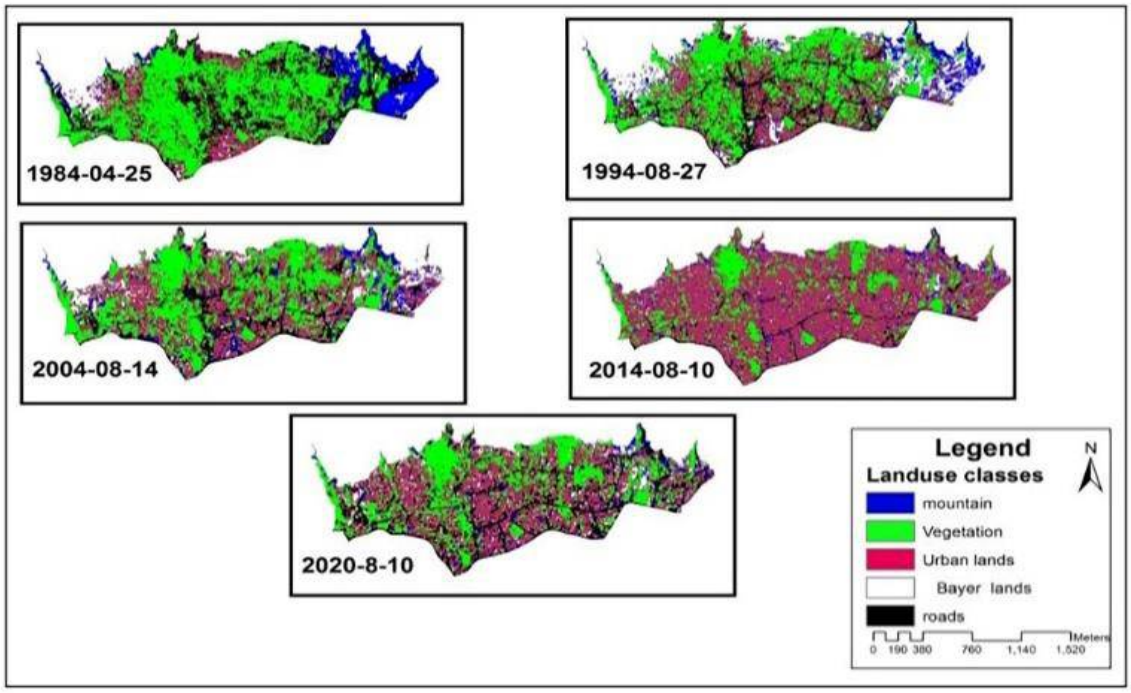

Figure 6. Land-use classification map

Table 9. The percentage of the area of each land-use class using Landsat images

Year	Land use area (%)					k coefficient (%)
	Vegetation	Urban	Barren lands	Mountains	Roads	
1984	32.597	16.795	24.039	18.594	7.976	96
1994	26.502	26.038	15.978	18.628	12.855	97
2004	26.015	32.834	11.679	15.754	13.718	97
2014	14.155	35.745	12.497	19.271	18.331	97
2020	22.065	35.949	9.909	12.820	19.257	97

According to Figure 6 and Table 9, vegetation cover was reduced from 32 % in 1984 to 26.5, 26, and 14 in 1994, 2004, and 2014, respectively, which recorded a downward trend, but increased to 22 % in 2020. Simply put, the overall trend from 1984 to 2020 was descending. Residential areas occupied 16 % of the city in 1984. After this time period, the mentioned trend took an ascending direction and reached 35 % in 2020. Moreover, barren lands decreased from 24 % to 9.9 %. According to the results of Figure 6 and Table 9, the number of mountains decreased from 18 % to 12 % and on the contrary, the number of paths in Region 1 increased from 7.9 % to 19 %.

The land use in the case study changed significantly from 1984 to 2020 and the urban field grew from 16 % in 1984 to 35 % in 2020 while vegetation cover was attenuated from 32 % in 1984 to 22 % in 2020. Barren lands decreased from 24 % in 1984 to 9 % and roads increased sharply from 7 % to 19 % in 2020. The trend of land use in our case study from the year 1984 to 2020 is accessible in Figure 7.

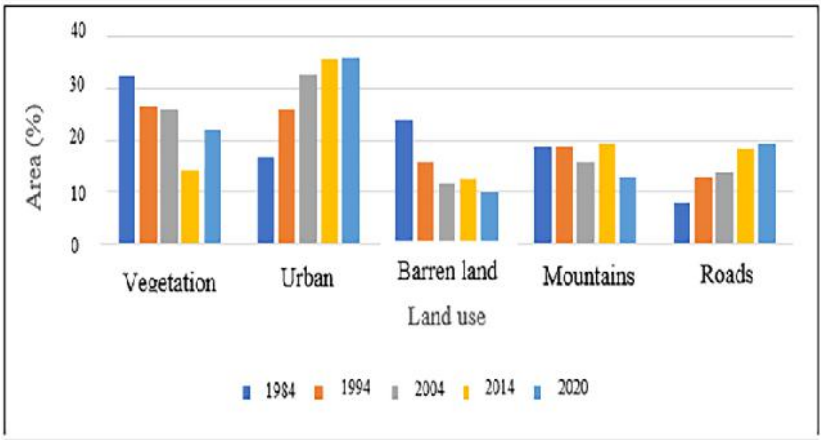

Figure 7. The trend of land-use change

Vegetation cover trends in District 1 was investigated using NDVI. This index was prepared for Landsat images in 1984, 1994, 2004, 2014, and 2020. In this map, the red dots indicate the areas devoid of vegetation, while the green dots indicate those with vegetation. However, the comparison of NDVI maps indicates the declining trend for vegetation cover over the past 38 years (Figure 8).

The results of the fitted linear regression model between weather station data and satellite images showed a significant correlation between them; therefore, the significance coefficient (Sig) of all stations was less than the confidence level of 0.05. The coefficient of variation (R) for all the stations had the desired value above 0.80. The regression analysis results indicate that the red and green classes had the highest correlation among other LST classes of satellite images (Table 10).

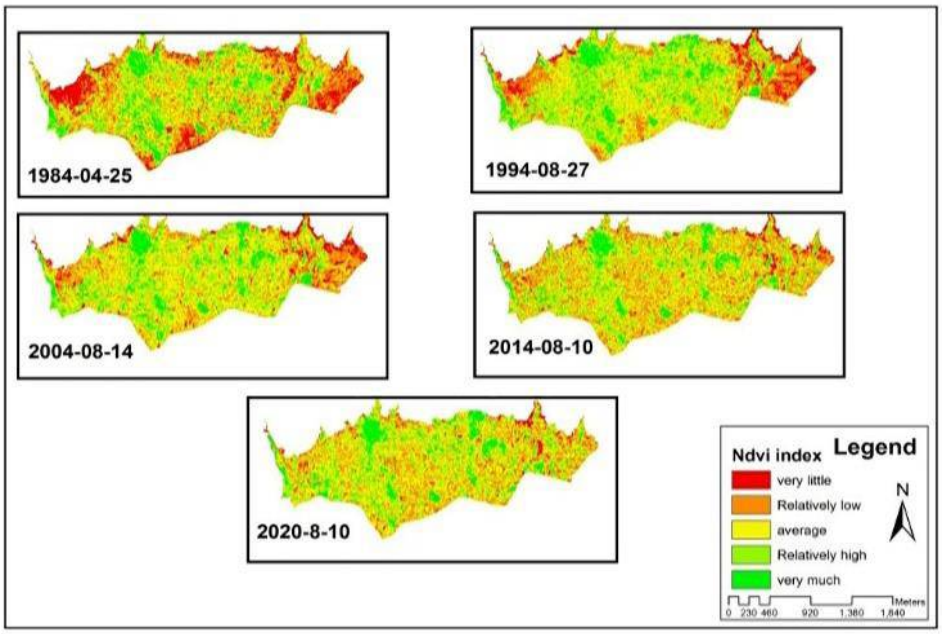

Figure 8. NDVI map

Table 10. Linear regression between satellite images and weather stations

Weather station	Class correlation	R	R^2	Durbin–Watson statistic	Sig	Regression model	Standardized beta coefficient	Non-standardized beta coefficient	The predicted SD
Tehran	Red	0.877	0.769	2.618	0.001	Forward	0.877	0.553	7.410
Shemiran	Green	0.881	0.776	2.988	0.001	Forward	0.881	0.584	6.374
Chitgar	Green	0.896	0.803	2.948	0.000	Forward	0.896	0.615	6.174
Geophysics	Green	0.815	0.664	2.185	0.004	Forward	0.815	0.572	8.261
	Yellow	0.904	0.817	2.185	0.003	Forward	0.904	0.623	6.507

4. CONCLUSIONS

According to the referenced findings (Galdies & Lau, 2020; Guo et al., 2020; Portela et al., 2020), the influencing factors in the formation of heat islands include the extent of vegetation cover, changes to the residential context, and the type of materials. The current study managed to investigate the changes to the residential context and the vegetation status of the area based on NDVI index. Galdies & Lau (2020) and Portela et al (2020) both investigated the thermal island utilizing LST. In this study, LST was also used to investigate the condition of thermal islands. In the present research, in addition to examining the thermal island, an exaggerated digital elevation model map of District 1 of Tehran was prepared and studied. In addition to the studies mentioned above, the correlation between the data was investigated, and due to the relative nature of the data, Pearson and Spearman tests were employed. This research made use of the regional survey to its advantage (past research is generally carried out in the country (Galdies & Lau, 2020) or carried out in the city (Portela et al., 2020). This study aimed to investigate the state of heat islands and the factors affecting them in District 1 of Tehran using RS technology, Landsat satellite images, and thermal bands from 1984 to 2020 with emphasis on LST, land use, vegetation, and changes in height and geometry shape is done. This research is seen as necessary for future planning.

The results indicate that the trend of temperature increased in District 1 from the year 1984 to 2020 in both summer and winter. Thus, the blue class in the summer of 1984 ranged between 10 and 15 °C and changed to 21 to 26 °C in 2020. Moreover, the red class with the highest density had a temperature between 30 and 32 °C in 1984, which reached 50 °C in 2014 and 47 °C in 2020. Land use in District 1 changed significantly over this period, with urban land use increasing

from 16 % (in 1984) to 35 % (in 2020) and vegetation declining from 32 % to 14 %. Vegetation analysis using NDVI showed a decreasing vegetation trend in the studied years. A significant correlation was seen between satellite images and the data collected from weather stations such as Tehran, Shemiran, Chitgar, and Geophysics stations to validate the study using the fitted linear regression model. The results of linear regression analysis demonstrated a significant correlation between satellite images and weather station data; therefore, the significance coefficient (Sig) in the case of all the stations was less than 0.05 with a 95 % confidence interval. Besides, the coefficient of variation (R) for all the stations was above 80 %. The regression analysis results show that the red and green classes had the highest correlation among other LST classes of satellite images. Another factor affecting temperature changes in District 1 of Tehran included the elevation and geometric and three-dimensional shape of this district such that most of the areas and neighborhoods of the district were located at high altitudes between 1400 and 1835. These high altitudes hinder the positive course of natural rainfall and other climatic factors which, in turn, increase the district's temperature compared to other districts over time. The findings illustrate that rising temperatures in District 1 of Tehran show no signs of putting on the brake any time soon. Unfortunately, land-use changes such as declining vegetation and increasing urban land use exacerbate this trend. In addition, population growth and the declining vegetation cover and rising number of buildings lead to the overheating of impermeable surfaces and excess heat penetrating the environment. Population growth and land-use change cause much vegetation to disappear, only to be replaced by buildings, roads, and other urban facilities. Reducing vegetation and turning it into high-rise buildings increase the temperature of the city. It must be emphasized that vegetation is one of the main factors in respiration, absorption of urban pollutants, and good biodiversity and prevents the rise of temperature in cities. In the end, we recommend further investigation into the effect of humidity on the thermal islands of the region as well as the type of materials and their relationship with these islands.

5. ACKNOWLEDGEMENT

The authors are very grateful for the valuable comments and suggestions of the reviewers and the journal editor, which improved the quality of this article.

REFERENCES

1. Ahmed, S. (2018). Assessment of urban heat islands and impact of climate change on socioeconomic over Suez Governorate using remote sensing and GIS techniques. *The Egyptian Journal of Remote Sensing and Space Sciences*, *21*(1), 15-25. https://doi.org/10.1016/j.ejrs.2017.08.001

2. Akbari, H. (2000). Consideration of temperature distribution pattern of Tehran using Landsat TM thermal data. [MA dissertation, Tarbiat Modarres University]. https://ganj.irandoc.ac.ir. (In Persian).

3. Al-Hatab, M., Amany, S., & Lamia, T. (2018). Monitoring and assessment of urban heat islands over the Southern region of Cairo Governorate, Egypt. *The Egyptian Journal of Remote Sensing and Space Sciences*, *21*(3), 311-323. https://doi.org/10.1016/j.ejrs.2017.08.008

4. Chander, G., Markham, B., & Helder, D. (2009). Summary of current radiometric calibration coefficients for Landsat MSS, TM, ETM+, and EO-1 ALI sensors. *Remote Sensing of Environment*, *113*. https://doi.org/10.1016/j.rse.2009.01.007

5. El-Hadidy, Sh.M. (2021). The relationship between urban heat islands and geological hazards in Mokattam plateau, Cairo, Egypt. *The Egyptian Journal of Remote Sensing and Space Sciences*, *24*. https://doi.org/10.1016/j.ejrs.2021.02.004

6. Galdies, C., & Lau, H.S. (2020). Urban heat island effect, extreme temperatures and climate change: A case study of Hong Kong SAR. *Climate Change, Hazards and Adaptation Options*. https://link.springer.com/chapter/10.1007/978-3-030-37425-9_20

7. Guo, A., Yang, J., Xiao, X., Xia, J., Jin, C., & Li, X. (2019). Influences of urban spatial form on urban heat island effects at the community level in China. *Sustainable Cities and Society*, *53*. https://doi.org/10.1016/j.scs.2019.101972

8. Harun, Z., Reda, E., Abdulrazzaq, A., Amer Abbas, A., Yusup, Y., & Zaki Sh.A. (2020). Urban heat island in the modern tropical Kuala Lumpur: Comparative weight of the different parameters. *Alexandria Engineering Journal*, *59*. https://doi.org/10.1016/j.aej.2020.07.053

9. Kabano, P., Lindley, S., & Harris, A. (2020). Evidence of urban heat island impacts on the vegetation growing season length in a tropical city. *Landscape and Urban Planning*, *206*. https://doi.org/10.1016/j.landurbplan.2020.103989

10. Koopmans, S., Heusinkveld, B.G., & Steeneveld, G.J. (2020). A standardized physical equivalent temperature urban heat map at 1-m spatial resolution to facilitate climate stress tests in the Netherlands. *Building and Environment*, *181*. https://doi.org/10.1016/j.buildenv.2020.106984

11. Lemus-Canovas, M., Martin-Vide, J., Moreno-Garcia, M.C., & Lopez-Bustins, J.A. (2019). Estimating Barcelona's metropolitan daytime hot and cold poles using Landsat-8 Land Surface Temperature. *Science of the Total Environment*, *699*. https://doi.org/10.1016/j.scitotenv.2019.134307

12. Li, H., Zhou, Y., Jia, G., Zhao, K., & Dong, J. (2021). Quantifying the response of surface urban heat island to urbanization using the annual temperature cycle model. *Geoscience Frontiers*, *13*. https://doi.org/10.1016/j.gsf.2021.101141

13. Lia, L., Zha, Y., & Zhang, J. (2020). Spatially non-stationary effect of underlying driving factors on surface urban heat islands in global major cities. *International Journal of Applied Earth Observation and Geoinformation*, *90*. https://doi.org/10.1016/j.jag.2020.102131

14. Liu, Ch., Yang, M., Hou, Y., Zhao, Y., & Xue, X. (2021). Spatiotemporal evolution of island ecological quality under different urban densities: A comparative analysis of Xiamen and Kinmen Islands, Southeast China. *Ecological Indicators*, *124*. https://doi.org/10.1016/j.ecolind.2021.107438

15. Makhdoom, M., Darwish Sefat, A., Jafarzadeh, H., & Makhdoom, A. (2004). *Environmental assessment and planning with geographic information systems "GIS"*. University of Tehran, Publishing and Printing Institute. https://www.gisoom.com/book/1826711/. (In Persian).

16. Macintyre, H.L., Heaviside, C., Cai, X., & Phalkey, R. (2021). The winter urban heat island: Impacts on cold-related mortality in a highly urbanized European region for present and future climate. *Environment International*, *154*. https://doi.org/10.1016/j.envint.2021.106530

17. Mendez-Astudillo, J., Lau, L., Tang, Y., & Moore, T. (2020). A new Global Navigation Satellite System (GNSS) based method for urban heat island intensity monitoring. *International Journal of Applied Earth Observations and Geoinformation*, *94*. https://doi.org/10.1016/j.jag.2020.102222

18. Portela, C.I., Massi, K.G., Rodrigues, T., & Alcântara, E. (2020). Impact of urban and industrial features on land surface temperature: Evidences from satellite thermal indices. *Sustainable Cities and Society*, *56*. https://doi.org/10.1016/j.scs.2020.102100

19. Rajeshwari, A., & Mani, N.D. (2014). Estimation of land surface temperature of Dindigul district using Landsat 8 data. *International Journal of Research in Engineering and Technology*, *3*. https://ijret.org/volumes/2014v03/i05/IJRET20140305025.pdf

20. Sadeghinia, A., Alijani, B., Ziaeian, P., & Khaledi, S. (2013). Application of spatial autocorrelation techniques in the analysis of the thermal island of Tehran. *Applied Research in Geographical Sciences*, *30*. https://www.sid.ir/en/Journal/ViewPaper.aspx?ID=354812. (In Persian).

21. Sekertekin, A., & Zadbagher, E. (2021). Simulation of future land surface temperature distribution and evaluating surface urban heat island based on impervious surface area. *Ecological Indicators*, *122*. https://doi.org/10.1016/j.ecolind.2020.107230

22. Tepanosyan, G., Muradyan, V., Hovsepyan, A., Pinigin, G., Medvedev, A., & Shushanik Asmaryan, Sh. (2020). Studying spatial-temporal changes and relationship of land cover and surface urban heat island derived through remote sensing in Yerevan. *Armenia Building and Environment*, *187*. https://doi.org/10.1016/j.buildenv.2020.107390

23. United Nations Department of Economic and Social Affairs. (2019). *World Urbanization Prospects: The 2018 Revision*, ISBN (PDF): 9789210043144. https://doi.org/10.18356/b9e995fe-en

24. VAN DE GRIEND, A.A., & OWE, M. (1993). On the relationship between thermal emissivity and the normalized difference vegetation index for natural surfaces. *International Journal of Remote Sensing*, *14*, 1119-1131. https://doi.org/10.1080/01431169308904400

25. Vasenev, V., Varentsova, M., Konstantinov, P., Romzaykina, O., Kanareykina, I., Dvornikov, V., & Manukyana, Y. (2021). Projecting urban heat island effect on the spatial-temporal variation of microbial respiration in urban soils of Moscow megalopolis. *Science of the Total Environment*, *786*. https://doi.org/10.1016/j.scitotenv.2021.147457

26. Wang, Y., Yi, G., Zhou, X., Zhang, T., Bie, X., Li, J., & Ji, B. (2021). Spatial distribution and influencing factors on urban land surface temperature of twelve megacities in China from 2000 to 2017. *Ecological Indicators*, *125*. https://doi.org/10.1016/j.ecolind.2021.107533

JREE: Vol. 10, No. 4, (Autumn 2023) 14-21

Journal of Renewable Energy and Environment

Journal Homepage: www.jree.ir

Materials and Energy Research Center

MERC

Research Article

Thermal Characterization of Eicosane/Graphite Nano-Composite-Based Phase Change Material

Ala Moradi [a], Hajar Es-haghi [b], Seyed Hasan Hashemabadi [a*], Majid Haghgoo [b], Zahra Emami [c]

[a] *Computational Fluid Dynamics (CFD) Research Laboratory, School of Chemical, Petroleum and Gas Engineering, Iran University of Science and Technology (IUST), Tehran, Iran.*
[b] *Iran Space Institute, P. O. Box: 13455/754, Tehran, Iran.*
[c] *Department of Material Science and Engineering, Sharif University of Technology, P. O. Box: 14588 89694, Tehran, Iran.*

P A P E R I N F O

Paper History:
Received: 19 September 2022
Revised: 21 December 2022
Accepted: 30 December 2022

Keywords:
Thermal Conductivity,
Phase Change Materials,
Graphite Nanoparticles,
Morphological Characterization

Phase Change Materials (PCMs) have received much consideration as thermal energy storage systems due to their high storage capacity. However, their heat transfer rate is limited because of the low thermal conductivity. Incorporating of carbon-based nanoparticles into the matrix of PCMs with good dispersion can be an efficient way to solve their deficiency. In this research, graphite nanoparticles were homogeneously dispersed within the Eicosane PCM matrix to prepare a Nano-Enhanced PCM (NEPCM). The main objective is to determine the optimum amount of graphite to maximize the thermal properties of NEPCM composites. The Scanning Electron Microscopy (SEM) images of the prepared nanocomposites confirmed the excellent dispersion of graphite nanoparticles within the Eicosane layers through an ultrasonic bath-assisted homogenization procedure followed by solidification. In addition, Differential Scanning Calorimetry (DSC) and Thermal Conductivity Evaluation (TC) of the samples were conducted to determine their heat capacity and thermal diffusivity. The results illustrated that the more the number of graphite nanoparticles, the larger the number of collisions between graphite and Eicosane. As the nanoparticle content increased, the thermal conductivity and diffusivity were enhanced, as well. Numerically, the maximum thermal conductivity was 4.1 W/m K for the composite containing 10 wt% graphite, 15.66 times that of the pure Eicosane. Furthermore, increasing crystal growth and reducing heat capacity for the large number of nanoparticles in the composite were discussed. The significantly improved thermal properties of the prepared NEPCMs with an optimal nanoparticle content could make them applicable for different thermal management applications.

https://doi.org/10.30501/jree.2023.362050.1454

1. INTRODUCTION

Nowadays, energy storage has become a vital issue for future generations. Energy storage-based technologies have widely been used to prevent increase in energy costs, loss of fossil fuel resources, and environmental unsustainability (Agresti et al., 2019; Al-Jethelah et al., 2019; Sampathkumar & Natarajan, 2022). Since thermal energy has been used extensively, reserving heat energy and advancing energy efficiency can be suggested to decrease environmental and energy problems. Hence, the latest proposed method is the utilization of heat-storage materials composed of adequate chemical stability, high latent heat, and outstanding thermal stability in industrial and homemade applications (Alshaer et al., 2015; Suraparaju & Natarajan, 2022).

PCMs, so-called latent heat-storage systems, could be efficiently utilized for stated applications due to high latent heat, high energy storage capacity, enormous diversity, and wide operating temperature (Eanest Jebasingh & Valan Arasu, 2020; Sampathkumar et al., 2022). Several organic and inorganic materials, mainly salt hydrates, clathrates, paraffin, and polyethylene glycol, can be used as effective PCMs (Sarı & Kaygusuz, 2002). Through many pieces of research, scientists declared paraffin-based hydrocarbons as a major PCM containing saturated and straight-chain organic compounds. Among different kinds of paraffin, Eicosane has been widely utilized due to its outstanding characteristics, such as excellent thermal stability, non-toxic, no phase separation during phase transformation, and good chemical stability. Therefore, Eicosane-based PCMs are a promising energy storage medium through a solid-liquid phase change at a low melting temperature. Despite its advantages, its performance has been restricted by its low thermal conductivity (Ebadi et al., 2018; Pahamli et al., 2017).

Numerous studies have been conducted to prevail over the shortage of thermal conductivity of paraffin waxes, which suggested the introduction of different inorganic (nanoparticles of metal oxides) and organic (polymer) materials to PCMs

*Corresponding Author's Email hashemabadi@iust.ac.ir (S.H. Hashemabadi)

URL: https://www.jree.ir/article_164908.html

Please cite this article as: Moradi, A., Es-haghi, H., Hashemabadi, S.H., Haghgoo, M., & Emami, Z. (2023). Thermal characterization of eicosane/graphite nano-composite-based phase change material. *Journal of Renewable Energy and Environment (JREE)*, *10*(4), 14-21. https://doi.org/10.30501/jree.2023.362050.1454.

(Mohamed et al., 2017). A summary of recent works on PCMs modified with additives, mainly nanoparticles, is represented in Table 1.

Table 1. Summary of the recent literature on modified PCMs with additives

PCM material	Additive	Maximum thermal conductivity (k) [W/m K]	Main finding	Ref.
Eicosane	Ag	0.5467	- The latent heat and the melting point of the samples decreased as the additives loading increased because of the reduction of the number of Eicosane molecules in the samples.	(Al Ghossein et al., 2017)
Eicosane	Graphene nanoplatelet (GNP)	2.1	- Decreased thermal interface resistance, attributed to the unique two-dimensional (2D) planar morphology of GNPs, was responsible for the improved performance of the composite.	(Fang et al., 2013)
n-docosane	Expanded-graphite	0.82	- The composite PCM with 10 wt % graphite was considered as form-stable allowing no leakage of melted paraffin throughout the liquid–solid phase change because of surface tension and capillary forces of graphite.	(Sari & Karaipekli, 2007)
Paraffin	Nano-graphite	0.9362	- The graphite layers were randomly dispersed within the paraffin, and the thermal conductivity was gradually enhanced with the graphite content.	(Li, 2013)
n-Eicosane	Expanded perlite & Carbon nanotube	-	- Compared to n-Eicosane/perlite composite, the utilization of carbon nanotubes improved the thermal conductivity without significantly affecting the compatibility of components, thermal stability, and thermal energy storage properties.	(Karaipekli et al., 2017)
n-Eicosane	Mesoporous silica	1.171	- The composite demonstrated a shorter heat-charging period because of excellent thermal conduction by their interconnecting mesopores silica matrix.	(Liu et al., 2019)
n-Eicosane	Fe_3O_4@SiO_2@Cu	1.3926	- The composite microcapsule exhibited excellent heat transfer capability due to its high thermal conductivity and high thermal energy storage–release performance via suppressing super cooling.	(Do et al., 2021)
n-Eicosane	Multilayer graphene	1.112	- The composite could effectively convert electricity into latent heat, in which its the electro-latent heat storage efficiency could exceed 59.9 % at 1.9 V.	(Zhang et al., 2021)

Al Ghossein et al., (2017) examined the effect of silver (Ag) nanoparticles on the thermal conductivity of Eicosane-based PCM. They found that an increasing thermal conductivity (k) trend emerges by adding Ag nanoparticles up to 2 wt %. However, there is no monotonic relationship between filler amount and thermal conductivity at higher Ag loadings. Carbon-based materials, such as carbon fiber, single and multi-walled carbon nanotubes, and nano-graphite, have shown high thermal conductivity (Bahiraei et al., 2017). Nano-graphite has a two-dimension (2D) layer structure and a large length-diameter ratio. Moreover, it has a larger specific surface area than expanded graphite and exfoliated graphite, which enables it to create the network architecture within PCM and enhance the heat transfer rate (Li & Kim, 2007). For example, Fang et al., (2013) studied the changes in thermal conductivity of Eicosane composite containing graphene nanoplatelet at various loadings, showing a 400 % improvement in thermal conductivity by adding 10 % filler.

Despite numerous studies on various types of paraffin as PCM, there is a lack of a complete study on the optimized thermal properties, primarily thermal conductivity, of an Eicosane-based PCM. In this study, the main aim is to find the optimum amount of nano-graphite, homogeneously dispersed within Eicosane matrix, to maximize the thermal properties of the composite for different PCM applications. Furthermore, the mechanism of heat transfer in the presence and absence of filler aggregation is discussed.

2. EXPERIMENTAL

2.1. Meterials

The materials used to synthesize the NEPCMs in the current study are as follows: pure Eicosane wax with a melting temperature (Tm) of ~ 38 °C was purchased from Parschemical Company. Nano graphite (with average particle sizes of 10-80

nm) and polyvinylpyrrolidone-40 (PVP) as the nanoparticle dispersant were supplied by IraNanotech.

2.2. Preparation of Eicosane/nano-graphite PCM

Different amounts of nano-graphite (2.5, 5, 7.5 and 10 wt %) and PVP as the surfactant were added to the melted PCM, denoted by EG2.5, EG5, EG7.5, and EG10, respectively. The mixture was stirred vigorously for 30 minutes at 75 °C to form a homogeneous mixture. The homogenization process of the mixture was facilitated using an ultrasonic bath for 2 hours at 90 °C followed by solidification in a short time (about 5 min). This procedure helped prevent the graphite nanoparticles from precipitation and ensured that the nanoparticles were well dispersed within the PCM matrix. The obtained mixture was evaluated during the repeated melting/freezing cycle at 50 to 25 °C and reverse order. A schematic representation of sample preparation is illustrated in Figure 1.

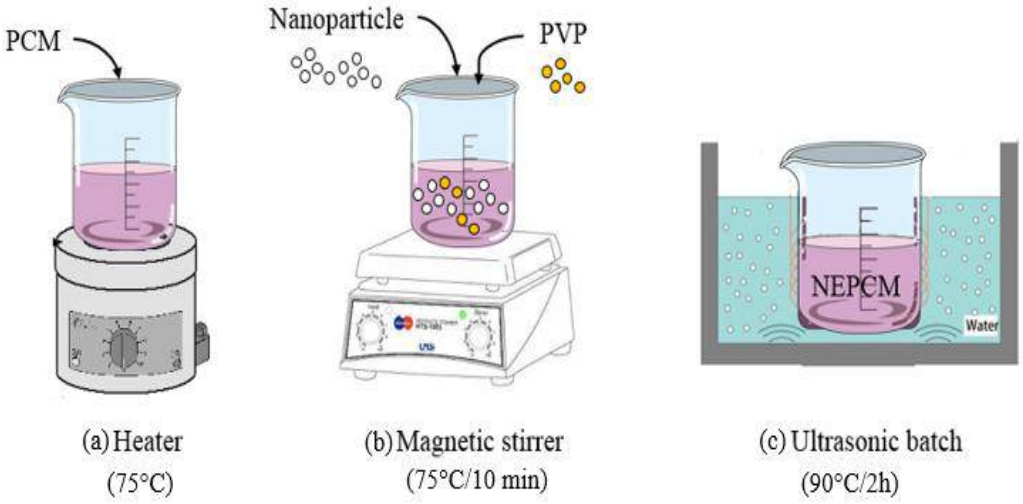

Figure 1. Schematic of sample preparation

2.3. Characterizations

The dispersion state of graphite nanoparticles into the synthesized NEPCMs was studied using scanning electron microscopy (SEM, Vega-TESCAN, Brno, Czech Republic), operating at 20 kV using a secondary electron detector. Differential scanning calorimetry (DSC) analysis (Mettler Toledo, Switzerland) assessed the phase change characterizations of pure substances and NEPCMs under nitrogen coolant gas. The samples by weight of about 10 mg were added into a sealed aluminum pan. The thermal diffusivity (α) of each sample was measured with a Linseis LFA 500 Light Flash. The specific heat capacity (C_P) of NEPCM samples was determined with a Differential Scanning Calorimeter (DSC, Mettler Toledo, Switzerland). Also, the density of samples was measured using the test method ASTM D792. According to thermal diffusivity definition, thermal conductivity (k) of samples is calculated based on the following relation:

$$k_{NEPCM} = \alpha_{NEPCM}(\rho C_P)_{NEPCM} \quad (1)$$

The thermal behavior of all NEPCMs was examined in the temperature range of 0-70 °C at a heating rate of 5 °C/min. All tests were conducted three times to ensure that the obtained results are reliable, and all the reported data is the averaged value with a deviation error within ± 5 %.

3. RESULTS AND DISCUSSION

3.1. SEM analysis

The morphology and surface structure of all samples, including graphite nanopowders, pure Eicosane, and the prepared nanocomposites, were analyzed by SEM images, as shown in Figure 2. In these micrographs, a laminar microstructure of the graphite nanoparticles (Figure 2a) and an excellent dispersion of nanoparticles between Eicosane layers (Figure 2b-2f) can be seen. However, some small aggregates are shown in the samples containing high nanoparticle concentration (above 5 %) due to graphite's high surface energy. Moreover, good interaction between Eicosane and graphite causes the integrated structure of nanocomposites without any loose interface.

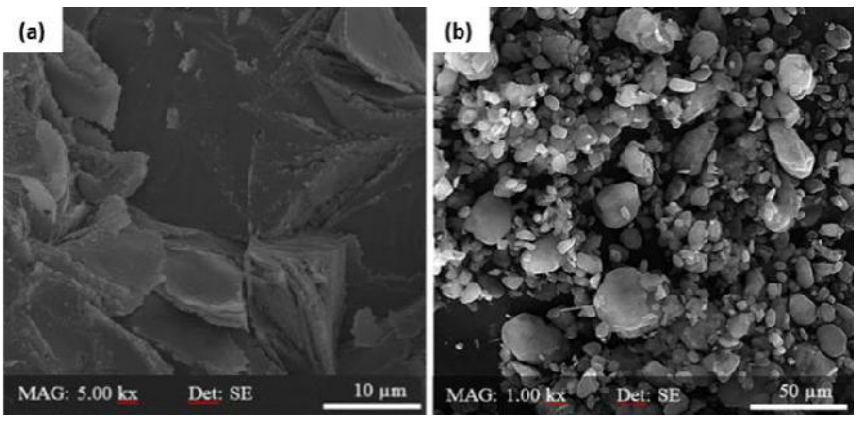

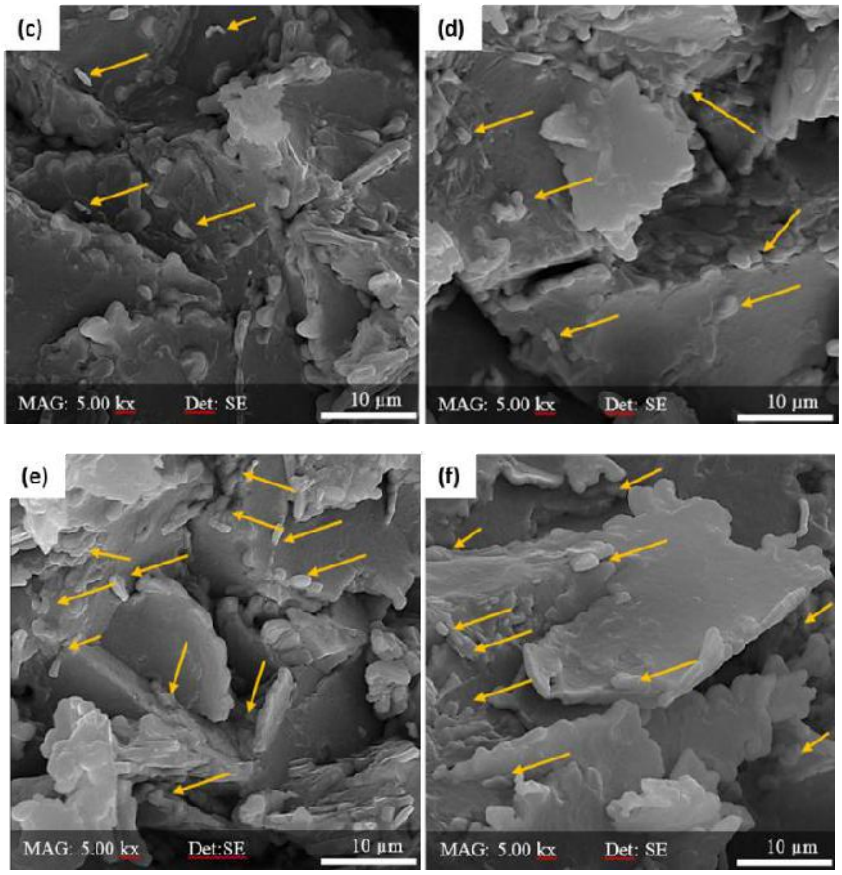

Figure 2. SEM images of (a) pristine Eicosane, (b) graphite nanopowders, (c) EG2.5, (d) EG5, (e) EG7.5, and (f) EG10 samples

3.2. DSC analysis

PCM-based thermal energy storage systems have been designed to collect energy during melting. The heat flow triggers the melting process into the PCM. Since the main state of PCMs is solid at room temperature, heat transfer initially occurs by conduction, in which heat energy is transmitted through the molecules of PCMs. When temperature equals the melting temperature, in the melted part, convection would be the heat transfer mechanism that occurs to move fluid from warm regions to cold due to variation of PCM density. Thus, during the phase change, a transition period is observed in which energy is transferred simultaneously through conduction and convection modes (Haghighi et al., 2020).

The DSC thermograms of pure Eicosane and NEPCM nanocomposites containing different concentrations of nanoparticles are shown in Figure 3 and Figure 4. Figure 3 presents the heating and cooling cycles of the pure Eicosane in the temperature range of 0 to 70 °C. The lower curve is related to the melting process, where PCM absorbs and stores thermal energy. The upper curve is associated with the freezing process where the PCM emits its stored energy to the ambience. The onset temperature is introduced as the baseline intersection with the melting curve (Manoj Kumar et al., 2021). The smaller peak (from 34 to 48 °C) indicates solid-solid phase change due to the remodeling of the crystalline structure. The more significant height (48 to 62 °C) exhibits solid-liquid phase change and the latent heat amount (Warzoha et al., 2012).

Figure 4 shows the melting curve of NEPCM nanocomposites and pure Eicosane. The NEPCM with 2.5 wt % graphite had the highest onset temperature at 48.9 °C, while the pure paraffin had an onset temperature of about 48.0 °C. Therefore, the insignificant influence of the graphite nanoparticles on the composite melting point is observed. All samples have determined the melting points at about 53 ± 0.2 °C. According to the investigation of nanoparticle effects on Eicosane in the literature (Murugan et al., 2018), Eicosane's melting temperature and thermal capacity are not affected by nanoparticles, but its thermal conductivity changes, which are in agreement with the current results.

The area under the melting peak is attributed to the enthalpy. The enthalpy value is expected to increase slightly after the small addition of nanoparticles due to the presence of different molecular interactions (wan der Waals) between nanoparticles and the PCM matrix (Bahiraei et al., 2017). However, the results of this study demonstrated that increasing nanoparticle concentration decreases the amount of latent heat in NEPCMs. As reported by (Warzoha & Fleischer, 2014), adding different fillers in paraffin-based PCMs leads to increasing or decreasing phase change enthalpy based on its impact on paraffin crystallinity. On the one hand, the phase change enthalpy of paraffin increased significantly by adding graphite due to an increase in NEPCM crystallinity; on the other hand, its value decreased with the addition of TiO_2 nanoparticles as a result of reduced NEPCM crystallinity. Table 2 reports the values of the enthalpy and thermal conductivity of all samples. The data indicated that a large amount of graphite caused a reduction in melt enthalpy due to reducing Eicosane mass and declining NEPCM crystallinity (Warzoha & Fleischer, 2014). However, it predicts better molecular heat transfer due to the presence of nanoparticles in NEPCM samples.

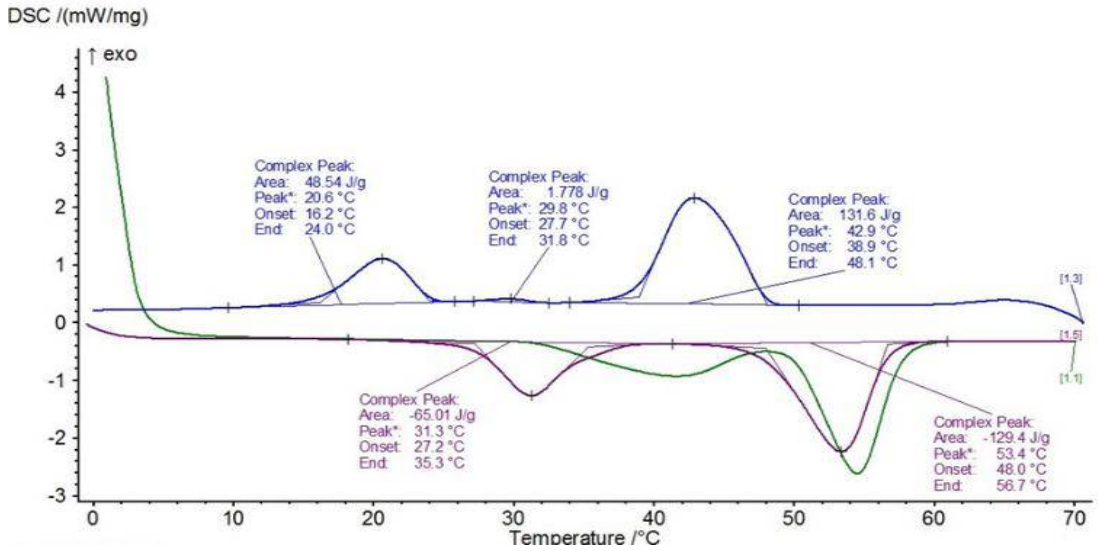

Figure 3. DSC graph of pure Eicosane

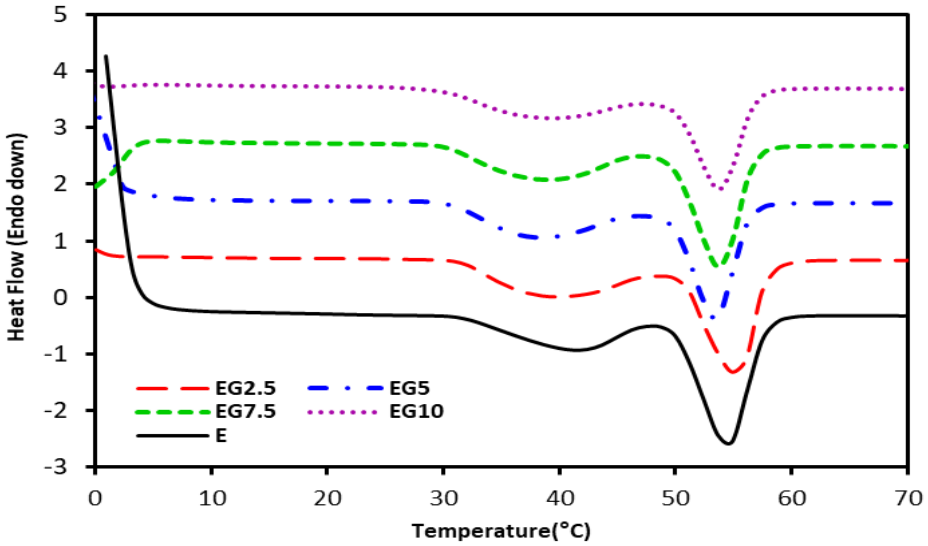

Figure 4. DSC graph of Eicosane-based samples; pristine PCM and NEPCMs at different mass fraction of graphite nanoparticles

Table 2. Enthalpy, thermal conductivity and density of pure Eicosane PCM and NEPCM samples

Sample	Enthalpy (J/g)	Thermal conductivity (W/m K)	Density (g/cm^3)
E	194.4	0.30	0.9207
EG2.5	179.2	0.51	0.9703
EG5	168.3	0.48	0.9708
EG7.5	148.7	0.40	0.9908
EG10	140.8	4.7	1.0388

3.3. Specific heat capacity of NPCMs

A proper phase change material should have a high specific heat capacity to be able to store more quantity of heat per unit volume (Haghighi et al., 2020). The specific heat capacity of nanocomposites depends on the type, size, shape, concentration, state of dispersion and distribution, and crystalline structure of the nanoparticles (Aqib et al., 2020).

Figure 5 shows the specific heat capacity profile of pure Eicosane and its nano-enhanced forms determined by DSC. The specific heat capacity of the NEPCM composite depends on the specific heat capacity of the nanoparticles and pure Eicosane, which causes the overall thermal absorbance in the composite. Since the nano-graphite has a lower heat capacity than Eicosane, adding it to the Eicosane matrix decreases C_p of the nanocomposite (Maher et al., 2021). Therefore, as the mass portion of nanoparticles increases or the mass portion of paraffin decreases, the specific heat capacity of composites is reduced due to the much lower specific heat of the nanomaterials than the pure paraffin.

Also, Figure 5 shows that increasing graphite concentration to 2.5 % leads to the reduction of C_p of the nanocomposite. The amount of C_p reduction is strongly influenced by the surface

energy of the nanoparticles (Warzoha et al., 2012). Adding 5 and 7.5 wt % graphite did not reduce heat capacity compared to the 2.5wt % graphite. Despite the independence of heat capacity with respect to network formation in the system (Chieruzzi et al., 2013), graphite aggregation at higher concentrations acts as a heterogeneous nucleation agent, which is advantageous for the crystallization growth of Eicosane (Kim et al., 2019). Hence, the competition between this phenomenon and heat capacity reduction due to the presence of nanoparticles causes the specific heat capacity to remain almost constant. For the sample EG10, heat capacity reduction may overcome the influence of crystallization growth, leading to the reduction of Cp of the sample.

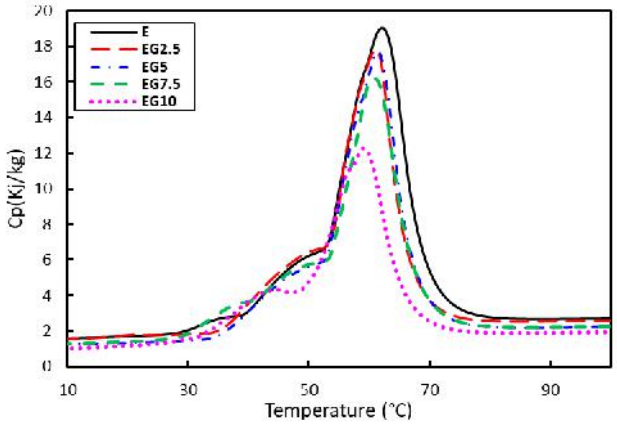

Figure 5. Specific heat capacity of pure Eicosane PCM and NEPCM samples contaning graphite nanoparticles

Thermal diffusivity in a material introduces heat conductivity ability compared to thermal energy storage. Therefore, a quantity, so-called "thermal diffusion coefficient", which is the ratio of the heat transferred by conduction mechanism to the heat stored by the unit volume of the substance, is represented by the symbol α correlated in Eq. 2.

$$\alpha = {}^{k}/_{\rho Cp} \quad (2)$$

According to the above equation, the thermal diffusion coefficient is inversely related to heat capacity and directly related to thermal conductivity. The high thermal conductivity intensified heat transmission through the material, representing high thermal diffusivity.

The values of the thermal diffusivity of the samples are reported in Figure 6. Adding graphite up to 7.5 wt % increased the thermal diffusivity by 1.8 times, while 10 wt % graphite enhanced that by approximately 27 times compared to pure Eicosane. This significant increase in thermal diffusivity of NEPCM at this loading level may be due to the formation of a percolation network (Warzoha et al., 2012). This also can be explained by trapping graphite in Eicosane's crystalline structures, enhancing the effective contact surface between the nanoparticles and the PCM (Bahiraei et al., 2017). Thus, increasing the collisions between Eicosane and graphite increases the thermal diffusivity and conductivity of nanocomposites.

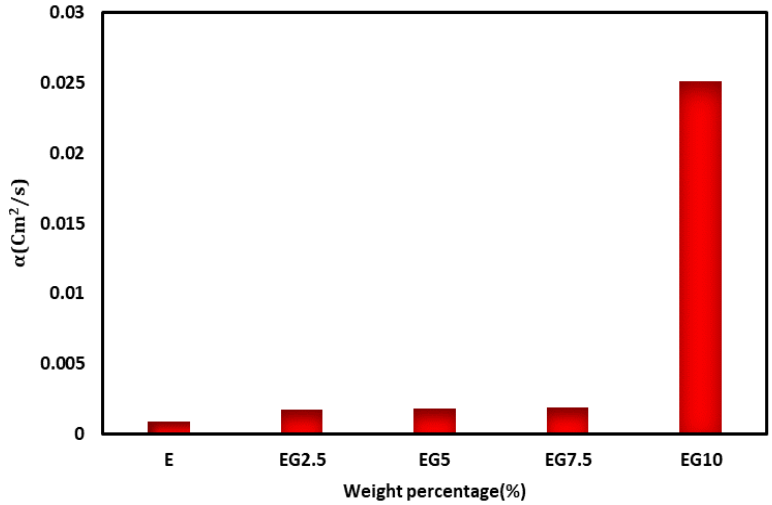

Figure 6. Thermal diffusivity for pure Eicosane PCM and NEPCM samples with different mass fractions of graphite nanoparticles at 25 °C

3.4. Thermal conductivity measurement

Figure 7 illustrates changes in the latent heat and thermal conductivity of composites as a function of nano-graphite percentage. Dispersion of nano-graphite layers in different directions in the Eicosane-based matrix creates a framework that promotes heat transfer in NEPCMs. This enhancement is related to the higher thermal conductivity of graphite (25-470 W/mK) compared to Eicosane. Additionally, in the presence of nanoparticles, a layer of melt Eicosane may form on the graphite surface, increasing interfacial heat conduction and decreasing interfacial thermal resistance (Srinivasan et al., 2017). Although NEPCM's thermal conductivity increases above the percolation threshold of graphite particles (Li & Kim, 2007), its values are strongly related to the dispersion state of the suspension. If the particles stick to each other and form clusters resulting in precipitation, this will drastically reduce the thermal conductivity of the composite. Thus, thermal conductivity enhancement in this work confirms the proper dispersion of nanofillers without significant precipitation. Numerically, the thermal conductivity was increased by 1550 % at a graphite loading of 10 wt %. The improvement of the thermal diffusivity is greater (Figure 6) than that in thermal conductivity, indicating the major impact of Cp on the thermal properties of PCMs. According to Figure 7, continuous increment in the thermal conductivity of NEPCM samples is accompanied by a gradual reeducation in the latent heat of the composite by enhancing graphite nanoparticle content.

Accordingly, the appropriate nanoparticle content must be carefully selected based on the desired PCM application.

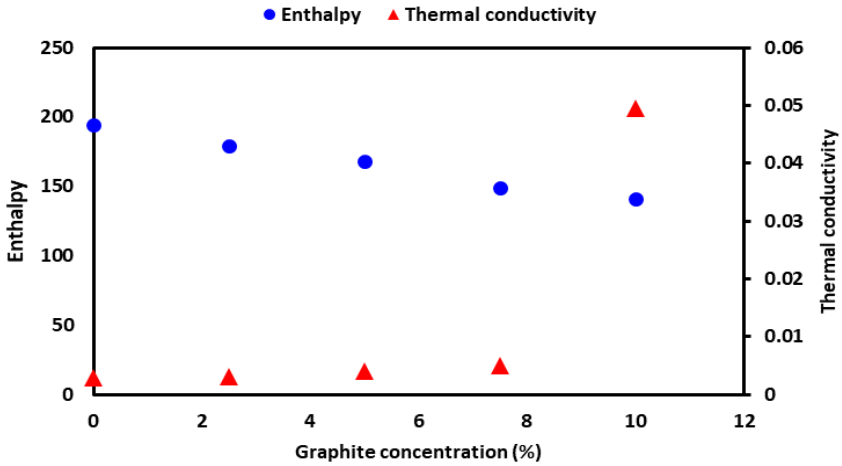

Figure 7. The enthalpy and thermal conductivity of the nanocomposite as a function of nano-graphite

4. CONCLUSIONS

The high thermal energy storage capacity of PCMs makes them applicable for different purposes, especially thermal management applications. However, their low thermal conductivity reduces the heating rate, resulting in lower system efficiency. In this study, we have shown that incorporating graphite nanoparticles in Eicosane-based PCMs can improve the thermal properties of NEPCMs, primarily their thermal conductivity. An ultrasonic bath-assisted homogenization procedure followed by solidification was harnessed to prepare homogenous PCM composites. The results exhibited that good dispersion of lamellar layers of graphite nanoparticles within the Eicosane matrix was responsible for the improved thermal properties. Although small aggregates at high nanoparticle loadings were observed, they had no impact on the heat transfer rate. However, aggregation of big nanoparticles affects the specific heat capacity due to its effect on the crystallization growth of Eicosane. Moreover, as the content of graphite nanoparticles increased, the thermal diffusivity was more affected than thermal conductivity. With the addition of graphite nanoparticles up to the optimal amount (10 wt %), the thermal conductivity and diffusivity of the composite PCM reached their maximum values of 4.7 W/m K and 0.025 cm^2/s, approximately 15.5 and 27 times those of the pure n-Eicosane, respectively. Due to the significant improvement in thermal conductivity of the PCM containing the optimal amount of nano-graphite, such composite PCMs could be promising in various applications, mainly aero-space systems and thermal management electronics.

5. ACKNOWLEDGEMENT

We appreciate and thank the financial support of the Space Research Institute.

NOMENCLATURE

Ag	Silver (k)
C_p	Specific heat capacity (kJ/kg°C)
DSC	Differential scanning calorimetry (mV/mg)
GNP	Graphene nanoplatelet
k	Thermal conductivity (W/mK)
NEPCM	Nano-enhanced phase change material
PCM	Phase change material
PVP	Polyvinylpyrrolidone
TC	Thermal conductivity evaluation (W/mK)

Greek letters

α	Thermal diffusivity

REFERENCES

1. Agresti, F., Fedele, L., Rossi, S., Cabaleiro, D., Bobbo, S., Ischia, G., & Barison, S. (2019). Nano-encapsulated PCM emulsions prepared by a solvent-assisted method for solar applications. *Solar Energy Materials and Solar Cells*, *194*, 268-275. https://doi.org/10.1016/J.SOLMAT.2019.02.021
2. Al Ghossein, R.M., Hossain, M.S., & Khodadadi, J.M. (2017). Experimental determination of temperature-dependent thermal conductivity of solid eicosane-based silver nanostructure-enhanced phase change materials for thermal energy storage. *International Journal of Heat and Mass Transfer*, *107*, 697-711. https://doi.org/10.1016/J.IJHEATMASSTRANSFER.2016.11.059
3. Al-Jethelah, M., Ebadi, S., Venkateshwar, K., Tasnim, S.H., Mahmud, S., & Dutta, A. (2019). Charging nanoparticle enhanced bio-based PCM in open cell metallic foams: An experimental investigation. *Applied Thermal Engineering*, *148*, 1029-1042. https://doi.org/10.1016/J.APPLTHERMALENG.2018.11.121
4. Alshaer, W.G., Nada, S.A., Rady, M.A., Del Barrio, E.P., & Sommier, A. (2015). Thermal management of electronic devices using carbon foam and PCM/nano-composite. *International Journal of Thermal Sciences*, *89*, 79-86. https://doi.org/10.1016/J.IJTHERMALSCI.2014.10.012
5. Aqib, M., Hussain, A., Ali, H.M., Naseer, A., & Jamil, F. (2020). Experimental case studies of the effect of Al_2O_3 and MWCNTs nanoparticles on heating and cooling of PCM. *Case Studies in Thermal Engineering*, *22*, 100753. https://doi.org/10.1016/j.csite.2020.100753
6. Bahiraei, F., Fartaj, A., & Nazri, G.A. (2017). Experimental and numerical investigation on the performance of carbon-based nanoenhanced phase change materials for thermal management applications. *Energy Conversion and Management*, *153*, 115-128. https://doi.org/10.1016/j.enconman.2017.09.065
7. Chieruzzi, M., Cerritelli, G.F., Miliozzi, A., & Kenny, J.M. (2013). Effect of nanoparticles on heat capacity of nanofluids based on molten salts as PCM for thermal energy storage. *Nanoscale Research Letters*, *8*(1), 448. https://doi.org/10.1186/1556-276X-8-448
8. Do, J.Y., Son, N., Shin, J., Chava, R.K., Joo, S.W., & Kang, M. (2021). n-Eicosane-Fe_3O_4@SiO_2@Cu microcapsule phase change material and its improved thermal conductivity and heat transfer performance. *Materials and Design*, *198*, 109357. https://doi.org/10.1016/j.matdes.2020.109357
9. Eanest Jebasingh, B., & Valan Arasu, A. (2020). A comprehensive review on latent heat and thermal conductivity of nanoparticle dispersed phase change material for low-temperature applications. *Energy Storage Materials*, *24*, 52-74. https://doi.org/10.1016/J.ENSM.2019.07.031

10. Ebadi, S., Tasnim, S.H., Aliabadi, A.A., & Mahmud, S. (2018). Melting of nano-PCM inside a cylindrical thermal energy storage system: Numerical study with experimental verification. *Energy Conversion and Management*, *166*, 241-259. https://doi.org/10.1016/J.ENCONMAN.2018.04.016
11. Fang, X., Fan, L.W., Ding, Q., Wang, X., Yao, X.L., Hou, J.F., Yu, Z. T., Cheng, G.H., Hu, Y.C., & Cen, K.F. (2013). Increased thermal conductivity of eicosane-based composite phase change materials in the presence of graphene nanoplatelets. *Energy and Fuels*, *27*(7), 4041-4047. https://doi.org/10.1021/ef400702a
12. Haghighi, A., Babapoor, A., Azizi, M., & Javanshir, Z. (2020). Optimization of the thermal performance of PCM nanocomposites. *Journal of Energy Management and Technology (JEMT)*, *4*(2), 14-19. https://doi.org/10.22109/JEMT.2019.152458.1134
13. Karaipekli, A., Biçer, A., Sarı, A., & Tyagi, V.V. (2017). Thermal characteristics of expanded perlite/paraffin composite phase change material with enhanced thermal conductivity using carbon nanotubes. *Energy Conversion and Management*, *134*, 373-381. https://doi.org/10.1016/j.enconman.2016.12.053
14. Kim, I.H., Sim, H.W., Hong, H.H., Kim, D.W., Lee, W., & Lee, D.K. (2019). Effect of filler size on thermal properties of paraffin/silver nanoparticle composites. *Korean Journal of Chemical Engineering*, *36*(6), 1004-1012. https://doi.org/10.1007/s11814-019-0282-2
15. Li, J., & Kim, J.K. (2007). Percolation threshold of conducting polymer composites containing 3D randomly distributed graphite nanoplatelets. *Composites Science and Technology*, *67*(10), 2114-2120. https://doi.org/10.1016/j.compscitech.2006.11.010
16. Li, M. (2013). A nano-graphite/paraffin phase change material with high thermal conductivity. *Applied Energy*, 106, 25-30. https://doi.org/10.1016/j.apenergy.2013.01.031
17. Liu, H., Niu, J., Wang, X., & Wu, D. (2019). Design and construction of mesoporous silica/n-eicosane phase-change nanocomposites for supercooling depression and heat transfer enhancement. *Energy*, *188*, 116075. https://doi.org/10.1016/j.energy.2019.116075
18. Maher, H., Rocky, K.A., Bassiouny, R., & Saha, B.B. (2021). Synthesis and thermal characterization of paraffin-based nanocomposites for thermal energy storage applications. *Thermal Science and Engineering Progress*, 22, 100797. https://doi.org/10.1016/j.tsep.2020.100797
19. Manoj Kumar, P., Sudarvizhi, D., Stalin, P.M.J., Aarif, A., Abhinandhana, R., Renuprasanth, A., Sathya, V., & Ezhilan, N.T. (2021). Thermal characteristics analysis of a phase change material under the influence of nanoparticles. *Materials Today: Proceedings*, *45*, 7876-7880. https://doi.org/10.1016/j.matpr.2020.12.505
20. Mohamed, N.H., Soliman, F.S., El Maghraby, H., & Moustfa, Y.M. (2017). Thermal conductivity enhancement of treated petroleum waxes, as phase change material, by α nano alumina: Energy storage. *Renewable and Sustainable Energy Reviews*, *70*, 1052-1058. https://doi.org/10.1016/J.RSER.2016.12.009
21. Murugan, P., Ganesh Kumar, P., Kumaresan, V., Meikandan, M., Malar Mohan, K., & Velraj, R. (2018). Thermal energy storage behaviour of nanoparticle enhanced PCM during freezing and melting. *Phase Transitions*, *91*(3), 254-270. https://doi.org/10.1080/01411594.2017.1372760
22. Pahamli, Y., Hosseini, M.J., Ranjbar, A.A., & Bahrampoury, R. (2017). Effect of nanoparticle dispersion and inclination angle on melting of PCM in a shell and tube heat exchanger. *Journal of the Taiwan Institute of Chemical Engineers*, *81*, 316-334. https://doi.org/10.1016/J.JTICE.2017.09.044
23. Sampathkumar, A., & Natarajan, S.K. (2022). Experimental analysis on single slope solar still by the inclusion of Agar-Agar (Eucheuma) Fibre and micro Phase Change Material for the productivity enhancement. *Journal of Energy Storage*, *50*, 104284. https://doi.org/10.1016/J.EST.2022.104284
24. Sampathkumar, A., Suraparaju, S.K., & Natarajan, S.K. (2022). Enhancement of yield in single slope solar still by composite heat storage material—Experimental and thermo-economic assessment. *Journal of Solar Energy Engineering*, *145*(2), 021005. https://doi.org/10.1115/1.4055100
25. Sari, A., & Karaipekli, A. (2007). Thermal conductivity and latent heat thermal energy storage characteristics of paraffin/expanded graphite composite as phase change material. *Applied Thermal Engineering*, *27*(8-9), 1271-1277. https://doi.org/10.1016/j.applthermaleng.2006.11.004
26. Sarı, A., & Kaygusuz, K. (2002). Thermal and heat transfer characteristics in a latent heat storage system using lauric acid. *Energy Conversion and Management*, *43*(18), 2493-2507. https://doi.org/10.1016/S0196-8904(01)00187-X
27. Srinivasan, S., Diallo, M.S., Saha, S.K., Abass, O.A., Sharma, A., & Balasubramanian, G. (2017). Effect of temperature and graphite particle fillers on thermal conductivity and viscosity of phase change material n-eicosane. *International Journal of Heat and Mass Transfer*, *114*, 318-323. https://doi.org/10.1016/j.ijheatmasstransfer.2017.06.081
28. Suraparaju, S.K., & Natarajan, S.K. (2022). Combined enhancement of evaporation and condensation rates in the solar still for augmenting the freshwater productivity using energy storage and natural fibres. *AQUA - Water Infrastructure, Ecosystems and Society*, *71*(5), 628-641. https://doi.org/10.2166/aqua.2022.017
29. Warzoha, R.J., & Fleischer, A.S. (2014). Improved heat recovery from paraffin-based phase change materials due to the presence of percolating graphene networks. *International Journal of Heat and Mass Transfer*, *79*, 314-323. https://doi.org/10.1016/j.ijheatmasstransfer.2014.08.009
30. Warzoha, R.J., Rao, A., Weigand, R., & Fleischer, A.S. (2012). *Experimental characterization of the thermal diffusivity of paraffin phase change material embedded with herringbone style graphite nanofibers*. Proceedings of ASME 2012 Heat Transfer Summer Conference collocated with the ASME 2012 Fluids Engineering Division Summer Meeting and the ASME 2012 10th International Conference on Nanochannels, Microchannels, and Minichannels, HT 2012, (pp. 307-315). USA. https://doi.org/10.1115/HT2012-58043
31. Zhang, B., Li, C., & Liu, Q. (2021). N-eicosane/multilayer graphene composite phase change materials for electro-thermal conversion and storage. *Thermal Science and Engineering Progress*, *25*, 101039. https://doi.org/10.1016/j.tsep.2021.101039

JREE: Vol. 10, No. 4, (Autumn 2023) 22-34

Journal of Renewable Energy and Environment

Journal Homepage: www.jree.ir

Materials and Energy Research Center

MERC

Research Article

An Improved Hottel-Whiller-Bliss Equation for the Nth Photo-Voltaic Thermal-Thermo-Electric Cooler Air Collectors Connected in Series: Exergy Analysis

Gopal Nath Tiwari [a], Prashant Bhardwaj [b*], Sujata Nayak [c]

[a] *BERS Pubic School, Margupur, P. O. Box: 221701, Chilkhar, Ballia (UP), India*
[b] *Department of Mechanical Engineering, Manav Rachna University, P. O. Box: 121004, Faridabad, Haryana, India*
[c] *Legato Health Technologies, P. O. Box: 560045, Bengaluru, Karnataka, India*

PAPER INFO

Paper history:
Received: 26 December 2022
Revised: 10 March 2023
Accepted: 11 March 2023

Keywords:
Photovoltaic Thermal (PVT),
Solar Energy,
Thermo-Electric Cooler (TEC)

ABSTRACT

This study considers N-photovoltaic thermal-thermo electric cooler (PVT-TEC) air collectors connected in series for thermal and electrical performance. An improved Hottel-Whiller-Bliss (HWB) equation and mass flow rate factor were derived for the nth PVT-TEC air collectors. The derivation is based on energy balance equation for each component of N-photovoltaic thermal-thermo electric cooler (PVT-TEC) air collectors connected in series. Further, thermal energy and electrical energy from PV module and TEC were analyzed based on a given design and climatic parameters along with the overall exergy of the proposed system on the hourly and daily bases. Numerical computations were conducted using MATLAB under Indian climatic conditions. The proposed thermal model is valid for all climatic and weather conditions. Based on the numerical computations carried out, the following conclusions were made:

i. The electrical power of PV module decreased with increase in the number of the n^th PVT-TEC air collectors as the electrical power of TEC increased.

ii. The overall instantaneous exergy efficiency decreased with increase in the number of the n^th PVT-TEC air collectors.

iii. Packing factor of TEC was found to be a very sensitive parameter for optimizing the number of PVT-TEC air collectors to ensure maximum overall exergy, and it was found to be β_tec=0.5. for N=7

https://doi.org/10.30501/jree.2023.376480.1516

1. INTRODUCTION

Solar energy is freely available, economical, environmentally-friendly, and sustainable source of energy and it find various applications in our daily lives. The analysis of a solar energy-based system basically depends on the operating temperature. One of the solar energy systems is the thermal system that operates in the medium temperature range (0°C<T<100°C). In this temperature range, a conventional flat plate water/air collector is used for water and air heating. The thermal analysis of conventional Flat Plate Collectors (FPC) has been carried out based on the first law of thermodynamics (energy conservation). The FPC enjoys better performance in the forced mode of operation and requires electrical power. To make FPC self-sustainable, the glass cover is replaced with a photovoltaic (PV) module, which is known as a photovoltaic thermal (PVT) collector (Tiwari et al., 2016; Tiwari & Dubey S., 2010). The PVT collector provides thermal (low-grade energy) and electrical power (high-grade energy). Hence, in order to analyze the PVT collector in the medium temperature range, it is important to consider both the thermal exergy and electrical energy concepts based on the second law of thermodynamics. The combination of both gives the overall exergy of the PVT collector. The exergy analysis is an efficient tool for energy policy-making in terms of quantity and quality of the energy sources including destruction unlike energy (Dincer, 2002; Dincer & Rosen, 2013). Hoseinzadeh et al. carried out exergoeconomic analysis and optimization of reverse osmosis (RO) desalination integrated with geothermal energy (Hoseinzadeh, Yargholi, et al., 2020). The study resulted in a reduction of the total cost rate by 10%. The multi-effect desalination (MED) system was also analyzed by Kariman et al. with negligible exergy destruction (Kariman et al., 2020). Kariman et al. conducted energetic and exergetic analyses of an evaporation desalination system integrated with mechanical vapor recompression circulation (Kariman et al., 2019). They found that the highest exergy destruction occurred in the boiler compartment. Recently, Hoseinzadeh et al. have conducted energy, exergy, and environmental (3E) analyses and optimization of a Coal-Fired 400 MW Thermal Power and micro hydro systems for hot climatic conditions (Hoseinzadeh, Ghasemi, et al., 2020; Hoseinzadeh & Heyns, 2020). Jafari et al. conducted an energy, exergy, and environmental (3E) optimal location assessment of flat-plate collectors for

*Corresponding Author's Email: prashant@mru.edu.in (P. Bhardwaj)
URL: https://www.jree.ir/article_170019.html

Please cite this article as: Tiwari, G. N., Bhardwaj, P., & Nayak, S. (2023). An Improved Hottel-Whiller-Bliss Equation for the Nth Photo-Voltaic Thermal-Thermo-Electric Cooler Air Collectors Connected in Series: Exergy Analysis, *Journal of Renewable Energy and Environment (JREE)*, 10(4), 22-34. https://doi.org/10.30501/jree.2023.376480.1516.

domestic hot water applications in Iran (Jafari et al., 2022).

The classifications of flat plate collectors are summarized as follows:

Conventional flat plate liquid collectors (FPC) operate by transmitting solar energy through a glazed surface, which is then absorbed by a blackened surface to heat the working fluid beneath it (Badiei et al., 2020; Duffie & Beckman W. A., 2013; Sarwar et al., 2020). This method provides only thermal energy and requires grid power for forced mode operation, which enhances its performance.

Photo-voltaic thermal (PVT) liquid collectors: In PVT collector, the glass of flat plate collector (FPC) is replaced by photovoltaic (PV) module. It gives both thermal and electrical energy to become self-sustained. It also operates in the medium range of temperatures (Arslan et al., 2020; Chow, 2010; Dupeyrat et al., 2014; Hocine et al., 2015; Tiwari & Dubey S., 2010; Zondag et al., 2003).

PVT-CPC collectors: When a compound parabolic concentrator (CPC) is integrated on top of a photovoltaic thermal (PVT) collector, the resulting system is called a PVT-CPC. This configuration allows for a more concentrated solar energy, resulting in more thermal energy production but lower electrical power output due to the high operating temperature. Additionally, PVT-CPC systems are self-sustained and can operate at higher temperatures compared to traditional PVT collectors (Atheaya et al., 2016; Cabral et al., 2019; Kostić et al., 2010; Proell et al., 2017; Tiwari et al., 2018).

PVT-TEC collectors: In this case, the thermo-electric cooler (TEC) is attached to the back of the absorber of PVT collector. In addition to PV module, TEC generates for additional electric power in addition to PV module due to Peltier effect with temperature difference. It is efficient and operates at medium temperature range (Dimri et al., 2018; Huen & Daoud, 2017; Ong et al., 2017; Sudharshan et al., 2016; Yin et al., 2017; Zhang et al., 2014; Zhu et al., 2016).

In all the cases mentioned above, the single collector was used. Furthermore, to increase both thermal energy and electrical energy, various researchers have analyzed the following combinations :

All PVT collectors were connected in series: Increasing the number of PVT collectors results in higher thermal output but lower electrical power output from the PV module due to the high temperature of the solar cell (Dubey & Tiwari, 2008; Li et al., 2020; Ma et al., 2020; Shyam et al., 2016; Tiwari et al., 2018).

Series and parallel separately: The operating temperature in the parallel configuration is lower than that in the series connection for a given total number of PVT collectors. Therefore, parallel connection is considered more efficient than series connection in this case (Kotb et al., 2019; Sharaf & Orhan, 2018; Vega & Cuevas, 2020).

The electrical efficiency of the solar cell in PVT-TEC air collectors is highly sensitive to the operating temperature (Evans, 1981; Skoplaki & Palyvos, 2009). When PVT air collectors are connected in series, the operating temperature of the PVT collector increases with an increase in the number of collectors. As a result, the electrical efficiency of the solar cell in the PVT collector decreases while the electrical efficiency of the TEC increases. However, this effect has not been considered for N-PVT-TEC collectors that are connected in series.

In this connection, we considered N-PVT-TEC air collectors connected in only series to evaluate the overall exergy of the PVT-TEC system which, to the best of our knowledge, has not been done before. Further, we derived an inproved Hottel-Wills- Beckman (HWB) equation and calculated the overall hourly exergy and exergy efficiency of the proposed system. The proposed system was evaluated based on the varying numbers of PVT-TEC collectors from n=1 to N. Additionally, we investigated the effect of the correction factor (CF) on the mass flow rate factor (F_(R,n^th)) .

2. WORKING PRINCIPLE OF OPAQUE PV-TEC AIR COLLECTOR

In the present case, we considered fully covering an opaque PV module with an air duct below it. The thermo-electrical cooler (TEC) module is attached to the base of PV module with packing factor (β_tec<1) less than one, as shown in Fig. 1a and suggested in (Sudharshan et al., 2016). By using the Eq. 1, the packing factor of TEC can be calculated.

$$\beta_{\text{tec}} = \frac{\text{Number of TEC cell area} \times \text{area of one TECcell}}{\text{Area of opaque PV modul}} \leq 1 \qquad (1)$$

In order to remove thermal energy from the bottom end of PV and TEC modules, the working fluid was considered as air and allowed to flow through an air duct. As a result, flowing air is heated and the bottom of TEC is cooled, giving rise a temperature difference across TEC that provides electrical current due to Peltier effect, as mentioned earlier. Therefore, the total electric power of PVT-TEC is the sum of electrical power generated from PV module and TEC. The schematic illustration of the opaque PV-TEC collector with air duct is shown in Fig. 1(a). To increase the temperature, the outlet of the first PVT-TEC air collector is connected to the inlet of the second collector, as shown in Fig.1b. This process continues until the Nth PVT-TEC air collector is reached. The number of PVT-TEC air collectors that can be connected in series depends significantly on the mass flow rate (0.025-0.25 kg/s) required to achieve the desired outlet air temperature. The design parameters of the PVT-TEC air collector are given in Table 1.

According to Fig. 1a, part of solar radiation is absorbed by solar cell of PV module $[\tau_g \alpha_{sc} I(t) bdx]$ after transmission through glass cover. Following the process of absorption, the solar cell of opaque PV module converts into electrical energy $[\eta_{sc} \tau_g I(t) bdx]$ depending upon its electrical efficiency (η_{sc}). Further, some portion of the absorbed radiation is directly transferred to ambient air through the top glass cover of the opaque PV module $[U_t(T_{sc} - T_a) bdx]$ and the remaining is indirectly transferred to the air flowing below the TEC $[U_{b,ca}(T_{sc} - T_f)(1 - \beta_{tec}) bdx]$. Moreover, thermal energy is transferred from the back of solar cells to the top of TEC $[h_t(T_{sc} - T_{tec,top})\beta_{tec} bdx]$ through the packing area of the TEC. The thermal circuit diagram of the PVT-TEC air collector is shown in Figure. 1c.

Table 1. Design parameters of the PVT-TEC air collector (Dimri et al., 2018)

A_m	0.1332 m^2	K_{tec}	1.82 W/mK
b	0.36 m	L_{tec}	0.004 m
L	0.37 m	K_i	0.166 W/mK
L_f	0.01 m	L_i	0.100 m
α_{sc}	0.9	K_f	0.02622 W/mK
τ_g	0.95	h_{tf}	2.21 W/m^2K
η_o	0.15	U_b	0.62 W/m^2K
η_{tec}	0.08	U_{tec}	435.2 W/m^2K
β_o	0.0045/K	$U_{tec,top-a}$	4.2118 W/m^2K
c_f	1005 J/kgK	$U_{tec,bottom-a}$	4.1714 W/m^2K
$\dot{m}_f$	0.003 kg/s	U_{fa}	2.3095 W/m^2K
R_c	10^{-4} m^2 K/W	h_{p1}	0.3618
K_g	0.816 W/mK	h_{p2}	0.9904
L_g	0.003 m	h_{p3}	0.6018
K_t	0.033 W/mK	$(\alpha\tau)_{eff}$	0.7225
L_t	0.005 m	$(\alpha\tau)'_{eff}$	0.2382

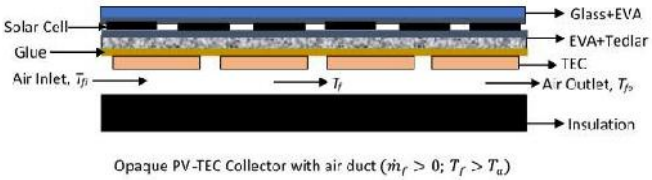

Figure 1a. Cross-sectional view of the single PVT-TEC air collector

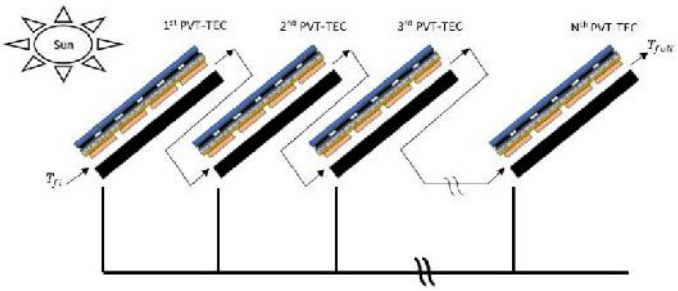

Figure 1b. The N-PVT-TEC air collectors connected in series

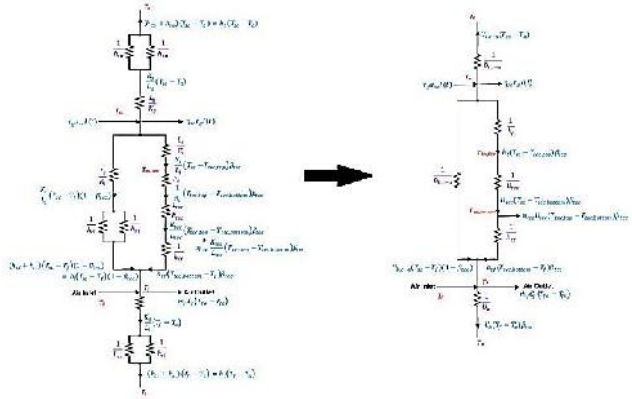

Figure 1c. Thermal circuit diagram of the PVT-TEC air collector (Sudharshan et al., 2016)

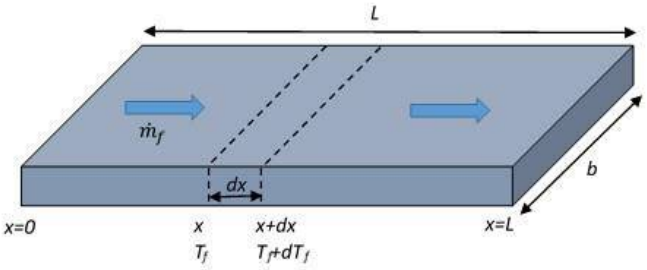

Figure 2. An elemental area of 'bdx' for flowing air below air duct

3. THERMAL MODELING

The following assumptions are made for thermal modeling:

(i) The proposed system is in a quasi-steady state
(ii) Thermal heat capacity of each component is neglected
(iii) No temperature stratification along thickness of each component is needed.
(iv) The flow of air is in a stream line.
(v) Design parameters and area $(A_m)$of each PVT-TEC air collectors are the same.

3.1 Energy Balance of PVT-TEC Air Collector (Dimri et al., 2018)

(a) Solar cell of the opaque PV module

$$\tau_g\alpha_{sc}I(t)bdx = U_{t,c-a}(T_{sc}-T_a)bdx + h_t(T_{sc}-T_{tec,top})\beta_{tec}bdx + U_{b,c-a}(T_{sc}-T_f)(1-\beta_{tec})bdx + \eta_{sc}\tau_g I(t)bdx \quad \ldots(2)$$

where

$$\beta_{tec} = \frac{NumberofTECmodules \times AreaofoneTECmodule}{AreaofPVmodule/collector}$$

(b) For tedlar:

$$h_t(T_{sc}-T_{tec,top})\beta_{tec}bdx = U_{tec}(T_{tec,top}-T_{tec,bottom})\beta_{tec}bdx \quad \ldots(3)$$

(c) For TEC module:

$$U_{tec}(T_{tec,top}-T_{tec,bottom})\beta_{tec}bdx = h_{tf}(T_{tec,bottom}-T_f)\beta_{tec}bdx + \eta_{tec}U_{tec}(T_{tec,top}-T_{tec,bottom})\beta_{tec}bdx \quad \ldots(4)$$

where U_{tec} is the overall heat transfer coefficient between TEC module and tedlar (Figure 1a). The numerical value of U_{tec} is calculated as:

$$U_{tec} = \left[R_c + \frac{L_{tec}}{K_{tec}}\right]^{-1} \quad \ldots(5)$$

where R_c is the thermal contact resistance at thermoelectric leg-electrode interfaces. The literature reports a range of thermal contact resistance levels that fall within $1 \times 10^{-6} - 5 \times 10^{-4}$ m^2Kelvin/W (Zhang et al., 2014). Thermal contact resistance (R_c) is chosen to be 10^{-4} m^2Kelvin/W in the current study.

(d) For air flowing below TEC module (Figure 2):

As mentioned above, the air flowing through the air duct received the rate of thermal energy $[h_{tf}(T_{tec,bottom} - T_f)\beta_{tec}bdx]$and $[U_{b,c-a}(T_{sc} - T_f)(1-\beta_{tec})bdx]$ and the energy balance can be written for the flowing air as follows:

$$h_{tf}(T_{tec,bottom} - T_f)\beta_{tec}bdx + U_{b,c-a}(T_{sc} - T_f)(1-\beta_{tec})bdx = \dot{m}_f c_f \frac{dT_f}{dx}dx + U_b(T_f - T_a)bdx \quad \ldots(6)$$

3.2 Analytical Expression for an Outlet Fluid Temperature of N-PVT-TEC Air Collector

By adopting the thermal mode proposed by various researchers (Dimri et al., 2018; Tiwari et al., 2016; Tiwari & Dubey S., 2010), an expression for solar cell temperature (T_{sc}), TEC top ($T_{tec,top}$), and TEC bottom ($T_{tec,bottom}$) temperatures can be obtained via the elimination process in Eqs. 1-4 as follows:

$$T_{sc} = \frac{(\alpha\tau)_{eff}I(t) + U_{t,c-a}T_a + U_{b,c-a}(1-\beta_{tec})T_f + h_t\beta_{tec}T_{tec,top}}{U_{t,c-a} + U_{b,c-a}(1-\beta_{tec}) + h_t\beta_{tec}} \quad \ldots(7)$$

$$T_{tec,top} = \frac{h_{p1}(\alpha\tau)_{eff}I(t) + U_{tec,top-a}T_a + U_{tec,top-f}T_f + U_{tec}\beta_{tec}T_{tec,bottom}}{U_{tec,top-a} + U_{tec,top-f} + U_{tec}\beta_{tec}} \quad \ldots(8)$$

$$T_{tec,bottom} = \frac{(\alpha\tau)'_{eff}I(t) + (1-\eta_{tec})U_{tec,bottom-a}T_a + [(1-\eta_{tec})U_{tec,bottom-f} + h_{tf}\beta_{tec}]T_f}{(1-\eta_{tec})U_{tec,bottom-a} + (1-\eta_{tec})U_{tec,bottom-f} + h_{tf}\beta_{tec}} \quad \ldots(9)$$

The expressions for $(\alpha\tau)_{eff}$, $(\alpha\tau)'_{eff}$, h_t, h_{p1}, h_{tf}, $U_{t,c-a}$, $U_{b,c-a}$, $U_{tec,top-a}$, $U_{tec,top-f}$, $U_{tec,bottom-a}$, and $U_{tec,bottom-f}$ are given in Appendix A (Dimri et al., 2018).

By using Eqs. (7) – (9), Eq. (6) can be rewritten as follows:

$$\frac{dT_f}{dx} + aT_f = f(t) \quad \ldots(10)$$

where

$a = \frac{(U_{fa}+U_b)b}{\dot{m}_f c_f}$, $f(t) = \frac{(\alpha\tau)_{m-eff}bI(t)+U_{Lm}bT_a}{\dot{m}_f c_f}$;

$\frac{f(t)}{a} = \frac{(\alpha\tau)_{m-eff}I(t)+(U_{fa}+U_b)T_a}{(U_{fa}+U_b)} = \left[\frac{(\alpha\tau)_{m-eff}}{U_{Lm}}I(t) + T_a\right]$

$(\alpha\tau)_{m-eff} = [h_{p3}(\alpha\tau)'_{eff} + h'_{p1}(\alpha\tau)_{eff} + h'_{p2}h_{p1}(\alpha\tau)_{eff} + h'_{p3}(\alpha\tau)'_{eff}]$ and $U_{Lm} = (U_{fa} + U_b)$

The expressions ofU_{fa}, U_b, h_{p3}, h'_{p1}, h'_{p2} and $h'_{p3}$are defined in Appendix A (Dimri et al., 2018)

The solution of Eq. 8 can be obtained through the initial condition, $i.e.,\ T_f|_{x=0} = T_{fi}$ (Dimri et al., 2018). The solution to Eq. (10) is as follows:

$$T_f = \left[\frac{(\alpha\tau)_{m-eff}}{U_{Lm}}I(t) + T_a\right](1 - e^{-ax}) + T_{fi}e^{-ax} \quad \ldots(11)$$

By using [Eq.11] and at x= $i.e.T_f|_{x=L} = T_{fo1}$, the fluid temperature at outlet (T_{fo1}) of the first PVT-TEC air collector can be calculated as

$$T_{fo1} = \left[\frac{(\alpha\tau)_{m-eff}}{U_{Lm}}I(t) + T_a\right]\left(1 - e^{-\frac{U_{Lm}A_m}{\dot{m}_f c_f}}\right) + T_{fi}e^{-\frac{U_{Lm}A_m}{\dot{m}_f c_f}} \quad \ldots(12)$$

The above equation is also derived from the referenced study (Dimri et al., 2018).

If an outlet of the first PVT-TEC air collector, T_{fo1} [Eq. 12], is connected to the inlet of the second PVT-TEC air collector, T_{fi2}, Figure 1b, then the expression of the outlet of the 2nd PVT-TEC will be as follows:

$$T_{fo2} = \left[\frac{(\alpha\tau)_{m-eff}}{U_{Lm}}I(t) + T_a\right]\left(1 - e^{-\frac{U_{Lm}A_m}{\dot{m}_f c_f}}\right) + T_{fo1}e^{-\frac{U_{Lm}A_m}{\dot{m}_f c_f}} \quad \ldots(13)$$

After substituting T_{fo1} from Eq. 12 into Eq. 13, we get:

$$T_{fo2} = \left[\frac{(\alpha\tau)_{m-eff}}{U_{Lm}}I(t) + T_a\right]\left(1 - e^{-\frac{2U_{Lm}A_m}{\dot{m}_f c_f}}\right) + T_{fi}e^{-\frac{2U_{Lm}A_m}{\dot{m}_f c_f}} \quad \ldots(14)$$

Now, the outlet of the second PVT-TEC air collector, T_{fo2}, will be the inlet of the third PVT-TEC air collector for series connection. Then, we have:

$$T_{fo3} = \left[\frac{(\alpha\tau)_{m-eff}}{U_{Lm}}I(t) + T_a\right]\left(1 - e^{-\frac{2U_{Lm}A_m}{\dot{m}_f c_f}}\right) + T_{fo2}e^{-\frac{2U_{Lm}A_m}{\dot{m}_f c_f}} \quad \ldots(15)$$

Upon solving Eq.15 as mentioned above, one gets:

$$T_{fo3} = \left[\frac{(\alpha\tau)_{m-eff}}{U_{Lm}}I(t) + T_a\right]\left(1 - e^{-\frac{3U_{Lm}A_m}{\dot{m}_f c_f}}\right) + T_{fi}e^{-\frac{3U_{Lm}A_m}{\dot{m}_f c_f}} \quad \ldots(16)$$

Similarly, for N-PVT-TEC air collectors connected in series, an expression for an outlet air temperature at the end of N-PVT-TEC air collector T_{foN} can be written as follows:

$$T_{foN} = \left[\frac{(\alpha\tau)_{m-eff}}{U_{Lm}} I(t) + T_a\right]\left(1 - e^{-\frac{NU_{Lm}A_m}{\dot{m}_f c_f}}\right) + T_{fi} e^{-\frac{NU_{Lm}A_m}{\dot{m}_f c_f}} \quad \ldots (17a)$$

The above equation is a new expression for N-PVT-TEC air collectors connected in series.

3.3 Improved Hottel-Whillier-Bliss (HWB) Equation

The rate of thermal energy at the n[th] PVT-TEC air collector will be as follows:

$$\dot{Q}_{uth,n^{th}} = \dot{m}_f C_f \left(T_{fon} - T_{fon-1}\right)$$

Substituting T_{fon} and T_{fon-1} from Eq. 17a in terms of T_{fi} into the above equation, we get:

$$\dot{Q}_{uth,n^{th}} = \dot{m}_f C_f \left\{\left[\frac{(\alpha\tau)_{m-eff}}{U_{Lm}} I(t) + T_a\right]\left(1 - e^{-\frac{nU_{Lm}A_m}{\dot{m}_f c_f}}\right) + T_{fi} e^{-\frac{nU_{Lm}A_m}{\dot{m}_f c_f}}\right\} - \left\{\left[\frac{(\alpha\tau)_{m-eff}}{U_{Lm}} I(t) + T_a\right]\left(1 - e^{-\frac{(n-1)U_{Lm}A_m}{\dot{m}_f c_f}}\right) + T_{fi} e^{-\frac{(n-1)U_{Lm}A_m}{\dot{m}_f c_f}}\right\}$$

$$\dot{Q}_{uth,n^{th}} = \dot{m}_f C_f \left(1 - e^{-\frac{U_{Lm}A_m}{\dot{m}_f c_f}}\right)\left\{\left[\frac{(\alpha\tau)_{m-eff}}{U_{Lm}} I(t) + T_a\right] - T_{fi}\right\} e^{-\frac{(n-1)U_{Lm}A_m}{\dot{m}_f c_f}}$$

$$\dot{Q}_{uth,n^{th}} = \dot{m}_f C_f \left(1 - e^{-\frac{U_{Lm}A_m}{\dot{m}_f c_f}}\right) CF\left[\frac{(\alpha\tau)_{m-eff}}{U_{Lm}} I(t) - \left(T_{fi} - T_a\right)\right] \quad \ldots (17b)$$

where

$$CF = e^{-\frac{(n-1)U_{Lm}A_m}{\dot{m}_f c_f}} = 1 \; for \; n = 1 \; otherwise < 1 \; for \; n > 1$$

The above equation is valid for $n < N$.

Instantaneous thermal efficiency of the n^{th} PVT-TEC air collector is given by

$$\eta_{i,n^{th}} = \frac{\dot{Q}_{uth,n^{th}}}{I(t)A_m} = \frac{\dot{m}_f C_f}{A_m U_{Lm}}\left(1 - e^{-\frac{U_{Lm}A_m}{\dot{m}_f c_f}}\right) CF\left[(\alpha\tau)_{m-eff} - U_{Lm}\frac{\left(T_{fi} - T_a\right)}{I(t)}\right] \quad \ldots (17c)$$

The above equation is the improved thermal characteristic equation of the n[th] PVT-TEC air collector (improved Hottel-Whillier-Bliss (HWB) equation) that is derived for the first time to be used for indoor testing under standard test conditions (STC). For n=1, Eq. 17c is reduced to the following:

$$\eta_{i,1^{st}} = \frac{\dot{Q}_{uth,n^{th}}}{I(t)A_m} = \frac{\dot{m}_f C_f}{A_m U_{Lm}}\left(1 - e^{-\frac{U_{Lm}A_m}{\dot{m}_f c_f}}\right)\left[(\alpha\tau)_{m-eff} - U_{Lm}\frac{\left(T_{fi} - T_a\right)}{I(t)}\right] \quad \ldots (17d)$$

which is Hottel-Whillier-Bliss (HWB) equation for conventional PVT-TEC air collector.

3.4 Improved Electrical Analysis

Now, an average fluid temperature of the n^{th} PVT-TEC air collector ($n < N$) can be expressed as follows:

$$\bar{T}_{f,n^{th}} = \frac{T_{fon} + T_{fon-1}}{2} \quad \ldots (18)$$

For the first PVT-TEC air collector, $T_{fon-1} = T_{fi}$.

At the known hourly numerical values of $\bar{T}_{f,n^{th}}$, average values of $\bar{T}_{sc}$, $\bar{T}_{tec,top}$, and $\bar{T}_{tec,bottom}$ can be determined using the following equations:

$$\bar{T}_{sc,n^{th}} = \frac{(\alpha\tau)_{eff} I(t) + U_{t,c-a}T_a + U_{b,c-a}(1-\beta_{tec})\bar{T}_{f,n^{th}} + h_t\beta_{tec}T_{tec,top}}{U_{t,c-a} + U_{b,c-a}(1-\beta_{tec}) + h_t\beta_{tec}} \quad \ldots (19)$$

$$\bar{T}_{tec,top,n^{th}} = \frac{h_{p1}(\alpha\tau)_{eff} I(t) + U_{tec,top-a}T_a + U_{tec,top-f}\bar{T}_{f,n^{th}} + U_{tec}\beta_{tec}T_{tec,bottom}}{U_{tec,top-a} + U_{tec,top-f} + U_{tec}\beta_{tec}} \quad \ldots (20)$$

$$\bar{T}_{tec,bottom,n^{th}} = \frac{(\alpha\tau)'_{eff} I(t) + (1-\eta_{tec})U_{tec,bottom-a}T_a + \left[(1-\eta_{tec})U_{tec,bottom-f} + h_{tf}\beta_{tec}\right]\bar{T}_{f,n^{th}}}{(1-\eta_{tec})U_{tec,bottom-a} + (1-\eta_{tec})U_{tec,bottom-f} + h_{tf}\beta_{tec}} \quad \ldots (21)$$

The efficiency of a PV module of the n^{th} PVT-TEC air collector is given as follows (Evans, 1981):

$$\eta_{m,n^{th}} = \tau_g\eta_o\left[1 - \beta_o\left(\bar{T}_{sc,n^{th}} - T_o\right)\right] \quad \ldots (22)$$

where η_o is the efficiency of the PV module at Standard Test Condition (STC), i.e., I(t) = 1000 W/m^2 and To = 25°C, and β_o is the temperature thermal expansion coefficient.

The rate of an electrical energy generated by PV module at the n^{th} PVT-TEC air collector for one packing ($\beta_{sc} = 1$) is given as follows:

$$\dot{E}_{PV,n^{th}} = \eta_{m,n^{th}} I(t) A_m \quad \ldots(23)$$

The rate of thermal energy received from the n^{th} PVT-TEC air collector using the TEC module for the packing area of $(\beta_{tec} A_m)$, i.e., $U_{tec}(\bar{T}_{tec,top,n^{th}} - \bar{T}_{tec,bottom,n^{th}})\beta_{tec} A_m$, when multiplied with η_{tec}, gives an expression for the electrical energy generated by the TEC module as (Dimri et al., 2018):

$$\dot{E}_{\mathrm{TEC,n^{th}}} = \eta_{tec} U_{tec}(\bar{T}_{tec,top,n^{th}} - \bar{T}_{tec,bottom,n^{th}})\beta_{tec} A_m \quad \ldots(24)$$

where η_{tec} is the conversion efficiency from thermal energy into electrical energy of the TEC module.

The total rate of electrical energy ($\dot{E}_{el,n^{th}}$) generated by the n^{th}opaque PV-TEC air collector can be calculated by adding electrical energy generated by PV module, $\dot{E}_{PV,n^{th}}$, according to Eq.15, and the electrical energy generated by the TEC module, $\dot{E}_{\mathrm{TEC,n^{th}}}$, according to Eq.17.

$$\dot{E}_{el,n^{th}} = \dot{E}_{PV,n^{th}} + \dot{E}_{TEC,n^{th}} \quad \ldots(25a)$$

The improved total rate of electrical energy, $\dot{E}_{e-N}$, generated by the n-opaque PV-TEC air collector can be evaluated as

$$\dot{E}_{el-N} = \sum_{i=1}^{N} \dot{E}_{eli,n^{th}} \quad \ldots(25b)$$

The overall instantaneous total electrical efficiency of the n^{th} opaque PV-TEC air collector can be obtained as follows:

$$\eta_{i,el,n^{th}} = \frac{\dot{E}_{el,n^{th}}}{A_m I(t)} \quad \ldots(26)$$

3.5 Overall Instantaneous Thermal Efficiency

The rate of useful thermal energy gained from the N-opaque PV-TEC air collector is calculated as follows:

$$\dot{Q}_{u,th-N} = \dot{m}_f c_f (T_{foN} - T_{fi}) \quad \ldots(27a)$$

Substituting $T_{foN}$from Eq. 17a into Eq. 27a, we get:

$$\dot{Q}_{u,th-N} = \dot{m}_f c_f \left(1 - e^{-\frac{NU_{Lm}A_m}{\dot{m}_f c_f}}\right)\left[\frac{(\alpha\tau)_{m-eff}}{U_{Lm}} I(t) - (T_{fi} - T_a)\right] \quad \ldots(27b)$$

Further, the overall instantaneous thermal efficiency, $\eta_{i,th-N}$, is defined as follows:

$$\eta_{i,th-N} = \frac{\dot{Q}_{u,th-N}}{NA_m I(t)} = \frac{\dot{m}_f c_f}{NA_m}\left(1 - e^{-\frac{NU_{Lm}A_m}{\dot{m}_f c_f}}\right)\left[\frac{(\alpha\tau)_{m-eff}}{U_{Lm}} - \frac{(T_{fi} - T_a)}{I(t)}\right]$$

or,

$$\eta_{i,th-N} = F_{RN}\left[(\alpha\tau)_{m-eff} - U_{Lm}\frac{(T_{fi} - T_a)}{I(t)}\right] \quad \ldots(27c)$$

where

$$F_{RN} = \frac{\dot{m}_f c_f}{NA_m U_{Lm}}\left(1 - e^{-\frac{NU_{Lm}A_m}{\dot{m}_f c_f}}\right)$$

Here, N=1 Eq. 27c is exactly the same as Eq. 17d.

Eq. 27c is the improved characteristic equation for the N-PVT_TEC air collector, derived for the first time, and it is similar to those derived by Hottel-Whillier-Bliss (HWB) for the flat plate collector (Duffie & Beckman W. A., 2013; Tiwari et al., 2016).

With reference to (Bejan, 1978; Cengel & Boles, 2015; Ouyang & Li, 2016), the exergy of hourly thermal energy$\dot{E}x_{u,th-N}$ (high-grade energy) obtained from the N-opaque PV-TEC air collector can be calculated through the following expression:

$$\dot{E}x_{u,th-N} = \dot{m}_f c_f \left[(T_{foN} - T_{fi}) - (T_a + 273) ln \frac{(T_{foN} + 273)}{(T_{fi} + 273)}\right] \quad \ldots(28)$$

From Eqs. 25b and 28, the overall hourly exergy, $\dot{E}x_{ou-N}$ of the N-opaque PV-TEC air collectors is written as:

$$\dot{E}x_{ou-N} = \dot{E}_{el-N} + \dot{E}x_{u,th-N} \quad \ldots(29)$$

The overall hourly instantaneous exergy efficiency,$\eta_{i,ov-ex}$,$\dot{E}x_{ou}$ of N-opaque PV-TEC air collectors is written as:

$$\eta_{i,ov-ex-N} = \frac{\dot{E}x_{ou-N}}{NA_M I(t)} \quad \ldots(30)$$

Here, N varies from 1 to N=12

Of note, the packing factor of the TEC module is taken as unity ($\beta_{tec} = 1$) in the numerical calculations for the N- opaque PV-TEC air collector.

4 METHODOLOGY FOR NUMERICAL COMPUTATION

The following methodology is developed:

Step 1: The input design and climatic parameters presented in Table 1 and Figure 3 are considered.

Step 2: First, the hourly variation of average fluid ($\bar{T}_{f,n^{th}}$) is determined according to Eq. 18 with help of Eq. 17 and then, the average solar cell ($\bar{T}_{sc,n^{th}}$), TEC top ($\bar{T}_{tec,top,n^{th}}$), and TEC bottom ($\bar{T}_{tec,bottom,n^{th}}$) are calculated using Eq. 19, Eq. 20, and Eq. 21, respectively, at the 12th air collector.

Step 3: Upon determining the hourly variation of average solar cell temperature ($\bar{T}_{sc}$), as outlined in Step 2, electrical

efficiency ($\eta_{i,el,n^{th}}$) at 1st, 3rd, 5th, 7th, 9th, and 12th PVT-TEC air collectors is evaluated.

Step 4: After determining average solar cell($\bar{T}_{sc,n^{th}}$)using Eq. 19, TEC top($\bar{T}_{tec,top,n^{th}}$) using Eq. 20, and TEC bottom($\bar{T}_{tec,bottom,n^{th}}$) using Eq.21 at 12th air collector from Step 2, the hourly variations of electrical energy from PV module ($\dot{E}_{PV,n^{th}}$) using Eq. 23 and TEC ($\dot{E}_{TEC,n^{th}}$) using Eq. 24 at 1st, 3rd, 5th, 7th, 9th, and 12th PVT-TEC air collectors are calculated.

Step 5: Hourly variation of total electrical energy($\dot{E}_{el,n^{th}}$) is calculated using Eq. 25a, which is the sum of electrical energy from PV and TEC, as outlined in Step 4, at the 1st, 3rd, 5th, 7th, 9th, and 12th PVT-TEC air collectors.

Step 6: Eq. 28 is used to compute hourly variation of the overall hourly exergy, $\dot{E}x_{ou}$ of N-opaque PV-TEC air collector at the 1st, 3rd, 5th, 7th, 9th, and 12th PVT-TEC air collectors.

Step 7: Variations of the instantaneous thermal efficiency ($\eta_{i,n^{th}}$) using Eq. 16c and total electrical efficiency ($\eta_{i,el,n^{th}}$) using Eq. 26 with $\frac{(T_{fi}-T_a)}{I(t)}$ are determined at the 1st, 3rd, 5th, 7th, 9th, and 12th PVT-TEC air collectors.

Step 8: Hourly variation of total exergy, Eq. 29 and its efficiency, Eq. 30 for N= 1.3.5.7.9 and 12 are calculated.

Step 9: Finally, the impacts of TEC packing factor β_{tec} (0,0.5 and 1) on the hourly variation of total exergy, Eq. 28, and efficiency, Eq. 30, for N= 7 are evaluated.

Step 10: Results for $T_{tec\text{-}bottom}$ are compared with the experimental findings of Dimri N. et al. (Dimri et al., 2018) to validate the viability of the proposed model, as shown in Figure 12

5 RESULTS AND DISCUSSION

The hourly variation of average fluid(T¯_(f,n^th)), solar cell(T¯_(sc,n^th)), TEC top(T¯_(tec,top,n^th)), and TEC bottom (T¯_(tec,bottom,n^th)) at the 2nd and 12th air collectors for design parameters given in Table 1 and climatic parameters given in Figure 3 are shown in Figure 4. Of note, the average solar cell temperature, T¯_(sc,n^th), is maximum at the 2nd PVT-TEC air collector and minimum at the 12nd PVT-TEC air collector. This indicates that inlet temperature of PVT-TEC in a series connection plays a notable role to determine thermal energy, electrical energy from PV module, and TEC of PVT-TEC air collector. This trend occurs after the 4th PVT-TEC air collector. Such observations have not been yet reported. It is further clear that solar cell temperature is maximum and the bottom of TEC material is minimum at the 12th PVT=TEC air collector (Figure 4b), compared to the 2nd PVT-TEC air collector (Figure 4a). In this case, electrical power from (i) solar cell, which depends only on solar cell temperature [Eq. 22], and (ii) TEC, which depends on difference of top and bottom temperatures, will be produced [Eq. 24]. Further, the temperature of the top surface of TEC is higher than the bottom temperature of TEC, as shown in all the nth PVT-TEC air collectors in Figure 4.

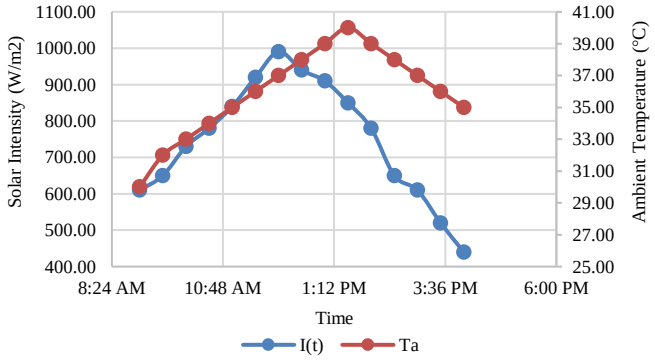

Figure 3. Hourly variation of solar intensity and ambient air temperature for a typical day of summer climatic conditions

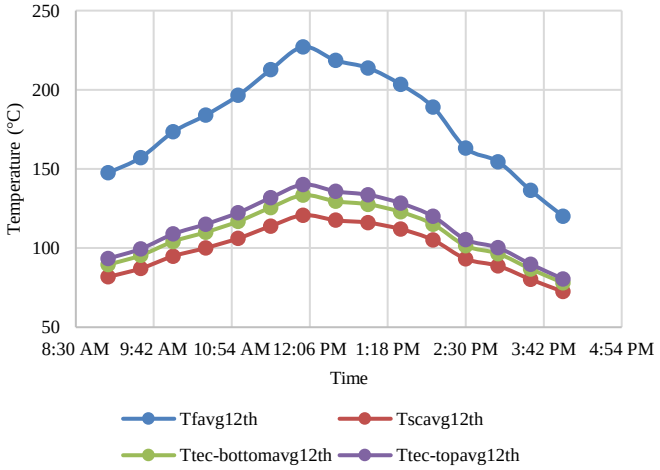

Figure 4a Hourly variation of average fluid($\bar{T}_{f,n^{th}}$) (Eq. 18), solar cell($\bar{T}_{sc,n^{th}}$) (Eq. 19), TEC top($\bar{T}_{tec,top,n^{th}}$) (Eq. 20), and TEC bottom($\bar{T}_{tec,bottom,n^{th}}$) (Eq.19) at the 12th air collector for $n^{th} = 2$ and $n < 4$

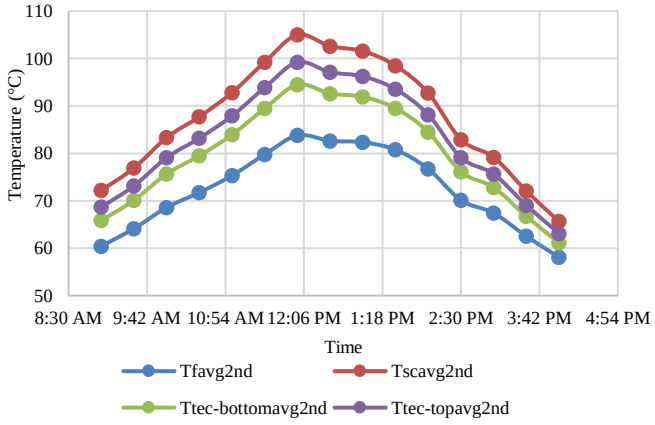

Figure 4b. Hourly variation of average fluid ($\bar{T}_{f,n^{th}}$) (Eq. 18), solar cell ($\bar{T}_{sc,n^{th}}$) (Eq. 19), TEC top ($\bar{T}_{tec,top,n^{th}}$) (Eq. 20), and TEC bottom ($\bar{T}_{tec,bottom,n^{th}}$) (Eq.21) at the 12th air collector

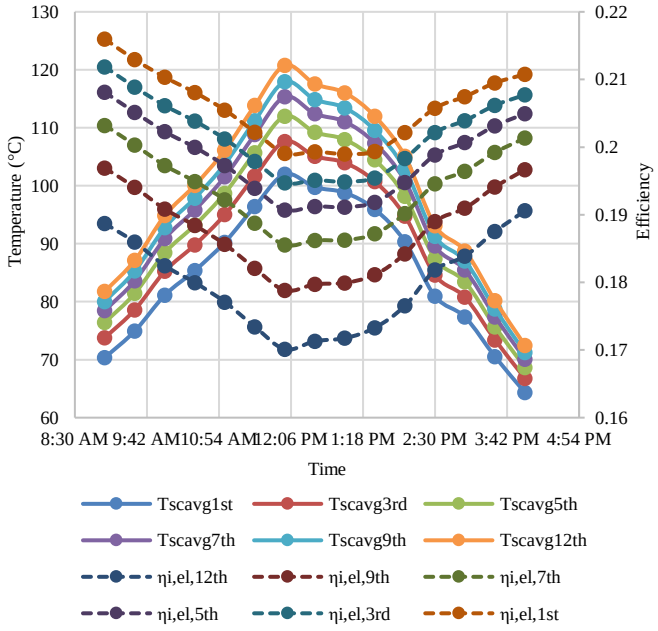

Figure 5. Hourly variation of average solar cell temperature($\bar{T}_{sc,n^{th}}$) ($Eq.19$) and electrical efficiency ($\eta_{i,el,n^{th}}$) (Eq. 22) at the 1st, 3rd, 5th, 7th, 9th, and 12th PVT-TEC air collectors

Figure 5 shows the hourly variation of average solar cell temperature($\bar{T}_{sc,n^{th}}$), Eq. 19, and electrical efficiency ($\eta_{i,el,n^{th}}$), Eq. 22, at the 1st, 3rd, 5th, 7th, 9th and 12th PVT-TEC air collectors. One can infer from Figure 5 that as the value of n in the nth PVT-TEC air collector increases, the average solar cell temperature($\bar{T}_{sc}$) increases, but increment in the average solar cell temperature($\bar{T}_{sc}$) slows down, especially after the 5thPVT-TEC air collector. Further, the electrical efficiency ($\eta_{i,el,n^{th}}$) decreases as the value of n in the nth PVT-TEC air collector increases due to the higher operating temperature per expectation. In this case, the decrement in electrical efficiency ($\eta_{i,el,n^{th}}$) is observed after the 5th PVT-TEC air collector. Therefore, it can be stated that the number of optimum PVT-TEC air collectors is five for design parameters shown in Table 1.

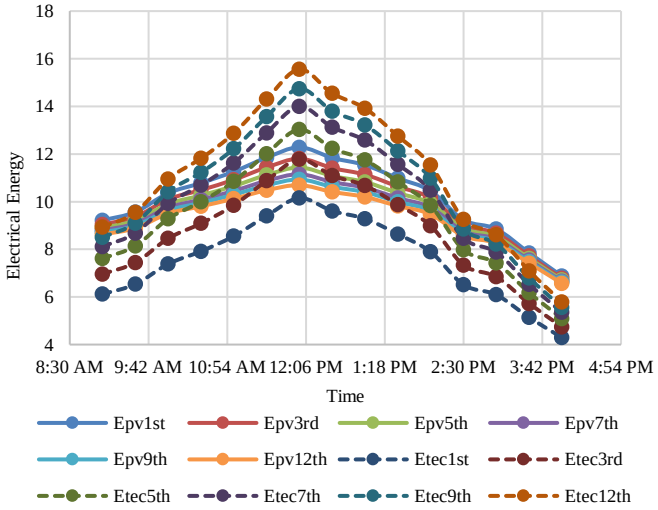

Figure 6a. Hourly variation of electrical energy from PV module ($\dot{E}_{PV,n^{th}}$), Eq. 23, and TEC ($\dot{E}_{TEC,n^{th}}$), Eq. 24, at the 1st, 3rd, 5th, 7th, 9th, and 12th PVT-TEC air collectors

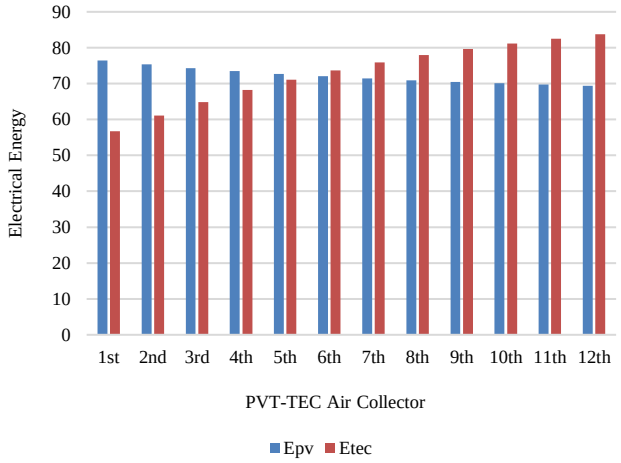

Figure 6b. Daily electrical energy from Opaque PV and TEC for different nth PV-TEC air collectors

Now, Figure 6a shows the hourly variation of electrical energy in W from PV module ($\dot{E}_{PV,n^{th}}$), Eq. 23, and electrical energy from TEC ($\dot{E}_{TEC,n^{th}}$), Eq. 24, from the 1st to 12th PVT-TEC air collectors. Figure 6b shows the daily electrical energy from PV and TEC for different nth PVT-TEC air collectors. It is noteworthy that the hourly and daily electrical energy from PV decreases with an increase in the number of nth PVT-TEC air collectors due to high thermal losses, as illustrated in Figure 5. However, the hourly and daily electrical energy from TEC increases because it depends on the difference in temperature between the top and bottom of the TEC, as shown in Figure 6. This difference increases as the number of the nth PVT-TEC increases. Therefore, in this case, the nth PVT-TEC air collector must be optimized for maximum electrical energy from PV as well as TEC. Further, one can conclude that both electrical energies from PV as well as TEC are approximately the same at the 5th PVT-TEC air collector.

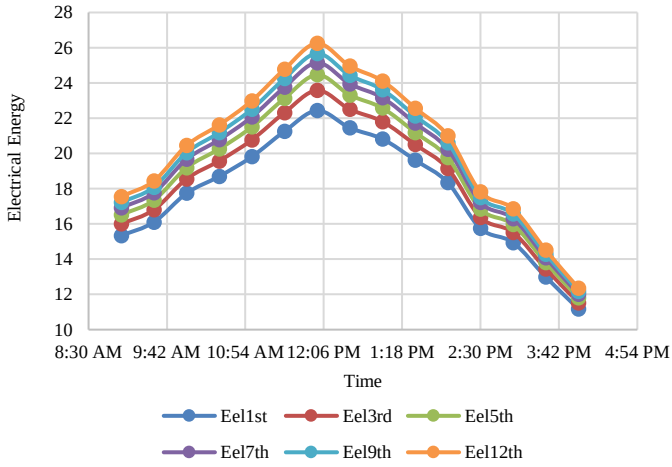

Figure 7. Hourly variation of total electrical energy($\dot{E}_{el,n^{th}}$), Eq. 23a at 1st, 3rd, 5th, 7th, 9th and 12th PVT-TEC air collector

In order to observe the hourly variation of total electrical energy in W for different nth PVT-TEC air collectors, Figure 7 is generated. It can be observed that the total electrical energy increases with an increase in the number of nth PVT-TEC air

collectors, unlike electrical energy from photo-voltaic module. In this case, increment in the total electrical energy is also reduced after the 5th PVT-TEC air collector and one can observe that the 5th PVT-TEC air collector is again optimum for given design parameters presented in Table 1. This optimization is only conducted from electrical energy point of view.

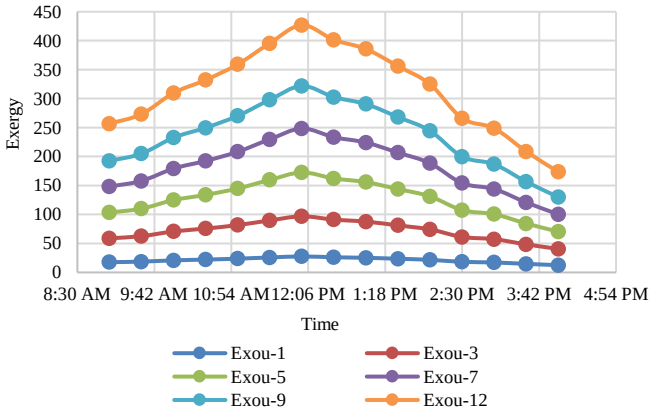

Figure 8. Hourly variation of the overall hourly thermal exergy, $\dot{E}x_{ou-N}$, Eq. 29, of N-opaque PV-TEC air collector at the 1st, 3rd, 5th, 7th, 9th, and 12th PVT-TEC air collectors

The hourly variations of the overall hourly exergy, $\dot{E}x_{ou-N}$, of the opaque PV-TEC air collector, Eq. 27, at the 1st, 3rd, 5th, 7th, 9th, and 12th PVT-TEC air collectors are shown in Figure 8. This figure illustrates that the overall exergy of the system increases with an increase in the number of nth PVT-TEC air collectors. However, the increment in the exergy becomes less significant compared to the total electrical energy, which is shown in Figure 7. Hence, the optimization of PVT air collector with respect to the overall thermal exergy is different from the earlier one, i.e., with respect to electrical energy (Figure 7).

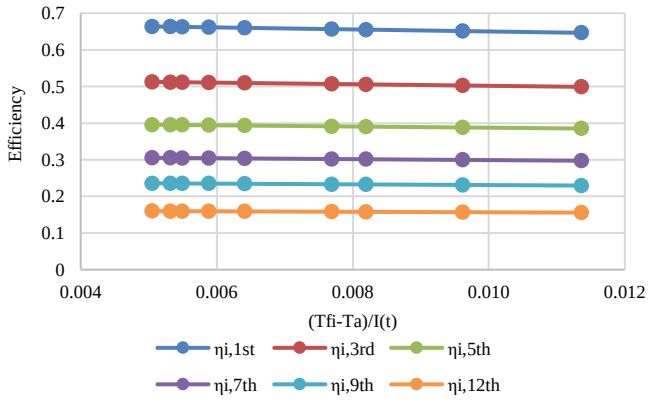

Figure 9a. Variation of instantaneous thermal efficiency $(\eta_{i,n^{th}})$ Eq. 17c with $\frac{(T_{fi}-T_a)}{I(t)}$ at the 1st, 3rd, 5th, 7th, 9th, and 12th PVT-TEC air collectors

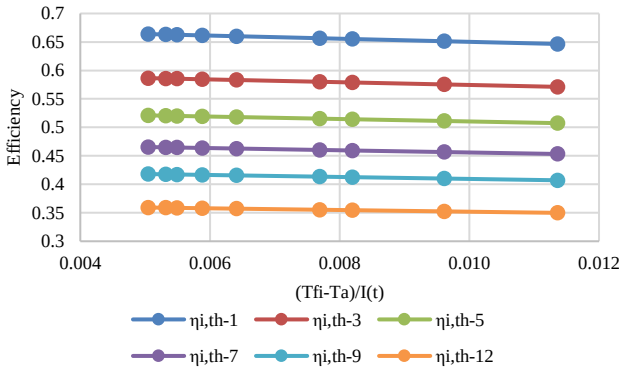

Figure 9b. Variation of instantaneous thermal efficiency $(\eta_{i,th-N})$ Eq. 27c with $\frac{(T_{fi}-T_a)}{I(t)}$ for N =1,3,5,7, 9, and 12 PVT-TEC air collectors

Figures 9a and 9b show the thermal characteristic curves for the nth and N PVT-TEC air collectors, respectively, which were drawn using Eqs. 17c and 27c. It can be observed that as n and N increase, the instantaneous thermal efficiency decreases due to an increase in operating temperature, resulting in higher thermal energy losses, as expected. It was also noted that the variation in both cases is marginal, possibly due to the considered mass flow rate of 0.003 kg/s as shown in Table 1. However, for n=N=1, the instantaneous thermal efficiency is approximately the same, but for higher values of n and N, the instantaneous efficiency is higher for the N case. This is due to the fact that the total thermal energy in this case becomes higher.

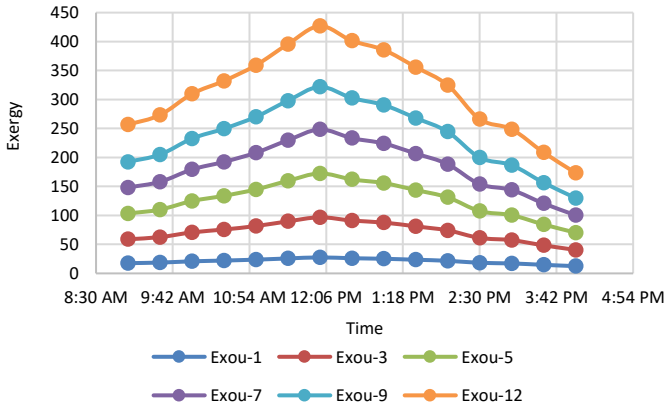

Figure 10a. Hourly variation of total exergy, Eq. 29, for N= 1.3.5.7.9, and 12

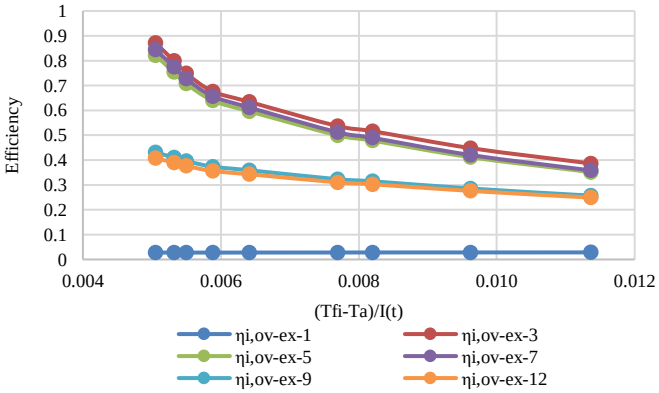

Figure 10b. Variation of the overall exergy efficiency, Eq. 30, and $\frac{(T_{fi}-T_a)}{I(t)}$.

The hourly variation of the total exergy in watts and exergy efficiency in fractions for N = 1, 3, 5, 7, 9, and 12 PVT-TEC air collectors is shown in Figure 10. It can be observed that electrical energy does not play a significant role in comparison to overall thermal exergy, as shown in Figure 7, due to its smaller value. Therefore, the exergy characteristic curve has a higher numerical value and variation in comparison to the thermal characteristic curve, as depicted in Figure 9. Furthermore, the exergy efficiency curve also increases up to the 5th PVT-TEC air collector and then begins to decrease. Hence, it can be concluded that the optimum value of n is five.

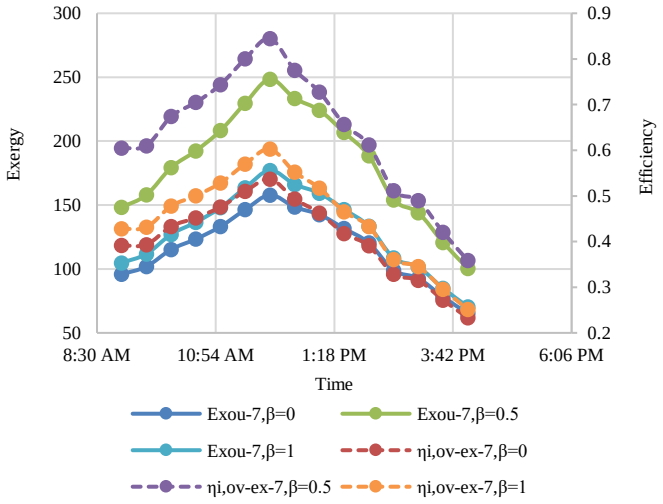

Figure 11. Effect of TEC packing factor β_{tec} (0,0.5 and 1) on the hourly variation of the total exergy (Eq. 29) and efficiency (Eq. 30) for N= 7

The effect of TEC packing factor β_{tec} on the hourly variation of total exergy for N=7 has been plotted in Figure11, considering β_tec values ranging from 0 to 1 (i.e., 0, 0.5, and 1). The results indicate that the hourly exergy is maximum for a packing factor of 0.5. Therefore, it can be concluded that the optimum value of the TEC packing factor in the case of PVT-TEC air collectors is 0.5. In this case, the temperature of the PV module and the temperature difference between the top and bottom of the TEC will determine the maximum electrical energy that can be obtained from the TEC.

6 EXPERIMENTAL VALIDATION

Equation 7 aims to ensure the experimental validation of $T_{tec,bottom}$ for the 1st PVT-TEC air collector based on the design and climatic parameters derived from the study of Dimri et. al. (Dimri et al., 2018). The hourly variation in the bottom temperature of TEC is shown in Figure 12 along with the experimental hourly variation obtained from Dimri et al. (Dimri et al., 2018). One can infer that there is reasonable agreement between theoretical results obtained by the present model and experimental value of Dimri et al. (Dimri et al., 2018). Accordingly, other hourly temperature variations can be validated by using the present model.

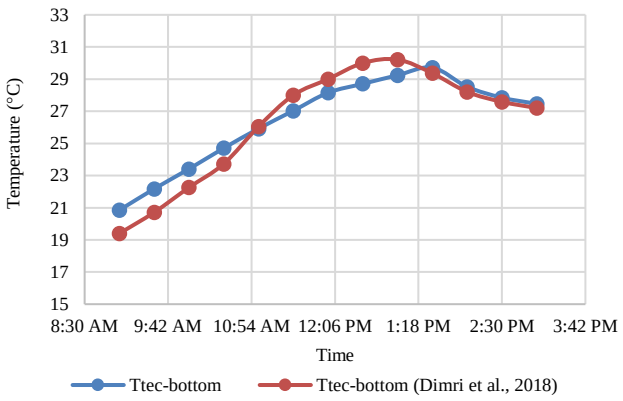

Figure 12. Comparison between the results for $T_{tec\text{-}bottom}$ and the experimental studies (Dimri et al., 2018)

7 CONCLUSIONS

Based on the present study on the N-PVT-TEC air collectors connected in series, the following conclusions were drawn:

(a) The trend in hourly variation of average solar cell temperature ($\bar{T}_{sc,n^{th}}$) and air fluid temperature changed after the 4th PVT-TEC air collector, ($\bar{T}_{f,n^{th}}$), while the trends in the top and bottom temperatures of TEC remained the same, as shown in Figure 4.
(b) The daily electrical energy from PV module decreased following an increase in the number of the nth PVT-TEC air collectors, unlike while electrical power from TEC, as shown in Figure 6b
(c) The optimum number of PVT-TEC air collectors was found to be five for the design parameters given in Table 1.
(d) The optimum packing factor of TEC was determined as 0.5 for maximum exergy and its efficiency, as given in Figure 11.

8 ACKNOWLDGEMENT

We would like to express our gratitude to Dr. M. S. Sodha for inspiring us in our research. Additionally, we extend our thanks to Dr. Neha Dimri and Dr. Arvind Tiwari for providing us with their research data, which we used to simulate our results.

APPENDIX A

The following relations are used in thermal modeling of opaque photovoltaic integrated thermoelectric cooler (PV-TEC) collector.

$$(\alpha\tau)_{eff} = \tau_g(\alpha_{sc} - \eta_{sc})$$

$$(\alpha\tau)'_{eff} = (1 - \eta_{tec})h_{p1}h_{p2}(\alpha\tau)_{eff}$$

$$U_{t,c-a} = \left[\frac{L_g}{K_g} + \frac{1}{h_o}\right]^{-1}$$

$$h_o = 5.7 + 3.8V$$

$$h_t = \frac{K_t}{L_t}$$

$$U_{b,c-a} = \left[\frac{L_t}{K_t} + \frac{1}{h_i}\right]^{-1}$$

$$h_i = 2.8 + 3V; V = 1m/s$$

$$h_{p1} = \frac{h_t\beta_{tec}}{U_{t,c-a} + U_{b,c-a}(1-\beta_{tec}) + h_t\beta_{tec}}$$

$$U_{tec,top-a} = \frac{h_t\beta_{tec}U_{t,c-a}}{U_{t,c-a} + U_{b,c-a}(1-\beta_{tec}) + h_t\beta_{tec}}$$

$$U_{tec,top-f} = \frac{h_t\beta_{tec}U_{b,c-a}(1-\beta_{tec})}{U_{t,c-a} + U_{b,c-a}(1-\beta_{tec}) + h_t\beta_{tec}}$$

$$h_{p2} = \frac{U_{tec}\beta_{tec}}{U_{tec,top-a} + U_{tec,top-f} + U_{tec}\beta_{tec}}$$

$$U_{tec,bottom-a} = \frac{U_{tec}\beta_{tec}U_{tec,top-a}}{U_{tec,top-a} + U_{tec,top-f} + U_{tec}\beta_{tec}}$$

$$U_{tec,bottom-f} = \frac{U_{tec}\beta_{tec}U_{tec,top-f}}{U_{tec,top-a} + U_{tec,top-f} + U_{tec}\beta_{tec}}$$

The heat transfer coefficient from the bottom-end of TEC module to fluid (h_{tf}) flowing below it, considering laminar flow, is calculated as:

$$h_{tf} = \frac{K_f}{L}Nu = \frac{K_f}{L} \times (0.332)Re^{\frac{1}{2}}Pr^{\frac{1}{3}} = \frac{0.02622}{0.37} \times (0.332) \times (1.10846 \times 10^4)^{\frac{1}{2}}0.708^{\frac{1}{3}} = 2.21W/m^2K$$

where Nu is Nusselt number, Pr is Prandtl number, and Re is Reynold number. Reynold number (Re) is obtained as follows:

$$Re = \frac{VL}{\nu} = \frac{\dot{m}_f L}{bL_f\rho\nu} = \frac{0.003 \times 0.37}{0.36 \times 0.01 \times 1.774 \times (15.68 \times 10^{-6})} = 1.10846 \times 10^4$$

The constants used in Eqs. are defined as:

$$U_b = \left[\frac{L_i}{K_i} + \frac{1}{h_i}\right]^{-1}$$

$$U_{fa} = U_{fa,1} + U_{fa,2} + U_{fa,3} + U_{fa,4}$$

$$U_{fa,1} = \frac{h_{tf}\beta_{tec}(1-\eta_{tec})U_{tec,bottom-a}}{h_{tf}\beta_{tec} + (1-\eta_{tec})U_{tec,bottom-a} + (1-\eta_{tec})U_{tec,bottom-f}}$$

$$U_{fa,2} = \frac{U_{t,c-a}U_{b,c-a}(1-\beta_{tec})}{U_{t,c-a} + U_{b,c-a}(1-\beta_{tec}) + h_t\beta_{tec}}$$

$$U_{fa,3} = \frac{h_t\beta_{tec}U_{b,c-a}(1-\beta_{tec})U_{tec,top-a}}{\left[U_{t,c-a} + U_{b,c-a}(1-\beta_{tec}) + h_t\beta_{tec}\right]\left[U_{tec,top-a} + U_{tec,top-f} + U_{tec}\beta_{tec}\right]}$$

$$U_{fa,4} = \frac{h_t\beta_{tec}U_{b,c-a}(1-\beta_{tec})U_{tec}\beta_{tec}(1-\eta_{tec})U_{tec,bottom-a}}{\left[U_{t,c-a} + U_{b,c-a}(1-\beta_{tec}) + h_t\beta_{tec}\right]\left[U_{tec,top-a} + U_{tec,top-f} + U_{tec}\beta_{tec}\right]\left[h_{tf}\beta_{tec} + (1-\eta_{tec})U_{tec,bottom-a} + (1-\eta_{tec})U_{tec,bottom-f}\right]}$$

$$h_{p3} = \frac{h_{tf}\beta_{tec}}{h_{tf}\beta_{tec} + (1-\eta_{tec})U_{tec,bottom-a} + (1-\eta_{tec})U_{tec,bottom-f}}$$

$$h'_{p1} = \frac{U_{b,c-a}(1-\beta_{tec})}{U_{t,c-a} + U_{b,c-a}(1-\beta_{tec}) + h_t\beta_{tec}}$$

$$h'_{p2} = \frac{h_t\beta_{tec}U_{b,c-a}(1-\beta_{tec})}{\left[U_{t,c-a} + U_{b,c-a}(1-\beta_{tec}) + h_t\beta_{tec}\right]\left[U_{tec,top-a} + U_{tec,top-f} + U_{tec}\beta_{tec}\right]}$$

$$h'_{p3} = \frac{h_t\beta_{tec}U_{b,c-a}(1-\beta_{tec})U_{tec}\beta_{tec}}{\left[U_{t,c-a} + U_{b,c-a}(1-\beta_{tec}) + h_t\beta_{tec}\right]\left[U_{tec,top-a} + U_{tec,top-f} + U_{tec}\beta_{tec}\right]\left[h_{tf}\beta_{tec} + (1-\eta_{tec})U_{tec,bottom-a} + (1-\eta_{tec})U_{tec,bottom-f}\right]}$$

NOMENCLATURE

A_m	Aea of module (m^2)
L	Length of collector (m)
b	Breadth of collector (m)
c_f	Specific heat of fluid (J/kgK)
dx	Elemental length (m)
I(t)	Global solar radiation (W/m^2)
mi	Mass flow rate of fluid (kg/s)
K_g	Thermal conductivity of glass (W/mK)
K_t	Thermal conductivity of tedlar (W/mK)
K_{tec}	Thermal conductivity of TEC module (W/mK)
K_i	Thermal conductivity of insulation (W/mK)
K_f	Thermal conductivity of fluid/air (W/mK)
L_g	Thickness of glass cover (m)
L_t	Thickness of tedlar (m)
L_{tec}	Thickness of TEC module (m)
L_i	Thickness of insulation (m)
L_f	Thickness of fluid/air column in the duct (m)
h_t	heat transfer coefficient from back of solar cells to the top end of TEC module (W/m^2K)
h_{tf}	Heat transfer coefficient from the bottom-end of TEC module to fluid (W/m^2K)
$U_{t,c-a}$	Overall heat transfer coefficient from top of solar cells to ambient through glass cover (W/m^2K)
U_b	Overall heat transfer coefficient from bottom of insulation to ambient (W/m^2K)
$U_{tec,top-a}$	Overall heat transfer coefficient from top-end of TEC module to ambient (W/m^2K)
$U_{tec,bottom-a}$	Overall heat transfer coefficient from bottom-end of TEC module to ambient (W/m^2K)
$U_{tec,top-f}$	Overall heat transfer coefficient from top-end of TEC module to fluid (W/m^2K)

$U_{tec,bottom-f}$	Overall heat transfer coefficient from bottom-end of TEC module to fluid (W/m^{2}K)
U_{fa}	Overall heat transfer coefficient from fluid to ambient (W/m^{2}K)
$U_{b,c-a}$	Overall heat transfer coefficient from bottom of solar cells to ambient through tedlar (W/m^{2}K)
h_{p1}	First penalty factor due to glass cover
h_{p2}	Second penalty factor due to tedlar
h_{p3}	Third penalty factor due to TEC module
η_o	Solar cell efficiency at standard test condition, i.e. I(t)=1000 W/m^2 and To=25°C
η_{tec}	Conversion efficiency from thermal energy to electricalenergy of TEC module
β_o	Temperature coefficient of solar cell efficiency (K−1)

Greek letters

α	Absorptivity
β	Packing factor
τ	Transmittivity
η	Efficiency
$(\alpha\tau)_{eff}$	Product of effective absorptivity and transmittivity

Subscripts

a	Ambient
eff	Effective
f	Fluid
fi	Fluid inlet
fo	Fluid outlet
g	Glass
m	Module
sc	Solar cell
tec	TEC module
t	Tedlar
i	Insulation

REFERENCES

1. Arslan, E., Aktaş, M., & Can, Ö. F. (2020). Experimental and numerical investigation of a novel photovoltaic thermal (PV/T) collector with the energy and exergy analysis. *Journal of Cleaner Production*, *276*, 123255. https://doi.org/10.1016/j.jclepro.2020.123255
2. Atheaya, D., Tiwari, A., & Tiwari, G. N. (2016). Exergy analysis of photovoltaic thermal (PVT) compound parabolic concentrator (CPC) for constant collection temperature mode. *Solar Energy*, *135*, 222–231. https://doi.org/10.1016/j.solener.2016.05.055
3. Badiei, Z., Eslami, M., & Jafarpur, K. (2020). Performance improvements in solar flat plate collectors by integrating with phase change materials and fins: A CFD modeling. *Energy*, *192*. https://doi.org/10.1016/j.energy.2019.116719
4. Bejan, A. (1978). General criterion for rating heat-exchanger performance. *International Journal of Heat and Mass Transfer*, *21*(5), 655–658. https://doi.org/10.1016/0017-9310(78)90064-9
5. Cabral, D., Gomes, J., & Karlsson, B. (2019). Performance evaluation of non-uniform illumination on a transverse bifacial PVT receiver in combination with a CPC geometry. *Solar Energy*, *194*, 696–708. https://doi.org/10.1016/j.solener.2019.10.069
6. Cengel, Y. A., & Boles, M. A. (2015). *Thermodynamics: An Engineering Approach*. McGraw- Hill Education, New York. https://www.mheducation.com/highered/product/thermodynamics-engineering-approach-cengel-boles/M9781259822674.html
7. Chow, T. T. (2010). A review on photovoltaic / thermal hybrid solar technology. *Applied Energy*, *87*(2), 365–379. https://doi.org/10.1016/j.apenergy.2009.06.037
8. Dimri, N., Tiwari, A., & Tiwari, G. N. (2018). Effect of thermoelectric cooler (TEC) integrated at the base of opaque photovoltaic (PV) module to enhance an overall electrical efficiency. *Solar Energy*, *166*(November 2017), 159–170. https://doi.org/10.1016/j.solener.2018.03.030
9. Dincer, I. (2002). The role of exergy in energy policy making. *Energy Policy*, *30*(2), 137–149. https://doi.org/10.1016/S0301-4215(01)00079-9
10. Dincer, I., & Rosen, M. A. (2013). Chapter 2 - Exergy and Energy Analyses. In I. Dincer & M. A. Rosen (Eds.), *Exergy (Second Edition)* (Second Edition, pp. 21–30). Elsevier. https://doi.org/10.1016/B978-0-08-097089-9.00002-4
11. Dubey, S., & Tiwari, G. N. (2008). *Thermal modeling of a combined system of photovoltaic thermal (PV / T) solar water heater*. *82*, 602–612. https://doi.org/10.1016/j.solener.2008.02.005
12. Duffie, J. A., & Beckman W. A. (2013). *Solar Engineering of Thermal Processes*. John Wiley & Sons, Inc. https://doi.org/10.1002/9781118671603
13. Dupeyrat, P., Ménézo, C., & Fortuin, S. (2014). Study of the thermal and electrical performances of PVT solar hot water system. *Energy and Buildings*, *68*, 751–755. https://doi.org/10.1016/j.enbuild.2012.09.032
14. Evans, D. L. (1981). Simplified method for predicting photovoltaic array output. *Solar Energy*, *27*(6), 555–560. https://doi.org/10.1016/0038-092X(81)90051-7
15. Hocine, H. B. C. El, Touafek, K., Kerrour, F., Haloui, H., & Khelifa, A. (2015). Model Validation of an Empirical Photovoltaic Thermal (PV/T) Collector. *Energy Procedia*, *74*, 1090–1099. https://doi.org/10.1016/J.EGYPRO.2015.07.749
16. Hoseinzadeh, S., Ghasemi, M. H., & Heyns, S. (2020). Application of hybrid systems in solution of low power generation at hot seasons for micro hydro systems. *Renewable Energy*, *160*, 323–332. https://doi.org/10.1016/j.renene.2020.06.149
17. Hoseinzadeh, S., & Heyns, P. S. (2020). Advanced Energy, Exergy, and Environmental (3E) Analyses and Optimization of a Coal-Fired 400 MW Thermal Power Plant. *J. Energy Resour. Technol.*, *143*(8), 082106 (9 pages). https://doi.org/10.1115/1.4048982
18. Hoseinzadeh, S., Yargholi, R., Kariman, H., & Heyns, P. S. (2020). Exergoeconomic analysis and optimization of reverse osmosis desalination integrated with geothermal energy. *Environmental Progress and Sustainable Energy*, *39*(5). https://doi.org/10.1002/ep.13405
19. Huen, P., & Daoud, W. A. (2017). Advances in hybrid solar photovoltaic and thermoelectric generators. *Renewable and Sustainable Energy Reviews*, *72*(October), 1295–1302. https://doi.org/10.1016/j.rser.2016.10.042
20. Jafari, S., Sohani, A., Hoseinzadeh, S., & Pourfayaz, F. (2022). The 3E Optimal Location Assessment of Flat-Plate Solar Collectors for Domestic Applications in Iran. *Energies*, *15*(10), 1–17. https://doi.org/10.3390/en15103589
21. Kariman, H., Hoseinzadeh, S., & Heyns, P. S. (2019). Energetic and exergetic analysis of evaporation desalination system integrated with mechanical vapor recompression circulation. *Case Studies in Thermal Engineering*, *16*, 100548. https://doi.org/10.1016/J.CSITE.2019.100548
22. Kariman, H., Hoseinzadeh, S., Heyns, S., & Sohani, A. (2020). Modeling and exergy analysis of domestic med desalination with brine tank. *Desalination and Water Treatment*, *197*, 1–13. https://doi.org/10.5004/dwt.2020.26105
23. Kostić, L. T., Pavlović, T. M., & Pavlović, Z. T. (2010). Optimal design of orientation of PV/T collector with reflectors. *Applied Energy*, *87*(10), 3023–3029. https://doi.org/10.1016/j.apenergy.2010.02.015
24. Kotb, A., Elsheniti, M. B., & Elsamni, O. A. (2019). Optimum number and arrangement of evacuated-tube solar collectors under various operating conditions. *Energy Conversion and Management*, *199*(September), 112032. https://doi.org/10.1016/j.enconman.2019.112032
25. Li, M., Zhong, D., Ma, T., Kazemian, A., & Gu, W. (2020). Photovoltaic thermal module and solar thermal collector connected in series: Energy and exergy analysis. *Energy Conversion and Management*, *206*(November 2019), 112479. https://doi.org/10.1016/j.enconman.2020.112479
26. Ma, T., Li, M., & Kazemian, A. (2020). Photovoltaic thermal module and solar thermal collector connected in series to produce electricity and high-grade heat simultaneously. *Applied Energy*, *261*(October 2019), 114380. https://doi.org/10.1016/j.apenergy.2019.114380
27. Ong, K. S., Naghavi, M. S., & Lim, C. (2017). Thermal and electrical performance of a hybrid design of a solar-thermoelectric system. *Energy Conversion and Management*, *133*, 31–40. https://doi.org/10.1016/j.enconman.2016.11.052
28. Ouyang, Z., & Li, D. (2016). Modelling of segmented high-performance thermoelectric generators with effects of thermal radiation, electrical and thermal contact resistances. *Scientific Reports*, *6*(April), 1–12. https://doi.org/10.1038/srep24123

29. Proell, M., Osgyan, P., Karrer, H., & Brabec, C. J. (2017). Experimental efficiency of a low concentrating CPC PVT flat plate collector. *Solar Energy*, *147*, 463–469. https://doi.org/10.1016/j.solener.2017.03.055

30. Sarwar, J., Khan, M. R., Rehan, M., Asim, M., & Kazim, A. H. (2020). Performance analysis of a flat plate collector to achieve a fixed outlet temperature under semi-arid climatic conditions. *Solar Energy*, *207*(April), 503–516. https://doi.org/10.1016/j.solener.2020.06.088

31. Sharaf, O. Z., & Orhan, M. F. (2018). Comparative thermodynamic analysis of densely-packed concentrated photovoltaic thermal (CPVT) solar collectors in thermally in-series and in-parallel receiver configurations. *Renewable Energy*, *126*, 296–321. https://doi.org/10.1016/j.renene.2018.03.026

32. Shyam, Tiwari, G. N., Fischer, O., Mishra, R. K., & Al-Helal, I. M. (2016). Performance evaluation of N -photovoltaic thermal (PVT) water collectors partially covered by photovoltaic module connected in series: An experimental study. *Solar Energy*, *134*, 302–313. https://doi.org/10.1016/j.solener.2016.05.013

33. Skoplaki, E., & Palyvos, J. A. (2009). On the temperature dependence of photovoltaic module electrical performance: A review of efficiency/power correlations. *Solar Energy*, *83*(5), 614–624. https://doi.org/10.1016/j.solener.2008.10.008

34. Sudharshan, K. Y., Kumar, V. P., & Barshilia, H. C. (2016). Performance evaluation of a thermally concentrated solar thermo-electric generator without optical concentration. *Solar Energy Materials and Solar Cells*, *157*, 93–100. https://doi.org/10.1016/j.solmat.2016.05.033

35. Tiwari, G. N., & Dubey S. (2010). Fundamentals of Photovoltaic Modules and Their Applications. *Royal Society of Chemistry (RSC), (UK)*. https://link.springer.com/book/9781849730204

36. Tiwari, G. N., Meraj, M., & Khan, M. E. (2018). Exergy analysis of N-photovoltaic thermal-compound parabolic concentrator (N-PVT-CPC) collector for constant collection temperature for vapor absorption refrigeration (VAR) system. *Solar Energy*, *173*, 1032–1042. https://doi.org/10.1016/j.solener.2018.08.031

37. Tiwari, G. N., Tiwari, A., & Shayam. (2016). *Handbook of solar energy*. Springer. https://doi.org/10.1007/978-981-10-0807-8

38. Vega, J., & Cuevas, C. (2020). Parallel vs series configurations in combined solar and heat pump systems: A control system analysis. *Applied Thermal Engineering*, *166*, 114650. https://doi.org/10.1016/j.applthermaleng.2019.114650

39. Yin, E., Li, Q., & Xuan, Y. (2017). Thermal resistance analysis and optimization of photovoltaic-thermoelectric hybrid system. *Energy Conversion and Management*, *143*, 188–202. https://doi.org/10.1016/j.enconman.2017.04.004

40. Zhang, J., Xuan, Y., & Yang, L. (2014). Performance estimation of photovoltaic-thermoelectric hybrid systems. *Energy*, *78*, 895–903. https://doi.org/10.1016/j.energy.2014.10.087

41. Zhu, W., Deng, Y., Wang, Y., Shen, S., & Gulfam, R. (2016). High-performance photovoltaic-thermoelectric hybrid power generation system with optimized thermal management. *Energy*, *100*, 91–101. https://doi.org/10.1016/j.energy.2016.01.055

42. Zondag, H. A., de Vries, D. W., van Helden, W. G. J., van Zolingen, R. J. C., & van Steenhoven, A. A. (2003). The yield of different combined PV-thermal collector designs. *Solar Energy*, *74*(3), 253–269. https://doi.org/10.1016/S0038-092X(03)00121-X

JREE: Vol. 10, No. 4, (Autumn 2023) 35-43

Journal of Renewable Energy and Environment

Journal Homepage: www.jree.ir

Materials and Energy Research Center

MERC

Research Article

Design, Fabrication, and Experimental Study of a Low-cost and Accurate Weather Station Using a Microcontroller System

Mahdi Pourbafrani, Hossein Ghadamian*, Meisam Moghadasi, Masoud Mardani

Department of Energy, Materials and Energy Research Center, Karaj, Iran.

PAPER INFO

Paper history:
Received: 31 January 2023
Revised: 13 March 2023
Accepted: 16 March 2023

Keywords:
Weather Station,
Anemometer,
Pyranometer,
Humidity Sensor,
Thermometer,
Microcontroller System

ABSTRACT

In this research study, a cost-effective and reliable weather station using a microcontroller system containing instruments and sensors for measuring and recording ambient variables was designed, fabricated, and tested. The dataset recorded and stored in the meteorological system can be applied to conduct various research in the field of energy and environment, especially in solar systems. Employing a microcontroller system reduces costs and provides special features such as accessing data on the web-based spreadsheets and adding control devices. In this system, meteorological information including solar radiation, air temperature, wind velocity, and air relative humidity is measured and saved in user-defined time intervals such as 30 seconds. The total cost for measuring equipment, sensors, and microcontroller along with a data logger is about 110 USD. To demonstrate the importance of using local meteorological data, in the vicinity of the case studies, the dataset provided by the local weather station was compared with the meteorological data of two nearby national stations for one month. The results revealed that the values reported by the national stations were different from the actual values measured by the local weather station. The deviations for solar radiation, wind velocity, air temperature and humidity values were at least 5, 9, 7%, and more than 100%, respectively.

https://doi.org/ 10.30501/JREE.2023.383796.1551

1. INTRODUCTION

Accurate weather data availability is vital for conducting research in the field of energy and environment and analyzing the performance of energy systems, especially renewable systems (Duffie and Beckman, 2013). For instance, one of the most significant factors in measuring the performance of a solar system is monitoring of both operating parameters and weather conditions. Also, development of energy performance indicators and energy baselines for energy management purposes requires historical data including meteorological variables (Moghadasi et al., 2021). In this regard, in most studies, national meteorological data have been applied to analyze the performance of these systems. The use of this meteorological information may cause errors in performance analysis due to possible differences between national and local data. Hence, the local weather measurements can enhance energy performance analysis. In the past, all systems for measuring ambient variables such as temperature, humidity, and wind velocity worked mechanically. Therefore, to record them, the only method was to read and record the measures manually in the specified time intervals. In previous years, by developing semiconductors, electronic circuits were used to measure meteorological parameters and display and record them digitally. The advantages of digital systems include high accuracy, fast response, automatic operation, small dimensions, long life cycles, and low price (Rafiquzzaman, 2014). In this regard, Pashchenko and Rassadin developed a microclimate weather station containing wireless sensors, a data collector, and an analytical tool in 2022. This system was part of a project to model building energy consumption. Data were collected from temperature, humidity, CO_2 concentration, and light intensity parameters in the location inside the studied building in Moscow city for the period of the Coronavirus quarantine lockdown. TD-11, Vega Smart-UM0101, ERS, and ERS CO_2 sensors were used to measure environmental parameters and the ELT-2 sensor was utilized for connecting through the LoRaWAN protocol (Pashchenko and Rassadin, 2022). Monteiro et al. built a microclimate weather station on the university campus in 2019. This research focuses on the development of a wireless network of ambient monitoring stations utilizing IoT technology to provide users with weather data for daily planning purposes. DSM501A sensor was used in the proposed device to monitor air pollution. Also, the parameters of CO, CO_2, temperature, humidity, and air pressure were measured by the system (Monteiro et al., 2019). Wang et al. investigated the performance of a microclimate monitoring system located on the SouthEast University campus with the help of long-term data from the urban weather station and EnergyPlus software tools. The results indicated that there was a significant difference between the three datasets. For example, the mean air temperatures in the microclimate station

*Corresponding Author's Email: h.ghadamian@merc.ac.ir (H. Ghadamian)
URL: https://www.jree.ir/article_169955.html

Please cite this article as: Pourbafrani, M., Ghadamian, H., Moghadasi, M. & Mardani, M. (2023). Design, Fabrication, and Experimental Study of a Low-cost and Accurate Weather Station Using a Microcontroller System. *Journal of Renewable Energy and Environment (JREE)*, 10(4), 35-43. https://doi.org/10.30501/JREE.2023.383796.1551.

were 1.2 and 2.2 ºC higher than the city climate station and EPW data (Wang et al., 2021). Moreover, Cureau et al. (2022) presented a wearable mobile system to monitor environmental parameters. BME280 sensor was used to measure the parameters of ambient temperature, humidity, and pressure, while the CV7-V sensor to measure the parameters of wind velocity and wind direction. Also, SP-510-SS, SE-421, TDS0037, PMS5003, OX-A431, NO_2-A43F, and NEO-M8 sensors were utilized to measure the parameters of solar irradiance, illuminance, CO_2 concentration, particulate matter concentrations, O_3 concentration, NO_2 concentration, and GPS unit, respectively. This system included the sensors connected to a control system that was portable and could be connected to other devices via Wi-Fi. By validating the data, it was concluded that the highest and lowest rates of measurement accuracy were assigned to the ambient temperature values and CO_2 concentration parameters with root mean square error equal to 0.46% and 49.42%, respectively (Cureau, Pigliautile and Pisello, 2022). Moghadasi et al. conducted an experimental study on a solar air heater with a specific geometry with access to data collected by a microclimate weather station, which was built and deployed at the data collection site. The parameters such as inlet and outlet temperature, radiation, wind velocity, ambient air temperature, and humidity were measured by the DS18S20, BH1750FVI, AM2302, and 652-1010 Robinson Cup type sensors, respectively (Moghadasi et al., 2022). Besides, this group used the weather station data in the development of machine learning prediction models for the purpose of optimal operation of the mentioned air heater (Moghadasi et al., 2023). Abbate et al. installed an automatic weather station connected to the network in the Alpine glacier (harsh weather conditions) in the north of Italy in 2013 (Abbate et al., 2013). Nsabagwaa et al. proposed an automatic weather station system at a low price in Uganda. The total cost of the proposed system was significantly cheaper than conventional types. The cost of the provided system was calculated as 1800 USD, while the price of conventional automatic weather station commercial data collection systems reached 7000 USD (Nsabagwa et al., 2019). In 2019, Netto and Neto designed an open-source automatic weather station to measure the effects of climate change on glaciers. They utilized a set of low-cost sensors, all of which were customized for use in natural glacier environment conditions (Netto and Arigony-Neto, 2019). Bernardes et al. (2022) introduced an affordable automatic weather station system using Commercial Off-The-Shelf and IoT technologies. A photovoltaic panel was applied to feed the system. An intelligent sensor calibration method was proposed to improve reliability (Bernardes et al., 2022).

Table 1. Detailed description of related works.

Author(s) / year	Collected parameters	Related accuracy	Main purpose of system development	Cost (USD)
Pashchenko and Rassadin / 2022	Temperature, humidity, CO_2 concentration, and light intensity	-	Building energy consumption modeling	-
Monteiro et al. / 2019	CO concentration, temperature, humidity, air pressure, and CO_2 concentration	-	Microclimate monitoring of a university campus using IoT	-
Wang et al. / 2021	Temperature, humidity, wind speed, and solar radiation	Temperature: ±0.21, humidity: ±2.5%, wind speed: ±4%, wind direction: ±5°, solar radiation: ±5%	Comparing local weather stations with meteorological and use in energy simulation	-
Cureau et al. / 2022	ambient temperature, humidity and pressure, wind velocity, wind direction, solar irradiance, illuminance, CO_2 concentration, particulate matter concentration, O_3 concentration, NO_2 concentration	Air temperature: ±1 °C, humidity: ±3%, atmospheric pressure: ±0.25%, wind direction: ±1°, solar radiation: ±5%, illuminance: ±5%, CO_2 concentration: ±2%,	Monitoring hyper-microclimate	-
Moghadasi et al. / 2022	Inlet and outlet air temperatures, radiation, wind velocity, ambient air temperature and humidity	Temperature: ±0.5°C, humidity: ±2%, solar radiation: ±2%, wind velocity: ±1%	Fabrication and testing of a new solar air heater – current present	110
Abbate et al. / 2013	Wind speed and direction, Snow height, Solar radiation, Air temp, and relative humidity	-	Installing an automatic weather station on a glacier	-
Nsabagwaa et al. / 2019	Temperature, Soil Moisture, Humidity, Wind Speed, Wind Direction, Solar Insolation, and atmospheric pressure	±0.5	Toward a robust and affordable Automatic Weather Station	1800
Netto and Neto / 2019	Atmospheric pressure, Humidity, Solar radiation, Temperature, Wind velocity, and direction	-	Investigation of effects of climate change on glaciers	202
Bernardes et al. / 2022	Wind speed and direction, Rain gauge, Temperature, pressure, and humidity	-	Natural disaster monitoring	-

According to the literature review, the high total cost of implementing local weather stations is one of the main factors that must be taken into account when considering the utilization of this system in the case study area. To solve this issue, in this research, a cost-effective weather station was designed, fabricated, and tested. The main features and advantages of the proposed system include (a) high accuracy, (b) low cost, (c) using a microcontroller system for recording and storing data, and (d) online monitoring using IoT.

2. MATERIALS AND METHODS

2.1. General Components of a Weather Station

In the analysis of the energy and environment systems, the most important meteorological parameters are solar irradiance, air temperature, wind speed, and relative humidity. In this sub-section, brief descriptions are provided in connection with common measuring equipment for monitoring these parameters.

2.1.1. Wind Speed

Anemometer instrument is employed to measure wind speed. The anemometers are divided into two categories according to the type of performance: (a) the first group measures the wind speed and (b) the other group measures wind pressure. Since the speed and pressure of the wind are related, the other can be calculated by measuring each of these two quantities. Conventional anemometers are:

(A) Cup anemometer: It is one of the most used types of anemometers. This speedometer usually has three cups at an angle of 120 degrees. The material of this blade differs from those in various models and it has several types of fiberglass, iron, aluminum, or plastic. These sensors measure the wind speed by detecting the rotation of the blade and counting the angular speed of the blade (Baseer et al., 2016).

(B) Vane anemometer: It has a propeller parallel to the vertical axis, which is connected to the speedometer. In this type, the rotation speed of the blades is converted into the equivalent wind speed and shown on the display (Pham, 2014).

(C) Ultrasonic anemometer: In this anemometer, two or three sound receivers are installed on the bowls at a perpendicular angle to each other. The electronic circuits inside the anemometer measure the difference between the round trip of the sound and convert it into the equivalent wind speed (Mustafa et al., 2016).

(D) Hot wire anemometer: In this type, the wind changes the temperature of the hot wire and the wind velocity is measured by the electric current required to keep the wire warm and exposed to the wind at a constant temperature. Figure 1 shows the types of anemometers (Ligęza, 2009).

a b c d

Figure 1. Types of Anemometer: (a) cup, (b) vane, (c) ultrasonic, (d) hot-wire.

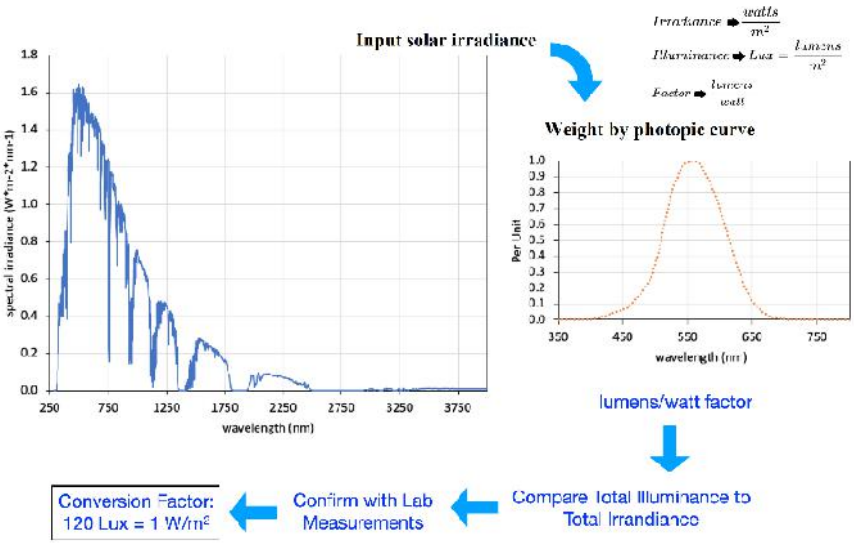

Figure 2. Stages of converting the ambient light into solar irradiance (Michael and Moreno, 2020).

2.1.2. Solar Irradiance

One of the most important meteorological parameters is solar irradiance. Pyranometers are generally employed to measure solar irradiance since they are the most accurate sensors to collect this parameter (Blum et al., 2022). Nevertheless, pyranometers are costly and their deployment throughout the territory, whether on local weather stations or specific locations, is not economically feasible. A simple and low-cost alternative way is to measure the ambient light and calculate the irradiance based on it, which is applied in this work. In 2020, Michael et al. presented a way to convert the ambient light into the amount of solar irradiance based on Figure 2. They measured ambient light and irradiance in different conditions and by comparing them, they found a linear relationship between them (Michael and Moreno, 2020).

As the main outcome, the measurement and analysis of modeling results proved that 120 lx of illumination was equal to 1 watt per square meter of solar irradiance.

2.1.3. Relative Humidity

It is possible to measure the relative humidity of the air directly with different sensors. DHT series sensors are often used in microcontroller systems. Among the features of these sensors are small size, low price, and high accuracy. In this type, relative humidity values are sent directly to the microcontroller (DHT22 technical details, 2023).

2.1.4. Air Temperature

There are different sensors to measure air temperature. The conventional and widely used sensor is a K-type thermocouple for measuring temperature. This sensor converts temperature into voltage and the microcontroller reports the measured temperature by converting this voltage into temperature (Radajewski, Decker and Krüger, 2019). The utilization of this sensor is constrained by limitations such as the length of the wire, the inability to add a wire to the sensor, and the need for regular calibration of the data logger. Another type is the digital temperature sensor that reports the temperature directly to the microcontroller and does not have the above limitations.

2.2. Design and Fabrication of the Proposed Weather Station

To use meteorological data in the analysis of the energy and environmental systems, especially solar systems, the range of changes in weather parameters have been considered according to Table 2 in the design and fabrication of the local weather station, in addition to the techno-economic criteria.

Table 2. The range of weather parameters values.

No.	Parameter	Most common natural range	Unit
1	Irradiance	0 to 1300	$W.m^{-2}$
2	Wind speed	0 to 30	$m.s^{-1}$
3	Air temperature	(-10) to (+50)	℃
4	Air humidity	10 to 100	%

2.2.1. Anemometer

By comparing four anemometer models, introduced in Subsection 2.1.1, the vane anemometer has the lowest price. Of note, this sensor must be placed perpendicular to the wind flow to measure the airspeed. Therefore, this anemometer is not suitable for continuous monitoring of the ambient wind velocity. Hence, the most suitable and economical sensor to measure this parameter is the cup anemometer. In this research, according to Figure 3a, the anemometer parts are designed by SolidWorks software (Bai et al., 2021) and made by laser cutting from the Plexiglas board following the reference sizes. Finally, they are connected together with the cups. The built anemometer is illustrated in Figure 3b.

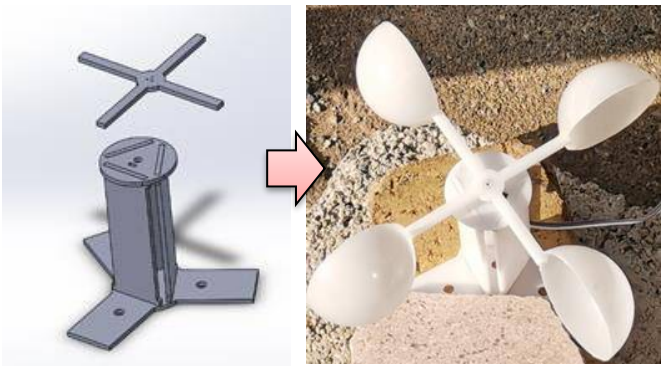

(a) (b)

Figure 3. (a) Anemometer design in SolidWorks software and (b) built anemometer.

In this anemometer, a low-mass magnet is attached to the vane. A pulse is sent to the microcontroller after each time the magnet passes in front of the Hall-effect sensor, which is installed on the body of the anemometer. In the microcontroller, the rotational speed of the anemometer is computed by calculating the time between the pulses. The wind speed calculation is as follows (Anemometer Instructions, 2005):

1- Determining the radius of rotation (r) by measuring the distance from the center of the cup to the center of rotation;
2- Obtaining the number of revolutions of the anemometer in one minute (n);
3- When one of the cups travels a full circle, it travels a distance equal to the circumference of the circle (S), which is calculated by Equation 1;

$$S = 2 \times \pi \times r \quad (1)$$

4- In the last step, the average wind speed (v) is calculated based on Equation 2 in one minute.

$$v\ (^{m}/_{s}) = \frac{n \times S}{60} \quad (2)$$

2.2.2. Digital Ambient Light Sensor

In this research, the ambient light was measured using the BH1750 sensor (refer to Figure 4.a). Then, the amount of irradiance was calculated using the linear relationship (120 lx of illumination = 1 $\frac{W}{m^2}$ of solar irradiance) (Michael and Moreno, 2020). The important specifications of the BH1750 (ROHM semiconductor Instructions, 2023) are as follows:

- Illuminance to digital converter,
- Wide range,
- Low current,
- Light noise reject function,
- 1.8V logic input interface, and
- Adjustable measurement result for the impact of optical windows.

2.2.3. Digital-output Relative Humidity Sensor

Air humidity is directly measured by the sensor DHT22 (refer to Figure 4.b). The main specifications of this sensor are (DHT22 technical specifiations, 2023):

- 3.3 V to 6 V DC,
- Digital signal via single-bus,
- Accuracy: ±2%,
- Resolution or sensitivity: 0.1%,
- Repeatability humidity: ±1%,
- Long-term stability,
- Sensing period average: two seconds, and
- Fully interchangeable property.

2.2.4. Digital-output Relative Humidity Sensor

One of the most common sensors is the DS18B20 temperature sensor (Figure 4.c), which is used in this research. This sensor measures the temperature with an accuracy rate of 0.5 °C. This sensor is advantageous as it does not require periodic calibration and has a low price, high accuracy, and suitability for long wire lengths. It also features a digital output that enables parallel connections of multiple sensors. Furthermore, the information transmitted by the sensors has a specific address, which can be separated in the microcontroller. The important specifications of the DS18B20 (DS18B20 technical details, 2023) are as follows:

- Multidrop capability,
- 3 – 5.5 V,
- Measuring range: -55 °C to +125 °C,
- ±0.5 °C accuracy,
- Wide applications in various systems.

a b c

Figure 4. (a) light sensor, (b) relative humidity sensor, (c) temperature sensor

3. EXPERIMENTAL SETUP

The proposed weather station consists of two main parts: (a) equipment for measuring environmental parameters and (b) a data logger. Environmental variables are measured by installing sensors of the anemometer, illuminance meter, ambient temperature, and relative humidity on special bases, as shown in Figure 5. In this regard, several considerations must be taken into account: (a) The anemometer should be placed away from any surfaces to avoid interference and ensure collection of data specific to the surrounding area. (b) The illuminance sensor (type BH1750) should be covered with a waterproof cover and installed in a location where it will not be affected by shadows during any time of day. (c) The temperature sensor (type DS18B20) is coated with waterproof steel and should not be exposed to direct sunlight. (d) The relative humidity sensor (Type DHT22) should be protected from sunlight and rain during installation**.**

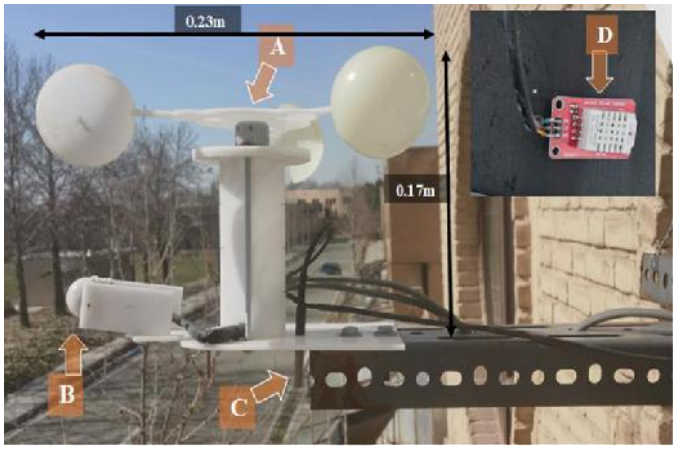

Figure 5. View of the proposed weather station and dimensions: (A) anemometer, (B) illuminance sensor with waterproof cover, (C) waterproof air temperature sensor, and (D) relative humidity sensor (installed on the backside of the device)

Based on Figure 6, monitoring and recording the measured data require a system consisting of a microcontroller, power supply, display screen, clock module, and SD memory card. This system has the ability to connect to the Wi-Fi network and can save the data locally (offline). Also, the data can be saved online (on the Google Sheets platform). The possibility of connecting to the network provides the ability to view real-time data, in addition to storing data and accessing them through the Internet.

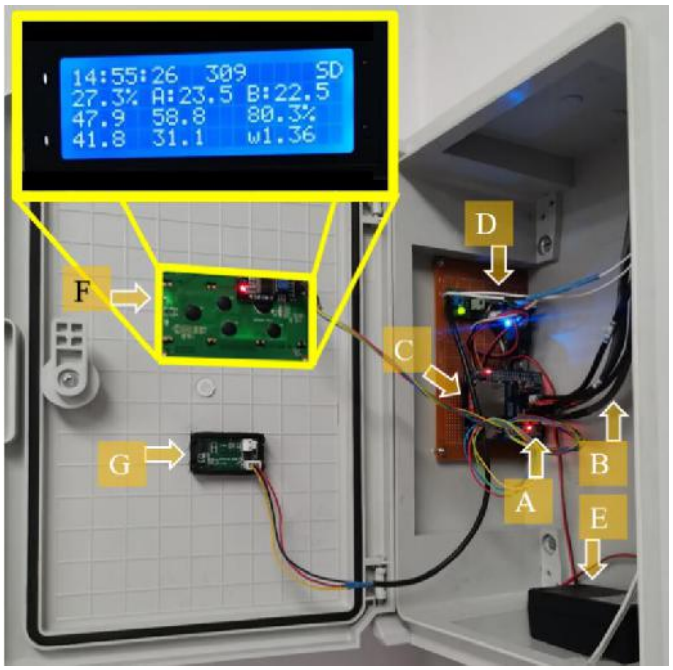

Figure 6. The data logger and components: (A) Wi-Fi-based microcontroller and datalogger module, (B) sensors wires, (C) SD card slot, (D) power module (voltage regulators), (E) power supply, (F) main screen, (G) second screen.

3.1. Weather Station Total Cost

One of the main advantages of the proposed meteorological station is the low total cost, which makes it affordable for wide applications such as performance analysis of energy and environmental systems. The total cost of building this station is about 110 USD and the relevant details are presented in Table 3.

Table 3. Details of the weather station components' price

No.	Item	Price (USD)
1	Air temperature sensor	5
2	Air humidity sensor	7
3	Anemometer	22
4	Illumination sensor	4
5	Microcontroller	7
6	Datalogger module (time and SD card module)	17
7	Power supply and voltage regulators	10
8	Display module	13
9	Structure, wiring, etc.	25
	Total cost is equal to:	**110 USD**

4. RESULTS AND DISCUSSION

4.1. Measurement Results

The ambient variables were experimentally measured in the winter of 2022 in the city of Karaj, Iran, at the location coordinates of 35°74′00" N, 50°95′00" E. Figure 7 showcases an instance of the measured data trend for three days.

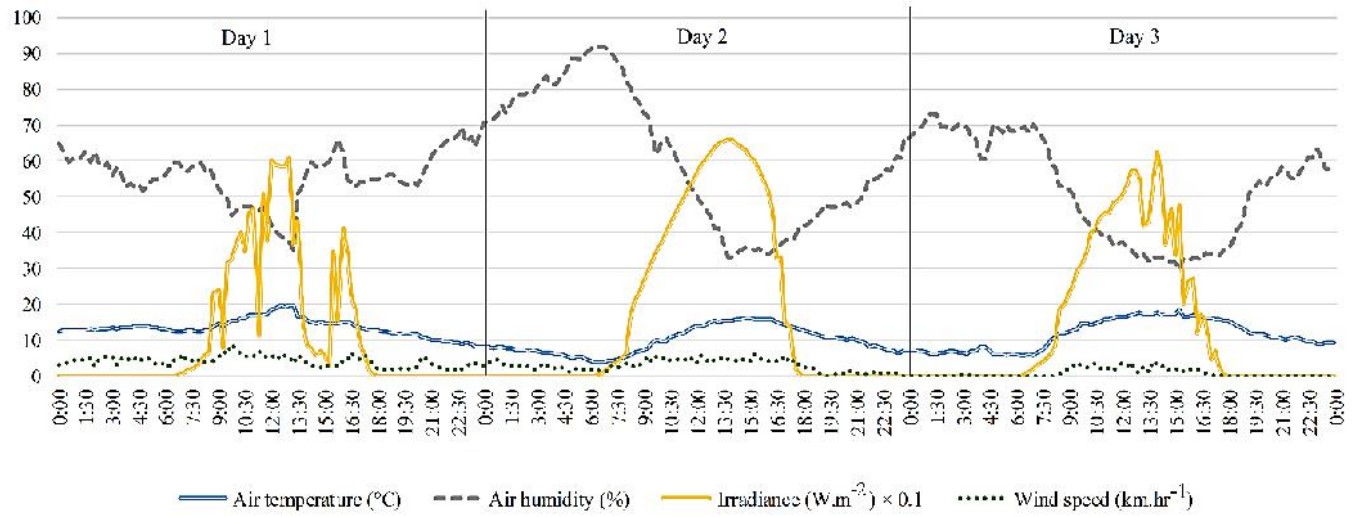

Figure 7. Trends of sample ambient parameters values.

Average data in 15-minute periods are plotted in Figure 7. As mentioned, one of the important advantages of the proposed weather station is access to real-time data on the Internet. Figure 8 illustrates a sample of an online data display.

4.2. Comparison of The Proposed Weather Station Data with National Meteorological Data

Most of the related studies have applied national meteorological data to analyze the performance of energy and environmental systems. Due to the difference in data, using this national meteorological information may cause errors in the performance analysis of the mentioned systems. In order to investigate this difference, the data recorded from the local station were compared with the data from two stations nearby the experiment site in November 2022. According to Figure 9, the closest national stations are the Alborz meteorological station with a distance of 4 km and the Chitgar meteorological station with a distance of 19 km. In addition, the geographical locations of stations are presented in Table 4.

Table 4. Geographical location of stations.

Location	Longitude (°)	Latitude (°)	Altitude above sea level (m)
Local Station	50.9575	35.7486	1248
Alborz Station	50.9395	35.7814	1263
Chitgar Station	51.1723	35.7492	1314

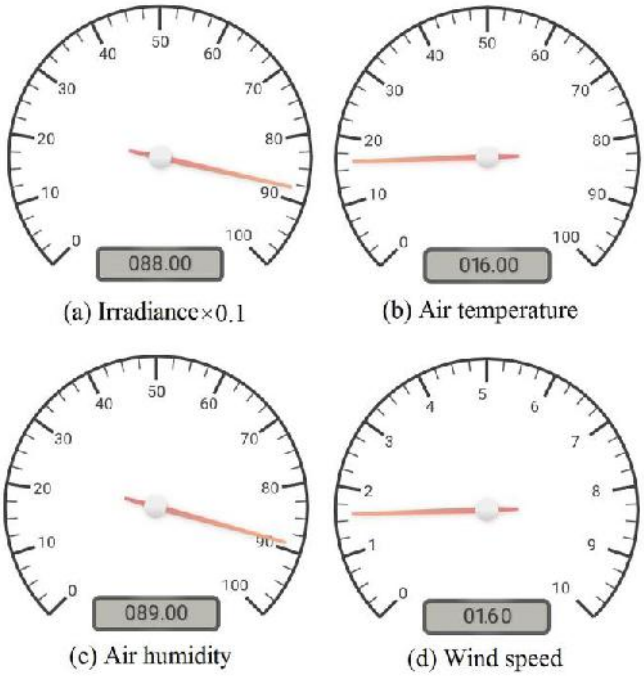

Figure 8. Online real-time data visualization

Figure 9. (A) The location of the proposed weather station, (B) Alborz meteorology office, and (C) Chitgar weather station

Daily average values were used to compare the data. Figure 10 shows the average daily air temperature in November.

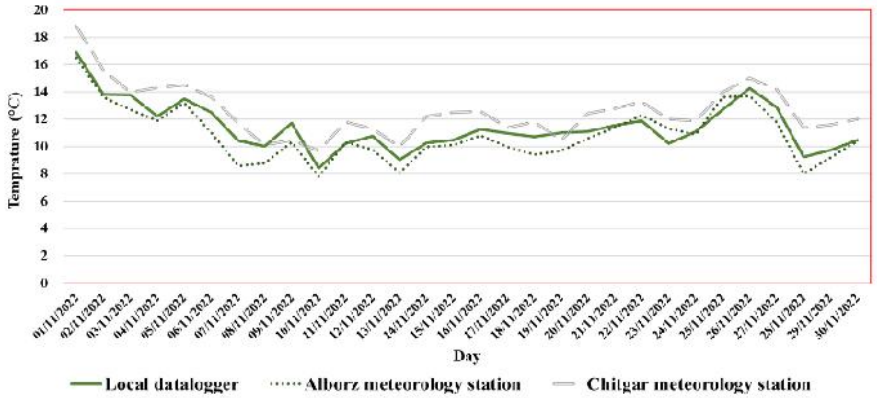

Figure 10. Daily average values of air temperature were reported by the weather stations

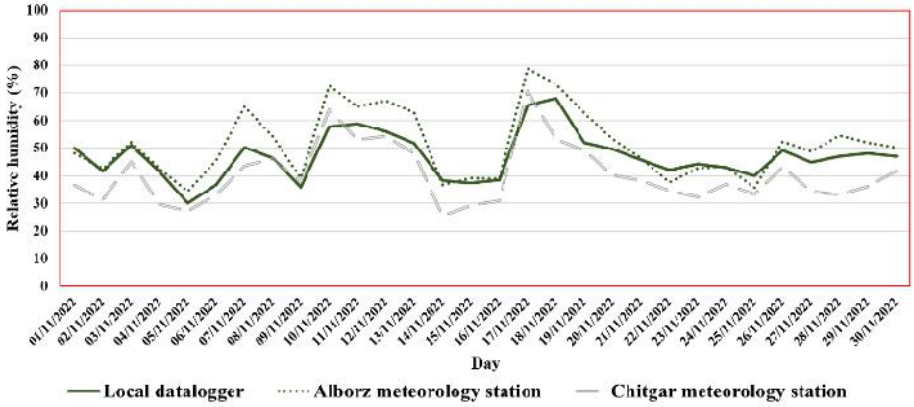

Figure 11. Daily average values of air relative humidity recorded by the weather stations

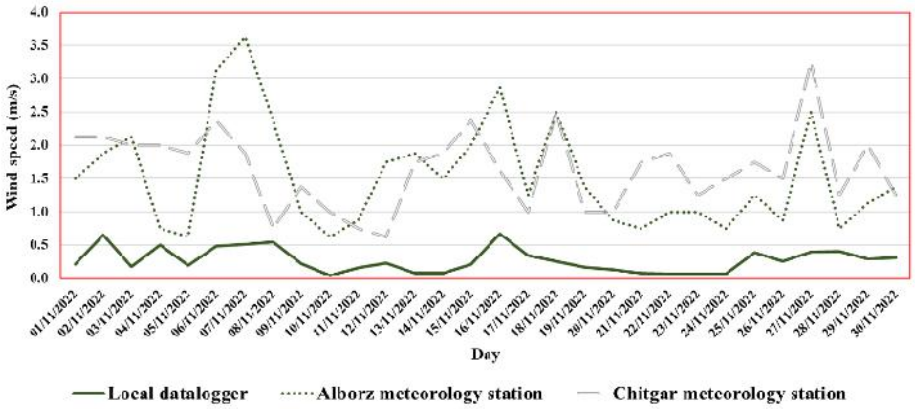

Figure 12. Daily average values of wind speed recorded by three weather stations

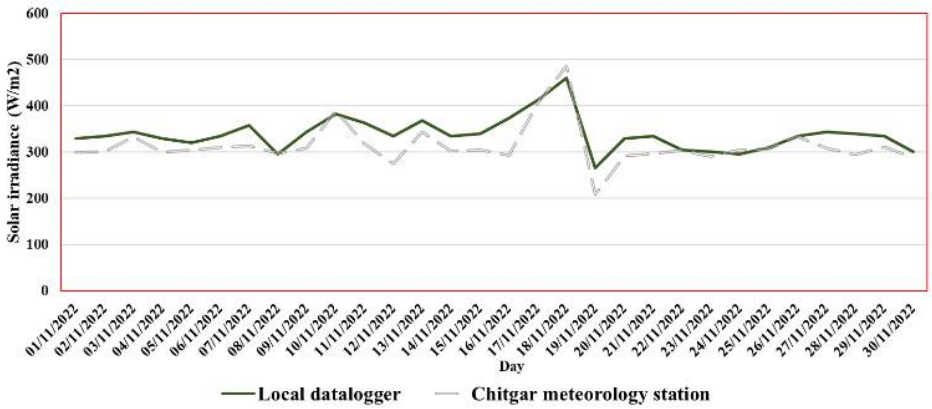

Figure 13. Daily average values of solar radiation reported by the weather stations

According to Figure 10, the trends of air temperature data are similar. Alborz station has recorded closer to the real world values than Chitgar station due to its proximity to the local station. The monthly average deviation of the local data from the Alborz station is 0.6°C (5%), and from the Chitgar station is 1.1°C (10%). Figure 11 displays the trend of air relative humidity in November.

Based on Figure 11, it can be observed that the average monthly difference in relative humidity between the local weather station and the Alborz weather station is 4.3% (9%), while it is 6.5% (14%) with the Chitgar weather station. Average daily wind speed values are presented in Figure 12.

The values of wind speed in 3 weather stations are very different, as shown in Figure 12. This issue results from the existence of the building at the location of the local station, the various urban structures, and also the relatively long distance between the stations**.** The average monthly difference in local wind velocity is 1.6 m/s (456% difference) compared to the Alborz weather station, and 1.4 m/s (498% difference) compared to the Chitgar weather station, as shown in Figure 12. Therefore, it is not practical to use this data. Finally, the average daily solar irradiance data sets are shown in Figure 13.

Alborz meteorological station measures and reports the values of wind velocity, ambient temperature, and humidity. Chitgar meteorological station also measures and reports solar irradiance, in addition to the three mentioned parameters. According to Figure 13, the average data difference in November at two local weather stations and Chitgar is 24 W/m^2 (7%). To review the measurement results, the lowest, highest, and average values of the meteorological variables are presented in Table 5.

Table 5. The range of daily data in November 2022.

Parameter (Unit)	Local station			Alborz station			Chitgar station		
	Min.	Max.	Mean	Min.	Max.	Mean	Min.	Max.	Mean
Air temp (°C)	8.44	16.86	11.45	7.80	16.50	10.86	9.70	18.8	12.58
Humidity (%)	30.1	68.0	47.0	34.5	78.9	51.3	25.6	70.8	40.5
Wind velocity (m.s^{-1})	0.05	0.67	0.28	0.63	3.63	1.53	0.63	3.25	1.65
Solar irradiance (W.m^{-2})	267	461	339	N/A	N/A	N/A	209	487	315

5. CONCLUSIONS

For analyzing the performance of energy and environmental systems, especially solar energy, the most important environmental parameters to consider are solar radiation, wind velocity, ambient temperature, and humidity. In this research, a weather station was designed, built, and tested to measure the above parameters at the data collection site. The important features of this weather station were portability, acceptable accuracy, and low cost (110 USD). This system contained two important parts including environmental measurement sensors and a data logger. By using the data logger, the meteorological data were stored online and offline at the specified time interval. By comparing the local station data with the national stations in November 2022, the following results are obtained:

- The average monthly difference between the local air temperature data and the Alborz station is 5%, and with the Chitgar station, it is 10%.
- The average monthly difference in relative humidity between the proposed weather station and the Alborz meteorological station is 9%, and 14% with the Chitgar station.
- The average monthly difference in local wind velocity data compared to Alborz and Chitgar meteorological stations is 1.6 m/s (456% difference) and 1.4 m/s (498% difference), respectively.
- The average monthly difference in irradiance data between the proposed local meteorological stations and the Chitgar station is 24 W.m^{-2}, equivalent to a 7% difference.

For future research, we recommend using new modeling methods with artificial intelligence and machine learning to predict environmental parameters. Also, the ambient data of the meteorological station will be used for the optimal operation of solar systems such as solar water heaters and solar air heaters.

6. ACKNOWLEDGEMENT

This work was supported by the Materials and Energy Research Center (MERC) under Grant No. 571398056.

NOMENCLATURE

IoT	Internet of things
n	Number of revolutions of the anemometer in one minute
S	Circle circumference (m)
r	Radius (m)
v	Wind speed (m.s^{-1})

REFERENCES

1. Abbate, S., Avvenuti, M., Carturan, L., Cesarini, D. (2013). Deploying a Communicating Automatic Weather Station on an Alpine Glacier. *Procedia Computer Science*, Volume 19, 1190-1195. https://doi.org/10.1016/j.procs.2013.06.170

2. Anemometer Instructions. (2005). science first, Available from: https://sciencefirst.com/wp-content/uploads/2017/05/24-0506-05-005-652-1010-anemometer.pdf

3. Bai, Y., Meng, X., Guo, H., Liu, D., Jia, Y., Cui, P. (2021). Design and validation of an adaptive low-power detection algorithm for three-cup anemometer, *Measurement*, Volume 172, 108887. https://doi.org/10.1016/j.measurement.2020.108887

4. Baseer, M.A., Meyer, J.P., Rehman, S., Mahbub Alam, Md., Al-Hadhrami, L.M., Lashin, A. (2016). Performance evaluation of cup-anemometers and wind speed characteristics analysis, *Renewable Energy*, Volume 86, 733-744. https://doi.org/10.1016/j.renene.2015.08.062

5. Bernardes, G.F.L.R., Ishibashi, R., Ivo, A.A.S., Rosset, V., Kimura, B.Y.L. (2023). Prototyping low-cost automatic weather stations for natural disaster monitoring, *Digital Communications and Networks*, 941-956. https://doi.org/10.1016/j.dcan.2022.05.002

6. Blum, N.B., Wilbert, S., Nouri, B., Lezaca, J., Huckebrink, D., Kazantzidis, A., Heinemann, D., Zarzalejo, L.F., Jiménez, M.J., Pitz-Paal, R., (2022). Measurement of diffuse and plane of array irradiance by a combination of a pyranometer and an all-sky imager. *Solar Energy*, 232: p. 232-247. https://doi.org/10.1016/j.solener.2021.11.064

7. Cureau, R.J., Pigliautile, I., Pisello, A.L. (2022). A New Wearable System for Sensing Outdoor Environmental Conditions for Monitoring Hyper-Microclimate. *Sensors*, 22(2), 502. https://doi.org/10.3390/s22020502

8. DHT22 temperature-humidity sensor technical details. (2023). Available from, Available from: https://www.adafruit.com/product/385

9. Duffie, J.A., Beckman, W.A. (2013). Solar engineering of thermal processes. 4th ed., *Hoboken*, N.J: Wiley. http://ndl.ethernet.edu.et/bitstream/123456789/87795/1/Solar%20Engineering%20of%20Thermal%20Processes%2C%204th%20Edition%20-%20GearTeam.pdf

10. Ligęza, P., (2009). An investigation of a constant-bandwidth hot-wire anemometer. *Flow Measurement and Instrumentation*, 20(3): p. 116-121. https://doi.org/10.1016/j.flowmeasinst.2009.02.002

11. Moghadasi, M., Ghadamian, H., Khodsiani, M., Pourbafrani, M. (2022). A comprehensive experimental investigation and dynamic energy modeling of a highly efficient solar air heater with octagonal geometry, *Solar Energy*, Volume 242, Pages 298-311, ISSN 0038-092X, https://doi.org/10.1016/j.solener.2022.07.030.

12. Moghadasi, M., Izadyar, N., Moghadasi, A., Ghadamian, H. (2021). Applying machine learning techniques to implement the technical requirements of energy management systems in accordance with iso 50001: 2018, an industrial case study, *Energy Sources, Part A: Recovery, Utilization, and Environmental Effects*, 1–18. https://doi.org/10.1080/15567036.2021.2011989

13. Moghadasi, M., Ghadamian, H., Moghadasi, M., Seidabadi, L. (2023). Prediction of outlet air characteristics and thermal performance of a symmetrical solar air heater via machine learning to develop a model-based operational control scheme—an experimental study. *Environ Sci Pollut Res*, 30, 27175–27190. https://doi.org/10.1007/s11356-022-24169-0

14. Monteiro, M.S., Caldas Filho, F.L.D., Barbosa, L.A., Martins, L.M.C.E., Menezes, J.T.M.D., Silva Filho, D.A.D. (2019). University Campus Microclimate Monitoring Using IoT in 2019 Workshop on *Communication Networks and Power Systems (WCNPS)*. https://doi.org/10.1109/WCNPS.2019.8896242

15. Mustafa, M., Xu, Y., Haritos, G., Kenji, K. (2016). Measurement of Wind Flow Behavior at the Leeward Side of Porous Fences Using Ultrasonic Anemometer Device. *Energy Procedia*, 85: p. 350-357. https://doi.org/10.1016/j.egypro.2015.12.261

16. Netto, G.T. and Arigony-Neto, J.(2019). Automatic Weather Station and Electronic Ablation Station for measuring the impacts of climate change on glaciers. *HardwareX*, 5: 1-13. https://doi.org/10.1016/j.ohx.2019.e00053

17. Nsabagwa, M., Byamukama, M., Kondela, M., Otim, J.S. (2019). Towards a robust and affordable Automatic Weather Station. *Development Engineering*, 4: p. 100040. https://doi.org/10.1016/j.deveng.2018.100040

18. Pashchenko, A.F., Rassadin, Y.M. (2022). Microclimate Monitoring System Design for the Smart Grid Analysis and Constructive Parameters Estimation. *IFAC-PapersOnLine*, 55(9): p. 479-484. https://doi.org/10.1016/j.ifacol.2022.07.083

19. Pham, Q.T. (2014). PHYSICAL MEASUREMENTS | Other Physical Measurements, in Encyclopedia of Meat Sciences (Second Edition), M. Dikeman and C. Devine, Editors, *Academic Press: Oxford*. p. 50-56. ISBN 978-0-12-384734-8, https://www.elsevier.com/books/encyclopedia-of-meat-sciences/devine/978-0-12-384731-7

20. Michael, P. R., Johnston, D. E., Moreno, W. (2020). A conversion guide: solar irradiance and lux illuminance. *Journal of Measurements in Engineering*, Vol. 8, No. 4, pp. 153–166. https://doi.org/10.21595/jme.2020.21667

21. Radajewski, M., Decker, S., Krüger, L. (2019). Direct temperature measurement via thermocouples within an SPS/FAST graphite tool. *Measurement*, 147: p. 106863. https://doi.org/10.1016/j.measurement.2019.106863

22. Rafiquzzaman, M., (2014). Fundamentals of digital logic and microcontrollers. Sixth edition, p-9781118855799, *Hoboken, New Jersey: Wiley*. ISBN: 978-1-118-85579-9. https://www.wiley.com/en-sg/Fundamentals+of+Digital+Logic+and+Microcontrollers%2C+6th+Edition-p-9781118855799.

23. ROHM semiconductor, Available from: https://www.mouser.com/datasheet/2/348/bh1750fvi-e-186247.pdf

24. Sparkfun, Available from: https://www.sparkfun.com/datasheets/Sensors/Temperature/DHT22.pdf

25. Sparkfun, Available from: https://cdn.sparkfun.com/datasheets/Sensors/Temp/DS18B20.pdf

26. Wang, W., Li, S., Guo, S., Ma, M., Feng, S., Bao, L. (2021). Benchmarking urban local weather with long-term monitoring compared with weather datasets from climate station and EnergyPlus weather (EPW) data. *Energy Reports*, 7: p. 6501-6514. https://doi.org/10.1016/j.egyr.2021.09.108

JREE: Vol. 10, No. 4, (Autumn 2023) 44-58

Journal of Renewable Energy and Environment

Journal Homepage: www.jree.ir

Materials and Energy Research Center

MERC

Research Article

A Novel Approach to Fast Determining the Maximum Power Point Based on Photovoltaic Panel's Datasheet

Sameer Hanna Khader[a]*, Abdel-Karim Khalid Daud[a]

[a] *Department of Electrical Engineering, Faculty of Engineering, Palestine Polytechnic University, P. O. Box: 198, Hebron, Palestine.*

PAPER INFO

Paper history:
Received: 13 September 2022
Revised: 18 January 2023
Accepted: 31 January 2023

Keywords:

Buck-Boost Converter,
Traditional SEPIC Converter,
Modified SEPIC Converter,
MPPT

ABSTRACT

This study proposes a novel approach to fast and direct determination of the Maximum Power Point (MPP) at any value of solar irradiation and cell temperature, without applying further mathematical processing to operate at that point. The current approach aims to reduce algorithm complexity, time consumption during the iteration, and oscillation to reach the point at which the panel generates maximum possible power. For avoiding or eliminating these drawbacks, the chopper duty cycle (D) at which the panel-generated power should be the maximum is determined using the panel datasheet with respect to voltage and power at different irradiation rates (G). Mathematical equations are derived for MPP voltage and power at any value of solar irradiation using the manufacturer Photovoltaic (PV) specification. The simulation results obtained by MATLAB/SIMULINK platform showed that the power had a linear change, while the voltage had a nonlinear one with narrow variations. The yield duty cycle controls the Modified Single Ended Primary Converter (MSEPIC) that regulates the load voltage through a wide range below and above the rated panel voltage. The simulation results showed the fast response of chopper operation with a negligible starting time required by the MPPT algorithm, no duty cycle oscillation, and shorter iteration time. Furthermore, the conducted approach is validated based on the data published in a reputed journal, and the obtained results gave rise to new aspects that helped reduce dependency on conventional MPPT algorithms and, consequently, enhance the system response, efficiency and cost reduction.

https://doi.org/10.30501/jree.2023.361697.1450

1. INTRODUCTION

Renewable energy sources enjoyed many different applications in three decades ago, mainly in photovoltaic and solar systems, wind energy systems, biogenertors, and other non-conventional sources. The great tendency for the growth of these sources is pushed ahead due to instability of international markets for fossil oils, conducted efforts for saving and protecting the environment, and high cost of traditional oil and gas as mentioned (Martini et al, 2015) and (Mahmoud Y. et al., 2012) in their studies. In addition, these sources suffer greatly from expected depletion in the near future. Consequently, intensive research is encouraged on the development of advanced renewable sources such as photovoltaic (PV) generators. (Khader et al, 2021) described a Photovoltaic generator consists of solar panels, DC chopper, smoothing unit, and power management unit for operating it at maximum extracted power called Maximum Power Point Tracker (MPPT). (Mastromauro et al, 2012) in their study described voltage and current control models using MPPT approach. Usually, PV systems are designed to operate at the point of maximum power called MPP in order to realize maximum efficiency and better utilization. Therefore, the need for MPPT module is an essential stage in energy conversion procedure to obtain maximum energy with reduced switching losses of the chopper and minimized overall system losses at high efficiency.

There are several MPPT techniques for tracking the maximum power of the PV system such as Perturb and Observation (P&O), which uses iteration procedures for reaching maximum power at the knee of power performance. (Femia et al, 2005) proposed optimization procedure for obtaining precise MPPT results. It is characterized by a simple mathematical approach and easy implantation, but with great voltage oscillation on the chopper electronic switch that cannot be completely avoided, leading to switching losses and excess of heat. The second technique is called Incremental Conductance (IC) method discussed by (Zegaoui, et al, 2011), which has a similar iteration procedure that uses the change of current rather than the change in power with respect to the voltage. The third technique is known as the Fuzzy Logic Control method (FLC) which was described by (Hasan et al, 2021) and is used very successfully in the implementation for MPP searching and the sliding mode control which was described by (Yatimi et al, 2016).

The P&O method stands out as the most relatively used method due to its simplicity. This method has a good operating behavior in slow changing solar irradiation and temperature change with respect to time. However, it is a time-consuming

*Corresponding Author's Email: *sameer@ppu.edu* (S. Khader)
URL: https://www.jree.ir/article_170661.html

Please cite this article as: Khader, S. & Daud, A. K. (2023). A Novel Approach to Fast Determining the Maximum Power Point Based on Photovoltaic Panel's Datasheet, *Journal of Renewable Energy and Environment (JREE)*, 10(4), 44-58. https://doi.org/10.30501/jree.2023.361697.1450.

method and hence, cannot track the MPP fast enough, leading to the loss of a certain amount of power before reaching the MPP value due to the iteration procedure and oscillation as well as generation of voltage stress across the chopper switch due to duty cycle variation.

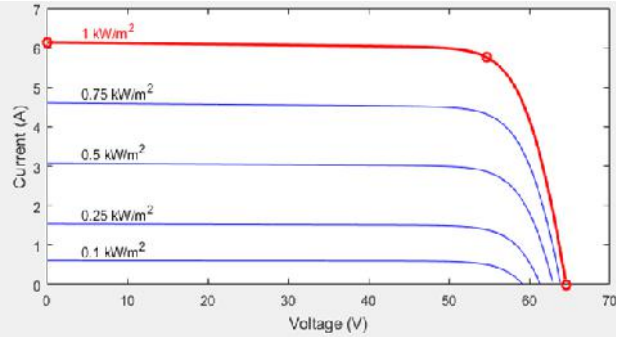

a) Panel P-V performance

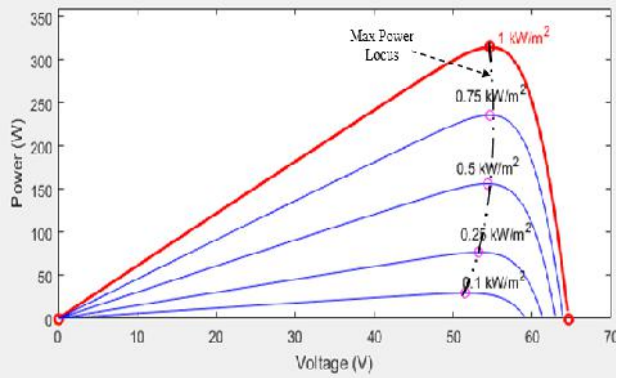

b) Panel I-V performance

Figure 1. Panel I-V and P-V characteristics.

Article main task and elements:

What is the article main task?

Usually, solar irradiation varies during the day time and this leads to continuous tracking of MPP point by various MPPT algorithms, meaning significant time delay, loss of energy, and excess of switching losses due to variation in the chopper duty cycle. Therefore, in order to avoid these drawbacks, it is necessary to immediately find the MPP voltage and power based on previously embedded equations V_{mpp} & P_{mpp} =f(G_T) for any irradiation rate during the day.

This article is organized as follows:

- Section 1: Introduction and overview about the development of electronic converters and their applications in solar energy and energy conversion.
- Section 2: Mathematical modeling for deriving a direct relationship between maximum power and solar irradiation using real data and specifications of manufactured solar panels.
- Section 3: Building the simulation model for direct detecting of the maximum power at any value of solar irradiation during the day time without oscillation around the MPP for Modified Single Primary Inductance Coil (MSEPIC) described by (Mahdavi et al, 2011) , (Bodetto et al, 2016) and (Fernão et al, 2016) .
- Section 4: Running the proposed model for simulation of power, voltage, and current at any time of the year without using the already known MPPT techniques.
- Section 5: Conducting various simulations for MPP power when the cell temperature varies below and above the Standard Test Conditions (STC) value.
- Section 6: Analysis of results and discussion are presented. Finally, some conclusions are drawn.

2. MATHEMATICAL MODELING

2.1. Panel's PV Current and Voltage

Most solar panel manufacturers provide the power voltage performance of a given real panel Ppv=f(Vpv) for solar irradiation starting with 100 Watt/m2 to 1000 Watt/m2 as shown in Figure 1, where the maximum values for voltage and power at the knee of the curves are stated in Table1 for SunPower-SPR-315E-WTH-D, (SUNPOWER datasheet, 2022).

With regard to the above issue for any type of PV panel, several methods can be used for MPP tracking. The only condition to build the required equation is to have PV data for small (may be minimum) and large (may be maximum) power spectra for a given type of panels. Table 2 presents the power range for various PV panel datasheets stored in MATLAB/Simulink database (MATLAB and Simulink (2016)).

Table 1. PV data at MPP for SPR315E-WHT-D.

G, Watt/m2	1000	750	500	250	100
Vmpp, V	54.7	54.65	54.34	53.38	51.64
Impp, A	5.76	4.32	2.88	1.44	0.576
Pmpp, Watt	315.1	236.1	156.5	76.88	29.75

In order to build the mathematical model and related simulation platforms, the following procedure is applied and graphically illustrated in Figure 2:

1. Read discrete values for the voltage and power of real solar panel and build the voltage performance Vmpp=f(G) and Pmpp=f(G) for irradiation points G=100, 250, 500, 750, and 1000 W/m^2.

Table 2. Examples of PV data at MPP for various panels at full Sun.

Panel Type	Range	Serial code	Vmpp, V	Impp, A	Pmpp, W
Sun Power	Small	SPR PL-PLT-63L-BLK-U	11.9	5.3	63.07
	Large	SPR-X20-445-Com	76.7	5.8	444.86
Canadian Solar	Small	CS5C-80M	17.5	4.58	80
	Large	CS7N-665MS	38.5	17.28	665
Soltech	Small	Soltech-1STH-215-P	29.35	7.34	215.1
	Large	Soltech-1STH-350-WH	43	8.15	350
Hanawa Q-cell	Small	Q-Cell 385	36.36	10.59	385
	Large	Q-Cell 585	45.10	12.97	585

2. Extract interpolation equations using MATLAB fitting tools for both voltage and power.
3. Build the continuous voltage equation V_{CON}=f(G) and P_{CON}=f(G).
4. Build/plot the continuous waveforms based on formulated equation for various panel datasheets.
5. Directly detect MPP for any given irradiation value.

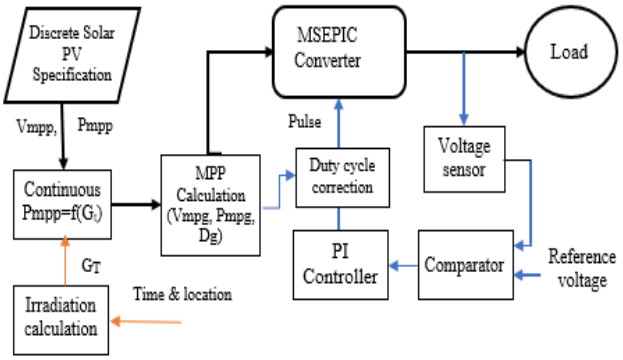

Figure 2. Model functional chart (Daud et al, 2022) .

where, $b_1 = 78.11;\ b_0 = 111.3$.

The obtained results related to voltage and power at MPP are displayed in Figure 4 for a power range of real panel types 1SOLTECH.

The same procedure is applied for another type of panels with a large power range related to HANAWA Q-Cell (Hanawa-Q Cell, 2022) , where the maximum rated panel power is 585 Watts peak with a rated voltage of 45V per panel, as shown in Figure 5, for which the voltage and power variation is displayed at MPP, as the solar irradiation varies as well.

2.3. Direct Detection of MPP`

After deriving the continuous voltage and power equations with respect to the solar irradiation, there is a need to derive a formula for directly determining the chopper duty cycle, voltage, and power at MPP without conducting any type of iteration procedures. To this end, it is necessary to determine the minimum power at a minimum irradiation rate, e.g., G=100W/m^2, and the rated panel power at G=1000W/m^2 is already known from the datasheet. With reference to Figure 4 (b), the MPP powers of performance 1 and performance 5 are known and represented in Figure 6, which are used to derive the power formula for two options:

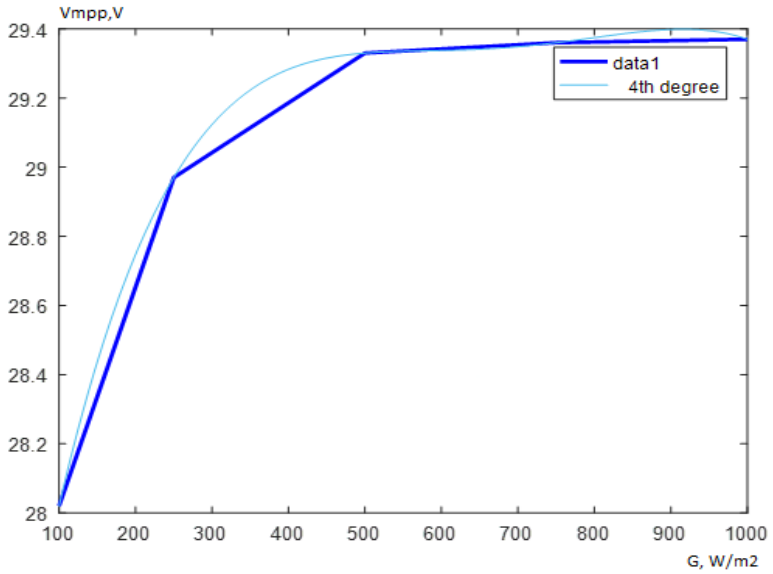

Figure 3. Vmpp at different irradiation rates.

6. Build the solar irradiation rate G=f(time) for any time of the year.
7. Combine the obtained equation V_{CON} and P_{CON} with G.
8. Build the Simulink model that combines the MPP performance with irradiation for any time of the year,

determine MPP for Pmpp and Vmpp at any value of G, and plot Vmpp and Pmpp=f(G).

2.2. Voltage and Power Equations`

Let us start with the data specification related to Solar panel Soltech-15TH-215-P, where the voltage is displayed in Figure 3 with the interpolated equation stated in (1), while the power performance versus irradiation has a linear change presented as a first-order equation. It is shown that the MPP voltage has a slight change when the irradiation varies between a weak and a full sun. The interpolated voltage equation is presented as follows:

$$V_{MPP} = \alpha_4 Z_V^4 + \alpha_3 Z_V^3 + \alpha_2 Z_V^2 + \alpha_1 Z_V + \alpha_0; \quad (1)$$

where, $Z_V = \left(\frac{G_T - \beta}{\delta}\right);\ \beta = 520;\ \delta = 370;$

$\alpha_4 = -0.23;\ \alpha_3 = 0.42;\ \alpha_2 = -0.17;\ \alpha_1 = 0.041;\ \alpha_0 = 29.$

While the power equation can be stated as follows:

$$P_{MPP} = b_1 Z_V + b_0; \quad (2)$$

Option 1: When the rated panel power $\mathbf{P_{mpp,\,i}}$ is located inside the power range "Performance A", the minimum power $\mathbf{P_{min,i}}$ is determined according to the following equation:

$$P_{min,i} = (P_{max,i} - P_{maxs})X_p + P_{mins} \quad (3)$$

where, $X_p = \frac{P_{minL} - P_{mins}}{P_{maxL} - P_{maxs}}$ presents the power ration of panel spectrum,

P_{mins}, P_{maxs}: the smallest min. and max. values of rated Pmpp of PV Panel's power range;

P_{mimL}, P_{maxL}: the largest min. and max. values of rated Pmpp of PV Panel's power range;

P_{mini}, $P_{max,i}$: the min. and max. values of rated Pmpp inside of PV Panel's power range;

$P_{min,o}$; $P_{max,o}$: the min. and max. values of rated Pmpp outside of PV Panel's power range.

Option 2: When the panel power $\mathbf{P_{mpp,o}}$ is located outside the power range "Performance **B**", the minimum power $\mathbf{P_{min,o}}$ is determined according to the following equation:

$$P_{min,o} = P_{max,o}X_p + \frac{\Delta P}{P_{maxL} - P_{maxs}}, \quad (4)$$

with, $\Delta P = P_{maxL} \cdot P_{mins} - P_{maxs} \cdot P_{minL}$

The instantaneous maximum power P_{mpp} (G) at given irradiation can be expressed as follows:

$$P_{mpp}(G) = M.(G - G_{min}) + P_{min} \quad (5)$$

with, $M = \frac{P_{max} - P_{min}}{G_{max} - G_{min}}$; presents the power slope.

and

$$P_{max} = \begin{cases} P_{max,i} & \text{for case 1} \\ P_{max,o} & \text{for case 2} \end{cases} \text{ and } P_{min} = \begin{cases} P_{min,i} & \text{for case 1} \\ P_{min,o} & \text{for case 2} \end{cases}$$

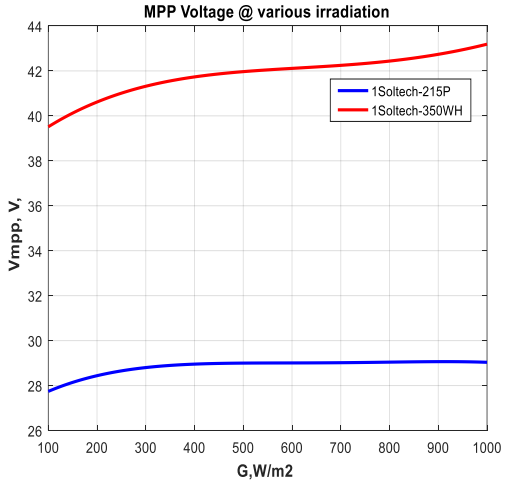

a) Voltage at MPP

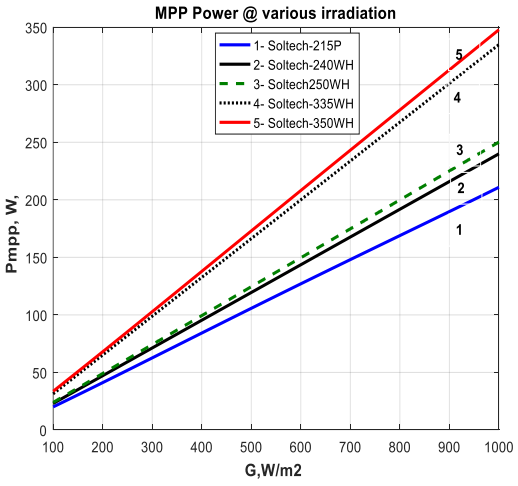

b) Power at MPP

Figure 4. Voltage and power at MPP for different irradiations of various SOLTECH panels.

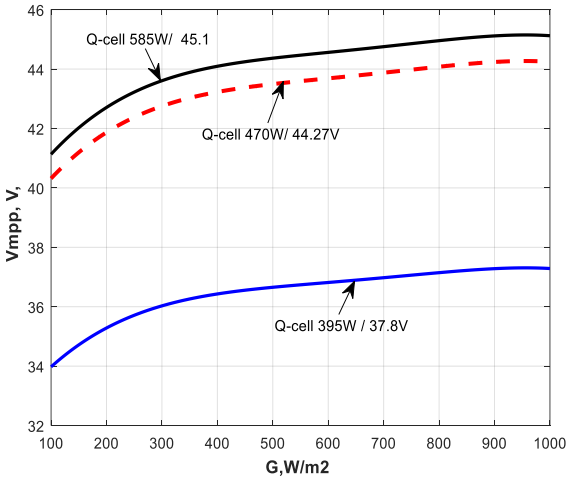

a) Voltage at MPP

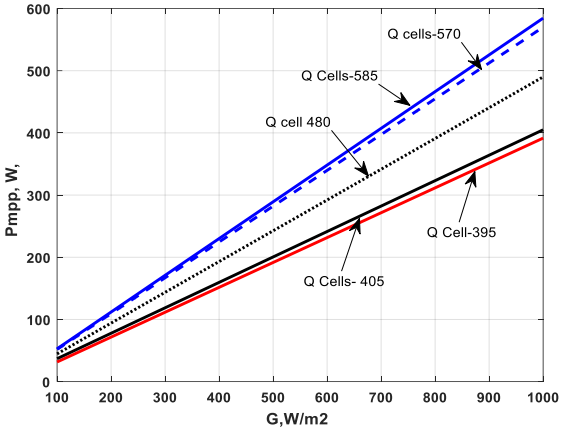

b) Power at MPP

Figure 5. Voltage and power at MPP for different irradiations of HANAWA Q-Cell (Hanawa-Q Cell, 2022).

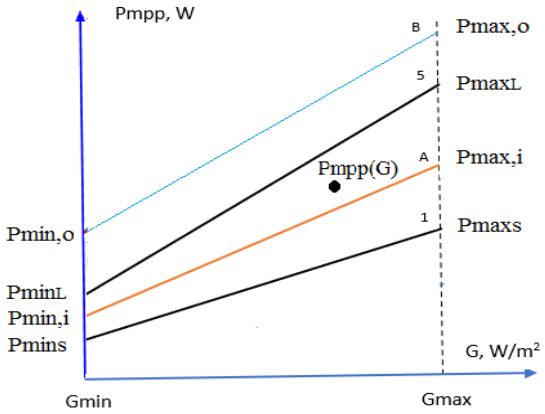

Figure 6. Exact MPP power at given G.

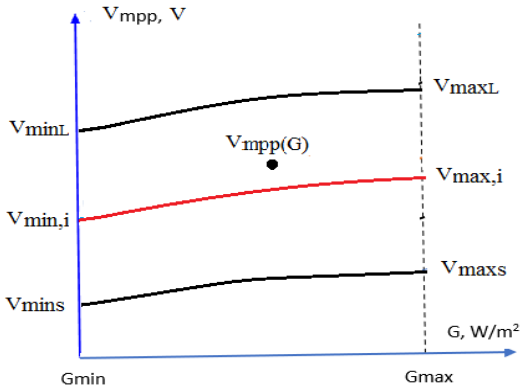

Figure 7. Exact MPP voltage at given G.

Referring to Figure 7, the MPP voltage V_{mpp} of PV panel within the power range can be calculated via the following voltage formula:

$$V_{mpp}(G)=\left(a_{4s}\cdot Z_V^4+a_{3s}\cdot Z_V^3+a_{2s}\cdot Z_V^2+a_{1s}\cdot Z_V+a_{0s}\right) \quad (6)$$

With

$$X_{V,i}=X_y\cdot\left[1+\alpha_p\cdot X_z\cdot\left(\frac{V_{minL}-V_{mins}}{V_{minL}+V_{mins}}\right)\right]$$

$$X_y=\frac{V_{max,i}}{V_{maxs}} \quad \text{and} \quad X_z=\frac{V_{maxL}}{V_{maxs}}.$$

$$\alpha_p=\text{f (Panel type)}\ \le 1\ .$$

Where, V_{mins}, V_{maxs}: the min. and max. values of rated Vmpp of PV Panel's power range;
V_{mimL}, V_{maxL}: the largest min. and max. values of rated Vmpp of PV Panel's power range;
$V_{min,i}$, $V_{max,i}$: the min. and max. values of rated Vmpp inside of PV Panel's power range;
a_{os}, a_{1s}, a_{2s}, a_{3s}, a_{4s}: Equation coefficient of the smallest power of PV panel power range;
α_P: Panel type's tuning coefficient (estimated value).
Equation (6) is applied for different panel types in order to determine the Vmpp voltage at any irradiation rate and panel's specification. Figure 8 shows the behaviors of Vmpp(G) for some well-known solar panels worldwide as stated (Robert Wortrich, 2022), keeping in mind that the rated power is selected to be 350W for all types.

It is clearly shown that Vmpp for the same radiation differs from one type to another with a percentage of change that goes up to 17%, as shown in the stated histogram.

It is imperative to look at the power behavior as shown in Figure 9 where all panel types have the same rated power of 350W. Now, by studying these performances, it can be noticed that there is a slight difference in the generated voltage and power amongst several types.
Based on the voltage generation according to Figure 8, the panel type "SunPower" had the highest value, while "Canadian" had the lowest value.

Based on the generated power according to Figure 9(b), it can be noticed that the panel type "Trina" generated the largest amount of energy. Therefore, the application of this approach provides clear information about the effectiveness of panels and helps better judge in the selection process.

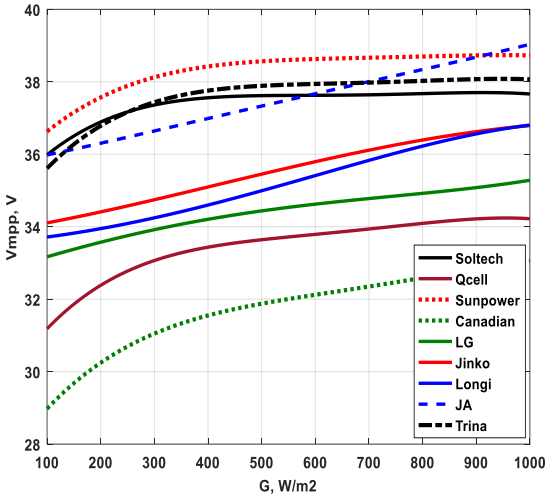

a) Continuous change of Vmpp

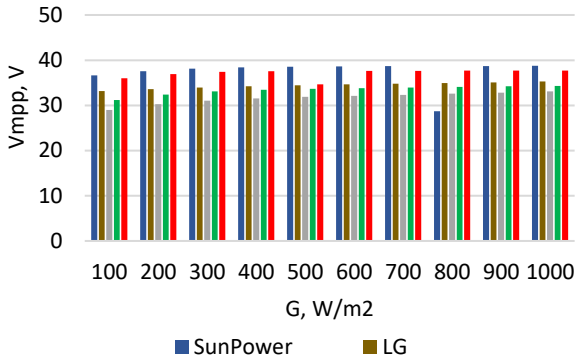

b) Histogram of selected 5 panels.

Figure 8. V_{MPP} voltage performance for various panel types with Pmpp=350W

2.4. Solar Irradiation Calculation

In order to determine the maximum power at given irradiation, it is necessary to determine the daily solar irradiation any time of the year as stated in (Gilbert M. Masters, 2017) as follows:

- The direct solar irradiation is given by:

$$G(t)=G_{max}\sin\left(\frac{\pi}{T_d}(t-t_{sr})\right);\text{for } t_{sr}\le t\le t_{sr}+T_d \quad (7)$$

where, t_{sr}, t_{ss}, T_d are the sunrise time, sunset time, and day duration, respectively.

$$t_{sr}=LT-\frac{T_d}{2}\ ;LT=LST-\frac{TC}{60}\ ;\ t_{ss}=LT+\frac{T_d}{2}\ ; \quad (8)$$

In addition, the daily duration can be presents as :

$$T_d=\frac{2}{15}\cos^{-1}(-\tan\phi\tan\delta)\ ; \quad (9)$$

where

$$\delta=23.45*\sin\left[\frac{360}{365}(n-81)\right].$$

ϕ=31.53° is the solar latitude;
n- is the day number ($1\le n\le 365$); and
LST and LT are the local solar time and local time, respectively.

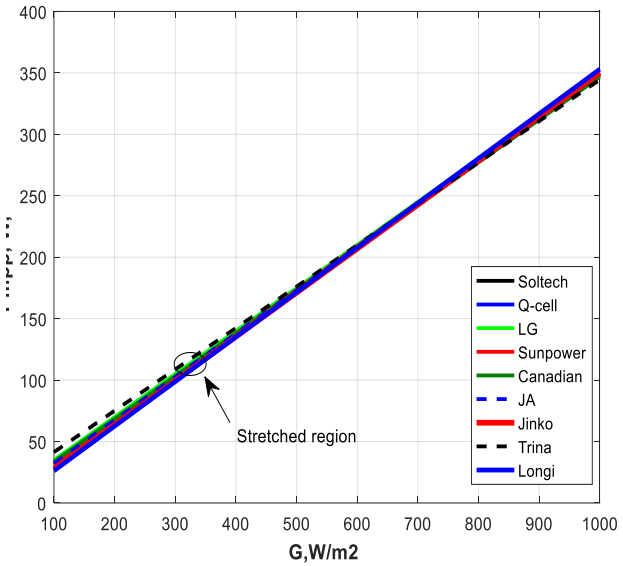

a) Full irradiation range

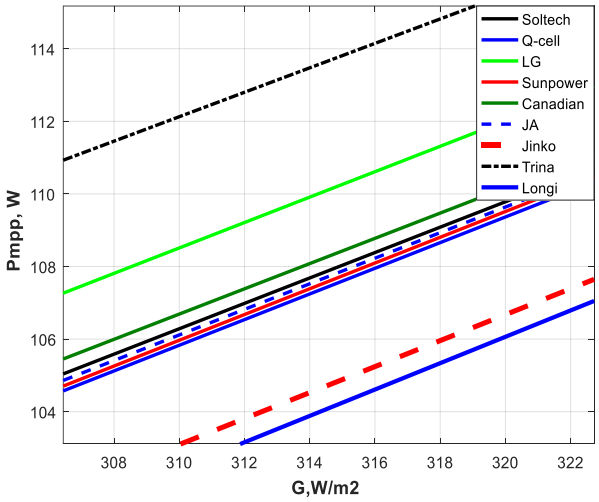

b) Stretched irradiation range.

Figure 9. P_{mpp} power performance for various panels' types.

The local time LT can be expressed as follows:

$$LT = 4 * (\varphi - LSTM) + EOT. \quad (10)$$

where φ= 35.1° is the longitude angle;
LSTM=15°.ΔTUC is the local standard time meridian;

$$EOT = 9.87 * \sin 2\beta - 7.53 * \cos\beta - 1.53 * \sin\beta; \quad (11)$$

where

$$\beta = \frac{360}{364}(n - 81).$$

3. SIMULATION RESULTS AND DISCUSSIONS

The derived equations for solar irradiation, power, and duty cycle at MPP are simulated using MATLAB/ SIMULINK platform for MSEPIC shown in Figure 10(a) where the conventional SEPIC converter circuit is also displayed. The built simulation model is illustrated in Figure 10(b), while Figures 10(c) to 10(j) illustrate the sub-models used in conducting the simulation process. The obtained results are hereby displayed:

3.1 Continuous Values Approach

The calculation of the MPP voltage and power based on discrete irradiation values yields a step-wide change in the voltage and power, which is somewhat far from real conditions, as shown in Figure 11 (and according to Table 1). In contrast, applying a continuous-value approach to calculating the voltage and power throughout the complete solar irradiation range yields closer results to those of real irradiation conditions.

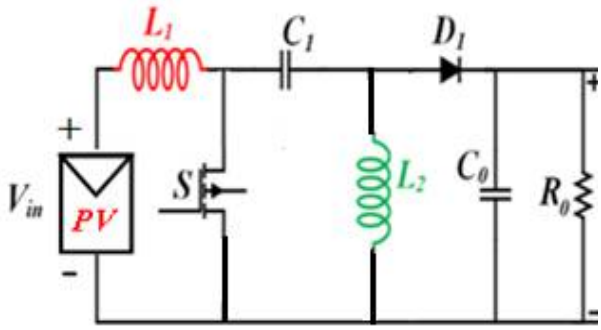

a1) SEPIC Converter

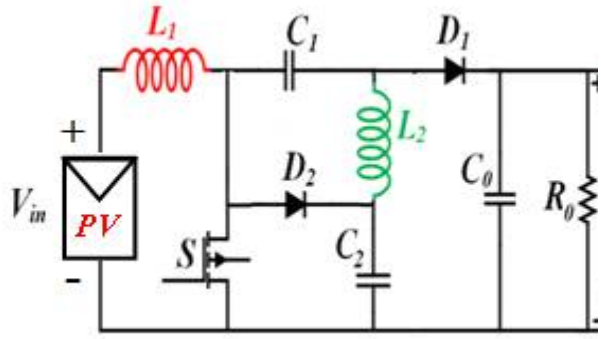

a2) Modified SEPIC Converter

(a) SEPIC and Modified SEPIC (Daud et al, 2022)

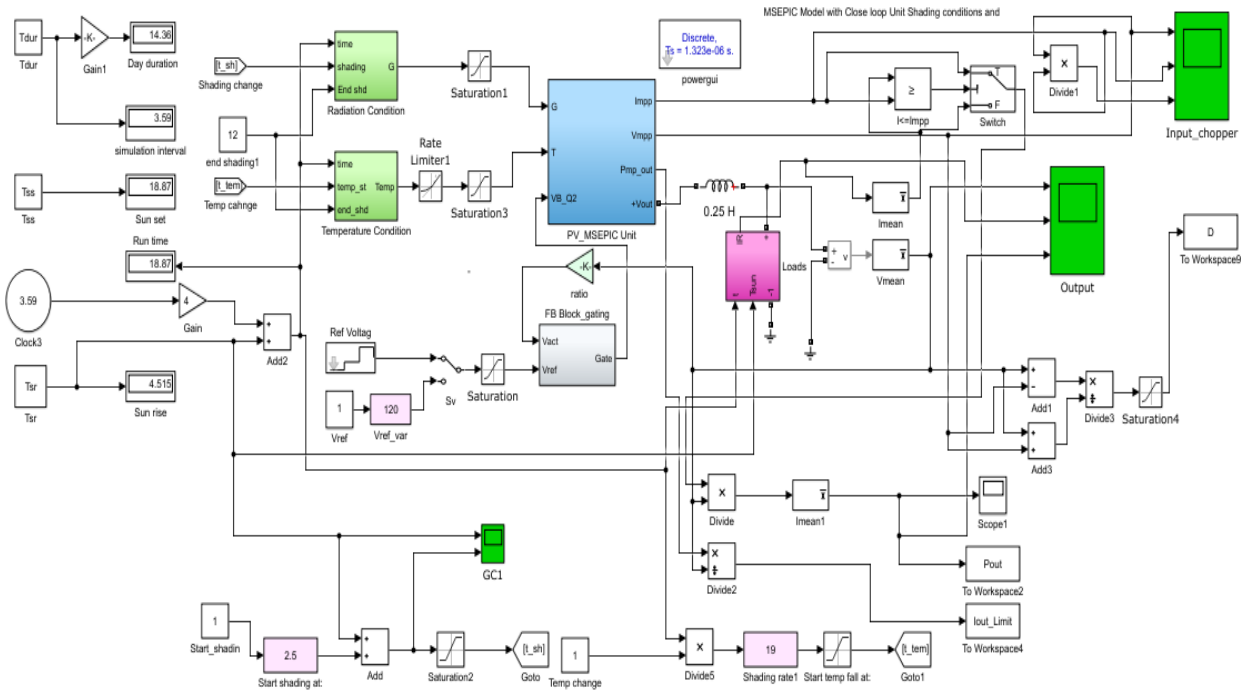

(b) Main Matlab/ Simulink Model

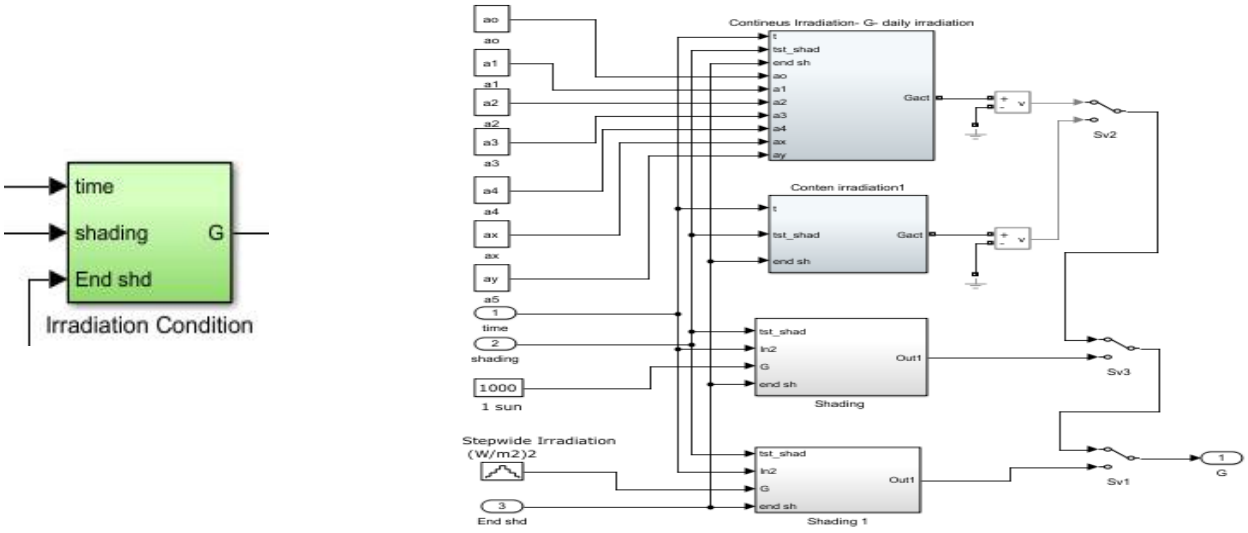

(c) IrradiationCoditions sub-model with a shading unit

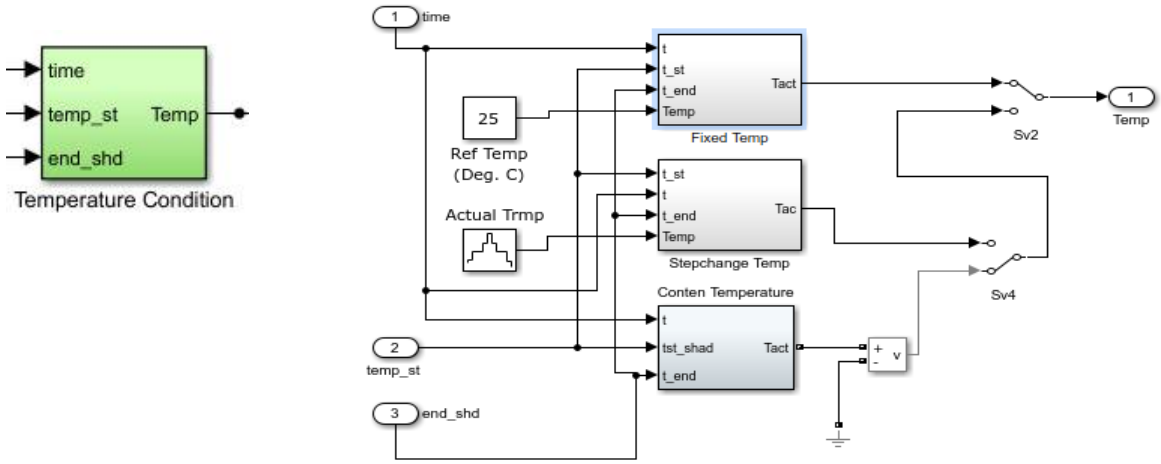

(d) Temperature Condtion sub-model

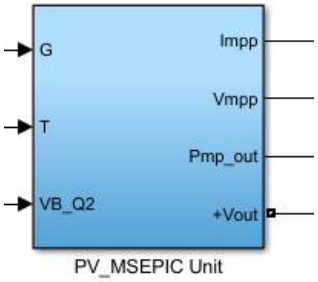

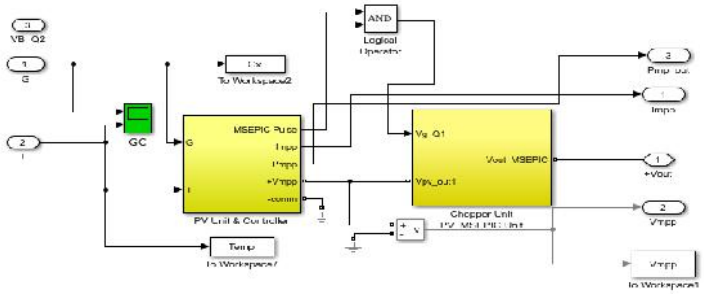

(e) PV & MSEPIC Chopper sub-models

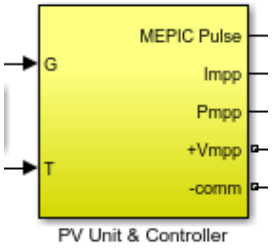

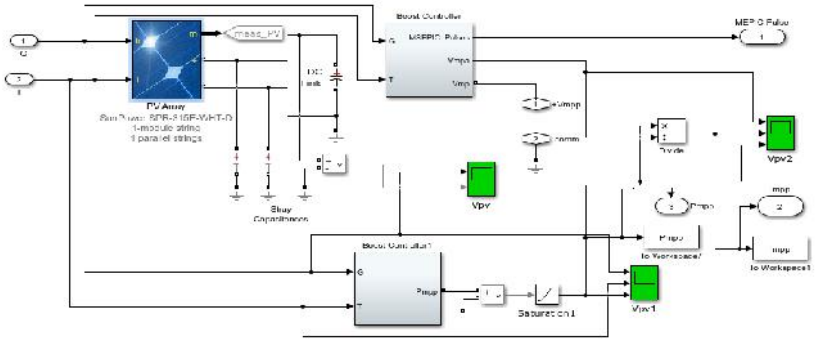

(f) PV Panel and MSEPIC controller

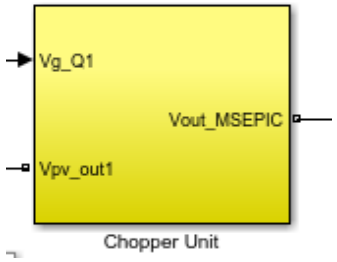

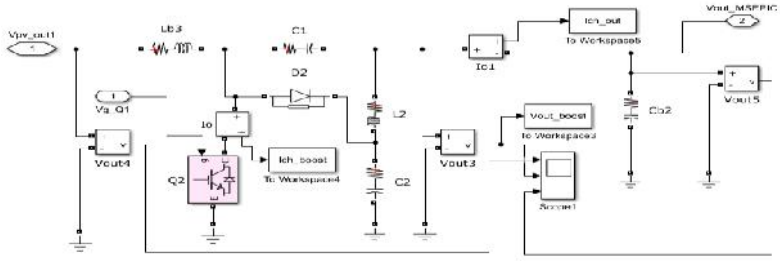

(g) MSEPIC simulation circuit

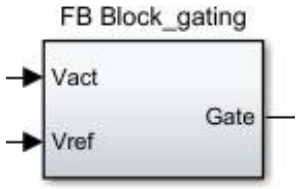

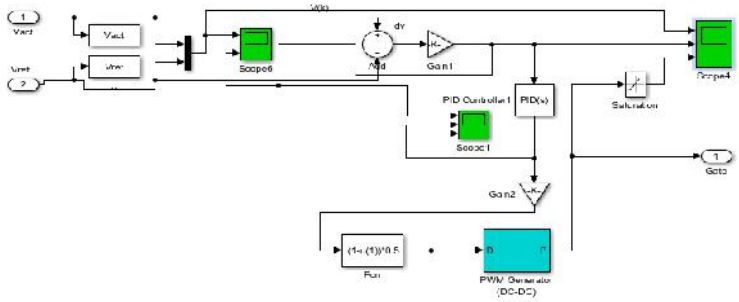

(h) Close-loop control with PID controlle

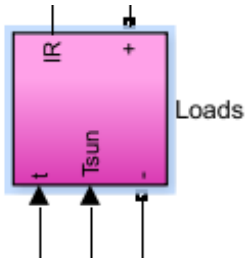

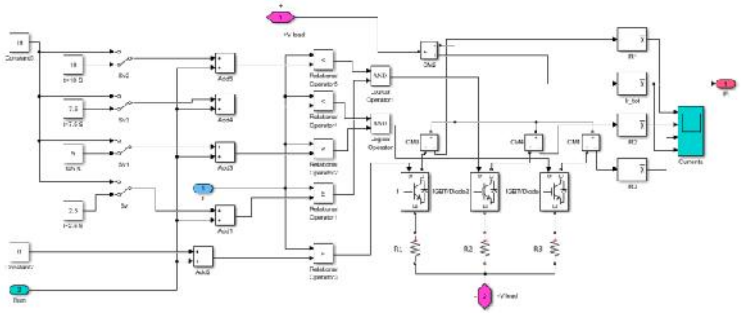

(i) Loading unit with R1, R2, and R3.

Figure 10. Electrical and simulation main and sub-modules.

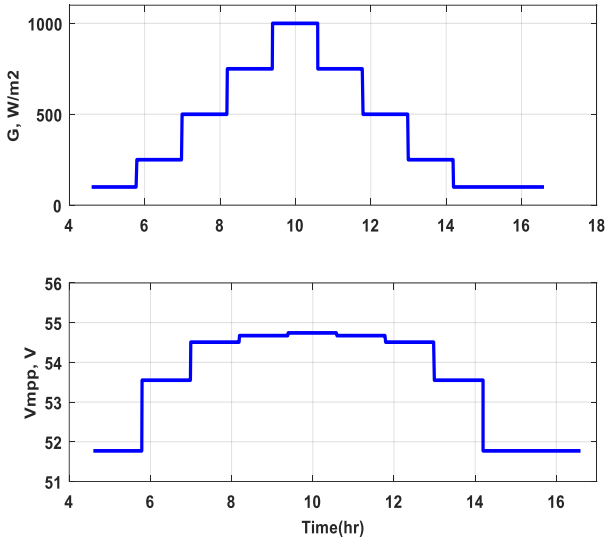

Figure11. Discrete values of solar irradiation and voltage at MPP.

Figure 12 illustrates the MPP voltage and power change, Vmpp, Pmpp=f(GT) with respect to the daily irradiation for both the 21st dates of June & December. It is shown that the day duration changes from June to December and related MPP voltage and power vary as well in standard test conditions.

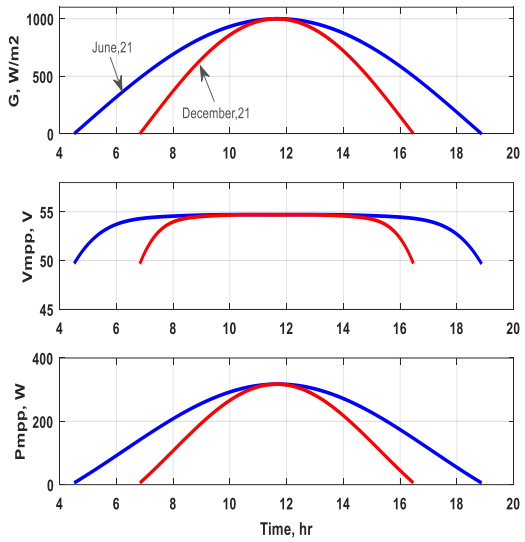

Figure 12. MPP voltage & power for the longest & shotest days of the year.

Figure13 illustrates the loading scenario in which the current changes according to connected loads and this current is projected over the panel capability with respect to MPP current for the same months. It is shown that a significant current shortage is observed during December month when Impp<Lout.

Figure 14 illustrates the effect of load changing over the output voltage at various irradiation rates for 21st June, in which it can be noticed that the negligible oscillation of the output voltage during the transition from one loading level to another.

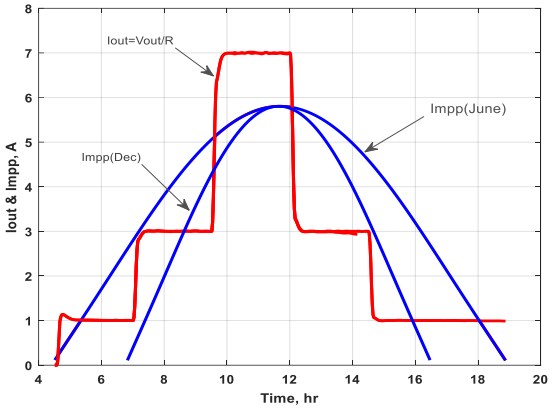

Figure13. Matching between load current (load changing) and MPP current.

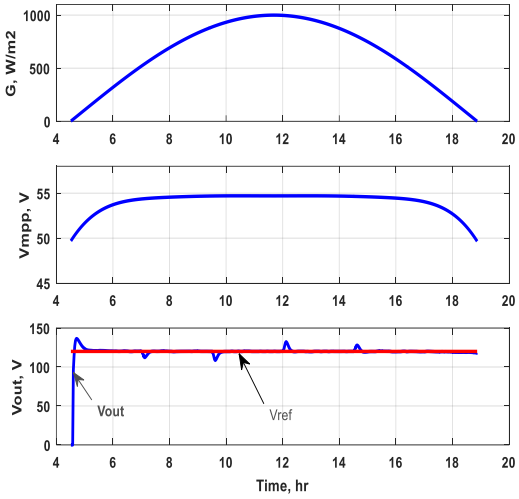

Figure 14. Output and reference voltage change.

3.2 MPP Power and Current for Real Measured Irradiation Data.

The proposed MPP approach is now applied for real measured data taken from a weather station installed over the rootop of the university buildings where the irradiation rate for May, 23,2022 is shown in Figure 15, but the real temperature measured for the same date is shown in Figure 16 (Solar Log 2000, 2022). The generated equations for irradiation (G) and temperature (Tt) are stated in (12) and (13) as follows.

$$G = \delta_4 Z_g^4 + \delta_3 Z_g^3 + \delta_2 Z_g^2 + \delta_1 Z_g + \delta_0; \quad (12)$$

where,

$$Z_g = \left(\frac{t - \beta_1}{\beta_{12}}\right);\ \beta_1 = 11.61;\quad \beta_2 = 4.062;$$
$$\delta_0 = 999.6;\ \delta_1 = 1.441e-13;\ \delta_2 = -410.71;$$
$$\delta_3 = 2.491e-14;\ \delta_4 = 25.46\ .$$

and

$$T_t = \tau_4 Z_t^4 + \tau_3 Z_t^3 + \tau_2 Z_t^2 + \delta_1 Z_t + \tau_0;$$

where,

$$Z_t = \left(\frac{t - \beta_\tau}{\delta_\tau}\right);\ \beta_\tau = 1.60;\quad \delta_\tau = 0.88;$$
$$\tau_0 = 19;\ 3.2;\ \tau_1 = 3.2;\ \tau_2 = -2.4;$$
$$\tau_3 = 3.2;\ \tau_4 = 0.21\ . \quad (13)$$

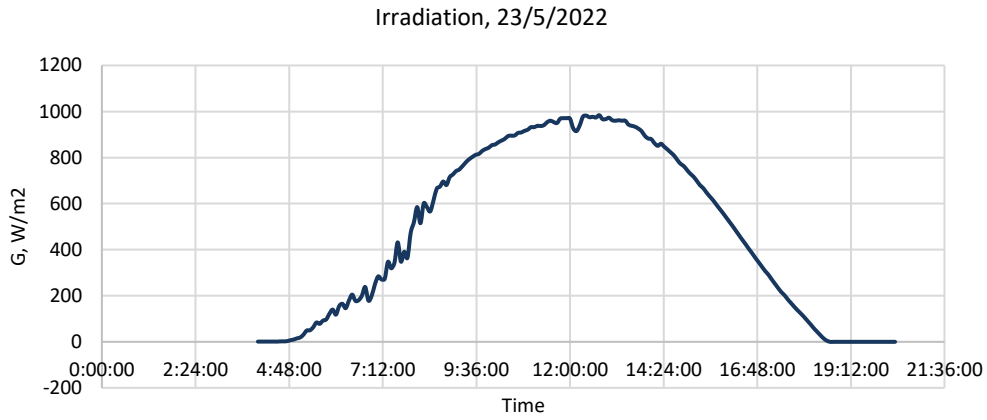

Figure 15. Measured real irradiation .

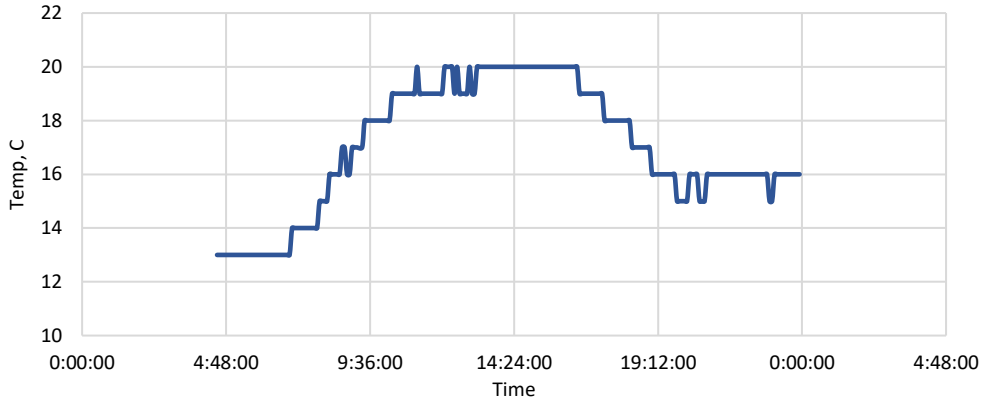

Figure 16. Measured real temperature..

After generating approximated equations for both irradiation and temperature, the MPP volage and power (Daud et al, 2022) are expressed according to (14) and (15) and displayed in Figure 17, taking into account the effect of temperature change for performance test conditions.

$$V_{MPP}(T_t) = V_{MPP}(STC) * \left[1 - \frac{\Delta V}{^\circ C}(T_t - 25)\right]; \quad (14)$$

$$P_{MPP}(T_t) = P_{MPP}(STC) * \left[1 - \frac{\Delta P}{^\circ C}(T_t - 25)\right]. \quad (15)$$

where

$$\frac{\Delta V}{^\circ C} = -0.27269\% \frac{V}{^\circ C}; \quad \frac{\Delta P}{^\circ C} = -0.016823\,\% \frac{W}{^\circ C_4}$$

V_{MPP} (STC) and P_{MPP} (STC) are the rated panel voltage and power in full sun and standard test conditions.

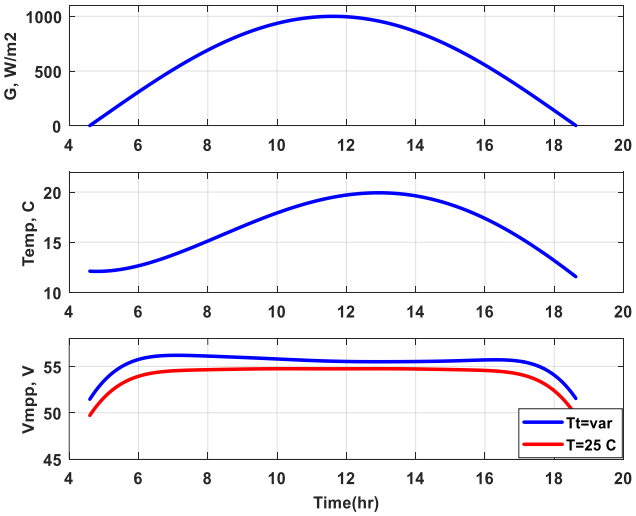

Figure 17. MPP voltage at different irradiations and temperature Tt.

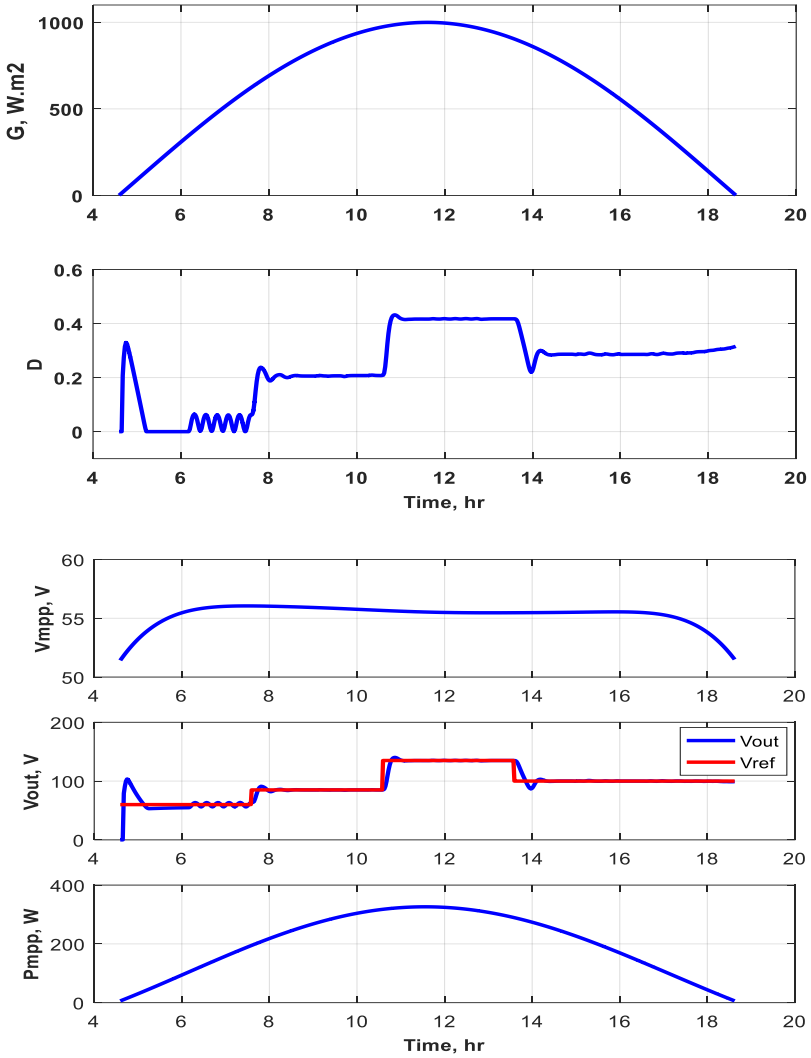

a) Main performances in the time domain

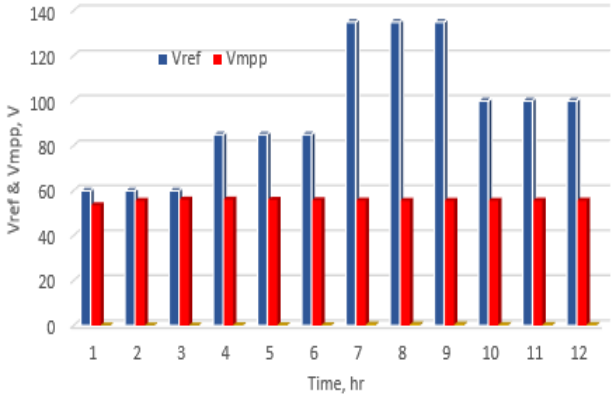

b) Histogram of voltages

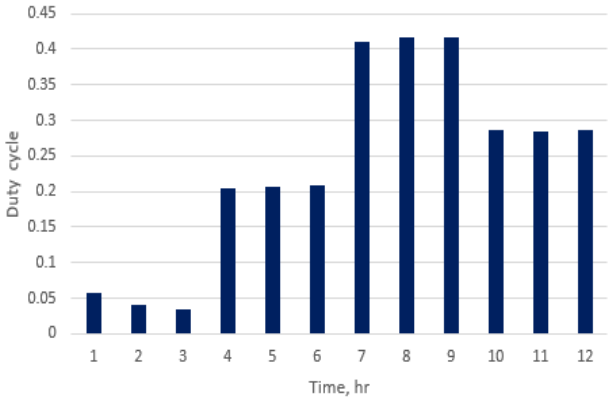

c) Histogram od duty cycle

Figure 18. Input-output performances at different loading voltages for May,23rd, 2022.

It can be noticed that the MPP voltage is higher than that of STC because the maximum temperature for that day (May 23rd , 2022) was detected around 20°C at noon time.

Figure 18 illustrates both the input-output performances in terms of irradiation, duty cycle, MPP voltage, and output voltage according to reference voltage with values V_{REF}= 60, 85, 135, and 100 V and with constant load of R=120 Ω.

In addition, the histogram for the voltage and duty cycle is displayed in the same figure.

The MSEPIC chopper duty cycle is expressed according to (16) in order to generate PWM pulses capable to regulate and boost up the MPP voltage according to the reference values mentioned by (Daud et al, 2022) :

$$D(t) = \frac{V_{REF}-V_{MPP}}{V_{REF}+V_{MPP}}. \quad (16)$$

It can be seen that at a low output reference voltage, the average duty cycle is tolerating around zero, i.e., D≅0, while at a high output reference voltage, where the difference between (V_{REF}-V_{MPP}) is high which requires the chopper to operate at a larger duty cycle, i.e., D≅0.42.

4. MPP TECHNIQUES COMPARISON WITH THE PRESENT APPROACH

There are several MPPT techniques used to operate the chopper at maximum power of the PV system as proposed in (Ben Ali et al,2022), (Pavithra et al, 2021) ,(Hossain et al, 2021), (Chowdhury et al, 2021) and (Boonraksa et al, 2022), where four techniques are described in this work as follows: Hill Climbing (HC), Incremental Conductance (INC), Perturb and Observe (P&O), and Fuzzy Logic Control (FLC).

These techniques have their pros and cons with respect to the fast response, starting time, output power variation, occurred chopper losses, and model simplicity. Three key decision elements can be taken for criteria judgment and precise estimation proposed by already conducted research done by Eltamaly and Rizk (Eltamaly et al, 2015) over solar panel type "Solarex MSX-60 "with data stated in Table 3.

Table 3 The key specifications for the Solarex MSX60 PV panel (Solarex PV Specifications, 2022) .

Vmpp,V	17.1	Voc, V	21
Impp, A	3.5	Isc, A	3.74
Pmpp, Watt	59.90	T, C	25

4.1. Starting Time

This is the time taken from the instant where the radiation changes till reaching the MPP value. Any significant increase in this time should cause additional energy loss and voltage stress over the chopper switch and excess of heat.

The variation of the generated PV power and duty cycle during starting time for mentioned techniques are illustrated in Figure 19, where all of them reach the maximum power Pmax within the time $\mathbf{t_{start}}$=**0.2** second.

While according to the present approach, there is no significant time to reach the maximum power under clear sky conditions as shown in Figure 20, i.e., $\mathbf{t_{st}} \cong$ **0.05** second.

4.2. Output Power Variation

As the solar irradiation varies, the generated MPP changes, as shown in Figure 21, for the mentioned techniques stated in (Eltamaly et al, 2015), where the observed uneven oscillation in duty cycle and power perturbation around the maximum value of the power point cause additional chopper losses due to frequent switching on and off.

These behaviors can be minimized through our proposed

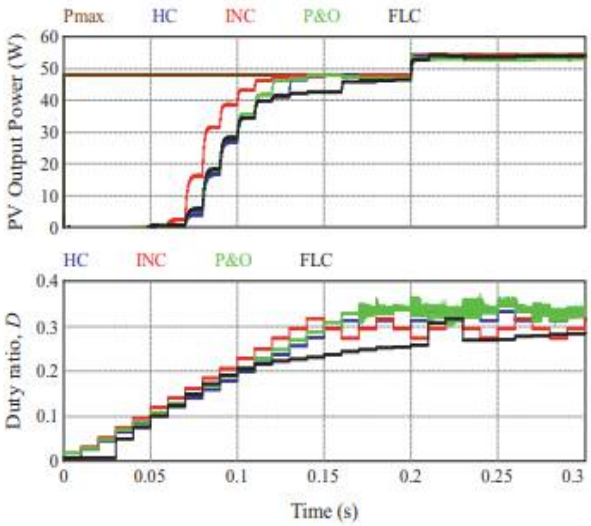

Figure 19. Power and duty cycle presented in (Eltamaly et al, 2015)

approach, as shown in Figure 22, for the constant reference

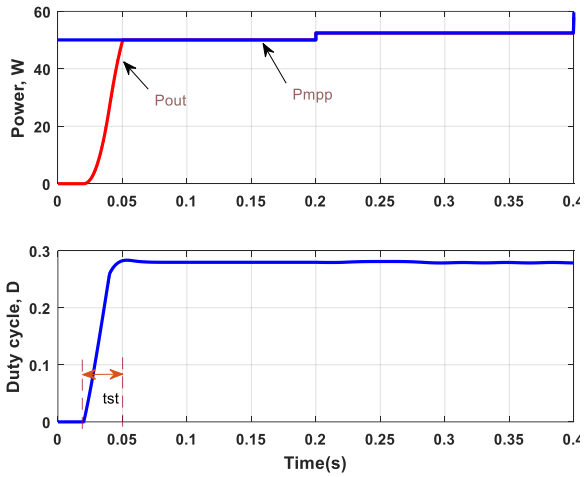

Figure 20. The power and parameters of the proposed approach in the full sun condition.

voltage of V_{ref}=30V and fixed load of R_1=15.5 Ω, where the irradiation changes 800, 850, and 1000 W/m^2.

It can be shown that the duty cycle varies within a small range with an average value of D_{avg}= 0.28.

Comparing the P&O algorithm of Figure 21 in terms of duty cycle with that of Figure 22, a stable change of D irrespective of the great change in solar irradiation during the day can be observed.

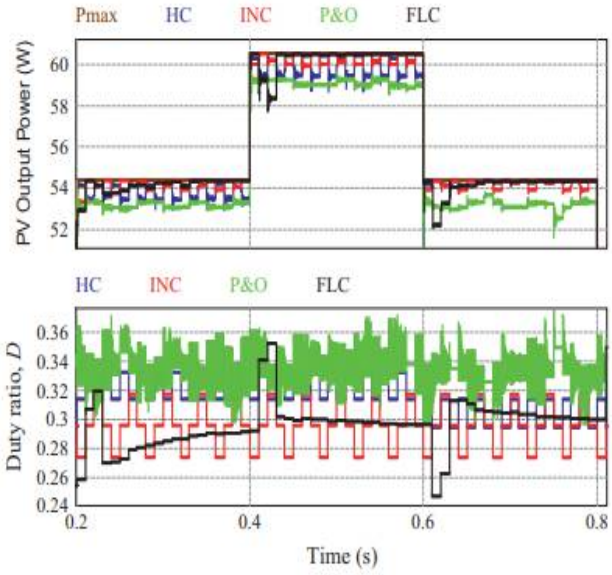

Figure 21. MPP power and duty cycle with variable irradiation described in (Eltamaly et al, 2015).

The above-mentioned techniques deal with a step-wide change in solar irradiations during the day being somewhat far from the real case of solar irradiation except in the case of sudden shadowing of the panel. Our proposed approach deals with a continuous change in solar irradiation, which causes further reduction in voltage stress across the chopper switch and conditioning elements of another chopper.

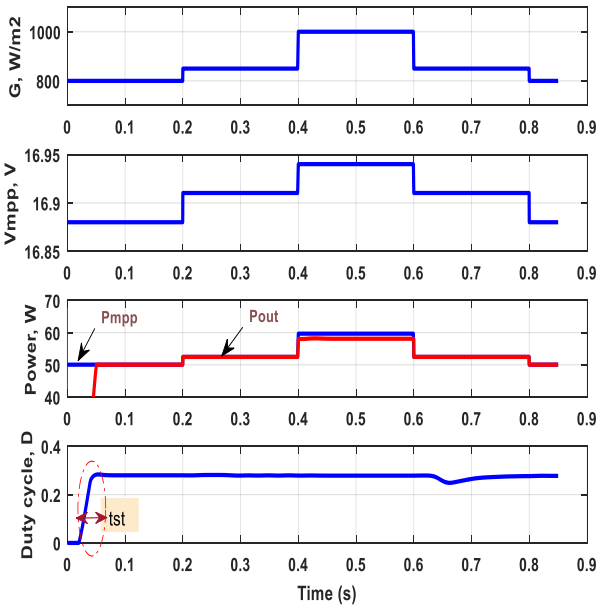

Figure 22. Main parameters of the proposed approach at different irradiation rates

5. CONTINUOUS CHARACTER OF MAXIMUM POWER AT A FIXED OUTPUT VOLTAGE

Figure 23(a) shows the continuous character of solar irradiation and corresponding reference voltage V_{out} = 20, 35, 50, and 40 V with a fixed load of R_1=60Ω , while Figure 23(b) shows the

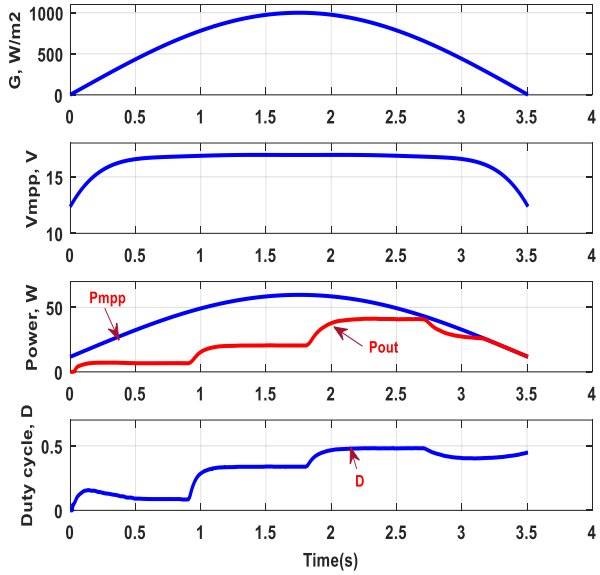

a) With variable output voltage and fixed load of R_1=60 Ω..

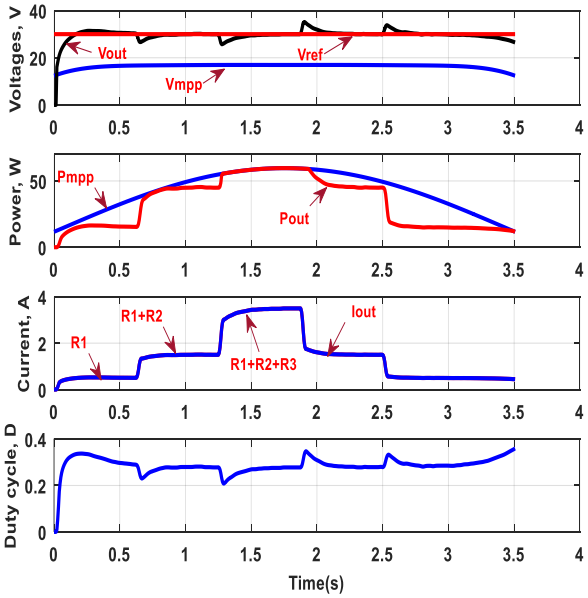

b) With fixed output voltage and variable loading of R_1, R_2, and R_3.

Figure 23. Main parameters of the proposed approach to continuous irradiation.

case when Vref=30V and the load varying with R_1=60Ω, R_2=30Ω, and R_3=15Ω.

It can be shown that keeping the voltage at a fixed reference value reduces the oscillations of the duty cycle and the load voltage. Furthermore, when various loads are added, the voltage sag is immediately recovered and the system returns to deliver an exact and stable output voltage.

6. CONCLUSION

A novel approach was applied to extract power at MPP without the need for conventional MPPT techniques. The proposed technique outperforms the conventional ones by eliminating the time needed to reach the point of maximum power and the

consequent loss of energy. In addition, frequent switching and voltage tension across the switching device were reduced.

The proposed approach used the PV key specification provided by the panel's manufacturer at different irradiation rates, where a continuous power function was derived for MPP points without running any kind of iteration procedures. The derived equation remained valid and regenerated itself for other panel data that belonged to the same manufacturer datasheet.

The PV power performance was built for any rated value of manufacturer's datasheet by merely noting the rated panel power. A variable loading was simulated at which the power, voltage, and current were tracked at the MPP.

The proposed model validation was verified based on the real measured data for solar irradiation and panel temperature. Furthermore, this model was compared to other published data in terms of the starting time and power fluctuations around the MPP (Eltamaly et al, 2015) .

Accordingly, the data published from used algorithms were reported around 0.2 second, while the starting time of our proposed model tended to about 0.05 second. Furthermore, the voltage stress and switching losses were significantly reduced.

The proposed model was projected over PV datasheets of nine solar companies with respect to the power and voltage at MPP, where a comparison analysis was conducted. The results showed a significant difference between these panels in terms of voltage and power at MPP, which in turn gave us a clear decision about panel selection.

The importance of the proposed model for the PV system manufacturers lies in reducing hardware complexity in the process of fabricating MPPT module and related accessories. Mainly, there is no need for voltage and current sensors to measure the PV voltage and current and no need for complicated microprocessor module, too. Furthermore, increase in the chopper lifetime due to reduced voltage stress was achieved besides reduced heatsink size. Given the reduction of the model complexity, the overall solar inverter performances were enhanced and the system footprint (size) and cost were achieved. The only restriction was that this model was valid for clear sky conditions with neglected effect of dust and eventual mismatching.

For future research, a hardware prototype model should be built and experimentally implemented in order to practically validate the discussed analytical and simulation results. This should be the main objective of the upcoming article.

CONFLICT OF INTEREST

The authors declare no conflicts of interest regarding the publication of this paper.

AUTHOR CONTRIBUTIONS

Sameer Khader implemented the SIMULINK model and presented building performances, conclusions, and paper preparation.

Abdel-Karim Daud carried out the mathematical model, analyzed the numerical results, discussed the results, and helped finalize the paper.

NOMENCLATURE

MPP	Maximum Power Point
MSEPIC	Modified Single Ended Coil
LSTM	Local Standard Time Meridian (hour)
ΔTUC	Differential Universal Coordinated Time
LT	Local Time (hour)
LST	Local Standard Time (hour)
EoT	Equation of Time (minute)
PV	Photovoltaic
STC	Standard test conditions
MPPT	Maximum Power Point Tracker
FLC	Fuzzy Logic Control
INC	Incremental Conductance
HC	Hill Climbing
P&O	Perturb and observe

Greek letters

δ	declination angle (degree)
Φ	Latitude angle (degree)
φ	Longitude angle (degree)
β	Parameter depends on the day number (degree).

REFERENCES

1. Ben Ali, I., Naouar, M.W. & Monmasson, E. (June, 2022). Parameters identification for a photovoltaic module: comparison between PSO, GA and CS metaheuristic optimization algorithms. *INDERSCIENCE*, 211-230. https://doi.org/10.1504/IJMIC.2021.123378

2. Bodetto, M., et al. (2015). Design of AC–DC PFC High-Order Converters with Regulated Output Current for Low-Power Applications. *IEEE Transactions on Power Electronics, Volume. 31*(3), 2012–2025. https://doi.org/10.1109/tpel.2015.2434937.

3. Boonraksa, P., Chaisa, A.T., et al. (March, 2022). Design and Simulation of Fuzzy logic controller based MPPT of PV module using MATLAB/ Simulink. *2022 International Electrical Engineering Congress (iEECON)*, 9-11. https://doi/ 10.1109/iEECON53204.2022.9741641.

4. Chowdhury, S., Kumar Das, D., & Hossain, M. S. (June, 2021), Power Performance Evaluation of a PV Module Using MPPT with Fuzzy Logic Control. *Journal of Engineering Advancements, Volume. 2*(1), 7-12. https://doi.org/10.38032/jea.2021.01.002.

5. Daud, A.K. & Khader, S. H. (2022). Closed Loop Modified SEPIC Converter for Photovoltaic System. *WSEAS Transaction on Circuits and Systems, Volume. 21*, 161-167. https://doi.org/ 10.37394/23201.2022.21.17.

6. Daud, A. K. & Khader, S. H. (2022). Comparison Analysis between Various Boost Chopper Configurations. *International Journal of Circuits and Electronics, Volume. 7*, 01-12. http://localhost:8080/xmlui/handle/123456789/8541.

7. Eltamaly, A. M. & Rezk, H. A. (2015). A comprehensive comparison of different MPPT techniques for photovoltaic systems. *Elsevier, Journal of Solar Energy, Volume. 112*, 1-12. https://doi.org/10.1016/j.solener.2014.11.010.

8. Femia, N., et al. (2005). Optimization of perturb and observe maximum power point tracking method. *IEEE Trans Power Electronics, Volume. 20* (4), 963–973. https://doi.org/10.1109/tpel.2005.850975.

9. Fernão, P. V., Foito, D., Baptista, F. & Fernando, S. J. (2016). Photovoltaic Generator System with A DC/DC Converter Based on An Integrated Boost-Ćuk Topology. *Elsevier, Solar Energy, Volume. 136*, 1–09. https://doi.org/10.1016/j.solener.2016.06.063.

10. Gilbert, M. M. (2017). *Renewable and Efficient Electric Power Systems. 2nd ed.* John Wiley & Sons, Inc. ch.4, 186-247. ISBN-13: 978-1118140628. http://www.a-ghadimi.com/files/Courses/Renewable%20Energy.

11. Hasan, J., Ferjana, S. & Chowdhury, S. (2021). Investigation of Power Performance of a PV Module with Boost Converter Using MATLAB Simulation. *American International Journal of Sciences and Engineering Research*, 01-13. https://doi.org/10.46545/aijser.v4i1.322.

12. Hanawa-Q Cell Specifications. (accessed 25 July, 2022). https://www.solaris-shop.com/hanwha-q-cells-q-peak-duo-blk-g5-315-315w-mono-solar-panel.

13. Hossain, Md. T., Rahman, Md. A. & Chowdhury, S. (Autumn, 2021). Evaluation of Power Performance of a PV Module with MPPT Solution Using MATLAB Simulation. *Journal of Renewable Energy and Environment, Volume. 8*(4), 101-107. https://www.jree.ir/article_137353_7bd16eed5df54abca03c789827fec020.pdf.

14. Khader, S. H. & Daud, A. K. (March, 2021). Boost chopper behaviors in Solar photovoltaic system. *Smart Grid and Renewable Energy,Volume. 12*(3), 31-52. https://doi.org/10.4236/sgre.2021.123003.

15. MATLAB and Simulink (2016) The MathWorks, Inc., version R2016b, http://www.mathworks.com.

16. Martini, S. S., Chebak, A. & Barka, N. (2015). Development of renewable energy laboratory based on integration of wind, solar and biodiesel energies through a virtual and physical environment. *3rd International Renewable and Sustainable Energy Conference, Marrakech*, 01-08. https://doi.org/10.1109/irsec.2015.7455086.

17. Mahmoud, Y., Xiao, W. & Zeineldin, H. H. (Jan, 2012). A simple approach to modeling and simulation of photovoltaic modules. *IEEE Trans. Sustain. Energy, volume. 3*(1), 185–186. https://doi.org/10.1109/tste.2011.2170776.

18. Mastromauro, R. A., Liserre, M. & Dell'Aquila, A. (May, 2012). Control issues in single-stage photovoltaic systems: MPPT, current and voltage control. *IEEE Trans. Ind. Information, volume. 8* (2), 241–254. https://doi.org/10.1109/tii.2012.2186973.

19. Mahdavi, M. & Farzanehfard, H. (Sept.,2011), Bridgeless SEPIC PFC Rectifier with Reduced Components and Conduction Losses. *IEEE Trans. Ind. Electronics, volume. 58* (9), 4253–4160, https://doi.org/10.1109/tie.2010.2095393.

20. Pavithra, K., Pooja, H., Tamilselvan, D. & Sudhakar, T. D. (2021). Solar power based positive output super-lift Luo converter using fuzzy logic controller. *Journal of Physics, Volume. 2040*, 01-12. https://doi.org/10.1088/1742-6596/2040/1/012034.

21. Robert, W. (May, 2022). The 10 best Solar Panels Manufacturers in the World, https://climatebiz.com/best-solar-panel-manufacturers/.

22. Solar-Log 2000, Palestine Polytechnic University. Industrial Synergy Center. (2022). https://isc.ppu.edu/en/campus/Productivity.

23. Solarex PV Specifications, (accessed 08 August, 2022) https://www.researchgate.net/figure/The-key-specifications-for-the-Solarex-MSX60-PV-panel-7_tbl2_283553910.

24. Solarex PV Specifications, (accessed 08 August, 2022). https://www.researchgate.net/figure/The-key-specifications-for-the-Solarex-MSX60-PV-panel-7_tbl2_283553910.

25. SUNPOWER Datasheet, SPR-315E-WHT-D. (accessed 25 July, 2022) http://www.solardesigntool.com/components/module-panel-solar/Sunpower/21/SPR-315E-WHT-D/specification-data-sheet.html.

26. Yatimi, H. & Aroudam, E. (2016). Assessment and control of a photovoltaic energy storage system based on the robust sliding mode MPPT controller. *Journal of Solar Energy, Volume. 139*. 557–568. https://doi.org/10.1016/j.solener.2016.10.038.

27. Zegaoui, A., Aillerie, M., Petit, P., Sawicki, J. P., Jaafar, A., Salame, C. & Charles, J. P. (2011). Comparison of two common maximum power point trackers by simulating of PV generators. *Energy Procedia, Volume. 6*, 678–687. https://doi.org/10.1016/j.egypro.2011.05.077.

JREE: Vol. 10, No. 4, (Autumn 2023) 59-65

Journal of Renewable Energy and Environment

Journal Homepage: www.jree.ir

Materials and Energy Research Center

MERC

Research Article

Experimental Study of Phase Change Process of the Paraffin as a PCM with Copper Foam and Iron Wool

Mohammad Saleh Barghi Jahromi[a], Vali Kalantar[a*], Mohammad Sefid[a], Masoud Iranmanesh[b*], Hadi Samimi Akhijahani[c]

a Department of Mechanical Engineering, Faculty of Mechanical Engineering, Yazd University, Yazd, Iran.
b Department of Energy, Institute of Science and High Technology and Environmental Sciences, Graduate University of Advanced Technology, Kerman, Iran.
c Department of BioSystems Engineering, Faculty of Agriculture, University of Kurdistan, Sanandaj, Iran.

PAPER INFO

Paper history:
Received: 22 October 2022
Revised: 26 November 2022
Accepted: 8 January 2023

Keywords:
Copper Foam and Iron Wool,
Copper Absorber Plate,
Energy Storage,
Phase Change Material

ABSTRACT

Paraffin waxes are widely used as commercial organic heat storage phase changes (PCM) for many applications due to their suitable properties. Significant heat from fusion, nonpoisonous and stable properties, no phase separation, and the phase process result in a small volume change. Meanwhile, they are subject to low thermal conductivity. The thermal conductivity of PCMs can be increased by different techniques such as the use of dispersion of particles or nanomaterials with high conductivity in PCM and the use of metal foams. The use of nanoparticles has such disadvantages as high cost and particle deposition after various cycles. Hence, in this study, some experiments were carried out to investigate the effect of porous media like copper foam and iron wool as the filler instead of nanomaterials on improving the heat conductivity of PCM. The results show that the porous foam increases the heat transfer and during the charging operation, the temperature of the porous plate wall increases continuously at the same rate as the paraffin. At 2400 s, the temperature of pure PCM, iron wool, and copper foam reaches 67.3, 72.5, and 73.27℃, respectively. The optimal mode is the one in which the copper absorber plate is connected to the copper foam, thus reducing the charging time by 600 s compared to pure PCM and saving 75% of energy. Connecting the copper absorber plate to the iron wool has a good thermal performance and stores 70.83% of energy. Thus, iron wool has an acceptable performance and is suitable for storage systems.

https://doi.org/10.30501/JREE.2023.365995.1483

1. INTRODUCTION

Energy consumption has significantly increased in recent years because of the swift development of human civilization and the economy. Based on recent research and studies, energy consumption in the world doubles every 20 years. Because of this problem, less renewable energy is used than fossil fuels. However, in recent years, there has been a growth in the usage of renewable energy, particularly solar energy (Iranmanesh et al., 2020; Jahromi et al., 2022). Thermal Energy Storage (TES) systems are utilized in various climatic conditions as temporary thermal energy storage or store preservatives. For many engineering applications, thermal energy storage is essential (Zhao et al., 2010). The word "TES" is not a new term; it has been applied for centuries in numerous industrial and agricultural endeavors, including drying procedures and building heating. Energy storage helps power systems operate more efficiently by regulating supplies and boosting dependability (Matofali and Massawe, 2016). TES plays an essential role in thermal energy saving by reducing the degree of time or uncertainty between supply and demand. Thermal energy can be stored in a liquid or solid with sufficient thermal insulation by changing the internal energy of the material, such as sensible heat or latent heat, or a combination thereof (Ali et al., 2019). Sensible heat, latent heat, and chemical energy are the three primary subtypes of TES. Depending on the material's thermo-physical characteristics, applications may vary (Zhang et al., 2017). Sensible Heat Storage (SHS) uses the heat capacity of a solid or liquid to raise its temperature while changing the material temperature during charging and discharging to store heat energy. The environment, temperature swings, and the value of the heat storage material all affect how much heat is stored (brahim et al., 2017; Dincer and Rosen, 2021). When a material section transitions from a base state into another state, Latent Heat Storage (LHS) depends on the absorption or desorption of thermal energy during that transition (liquid to gas, solid to liquid, or vice versa) (Zhang et al., 2017; Barghi Jahromi et al., 2020). Given the latent heat in the PCM material, the heat storage process takes place at a temperature close to the melting point of the PCM, which increases the density of energy storage in two units of mass and volume in a cycle of approximately the same temperature (Zhao et al., 2010; Abhat, 1983). PCMs use chemical bonds to store and unleash heat. When the PCM materials regenerate from

*Corresponding Author's Email: vkalantar@yazd.ac.ir (V. Kalantar)& m.iranmanesh@kgut.ac.ir (M. Iranmanesh)
URL: https://www.jree.ir/article_164809.html

Please cite this article as: Barghi Jahromi, M. S., Kalantar, V., Sefid, M., Iranmanesh, M. & Samimi Akhijahani, H. (2023). Experimental Study of Phase Change Process of the Paraffin as a PCM with Copper Foam and Iron Wool, *Journal of Renewable Energy and Environment (JREE)*, 10(4), 59-65. https://doi.org/10.30501/JREE.2023.365995.1483.

solid to liquid or liquid to solid, the chemical connections are disrupted and heat transmission occurs (Kumar and Gupta, 2021). Therefore, storing thermal energy in the latent heat of PCM is an exclusive benefit of increasing the value of thermal energy in the system. PCM materials fall into three main categories: organic, inorganic, and eutectic. The required temperature range is 0-150℃, which is very suitable for solar applications (Ali et al., 2019; Usman et al., 2018). For many applications, the PCM needs higher latent heat, higher thermal conductivity, and lower volume expansion (brahim et al., 2017). The thermal conductivity of PCMs, which ranges from 0.1 to $0.3^{W}/_{m \cdot k}$, is relatively low, but has a significant latent heat value. If the thermal conductivity is low, the heat transfer coefficient when releasing the stored heat will decrease.

With a variety of methods, many researchers have tried to increase heat transport in PCMs. Due to the low thermal conductivity coefficient of PCM and increasing heat transfer, surfaces or containers with a higher thermal conductivity coefficient such as spiral copper tubes (Iranmanesh et al., 2020; Ebrahimi et al., 2021), aluminum containers (Shalaby and Bek, 2015; Bhardwaj et al., 2021), fins (Ali and Arshad, 2017; Arshad et al., 2018; Arshad et al., 2017), honeycomb structures (Xie et al., 2015; Wang et al., 2015), microencapsulation (Agyenim et al., 2010), and nanoparticle additives (brahim et al., 2017) can be used. To speed up heat transfer in PCMs, porous materials or porous metal plates are utilized. Highly conductive foams like copper, aluminum, iron, nickel, and others can be employed. To improve heat transfer, PCM is incorporated into a porous material. Foam exists in pores and different densities, affecting the heat transfer rate. In the applications of energy storage and increasing heat transfer, the porous copper plate should be used because it has a high thermal conductivity coefficient and a higher volume than the volume of the material filled in the porous plate. Research has been done on the melting variation of the phase change material in copper and iron foams. Zhang et al (Zhang et al., 2017), investigated the phase transition properties of a composite material comprised of metal porous plate and paraffin. The findings demonstrate that the unbalanced thermal effect on the heat transmission between the paraffin and the porous copper plate caused a significant temperature difference between the copper ligaments and the paraffin porous plate. The use of the two-temperature energy method correctly answers the characteristics related to heat transfer because in the research of most researchers, the experimental and simulation results have a low percentage of error. In order to store thermal energy, Nie et al (Nie et al., 2021), investigated the effect of geometry adjustment on the thermal response of metal porous plate/phase change composite materials. The findings demonstrate that compared to the cylinder system, the conical shell system boosts natural convection. The frustum tube arrangement, however, boosts convection as well as conduction. The performance of the composite metal/PCM porous plate in terms of heat transfer is largely unaffected by variations in geometry. For pure PCM and composite metal/PCM porous plates, the change in geometry reduces the full melting time by at least 9.2% and 5.6%, respectively. Zhao et al (Zhao et al., 2010), investigated the use of porous metal plates embedded in phase transition materials to enhance heat transfer to store thermal energy (PCM). Depending on the structure and composition of the porous plate metal, the porous metal plate was able to boost the overall heat transfer rate by 3 to 10 times in the melting process (two-phase zone) and the pure liquid region compared to PCM. Baby and Balaji (Baby and Balaji, 2013), performed experimental studies on the increase in thermal performance and the effect of orientation on a PCM-based heat sink filled with a porous plate. The working time of a PCM with a porous metal plate filled with PCM is compared to a PCM without a porous metal plate but filled with PCM 7.5 at 10 watts to determine the enhancement ratio and to determine the maximum PCM increase ratio. The PCM-based heatsink operation ratio is full of the porous metal plate to metal porous plate heatsink, but without PCM 3 at 7 watts for the set point temperature of 52℃. In addition, the results of heat sinks based on PCM with the aluminum metal porous plate were also very similar to the previous case. Cui (Cui, 2012), conducted an experimental investigation of the thermal charging procedure using a paraffin-filled high-porosity copper porous plate. The findings demonstrate that a metal porous plate can, therefore, be used to decrease the charging time and speed up the melting process by 36%. A myristyl alcohol/metal porous plate was used by Huang et al (Huang et al., 2017), to study the thermal characteristics and improved thermal conductivity of composite phase change materials for solar thermal storage. The latent heat when using PCM metal porous plate composite is reduced by 3-29% in the melting process compared to the latent heat of Myristyl pure alcohol. Jin et al (Jin et al., 2017), examined a visualized pore-scale study of the heat transfer of a molten paraffin wax saturated in a porous copper plate and the effects of pore size. The results showed that at a wall superheat of 20℃, 30 PPI and 50 PPI copper porous plates result in approximately the same overall melting rate, which is much faster than the 15 PPI melting rate. In order to store energy for electronic thermal management, Ali et al (Ali et al., 2020), conducted experimental research on the thermal behavior of paraffin in open-cell copper and nickel-iron foams. The results showed that the heatsink based on a porous copper plate at 5 to 6 ℃ exhibited a lower base temperature than a nickel-iron porous plate. When examining the effect of porous plate porosity, porous copper plate with less porosity (95%) at the end of the charge cycle exhibited an 11% lower base temperature. Using experimental and numerical methods, Marri and Balaji (Marri and Balaji, 2021), investigated the impact of metal foams' porosity and PPI gradients on the thermal efficiency of a composite phase change heat sink. The findings indicate that the porosity performs better than heatsink settings with uniform porosity and PPI density in terms of time to reach the set point temperature by 28 and 45%, respectively. It is clear from the numerical simulations that the convection velocity cells are dramatically altered by the PCM melt percentage, which impacts the PCM melting dynamics. Babapour and Karimi (Babapoor and Karimi, 2015), investigated the thermal storage optimization of paraffin composites with different nanoparticles. The results showed that Al2O3 nanoparticles had the ability to promote the thermal storage properties of paraffin. Bahari et al (Bahari et al., 2020), investigated the effect of paraffin nanocomposite with AL2O3 in an indirect solar dryer. The results showed that the addition of AL2O3 nanofluid to paraffin reduced the drying time of the product. A summary of experimental studies on the PCM material melting process in porous plates is presented in Table 1.

The examined literature indicates that the melting of PCM material in two copper and iron foams (iron wool) connected to the copper absorber plate has not been studied. Due to the low thermal conductivity of paraffin as a phase change material, copper and iron foams (iron wool) were used, and the charging

and discharging processes of PCM and the effect of the implementation of the copper absorber plate on the charging and discharging processes of PCM materials were investigated and the results were compared to each other. This new study can be widely used for solar storage applications, especially solar panels, types of solar collectors (FPSC, ETSC, and PTSC), solar air heaters (SAH), solar desalination systems, and solar dryers that are capable of using porous foams. The obtained results were achieved using the solar simulation device, which would significantly help scientists in the field of renewable energy in future research.

Table1. Several experimental research papers on the charging and discharging of PCMs in copper and iron foams.

Ref.	Type of PCM / melting temperature	Type of porous foam	Important results
(Zhang et al., 2017)	Paraffin / 54.43-64.11	copper foam	-Due to its high latent heat, paraffin warmed up slowly during the melting process, but porous copper plate warmed up more quickly. - The paraffin/ copper porous plate composite performed better in heat transmission than pure paraffin due to the solid thermal conductivity of the copper foam. Compared to paraffin, which is pure paraffin, the temperature distribution of the paraffin/foam copper composite was more even.
(Chen et al., 2016)	Paraffin / 54-56	copper foam	-To improve heat transfer, the FSPCMs (form-stable phase change materials) can infuse into the porous metal plate. -To improve heat transfer, the FSPCMs can impregnate porous metal plates.
(Li et al., 2012)	Paraffin / 46.48-60.39	copper foam	-The foam-PCM composite's ultimate overall thermal resistance was lower than that of PCM. - By either reducing the pore density to speed up natural convection or reducing the porosity to improve the effective thermal conductivity, the temperature distribution within the foam-PCM composite becomes more uniform.
(Li et al., 2017)	Sodium acetate trihydrate / 56.75	copper foam	-Copper porous plate /SAT has a thermal conductivity rate 11 times greater than pure SAT. -Copper porous plate /SAT composite PCM has an energy storage density up to $467 MJ/m^3$.
(Mancin et al., 2015)	Paraffin wax / 52-60	copper foam	-The function of PCM heat transmission is significantly improved by copper foams. -Using a copper foam structure allows for the elimination of severe freezing issues associated with asymmetric heating.
(Zhu et al., 2020)	lauric acid / 41-45	Iron foam	-The latent heat and melting point of the composites are 177.88 kJ/kg and 44.36℃. -Composites are made of lauric acid and porous iron plate that contain graphene offer good thermal stability and dependability.
(Ali et al., 2020)	Paraffin wax / 34-36	Iron-Nickel foam	- By examining the heat transfer, it can be concluded that foam with less porosity will perform better during charging and discharging. - Minimal melting point PCMs work well with light heating loads.
Present study	Paraffin wax / 57-60	Copper Foam and Iron wool	- The copper absorber plate attached to the copper foam accelerated the melting rate to a pure PCM of 600s. - Energy saving in the case of using the copper absorber plate connected to the copper foam had the highest value of 75%.

2. EXPERIMENTAL

An experimental system including a solar simulator, data logger and K-type thermocouple, pyranometer, and Teflon insulation was set up to place samples. Tests were performed at the "Institution of Science and High Technology and Environmental Sciences, Kerman." Figure 1 shows the experimental settings used. Test boxes made out of Teflon insulation with dimensions of $5 \times 5 \times 2\ cm$ and the samples were placed inside the cubic hole in the middle compartment of Teflon with dimensions of $4 \times 4\ cm$. Copper foam and iron wool were both $3 \times 3\ cm$ in size and $1\ cm$ in thickness. The thermo-physical properties of copper foam and iron wool and PCM material (paraffin RT57-60) are given in Table 2.

The porosity effect was considered for copper foam with a constant PPI density of 10. The solar simulator provided the heat required for melting PCM in terms of LUX. Therefore, a pyranometer was placed in the solar simulator to measure irradiation intensity and heat flux. In all experiments, the heat flux was $3.824^{kw}/_{m^2}$. The features of the solar simulator are given in Table 3.

As shown in Figure 2a, the sample preparation steps include: (1) calculating the weight of PCM material and porous foams, (2) melting PCM material with an electric heater, (3) filling copper and porous iron plates with PCM material, and (4) placing samples in Teflon insulted box. The next step, shown in Figure 2b, is to place the copper plate using solder on copper and iron foams and, then, to fill it with PCM. The melting temperature fluctuations of PCM material were investigated using pre-calibrating K-type thermocouples. K-type thermocouples were affixed to the paraffin-filled inside of the foam, and a 16-channel data logger was employed to capture temperature data (Model: 32M96, Hioki, Japan, precision 0.1). Pyranometer (KIPP ZONEN, CMP6, precision 4W/m2) was used to gauge the radiation output of the solar simulator. Therefore, by analyzing the collected data, it is possible to determine the melting rate of PCM materials and their heat storage capability. A sample of pure paraffin core (without any porous metal plate) was examined for comparison to investigate the increase in heat transmission caused by copper and iron foams. Moreover, the impact of the structure (porosity) of porous foams on the transfer of heat from solid to liquid was examined. DSC analysis was also carried out to obtain the thermo-physical attributes of paraffin, as shown in Figure 3.

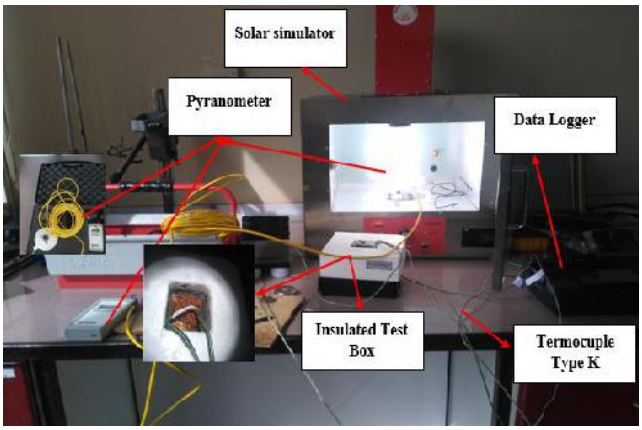

Figure 1. Image of test setup and measuring instruments.

Table 2. Thermo-physical attributes of paraffin and selected foams

Feature	Copper Foam	Iron Wool	PCM (paraffin RT57-60)
Porosity (%)	85	95.2-98.3	-
Melting range (℃)	-	-	57-60
Thermal conductivity (W/m.K)	378	81	0.2
Latent heat (J/g)	-	-	169.51
Apparent density (kg/m3)	200	180	783

Table 3. Technical specifications of the tested solar simulator

Components	Details and Dimension
Chamber solar simulator	12 inches wide, 12 inches deep, and 8.5 inches high are the internal dimensions. External dimensions are 18 inch wide, 13.75 inches deep, and 26 inches high. Weight 31 pounds and output current 110 or 220 VAC with 6 amps. The external and internal materials of the body are stainless steel and aluminum alloy (highly reflective), respectively.
Lamp	A 300W Cermax Xenon light is used by the device. There is also a dimmer switch so that power output can be adjusted to meet AM 1.5 intensity.
Filter	A single 2-inch round filter is positioned at the chamber's top (in the filter holder).
Lense	Lenses with a diameter of 2" can fit the filter adaptor. This beam can modify the output intensity by expanding or contracting the beam.

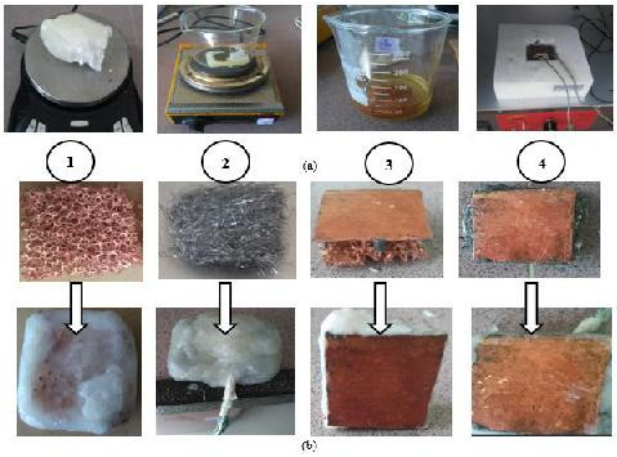

Figure 2. (a) Sample preparation steps; (b) Paraffin filling in cases with copper foam, iron wool, copper foam with copper absorber, and iron wool with copper absorber.

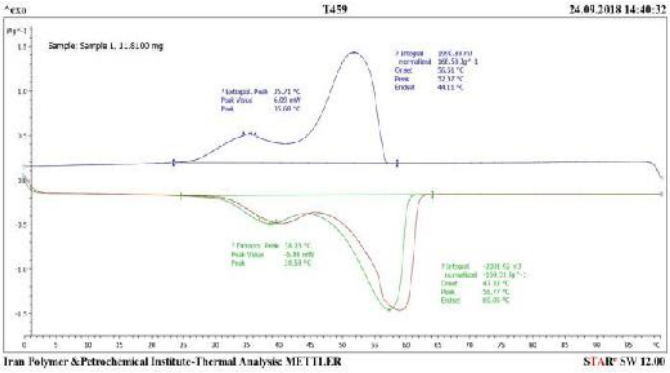

Figure 3. The melting curve of paraffin from DSC.

3. UNCERTAINTY ANALYSIS

The measurement error in the case of the input heat flux and temperature is responsible for the overall uncertainty. Test uncertainty in this research was conducted using Equation 1 (Zhao et al., 2010). With δT_{TC} being ±0.1ºC (±0.43 %) for thermocouples, the uncertainty of the solar simulator is ±0.5 %. Using Eq. (1), the test's overall degree of uncertainty was calculated as 1.41%.

$$U_T = \sqrt{\left(\frac{\delta T_{TC}}{T_{TC}}\right)^2 + \left(\frac{\delta q_{PM}}{q_{PM}}\right)^2} \times 100\% \quad (1)$$

4. RESULTS AND DISCUSSION OF EXPERIMENTS

Figure 4 depicts the PCM sample outcome when two pieces of foam made of copper and iron are involved. The wall temperature rises steadily at the same rate as paraffin throughout the charging process. The 2400s pure PCM reaches 67.3℃, i.e., above the melting point; copper foam and iron foam reach 73.27℃ and 72.5℃, respectively.The increase in heat transfer via copper foam is due to the excellent heat conduction of metal foam solid structures. The temperature line experiences a significant drop following the successful transition of the pure PCM from solid to liquid. The increase in heat transmission brought about by the inherent convection effect of the liquid phase can be the cause of it. Foam can make the temperature distribution more homogeneous in the discharging process. The heat from the PCM can be efficiently dissipated via a foam structure, resulting in a reduction process for copper and iron foams. Therefore, using metal foams significantly improves the PCM heat transfer efficiency, similar to the charging process.

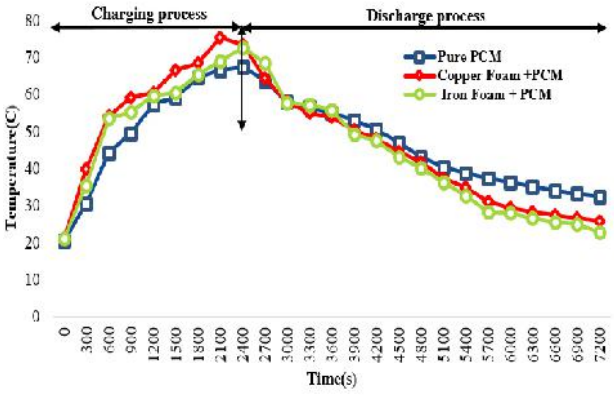

Figure 4. Comparison between three different modes of pure PCM: PCM with copper foam and PCM with iron foam in the charging and discharging processes.

In Figure 5, upon the addition of a copper absorber plate to copper and iron foams, the melting process of PCM material and the effect of heat transfer are investigated. As can be seen, by adding the absorber plate, the heat transfer increases and the maximum value is 77.41℃ for copper foam and 74.67℃ for iron foam. The reason for this can be the effect of conductive heat transfer between the copper absorber plate and the foam structure containing PCM. For copper and iron foams, a foam structure can quickly dissipate heat from the PCM and reduce discharging. However, when the copper absorber plate is added to copper and iron foams, the process does not decrease during discharge and the heat present in the copper absorber plate, which still transfers to the foam containing PCM, can explain the reason.

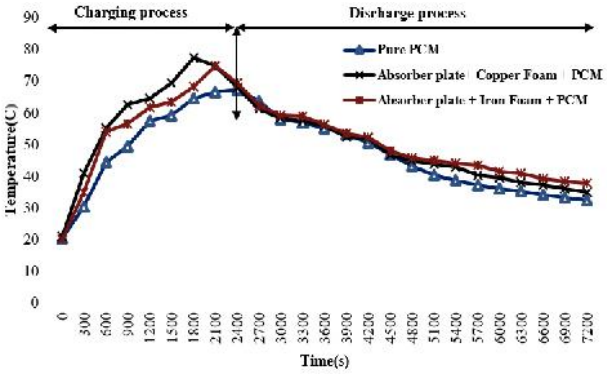

Figure 5. Comparison between pure PCM samples and copper and iron foam samples with copper absorber plate during the melting process

Figure 6 depicts a diagram showing the temperature of the absorber plate when mounted on copper and iron foams while they are melting PCM. The maximum temperature of the absorber plate reaches 104℃ in the 1800s. Moreover, at 3000s to 7200s, the temperature of the absorber plate slowly declines. Figures 4 and 5 show that the onset of phase change of PCM material from liquid to solid is in the 2400s. As shown in Figure 7, when copper and iron foam are used, the phase changes in the time of the PCM material are 2100 and 2390s, respectively. When the copper absorber plate is added to the copper and iron foam, the phase changes in the time of the PCM material are 1800 and 2100s, respectively. Therefore, the best case is when the copper absorber plate is connected to the copper foam containing PCM. However, when the copper absorber plate is connected to the iron foam, it can provide acceptable results.

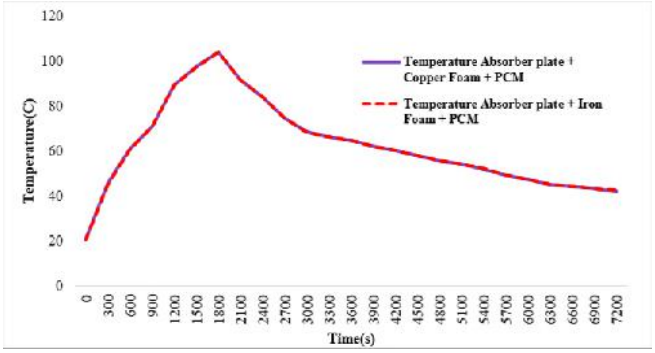

Figure 6. Temperature absorber plate used when melting PCM

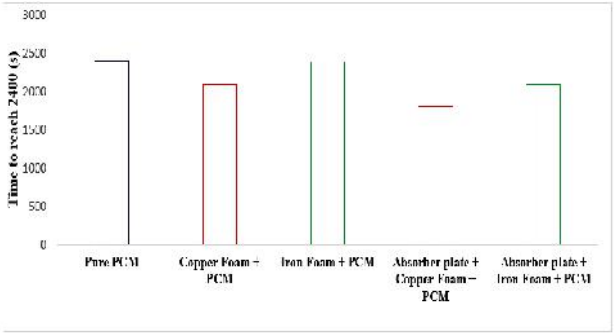

Figure 7. Comparison of paraffin melting time in different modes

To calculate the energy saving of PCM materials in different modes, the start time of the phase change process can be reduced from the total phase change time (7200s) and divided by 7200s. In Figure 8, when copper and iron foam are used, the stored energy reaches 70.83% and 66.8%, respectively.

However, when the copper absorber plate is used, it reaches 75% and 70.83%, respectively. The best case is when the copper absorber plate is attached to the copper foam.

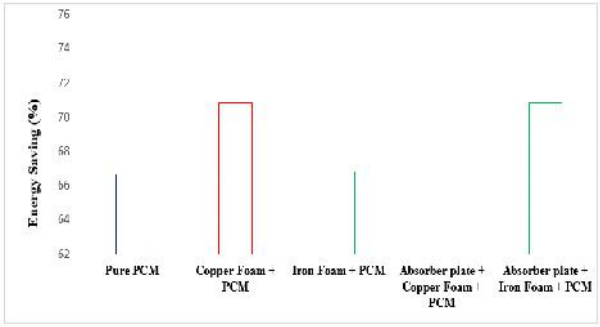

Figure 8. Comparison of melting paraffin energy saving in different modes

5. CONCLUSIONS

This study used pure paraffin filled with and without porous copper plate and iron wool, as well as pure paraffin with the addition of a copper absorber plate to the copper and iron wool, to melt PCM. The findings demonstrated that adding metal foams could significantly increase the effective thermal conductivity of the melting process. Given that it uses a porous copper plate and iron wool, the highest temperature of PCM reaches 73.27°C and 72.5°C, respectively. By adding copper absorber plates to copper porous plate and iron wool, the highest PCM temperature reached 77.41°C and 74.67°C, respectively. The heat transfer rate increased by 14% when the copper porous plate was combined with a copper absorber plate. Therefore, using metal foam with a copper absorber plate might hasten its melting and cut down on charging time. Natural convection can boost heat transfer efficiency and lower the temperature discrepancy between the wall and the PCM when the PCMs start to melt. The best case is when the copper absorber plate is connected to the porous copper plate, which reduces the charging time by 600 seconds compared to the pure PCM and saves 75% of the energy, while the pure PCM saves 66.66% of the energy. In addition, connecting the copper absorber plate to iron wool ensure viable thermal performance and stores 70.83% of the energy. The most important disadvantage of porous copper plates is their high cost, which makes them less popular for use in storage systems. Therefore, according to the results of this research, iron wool exhibits acceptable performance in terms of increasing heat transfer and speeding up the melting of PCM materials, and it can be used in storage systems.

6. ACKNOWLEDGEMENT

The authors express their gratitude to the Research institution of Higher Science and Technology and Environmental Sciences and the Kerman Graduate University of Technology (KGUT) for using laboratory equipment in this research.

Nomenclature

U_T	Uncertainty total (%)
ETSC	Evacuated tube solar collector
FPSC	Flat plate solar collector
LHS	Latent Heat Storage
PCM	Phase change material
SAH	Solar air heater
SHS	Sensible Heat Storage
TES	Thermal energy storage

REFERENCES

1. Abhat, A. (1983). Low temperature latent heat thermal energy storage: heat storage materials. *Solar energy*, *30*(4), 313-332. https://doi.org/10.1016/0038-092X(83)90186-X

2. Agyenim, F., Hewitt, N., Eames, P., & Smyth, M. (2010). A review of materials, heat transfer and phase change problem formulation for latent heat thermal energy storage systems (LHTESS). *Renewable and sustainable energy reviews*, *14*(2), 615-628. https://doi.org/10.1016/j.rser.2009.10.015

3. Ali, H. M., Janjua, M. M., Sajjad, U., & Yan, W. M. (2019). A critical review on heat transfer augmentation of phase change materials embedded with porous materials/foams. *International Journal of Heat and Mass Transfer*, *135*, 649-673. https://doi.org/10.1016/j.ijheatmasstransfer.2019.02.001

4. Ali, H. M., & Arshad, A. (2017). Experimental investigation of n-eicosane based circular pin-fin heat sinks for passive cooling of electronic devices. *International Journal of Heat and Mass Transfer*, *112*, 649-661. https://doi.org/10.1016/j.ijheatmasstransfer.2017.05.004

5. Ali, H. M. (2020). Experimental study on the thermal behavior of RT-35HC paraffin within copper and Iron-Nickel open cell foams: Energy storage for thermal management of electronics. *International Journal of Heat and Mass Transfer*, *146*, 118852. https://doi.org/10.1016/j.ijheatmasstransfer.2019.118852

6. Arshad, A., Ali, H. M., Khushnood, S., & Jabbal, M. (2018). Experimental investigation of PCM based round pin-fin heat sinks for thermal management of electronics: effect of pin-fin diameter. *International Journal of Heat and Mass Transfer*, *117*, 861-872. https://doi.org/10.1016/j.ijheatmasstransfer.2017.10.008

7. Arshad, A., Ali, H. M., Ali, M., & Manzoor, S. (2017). Thermal performance of phase change material (PCM) based pin-finned heat sinks for electronics devices: Effect of pin thickness and PCM volume fraction. *Applied Thermal Engineering*, *112*, 143-155. https://doi.org/10.1016/j.applthermaleng.2016.10.090

8. Babapoor, A., & Karimi, G. (2015). Thermal properties measurement and heat storage analysis of paraffinnanoparticles composites phase change material: Comparison and optimization. *Applied Thermal Engineering*, *90*, 945-951. https://doi.org/10.1016/j.applthermaleng.2015.07.083

9. Baby, R., & Balaji, C. (2013). Experimental investigations on thermal performance enhancement and effect of orientation on porous matrix filled PCM based heat sink. *International Communications in Heat and Mass Transfer*, *46*, 27-30. https://doi.org/10.1016/j.icheatmasstransfer.2013.05.018

10. Barghi Jahromi, M., Kalantar, V., & Abdolrezaie, M. (2020). Experimental Study of Effect of Storage Phase Change Materials (PCM) on the Function of a Passive Solar Ventilator. *Modares Mechanical Engineering*, *20*(7), 1709-1717. http://mme.modares.ac.ir/article-15-38118-en.html

11. Bahari, M., Najafi, B., & Babapoor, A. (2020). Evaluation of α-AL2O3-PW nanocomposites for thermal energy storage in the agro-products solar dryer. *Journal of Energy Storage*, *28*, 101181. https://doi.org/10.1016/j.est.2019.101181

12. Bhardwaj, A. K., Kumar, R., Kumar, S., Goel, B., & Chauhan, R. (2021). Energy and exergy analyses of drying medicinal herb in a novel forced convection solar dryer integrated with SHSM and PCM. *Sustainable Energy Technologies and Assessments*, *45*, 101119. https://doi.org/10.1016/j.seta.2021.101119

13. Brahim, N. I., Al-Sulaiman, F. A., Rahman, S., Yilbas, B. S., & Sahin, A. Z. (2017). Heat transfer enhancement of phase change materials for thermal energy storage applications: A critical review. *Renewable and Sustainable Energy Reviews*, *74*, 26-50. https://doi.org/10.1016/j.rser.2017.01.169

14. Chen, P., Gao, X., Wang, Y., Xu, T., Fang, Y., & Zhang, Z. (2016). Metal foam embedded in SEBS/paraffin/HDPE form-stable PCMs for thermal energy storage. *Solar Energy Materials and Solar Cells*, *149*, 60-65. https://doi.org/10.1016/j.solmat.2015.12.041

15. Cui, H. T. (2012). Experimental investigation on the heat charging process by paraffin filled with high porosity copper foam. *Applied*

thermal engineering, *39*, 26-28. https://doi.org/10.1016/j.applthermaleng.2012.01.037

16. Dincer, I., & Rosen, M. A. (2021). Thermal energy storage: systems and applications. *John Wiley & Sons.* https://scholar.google.com/scholar?hl=en&as_sdt=0%2C5&q=I.+Dincer+and+M.+A.+Rosen%2C+Thermal+energy+storage+systems+and+applications.+John+Wiley+%26+Sons%2C+2021.&btnG=
17. Ebrahimi, H., Akhijahani, H. S., & Salami, P. (2021). Improving the thermal efficiency of a solar dryer using phase change materials at different position in the collector. *Solar Energy*, *220*, 535-551. https://doi.org/10.1016/j.solener.2021.03.054
18. Huang, X., Lin, Y., Alva, G., & Fang, G. (2017). Thermal properties and thermal conductivity enhancement of composite phase change materials using myristyl alcohol/metal foam for solar thermal storage. *Solar Energy Materials and Solar Cells*, *170*, 68-76. https://doi.org/10.1016/j.solmat.2017.05.059
19. Iranmanesh, M., Akhijahani, H. S., & Jahromi, M. S. B. (2020). CFD modeling and evaluation the performance of a solar cabinet dryer equipped with evacuated tube solar collector and thermal storage system. *Renewable Energy*, *145*, 1192-1213. https://doi.org/10.1016/j.renene.2019.06.038
20. Jahromi, M. S. B., Kalantar, V., Akhijahani, H. S., & Kargarsharifabad, H. (2022). Recent progress on solar cabinet dryers for agricultural products equipped with energy storage using phase change materials. *Journal of Energy Storage*, *51*, 104434. https://doi.org/10.1016/j.est.2022.104434
21. Jin, H. Q., Fan, L. W., Liu, M. J., Zhu, Z. Q., & Yu, Z. T. (2017). A pore-scale visualized study of melting heat transfer of a paraffin wax saturated in a copper foam: Effects of the pore size. *International Journal of Heat and Mass Transfer*, *112*, 39-44. https://doi.org/10.1016/j.ijheatmasstransfer.2017.04.114
22. Kumar, N., & Gupta, S. K. (2021). Progress and application of phase change material in solar thermal energy: An overview. *Materials Today: Proceedings*, *44*, 271-281. https://doi.org/10.1016/j.matpr.2020.09.465
23. Li, W. Q., Qu, Z. G., He, Y., & Tao, W. (2012). Experimental and numerical studies on melting phase change heat transfer in open-cell metallic foams filled with paraffin. *Applied Thermal Engineering*, *37*, 1-9. https://doi.org/10.1016/j.applthermaleng.2011.11.001
24. Li, T. X., Wu, D. L., He, F., & Wang, R. Z. (2017). Experimental investigation on copper foam/hydrated salt composite phase change material for thermal energy storage. *International Journal of Heat and Mass Transfer*, *115*, 148-157. https://doi.org/10.1016/j.ijheatmasstransfer.2017.07.056
25. Mancin, S., Diani, A., Doretti, L., Hooman, K., & Rossetto, L. (2015). Experimental analysis of phase change phenomenon of paraffin waxes embedded in copper foams. *International Journal of Thermal Sciences*, *90*, 79-89. https://doi.org/10.1016/j.ijthermalsci.2014.11.023
26. Marri, G. K., & Balaji, C. (2021). Experimental and numerical investigations on the effect of porosity and PPI gradients of metal foams on the thermal performance of a composite phase change material heat sink. *International Journal of Heat and Mass Transfer*, *164*, 120454. https://doi.org/10.1016/j.ijheatmasstransfer.2020.120454
27. Matofali, A. X., & Massawe, E. S. (2016). Investigation of effect of rock storage system parameters on thermal cooling performance. https://article.sciencepublishinggroup.com/html/10.11648.j.acm.20160501.12.html
28. Nie, C., Liu, J., & Deng, S. (2021). Effect of geometry modification on the thermal response of composite metal foam/phase change material for thermal energy storage. *International Journal of Heat and Mass Transfer*, *165*, 120652. https://doi.org/10.1016/j.ijheatmasstransfer.2020.120652
29. Shalaby, S. M., & Bek, M. A. (2015). Drying nerium oleander in an indirect solar dryer using phase change material as an energy storage medium. *Journal of Clean Energy Technologies*, *3*(3), 176-180. 10.7763/JOCET.2015.V3.191
30. Usman, H., Ali, H. M., Arshad, A., Ashraf, M. J., Khushnood, S., Janjua, M. M., & Kazi, S. N. (2018). An experimental study of PCM based finned and un-finned heat sinks for passive cooling of electronics. *Heat and Mass Transfer*, *54*, 3587-3598. https://doi.org/10.1007/s00231-018-2389-0
31. Wang, Z., Zhang, Z., Jia, L., & Yang, L. (2015). Paraffin and paraffin/aluminum foam composite phase change material heat storage experimental study based on thermal management of Li-ion battery. *Applied Thermal Engineering*, *78*, 428-436. https://doi.org/10.1016/j.applthermaleng.2015.01.009
32. Xie, B., Cheng, W. L., & Xu, Z. M. (2015). Studies on the effect of shape-stabilized PCM filled aluminum honeycomb composite material on thermal control. *International Journal of Heat and Mass Transfer*, *91*, 135-143. https://doi.org/10.1016/j.ijheatmasstransfer.2015.07.108
33. Zhao, C. Y., Lu, W., & Tian, Y. (2010). Heat transfer enhancement for thermal energy storage using metal foams embedded within phase change materials (PCMs). *Solar energy*, *84*(8), 1402-1412. https://doi.org/10.1016/j.solener.2010.04.022
34. Zhang, P., Meng, Z. N., Zhu, H., Wang, Y. L., & Peng, S. P. (2017). Melting heat transfer characteristics of a composite phase change material fabricated by paraffin and metal foam. *Applied Energy*, *185*, 1971-1983. https://doi.org/10.1016/j.apenergy.2015.10.075
35. Zhu, C., Ran, F., & Fang, G. (2020). Thermal properties improvement of lauric acid/iron foam composites with graphene nanoplates as thermal energy storage materials. *Journal of Energy Storage*, *27*, 101163. https://doi.org/10.1016/j.est.2019.101163

JREE: Vol. 10, No. 4, (Autumn 2023) 66-77

Journal of Renewable Energy and Environment

Journal Homepage: www.jree.ir

Materials and Energy Research Center

MERC

Research Article

Techno-Environmental Analysis of Hybrid Energy System for Offshore Oil Rig Black Start

Abraham Olatide Amole[a*], Adebimpe Oluwaseun Adeyeye[a], Daniel Oluwaseun Akinyele[b], Kehinde Adeleye Makinde[c], Stephen Oladipo[d]

[a] *Department of Electrical, Electronics, and Telecommunication Engineering, College of Engineering, Bells University of Technology, Ota, Nigeria.*
[b] *Department of Electrical and Electronics Engineering, Olabisi Onabanjo University, Ago-Iwoye, Nigeria.*
[c] *School of Computing, Design and Digital Technologies, Teesside University, Middlesbrough, UK.*
[d] *Department of Electrical and Electronics Engineering, University of Johannesburg, Johannesburg, 2006, South Africa*

PAPER INFO

Paper history:
Received: 13 July 2022
Revised: 30 October 2022
Accepted: 07 November 2022

Keywords:
Oil Rig,
Black Start,
Energy Systems,
Technical,
Environmental,
Analysis

ABSTRACT

The use of Diesel Generators (DGs) and gas turbines to power oil rigs is characterized by pollution due to the emission of harmful gases like carbon dioxide, very high noise levels, high maintenance costs, and the inability to start the platform if the DG fails. Offshore wind energy generation system provides a viable alternative means of powering the oil rig and can also be integrated to operate in parallel with gas turbines. However, offshore wind energy might fail if not properly designed due to the high variability of wind resources. Hence, the objective of this work is to design offshore Wind Turbine Generator (WTG) energy generation system, DG, and hybrid DG-WTG for the black start of an offshore oil rig. The designed energy systems are simulated using HOMER Pro. Furthermore, the performance of the simulated systems was evaluated using the electrical production, unmet load, and emission profile as the performance metrics. The results of the hybrid DG-WTG powered black start revealed that 150kW DG generated 322,071kWh/yr representing 6.77% of the total generation and 1.5MW WTG generated 4,434,632kWh/yr representing 93.2% of the total generation. The comparison of the emissions from DG and DG-WTG revealed that 294,058kg/yr, 1,945kg/yr, 80.9kg/yr, 9.02kg/yr, 720kg/yr, and 688kg/yr of CO_2, CO, UH, PM, SO_2, and NO, respectively, were released into the atmosphere by DG-WTG which is very low compared to 969,129kg/yr, 6,109kg/yr, 267kg/yr, 37kg/yr, 2373kg/yr, and 5739kg/yr of CO_2, CO, UH, PM, SO_2, and NO, respectively, released into the atmosphere by DG. The sensitivity analysis revealed that while the electrical production of 100kW and 50kW DGs decreased with an increase in WTG height, the electrical production of 1.5MW WTG increased with an increase in WTG height. It was further revealed that the higher the WTG height the smaller the quantity of the emission released into the atmosphere.

https://doi.org/10.30501/jree.2022.350408.1402

1. INTRODUCTION

The conventional means of generating energy poses a lot of challenges emanating from high costs and emissions. Nigeria is currently battling with energy deficiency arising from poor power networks, ageing power infrastructure, and insufficient generation (Makinde et al, 2021; Amole et al., 2020). According to Ijeoma, 2012), there are numerous obstacles militating against the development and the present state of energy generation and utilization. The author also discussed the ways the Nigerian government is operating the existing power sector and the plans to attract private companies to contribute to the growth of the sector. The global communities continue to develop interest in renewable energy as a means of addressing global energy challenges and climate change issues and significant efforts have been made to develop and create eco-friendly alternative energy generation techniques (Attabo, 2019; Chakraborty et al., 2011). A comparative study of renewable energy sources in (Salih et al., 2014) revealed that wind energy was the most promising, economical, and fast-growing renewable energy source. The market potential, ample availability, and cost competitiveness of wind energy led to a consistent technological development, which has made it easier and more effective to exploit its energy potential (Aazami et al., 2022; Hosseini et al., 2022). Another renewable energy source that has similar potential is solar photovoltaics. Both have been widely utilized in replacing conventional energy generation sources such as gas, crude oil, and coal (Ajibola and Balogun, 2019) and have helped to reduce atmospheric pollution and the level of harmful gas emissions.

In response to the growing demand for environmentally-friendly energy generating sources, energy providers are making significant investments in the development of wind energy (Kumar et al., 2018, Brimmo et al., 2016). Electricity generation using wind energy has the fastest growth and development rate among other renewable energy sources, as reported in (Lop´ez-Guevara et al., 2020). Nigeria is still lagging behind in the implementation of these eco-friendly energy-generating technologies. The United State wind energy generating capacity stood at 16,818 MW in 2007 with additional 8,358 MW in 2008 and 9,922 MW in 2009 (Olalekan

*Corresponding Author's Email: *aoamole@*bellsuniversity.edu.ng (A. O. Amole)
URL: https://www.jree.ir/article_161982.html

Please cite this article as: Amole, A. O., Adeyeye, A. O., Akinyele, D. O., Makinde, K. A. & Oladipo, S. (2023). Techno-Environmental Analysis of Hybrid Energy System for Offshore Oil Rig Black Start, *Journal of Renewable Energy and Environment (JREE)*, 10(4), 66-77. https://doi.org/10.30501/jree.2022.350408.1402.

et al., 2020). As of the beginning of 2010, the generation capacity increased to 35,098 MW, which is double what was generated in 2007 (Ajayi et al., 2014, Pritesh et al., 2016). Today, offshore WTGs with capacities as high as 10 MW to 14 MW are available. Further, several manufacturers have announced and are testing offshore WTGs up to 14 MW. Yet, no WTGs larger than 15 MW have been announced (Energinet, 2015).

Further development has been made to maximize the energy being generated from the WTG (Arshad and O'kelly, 2013, Adedipe et al., 2018). Offshore wind energy has been one of the most significant outcomes of this development since there are enough wind resources to harness offshore. Therefore, the development of WTG with a higher energy-generating capacity has been made possible (Aardal et al. 2012). One of the major challenges of energy generation using wind energy is the availability and variability of wind resources (Arshad and O'kelly, 2013, Kumar et al., 2021, Ajibola and Balogun, 2019). These challenges are mostly responsible for the failure of several wind energy system installations (Pham and Shin, 2020). Installation of WTGs offshore has offered better wind availability and less variability, making the generation of electricity through this means more efficient and reliable (Rohan et al., 2020). Offshore wind energy eliminates the cost of transmitting energy from the grid or onshore wind farm for offshore usage since the offshore wind turbines are much closer to such loads (Vales and Soares, 2020).

Renewable energy has found usage in different areas, thereby lessening the demand for conventional energy sources. For example, solar PV has been variously used to energize different loads such as residential (Dioha and Kumar, 2018; Makinde et al., 2021; Hosseinian et al., 2016; Imam et al., 2020), telecommunications (Anayochukwu and Onyeka 2014; Amole et al., 2021), water supply (Okakwu et al., 2022; Stoyanov et al., 2021), and healthcare (Babatunde et al., 2019; Olatomiwa et al., 2018, Oladigbolu et al., 2021). In the same manner, the wind energy system has been used to provide the required energy for several services and businesses among which one include water supply (Ayodele et al., 2018) and electricity supply (Ohunakin et al., 2012). Grid integration of wind energy systems is one of the most common phenomena in renewable energy system design and implementation as it has been found to offer several advantages such as strengthening of weak transmission lines (Butt et al., 2022), real power loss reduction (Mahat, 2006), and WTG performance improvement (Aazami et al., 2022). The biogas energy system is another fast-growing renewable energy source that aids a cleaner environment and an energy-sufficient world (Akinbomi et al., 2014; Odekanle et al., 2020). Energy from bio-gasifier has been used for powering rural healthcare facilities (Achirgbenda et al., 2020) and providing support to the grid (Jumare et al., 2020). Hybridization of these renewable energy sources has been widely adopted for design and performance improvement (Ndukwe et al., 2019; Teo and Go, 2021; Gabbar et al., 2020; Mazzeo et al., 2021). The idea behind hybridizing energy sources is to increase the reliability of the system, which is the desired factor for efficient operation (Kitindi 2021). This also helps reduce the generator running time, thereby reducing fuel usage and running cost. Then, it backs up the system during the period where the wind speed is not enough to drive the WTG to produce enough energy (Jayswal, 2017).

Generally, the sustainability of renewable energy depends on many factors that are complex and highly dynamic. The STEEP model is a model that gives a comprehensive account of factors that generally affect renewable energy systems (Akinyele et al., 2021). The model has been used to evaluate different designs of renewable energy systems. For instance, techno-environmental studies (Erixno and Rahim, 2020; Lubritto et al., 2011; Aberilla et al., 2019; Amole et al., 2021) of different energy systems allow for technical evaluation and environmental impacts of such systems. While techno-economic analysis (Gabbar et al., 2020; Oladigbolu et al., 2019; Jahid et al., 2020; Imam et al., 2020; Jamil et al., 2012) of renewable energy systems permits technical assessment and economic implications of such systems, techno-economic and environmental studies (Butt, 2022; Kitindi, 2021; Akinbulire et al., 2014; Masrur et al., 2020) give a broader view of technical, economic, and environmental assessments of renewable energy systems in general. The social and policy implications (Kumar, 2020) of any renewable energy system can also be measured with the STEEP model.

Oil rig platforms, which are usually of larger capacities, can be located onshore and offshore. Effective running of the rig depends on reliable and large amounts of electricity (Zhang et al., 2019). The black start unit is a very essential unit of the oil rig platform that provides electricity supply for platform startup and emergency loads, including platform lighting and other loads in the living quarters when the gas turbine is not running. The black start unit provides electricity supply to the gas turbine compressors and pumps that need to be operated even when the rig is not in operation.

Traditionally, oil rig platforms are powered using both DG and gas turbine that involves burning fossil fuel (Agung et al., 2022). The use of gas turbines and DG is, however, accompanied by the emission of carbon dioxide (CO_2), particulate matter (PM), Sulphur dioxide (SO_2), and nitrate-oxide (NO) which are harmful to the eco-system and high running costs. It has been reported that 80% of the greenhouse gas emission from offshore drilling results from these generators (Wu and Re, 2012). In this paper, attention is given to the black start of ExxonMobil offshore platform, Bonny Island, Nigeria which is the DG.

A review of relevant literature presented in the subsequent section indicates that wind energy has been widely used for different applications. However, it has been found that the wind energy system is mostly used in the complementary mode with other energy sources due to its high variability for effective performance. Also, it has been claimed a number of times that there is abundant wind energy offshore and in the coastal areas. However, these resources are yet to be explored for offshore applications. Consequently, this paper examines WTG, DG, and hybrid offshore DG-WTG for the black start of ExxonMobil offshore platform, Bonny Island, Nigeria by considering both the techno-environmental aspect of an offshore hybrid DG-WTG system and the sensitivity analysis since the height of the WTG is a major factor that determines the number of wind resources that WTG can access (Vorpahl et al., 2013). The variability of wind speed remains a major factor that affects the offshore WTG power output and this can severely impact its performance. This is a great disadvantage to the oil rig as the WTG may not be able to generate as much energy as required for the oil rig operation (Yang et al., 2022). Hence, the need to have a hybrid offshore DG-WTG system to provide ancillary support in cases where offshore wind energy is unable to meet the rig black start energy demands for some periods due to wind variability (EWEA, 2009).

2. LITERATURE REVIEW

Despite its abundance of renewable energy resources, wind energy is underused in West African nations such as Nigeria. Wind energy, on the other hand, has been highlighted as a feasible solution to Nigeria's energy poverty and insecurity. According to reports, North African countries remains at the forefront of the African wind energy market while South and Eastern African countries were predicted to make efforts that would reduce the gap. However, the implementation of wind farm projects is scarce in Central Africa and West African countries (Ajayi et al., 2014). In Nigeria, the notion to tackle energy insecurity through sustainable sources has made researchers and some other governmental bodies evaluate the nation's potential for power generation using wind and solar energy, in which some areas have been identified to have good wind resources. The Nigeria Metrological Station identified some states with good wind resources including Jos, Katsina, and Maiduguri with wind speeds as high as 8.07m/s, proving that there is a high onshore wind speed in the Northern part of Nigeria. Although the wind resources in the southwestern region of Nigeria are not so encouraging, few offshore areas in Lagos through Ondo were identified with strong wind potential and others in Bayelsa, Akwa Ibom and River State (Adedipe et al., 2018; Olujobi et al., 2022).

Several studies have gathered data on wind resources in different parts of Nigeria and evaluated the performance of wind energy conversion systems. A study in (Izelu et al., 2013) utilized the wind resources in Port Harcourt to meet the electricity requirement of the University of Port Harcourt (UNIPORT) and at its Teaching Hospital (UPTH), the WTG was installed along the Choba banks of the New Calabar River. It was demonstrated that for a projected power requirement of 21 MW in 20 years, an airfoil shape of NACA 2412 WTGs of 1.5 MW capacity would be needed for a wind velocity of 17.5 [m/s]. The economic value of the system when compared with the existing diesel plant demonstrated a saving of N8,633,032,101.98. An LCOE and present cost-based analysis of WECSs in a different part of Nigeria was carried out in (Ohunakin et al., 2013). It was found that the hub height played a significant role in the amount of energy generated by the WECS.

Grid integration of renewable technologies is another viable solution to achieving sufficient and sustainable energy in Africa. The opportunities and the associated challenges with the integration of renewable energy into Nigeria's power network were extensively discussed in (Adebanji et al., 2022; Uguru-Okorie et al., 2015). The impact of the integration of WECS on the voltage stability of the Nigerian 330 kV power grid was investigated using DIgSILENT Power Factory and MATLAB (Adeokun et al., 2021). The work revealed that DFIG-based WECS was effective in overcoming the overvoltage problem in the Northern region of the country with a Penetration Level (PL) satisfying a bus voltage criterion of 1.0 ± 0.05p.u. The work further demonstrated that loading of all critical power system equipment was 35% and hence, it proffered a viable solution for voltage instability on the weak National grid. Similarly, the fuzzy logic-based peak load-sharing technique for grid-connected wind energy systems was studied in (Ashraf et al., 2017). The result obtained from the work revealed that the improved Pitch Frequency Control (PFC) of the wind energy system was achieved with minimal percentage overshoot and settling time. The General Algebraic Modeling System (GAMS) was adopted for the study of power management in smart 33-bus distribution networks augmented with wind turbines and solar PV (Mehbodniya et al., 2022). The results presented in the work in comparison to conventional power flow studies showed improvement rates of 40.7%, 33%, 36%, and 74.7% for the active and reactive power losses, network energy costs, and voltage deviations, respectively.

The hybridization of different energy sources has proven to be one of the most promising means of providing affordable and clean energy to the growing population. Therefore, several studies have considered hybrid renewable energy technologies for a reliable supply of electricity (Ohiero et al., 2018; Asif and Khanzada, 2015; Kitindi, 2021). Genetic algorithm-based optimization of a hybrid PV-WTG energy system for the Patani community was examined by the authors in (Nyeche and Diemuodeke, 2019) using HOMER, MATLAB, and MS Excel spreadsheet. The result showed that for satisfactory performance of the system, the peak rated powers of 217 kWp and 226050 kW were required for PV and WTG, respectively. The study further illustrates that with a loss of load probability of 0.1086, the Levelized Cost of Energy (LCOE) obtained for the system is 0.27 $/kWh. The Grasshopper Optimization Algorithm (GOA) was employed in (Bukar et al., 2019) for effective energy management in a microgrid comprising solar PV, wind turbine, and diesel generator. A comparison of GOA with Particle Swarm Optimization (PSO) and Cuckoo Search (CS) through MATLAB simulation showed that GOA was optimal sizing using the Cost of Energy (COE) and system capital cost as a benchmark.

The technical and economic aspects of an advanced combined power generation cycle were considered in (Hosseinpour et al., 2020). The system consisted of a biomass gasifier, a cascaded humidified advanced turbine (CHAT), and a steam turbine. The economic result indicates a positive Net Present Value (NPV) with an investment cost per unit of energy of about 909 USD per kW. For a typical building integrated Photovoltaic (BIPV), the energy, economics, and environment were reflected for solar cells slope and azimuth as sensitivity analysis variables in (Dehkordi and Jahangiri, 2022). It was demonstrated that a 30-degree slope and zero azimuth at the per kWh of energy was found to be $0.09 and is the optimal configuration for the BIPV. Recent studies on renewable energy systems have focused more on the technical and economic implications of these systems (Peña Sánchez et al., 2021; Peloriadi et al., 2022). For instance, the hybrid renewable energy systems for electric vehicle charging applications were presented in (AlHammadi et al., 2022) with the techno-economic indices as the variables of interest. Also, off-grid renewable energy electrification models in rural Namibia were considered with an emphasis on the technical and economic parameters (Amupolo et al., 2022). In recent studies by independent researchers, environmental and economic parameters were prioritized for a standalone hybrid energy system (Chowdhury et al., 2022) and integrated anaerobic co-digestion power plant (Hamedani, 2020).

Subsequently, methods for acquiring data with respect to the energy input and load profiles were determined, and a techno-economic analysis was performed using Hybrid Optimization of Multiple Energy Resources (HOMER) software. The results demonstrated that the optimal electric vehicle charging model comprising solar photovoltaics, wind turbines, batteries, and a distribution grid was superior to the other studied configurations from the technical, economic, and environmental perspectives. An optimal model could produce excess electricity of 22,006 kWh/year with an energy cost of 0.06743 USD/kWh. Furthermore, the proposed battery–grid–

solar photovoltaics–wind turbine system had the highest renewable penetration and, thus, reduced carbon dioxide emissions by 384 tons/year. The results indicated that the carbon credits associated with this system could result in savings of 8786.8 USD/year.

Some WTG-based studies are reported in Table 1 and they demonstrated that wind energy was mostly used in a hybrid mode with other energy sources like solar PV and DGs. The table further indicates that technical, economic, and environmental parameters are predominantly used for quantifying these systems with applications in telecommunications, healthcare, and generic electricity production. The background so far laid has revealed that wind energy has been used for diverse onshore applications. However, despite the enormous wind potential offshore, it is glaring that this potential remained untapped. The offshore oil rig is the right means for harnessing this untapped offshore wind energy. This will ensure a healthier environment for the aquatic lives that are greatly affected by DG emissions and oil rig activities. Consequently, in this work, the feasibility of wind energy deployment for powering the black start load of the oil rig is explored.

Table 1. Some WTG-based studies

Author(s)	System Configuration	Results	Applications
Jahid et al., 2020).	Grid, Solar PV, WTG, and DG	Technical, Economic, and Environmental	Telecommunication
Ajewole et al., 2019) Okundamiya et al., 2014)	Solar PV, WTG	Technical, Economic, and Environmental	Telecommunication
Kitindi, 2021), Abdulmula et al., 2022)	Solar PV, WTG, and DG	Technical, Economic, and Environmental	Telecommunication
Babatunde et al., 2019), Oladigbolu ,. 2021), Gbadamosi and Nwulu, 2022), Babatunde et al., 2018)	Solar PV, WTG, and DG	Technical, Economic, Environmental, and Policy	Healthcare
Kumar et al., 2019)	Solar PV	Technical, Economic,	Healthcare
Diyoke et al. 2022)	Hydro, Solar PV, and WTG	Technical, Economic, and Environmental	Electricity
Adaramola et al., 2012)	Solar PV, WTG	Technical, Economic	Electricity
Ajibola and Balogun, 2019)	Grid, Solar PV, WTG, and DG	Technical, Economic, and Environmental	Telecommunication
Kumar et al., 2018), Brinmo et al., (2016)	Solar PV, WTG	Technical, Economic, and Environmental	Telecommunication
Lop´ez-Guevara et al., 2020), Olalekan et al., 2020)	Solar PV, WTG, and DG	Technical, Economic, and Environmental	Telecommunication
Ajayi et al., 2014), Pritesh et al., 2016), Energinet, 2015), Arshad and O'kelly, 2013)	Solar PV, WTG, and DG	Technical, Economic, Environmental, and Policy	Healthcare
Adedipe et al., 2018)	Solar PV	Technical, Economic,	Healthcare
Aardal et al,. 2012)	Hydro, Solar PV, and WTG	Technical, Economic, and Environmental	Electricity
Kumar et al., 2021)	Solar PV, WTG	Technical, Economic	Electricity

3. MATERIALS AND METHODS

The materials and the methods used in this work are presented step by step in this section.

3.1 Description of case study

The study area for this research is the ExxonMobil offshore production platform with a water depth of (26-34m) which is located about 28km off southeast, Bonny Island, Nigeria (latitude 4˚ 26′ 34.19″ N and longitude 7˚ 14′ 14.40″ E). This is the only oil and gas platform operating offshore presently in Nigeria. This is floating production storage and offloading platform as shown in Figure 1. The estimated 1.2MW load requirement of the black start is presented in Table 2 showing different pumps, vent fans, compressors, etc.

3.2 Wind resources and WTG model

The monthly average wind data of the study area for the years 2010 and 2011 are given in Table 3 as obtained at 10m anemometer hub height. The wind speed at the WTG hub height can be obtained from the wind speed at the anemometer hub height according to Equation (1), where U_H is the wind speed at the hub height of the WTG (m/s), U_A is the wind speed at anemometer height (m/s), Z_H denotes the hub height of the WTG (m), Z_A is the anemometer height (m), and Z_0 represents the surface roughness length (m). It should be noted that the WTG hub height of 80m is considered in this work and the corresponding wind speed is presented in Figure 2. The energy available in the wind can be harnessed with WTG designed based on Equation (2). Here, ρ, A, and v denote the air density (1.225 kg/m^3), WTG rotor swept area (m^2), and the wind speed (m/s). P_{WTG} is the WTG rated power and is equal to 1.5MW for a black start load of 1.2MW considering a safe operating condition of 0.2. The wind data used in this work is obtained at 80m hub height. The WTG rotor diameter can be calculated using Equation (3), where r is the length of the blade or radius of the rotor.

3.3 DG model

The peak load demand is a key parameter to consider in determining the rated capacity of a DG because the DG is expected to meet maximum demand at all times. The mathematical relation can be described by Equation (4). Here, D_{pk} and σ represent the peak load (kW) and safety factor (%) that accounts for the difference between the DG capacity and the peak load. The DG fuel consumption is calculated by Equation (5), where P_o, P_r, A, and B are the DG's operating power output (kW), DG's power rating (kW), fuel curve slope (0.246 L/kWh), and fuel curve intercept coefficient (0.08415 L/kWh), respectively.

Figure 1. ExxonMobil offshore platform, Bonny Island, Nigeria.

Table 2. Black start equipment and specifications

Equipment	Specification/capacity (y)	Quantity
Hydraulic starter pump	149kW, 415VAC	1
Generator lube oil pump	50kW, 415VAC	1
Vent fans	(150×2)kW, 415VAC	2
Instrument load	Approximately 8kW	1
Compressor	330kW, 415VAC	1
Others (lighting, heating, ventilation and living quarters)	350kW	Quite a few

Table 3. Average wind data for the years 2010 and 2011 at 10m anemometer height

Month	Average wind speed (m/s) Year 2010	Average wind speed (m/s) Year 2011
January	4.67	4.15
February	4.88	4.56
March	4.52	4.27
April	4.96	4.25
May	5.56	6.05
June	6.58	6.87
July	6.56	6.78
August	6.73	6.76
September	6.41	6.09
October	5.82	5.63
November	5.00	5.25
December	4.36	4.94

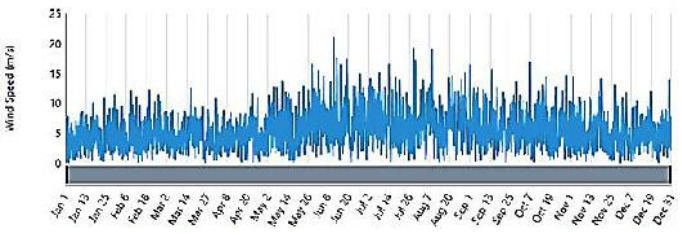

Figure 2. Daily Wind Resources of the area under study at 80m anemometer height

3.4 Design of hybrid DG-WTG

The design of the hybrid DG-WTG is based on Figure 3 using Equations 2 and 4 as presented in Table 4. The control unit is responsible for coordinating the energy interplay among the WTG, DG, and the load, as shown in Figure 4. It should be noted that the DG configuration is such that 50kW and 100kW DGs were synchronized prior to synchronization with the WTG. If P_{WTG} represents the WTG turbine power, P_{DG} represents DG power, and P_L is the black start load, then the power coordination for the control unit is based on Equations 6 to 9. Equation 6 implies that as long as the power available from the WTG is sufficiently greater than the required power by the load, the load is powered by the WTG. Also, Equation 7 implies that when no power is available from the WTG, the DG is fully called into operation. In Equation 8, ΔP represents the power deficit between the WTG and the load. ΔP is dynamic based on wind variability and is equal to P_{DG}. In a condition where the WTG power is less than the load power as in Equation 9, the DG is called into operation to augment the WTG power. It should be noted that the control unit has synchronization capability. The designs in 3.2, 3.3, and 3.4 were simulated using HOMER pro in Figure 5 and the performance of the energy systems was evaluated based on the metrics presented in Subsection 3.6.

Table 4. System model equations

Model Equations	Equations No.
$U_H = U_A\left[\ln\left(\frac{Z_H/Z_0}{Z_A/Z_0}\right)\right]$	(1)
$P_{WTG} = \frac{1}{2}\rho A v^3$	(2)
$r = \sqrt{\frac{2P_{WTG}}{\rho\pi v^3}}$	(3)
$DG_c = D_{pk}(1+\sigma)$	(4)
$DG_{fc} = AP_o + BP_r$	(5)
$P_{WTG} \geq P_L, \quad P_{WTG}$	(6)
$P_{WTG} = 0, \quad P_{DG}$	(7)
$\Delta P = P_{WTG} - P_L \approx P_{DG}$	(8)
$P_L \geq P_{WTG}, \quad \Delta P + P_{WTG}$	(9)

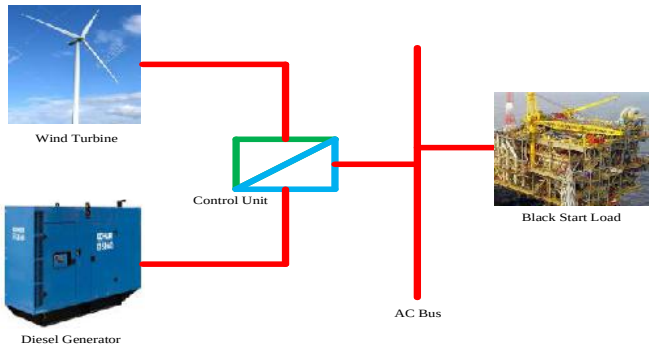

Figure 3. Hybrid DG-WTG Energy System Configuration

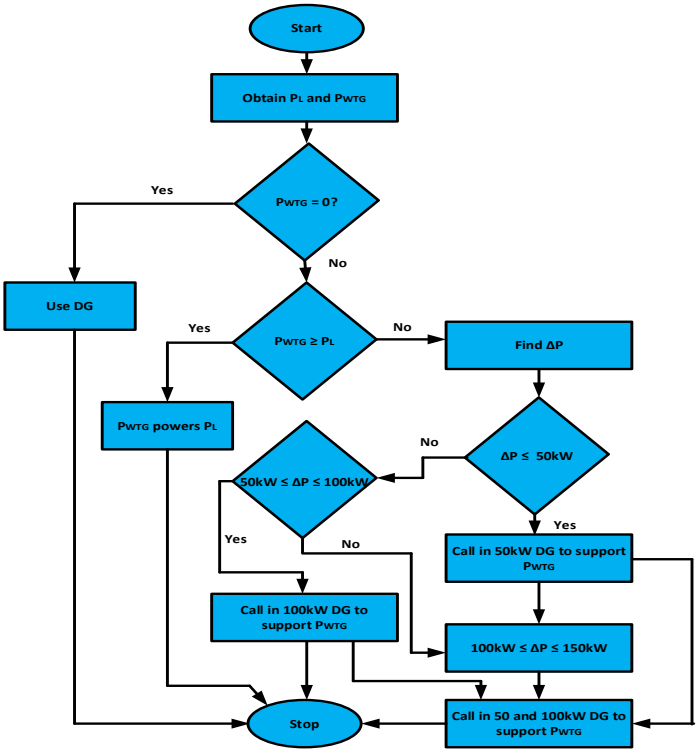

Figure 4. System energy management flowchart

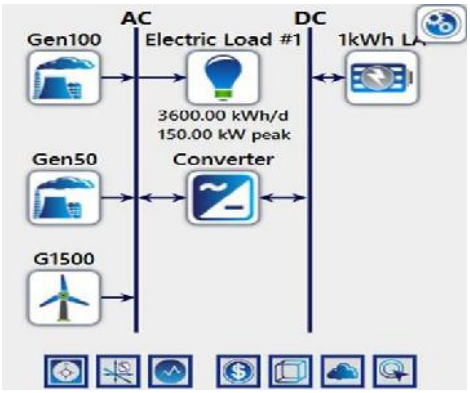

Figure 5. HOMER simulation diagram

3.5 Sensitivity analysis

The independent variable for this analysis is the hub height and it varies from 25m (for smaller WTGs of 50kW or less) to 100m (for larger WTGs of 100kW or more) and even heights higher than 100m in offshore technology for very large wind turbines of multi-megawatt. The effect of the variation in hub height on other variables that determine the quality of the hybrid generator is studied. The impact of the variation in WTG hub height with electrical production, unmet load, fuel summary, and emissions is also examined.

3.6 Evaluation of the hybrid energy system

The following parameters were used to measure the performance of the WTG, DG, and hybrid DG-WTG energy generators for the oil rig black start.

3.6.1 Electrical load served

The electrical load served is the total amount of load the electrical generating system is able to supply adequate power for proper operation. In case of excess production, the excess can be sold to the national grid.

3.6.2 Unmet electrical load

Following the simulation, there were instances when the simulation results revealed that some of the loads in the system did not get the electrical power required for operation; such loads are referred to as an unmet load. It happens when the electricity demand exceeds the supply. HOMER measures the cumulative unmet load as well as the unmet load fraction for each device over the year. By default, the software regards any power system with an unmet load as inadequate because a good power system should be able to cater for the power need of the entire system.

3.6.3 Emission

Emission is a major parameter that must be factored into the design of a power system. The focus of this work is to design a system with minimal emission with the use of WTG.

4. RESULTS AND DISCUSSION

The simulation results of the offshore DG, WTG, and hybrid DG-WTG-powered black start for the platform are presented in the subsequent subsections.

4.1 Simulation results for WTG-powered black start

Table 5 presents the simulation results of the WTG-powered black start. It is shown that 4,434,623KWh/yr is generated by the 1.5MW WTG at a height of 60m. An estimated load of 101,093 kWh/yr equivalent to 7.69% was not served by the WTG-powered black start, which is not acceptable considering the importance of the load being powered by this system. It should be noted that this system poses no environmental concerns as no fuel is used in this system as revealed by the fuel summary. Figure 6 depicts the electricity production of the WTG-powered black start, which indicates that the highest electricity, about 700kW monthly average, was generated in June, while the lowest electricity, about 280kW monthly average, was produced in January. The output power of the 1.5MW WTG is presented in Figure 7 from which it is observed that about 1500kW power is produced by the WTG for most of the periods between May and November. The unmet electric load of the WTG-powered black start is presented in Figure 8, which shows that the system is predominantly unable to serve the start between January to April and the latter part of the year.

Table 5: Simulation results of the WTG-powerd black start

Parameters	Value
WTG Turbine Size	1.5 MW
WTG Hub Height	60m
Electricity Generated	4,434,623 kWh/yr
Unmet Electricity	101,093 kWh/yr (7.69%)
Fuel Summary	0

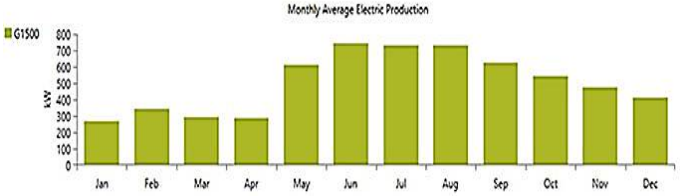

Figure 6. Monthly Average Electricity Production of WTG-Powered Black Start

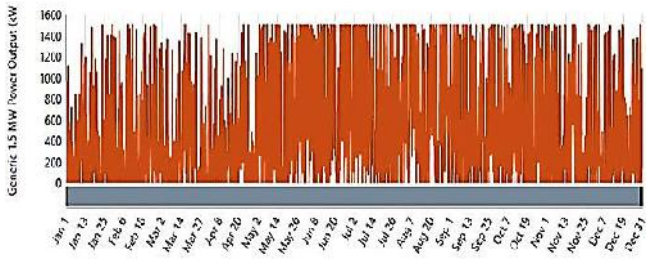

Figure 7. Daily Power Output of the 1.5MW WTG

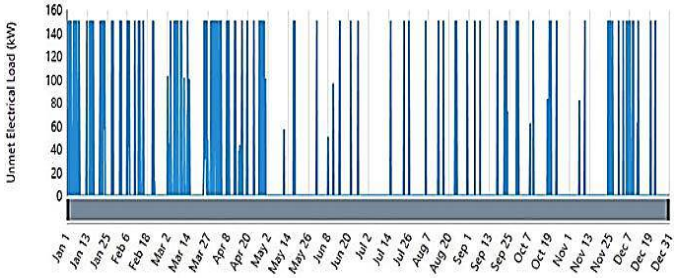

Figure 8. Daily Unmet Electrical Load

4.2 Simulation results for DG-powered black start

The simulation results of the DG-powered black start are presented in Table 6. The table 6 shows that the DG generated 1,314,000 kWh/yr of electricity with a 0% unmet electrical load, which is desirable given the significance of the load this system is powered by. However, it is noteworthy that this system poses a great environmental threat with 969,129kg/yr of CO_2, 6,109kg/yr of CO, 267kg/yr of UH, 37kg/yr of PM, 2373kg/yr of SO_2, and 5739kg/yr of NO released into the atmosphere from 370,234 L/yr of diesel fuel, as presented in Table 8. These emissions are high and must be reduced to enhance a cleaner environment for human beings and aquatic lives. The monthly average electricity production of the DG is presented in Figure 9, illustrating that constant electricity of 150kW was produced by the DG round the year, whereas the monthly average fuel consumption of the DG is shown in Figure 10. The monthly average of about 42L/hr is consumed by the DG around the year. The daily power output by the DG is presented in Figure 11 where a constant power output of 150kW is observed. The result shows no unmet electrical load.

Table 6. Summary of emissions by the DG-powered black start

Parameters	Value
Diesel Generator Size	150 kW
Electricity Generated	1,314,000 kWh/yr
Unmet Electricity	0 kWh/yr
Fuel Summary	370,234 L/yr

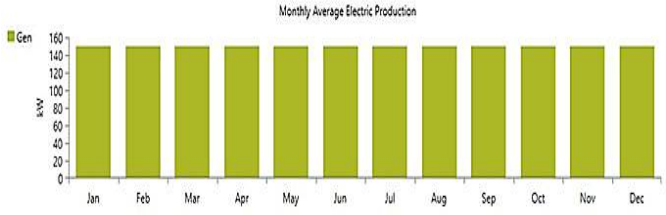

Figure 9. Monthly average electric production of DG

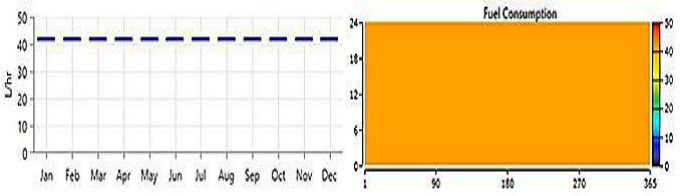

Figure 10. Monthly average fuel consumption of DG

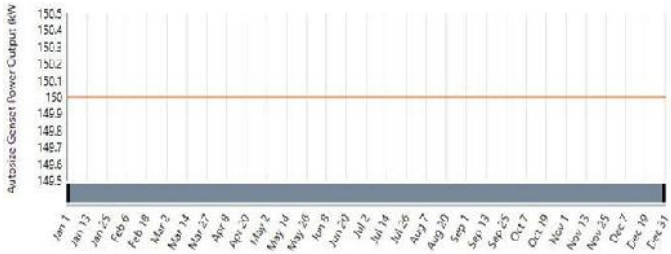

Figure 11. Daily power output of DG

4.3 Simulation results for hybrid DG-WTG-powered black start

The results of the hybrid DG-WTG-powered black start are presented in Table 7. The table shows that the 1.5MW WTG produced 4,434,632kWh/yr, which is 93.2% of the total production, while the 150kW DG produced 322,071kWh/yr, which is 6.77% of the total output. It can be inferred from this result that the WTG provides the backbone of the generation while the DG only provides ancillary support to the system. The table further presents the desired 0% system unmet electrical load with a less environmental threat in terms of emissions from 112,392 L/yr consumed by the system. The comparison of the emissions from DG and DG-WTG-powered black is presented in Table 8. It is evident that 294,058kg/yr of CO_2, 1,945kg/yr of CO, 80.9kg/yr of UH, 9.02kg/yr of PM, 720kg/yr of SO_2, and 688kg/yr of NO were released into the atmosphere by DG-WTG, which is very low compared to 969,129kg/yr, 6,109kg/yr, 267kg/yr, 37kg/yr, 2373kg/yr, and 5739kg/yr of CO_2, CO, UH, PM, SO_2, and NO, respectively, released into the atmosphere by DG powered black start. Figure 12 depicts the monthly average electric output of the DG-WTG powered system, revealing that the maximum electricity, about 800kW, was generated from June to August, with the lowest, nearly 340kW, produced in January. This indicates that the DG is only called into operation when the WTG cannot power the black start load due to wind resources variability.

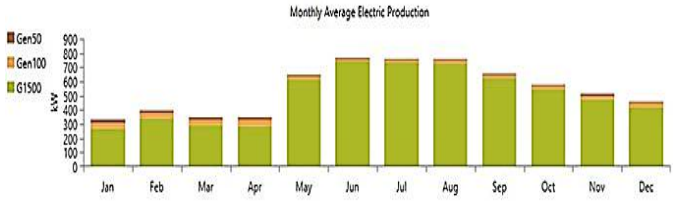

Figure 12. Monthly average electric production by the hybrid DG-WTG powered system

Table 7. Simulation results of the hybrid DG-WTG powered black start

Height (m)	Electrical Production (kWh/yr)		Unmet Electricity (kWh/yr)	Fuel Summary (L/yr)
60	100kW	265,496 (5.58%)	0 (0%)	112,392
	50kW	56,575 (1.19%)		
	1.5MW wind	4,434,632 (93.2%)		

The output powers of the 50kW DG, 100kW DG, and 1.5MW WTG are presented in Figures 13, 14, and 15, respectively. From these figures, it is observed that about 1500kW power is produced by the WTG between May and November, while that of 50kW DG and 100kW DG remains constant around the year. The percentage renewable penetration of the hybrid DG-WTG powered black start is presented in Figure 16, where it is observed that the WTG contributes largely to the total power output of the system.

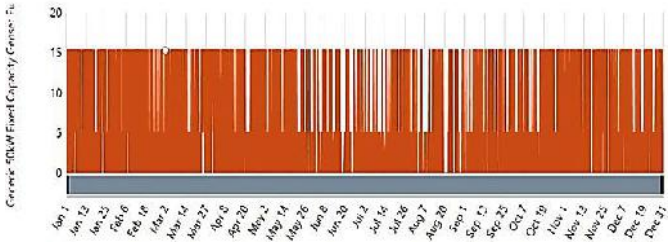

Figure 14. The 50kW fixed capacity of the hybrid DG-WTG powered black start

Table 8. Emission Summary of DG and DG-WTG

System	Height (m)	Emissions (kg/yr)					
		CO_2	CO	UH	PM	SO_2	NO
DG	-	969,129	6,109	267	37	2373	5739
DG-WTG	60	294,058	1,945	80.9	9.02	720	688

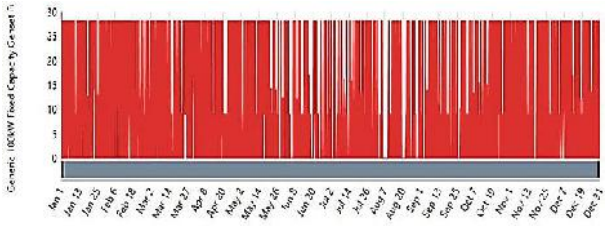

Figure 15. The 100kW fixed capacity of the hybrid DG-WTG powered black start

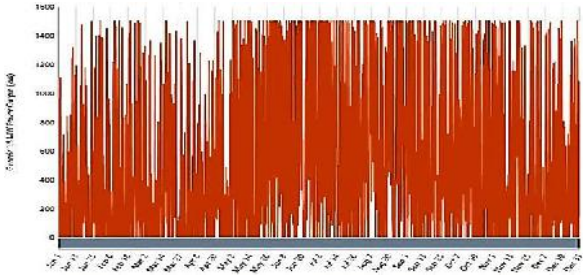

Figure 16. The 1.5MW WTG output of the hybrid DG-WTG powered black start

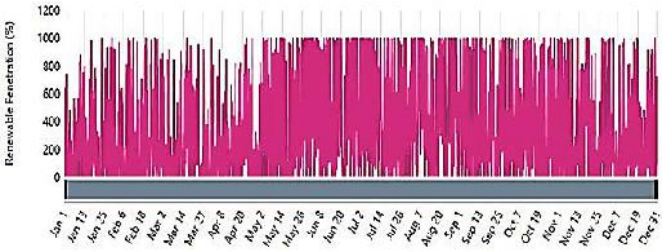

Figure 17: The percentage of renewable penetration of the hybrid DG-WTG powered black start

44.4 Sensitivity analysis results

The sensitivity analysis results of DG-WTG powered black start at varying WTG heights is presented in this section. Figure 17 shows the comparison of electrical production with the variation of WTG height for 100kW, 50kW, and 1.5MW. According to the Figure 17, the electrical production of 50kW and 100kW DGs decreases with an increase in the WTG height. This suggests that at a higher height, the WTG can produce more electrical energy, thereby reducing the energy demand from the DGs. The figure shows that the electrical production of 1.5MW WTG increases with WTG height, implying that at a greater height, there are more wind resources and, hence, WTG generates greater electrical energy. Generally, it can be inferred that while the electrical production of DGs decreases with an increase in WTG height, the electrical production of WTG increases with an increase in WTG height.

The comparison of the variation of hub height with the unmet electrical load and fuel summary of the hybrid DG-WTG powered black start is presented in Figure 18. The figure reveals that the unmet electricity of the hybrid DG-WTG powered black start decreases with an increase in the WTG height, which attests to the availability of more wind resources at a higher height, thereby resulting in reduced unmet electricity. In addition, Figure 19 shows that the fuel summary of the hybrid DG-WTG-powered black start decreases with an increase in WTG height. This shows that as a result of more energy produced by WTG at higher heights due to the availability of more wind resources, the DGs are not running at full capacity leading to a decrease in fuel summary.

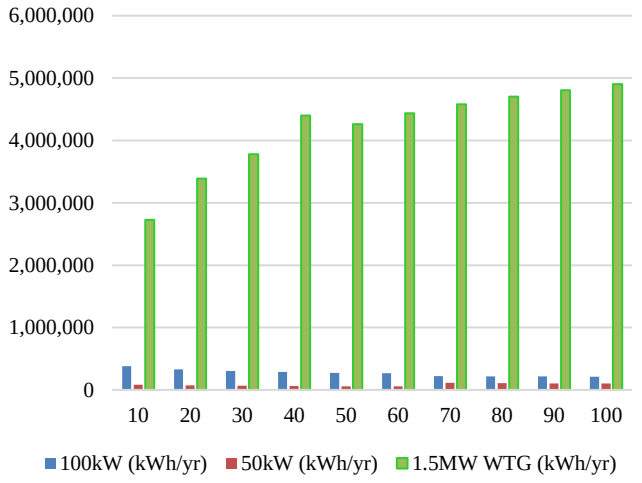

Figure 18. Comparison of electrical production of 100kW DG, 5kW DG, and 1.5MW WTG at different heights

Table 9 presents the summary of emissions by the hybrid DG-WTG powered black start at different heights from which six gases namely carbon dioxide (CO_2), carbon-monoxide (CO), unburned hydrocarbon (UH), particulate matter (PM), sulphur dioxide, SO_2, and nitrate-oxide (NO) were emitted into the environment.
Table 9 shows that a large amount of gas was released at a lower WTG height (10m), whereas less was released at the maximum WTG height (100m), which is consistent with the fuel summary stated before. 100m because greater electricity is produced with less diesel fuel at a reduced emission quantity.

Table 9. Summary of emissions by the hybrid DG-WTG-powered black start at different heights

Height (m)	Emissions (kg/yr)					
	CO_2	CO	UH	PM	SO_2	NO
10	362,953	2,431	99.9	10.6	889	564
20	314,843	2,109	86.7	9.17	771	486
30	289,987	1,942	79.8	8.45	711	446
40	274,162	1,826	75.5	7.98	672	421
50	262,537	1,729	72.3	7.64	643	402
60	253,356	1,697	69.7	7.38	621	388
70	258,088	1,702	71.0	8.00	632	648
80	253,022	1,671	69.6	7.81	602	619
90	247,811	1,637	68.2	7.64	607	602
100	242,332	1,600	66.7	7.48	594	592

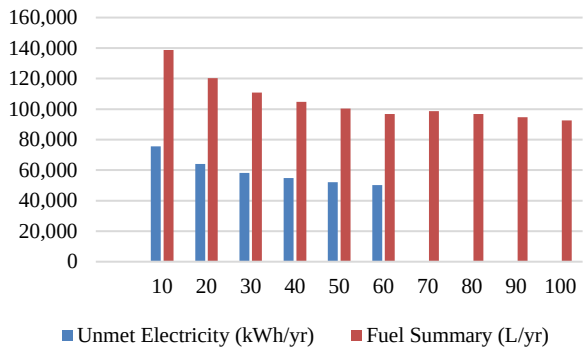

Figure 19. Comparison of unmet electricity and fuel summary with WTG height

A general study of the Table 9 shows that the higher the WTG height, the smaller the quantity of gases emitted into the environment. Finally, it can be concluded from this section that the optimal WTG height for this work is

5. CONCLUSIONS AND FUTURE DIRECTIONS

The use of renewable energy to provide the needed power for various applications is constantly on the rise. The use of wind energy is gaining acceptance due to its ability to power inductive loads. However, its high variability limits the reliability. According to the literature review conducted for this study, wind energy has mostly been employed in the generation of general electricity, healthcare, and telecommunications industry. It was further revealed that wind energy system was mostly used in the hybrid mode to improve the overall system reliability. Consequently, the possibility of harnessing the abundant offshore wind energy to power the black start load of an oil rig in place of DG was presented in this work. It was shown through HOMER Pro simulations that though the WTG provides clean energy to power the black start of the oil rig, it exhibits some unmet electrical load which necessitates the need for the hybrid DG-WTG. Furthermore, it was established that while DG had a relatively high emission profile compared to zero emissions of the WTG, the DG-WTG had a lower emission profile with no unmet electrical loads. Hence, it can be concluded from this work that the hub height of the WTG plays a significant role in the performance of the system. Moreover, the more the WTG height, the more energy produced by the WTG. Moreover, the greater the WTG height, the less the fuel summary and, hence, the less the emissions released into the atmosphere. Finally, it was demonstrated that the optimal WTG height for this work was 100m. This work opened up the possibility of harnessing the abundant offshore wind energy for offshore applications. Future studies will investigate the feasibility of harnessing the offshore wind energy for onshore applications and usage.

6. ACKNOWLEDGEMENT

The authors wish to acknowledge ExxonMobil, Bonny Island, Nigeria for providing the necessary data and information used in this work.

NOMENCLATURE

DG	Diesel Generators
WTG	Wind Turbine
CO_2	Carbon Dioxide
CO	Carbon Monoxide
UH	Unburn Hydrocarbon
PM	Particulate Matter
SO_2	Sulphur Dioxide
NO	Nitrae-oxide
MW	Mega Watts
PV	Photovoltaics
STEEP	Social, Technical, Economic, Environmental, and Policy
WECS	Wind Energy Conversion System
LCOE	Levelized Cost of Energy
MATLAB	Matrix Laboratory
PL	Penetration Level
PFC	Pitch Frequency Control
GAMS	General Algebraic Modeling System HOMER Hybrid Optimization of Multiple Energy Resource
GOA	Grasshopper Optimization Algorithm
PSO	Particle Swarm Optimization
CS	Cuckoo Search
CHAT	Cascaded Humidified Advanced Turbine
NPV	Net Present Value
BIPV	Building Integrated Photovoltaic
kWh	kilo Watt hour
USD	US dollar
L/kWh	Litre per kiloWatt hour
kWh/yr	kiloWatt hour per year
L/hr	Litre per hour
L/yr	Litre per year
Kg/yr	kilogram per year

REFERENCES

1. Aardal A. R., Marvik J. I., Svendsen H., & Giaever Tande J. O., (2012). Offshore wind as power supply to oil and gas platforms, *Offshore Technol. Conf. Proc.*, *vol. 2*, no. May, pp. 1624–1631, https://doi.org/10.4043/23245-ms.

2. Aazami R., Heydari O., Tavoosi J., Shirkhani M., Mohammadzadeh A., & Mosavi A., (2022) "Optimal Control of an Energy-Storage System in a Microgrid for Reducing Wind-Power Fluctuations," *Sustainability*, *vol. 14*, no. 10, p. 6183, , https://doi.org/10.3390/su14106183.

3. Abdulmula A. Sopian K., Ludin N. A., & Haw L. C., (2022). Micropower system optimization for the telecommunication towers based on various renewable energy sources Micropower system optimization for the telecommunication towers based on various renewable energy sources," *International Journal of Electrical and Computer Engineering (IJECE)*, pp. 1069–1076,, https://doi.org/10.11591/ijece.v12i2.pp1069-1076.

4. Aberilla J. M., Gallego-Schmid A., Stamford L., & Azapagic A. (2020). Design and environmental sustainability assessment of small-scale off-grid energy systems for remote rural communities, *Appl. Energy*, vol. 258, no. October, p. 114004,, https://doi.org/10.1016/j.apenergy.2019.114004.

5. Achirgbenda V. T., Kuhe A., & Okoli K., (2020). Techno-economic feasibility assessment of a solar-biomass-diesel energy system for a remote rural health facility in Nigeria, *Energy Sources, Part A Recover. Util. Environ. Eff.*, *vol. 00*, no. 00, pp. 1–18, https://doi.org/10.1080/15567036.2020.1813848.

6. Adaramola M. S., Oyewola O. M., & Paul S. S., (2012). Technical and economic assessment of hybrid energy systems in South-West Nigeria, *Energy Exploration & Exploitation ,vol. 30*, no. 4, pp. 533–551, https://doi.org/10.1260/0144-5987.30.4.

7. Adebanji B., Ojo A., Fasina T., Adeleye S., & Abere J., (2022) Integration of Renewable Energy with Smart Grid Application into the Nigeria's Power Network: Issues, Challenges and Opportunities, *Eur. J. Eng. Technol. Res.*, *vol. 7*, no. 3, pp. 18–24, https://doi.org/10.24018/ejeng.2022.7.3.2792.

8. Adedipe O., Abolarin M. S., & Mamman R. O., (2018) "A Review of Onshore and Offshore Wind Energy Potential in Nigeria," *IOP Conf. Ser. Mater. Sci. Eng.*, *vol. 413*, no. 1, https://doi.org/10.1088/1757-899X/413/1/012039.

9. Adetokun B. B. & Muriithi C. M., (2021). Impact of integrating large-scale DFIG-based wind energy conversion system on the voltage stability of weak national grids: A case study of the Nigerian power grid," *Energy Reports*, *vol. 7*, pp. 654–666, https://doi.org/10.1016/j.egyr.2021.01.025.

10. Agung, I. G., Angga, G., Bellout, M., Strand, B., Per, K., & Strand, E. (2022). Effect of - CO 2 tax on energy use in oil production : waterflooding optimization under different emission costs. *SN Applied Sciences*. https://doi.org/10.1007/s42452-022-05197-4.

11. Ajayi O. O., Fagbenle R. O., Katende J., Ndambuki J. M., Omole D. O., & Badejo A. A., (2014). Wind energy study and energy cost of wind electricity generation in Nigeria: Past and recent results and a case study for South West Nigeria, *Energies*, *vol. 7*, no. 12, pp. 8508–8534, (2014), https://doi.org/10.3390/en7128508.

12. Ajewole M. O., Owolawi P. A., Ojo J. S., & Oyedele O. M., (2019). Hybrid renewable energy system for 5G mobile telecommunication applications in Akure, Southwestern Nigeria," *Niger. J. Pure Appl. Phys.*, vol. 8, no. 1, p. 27, https://doi.org/10.4314/njpap.v8i1.4.

13. Ajibola O. O. E. & Balogun O. J. (2019). Stochastic analysis of energy potentials of wind in Lagos metropolis, *Lect. Notes Eng. Comput. Sci.*, vol. 2019-Octob, pp. 198–203, https://www.iaeng.org/publication/WCECS2019/WCECS2019_pp198-203.pdf.

14. Akinbomi J., Brandberg T., Sanni S. A., & Taherzadeh M. J. (2014). Development and Dissemination Strategies for Accelerating Biogas Production in Nigeria, *BioResources*, *vol. 9*, no. 3, pp. 5707–5737, https://doi.org/10.15376/biores.9.3.5707-5737.

15. Akinbulire T. O., Oluseyi P. O., & Babatunde O. M., (2014). Techno-economic and environmental evaluation of demand side management techniques for rural electrification in Ibadan, Nigeria, *Int. J. Energy Environ. Eng.*, *vol. 5*, no. 4, pp. 375–385, https://doi.org/10.1007/s40095-014-0132-2.

16. Akinyele D., Amole A., Olabode E., Olusesi A., & Ajewole T. (2021). Simulation and Analysis Approaches to Microgrid Systems Design : Emerging Trends and Sustainability Framework Application, Sustainability, 13, 11299. https://doi.org/10.3390/su132011299.

17. AlHammadi A., Al-Saif N., Al-Sumaiti A. S., Marzband M., Alsumaiti T., & Heydarian-Forushani E. (2022). Techno-Economic Analysis of Hybrid Renewable Energy Systems Designed for Electric Vehicle Charging: A Case Study from the United Arab Emirates, *Energies*, *vol. 15*, no. 18, https://doi.org/10.3390/en15186621.

18. Amole A. O., Akinyele D. O., Olabode O. E., Idogun O. O., Adeyeye A. O., & Olarotimi B. S. (2021). Comparative Analysis of Techno-Environmental Design of Wind and Solar Energy for Sustainable Telecommunications Systems in Different Regions of Nigeria, *International Journal of Renewable Energy and Research*, *Vol. 11*., No. 4, Pp: 1776 – 1792, https://doi.org/10.20508/ijrer.v11i4.12524.g8329.

19. Amole A. O., Okelola M. O., & Amole G. O. (2020). Reliability Assessment of some Selected 11 kV Feeders within Ibadan Distribution Network, *Jurnal Ilmiah Teknik Elektro Komputer dan Informatika (JITEKI)*, *vol. 6*, no. 2, pp. 39–46, https://doi.org/10.26555/jiteki.v6i2.18970.

20. Amupolo A., Nambundunga S., Chowdhury D. S. P., & Grün G. (2022). Techno-Economic Feasibility of Off-Grid Renewable Energy Electrification Schemes: A Case Study of an Informal Settlement in Namibia," *Energies*, *vol. 15*, no. 12, https://doi.org/10.3390/en15124235.

21. Anayochukwu A. V. & Onyeka A. E., (2014). Simulation of Solar-Photovoltaic Hybrid Power Generation System with Energy Storage and Supervisory Control for Base Transceiver Station (BTS) Site Located in Rural Nigeria, *International Journal of Renewable Energy Research*, *vol. 4*, no. 1, https://doi.org/10.20508/ijrer.v4i1.978.g6239.

22. Arshad M. & O'kelly B. C. (2013). Offshore wind-turbine structures: A review, *Proc. Inst. Civ. Eng. Energy*, *vol. 166*, no. 4, pp. 139–152, https://doi.org/10.1680/ener.12.00019.

23. Ashraf M. M, Abu Bakar Waqas A & Malik T. N. (2017). Grid Connected Wind Energy Conversion System for Peak Load Sharing Using Fuzzy Logic Controller, *International Journal of Renewable Energy Research*, *Vol.7*, No.4, Pp: 1767-1778, https://doi.org/10.20508/ijrer.v7i4.6254.g7217.

24. Asif R. & Khanzada F. (2015). Cellular Base Station Powered by Hybrid Energy Options, *Int. J. Comput. Appl.*, *vol. 115*, no. 22, pp. 35–39, https://doi.org/10.5120/20286-2842.

25. Attabo A. A., Ajayi O. O., & Oyedepo S. O. (2019). Wind energy generation from Nigeria continental shelf: A review, *IOP Conf. Ser. Earth Environ. Sci.*, *vol. 331*, no. 1, https://doi.org/10.1088/1755-1315/331/1/012019.

26. Ayodele T. R., Ogunjuyigbe A. S. O., & Amusan T. O. (2016). Techno-economic analysis of utilizing wind energy for water pumping in some selected communities of Oyo State , Nigeria, *Renew. Sustain. Energy Rev.*, *vol. 91*, no. (2016), pp. 335–343, 2018, https://doi.org/10.1016/j.rser.2018.03.026.

27. Babatunde, O. M., Adedoja, O. S., Babatunde, D. E., & Denwigwe, I. H. (2019). Off-grid hybrid renewable energy system for rural healthcare centers: A case study in Nigeria. *Energy Science and Engineering*, *7*(3), 676–693. https://doi.org/10.1002/ese3.314.

28. Brimmo A. T., Sodiq A., Sofela S., & Kolo I. (2016). Sustainable energy development in Nigeria : Wind , hydropower , geothermal, *Renew. Sustain. Energy Rev.*, *vol. 74*, no. pp. 474–490, 2017, https://doi.org/10.1016/j.rser.2016.11.162.

29. Bukar A. L., Tan C. W., & Lau K. Y., (2019). Optimal sizing of an autonomous photovoltaic/wind/battery/diesel generator microgrid using grasshopper optimization algorithm, *Sol. Energy*, *vol. 188*, no. March, pp. 685–696, https://doi.org/10.1016/j.solener.2019.06.050.

30. Butt, R. Z., Kazmi, S. A. A., Alghassab, M., Khan, Z. A., Altamimi, A., Imran, M., & Alruwaili, F. F. (2022). Techno-Economic and Environmental Impact Analysis of Large-Scale Wind Farms Integration in Weak Transmission Grid from Mid-Career Repowering Perspective. *Sustainability (Switzerland)*, *14*(5). https://doi.org/10.3390/su14052507.

31. Chakraborty S, Dutta S., & Biswas N. (2011). A Review Paper of Wind Energy, *Natl. Conf. Adv. Res. Electr. Syst. Technol.*, no. l, pp. 202–206, https://www.researchgate.net/publication/303736666_A_REVIEW_PAPER_0F_WIND_ENERGY.

32. Chowdhury, T., Hasan, S., Chowdhury, H., Hasnat, A., Rashedi, A., Asyraf, M. R. M., Hassan, M. Z., & Sait, S. M. (2022). Sizing of an Island Standalone Hybrid System Considering Economic and Environmental Parameters: A Case Study. *Energies*, *15*(16). https://doi.org/10.3390/en15165940.

33. Dehkordi S. R. & Jahangiri M. (2022). Sensitivity Analysis for 3E Assessment of BIPV System Performance in Abadan in Southwestern Iran, *J. Renew. Energy Environ.*, *vol. 9*, no. 1, pp. 1–12, https://doi.org/10.30501/jree.2021.262420.1173.

34. Dioha M. O. & Kumar A., (2018). Rooftop solar PV for urban residential buildings of Nigeria: A preliminary attempt towards potential estimation, *AIMS Energy*, *vol. 6*, no. 5, pp. 710–734, https://doi.org/10.3934/energy.2018.5.710.

35. Diyoke C., Eja, L. E. & Chikwado U. K. (2022). Hydro Backed-up Hybrid Renewable System for Off-grid Power in Nigeria, *American Journal of Electrical Power and Energy Systems, vol. 11*, no. 2, pp. 31–47, https://doi.org/10.11648/j.epes.20221102.12.

36. Energinet, (2015). Report - Technical Project Description for Offshore Wind Farms (200 MW) - Offshore Wind Farms at Vesterhav Norf, Vesterhav Syd, Saeby, Sejero Bugt, Smalandsfarvandet and Bornholm, no. 00 , pp. 1–73, https://docplayer.net/19063897-Technical-project-description-for-offshore-wind-farms-200-mw.html.

37. Erixno O. & Rahim N. A. (2020). A techno-environmental assessment of hybrid photovoltaic-thermal based combined heat and power system on a residential home, *Renew. Energy*, *vol. 156*, pp. 1186–1202, https://doi.org/10.1016/j.renene.2020.04.101.

38. EWEA, (2009). Executive Summary, *Wind Energy – Facts*, https://www.ewea.org/fileadmin/files/library/publications/reports/Offshore_Report_2009.pdf.

39. Gabbar H. A., Abdussami M. R., & Adham M. I. (2020). Techno-economic evaluation of interconnected nuclear-renewable micro hybrid energy systems with combined heat and power, *Energies*, *vol. 13*, no. 7, https://doi.org/10.3390/en13071642.

40. Gbadamosi S. L. & Nwulu, N. I. (2022). Optimal Configuration of Hybrid Energy System for Rural Electrification of Community Healthcare Facilities, *Appl. Sci. 12*, 4262. https://doi.org/10.3390/app12094262.

41. Hamedani, S. R., Villarini, M., Colantoni, A., Carlini, M., Cecchini, M., Santoro, F., & Pantaleo, A. (2020). Environmental and economic analysis of an anaerobic co-digestion power plant integrated with a compost plant. *Energies*, *13*(11). https://doi.org/10.3390/en13112724.

42. Hosseini E., Behzadfar N., Hashemi M., Moazzami M., & Dehghani M., (2022). Control of Pitch Angle in Wind Turbine Based on Doubly Fed Induction Generator, *Journal of Renewable of Energy and Environment*, *vol. 9*, no. 2, pp. 1–7, https://doi.org/10.30501/jree.2021.293546.1226.

43. Hosseinian Y. H., Shahnia F., & Islam S. M. (2016). Disconnection of single-phase rooftop PVs after short-circuit faults in residential feeders, *Aust. J. Electr. Electron. Eng.*, *vol. 13*, no. 2, pp. 151–165, https://doi.org/10.1080/1448837X.2016.1221637.

44. Hosseinpour S., Hosseini S. A., Mehdipour R., Hemmasi A. H., & Ozgoli H. A. (2020). Energy Modeling and Techno-Economic Analysis of a Biomass Gasification-CHAT-ST Power Cycle for Sustainable Approaches in Modern Electricity Grids, *Jree.Ir*, *vol. 7*, no. 2, pp. 43–51, [Online]. Available: http://www.jree.ir/article_106780.html.

45. Ijeoma V. (2012). Renewable energy potentials in Nigeria, *'IAIA12 Conference Proceedings' 32nd Annual Meeting of the International Association for Impact Assessment 27 May- 1 June (2012)*, Centro de Congresso da Alfândega, Porto - Portugal (www.iaia.org) pp. 1–6, https://conferences.iaia.org/2012/pdf/uploadpapers/Final%20papers%20review%20process/Vincent-Akpu,%20Ijeoma.%20%20Renewable%20energy%20potentials%20in%20Nigeria.pdf.

46. Imam A. A., Al-Turki Y. A., & Kumar R. S., (2020). Techno-economic feasibility assessment of grid-connected PV systems for residential buildings in Saudi Arabia-A case study, *Sustain.*, *vol. 12*, no. 1, https://doi.org/10.3390/su12010262.

47. Izelu C. O., Agberegha O. L., & Oguntuberu O. B., (2013). Wind energy conversion system for electrical power generation in UNIPORT and UPTH, port harcourt, rivers state, Nigeria, *Int. J. Renew. Energy Res.*, *vol. 3*, no. 3, pp. 615–626, https://doi.org/10.20508/ijrer.49835.

48. Jahid A., Hossain M. S., Monju M. K. H., Rahman M. F., & Hossain M. F., (2020). Techno-Economic and Energy Efficiency Analysis of Optimal Power Supply Solutions for Green Cellular Base Stations, *IEEE Access*, *vol. 8*, pp. 43776–43795, (2020), https://doi.org/10.1109/ACCESS.2020.2973130.

49. Jamil M., Kirmani S., & Rizwan M., (2012). Techno-Economic Feasibility Analysis of Solar Photovoltaic Power Generation: A Review, *Smart Grid Renew. Energy*, *vol. 03*, no. 04, pp. 266–274, https://doi.org/10.4236/sgre.2012.34037.

50. Jayswal G., (2017). Techno-Economic and Environmental Analysis of Wind-Diesel Power System, *International Journal of Trend in Scientific Research and Development, Volume 1(4)*, (2017), ISSN: 2456-6470, pp. 369–374, https://doi.org/10.31142/ijtsrd157.

51. Jumare I. A., Bhandari R., & Zerga A., (2020). Assessment of a decentralized grid-connected photovoltaic (PV) / wind / biogas hybrid power system in northern Nigeria, *Energy. Sustain. Soc.*, *vol. 10*, no. 1, pp. 1–25, https://doi.org/10.1186/s13705-020-00260-7.

52. Kitindi E. J., (2021). Techno-Economic and Environmental Analysis for Off-Grid Mobile Base Stations Electrification with Hybrid Power System in Tanzania, *Ijarcce*, *vol. 10*, no. 4, pp. 47–60,, https://doi.org/10.17148/ijarcce.2021.10408.

53. Kumar A., Khan M. Z. U., & Pandey B., (2018). Wind Energy: A Review Paper, *Gyancity J. Eng. Technol.*, *vol. 4*, no. 2, pp. 29–37, https://doi.org/10.21058/gjet.2018.42004.

54. Kumar G., Sarkar A., Ley C., & Matsagar V., (2021). Identification of optimum wind turbine parameters for varying wind climates using a novel month-based turbine performance index, *Renew. Energy*, *vol. 171*, pp. 902–914, https://doi.org/10.1016/j.renene.2021.02.141.

55. Kumar M., (2020). Social, Economic, and Environmental Impacts of Renewable Energy Resources, *Wind Sol. Hybrid Renew. Energy Syst. [Working Title]*, pp. 1–11, https://doi.org/10.5772/intechopen.89494.

56. Kumar N. M., Vishnupriyan J., & Sundaramoorthi P., (2019). Techno-economic optimization and real-time comparison of sun tracking photovoltaic system for rural healthcare building, *J. Renewable Sustainable Energy*, *11*, 015301, https://doi.org/10.1063/1.5065366.

57. Lop´ez-Guevara J. A., del Puerto-Flores d., Zuniga P., & Barocio E., (2020). Power-Scale Emulator Design of a DFIG-Based Variable Speed Wind Turbine. *Memorias del Congreso Nacional de Control Automático* ISSN: 2594-2492, http://www.amca.mx/RevistaDigital/cnca2020/pdf/0049_FI.pdf.

58. Lubritto, C., Petraglia, A., Vetromile, C., Curcuruto, S., Logorelli, M., Marsico, G., & D'Onofrio, A. (2011). Energy and environmental aspects of mobile communication systems. *Energy, 36(2), 1109–1114.* https://doi.org/10.1016/j.energy.2010.11.039.

59. Mahat, P. (2006). Optimal placement of wind turbine DG in primary distribution systems for real loss reduction. *Proceedings of Energy for*, *4*. http://www.aseanenergy.info/Abstract/33005492.pdf.

60. Makinde K. A, Akinyele D. O., & Amole A. O. (2021). Voltage Rise Problem in Distribution Networks with Distributed Generation : A Review of Technologies , Impact and Mitigation Approaches, *Indonesian Journal of Electrical Engineering and Informatics vol. 9*, no. 3, pp. 575–600, (2021), https://doi.org/10.52549/ijeei.v9i3.2971.

61. Makinde K. A., Adewuyi O. B., Amole A. O., & Adeaga O. A., (2021). Design of Grid-connected and Stand-alone Photovoltaic Systems for Residential Energy Usage: A Technical Analysis," *J. Energy Res. Rev.*, *vol. 8*, no. 1, pp. 34–50, (2021), https://doi.org/10.9734/jenrr/2021/v8i130203.

62. Masrur H.,. Howlader H. O. R, Lotfy M. E., Khan K. R., Guerrero J. M., & Senjyu T., (2020). Analysis of techno-economic-environmental suitability of an isolated microgrid system located in a remote island of Bangladesh," *Sustain.*, *vol. 12*, no. 7, (2020), https://doi.org/10.3390/su12072880.

63. Mazzeo D., Matera N., De Luca P., Baglivo C., Congedo P. M., & Oliveti G., (2021). A literature review and statistical analysis of photovoltaic-wind hybrid renewable system research by considering the most relevant 550 articles: An upgradable matrix literature database, *J. Clean. Prod.*, *vol. 295*, p. 126070, https://doi.org/10.1016/j.jclepro.2021.126070.

64. Mehbodniya A., A. Paeizi A, Rezaie M., Azimian M., Masrur H., & Senjyu T., (2022). Active and Reactive Power Management in the Smart Distribution Network Enriched with Wind Turbines and Photovoltaic Systems, *Sustain.*, *vol. 14*, no. 7, https://doi.org/10.3390/su14074273.

65. Ndukwe C., Iqbal T., Liang X., & Khan J., (2019). Optimal Sizing and Analysis of a Small Hybrid Power System for Umuokpo Amumara in Eastern Nigeria," *Int. J. Photoenergy*, *vol. 2019*, no. i, https://doi.org/10.1155/2019/6960191.

66. Nyeche E. N. & Diemuodeke E. O., (2019). Modelling and Optimisation of a Hybrid PV-Wind Turbine-Pumped Hydro Storage Energy System for Mini-Grid Application in Coastline Communities, *J. Clean. Prod.*, https://doi.org/10.1016/j.jclepro.2019.119578.

67. Odekanle E. L., Odejobi O. J., Dahunsi S. O., & Akeredolu F. A., (2020). Potential for cleaner energy recovery and electricity generation from abattoir wastes in Nigeria, *Energy Reports*, *vol. 6*, pp. 1262–1267, https://doi.org/10.1016/j.egyr.2020.05.005.

68. Ohiero P. O., Odey P. O., & Ukang J. U., (2018). Design and Evaluation of Solar – Pumped Storage hybrid Power System for Rural Communities in Nigeria, *International Research Journal of Engineering and Technology (IRJET)*, https://www.irjet.net/archives/V5/i7/IRJET-V5I7449.pdf, pp. 2263–2269.

69. Ohunakin O. S., Oyewola O. M., & Adaramola M. S., (2013). Economic analysis of wind energy conversion systems using levelized cost of electricity and present value cost methods in Nigeria, *International Journal of Energy and Environmental Engineering*, 4:2, pp. 2–9 http://www.journal-ijeee.com/content/4/1/2.

70. Ohunakin S. O., Ojolo S. J., Ogunsina S. B., & Dinrifo R. R., (2012). Analysis of cost estimation and wind energy evaluation using wind energy conversion systems (WECS) for electricity generation in six selected high altitude locations in Nigeria, *Energy Policy*, *vol. 48*, pp. 594–600, https://doi.org/10.1016/j.enpol.2012.05.064.

71. Okakwu I. K., Alayande A. S., Akinyele D. O., Olabode O. E., & Akinyemi J. O., (2022). Effects of total system head and solar radiation on the techno-economics of PV groundwater pumping irrigation system for sustainable agricultural production, *Sci. African*, *vol. 16*, no. April, p. e01118, https://doi.org/10.1016/j.sciaf.2022.e01118.

72. Okundamiya M. S., Emagbetere J. O., & Ogujor E. A., (2014). Assessment of renewable energy technology and a case of sustainable energy in mobile telecommunication sector," *Sci. World J.*, *vol. 2014*, https://doi.org/10.1155/2014/947281.

73. Oladigbolu J. O., Ramli M. A. M., & Al-Turki Y. A., (2019). Techno-economic and sensitivity analyses for an optimal hybrid power system which is adaptable and effective for rural electrification: A case study of Nigeria," *Sustain.*, *vol. 11*, no. 18, https://doi.org/10.3390/su11184959.

74. Oladigbolu, J. O., Al-turki, Y. A., & Olatomiwa, L. (2021). Comparative study and sensitivity analysis of a standalone hybrid energy system for electrification of rural healthcare facility in Nigeria. *Alexandria Engineering Journal*, *60*(6), 5547–5565. https://doi.org/10.1016/j.aej.2021.04.042.

75. Olalekan Idris W., Ibrahim M. Z., & Albani A., (2020). The status of the development of wind energy in nigeria," *Energies*, *vol. 13*, no. 23, pp. 1–16, (2020), https://doi.org/10.3390/en13236219.

76. Olatomiwa L, Blanchard R, Mekhilef S., & Akinyele D., (2018). Hybrid renewable energy supply for rural healthcare facilities : An approach to quality healthcare delivery," *Sustain. Energy Technol. Assessments*, *vol. 30*, no. August, pp. 121–138, https://doi.org/10.1016/j.seta.2018.09.007.

77. Olujobi O. J., Ufua, D. E., Olokundun M & Olujobi, M. (2022). Conversion of organic wastes to electricity in Nigeria : legal perspective on the challenges and prospects. *International Journal of Environmental Science and Technology*, *19*(2), 939–950. https://doi.org/10.1007/s13762-020-03059-3.

78. Peloriadi K., Iliadis P., Boutikos P., Atsonios K., Grammelis P., & Nikolopoulos A., (2022). Technoeconomic Assessment of LNG-Fueled Solid Oxide Fuel Cells in Small Island Systems: The Patmos Island Case Study, *Energies*, *vol. 15*, no. 11, pp. 1–20, https://doi.org/10.3390/en15113892.

79. Peña Sánchez E. U., Ryberg S. D., Heinrichs H. U., Stolten D., & Robinius M., (2021). The potential of variable renewable energy sources in mexico: A temporally evaluated and geospatially constrained techno-economical assessment, *Energies*, *vol. 14*, no. 18, https://doi.org/10.3390/en14185779.

80. Pham T. D., & Shin H., (2020). The effect of the second-order wave loads on drift motion of a semi-submersible floating offshore wind turbine, *J. Mar. Sci. Eng.*, *vol. 8*, no. 11, pp. 1–13, https://doi.org/10.3390/jmse8110859.

81. Pritesh P. S., Anant P. & Ajit S., (2016). Solar-Wind Hybrid Energy Generation System, *International Journal of Engineering Research and General Science*, *Vol. 4*, Issue 2, ISSN 2091-2730, http://pnrsolution.org/Datacenter/Vol4/Issue2/75.pdf.

82. Rohan K. Tim S., & Peter K. S., (2016). Large-scale offshore wind energy installation in northwest India: Assessment of wind resource using Weather Research and Forecasting and levelized cost of energy, *Wind Energy*, pp; 1–19, https://doi.org/10.1002/we.2566

83. Salih, T., Wang, Y., & Adam, M.A.A., (2014). Renewable micro hybrid system of solar panel and wind turbine for telecommunication equipment in remote areas in Sudan, *Energy Procedia 61*, 80–83, https://doi.org/10.1016/j.egypro.2014.11.911.

84. Stoyanov, L., Bachev, I., Zarkov, Z., Lazarov, V., & Notton, G. (2021). Multivariate analysis of a wind–pv-based water pumping hybrid system for irrigation purposes. *Energies*, *14*(11), 1–28. https://doi.org/10.3390/en14113231.

85. Teo Y. L. & Go Y. I., (2021). Techno-economic-environmental analysis of solar/hybrid/storage for vertical farming system: A case study, Malaysia, *Renew. Energy Focus*, *vol. 37*, no. June, pp. 50–67, https://doi.org/10.1016/j.ref.2021.02.005.

86. Uguru-Okorie D. C, Kuhe A & Ikpotokin I., (2015). Stand-alone wind energy systems for power generation in Nigeria, *International Journal of Advanced Information Science and Technology (IJAIST), ISSN: 2319:2682 vol. 4*, no. 6, pp. 56–65, (2015), https://doi.org/10.15693/ijaist/2015.v4i6.56-65.

87. Vales, Z. A. & Soares, J. (2020). Overview of Applications in Power and Energy Systems. *Applications of Modern Heuristic Optimization Methods in Power and Energy Systems*, *1*(1), 21–37. https://doi.org/10.1002/9781119602286.ch2

88. Vorpahl F., Schwarze H., Fischer T., Seidel M., & Jonkman J., (2013). Offshore wind turbine environment, loads, simulation, and design, *Wiley Interdiscip. Rev. Energy Environ.*, *vol. 2*, no. 5, pp. 548–570, https://doi.org/10.1002/wene.52.

89. Wu, J., & Re, J. (2012). Research and Application of Solar Energy Photovoltaic-Thermal Technology. *Solar Power*, *(2012)*. https://doi.org/10.5772/27897.

90. Yang, X., Wang, Z., Zhang, H., Ma, N., Yang, N., Liu, H., Zhang, H., & Yang, L. (2022). A Review: Machine Learning for Combinatorial Optimization Problems in Energy Areas. *Algorithms*, *15*(6), 205. https://doi.org/10.3390/a15060205.

91. Zhang A., Zhang H., Qadrdan M., Yang W., Jin X., & Wu J., (2019). Optimal planning of integrated energy systems for offshore oil extraction and processing platforms," *Energies*, *vol. 12*, no. 4, https://doi.org/10.3390/en12040756.

JREE: Vol. 10, No. 4, (Autumn 2023) 78-88

Journal of Renewable Energy and Environment

Journal Homepage: www.jree.ir

Materials and Energy Research Center

MERC

Research Article

Impact of Dust and Degradation on the Electrical Properties of PV Panels

Samir Tabet[a,b], Razika Ihaddadene[a,c*], Belhi Guerira[d], Nabila Ihaddadene[a,c]

[a] *Department of Mechanical Engineering, Faculty of Technology, University of Med Boudiaf, M'sila, Algeria.*
[b] *Laboratory of Materials and Mechanics of Structure L.M.MS, University of Med Boudiaf, M'sila, Algeria.*
[c] *Laboratory of Renewable Energy and Sustainable Development L.R.E.S.E, University of Mentouri Brothers, Constantine, Algeria.*
[d] *Laboratory of Mechanical Engineering L.M.G, University Mohamed Khider , Biskra, Algeria.*

P A P E R I N F O

Paper history:
Received: 05 November 2022
Revised: 01 November 2022
Accepted: 11 December 2022

Keywords:
Dust Accumulation,
Solar PV Performance,
Degradation Rate,
Degradation Mechanisms,
Electrical Characteristics

A B S T R A C T

Dust accumulation on PV surface panels is a crucial factor affecting their performance. It is more frequently noted in the desert zones. The effect of dust on the electrical behavior of damaged PV panels was investigated in this study. Three panels are used: the degraded panels (with and without dust) and the reference panels; they are located in an industrial zone with a continental climate (Bordj Bou Arréridj, Algeria). The I-V and P-V characterization and degradation mechanism visualization are used. Also, a numerical simulation was conducted to calculate the five parameters of the three modeled PV panels (diode ideality factor (a), series resistance (Rs), Shunt resistance (Rp), photocurrent (Ipv), and diode saturation current (I0)). These parameters were utilized for the first time to study the impact of dust on their degradation rate and the PV panel behavior. The degradation rate and the annual degradation rate of each parameter are affected by dust differently. The power degradation rate is increased by 5.45%. The Isc and Imax degradation rates are climbed by 6.97% and 6.0%, respectively. Vmax and Voc degradation rates decrease by 1.20% and 0.35%, respectively. Dust increased the rate of degradation for a, Iph, and I0 by 4.12%, 6.99%, and 68.17%, respectively. For Rs and Rp, the degradation rate was reduced by 4.51% and 20.01%, respectively. An appropriate netoiling approach must be considered because dust, even in non-desert areas and industrial zones, has a significant impact on the electrical characteristics degradation of a PV panel.

https://doi.org/10.30501/jree.2023.367573.1491

1. INTRODUCTION

Solar chimneys, photovoltaic (PV), and concentrated-solar power plants are a few examples of solar utilizations that have been observed in the electricity industry (Franzese et al., 2020). Thermoelectric (TE) technology is an approach that directly converts the heat available from automobiles, industries, etc. into electricity without any intermediate conversion (Seebeck effect and Peltier effect) (Subbarama et al., 2019). Similarly, TEG converts electricity into thermal energy for the required heating or cooling applications. In order to achieve the high conversion efficiency and spread its wings for all applications, extensive research into the TE technology and its materials was conducted (Subbarama et al., 2019). A recent invention involving the combination of TEG with solar concentrator technologies to generate electricity has been welcomed (Sahu et al., 2021).

Electricity can be produced directly from chemical energy in reactants by electrochemical devices known as fuel cells. Proton Exchange Membrane Fuel Cells (PEMFC) have received significant attention among all fuel cell types and have been viewed as the best option for both portable electronics like laptops and future transportation applications. Numerous studies have looked into different PEMFC performance facets in relation to operating parameters. The results of numerical simulations indicated that the presence of a substantial Gas Diffusion Layer (GDL) could enhance the movement of species across porous layers, increasing the performance of fuel cells (Ahmadi et al., 2015). Besides, the circular and elliptical channel cross-sections produced higher current densities, as compared to the traditional model (Ashkan et al., 2014).

The PV application has been developed in terms of its technology and electricity production, leading to price reduction (Darwish et al., 2013). The susceptibility of this technology to various outside climate parameters like humidity levels, temperature, wind, clouds, and lack of solar radiation in some regions is a drawback (Chaichan & Kazem, 2016). These climatic parameters have a significant impact on the efficiency of PV systems (Ihaddadene et al., 2022; Sendhil & Subbarama, 2019).

The impact of dust on PV performance on a global scale was recognized in (Mani & Phillai, 2010; Chaichan et al., 2015; Kazem et al., 2017; Vidyanandan, 2017; Chen et al., 2020). By serving as a barrier between the PV and the radiation, dust attenuates the transmittance of cellular glazing (Chaichan et al., 2015) in dusty countries and in desert regions. In dusty

*Corresponding Author's Email: razika.ihaddadene@univ-msila.dz (R. Ihaddadene)
URL: https://www.jree.ir/article_165693.html

Please cite this article as: Tabet, S., Ihaddadene, R., Guerirad, B. & Ihaddadene, N. (2023). Impact of Dust and Degradation on the Electrical Properties of PV Panels, *Journal of Renewable Energy and Environment (JREE)*, 10(4), 78-88. https://doi.org/10.30501/jree.2023.367573.1491.

countries and desert regions, it reduces cellular glazing transmittance (Chaichan et al., 2015) by acting as a barrier between the PV and the radiation. Dust collects particles with a diameter less than 500 m (Tanesab et al., 2019; Pan et al., 2019). Its composition, structural morphology, and deposition are related to its localization characteristics (Aissa et al., 2017). Noting that many contaminants and dirt, such as sand, dust, pollutants, smoke, dirt, pollen, and so on that result from human activities are suspended in the air and these have been expressed as dust in most studies. PV module performance is heavily influenced by the particle size and surface density of dust deposited on the panels (Styszko et al., 2019). Indeed, studies on this phenomenon have been reported for different solar energy technologies, in particular PV, CSP, CPV, and thermal solar (Menoufi,2017; Chaichan et al., 2018).

Dust collection on a panel may cause the cells to warm up, acting as a barrier to the power produced (Kazem et al., 2017). This tendency results in a major decline in efficiency and even the formation of a hot spot, which may eventually harm the PV module (Tripathi et al., 2017). However, there have been numerous suggestions for cleaning PV to increase efficiency. The cleaning of PV modules cannot rely on occasional rain and should be planned based on the regular density accumulated. PV system tilt-angle and orientation, ambient temperature and humidity, site characteristics, dust properties, wind speed velocity, and glazing characteristics are all factors that influence dust settlement (Mani & Phillai, 2010). Specifically, in arid areas where the use of water is challenging due to its scarcity, the presence of relatively high humidity in the air combined with dust may result in the development of thin surface layers on the PV. These layers cannot be removed by wind or any conventional cleaning techniques (Hachicha et al., 2019). The wind decelerates after a dust storm, and granules start to gather and settle. Consequently, due to their size and weight, small molecules can stay in the atmosphere for days or even months (Namdari et al., 2018).

The performance of PV systems is impacted by soiling and condensation in arid regions with high dust frequencies and high relative humidity levels, which can significantly reduce their power production. Recently, Amer et al. (Amer et al., 2022) developed a new technique to lessen the impact of moisture and soiling accumulation on PV performance using superhydrophobic and superhydrophilic coating on the PV module surface. The effect of condensation and the buildup of soiling, which could damage the performance of the PV panels and lower their efficiencies, was successfully reduced by this technique.

Due to its assistance, especially in primarily desert nations which make up the solar belt zone and its environs, the effects of dust deposits on PV panel surfaces have been extensively researched. Based on the plant location, it was found that the daily reduction in PV productivity in hot climates without precipitation may reach 0.2%/day or reduce PV productivity by 56.2% per year (Kimber et al., 2007). The findings revealed a 31–35% decline in PV performance in August 2010 in Jordan (Essalaimeh et al., 2013). The impact of dust on PV cell efficiency was examined in Baghdad (Iraq) (Mani & Phillai, 2010). The reported finding shows that dirt and pollution reduced the performance of PV despite a brief time without washing. The efficiency of the filthy and contaminated PV cells was about 12 % less than that of the clean cell. Prolonged exposure times cause the aggregation of dust particles (Waved et al., 2017). Five distinct types of dust (carbon, cement, and various classes of limestone) were used in an indoor experiment to examine if they could impact the output power of solar cells (El-Shobokshy & Hussein, 1993). They discovered that the PV efficiency was considerably worsened by finer particles.

Another study examined the effects of traffic-related pollutants and the dirt arising from them. This study discovered that this type of dust and pollutants accumulates quickly, clearly reducing the performance of PV by 20% (Dorobantu et al., 2017). The study findings also indicate that even a very thin layer of this kind of dirt buildup can result in a 40% decrease in PV efficiency. Significantly less short-circuit current is produced, especially at high dust density (Hachicha et al., 2019). Following a 1.7%/g/m^2 decline, a linear relation is found between normalizing PV power and dust collection on the PV surface. Both indoor and outdoor circumstances were validated for this correlation.

It should be mentioned that studies on the impact of dust on solar panels are frequently carried out in desert areas. Also, degraded panels were not used in these studies. According to the findings of the current research, maximum power (P_{max}), short-circuit current (I_{sc}), open-circuit voltage (V_{oc}), and shape factor (FF) all degrade at different rates. Several studies on the effect of dust on the degradation of resistances (R_s and R_p) are also mentioned. The present paper investigates the impact of dust on the degraded panels under outdoor conditions in an industrial zone located in a non-desert region characterized by a continental climate.

The first part of this work is devoted to the effect of dust and degradation on all the parameters of the curves (I-V and P-V), including I_{sc}, V_{oc}, P_{max}, I_{max}, and V_{max}. Of note, the evolution of these curves is performed using a PV simulator, which allows them to be plotted precisely under normal conditions (1000 W/m^2 and 25 °C). Furthermore, degradation mechanisms of the degraded panel in this zone are visualized.

The second section of this paper employs a numerical simulation to compute five electrical parameters (a, R_s, R_p, I_{pv}, and I_0) of the three panels namely degraded (with and without dust) and reference panels. This simulation uses a mathematical model to simulate the behavior of the PV panel. For the first time, degraded panels are used in this simulation. The obtained results allow calculating the degradation rate and annual degradation rate of these five parameters as well as evaluating the effect of dust on their degradation. Of note, the two mentioned rates have been calculated for the first time ever.

2. MATERIALS AND METHODS

This study concentrates on the monocrystalline PV modules (CEM235P-60) installed on the roof of Condor company in Bordj Bou Arréridj (BBA-Algeria), as shown in Figure 1 in detail. Despite being mounted on the roof, these panels did not produce any electricity. They are made up of 60 cells that are linked in series and have the properties of their manufacturers under typical conditions, as shown in Table 1. One panel, known as a "degraded panel with dust," has been degrading naturally for six years (it has not been cleaned). It is referred to as a "degraded panel without dust" after cleaning. Of note, in the experiments, soiling from rain and airborne dust particles, particularly in this industrial zone, constitutes the majority of the dirt accumulation. A new panel with the same settings was utilized as a reference panel.

BBA is located on a high plateaux in the north-east of Algeria (Figure 2). It is placed between 35° and 37° parallels of latitude north and between the meridians of longitudes 4° and 5° east. It is characterized by a continental climate that offers hot temperatures in the summer and very cold temperatures in winter, among the lowest in Algeria. The annual rainfall ranges from 300 to 700 mm. Winters are long, extremely cold, and frequently cloudy in BBA, whereas summers are brief, hot, dry, and mostly clear. The average annual temperature ranges from 1°C to 34°C, rarely falling below -3°C or rising above 37°C (Weather Spark. 2022).

Figure 1. Used panels from left to right :(a) Reference panel, (b) degraded panel with dust and (c) degraded panel without dust.

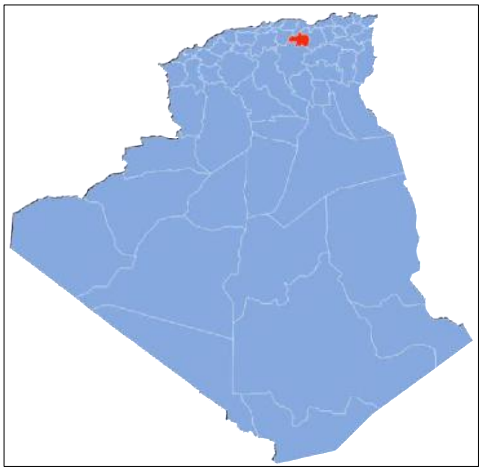

Figure 2. Geographical location of BBA region in Algeria (Wikipedia, 2022).

The performance of photovoltaic panels was evaluated using a photovoltaic simulator at Condor Company in BBA (Algeria) (Figure 3). This LED sun simulator (simulator of the A+A+A++ class), known as Ecosun Plus, was designed to carry out semi-automatic quality checks based on artificial lighting and a replication of the normal operating state for the module (STC). The high LED output allows for the recreation of solar irradiance in comparable settings, simulating the solar spectrum in accordance with IEC 60904 editions 2 and 3.

The solar simulator measures the courbes I-V and P-V, one of many variables that are crucial for determining the module power and efficiency. With the option to repeat tests without losing time between them, the same simulator offers an immediate response, good stability, and repeatability. In other words, the solar simulator is crucial for determining potential power losses in finished modules and checking the quality of the modules in the couse of solar panel testing. Ecosun Plus can be exploited for all existing solar cell technologies, including HIT, PERC, MWT, bifaciales, and hybrid silicon cells and also photovoltaic modules of all shapes and sizes, from crystal to "couche mince" for back-contact cells. In this study, this simulator was used for investigating solar panels to give the I–V and P–V curves under the STC test.

Figure 3. LED Sun Simulator in Condor company.

The degradation rate and the annual degradation rate of the degraded panel with dust are denoted by R_{DD} and R_{AD}, respectively. The degradation rate and the annual degradation rate of the degraded panel without dustn(cleaned) are given as R_{DC} and R_{ADC}, respectively. The degradation rate and the annual degradation rate of each performance parameter (open circuit voltage (V_{oc}), short-circuit current(I_{sc}), maximum power (P_{max}), maximum voltage (V_{max}), and maximum current (I_{max})) in a standard condition are calculated using the following equations (Bandou et al., 2015, Bouaichi et al., 2019):

$$R_{DD(C)}(Y) = \left(1 - \frac{Y}{Y_0}\right) \times 100 \quad (1)$$

$$R_{ADD(C)}(Y) = \frac{R_{DD(C)}(Y)}{N} \quad (2)$$

The performance parameters of the degraded panel with dust or without dust (cleaned) and reference panel are denoted by Y = [I_{sc}, V_{oc}, P_{max}, V_{max}, I_{max}] and Y0 = [P_{max0}, V_{max0}, I_{max0}, I_{sc0}, V_{oc0}], respectively. N is the year number of module exposure duration in real conditions. The reference performance parameters and the degraded performance parameters (with and without dust) are determined experimentally using the Led Sun simulator in standard conditions.

Table 1. The electrical parameters of the used PV panel at STC (Condor, 2022).

Parameters	Values.
Nominal power (P_{max})	235 W
Short-circuit current (I_{sc})	8.4 A
Open-circuit voltage (V_{oc})	37.4 V
Maximum power current (I_{max})	7.78 V
Maximum power tension (V_{max})	30.2 V
Cells number (N_s)	60
Temperature coefficient of I_{sc} (k_I)	+0.06%/°C
Temperature coefficient of V_{oc} (k_V)	+0.32%/°C
Temperature coefficient of P_{max} (k_P)	+0.41%/°C

3. RESULTS AND DISCUSSION

3.1. Degradation rates

After analyzing the degraded PV panel (with and without dust) and reference PV panel in the STC using the Ecosun Plus simulator, the I-V and P-V curves of each panel are plotted, the parameter values (I_{sc}, V_{oc}, P_{max}, I_{max}, and V_{max}) extracted for each case, and the degradation rate and the annual degradation rate calculated for the degraded panels (with and without dust).

A. Degraded panel without dust

The I-V and P-V evolutions of the degraded panel (without dust) and the reference panel are illustrated in Figures 4 and 5, respectively. All the electrical parameters (I_{sc}, V_{oc}, P_{max}, I_{max}, and V_{max}) are degrading at different rates, as noted in Table 2.

The power rate degradation was 4.32% with an annual degradation rate of 0.86%/y. These findings are consistent with the Algerian power degradation rate in several climates, including the Saharan environment (Adrar), where annual power degradation rate ranges from 0.85%/y to 2.26%/y (Bandou et al., 2015), and the Mediterranean climate in the Bouzareah, where annual power degradation rate varies from 0.82%/y to 1.47%/y (Belhaouas, 2022). In Adrar region, higher power degradation rates are observed (3.33%/year to 4.64%/year) (Kahoul et al., 2017) than that noted in BBA with continental climate conditions. V_{oc} has the lowest degradation rate (0.91%) with an annual degradation rate of 0.18%/y. Both currents I_{sc}(1.17%-0.23%/y) and I_{max}(1.13%-0.23%/y) experienced similar degradation rates. A high degradation rate for V_{max} (3.24%-0.65%/y) is noted .

B. Degraded panel with dust

Figures 6 and 7 illustrate the I-V and P-V evolutions of the reference and degraded panels with dust, respectively. The two curves I-namely V and P-V of the degraded panel with dust have the same pattern as those of the reference panel. In this case, the power rate degradation was 9.50 % with an annual degradation rate of 1.90%/y. As a result, the presence of dust reduced the maximum power generated by the degraded panel by 5.45 %.

The degradation rate of V_{oc} for the panel degraded with dust was 0.56%, with an annual degradation rate of 0.11%/y and a minimal rise of 0.35 % compared to the degraded panel without dust.

The highest degradation rates were registered for the currents, namely I_{sc}(8.06%-1.61%/y) and I_{max}(7.65%-1.53%/y), with the increase rates of 6.97% and 6.0% in the presence of dust. The degradation rate of V_{max} for the degraded panel with dust was 2.08% (0.42%/y) with a reduction of 1.20% in the presence of dust.

As noted, the presence of dust affects the degradation rate and the annual degradation rate of all the parameters (I_{sc}, V_{oc}, P_{max}, I_{max}, V_{max}) with different values, and this finding in agreement with the results of Hachicha et al. (2019). Also, in this case, the I_{sc} degradation rate was more significant than V_{oc} degradation rate; this finding is consistent with high dust density (Hachicha et all., 2019) and various industrial dusts (Dorobantu et al., 2017). Therefore, dust accumulation had no significant impact on V_{oc} as seen in Figures 6 and 7. (Andrea, 2019) found similar results using different industrial dusts (fertilizer, gypsum, aggregate crusher, and coal mine industries) under a tropical climatic condition of Arusha, Tanzania.

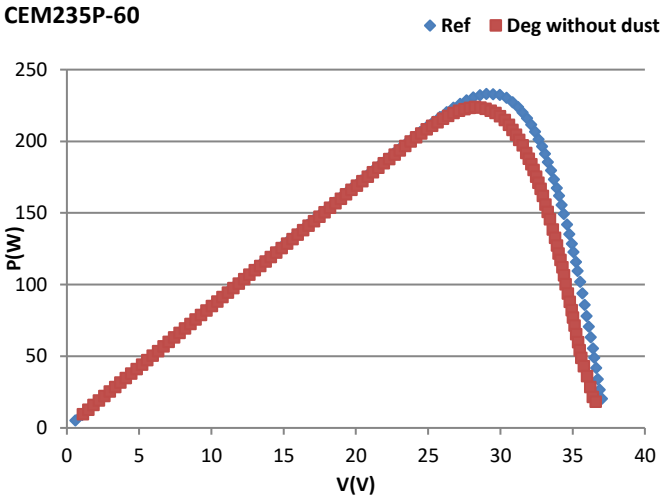

Figure 5. P-V curves for the reference panel and degraded without dust panel.

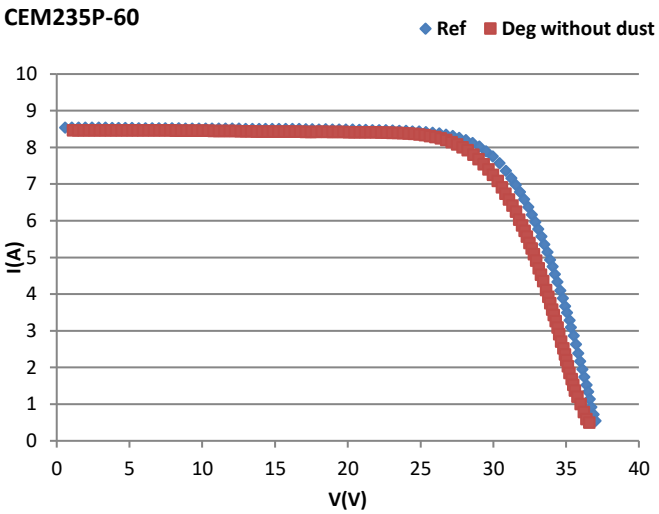

Figure 4. I-V curves for the reference panel and the degraded without dust panel.

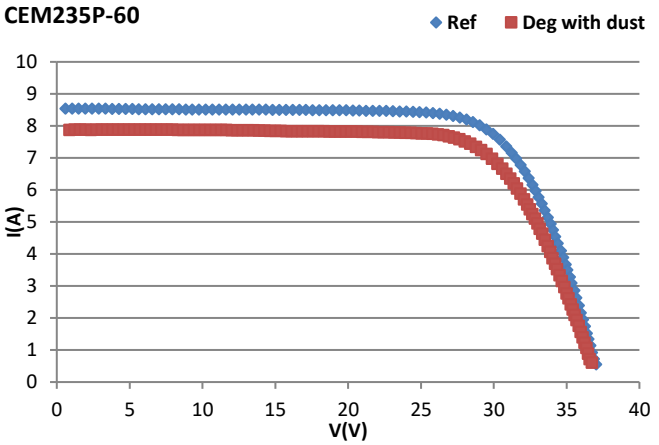

Figure 6. P-V curves for the reference panel and degraded without dust panel.

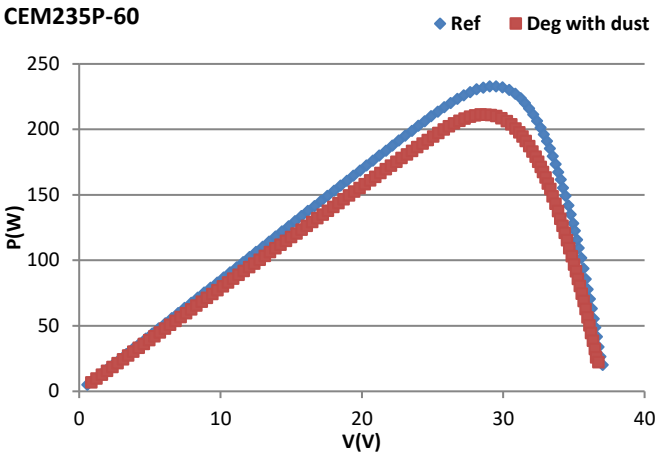

Figure 7. P-V curves for the reference panel and degraded without dust panel.

3.2. Degradation mechanisms

Visual analysis was carried out to determine the PV panel degradation modes that took place during the exposed period in the BBA climate. The following defects have been identified:

A. Discoloration of capsulant

Discoloration of encapsulant is one of the most prevalent types of visual degradation that has been noted (Figure 8a). Encapsulant discoloration (EVA degradation) occurs when a clear encapsulant turns yellow or even brown, causing the light to transmit towards the solar cells. This phenomenon may lead to the reduction of I_{sc} module and attenuated power output. According to Yang & Whitfield, (2012), the yellowness index of the encapsulant is proportionally correlated with the degradation of the Isc of the modules. The performance of the module can be reduced by as much as 50% due to encapsulant browning (Munoz et al., 2011).

B. Snail track

This mode of degradation is one of PV defects (Figure 8b) that can be detected either visually or by EL imaging. It appear as discoloration of the grid fingers of the silicon solar panel front side, resembling a snail track (Yang & Jiang, 2019). A snail track is caused by discoloration of the silver paste of the front side metallization of silicon solar cells, which occurs at the edge of the solar cell and usually traces invisible cell cracks. Some studies claim that the snail track shortage will show symptoms within 3–5 months (Meyer et al., 2013), while others claim it could take up to 2 years (Dobaria et al., 2018; Bouaichi et al., 2019). The cracks are caused by thermal stress and high temperatures, and the presence of moisture seeping through the microcracks causes the snail track to emerge.

Due to the discoloration of the snail trails, the ability of PV cells to absorb solar irradiance is diminished, which adversely affects the performance of the PV modules. Numerous studies, however, demonstrate that this kind of failure does not significantly lower electrical performance (Yang et al. 2018). Moreover, the performance of the PV module is mostly impacted by the broken PV cells (Dolara et al., 2016).

C. Hot spot

The hot spot behavior in crystalline silicon solar cells, which has been well reported in many research studies, may result from shading, soiling, damaged cells, or connections (metallization, interconnects), as well as places where high currents flow via resistive zones (Simon & Mayer, 2010). This type of degradation was noted in the studied panel, as noted in Figure 8c. Hot spots are cell regions with increased temperatures that have the ability to severely degrade modules and hasten the emergence and spread of further failure mechanisms (Kato, 2011).

D. Corrosion

To safeguard the glass borders and provide mounting points for other modules, the majority of commercial modules are enclosed. The most popular frame material is anodized aluminum due to its great strength, low weight, and inexpensive price. Over time, frames may become corroded, deformed, or loose (Mathiak et al., 2012). Mechanical loading or subpar manufacturing quality can both cause or hasten them. An example of this kind of corrosion was noted in the studied panel, as seen in Figure 8d. The frame degradation mode was a less frequent failure mode than the other failure modes (Halwachs et al., 2019).

The junction box is a rather typical source of failure in the reported module field failures (Leva & Aghaei, 2018). Detachment (from the module backsheet), improperly sealed or closed boxes, corrosion, and arcing because of defective or deteriorated wiring are the main failure modes for junction boxes. Figure 8e illustrates the corrosion of the junction box noted in the analyzed panel. Due to the high current levels passing through, junction box component deterioration and failure can result in significant performance losses and safety risks (Kontges et al., 2014).

The oxidation of metallic contacts such as cell interconnect ribbon was also noted in this panel, as illustrated in Figure 8f. This can be caused by several factors, such as humidity ingress, higher moisture absorption of encapsulant, the combination of higher temperature and humidity, and high system voltage. This defect increases the series resistance and degrades the fill factor, leading to reduced output power (Kim et al., 2014).

Table 2. The electrical parameters associated with the degradation rate of the used PV panel in STC.

Parameters	Ref Panel	Deg cleaned Panel	Deg with dust Panel	R_{DC}(%)	R_{DD}(%)	R_{ADC}(%/y)	R_{ADD}(%/y)
I_{sc}	8.56	8.46	7.87	1.17	8.06	0.23	1.61
V_{oc}	37.36	37.02	37.15	0.91	0.56	0.18	0.11
I_{max}	7.97	7.88	7.36	1.13	7.65	0.23	1.53
V_{max}	28.37	28.37	28.71	3.24	2.08	0.65	0.42
P_{max}	233.58	223.49	221.38	4.32	9.5	0.86	1.90

E. Finger interrupts

The finger interrupts that happen in cell metallization and module connections are also a typical external problem in PV modules. This defect frequently leads to a rise in R_s, which diminishes power rating (Zafifirovska et al., 2017). It was noted in the tested module, as illustrated in Figure 8g. The efficiency of the solar cell is directly impacted by the its finger shape, aging, and fabrication quality (Li et al., 2022).

3.3. The five electrical parameters' degradation rate

The values of the characteristic parameters (a, R_s, R_p, I_{ph}, and I_0) of the employed PV panels (degraded (with and without dust) and the reference panel under standard conditions were evaluated using the extraction method provided by Hussein, (2017). There are two steps in this method. The first step is concentrated on the determination of the four parameters namely R_s, R_p, I_{ph}, and I_0 using the characterization equations of the points: short-circuit current (I_{sc}), open-circuit voltage (V_{oc}), and the maximum power P_m with the corresponding voltage (V_m) and courent (I_m). In the following step, the ideality factor (a) value is adjusted by comparing the experimental and simulated I-V curves. The optimization of the NRMSE error was used to accomplish this improvement. This procedure is to be resumed as in the following:

Values of the constants A, B, and C are assumed to be as follows:

$$A = \exp\left(\frac{V_{oc}}{aV_t}\right) - 1 \quad (3)$$

$$B = \exp\left(\frac{R_s I_{sc}}{aV_t}\right) - 1 \quad (4)$$

$$C = \exp\left(\frac{V_m + R_s I_{max}}{aV_t}\right) - 1 \quad (5)$$

The thermal voltage V_t is given as:

$$V_t = \frac{a \times Ns \times k \times T}{q} \quad (6)$$

Where a and Ns are the diode ideality factor and the number of series-connected solar cells in the panel, respectively. q and k are the electron charge and Boltzmann constant, respectively, and T is the working temperature in Kelvin.

The equations of the specific points cited above can be given as follows (Hussein, 2017):

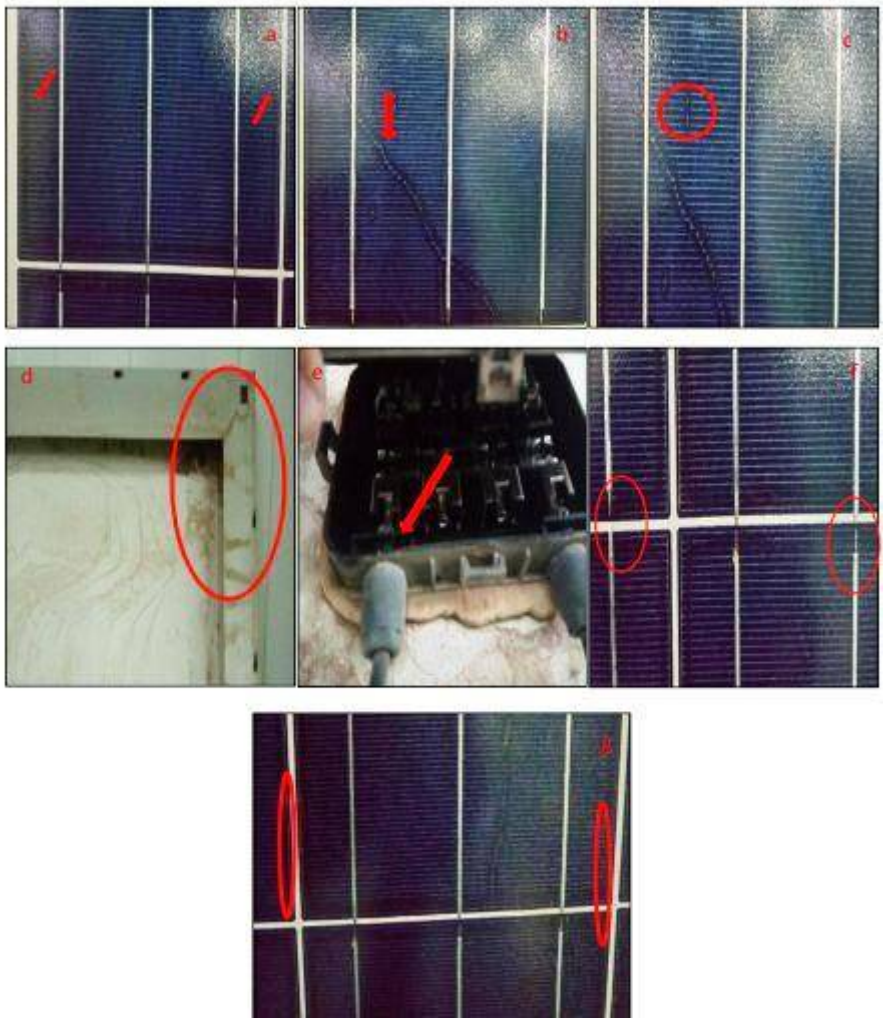

Figure 8. Degradation mechanisms recorded.
(a) Discoloration, (b) Snail track, (c) Hot spot, (d) Corrosion of aluminum frame, (e) Corrosion of the junction box, (f) Corrosion of interconnections, and (g) Finger interrupts.

$$I_0 = \frac{I_{ph}}{A} - \frac{V_{oc}}{AR_p} \quad (7)$$

$$I_{sc}(1 + \frac{R_s}{R_p}) = I_{ph} - BI_0 \quad (8)$$

$$I_{max}(1 + \frac{R_s}{R_p}) = I_{ph} - I_0 C - \frac{V_{max}}{R_p} \quad (9)$$

By substituting Eq.7 into Eq.9, the following equation is obtained:

$$I_{max}(\frac{R_s+R_p}{R_p}) = I_{ph}(\frac{A-C}{A}) + \frac{CV_{oc}-AV_{max}}{AR_p} \quad (10)$$

By substituting Eq.7 into Eq.8 , the following equation is obtained:

$$I_{ph} = \frac{AI_{sc}(1+\frac{R_s}{R_p})-B\frac{V_{oc}}{R_p}}{(A-B)} \quad (11)$$

From Eq.10 and Eq.11, maximum power can be written as follows (Hussein, 2017):

$$I_0(C + \frac{(C+1)V_{max}}{V_t}) - I_{ph} - \frac{2V_{max}}{R_p} = 0 \quad (12)$$

The four parameters namely R_s, R_p, I_0, and I_{ph} are determined by solving the following system of equations, Eq.7, Eq.8, Eq.9, and Eq.12, respectively. These equations can be rearranged to obtain an equation with only one variable, R_s, as follows (Hussein, 2017):

$$f(R_s) = V_{max}(C+1)[I_{sc}V_{oc} - I_{sc}V_{max} - I_{max}V_{oc}] - (A-C)I_{sc}V_{max}V_t + (B-C)I_{max}V_{oc}V_t + 2(A-B)I_{max}V_{max}V_t \quad (13)$$

As shown, this equation has one variable only R_s, and it is easy to find its value using the solver in the Excel software. Once the value of Rs is determined, the values of R_p and I_{ph} are estimated using the following equations (Hussein, 2017):

$$R_p = \frac{(C-B)V_{oc} - (A-B)V_{max}}{(A-B)I_{max} - (A-C)I_{sc}} - R_s \quad (14)$$

$$I_{ph} = \frac{A(1+\frac{R_s}{R_p})I_{sc} - \frac{V_{oc}}{R_p}}{(A-B)} \quad (15)$$

As mentioned in Eq. 7, the value of I_0 is calculated using the estimated values of R_p and I_{ph}.

Noting that the four unknown parameters, R_s, R_p, I_{ph}, and I_0, must be calculated using a proposed algorithm, which must be based on an initial value of the ideality factor a_0. The optimum values of these four parameters are then determined by minimizing the Normal Root Mean Square Error (NRMSE) between measured current (I_m) and simulated current (I_s) values, as noted as an objective function. The NRMSE is calculated as follows (Maouhoub, 2018):

$$NRMSE(\%) = \frac{100}{\frac{\sum_{i=1}^{N} I_{m,i}}{N}} \times \left(\frac{\sum_{i=1}^{N}(I_{m,i}-I_{s,i})^2}{N}\right)^{0.5} \quad (16)$$

The values $I_{m,i}$ and $I_{s,i}$ are the measured and simulated currents of the i^{th} point, respectively, and N is the total number of experimental points used.

A program in the Excel software was developed to perform the determination of all these parameters for the three panels studied. The values of the five parameters are gathered in Tableau 3 for the reference panel and the degraded panel (both with and without dust) in the standard conditions.

Figures 9, 10, and 11 show the validity of these findings by comparing the experimentally measured and simulated curves (I-V and P-V) for the three panels (reference, degraded ones (with and without dust)). It should be noted that the Husein method accurately defines the parameters (a, R_s, R_p, I_{ph}, and I_0).

The reference panel has a coefficient of determination (R^2) of 0.9999, an NRMSE value of 0.00813% for I-V curve, a R^2 value of 0.9995, and an NRMSE value of 0.0147% for P-V curve. The degraded panel without dust revealed 0.9995 (R^2) and 0.026% (NRMSE) values for the I-V curve and 0.9897 (R^2) and 0.0588% (NRMSE) values for the P-V curve. The degraded panel with dust showed 0.9999(R^2) and 0.004% (NRMSE) values for the I-V curve, and 1 (R^2) and 0.006% (NRMSE) values for the P-V curve.

For each of the five parameters (a, R_s, R_p, I_{ph}, and I_0), the degradation rate and annual degradation rate are determined in order to investigate the effects of degradation and dust on those parameters. As noted in Table 3, degradation and the presence of dust have an effect on the five parameters.

The ideality factors(a) including degradation rate and annual degradation rate were 7.93% and 1.59%/y, respectively. When dust is present, this factor increases by 4.18%, reaching 11.77% (2.36%/y). The I_{ph} degraded rate is the lowest at 1.04% (0.21%/y); then, it increases to 7.96% (1.98%/y) with a pourcentage of 6.99% in the presence of dust. However, when the I_0 degradation rate is the highest at 76.87% (18.53%/y), it jumps to 92.64% (18.53%/y), with a rise of 68.17% due to the presence of dust.

Table 3. The electrical parameters associated with the degradation rate of the used PV panel in STC.

Parameters	Ref Panel	Deg cleaned Panel	Deg with dust Panel	R_{DC}(%)	R_{DD}(%)	R_{ADC}(%/y)	R_{ADD}(%/y)
a	1.274	1.173	1.124	7.93	11.77	1.59	2.35
R_s	0.3254	0.4502	0.4705	-38.35	-44.59	-7.67	-8.92
R_p	372.5177	341.2018	409.4662	8.41	-9.92	1.68	1.98
I_{ph}	8.56	8.4712	7.879	1.04	7.96	0.21	1.59
I_0	4.63011x10^{-8}	10171x10^{-8}	3.80x10^{-9}	76.87	92.64	15.37	18.53

The R_s increased during this time; its degradation rate was -38.35%, with an annual rate of -7.67%/y, and this can be related to the detected degradation mechanisms (oxidation of metallic contacts and finger interrupts, as described in Section 3.3) and inducing power degradation, as noted in Table2. In arid climates, the same evolution of R_s resistance was observed (Younes et al., 2020), but with much high values ranging from 137.84% to 229.73%. When dust is present, this R_s degradation decreases to -44.59% (-8.92%/y), with the decrease of 4.51%. In this case, the dust acts as a barrier between the PV and the radiation, reducing the transmittance of cellular glazing (Chaichan et al., 2015) and the output power, as shown in Table 2.

The R_p degradation rate was 8.41%, with an annual rate of 1.68%/y. A similar decrease in R_p was seen in a desert climate (Younes et al., 2020), with an elevated value of 65%. The decrease in R_p contributes to the current reduction (Younes et al., 2020), hence the decrease in the power, maximum voltage, and maximum current, as noted in Table 2. Due to the impact of dust being present, the mentioned rate degraded by -9.92% (-1.98%/y), with a -20.01% decrease, which increased the current, as shown in Figure 6 compared with Figure 4.

The climate conditions of the BBA region across the six-year study period have a variable impact on the five characteristic parameters of the panels. I_0 is the parameter most affected by the mentioned conditions, followed by resistance R_s , which degrades at a negative rate, followed by R_p and a, which degrade at a similar rate, and finally I_{pv} ,which degrades at the slowest rate. These degradation rates vary when dust is present on the PV panel. I_0 suffers another degradation (severe) on the order of 68.17%. The resistance R_p rises by 20.01%, the I_{pv} deteriorates by 6.99%, and the resistance Rs rises by 4.51%, as well. The ideality factor (a) has decreased by 4.18%.

5. CONCLUSIONS

Photovoltaic module performance was found to be susceptible to the climate, particularly in desert areas. In addition to these climate factors, dust collection is another problem that has an impact on the functioning of the PV system. Noting that the desert areas are not the only ones with this problem, this study considers the impact of dust on the degraded panels under outdoor conditions in an industrial zone in the BBA (Algeria) region with a continental climate. The degradation rate and the annual degradation rate of the five parameters characterizing the behavior of a degraded PV panels were carried out for the first time.

In order to analyze the I-V and P-V curves for the tested panels and to identify the degraded mechanisms noticed under this climate after six years of exposure, three panels including SEM235P-60 (degraded panels (with and without dust) and a reference panel) were examined.

The power degradation rate for the degraded panel without dust was 4.32% (0.86%/y), which was comparable to the literature finding and lower than the results observed in desert regions. V_{max} had the highest rate of degradation rate (3.24%-0.65%/y), followed by I_{sc} (1.17%-0.23%/y) and I_{max} (1.17%-0.23%/y) with comparable degradation rates, while V_{oc} had the lowest rate of degradation (0.91% (0.18%/y)). These degradation rates were related to the mechanisms of degradation identified in the tested panel.

For the degraded panel with dust, the power degradation rate was 9.50% (1.90%/y), with an increase of 5.45% compared to the panel without dust. The V_{oc} degradation rate was 0.56% (0.11%/y) with a non-significant degradation of 0.35% in the presence of dust. Isc (8.06%-1.61%/y) and I_{max} (7.65%-1.53%/y) experienced the highest degradation rates, with 6.97% and 6.0% increases in the presence of dust, respectively. The V_{max} degradation rate was 2.08% (0.42%/y), with a reduction of 1.20% compared to the panel without dust.

The determination of the five parameters (a, R_s, R_p, I_0, and I_{pv}) of the PV panels studied was carried out according to the Hussien model. This model is quite effective for both the reference panel and the gradient panels (with and without dust). With the help of these results, the degraded rate and annul degraded rate of the five characteristics, as well as how dust affects these parameters, were determined.

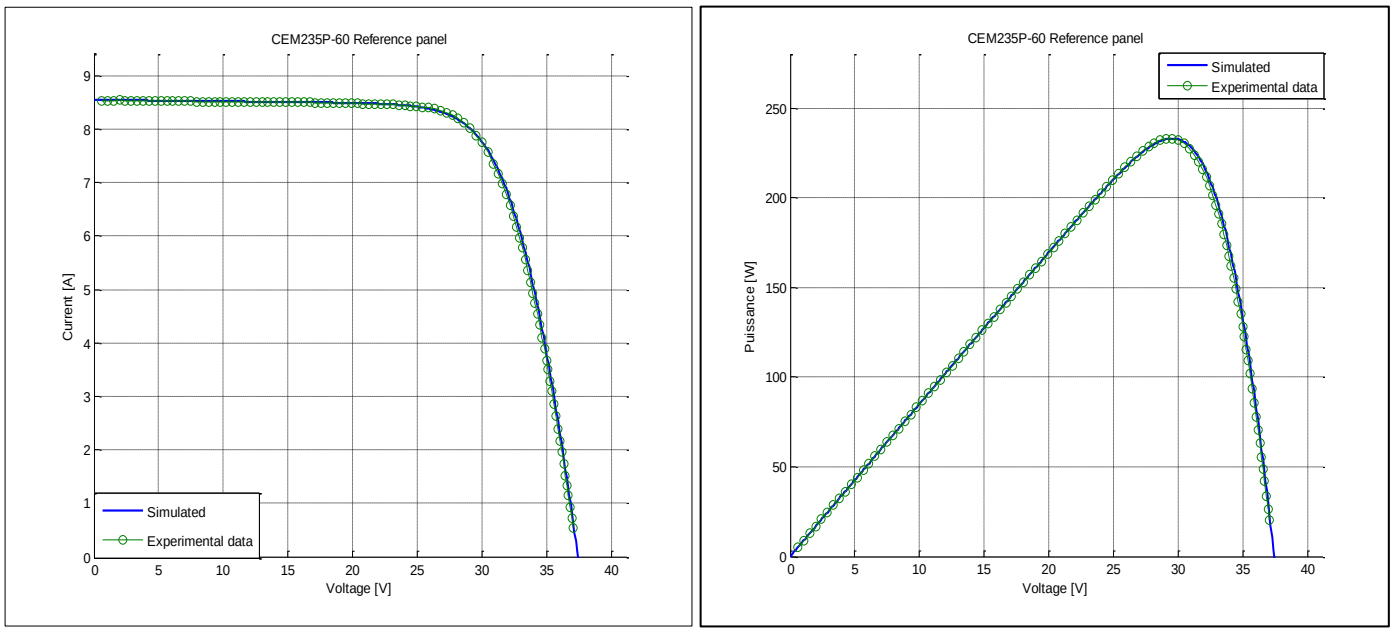

Figure 9. Comparaison of the measured and simulated curves (I-V and P-V) for the reference panel.

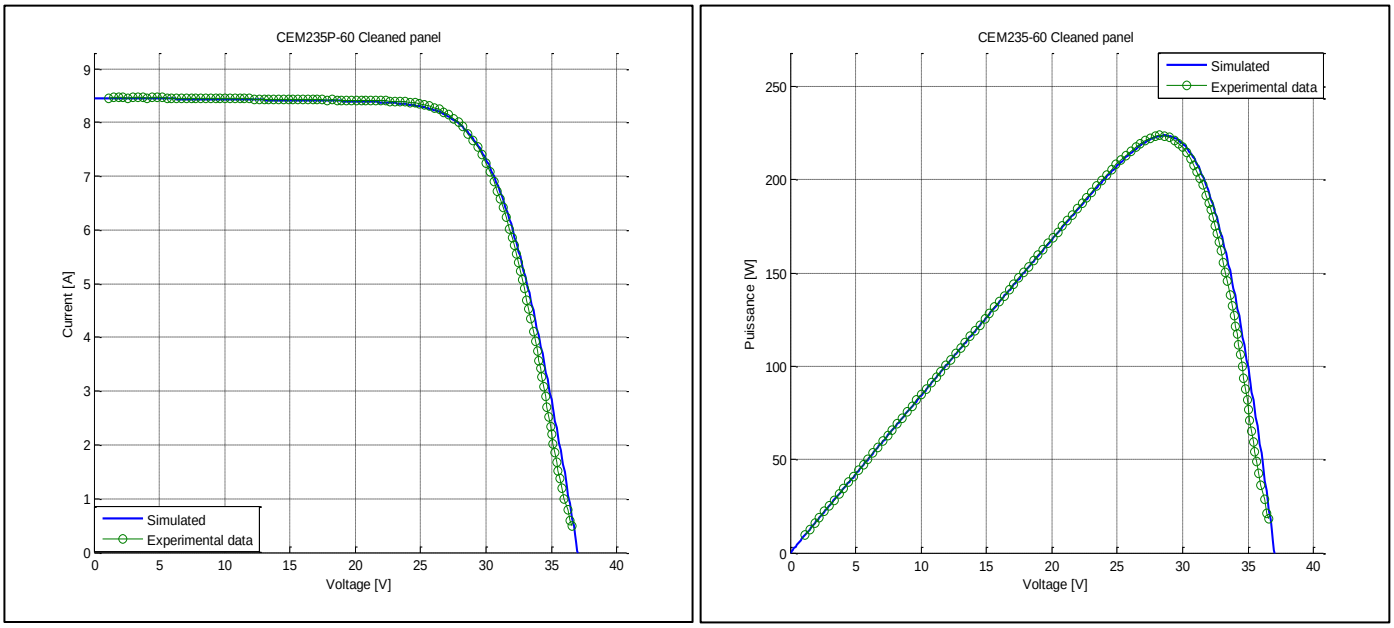

Figure 10. Comparaison of the measured and simulated curves (I-V and P-V) for the degraded panel without dust.

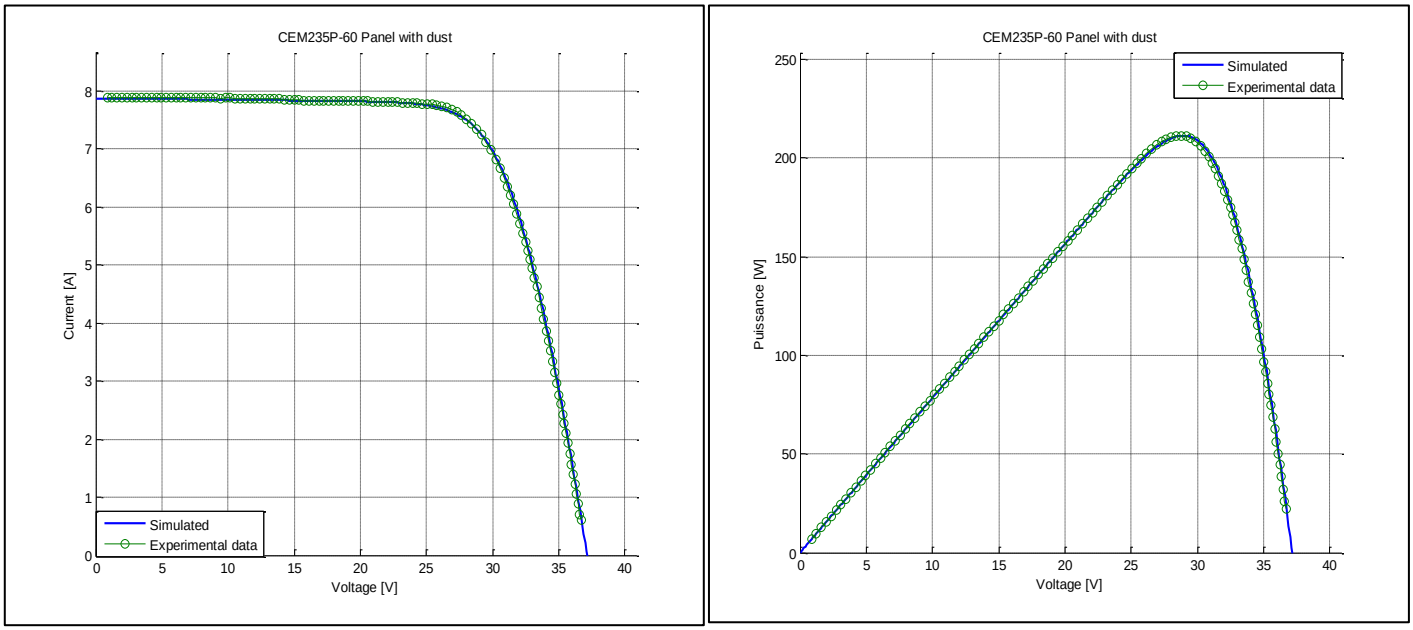

Figure 11. Comparaison of the measured and simulated curves (I-V and P-V) for the degraded panel with dust.

The degraded panel without dust had an ideality factor(a) degraded rate of 7.93% and (1.59%/y). This factor rose by 4.18% when dust was present, reaching 11.77% (2.36%/y). The I_{ph} degradation rate was the lowest at 1.04% (0.21%/y); then, it increased to 7.96% (1.98%/y), which is 6.99%, in the presence of dust. However, the I_0 degradation rate was the highest at 76.87% (18.53%/y) and jumped to 92.64% (18.53%/y) with a rise of 68.17% when dust was present.

The degradation rate of the R_s was -38.35% (-7.67%/y), which could be attributed to the indicated degradation mechanisms, and it caused power degradation. When dust was present, the R_s degradation decreased to -44.59% (-8.92%/y), which is a 4.51% decrease. In this instance, the dust acts as a shield between the PV and the radiation, reducing the cellular. glazing transmittance and as a result, the output power is reduced R_p degradation rate was reduced by 8.41% (1.68%/year), which was related to the loss of current and consequently power (maximum voltage and maximum current). In the presence of dust, R_p degradation rate was -9.92% (-1.98%/year), with a drop of -20.01% compared to the absence of dust.

The appropriateness of netoiling methods must be considered because dust, even in non-desert climates, has a significant impact on the electrical characteristics of a PV panel.

6. ACKNOWLEDGEMENT

The authors would like to thank all the staff of the BBA Condor Society for providing access and their help during the realization of this work.

NOMENCLATURE

Ns	Number of cells
P	Generated power by the PV module [W]
P_{max}	Maximum power [W]
q	Electronic charge (1.6x10-^{16} C)
R^2	Coefficient of determination
R_{ADC}	Annual degradation rate of the degraded panel without dust [%/Y]
R_{ADD}	Annual degradation rate of the degraded panel with dust [%/Y]
R_{DC}	Degradation rate of the degraded panel without dust [%]
R_{DD}	Degradation rate of the degraded panel with dust [%]
R_p	Shunt resistance [Ω]
R_s	Series resistance [Ω]
T	Cell temperature [K]
V	Generated voltage [V]
V_{max}	Maximum power tension [V]
V_{oc}	Open circuit voltage [V]
Vt	Thermal voltage

REFERENCES

1. Ahmadi, N., Rezazadeh, S., Dadvand, A., & Mirzaee, I. (2015). Numerical Investigation of the Effect of Gas Diffusion Layer with Semicircular prominences on Polymer Exchange Membrane Fuel Cell Performance and Species Distribution. *Journal of Renewable Energy and Environment*, 2(2), 36-46. https://doi.org/10.30501/jree.2015.70069.

2. Aïssa, B.,Isaifan, R. J., Madhavan, V. E., & Abdallah, A. A. (2016) Structural and physical properties of the dust particles in Qatar and their influence on the PV panel performance. *Scientific Reports*. 6(1), 1–12. https://doi.org/ 10.1038/srep31467.

3. Amer, A., Abdelsalam A., Yashar A., Mamdouh E. H. A., Shubham, Sh., Reza A. (2022). Reducing PV soiling and condensation using hydrophobic coating with brush and controllable curtains. *International Journal of Low-Carbon Technologies*, 17, 919–930. https://doi.org/10.1093/ijlct/ctac056

4. Andrea, Y., Pogrebnaya, T., and Kichonge. B. (2019). Effect of Industrial Dust Deposition on Photovoltaic Module Performance: Experimental Measurements in the Tropical Region. *Hindawi Intnational Journal of Photoenergy*. https://doi.org/10.1155/2019/1892148

5. Ashkan, T., S. Mehdi, P., Farzin, R., Nima, A., Hadi, Shahmohammadi. (2014). Design of Innovative Channel Geometrical Configuration and Its Effect on Species Distribution. *Journal of Renewable Energy and Environment*, 1(1), 20-29. https://doi.org/10.30501/jree.2014.70053.

6. Bandou, F., Hadj Arab, A., Belkaid. M.S., Logerais. P.O., Riou. O., et al. (2015). Evaluation performance of photovoltaic modules after a long time operation in Saharan environment. *International Journal of Hydrogen Energy*, 40, 13839–13848. http://dx.doi.org/10.1016/j.ijhydene.2015.04.091

7. Belhaouas, N., Mehareb, F., Kouadri-Boudjelthia, E., Assem, H., Bensalem, S., Hadjrioua, F., Aissaoui, A., Hafdaoui, H., Chahtou, A., Bakria, K., Saheb-Koussa, D. (2022). The performance of solar PV modules with two glass types after 11 years of outdoor exposure under the Mediterranean climatic conditions. *Sustainable Energy Technologies and Assessments*, 49(101771), https://doi.org/10.1016/j.seta.2021.101771

8. Bouaichi, A., Alami M. A. Hajjaj, Ch., Messaoudi, C., Ghennioui, A., Benlarabi, A., Ikken, B., El Amrani, A., Zitouni, H. (2019). In-situ evaluation of the early PV module degradation of various technologies under harsh climatic conditions: The case of Morocco. *Renewable Energy*, 143(C), 1500-1518. https://doi.org/10.1016/j.renene.2019.05.091.

9. Chaichan, M.T., Abass, K.I., Kazem, H.A. (2018). Energy yield loss caused by dust and pollutants deposition on concentrated solar power plants in Iraq weathers. *International Research Journal Advanced Engineering Science*, 3, 160-169. https://web.archive.org/web/20180410180634/http://irjaes.com/pdf/V3N1Y17-IRJAES/IRJAES-V3N1P621Y18.pdf

10. Chaichan, M.T., Kazem, H.A. (2016). Experimental analysis of solar intensity on photovoltaic in hot and humid weather conditions. *International Journal Scientific and Engineering Research*, 7, 91-96.https://web.archive.org/web/20180410180634/http://irjaes.com/pdf/V3N1Y17-IRJAES/IRJAES-V3N1P621Y18.pdf

11. Chaichan, M.T., Mohammed, B.A., Kazem, H.A. (2015). Effect of Pollution and Cleaning on Photovoltaic Performance Based on Experimental Study. *International Journal Scientific and Engineering Research*, 6(4), 594-601. https://www.uotechnology.edu.iq/paper/PDF/power/No.%2020.pdf

12. Chen, J., Pan, G., Ouyang, J., Ma, J., Fu, L., Zhang, L. (2020). Study on impacts of dust accumulation and rainfall on PV power reduction in East China. *Energy*, 194. https://doi.org/10.1016/j.energy.2020.116915.

13. Condor. (2022). Catalogue Produits Solar Photovoltaiques. Available from:https://www.condor.dz/images/pdf/CatalogueProduitsSolairesPhotovoltaiques_min.pdf

14. Darwish, Z.A., Kazem, H.A., Sopian, K., Alghoul, M.A., Chaichan, M.T. (2013). Impact of some environmental variables with dust on solar photovoltaic (PV) performance: review and research status. *Researchgate*. Net 7, 152-159. https://doi.org/10.1021/ie301985y.

15. Dobaria, B.V., Sharma, V., Deshara, A. A. (2018). Investigation of failure and degradation types of solar PV plants in a composite climate: abstract after 4-6 Years of field operation, in: *Advances in Smart Grid and Renewable Energy*, Springer, Singapore, 227-235. https://doi.org/ 10.1007/978-981-10-4286-7_22.

16. Dolara, A., Lazaroiu, GC., Leva, S., Manzolini, G., Votta, L. (2016). Snail trails and cell microcrack impact on PV module maximum power and energy production. *IEEE Journal of Photovoltaic*, 6(5), 1269–77. https://doi.org/10.1109/JPHOTOV.2016.2576682

17. Dorobantu, L., Popescu, M.O., Popescu, C.I., Craciunescu, A. (2017). The effect of surface impurities on photovoltaic panels. *Renewable. Energy Power Quality Journal*, 1, 622-626. https://doi.org/10.24084/repqj09.405.

18. El-Shobokshy, S., Hussein, F.M. (1993). Effect of dust with different physical properties on the performance of photovoltaic cell. *Solar Energy*, 51(6), 505-511. https://doi.org/10.1016/0038-092X(93)90135-B

19. Essalaimeh, S., Al-Salaymeh, A., Abdullat, Y. (2013). Electrical production for domestic and industrial applications using hybrid PV-wind system. *Energy Conversion Management*, 65, 736-743. https://doi.org/10.1016/j.enconman.2012.01.044

20. Franzese, N., Dincer, I., Sorrentino, M., A. (2020). New multigenerational solar-energy based system for electricity, heat and hydrogen production. *Applied Thermal Engineerig*, 171, No 115085. https://doi.org/10.1016/j.applthermaleng.2020.115085.

21. Hachicha, A.A., Al-Sawafta, I., Said, Z. (2019). Impact of dust on the performance of solar photovoltaic (PV) systems under United Arab Emirates weather conditions. *Renewable Energy*, 141, , 287-297. https://doi.org/10.1016/j.renene.2019.04.004.

22. Halwachs, M., Neumaier, L., Vollert, N., Maul, L., Dimitriadis, S., Voronko, Y., et al. (2019). Statistical evaluation of PV system performance and failure data among different climate zones. *Renewable Energy*, 139, 1040–60. https://doi.org/10.1016/j. renene.2019.02.135.

23. Hussein, A. M. (2017). Extraction of Unknown Parameters of PV Modules", 9th IEEE-GCC Conference and Exhibition (GCCCE). https://doi.org/10.1109/ieeegcc.2017.8448245

24. Ihaddadene, R., Jed, M.E.H., Ihaddadene, N., Souza. A. (2022). Analytical assessment of Ain Skhouna PV plant performance connected to the grid under a semi-arid climate in Algeria. Solar Energy, 232, 52–62. https://doi.org/10.1016/j.solener.2021.12.055.

25. Kahoul, N., Chenni, R., Cheghib, H., Mekhilef, S. (2017). Evaluating the reliability of crystalline silicon photovoltaic modules in harsh environment. *Renewable Energy*, *109*, 66–72. https://doi.org/10.1016/j.renene.2017.02.078.

26. Kato, K. (2011). PVRessQ!: a research activity on reliability of PV systems from an user's viewpoint in Japan. In: Dhere NG, Wohlgemuth JH, Lynn KW, editors. 81120K. https://doi.org/10.1117/12.896135.

27. Kazem, H.A., Chaichan, M.T., Alwaeli, A.H., Mani, K. (2017). Effect of shadows on the performance of solar photovoltaic, Mediterranean green buildings and renewable energy", *selected papers from the world renewable energy network's med green forum*. https://doi.org/10.1007/978-3-319-30746-6_27.

28. Kim, J.H., Park, J., Kim, D., Park, N. (2014). Study on mitigation method of solder corrosion for crystalline silicon photovoltaic modules. International. *Journal of Photoenergy*, http://dx.doi.org/10.1155/2014/809075.

29. Kimber, A., Mitchell, L., Nogradi, S., Wenger, H. (2007). The effect of soiling on large grid-connected photovoltaic systems in California and the Southwest Region of the United States. Conf. Rec. 2006 IEEE 4th *World Conf. Photovolt. Energy Conversion, WCPEC- 4 2*, 2391-2395 https://doi.org/10.1109/ WCPEC.2006.279690.

30. Kontges, M., Kurtz, S., Packard, CE., Jahn, U., Berger, K., Kato, K., et al. (2014). Review of failures of photovoltaic modules. *IEA PVPS Task 13 External final report IEA-PVPS*. https://doi.org/978-3-906042-16-9.

31. Li, L., Tu, J., Wu. J., Hu, K., Yu, S. (2022). Effect of finger interruption mode on the performance of crystalline silicon solar cells. *Solar Energy*, *238*(15), 381-391. https://doi.org/10.1016/j.solener.2022.03.065.

32. Leval,S., Aghaei M. (2018). Failures and defects in PV systems review and methods of analysis. In: Badescu Viorel, George Cristian Lazaroiu LB, editors. Power Eng. Adv. Challenges Part B Electr. Power. first ed. CRC Press; 56–84. https://re.public.polimi.it/handle/11311/1073064

33. Maouhoub, N. (2018). Photovoltaic module parameter estimation using an analytical approach and least squares method. *Journal of Computational. Electronics*, *Vol. 17*, No 2, 784–790. https://doi.org/10.1007/s10825-017-1121-5.

34. Mani, M., Pillai, R. (2010). Impact of Dust on Solar Photovoltaic (PV) Performance: Research Status, Challenges and Recommendations. Renewable and Sustainable *Energy Reviews*, *14*(9), 3124-3131. https://doi.org/10.1016/j.rser.2010.07.065

35. Mathiak, G., Althaus, J., Menzler, S., Lichtschlager, L., Herrmann, W. (2012). PV Module Corrosion from ammonia and salt mist - experimental study with full-size modules. In: 27th Eur. Photovolt. *Sol. Energy conf. Exhib. WIP*, 3536–40. https://doi.org/10.4229/27thEUPVSEC2012-4BV.3.44.

36. Menoufi, K. (2017). Dust accumulation on the surface of photovoltaic panels: introducing the photovoltaic soiling index (PVSI). Sustainability, 9(6). https://doi.org/10.3390/su9060963.

37. Meyer, S., Richter, S., Timmel, S., Glaser, M., Werner, M., Swatek, S., Hagendorf, C. (2013). Snail trails: root cause analysis and test procedures ", *Energy Procedia. 38*, 498-505. https://doi.org/10.1016/j.egypro.2013.07.309.

38. Munoz, M.A., Alonso-Garcia, M.C., Vela, N., Chenlo, F. (2011). Early degradation of silicon PV modules and guaranty conditions. *Solar Energy*, *85*, 2264–2274. https://doi.org/10.1016/j.solener.2011.06.011.

39. Namdari, S., Karimi, N., Sorooshian, A., Mohammadi, G.H., Sehatkashani, S. (2018). Impacts of climate and synoptic fluctuations on dust storm activity over the Middle East. *Atmospheric. Environment*, *173*, 265-276. https://doi.org/10.1016/ j.atmosenv.2017.11.016.

40. Pan, A., Lu, H., and Zhang, L.-Z. (2019). Experimental investigation of dust deposition reduction on solar cell covering glass by different self-cleaning coatings. *Energy*, *181*, 645–653. https://doi.org/10.1016/j.seta.2018.12.024.

41. Sahu, S.K., Singh K. A., Natarajan, S.K. (2021). Electricity generation using solar parabolic dish system with thermoelectric generator—An experimental investigation, *Heat Transfer*, 1-14. https://doi.org/10.1002/htj.22253.

42. Sendhil, K. N., Subbarama, K. S., Elavarasan. E and Arjun Singh. K. (2019). Performance analysis of solar photovoltaic panel at Karaikal weather conditions. *IOP Conference Series: Earth and Environmental Science, 312*, , 312012013. https://doi.org/10.1088/1755-1315/312/1/012013.

43. Simon, M., Meyer, EL. (2010). Detection and analysis of hot-spot formation in solar cells. *Solar Energy Materials and Solar Cells*, *94*, 106–13. https://doi.org/10.1016/j. solmat.2009.09.016.

44. Styszko, K., Jaszczur, M., Teneta, J., et al., (2019). An analysis of the dust deposition on solar photovoltaic modules. Environnemental Science *Pollution Reserch*, *26*(9), 8393–8401. http://dio.org/10.1007/s11356-018-1847-z.

45. Subbarama, K. A., Gudapati, K., Gummalla, V. S. R., and Sendhil K. N. (2019). A short review on recent trends and applications of thermoelectric Generators. *IOP Conferences Series: Earth Environmental Sciences*, 312 012013. https://doi.org/10.1088/1755-1315/312/1/012013.

46. Tanesab, J., Parlevliet, D., Whale, J., and Urmee, T. (2019). The effect of dust with different morphologies on the performance degradation of photovoltaic modules. *Sustainable Energy Technologies Assessments*, *31*, 347–354. https://doi.org/10.1016/j.seta.2018.12.024.

47. Tripathi, A. K,. Aruna, M., and Murthy, C. S. N. (2017). Performance of a PV panel under different shading strengths. *International Journal of Green Energy*, *40*(3), 248–253. https://doi.org/10.1080/01430750.2017.1388839.

48. Vidyanandan K. (2017). An Overview of Factors Affecting the Performance of Solar PV Systems. 27, *Energy Scan House J Corp Plan NTPC Ltd, New Delhi*. https://www.researchgate.net/profile/Kv-Vidyanandan/publication/319165448_An_Overview_of_Factors_Affecting_the_Performance_of_Solar_PV_Systems/links/5996ae170f7e9b91cb10967b/An-Overview-of-Factors-Affecting-the-Performance-of-Solar-PV-Systems.pdf

49. Waved, W., et al., (2017). Characterization of dust accumulated on photovoltaic panels in Doha, Qatar. *Solar Energy*, *142*, 123-135. https://doi.org/10.1016/j.solener.2016.11.053.

50. Weather Spark. (2022). Weather conditions in BBA. Available from: https://fr.weatherspark.com/y/50132/M%C3%A9t%C3%A9o-moyenne-%C3%A0-Bordj-Bou-Arreridj-Alg%C3%A9rie-tout-au-long-de-l'ann%C3%A9e.

51. Wikipedia. (2022). Geographica Situation of BBA. Available from: https://fr.wikipedia.org/wiki/Wilaya_de_Bordj_Bou_Arreridj.

52. Yang, H., He, W., Wang, H., Huang, J., Zhang, J. (2018). Assessing power degradation and reliability of crystalline silicon solar modules with snail trails. *Solar Energy Materials Solar Cells*, *187*, 61–8. https://doi.org/10.1016/j.solmat.2018.07.021.

53. Yang, S., and Jiang, L. (2019). Crystalline Silicon PV Module Field Failures. Durability and Reliability of Polymers and Other Materials in Photovoltaic Modules, 177-216. https://doi.org/10.1016/B978-0-12-811545- 9.00008-2.

54. Yang, S., Whitfield, K. (2012). Thermal Endurance Study of Polymers Used in Low Concentration Photovoltaic Modules", *Journal of Photonics for Energy*, *2*(1). https://doi.org/ 10.1117/1.JPE.2.021803.

55. Younes, M., Labed, D., Kahoul, N., Cheghib, H., Kherici, Z., Affari, B. C., & De Cardona, M. S. (2020). Silicon solar cells performance in Algerian desert. *11th International Renewable Energy Congress (IREC)*. https://doi.org/10.1109/irec48820.2020.9310366.

56. Zafifirovska, I., Juhl, M.K., Weber, J.W., Wong, J., Trupke, T. (2017). Detection of Finger Interruptions in Silicon Solar Cells Using Line Scan Photoluminescence Imaging. *IEEE Journal of Photovoltaic*, *7*, 1496–1502. https://doi.org/10.1109/JPHOTOV.2017.2732220.

JREE: Vol. 10, No. 4, (Autumn 2023) 89-98

Journal of Renewable Energy and Environment

Journal Homepage: www.jree.ir

Materials and Energy Research Center

MERC

Research Article

Phenolic Compound Removal Technique for Efficient Biobutanol Production Using Oil Palm Fronds Hydrolysate

Abdurrahman Abubakar[a&b], Madihah Binti MD Salleh*[a], Adibah Yahya[a], Chong Chun Shiong[a], Shaza Eva Mohamad[a], Suraini Binti Abd-Aziz[c], Huszalina Hussin[a]

[a] *Department of Biosciences, Faculty of Sciences, Universiti Teknologi Malaysia, P. O. Box: 81310, Skudai, Johor, Malaysia*

[b] *Department of Biological Sciences, Faculty of Science, Federal University of Kashere, P. O. Box: 0182, Gombe, Gombe State, Nigeria.*

[c] Department of Bioprocess Technology, Faculty of Biotechnology and Biomolecular Sciences, Universiti Putra Malaysia, *P. O. Box:* 43400 Seri Kembangan, Selangor, Malaysia

PAPER INFO

Paper history:
Received: 07 December 2022
Revised: 01 March 2023
Accepted: 09 April 2023

Keywords:
ABE Fermentation,
Biobutanol,
Detoxification,
Phenolic Compounds,
Oil Palm Frond Hydrolysate

ABSTRACT

Oil Palm Frond (OPF) juice has been the focus of Malaysian bioenergy producers through acetone-butanol-ethanol (ABE) fermentation. However, due to the high concentration of phenolic compounds in the hydrolysate, usually gallicacid and ferulic acids, the fermentation medium turns acidic which hinders the growth of most microorganisms. A suitable method of phenolic compound removal with a minimal effect on the sugar stability of OPF juice has been employed using Amberlite XAD-4 resin. During the detoxification process, the effects of temperature and pH on the removal of phenolic compounds and sugar stability were also assessed. The Amberlite XAD-4 resin managed to adsorb about 32% of phenolic compound from the OPF hydrolysate at an optimum temperature of 50 °C and hydrogen ion concentration (pH) of 6. In addition, it maintained as much as 93.7 % of the sugar in the OPF juice. The effect of detoxifying OPF hydrolysate was further tested for biobutanol production in batch culture using strain *Clostridium acetobutylicum* SR1, L2, and A1. Strain L2 gave the highest improvement in biobutanol and total solvent production by 22.7% and 14.41%, respectively, in medium with detoxified OPF juice. Meanwhile, compared to non-detoxified OPF juice, the acid production of strain L2 significantly decreased by 2.99-fold when using detoxified OPF juice, despite a 1.2-fold increase in sugar consumption. Conclusively, using Amberlite XAD-4 resin to detoxify OPF hydrolysate at pH 6 and 50 °C removed the phenolic compound while increasing the strain L2 capability to improve biobutanol and total solvent production.

https://doi.org/10.30501/jree.2023.374488.1512

1. INTRODUCTION

Oil palm frond (OPF), empty fruit brunch (EFB), palm kernel shell (PKS), oil palm trunk (OPT), palm oil mill effluent (POME), and mesocarp fibre are generated annually in huge amounts, especially after pruning or harvesting the fresh bunch. According to the 2013report by Malaysian Palm Oil Board (MPOB), Malaysia in its agricultural activities produces approximately 168 million tonnes of biomass waste. Of all the biomass generated in the oil palm industry, OPF accounts for more than 50% of the total quantity. As a result, it has become one of the most significant biomass materials generated during oil palm production (Kumneadklang et al., 2019). The use of its juice as a substrate for bioenergy production has currently derived a remarkable interest from bioenergy producers as an appropriate feedstock for sustainable, economic, and environmentally-friendly energy production. Among the different types of solvents produced as bioenergy, biobutanol is considered the most attractive. It undoubtedly possesses superior properties over ethanol owing to its high energy density, low volatility, hygroscopicity, and low greenhouse gas emission(Nimbalkar et al., 2019). Apart from being a solvent for various industrial applications, biobutanol is an essential chemical precursor for producing paints, polymers, and plastic Numerous researchers have attempted to use OPF hydrolysate for biobutanol production, and recent studies have highlighted its potential as a rich source of reducing sugars suitable for various industrial applications (Kee et al., 2022), (Asri et al., 2019). However, one of the major challenges of using the juice from OPF biomass as the substrate to produce biobutanol is the generation of various inhibitory compounds during pretreatment (Satari et al., 2019). Microbes are generally sensitive to these phenolic inhibitors such as ferulic, gallic acid, ρ-coumaric, and vanillic acids in the resulting hydrolysate, which hindered their metabolism and, as a result, biobutanol production (Kourilova et al., 2021). For efficient conversion of this hydrolysate into biobutanol, it is important to get rid of these compounds to permit the efficient activity of the microbe during acidogenesis and solventogenesis. However, these

*Corresponding Author's Email: *madihah@fbb.utm.my* (M. MD Salleh)
URL: https://www.jree.ir/article_169887.html

Please cite this article as: Abubakar, A., MD Salleh, M., Yahya, A., Shiong, C. C., Mohamad, S. E., Abd-Aziz, S. & Hussin, H. (2023). Phenolic Compound Removal Technique For Efficient Biobutanol Production Using Oil Palm Fronds Hydrolysate, *Journal of Renewable Energy and Environment (JREE)*, 10(4), 89-98. https://doi.org/10.30501/JREE.2023.374488.1512.

compounds are completely mixed with the hydrolysate, making it difficult to separate them from the reducing sugars(Galbe and Wallberg, 2019).

Scientists have recently focused on developing a method to facilitate fermentation activity by removing these inhibitory compounds from the hydrolysate before inoculating the microbes. Detoxification of hydrolysate to improve fermentation efficiency has been demonstrated through physical, chemical, and biological methods (Kordala et al., 2021; Singh et al., 2019). However, most of the current methods are very expensive due to the ineffectiveness of the method to remove a significant percentage of these phenolic compounds produced in the hydrolysate as a result of lignin degradation while retaining a greater amount of its original sugars.

In recent years, there have been quite a number of compound extraction methods that involve the ion-exchange process, such as electro-membrane extraction and hollow-fibre liquid-phase microextraction (Pedersen-Bjergaard, 2019). One of these techniques that has a high potential for removing phenols from hydrolysate is ultrafiltration with prior polymerization by the use of laccase (EC 1.10.3.2), i.e., a multi-copper oxidase that catalyzes the oxidation of one electron of a wide range of phenolic compounds in the presence of excess molecular oxygen. In this method, the reactive phenolic compounds that serve as toxic compounds are oxidized by laccase and they react spontaneously further with polymers with a large molecular weight. In doing so, the juice is detoxified as the polyphenols are retained by the ultrafiltration(Morsi et al., 2020). However, this method cannot always be applied due to the loss of natural juice properties, which could vehemently affect the sugar contents. While Zeolites are known to selectively remove hydroxymethylfurfural, furfural, and vanillin from juices, enabling efficient inhibitor recovery, they are also associated with significant sugar loss (Wikandari et al., 2019).

A process used to separate phenolic compounds from apple pomace involves the adsorption of phenolic constituents by a hydrophobic styrene-divinylbenzene copolymer. After elution with methanol, the polyphenolics usually become concentrated in vacuum and stabilized by lyophilization. Finally, an Amberlite XAD 16HP is used for the adsorptive removal of phenolic compounds with the resin (Wikandari et al., 2019). Even though this technique provides an efficient and reliable method for phenol removal from fruit and vegetable juices, there are no reports in the literature concerning the effect of using this method on the sugar content of the juices. Hence, the technique still needs further investigation in order to stabilize juices after removing phenolics. Besides, there are various factors that affect the adsorption capacity of resins for the removal of phenols (Mohammed et al., 2019). Temperature and hydrogen ion concentration (pH) are key factors influencing the adsorption of phenolic compounds (Chen et al., 2022; Liu et al., 2019). It has been reported that at acidic pHs, the uptake of phenolics by different adsorbents is enhanced because the phenols are undissociated and the dispersion interactions predominate, whereas at alkaline pH, adsorption decreases since dissociation of hydroxyl from carboxyl groups occurs(Wei et al., 2021). However, another report indicated zero influence of pH (keeping in the acidic range) on the adsorption of phenolic on resins (Waheed et al., 2019). Temperature also influences adsorption in two ways: (i) by increasing the rate of transport across the external boundary layer and within the pores due to decreased solution viscosity, and (ii) by changing the capacity of the adsorbent. High temperatures may promote irreversible interactions (Karimi et al., 2019). Therefore, both positive and negative effects of temperature have been reported, especially for ACs, minerals, and resins, whereas in some applications, higher temperatures favor adsorption. The current study investigated the effects of hydrolysate temperature and pH on Amberlite XAD-4 adsorption efficiency and sugar stability and then, compared the bacteria ability to ferment both detoxified and non-detoxified OPF hydrolysates for biobutanol production.

2. METHODOLOGY

2.1 Oil Palm Frond Collection and Preparation

Fresh and basal parts of OPF petioles with an average length of 1-1.5 m were obtained from Kampung Terjun Rimba, Pontian Johor, Malaysia, located at latitude 1° 27' 59.20" N, longitude 103° 27' 20.50" E. To minimize the intrusion of microbes and dirt, freshly harvested petioles were cut at both edges and spread with 70 % (v/v) ethanol just before being put in sealed plastic bags and immediately transported to the juice processing site for juice extraction. To obtain the juice, a sugarcane juicing machine (Hisaki, TFS3777) was employed to press the OPF petiole repeatedly until the juice content could be completely removed. To collect juice, 1 L of sterilized Scott bottle was used.

2.2.1 OPF Juice Detoxification

In this part of the study, a polymeric Amberlite XAD-4 resin with particle size of 20-60 mesh and surface area of 750m^2/g was used for the adsorptive removal of phenolic compounds. 40 g of the resin was poured into a glass column (XK 50×100) in three different beds, which were then demarcated with very thin cotton and washed with five volumes of distilled water to remove impurities (Fan et al., 2021). The OPF juice was then applied to the column at a flow rate of 100 mL/h (Nagasawa et al., 2019), and the initial fractions of sugar-containing juice were collected separately in conical flasks (Figure 1) for sugar and phenolic compounds analysis. To investigate the effect of temperature on phenolic removal and sugar stability, the OPF juice extract was preheated in a water bath for 25 minutes (until thermal equilibrium was reached) before being applied to the column, while the control treatment was performed without any prior heating of the OPF juice. The effect of 5 different pH levels was assayed (3, 4, 5, 6, and 7), and 1 M of NaOH and/or HCl was used for the pH adjustment. All the experiments were conducted in triplicate, and the averages of the results were recorded as responses.

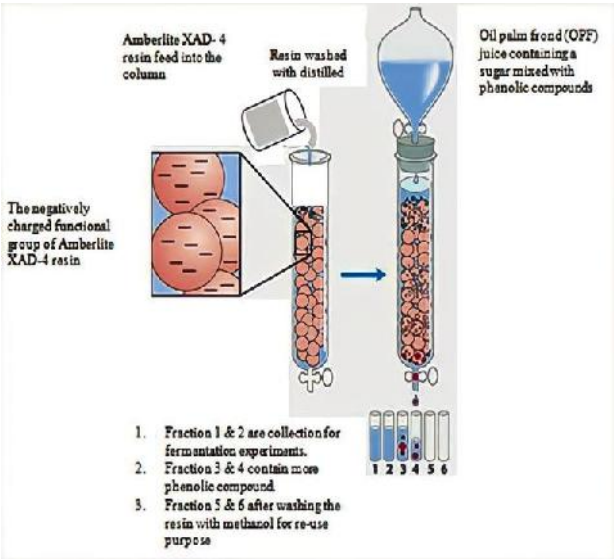

Figure 1. Oil palm frond juice detoxification technique using Amberlite XAD-4 resin.

2.2.2 Resin Regeneration

Regeneration of resin is an economic practice that takes exhausted ion exchange resin beads and removes the ions that have been adsorbed during the filtration process so that the resin can be re-used. This process varies depending on the resin properties and the type of compound adsorbed. Phenolic compounds are reported to have high affinity to Amberlite XAD-4 resin, and the regeneration recovery strategies may therefore depend on the solvent used (Din et al., 2021). While some studies have achieved >80% resin recovery, most studies have failed to achieve even 70% recovery due to the low concentration of solvent used. Hence, the current research regenerates the resin by pre-washing it with 95 % methanol (32.02 g/mol) to release the adsorbed phenolic compound from the resin, as described by Pailliè-Jiménez et al. (2020). However, the methanol was allowed to completely evaporate, and the residual water was removed by lyophilization, making >80% of the resin ready for re-use.

2.3 Microorganism Procurement and Preparation

The solvent-producing bacteria, *Clostridium acetobutylicum* SR1, L2, and A1, used in this study were obtained from the Biorefinery Technology Laboratory, Department of Bioscience, Universiti Teknologi Malaysia. The Reinforced Clostridial Medium (RCM) was used for the development of inoculums. Before being transferred into the inoculum bottles, the stock culture was heat-shocked at 80 °C for 10 minutes to activate bacterial spore germination and kill both the vegetative forms of the bacteria and the weaker spores(Narita et al., 2020). After cooling, 1 mL of stock culture was transferred into an inoculum bottle (100 mL) containing RCM medium and incubated at 35 °C until cells reached a stable exponential phase (24 hours).

2.4Maintenance Medium- Reinforced Clostridia Medium (RCM)

Reinforced Clostridia Medium (RCM) was used for the growth of the microorganisms. This medium served as an enrichment medium, which allowed the growth of *Clostridium* sp**.** and specific bacterial strains that could grow in anaerobic conditions. During the preparation of the medium in a 100 mL serum bottle, the medium was filled to a volume where a small space on top of the bottle was left empty. This space was required to provide anaerobic conditions for the culture. The inoculated medium was kept at room temperature prior to the experiment. The RCM was prepared by adding meat extract (10 g), peptone (10 g), yeast extract (3 g), glucose (5 g), starch (1 g), NaCl (5 g), and sodium acetate (3 g). The contents were sterilized by autoclaving at 121 °C for 15 minutes. After cooling the contents to room temperature, L-cysteine HCl (0.5 g), para-aminobenzoic acid (0.001 g), and biotin (0.008 g) were added separately via filter sterilization using an Agilent PTFE 0.2 µm membrane filter.

2.5 Production Medium (P2 medium)

In order to conduct the fermentation using detoxified OPF juice, production medium (P2) was used as fermentation medium containing the following composition (in g/L): yeast extract, 5; $MgSO_4.7H_2O$, 0.2; $MnSO_4.7H_2O$, 0.01; $FeSO_4.7H_2O$, 0.01; NaCl, 0.01; and ammonium acetate, 2.0. About70 % v/v of detoxified and non-detoxified OPF hydrolysates containing a total of 47.5 g/L of reducing sugar was used as the sole carbon source for bacterial growth and metabolism (Khunchit et al., 2020). After autoclaving the samples at 121ºC for 15 minutes, KH_2PO_4, 0.5 g/L; K_2HPO_4, 0.5 g/L, and vitamin solution containing 0.001 g/L of para-aminobenzoic acid, thiamin, and biotin were filter-sterilized into the sample mixture using an Agilent PTFE 0.2µm membrane filter **(**pore size 47 mm diameter). Then, 140 mL of the samples were dispensed into their respective 150-mL serum bottles until there was only a small space at the top, which was used to degas the sample with oxygen-free nitrogen gas. The medium was degassed following a slight modification of the method described by Miller and Wolin (1974). This experiment was conducted in duplicate, while samples were withdrawn from the fermentation broth every 6 hours for the analysis of acids, solvent, reducing sugar utilization, and bacterial growth.

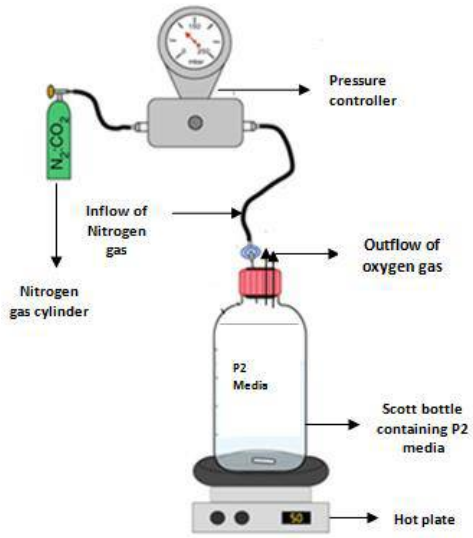

Figure 2. Process of media degassing for efficient anaerobic culture.

2.6 Functional Group Analysis Using Fourier Transform Infrared Spectroscopy (FTIR)

The chemical structure of the resulting oil palm frond juices was studied, and the infrared spectra of oil palm frond juice were measured with an FTIR spectrophotometer (Nicolet iS5FT-IR Spectrometer, Thermo Fisher Scientific Inc., USA) to elucidate the functional groups that are present in the juice before and after the resin adsorptive detoxification process. This technique was used to provide important information about the structure modification of oil palm frond juice, which is widely used for other structural characterizations. To accomplish this, approximately 0.2-0.5 mL of juice samples were placed on the provided sample area; the spectra were recorded between 600-3500 cm^{-1} and the samples were scanned for available compounds.

2.7 Determination of Reducing Sugar and Phenolic Compounds

The total reducing sugar concentration was determined via the dinitrosalicyclic (DNS) method (Miller, 1959). A glucose monohydrate solution of 1 g/L was used as a standard solution, and the absorbance of both the samples and the standards was read at 540 nm. On the other hand, the Folin-Ciocalteu technique was utilized to determine total phenolic compounds before and after the detoxification with an absorbance read at 765nm and here, gallic acid was utilized as the benchmark (Way et al., 2020). The concentration of individual sugars in the hydrolysate was determined using an Agilent 1100 series high-performance liquid chromatography (HPLC) technique with Rezex RPM-monosaccharide Pb^{+2} columns and a lead ion (Pb^{2+}) as the stationary phase. Glucose, fructose, sucrose, xylose, arabinose, mannose, and galactose were used as the sugar standards. To determine the individual phenolic compounds in the hydrolysate using HPLC, a C18 column was used following the method described by Krstonošić et al. (2020) and finally, gallic acid was set as the standard solution.

2.8 Determination of Acids and Solvent Using Gas Chromatography (GC)

The concentration of acids such as acetic acid and butyric acid and solvents such as acetone, butanol, and ethanol were determined using gas chromatography equipped with a DB-WAX column and Flame Ionized Detector (FID). The carrier gas was helium, with a flow rate of 25 mL/minute. The temperatures of the oven, column inlet, and detector were 200, 300, and 300 °C, respectively (Abe et al., 2020). Prior to the GC analysis, solvent-solvent extraction was conducted to separate the products (acids and solvents) from the broth. At first, 0.1 M of HCl was used to acidify the broth in order to separate the culture from the sample, and the acidified sample was extracted with an equivalent amount of dichloromethane (DCM). The mixture was then centrifuged at 10,000 rpm for 30 minutes, where the top layer was discarded and the bottom, which is expected to contain the acids and solvents, including the DCM, was injected into the column using auto-injection. Acids and solvents of analytical grade (Sigma Aldrich, USA) were used as standards. The concentration of acids and solvents in the sample was determined by comparing the areas of the peaks of each sample with those of standards for acids (acetic acid and butyric acid) and solvents (acetone, butanol, and ethanol) (Raganati et al., 2020).

3. RESULTS AND DISCUSSION

3.1. Phenolic compounds removal from oil palm frond juice.

The result for the phenolic compound removal from OPF hydrolysate using Amberlite XAD-4 resin for an adsorptive filtration is shown in Table 1, and the total concentration of phenolic compounds and fermentable sugars is compared with their original amounts in the juice before the removal. It is found that the resin filtration is able to remove about 21% of the total concentration of phenolic compounds when compared with the control, that is, from 0.332 ± 0.04 (control) to 0.261 ± 0.07 g/L (filtered). Nevertheless, a slight reduction of sugar, which is about 5.5% of the total concentration of the fermentable sugar, was observed. The 21% of the phenolic compound removed that is observed in this study is relatively lower than the percentage of phenolic compound removed from orange juice by the same resin, which is about 32.97% (even though the resin applications considerably reduced some bioactive compounds such as ascorbic acid)(Akyıldız et al., 2022). However, temperature, pH, feed composition, and concentration are some of the factors that influence the adsorption capacity of resins for the removal of phenolic compounds. According to the research conducted by Phung et al. (2015), solution viscosity is very critical in determining the rate at which transport occurs across and within the resin pores, thereby changing the capacity of the adsorbent. Temperature can thus enhance or limit phenolic compound removal depending on the material used as an adsorbent and the type of hydrolysate. It is therefore important to further investigate the effect of various temperatures and pH on the phenol removal and sugar stability of the OPF hydrolysate for effective utilization in biobutanol production.

Table 1. Comparison of biobutanol production using detoxified and non-detoxified OPF juices

Parameters	Before detoxification of OPF juice	After detoxification of OPF juice	% of reduction
Initial total phenolic compound (g/L)	0.332 ± 0.04	0.261 ± 0.07	21.39
Gallic acid concentration (g/L)	0.264 ± 0.01	0.212 ± 0.05	19.70
Ferulic acid concentration (g/L)	0.061 ± 0.02	0.043 ± 0.00	29.51
Total fermentable sugar (g/L)	69.03 ± 1.61	65.16 ± 2.18	5.61
Glucose concentration (g/L)	43.61 ± 1.45	43.27 ± 1.02	0.46
Fructose concentration (g/L)	16.53 ± 0.85	14.24 ± 0.41	13.86
Sucrose concentration (g/L)	8.19 ± 1.25	6.94 ± 0.43	15.26

3.2 Effect of Temperature

Table 2 shows the effect of temperature on the resin adsorptive performance on phenolic compound removal and the sugar stability of OPF hydrolysate**.** It was observed that the adsorptive performance increased with an increase in temperature up to a certain level. The removal of phenolic compounds at 50ºC yielded the highest percentage of approximately 31% with a fermentable sugar loss of only 0.04%. This indicated that the increase in temperature up to 50ºC did not significantly affect the stability of the sugar content of the hydrolysate. However, a further increase in temperature to 60ºC did not show an increase in phenol removal, but also exhibited a decrease in the sugar content of the hydrolysate, indicating the loss of sugar content at temperatures higher than 50ºC(Ghorbannezhad and Abbasi, 2021).

The amounts of glucose and fructose remain stable after cycles 1 and 2 of phenolic compound removal. However, the concentration of sucrose continually decreases by about 11.4 %, which is from 8.19 ± 1.25 to 7.05 ± 0.54 across the temperature range of 40 to 70ºC. This might be due to the disaccharide nature of the sucrose, which is more susceptible to hydrolysis at higher temperatures(Milewska et al., 2022). A significant effect of higher temperature on hydrolysate detoxification via resin filtration was observed for ferulic acid as well as another phenolic compound (gallic acid). Even though the concentration of gallic acids fluctuated, the concentration of ferulic acid continually decreased as the temperature increased to 60ºC (though it remained the same at 70ºC), indicating the effectiveness of resin for the adsorptive removal of ferulic acid from OPF hydrolysate. Hence, the present study suggests that the most favorable temperature for phenolic compound removal from oil palm frond hydrolysates is at 50ºC.

Table 2. Effect of OPF hydrolysate temperature on the Amberlite XAD-4 resin adsorptive performance

Parameters	Different temperature(°C)				
	30	40	50	60	70
Initial total phenolic compound (g/L)	0.332± 0.04	0.332± 0.04	0.332± 0.04	0.332± 0.04	0.332± 0.04
Final total phenolic compound (g/L)	0.267± 0.02	0.251± 0.01	0.228± 0.03	0.262± 0.01	0.281± 0.02
Total phenolic compound removed (%)	19.58	24.40	31.32	21.08	15.36
Initial gallic acid (g/L)	0.264± 0.01	0.264± 0.01	0.264± 0.01	0.264± 0.01	0.264± 0.01
Final gallic acid (g/L)	0.211± 0.03	0.195± 0.04	0.207± 0.02	0.218± 0.02	0.237± 0.01
Initial ferulic acid (g/L)	0.061± 0.02	0.061± 0.02	0.061± 0.02	0.061± 0.02	0.061± 0.02
Final ferulic acid (g/L)	0.050± 0.01	0.055± 0.01	0.060± 0.04	0.044± 0.02	0.044± 0.03
Initial total fermentable sugar (g/L)	69.03± 1.61	69.03± 1.61	69.03± 1.61	69.03± 1.61	69.03± 1.61
Final total fermentable sugar (g/L)	66.49± 1.14	68.27± 0.53	68.33± 0.24	68.80± 0.12	68.14± 0.026
Fermentable sugar stability (%)	96.30	98.80	98.90	99.60	98.70
Initial glucose (g/L)	43.61± 1.45	43.61± 1.45	43.61± 1.45	43.61± 1.45	43.61± 1.45
Final glucose (g/L)	41.53± 2.04	43.41± 0.62	42.56± 0.44	43.50 ± 0.02	42.67± 0.03
Initial fructose (g/L)	16.53± 0.85	16.53± 0.85	16.53± 0.85	16.53± 0.85	16.53± 0.85
Final fructose (g/L)	15.31± 0.17	15.87± 0.04	16.53± 0.02	16.42± 0.18	16.98± 0.01
Initial sucrose (g/L)	8.19± 1.25	8.19± 1.25	8.19± 1.25	8.19± 1.25	8.19± 1.25
Final sucrose (g/L)	8.00± 0.07	8.11± 0.02	7.91± 0.42	7.05± 0.54	7.05± 0.61

3.3 Effect of pH

Compared to the temperature effect, the pH of the OPF hydrolysate had a lesser impact on the adsorptive performance of the resin for removing phenolic compounds from the hydrolysate. Substrate pH values of 3, 4, 5, 6, and 7 were tested in this experiment to determine the most suitable and optimum substrate pH for the adsorptive efficiency of resin for phenolic compound removal from OPF hydrolysate. As can be observed in Table 3, the highest amount of phenolic compound removed from the hydrolysate was attained at pH 6, which is about 32.64%. However, good phenolic compound removal efficiency was also demonstrated at other substrate pH values of 3, 4, and 5. However, at a pH of 7, the efficiency was found to decrease by about 22.6% when compared to the efficiency at pH 6. Even though some scientists reported a zero effect of pH on the performance of resin for the removal of phenolic compounds (Wei et al., 2021), the research only focused on the acidic pH, which was also observed with less effect in the present research. This is in agreement with the study conducted on the cobalt removal from environmental water samples, showing that an increase in the pH level to a certain level enhanced the cobalt extraction and recovery (Ghasemi et al., 2021). On the other hand, the effect of OPF juice pH on sugar stability after the resin adsorptive removal of phenols was assessed. An increase in pH from 5 up to 7 was found to negatively affect the sugar stability by almost 6.3 %, which is 2 folds higher than when the substrate pH was between 3 and 4. Although the acidic pH demonstrated good sugar stability compared to alkaline, the improvement of phenolic compound removal provides a superior advantage for bacterial growth and metabolism.

Table 3. Effect of OPF hydrolysate pH on the Amberlite XAD-4resin adsorptive performance

Parameters	pH				
	3	4	5	6	7
Initial total phenolic compound (g/L)	0.332± 0.04	0.332± 0.04	0.332± 0.04	0.332± 0.04	0.332± 0.04
Final total phenolic compound (g/L)	0.223± 0.01	0.236± 0.01	0.225± 0.03	0.221± 0.02	0.247± 0.06
Total phenolic compound removed (%)	30.23	29.12	32.23	32.64	25.61
Initial gallic acid (g/L)	0.264± 0.01	0.264± 0.01	0.264± 0.01	0.264± 0.01	0.264± 0.01
Final gallic acid (g/L)	0.191± 0.03	0.190± 0.02	0.186± 0.02	0.191± 0.03	0.203± 0.01
Initial ferulic acid (g/L)	0.061± 0.02	0.061± 0.02	0.061± 0.02	0.061± 0.02	0.061± 0.02
Final ferulic acid (g/L)	0.032± 0.01	0.043± 0.02	0.043± 0.02	0.030± 0.01	0.044± 0.00
Initial total fermentable sugar (g/L)	69.03± 1.61	69.03± 1.61	69.03± 1.61	69.03± 1.61	69.03± 1.61
Final total fermentable sugar (g/L)	67.54± 1.11	67.17± 0.70	67.25± 0.29	64.70± 0.84	65.46± 0.36
Fermentable sugar stability (%)	97.8	97.3	97.4	93.7	94.8
Initial glucose (g/L)	43.61± 1.45	43.61± 1.45	43.61± 1.45	43.61± 1.45	43.61± 1.45
Final glucose (g/L)	41.23± 0.01	42.41± 0.01	42.44± 0.02	40.17± 0.01	41.48± 0.03
Initial fructose (g/L)	16.53± 0.85	16.53± 0.85	16.53± 0.85	16.53± 0.85	16.53± 0.85
Final fructose (g/L)	16.01± 0.01	16.42± 0.06	16.30± 0.05	16.24± 0.14	15.98± 0.62
Initial sucrose (g/L)	8.19± 1.25	8.19± 1.25	8.19± 1.25	8.19± 1.25	8.19± 1.25
Final sucrose (g/L)	8.69± 0.02	8.61± 0.05	7.88± 0.12	7.41± 0.32	7.35± 0.19

3.4 Functional Group Analysis of OPF Segments using FTIR Spectroscopy

The spectroscopic investigation of OPF hydrolysates was conducted to determine the functional groups and conformational structural changes that occur on the substrate after the detoxification process. The functional group of the non-detoxified sample was equally determined and served as a control. The spectra produced a profile of the samples with a distinctive molecular fingerprint, which was used to scan the samples for many different components, and the results are presented in Figure 3 (a & b).

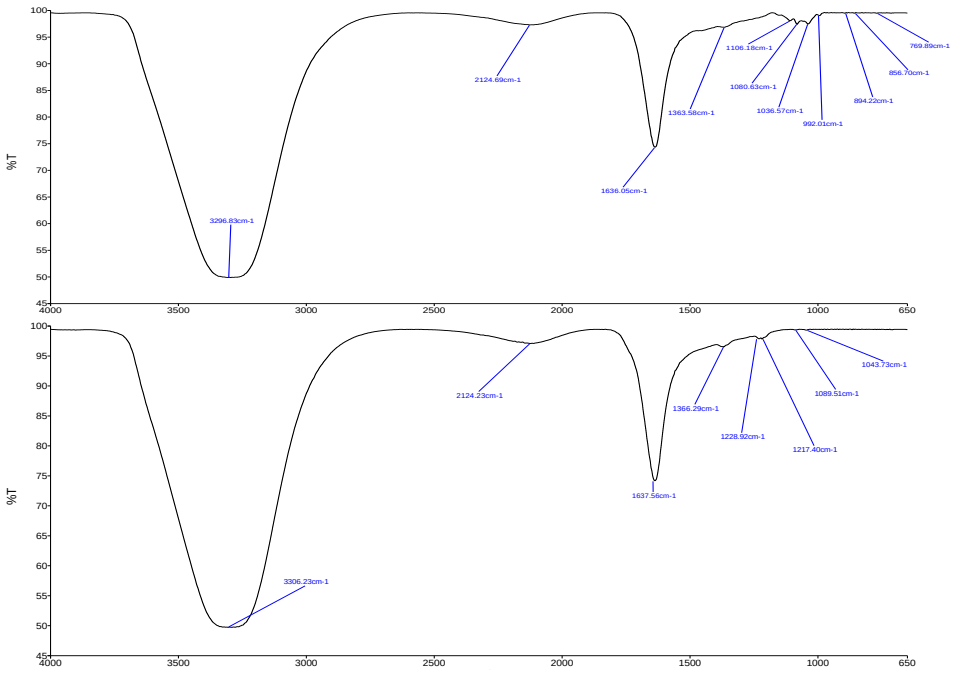

Figure3. FTIR-ATR spectra showing structural modification between (a) OPF juice before detoxification and (b) OPF juice after detoxification

Table 4. Effect of juice detoxification on the functional groups in the OPF juice

S/N	Wave number cm^{-1}	Juice before detoxification	Juice after detoxification	Vibration	Source
1.	769-992	×	✓	C-C	Alkene
2.	1020-1220	increased	Reduced	C-O Hydroxyl group	Phenols
3.	1363.58	✓	✓	O-H bending	Phenols
4.	2126	✓	✓	C-N	
5.	1637	✓	✓	OH (water)	Water
6.	3296-3306	✓	✓	O-H linked shearing	Sugars

The most observed differences between the two spectra of oil palm frond hydrolysate (before and after detoxification) were found within the region from 1400 to 700 cm^{-1}. The absorption bands at 1228 and 1217 cm^{-1} were not clearly observed in the spectra of the hydrolysate after detoxification (Figure. 2b). These absorptions are attributed to the esterified phenolic functional groups that are associated with phenolic compounds before the oil palm frond hydrolysate is detoxified. Figure 2a shows absorption bands that must be emphasized; the bands at 1080 and 1036 cm^{-1} show a drastically reduced spectrum from the original juice before detoxification. These two absorption bands are important because the reduction of the detoxified OPF hydrolysate spectra indicated that some of the phenol compounds were removed. The removal of phenolic compounds was confirmed by the HPLC results presented in Table 4, which showed reduced amounts of gallic acid and ferulic acid in the hydrolysate of the detoxified sample

3.5 Effect of Detoxification Process of OPF Hydrolysate on Biobutanol Production

Table 5 shows the effect of ABE fermentation by three Clostridial species using detoxified OPF hydrolysate containing 47.5 g/L reducing sugar concentration. The fermentation using a non-detoxified OPF hydrolysate containing the same initial sugar concentration using these isolates was equally performed as a control. The results indicated that all three strains of bacteria demonstrated improved biobutanol production (1.3 folds) from detoxified OPF hydrolysate when compared with the ABE produced from the controls (non-detoxified OPF hydrolysate). As shown in Table 5, the butanol production from detoxified OPF hydrolysate using strain L2 to ferment demonstrated the highest improvement towards biobutanol production when compared with the other two isolates. The solvents and acids produced by the strain L2 were almost 1.77 times higher than the control using the same isolate and fermentation conditions. The maximum butanol of 2.64± 0.03 g/L and total solvent of 5.41± 0.07 g/L were produced with a butanol productivity of 0.29×10^{-3} g/L/h, being about 1.3 folds as compared with the control, in which only 2.04± 0.01 g/L of butanol was produced with a productivity of 0.21×10^{-3} g/L/h and total solvent of 4.63± 0.08 g/L. This enhancement was achieved because of the reduction of the phenolic compound that was present in the hydrolysate, which could have distressed bacterial metabolisms

Similar enhancements were observed with a relatively low improvement from the fermentations of detoxified OPF hydrolysate using strain A1. Here, the results indicated 1.23 folds of butanol production when comparing the fermentation of detoxified and non-detoxified OPF hydrolysates using the same A1 strain. However, for *C. acetobutylicum* SR1, only a 1.02-foldenhancement was observed in the biobutanol yields. Nevertheless, the improvement of the fermentation products, particularly when the detoxified OPF hydrolysate was fermented by strain L2, indicated that the phenolic compound concentration had a great negative impact on the fermentation media and that the isolates could better adopt a medium with a lower concentration of phenolic compounds than the higher (Khanna et al., 2019). This was further proved by the rapid growth of all three isolates in the media containing the detoxified OPF hydrolysate when compared with their growth in the media with non-detoxified samples. Even though folic acid, which is also a phenol compound, has been shown to stimulate bacterial metabolism during ABE fermentation, leading to increased butanol production (Shahryari et al., 2018), its effects are only efficient when present at very low concentrations (1-100 mg/L) in the fermentation medium (Mosele et al., 2015), which is far below the amount of gallic acid present in the OPF hydrolysate. The current study aims to reduce both the total and individual amounts of phenolic compounds.

During the 96 hours of batch culture fermentation, it was observed that the acidogenic phase of most of the strains ranged between 12 and 24 hours of the fermentation, where acetic acid and butyric acid were the main products produced. The specific growth rates of the isolates were 0.127, 0.025, and 0.015 g/L/h for ***C. acetobutylicum*** SR1, L2, and A1, respectively, which were faster than the growth rates of the isolates in the non-detoxified samples with 0.121, 0.019, and 0.007 g/L/h. The growth of these isolates was also seen in terms of their sugar utilization. Strain L2, which was seen to have utilized 62% of its sugar at a rate of 0.37 g/L/h using the non-detoxified OPF hydrolysate, was able to utilize 69% of its reducing sugar (almost 1.2 folds) at a rate of 0.31 g/L/h. This result further supports the suggestions made by several researchers that phenolic compounds not only inhibit the growth of bacteria but also hinder the rate of sugar utilization, ultimately reducing the metabolic processes of the microorganisms (Bottery et al., 2021; Robak and Balcerek, 2018).

Table 5. Comparison of biobutanol production using unfiltered and partially optimized filtered OPF juices

Parameters	Result obtained from fermentation of ND-OPFJ and D-OPFJ Using three strains					
	Strain SR1		Strain L2		Strain A1	
	ND-OPFJ	D-OPFJ	ND-OPFJ	D-OPFJ	ND-OPFJ	D-OPFJ
Acetone (g/L)	0.38± 0.02	**0.72± 0.05**	0.92± 0.04	**1.25± 0.01**	2.59± 0.03	**1.82± 0.04**
Butanol (g/L)	1.96± 0.04	**2.01± 0.02**	2.04± 0.01	**2.64± 0.03**	2.12± 0.05	**2. 32± 0.03**
Ethanol (g/L)	2.30± 0.06	**1.53± 0.05**	1.67± 0.03	**1.51± 0.02**	1.53± 0.05	**0.11± 0.23**
Total ABE (g/L)	4.58± 0.11	**3.61± 0.12**	4.63± 0.08	**5.41± 0.07**	6.44± 0.12	**5.05± 0.31**
Acetic acid (g/L)	1.35± 0.04	**0.18± 0.06**	0.25± 0.02	**1.31± 0.03**	0.19± 0.06	**0.23± 0.02**
Butyric acid (g/L)	2.90± 0.03	**1.23± 0.01**	0.90± 0.06	**1.54± 0.02**	1.23± 0.04	**0.65± 0.06**
Total acid (g/L)	4.25± 0.07	**1.42± 0.07**	1.05± 0.08	**2.85± 0.05**	1.42± 0.10	**0.89± 0.08**
Acetone productivity (g/L/h)	0.03×10^{-3}	$\mathbf{0.1\times10^{-3}}$	0.08×10^{-3}	$\mathbf{1.7\times10^{-3}}$	0.15×10^{-3}	$\mathbf{3.4\times10^{-3}}$
Butanol productivity (g/L/h)	6.0×10^{-3}	$\mathbf{0.12\times10^{-3}}$	0.21×10^{-3}	$\mathbf{0.29\times10^{-3}}$	0.33×10^{-3}	$\mathbf{0.14\times10^{-3}}$
Ethanol productivity (g/L/h)	10.0×10^{-3}	$\mathbf{0.5\times10^{-3}}$	1.2×10^{-3}	$\mathbf{20\times10^{-3}}$	13.0×10^{-3}	$\mathbf{1.2\times10^{-3}}$
Acetic acid productivity (g/L/h)	0.02×10^{-3}	$\mathbf{0.04\times10^{-3}}$	0.06×10^{-3}	$\mathbf{0.05\times10^{-3}}$	0.02×10^{-3}	$\mathbf{0.02\times10^{-3}}$
Butyric acid productivity (g/L/h)	0.6×10^{-3}	$\mathbf{0.13\times10^{-3}}$	0.08×10^{-3}	$\mathbf{3.2\times10^{-3}}$	0.08×10^{-3}	$\mathbf{0.09\times10^{-3}}$
Overall acetone productivity (g/L/h)	0.02×10^{-3}	$\mathbf{0.07\times10^{-3}}$	0.05×10^{-3}	$\mathbf{0.13\times10^{-3}}$	0.11×10^{-3}	$\mathbf{0.13\times10^{-3}}$
Overall butanol productivity (g/L/h)	0.04×10^{-3}	$\mathbf{0.09\times10^{-3}}$	2.1×10^{-3}	$\mathbf{0.15\times10^{-3}}$	0.21×10^{-3}	$\mathbf{0.13\times10^{-3}}$
Overall ethanol productivity (g/L/h)	0.62×10^{-3}	$\mathbf{0.39\times10^{-3}}$	0.93×10^{-3}	$\mathbf{1.5\times10^{-3}}$	0.08×10^{-3}	$\mathbf{0.12\times10^{-3}}$
Overall total solvent productivity (g/L/h)	0.13×10^{-3}	$\mathbf{0.55\times10^{-3}}$	0.36×10^{-3}	$\mathbf{3.0\times10^{-3}}$	0.4×10^{-3}	$\mathbf{0.24\times10^{-3}}$
Overall acetic acid productivity (g/L/h)	0.010×10^{-3}	$\mathbf{0.17\times10^{-3}}$	0.021×10^{-3}	$\mathbf{0.3\times10^{-3}}$	0.01×10^{-3}	$\mathbf{0.01\times10^{-3}}$
Overall butyric acid productivity (g/L/h)	0.23×10^{-3}	$\mathbf{0.065\times10^{-3}}$	0.061×10^{-3}	$\mathbf{2.4\times10^{-3}}$	0.74×10^{-3}	$\mathbf{0.03\times10^{-3}}$
Overall total acids productivity (g/L/h)	0.24×10^{-3}	$\mathbf{0.182\times10^{-3}}$	0.082×10^{-3}	$\mathbf{2.7\times10^{-3}}$	0.75×10^{-3}	$\mathbf{0.042\times10^{-3}}$
Initial total fermentable sugar (g/L)	47.50± 1.06	**47.50**± 1.06	47.50± 1.06	**47.50**± 1.06	47.50± 1.06	**47.50**± 1.06
Final total fermentable sugar (g/L)	18.2	**15.4**	19.5	**12.2**	13.4	**14.7**
Percentage of sugar consumed (%)	66.7	**67.4**	59.1	**68.2**	69.1	**71.8**
Sugar utilization rate (g/L/h)	0.33	**0.36**	0.31	**0.37**	0.35	**0.34**
Xmax (g/L)	0.317	**0.364**	1.051	**1.138**	0.372	**0.425**
Specific growth rate (g/L/h)	0.121	**0.127**	0.019	0.025	0.007	**0.015**
Maximum specific growth rate (h^{-})	0.993	**0.254**	0.038	**0.050**	0.014	**0.010**
Doubling time td (h^{-})	1.395	**2.728**	0.659	**0.609**	1.863	**1.630**

Note: **ND-OPFJ** = Non detoxified oil palm frond juice and **D-OPFJ** = detoxified oil palm frond juice

3.6 Toxicity tolerance of the isolates

The toxicity tolerance of the three tested strains during the fermentation using non-detoxified OPF hydrolysate is presented in Table 5. Strain A1 was found to produce the highest concentration of butanol and other solvents with a better production rate and faster biomass formation compared to strains SR1 and L2. However, after the detoxification of the OPF hydrolysate, the strain L2 exhibits the most significant improvement (1.3 folds) in the biobutanol production, biomass formation, and sugar utilization compared to the SR1 and A1. This could possibly be explained due to the differences in phenolic compound resistance conferred by the various isolates. This assertion is in agreement with the suggestions previously made on the response of different microbes to certain inhibitors, such that some inhibitors are highly detrimental to a particular strain while some strains resist them (Ezeji et al., 2007). Hence, depending on the type of inhibitor, concentration, and other physicochemical parameters of the culture medium, such as temperature and pH, the effects of a variety of phenolic compounds usually vary among different organisms and strains applied for the fermentation process. For example, acetates, furfural, and HMF at concentrations less than 1.9 g/L were reported to be less toxic to *C. beijerinckii* BA101 growth or butanol production (Nimbalkar et al., 2019), whereas solvent production by *C. acetobutylicum* was reported to have collapsed, particularly when the cells were in a medium with pH decline due to rapid accumulation of acetic and butyric acids (Nimbalkar et al., 2019).

4. CONCLUSIONS

With the increasing concerns about the low biobutanol production from lignocellulosic hydrolysate, it has been speculated that the presence of phenolic compounds could be responsible for the poor fermentation. Ferulic, gallic, ρ-coumaric, and vanillic acids are known as phenolic compounds with a critical inhibitory effect on Gram-positive bacteria, especially solvent-producing Clostridia. However, the current research uses the resin filtration technique as a means to decrease the amount of these inhibitory compounds in OPF hydrolysate. The results of the research indicated a significant removal of phenolic compounds at an optimum temperature of 50 °C and pH 6. The removal of approximately 32% of the phenolic compound from the hydrolysate resulted in improved biobutanol production and productivity, as well as decreased acid production that may have hindered the fermentation process. The impact of the detoxification process also seems to improve and hasten biomass formation as well as sugar utilization.

5. DECLARATION OF COMPETING INTEREST

The authors declare that they have no known competing financial interests or personal relationships that could have appeared to influence the work reported in this paper.

6. ACKNOWLEDGEMENT

The Authors are very gratefull for the fund received from UTM High Impact Research Grant (Q.J130000.2454.09G06) under the Universiti Teknologi Malaysia. The first author also acknowledged TETFund, Nigeria for financial assistance during his PhD studies.

REFERENCES

1. Abe, K., Hori, Y., & Myoda, T. (2020). Characterization of key aromacompounds in aged garlic extract. *Food chemistry*, 312, 126081. https://doi.org/10.1016/j.foodchem.2019.126081
2. Akyıldız, A., Önür, E., Ağçam, E., Kirit, B. D., & Türkmen, F. U. (2022). Changes in quality parameters of orange juice deacidified by ion exchange resins. *Food Chemistry*, 375, 131837. https://doi.org/10.1016/j.foodchem.2021.131837
3. Asri, F., Masngut, N., & Zahari, M. (2019). Biobutanol production from oil palm frond juice in 2 L stirred tank bioreactor with in situ gas stripping recovery. *In* "IOP Conference Series: Materials Science and Engineering", Vol. 702, pp. 012004. IOP Publishing. https://doi.org/10.1088/1757-899X/702/1/012004
4. Bottery, M. J., Pitchford, J. W., & Friman, V.-P. (2021). Ecology and evolution of antimicrobial resistance in bacterial communities. *The ISME Journal*15, 939-948.https://www.nature.com/articles/s41396-020-00832-7
5. Chen, Z., Zeng, J., Zhang, Z.-B., Zhang, Z.-J., Ma, S., Tang, C.-M., & Xu, J.-Q. (2022). Preparation and application of polyethyleneimine-modified corncob magnetic gel for removal of Pb (ii) and Cu (ii) ions from aqueous solution. *RSC advances*12, 1950-1960.https://doi.org/10.1039/D1RA08699E
6. Din, N. A. S., Lim, S. J., Maskat, M. Y., Mutalib, S. A., & Zaini, N. A. M. (2021). Lactic acid separation and recovery from fermentation broth by ion-exchange resin: A review. *Bioresources and Bioprocessing***8**, 1-23. https://doi.org/10.1186/s40643-021-00384-4
7. Ezeji, T., Qureshi, N., & Blaschek, H. P. (2007). Butanol production from agricultural residues: impact of degradation products on Clostridium beijerinckii growth and butanol fermentation. *Biotechnology and bioengineering*, 97, 1460-1469. https://doi.org/10.1002/bit.21373
8. Fan, L., Wang, G., Holzheid, A., Zoheir, B., & Shi, X. (2021). Sulfur and copper isotopic composition of seafloor massive sulfides and fluid evolution in the 26° S hydrothermal field, Southern Mid-Atlantic Ridge. *Marine Geology*, 435, 106436. https://doi.org/10.1016/j.margeo.2021.106436
9. Galbe, M., & Wallberg, O. (2019). Pretreatment for biorefineries: a review of common methods for efficient utilisation of lignocellulosic materials. *Biotechnology for biofuels*, 12, 1-26. https://link.springer.com/article/10.1186/s13068-019-1634-1
10. Ghasemi, A., Jamali, M. R., & Es' haghi, Z. (2021). Ultrasound assisted ferrofluid dispersive liquid phase microextraction coupled with flame atomic absorption spectroscopy for the determination of cobalt in environmental samples. *Analytical Letters*, 54, 378-393. https://doi.org/10.1080/00032719.2020.1765790
11. Ghorbannezhad, P., & Abbasi, M. (2021). Optimization of Pyrolysis Temperature and Particle Size on the Phenols and Hemicellulose Fast Pyrolysis Products in a Tandem Micro-Pyrolyzer. *Journal of Renewable Energy and Environment*, 8, 68-74. https://doi.org/10.30501/jree.2021.255248.1155
12. Karimi, S., Yaraki, M. T., & Karri, R. R. (2019). A comprehensive review of the adsorption mechanisms and factors influencing the adsorption process from the perspective of bioethanol dehydration. *Renewable and Sustainable Energy Reviews*, 107, 535-553. https://doi.org/10.1016/j.rser.2019.03.025
13. Kee, S. H., Ganeson, K., Rashid, N. F. M., Yatim, A. F. M., Vigneswari, S., Amirul, A.-A. A., Ramakrishna, S., & Bhubalan, K. (2022). A review on biorefining of palm oil and sugar cane agro-industrial residues by bacteria into commercially viable bioplastics and biosurfactants. *Fuel*, 321, 124039. https://doi.org/10.1016/j.fuel.2022.124039
14. Khanna, K., Kohli, S. K., Ohri, P., Bhardwaj, R., Al-Huqail, A. A., Siddiqui, M. H., Alosaimi, G. S., & Ahmad, P. (2019). Microbial fortification improved photosynthetic efficiency and secondary metabolism in Lycopersicon esculentum plants under Cd stress. *Biomolecules*9, 581. https://doi.org/10.3390/biom9100581
15. Khunchit, K., Nitayavardhana, S., Ramaraj, R., Ponnusamy, V. K., & Unpaprom, Y. (2020). Liquid hot water extraction as a chemical-free pretreatment approach for biobutanol production from Cassia fistula pods. *Fuel*279, 118393. https://doi.org/10.1016/j.fuel.2020.118393
16. Kordala, N., Lewandowska, M., & Bednarski, W. (2021). Effect of the method for the elimination of inhibitors present in Miscanthus giganteus hydrolysates on ethanol production effectiveness. *Biomass Conversion and Biorefinery*, 1-9. https://link.springer.com/article/10.1007/s13399-020-01255-2
17. Kourilova, X., Novackova, I., Koller, M., & Obruca, S. (2021). Evaluation of mesophilic Burkholderiasacchari, thermophilic Schlegelellathermodepolymerans and halophilic Halomonas halophila for polyhydroxyalkanoates production on model media mimicking lignocellulose hydrolysates. *Bioresource Technology*, 325, 124704. https://doi.org/10.1016/j.biortech.2021.124704
18. Krstonošić, M. A., Hogervorst, J. C., Mikulić, M., & Gojković-Bukarica, L. (2020). Development of HPLC method for determination of phenolic compounds on a core shell column by direct injection of wine samples. *Acta Chromatographica*, 32, 134-138. https://doi.org/10.1556/1326.2019.00611
19. Kumneadklang, S., Sompong, O., & Larpkiattaworn, S. (2019). Characterization of cellulose fiber isolated from oil palm frond biomass. *Materials Today: Proceedings*17, 1995-2001. https://doi.org/10.1016/j.matpr.2019.06.247
20. Liu, S., Wang, J., Huang, W., Tan, X., Dong, H., Goodman, B. A., Du, H., Lei, F., & Diao, K. (2019). Adsorption of phenolic compounds from water by a novel ethylenediamine rosin-based resin: Interaction models and adsorption mechanisms. *Chemosphere*, 214, 821-829. https://doi.org/10.1016/j.chemosphere.2018.09.141
21. Milewska, M., Milewski, A., Wandzik, I., & Stenzel, M. H. (2022). Structurally analogous trehalose and sucrose glycopolymers–comparative characterization and evaluation of their effects on insulin fibrillation. *Polymer Chemistry*13, 1831-1843. https://doi.org/10.1039/D1PY01517F
22. Miller, G. L. (1959). Use of dinitrosalicylic acid reagent for determination of reducing sugar. *Analytical chemistry*, 31, 426-428.https://doi.org/10.1021/ac60147a030
23. Miller, T. L., & Wolin, M. (1974). A serum bottle modification of the Hungate technique for cultivating obligate anaerobes. *Applied microbiology*27, 985-987.https://doi/pdf/10.1128/am.27.5.985-987.1974
24. Mohammed, B. B., Yamni, K., Tijani, N., Alrashdi, A. A., Zouihri, H., Dehmani, Y., Chung, I.-M., Kim, S.-H., & Lgaz, H. (2019). Adsorptive removal of phenol using faujasite-type Y zeolite: Adsorption isotherms, kinetics and grand canonical Monte Carlo simulation studies. *Journal of Molecular Liquids*, 296, 111997.https://doi.org/10.1016/j.molliq.2019.111997
25. Morsi, R., Bilal, M., Iqbal, H. M., & Ashraf, S. S. (2020). Laccases and peroxidases: the smart, greener and futuristic biocatalytic tools to mitigate recalcitrant emerging pollutants. *Science of the total environment*, 714, 136572.https://doi.org/10.1016/j.scitotenv.2020.136572
26. Mosele, J. I., Macià, A., & Motilva, M.-J. (2015). Metabolic and microbial modulation of the large intestine ecosystem by non-absorbed diet phenolic compounds: A review. *Molecules*, 20, 17429-17468.https://doi.org/10.3390/molecules200917429
27. Nagasawa, T., Sato, K., & Kasumi, T. (2019). Efficient Continuous Production of Lactulose Syrup by Alkaline Isomerization Using an Organogermanium Compound Continuous Production of Lactulose Syrup Using an Organogermanium Compound. *Journal of Applied Glycoscience*, 66, 121-129.https://doi.org/10.5458/jag.jag.JAG-2019_0012
28. Narita, K., Asano, K., Naito, K., Ohashi, H., Sasaki, M., Morimoto, Y., Igarashi, T., & Nakane, A. (2020). Ultraviolet C light with wavelength of 222 nm inactivates a wide spectrum of microbial pathogens. *Journal of Hospital Infection*, 105, 459-467.https://doi.org/10.1016/j.jhin.2020.03.030

29. Nimbalkar, P. R., Khedkar, M. A., Chavan, P. V., & Bankar, S. B. (2019). Enhanced biobutanol production in folic acid-induced medium by using Clostridium acetobutylicum NRRL B-527. *ACS omega*, 4, 12978-12982.https://doi.org/10.1021/acsomega.9b00583

30. Pailliè-Jiménez, M. E., Stincone, P., & Brandelli, A. (2020). Natural pigments of microbial origin. *Frontiers in Sustainable Food Systems*, 4, 590439.https://doi.org/10.3389/fsufs.2020.590439

31. Pedersen-Bjergaard, S. (2019). Electromembrane extraction—looking into the future. *Analytical and bioanalytical chemistry*411, 1687-1693.https://link.springer.com/article/10.1007/s00216-018-1512-x

32. Phung, Q. T., Maes, N., Jacques, D., Bruneel, E., Van Driessche, I., Ye, G., & De Schutter, G. (2015). Effect of limestone fillers on microstructure and permeability due to carbonation of cement pastes under controlled CO2 pressure conditions. *Construction and Building Materials*, 82, 376-390.https://doi.org/10.1016/j.conbuildmat.2015.02.093

33. Raganati, F., Procentese, A., Olivieri, G., Russo, M. E., Salatino, P., & Marzocchella, A. (2020). Bio-butanol recovery by adsorption/desorption processes. *Separation and Purification Technology*, 235, 116145.https://doi.org/10.1016/j.seppur.2019.116145

34. Robak, K., & Balcerek, M. (2018). Review of second-generation bioethanol production from residual biomass. *Food technology and biotechnology*56, 174.https://doi.org/10.17113%2Fftb.56.02.18.5428

35. Satari, B., Karimi, K., and Kumar, R. (2019). Cellulose solvent-based pretreatment for enhanced second-generation biofuel production: a review. *Sustainable energy & fuels*, 3, 11-62.https://doi.org/10.1039/C8SE00287H

36. Shahryari, S., Zahiri, H. S., Haghbeen, K., Adrian, L., & Noghabi, K. A. (2018). High phenol degradation capacity of a newly characterized Acinetobacter sp. SA01: bacterial cell viability and membrane impairment in respect to the phenol toxicity. *Ecotoxicology and Environmental Safety*, 164, 455-466.https://doi.org/10.1016/j.ecoenv.2018.08.051

37. Singh, B., Kumar, P., Yadav, A., & Datta, S. (2019). Degradation of fermentation inhibitors from lignocellulosic hydrolysate liquor using immobilized bacterium, Bordetella sp. BTIITR. *Chemical Engineering Journal*361, 1152-1160.https://doi.org/10.1016/j.cej.2018.12.168

38. Waheed, A., Mansha, M., Kazi, I. W., & Ullah, N. (2019). Synthesis of a novel 3, 5-diacrylamidobenzoic acid based hyper-cross-linked resin for the efficient adsorption of Congo Red and Rhodamine B. *Journal of hazardous materials*369, 528-538.https://doi.org/10.1016/j.jhazmat.2019.02.058

39. Way, M. L., Jones, J. E., Nichols, D. S., Dambergs, R. G., & Swarts, N. D. (2020). A comparison of laboratory analysis methods for total phenolic content of cider. *Beverages*, 6, 55.https://doi.org/10.3390/beverages6030055

40. Wei, W., Li, J., Han, X., Yao, Y., Zhao, W., Han, R., Li, S., Zhang, Y., & Zheng, C. (2021). Insights into the adsorption mechanism of tannic acid by a green synthesized nano-hydroxyapatite and its effect on aqueous Cu (II) removal. *Science of The Total Environment*, **778**, 146189.https://doi.org/10.1016/j.scitotenv.2021.146189

41. Wikandari, R., Sanjaya, A. P., Millati, R., Karimi, K., & Taherzadeh, M. J. (2019). Fermentation inhibitors in ethanol and biogas processes and strategies to counteract their effects. *In* "Biofuels: alternative feedstocks and conversion processes for the production of liquid and gaseous biofuels", pp. 461-499. Elsevier. https://doi.org/10.1016/B978-0-12-816856-1.00020-8

JREE: Vol. 10, No. 4, (Autumn 2023) 99-106

Journal of Renewable Energy and Environment

Journal Homepage: www.jree.ir

Materials and Energy Research Center

MERC

Research Article

Application of Thermal Energy Accumulators Based on Paraffin Phase Change Materials in Convective-Vacuum Impulsive Drying Units: A Brief-Focused Overview of Characteristics and Thermal Conductivity Enhancement Techniques

Mohammed Ali Sami Mahmood[a,b*], Rodionov Yuriy Viktorovich[a], Shchegolkov Alexandr Viktorovich[c]

[a] *Department of Mechanics and Engineering Graphics, Tambov State Technical University, Tambov, Russia.*
[b] *Department of Machines and Equipment Engineering Techniques, Al-Mussaib Technical College, Al-Furat Al-Awsat Technical University, Babil, Iraq.*
[c] *Department of Technology and Methods of Nanoproducts Manufacturing, Tambov State Technical University, Tambov, Russia.*

PAPER INFO

Paper history:
Received: 19 November 2022
Revised: 06 January 2023
Accepted: 17 January 2023

Keywords:
Thermal Energy Accumulator,
Paraffin,
Phase Change Material,
Convective Drying,
Convective-vacuum Impulsive Drying,
Energetic Efficiency

ABSTRACT

Researchers worldwide are studying thermal energy storage with phase change materials because of their substantial benefits in the enhancement of energy efficiency of thermal drying systems. A two-stage convective-vacuum impulsive drying plant is a technology for the manufacturing of chemical and food products with high quality and low energy costs. Energy consumption during the drying process is the main indicator in terms of economy. In this paper, a brief and focused review of the peculiarities of TEAs with PPCMs and opportunities of their application in such drying systems is done and discussed. The paper described the mentioned manufacturing system. The advantages of paraffin wax and thermal conductivity improvement techniques were demonstrated for their use as heat storage materials in CVID drying units. The results of similar previous studies were presented. The results of the experimental studies conducted by the researchers proved that the use of heat accumulators with PCMs increased the overall energy efficiency of drying systems. Finally, integration of TEAs based on modified PPCMs in the CVID system was recommended to intensify thermal energy, reduce thermal influence on the main indicators of the vacuum pump during the evacuation process, and decrease production costs.

https://doi.org/10.30501/jree.2023.370842.1501

1. INTRODUCTION

1.1. General background

Drying is a traditional preservation technique for the preservation of food products and the processing of various chemical materials. It is a process of dehumidification from substances. It is a time-consuming and energy-intensive process (Azzouz et al., 2018; Iqbal et al., 2019). The energy needed to remove moisture content can be procured from traditional and non-traditional sources (Aktaş et al., 2016; Malakar and Arora, 2022). Reliance on fossil fuels as a source of energy (heat) during the drying process of raw materials leads to major environmental problems. Currently, preserving the environment and finding alternative energy sources are among the most important issues in developing countries (Bahari et al., 2020; Srinivasan et al., 2021). In most industrial and technological processes, the operation of machines and devices is accompanied by the release of heat, which is poorly used, hence heat loss. The application of thermal accumulators based on phase change materials with various thermal performance improvement techniques works to manage the thermal energy in the drying system and increases the drying speed, thus reducing energy costs (Ahmadi Mezjani et al., 2022; Babapoor et al., 2015; Babapoor et al., 2022; Bahari et al., 2020; Srinivasan et al., 2021). In this review, a beneficial insight is provided on the main characteristics of PCMs with a focus on paraffin waxes and methods for improving thermal conductivity as materials for storing heat energy during thermal processing of raw materials to intensify the thermal energy consumed by a two-stage Convective-Vacuum Impulsive Drying (CVID) plant. The aim of this paper is to study the potential of thermal energy storage and recirculating stored heat depending on the TEAs with PPCM to be integrated in CVID units.

1.2. Working principle description of convective-vacuum impulsive drying unit

The convective-vacuum impulsive drying plant is a two-stage drying technology used for the manufacturing of products with high quality and low energy consumption in the food and chemical industries (Didone and Tosello, 2016; Zubov and Khamitova, 2011; Nikitin et al., 2021). The first stage is the processing of materials using the traditional hot air convective dryer (Figure 1a) to remove the free moisture content from the external surface of the material. It involves two main processes.

*Corresponding Author's Email: mohammed.sami@atu.edu.iq (M.A.S. Mahmood)
URL: https://www.jree.ir/article_165735.html

Please cite this article as: Mahmood, M. A. S., Viktorovich, R. Y. & Viktorovich, S. A. (2023). Application of thermal energy accumulators based on paraffin phase change materials in convective-vacuum impulsive drying units: A brief-focused overview of characteristics and thermal conductivity enhancement techniques, *Journal of Renewable Energy and Environment (JREE)*, 10(4), 99-106. https://doi.org/10.30501/jree.2023.370842.1501 .

The first is transfer (supply) of the thermal energy from the surrounding environment to the materials (solid) (5). The hot air heated by heater (3) to a desired temperature is provided using blower (1). Regulator (2) controls the flow rate of the supply air. The second process is the transfer of humidity from within the materials (removing moisture) in the drying chamber (7). The control panel (6) contains devices to control and display the main parameters of the drying process. As a result, it may be thought of as a simultaneous process of mass and heat transmission. It is worth noting that convection drying for the first stage can be done using a tray dryer as shown in Figure 1b. The second stage is the removal of bound moisture from the substance by means of vacuum impulsive cabinets with auxiliary equipment (Figure 1c). In this technology, the evacuation process takes place at a lower temperature and a higher mass transfer rate; as a result, the energy consumption during drying is reduced. The mechanism of action consists of the following periods: The first period is the heating of the material placed in the drying cabinet (9) through heated air by an electric heater (7) at a desired drying temperature. In this period, the temperature of substance and drying rate is constant. The second period is the removal of bound moisture by vacuumization using a liquid ring vacuum pump (LRVP) (1). The control panel (10) with needful controllers is used to adjust the parameters of the drying process. The pneumatic valves are employed to regulate the flow rate in air pipelines. The hydrodynamic valves are applied to controlling the indispensable working fluid for the normal operation of the LRVP. A chiller (5) is employed to cool the recirculated working fluid and to prevent liquid evaporation in the working cavity of LRVP. The set temperature and periods of heating and evacuation depend on the characteristic of products to be dried. The cycle is repeated until the required moisture content of the product is obtained. Figure 2 presents the 3D of the CVID system.

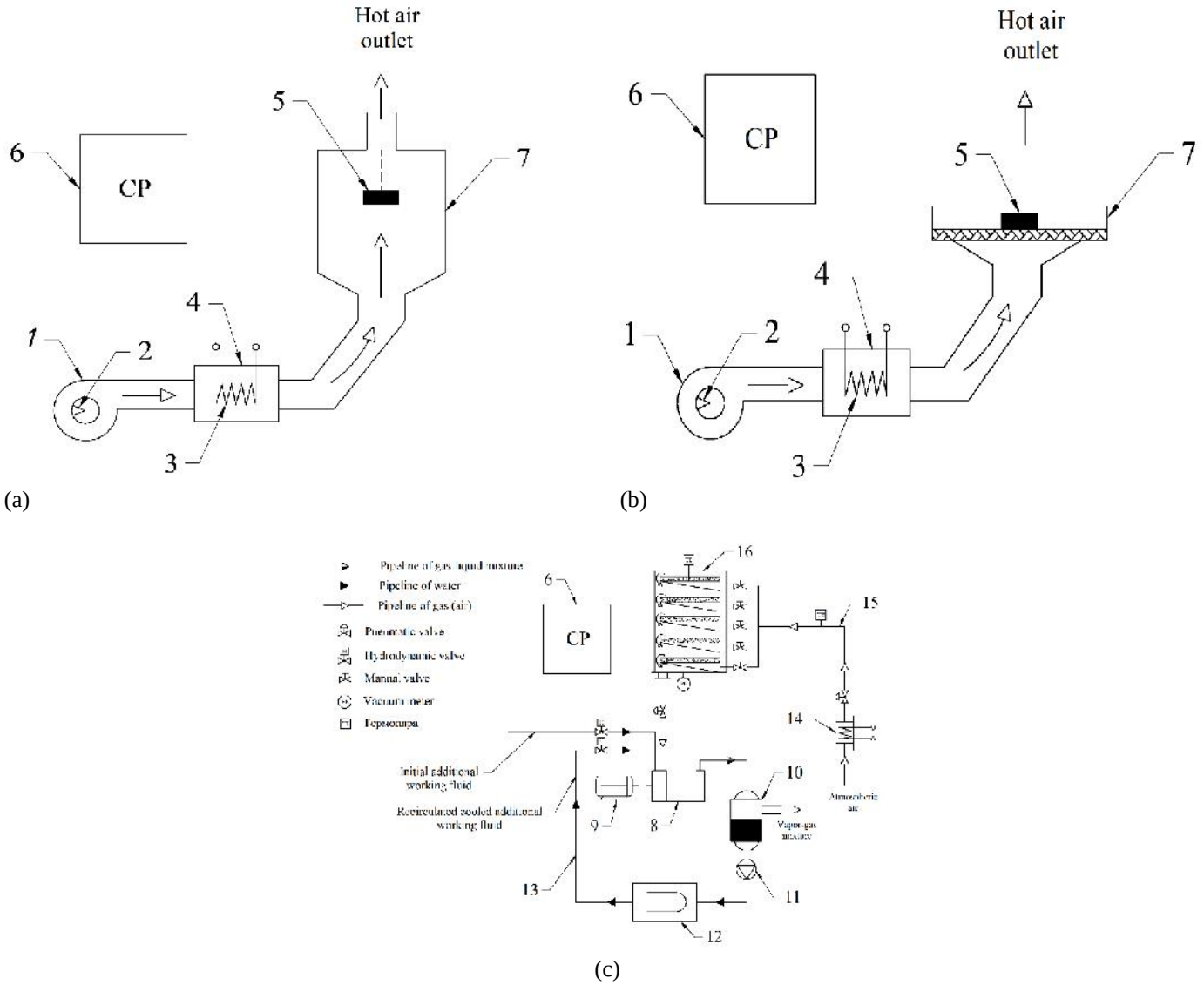

Figure 1. Schematic diagram of a two-stage drying plant (Zorin, 2019): (a) the first stage of hot air convective dryer with a suspended swirling layer; (b) the first stage of hot air convective tray dryer; (c) the second stage of vacuum impulsive cabinets with recirculation of working fluid of LRVP: 1 – blower, 2 – air flow regulator, 3 – electric heater, 4 – heating unit, 5 – sample of material, 6 – control panel, 7 – drying chamber, 8 – LRVP, 9 – electric motor, 10 – gas-liquid phase separator, 11 – water circulation pump, 12 – chiller for cooling of recirculated working liquid, 13 – water pipeline, 14 – electric heater (resistance), 15 – air pipeline, and 16 – drying cabinet.

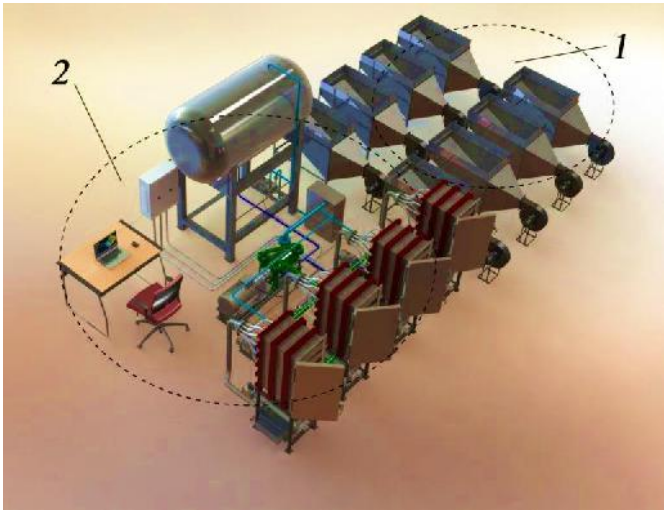

Figure 2. 3D configuration of a two-stage CVID (Petrovna, 2016): 1 – The first stage of hot air convective tray dryers, 2 – The first stage of vacuum impulsive cabinets with auxiliary equipment.

2. THERMAL ENERGY ACCUMULATORS

Thermal Energy Accumulators (TEAs) are units or apparatuses that are used to temporarily store thermal energy for use at a later time (Zorin, 2019). The energy demand varies with time according to thermal drying system requirements. This change can be controlled through the integration of TEAs with PCMs (Socaciu, 2012). The selection of TEAs for a drying plant depends on many factors, such as supply temperature requirement, economics, storage duration, heat losses, storage capacity, and available space (Ibrahim and Marc, 2011). There are two main kinds of TEAs: sensible and latent. Sensible TEA systems accumulate TE by modifying the temperature of the utilized storage medium, like soil, brine, water, rock, etc. Latent systems accumulate TE by phase change, e.g., the storage of heat through melting paraffin waxes and cold storage water/ice. In addition, TAs can be performed through chemical reactions (Abedin, 2011; Socaciu, 2012). Figure 3 illustrates the categories of TEA units (Sarbu and Sebarchievici, 2018).

2.1. Phase change materials

PCMs are latent heat storage materials that have been used in many thermal applications due to their thermo-physical peculiarities (Du et al., 2018). Heat is mostly accumulated during the phase change process and is directly connected to the substance's latent heat. The application of TEAs with PCMs is considered an efficient and desirable technology because they provide isothermal and high thermal energy storage (Sarbu and Sebarchievici, 2018). PCMs are classified into several types, as shown in Figure 4. TEAs with PCMs typically involve three stages: charging, storing, and discharging. They are a reliable technology dependent on the storage of latent heat energy (Mondal, 2008), where PCM absorbs or releases heat with time during the charging and discharging process (phase change period), with a high heat of fusion (Ghoneim, 1989; Morrison, 1978), as shown in Figure 5.

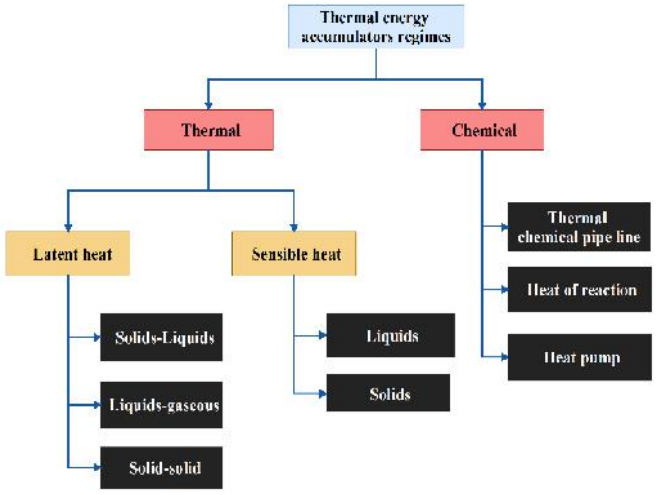

Figure 3. Classifications of the thermal energy accumulator regimes (Sarbu and Sebarchievici, 2018).

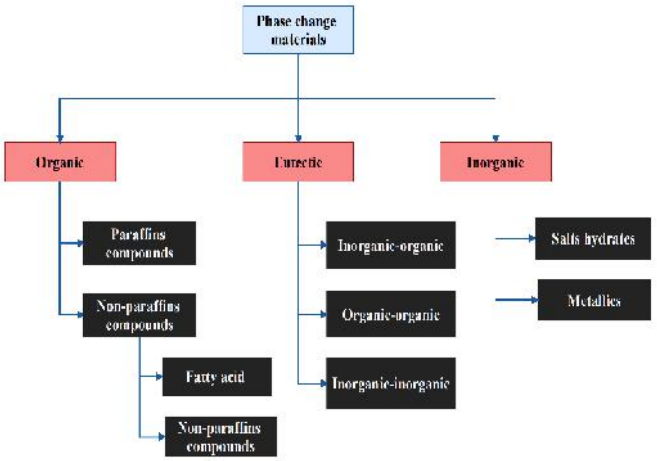

Figure 4. Classifications of PCMs (Sarbu and Sebarchievici, 2018).

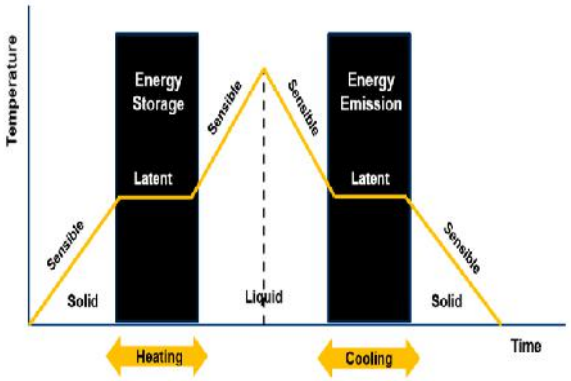

Figure 5. Regime representation TEAs-PCMs, cycle of charging, storing and discharging in case of cooling and heating (Du et al., 2018).

The amount of stored sensible heat depends on the average specific heat of the medium, the quantity of storage material, and the temperature change. The sensible heat for various materials can be calculated as follows (Kumar and Shukla, 2015):

$$Q_s = c_p\, m \int_{T_i}^{T_f} dT = c_p\, m \left(T_f - T_i\right) \quad (1)$$

where Q_s is the amount of sensible heat stored in, J; c_p is the specific heat of the materials, J/kg.°C; T_f, T_i are the final and initial temperatures, °C. The accumulated latent heat via PCMs can be calculated using the following equation (Kumar and Shukla, 2015):

$$Q_{LHS} = \int_{T_i}^{T_m} m_{PCM}\, c_{ps}\, dT + m_{PCM}\, q_{hf} + \int_{T_m}^{T_f} m_{PCM}\, c_{pl}\, dT \quad (2)$$

$$Q_{LHS} = m_{PCM}\left[c_{ps}\left(T_m - T_i\right) + q_{hf} + c_{pl}\left(T_f - T_m\right)\right] \quad (3)$$

where m_{PCM} is the mass of PCM medium, kg; T_m is the melting temperature, °C; c_{pl} is the average specific heat of the liquid phase between T_m and T_f, J/(kg·K); q_{hf} is the latent heat of fusion (J/kg) at the temperature of phase change T_{pc}; c_{ps} is the average specific heat of the solid phase between T_i and T_m, kJ/(kg·K). The reported advantages and disadvantages for several PCMs are tabulated in Table 1 (Pahamli and Valipour, 2021). In thermal energy storage applications, paraffins, fatty acids, and hydrated salts are the most common widespread used materials (Sarbu and Sebarchievici, 2018). Ice water is frequently utilized in cold storage, as well (Sarbu and Sebarchievici, 2018). The important thermophysical properties of some indispensable PCMs are presented in Table 2.

2.2 Paraffins as latent PCMs

2.2.1. General overview

Among many types of PCMs currently available, paraffin waxes have been used in many types of thermal applications. They belong to groups of organic PCMs with greater processing options than the other types illustrated in Figure 4. Furthermore, because of their widespread accessibility, safe operation, and low cost, they are a remarkable choice to enhance the thermal efficiency of the drying system (Srinivasan et al., 2021). Paraffin is a hydrocarbon combination and is derived basically from waste products of the petroleum. Depending on the number of carbon atoms, the state of the phase is distinguished. They are in a gaseous state under room conditions with a number of carbon atoms ranging from 1 to 4 and carbon atoms from 5 to 17 being in a liquid state and waxes with a number of carbon atoms more than 17 (Al-yasiri, 2021). Typical paraffin properties are listed in Table 3. Figure 6 presents the appearance of paraffin available in local markets.

Table 3. General properties related to paraffins (Hamad, 2021).

Property	Liquid phase	Solid phase
Boiling point	> 370 °C	
Melting temperature	57 °C	57 °C
Thermal conductivity	0.25 W/m °C	0.23 W/m °C
Specific heat capacity	1.6 kJ/kg °C	2 kJ/kg °C
Latent Heat of Fusion	2.1 kJ/kg °C	
Chemical formula	C_nH_2n+2	
Appearance	According to source of paraffin and composition	

Figure 6. Appearance of paraffin wax (Al-yasiri, 2021).

Table 1. Advantages and disadvantages of PCMs (Pahamli and Valipour, 2021).

Indicator	Organic Material	Inorganic Material	Eutectic Material
Advantages	- Good chemical and thermal stability, - Non-corrosive, - Low vapor pressure, - No supercooling, - High heat of fusion, - Nontoxic.	- Inexpensive, - Nonflammable, - Good thermal conductivity, - High heat of fusion.	- Wide range of phase change temperature, - Good chemical and thermal stability, - High heat capacity, - No or little supercooling.
Disadvantages	- Low thermal conductivity, - Low phase change enthalpy, - High changes in volumes during the phase transition.	- Corrosion, - Phase decomposition, - High supercooling effect, - Loss of hydrate throughout the process, - Insufficient thermal stability, - Weight problem.	- Leakage during the phase transition, - Low thermal conductivity.

Table 2. Properties of the main PCMs (Sarbu and Sebarchievici, 2018).

PCM	Melting enthalpy (kJ/kg)	Melting Temperature (°C)	Density (g/cm^3)
Ice	333	0	0.92
Na-acetate trihidrate	250	58	1.30
Paraffin	150 - 240	- 5 - 120	0.77
Erytritol	340	118	1.30

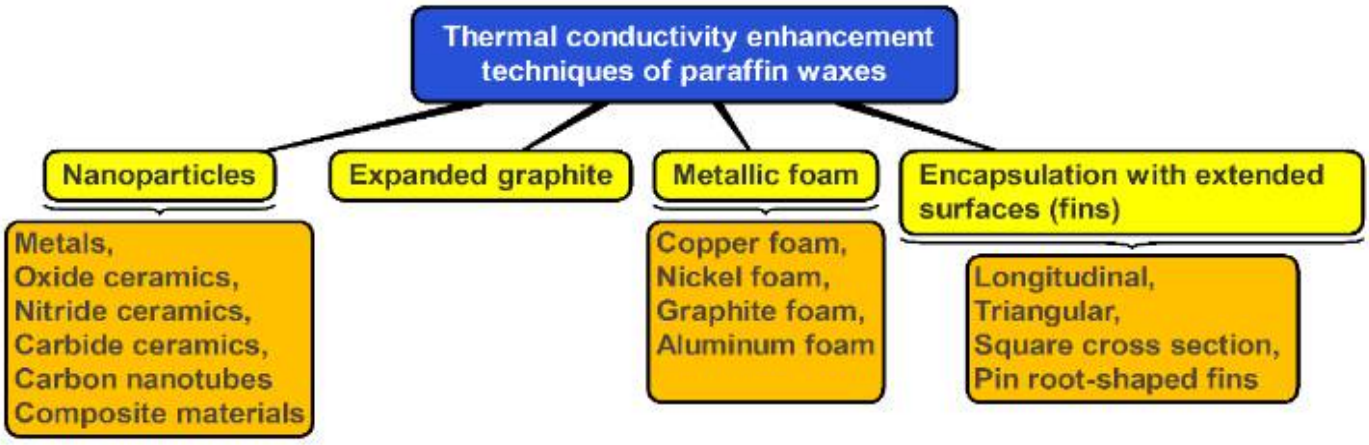

Figure 7. TC enhancement methods of paraffin PCM.

2.2.2. Thermal conductivity enhancement techniques of paraffin

Despite the many advantages of paraffin such as no sub-cooling, non-toxic, low-cost, high latent heat, eco-friendly, non-corrosive, and chemical stability (Sharma et al., 2009), they are renowned for their poor thermal conductivity (TC), causing melting and solidification to take longer and have an influence on thermal performance of convective and TVID plant. Five known methods exist to improve the TC of paraffin, as shown in Figure 7. Recently, nanoparticles (NPs) have been used to increase the TC of paraffin. In this regard, many studies have been conducted in depth and the results are attractive (Wang et al., 2019; Zhang, 2020). The use of NPs with paraffin activates the charging and discharging time, which is positively reflected on the thermal system performance. Modified paraffin by NPs is manufactured in the same way as nanofluids (Al-yasiri et al., 2021; Sundar et al., 2017). Figure 8 shows the manufacturing stages of PPCM-NPs. The other method is to use expanded graphite (EG) as a supplement material with paraffin to increase the TC (Kenisarin et al., 2019). It is a novel approach to improving the TC of paraffin. As the mass fraction of EG increases, the TC of paraffin increases (Zhang et al., 2020). The steps of PPCM-EG are shown in Figure 9. Metallic foam is another important way to improve the TC of PPCM. High TC of the base materials makes metallic foams an excellent choice. Moreover, their better properties, such as long-term stability and lower density, make them preferred over NPs (Qureshi et al., 2018). The effectiveness of metallic foams is determined by the density of the pores, the size of the pores, and the type of foam material (Tauseef-ur- Rehman, 2018). Figure. 10 illustrates the stages of preparation. The TC of PPCM can considerably improve by encapsulating it in finned containers (internal and/or external fins). This technology is a cost-effective solution that has demonstrated significant improvement when used with high-TC materials like stainless steel aluminum, and copper. Fins speed up the melting and solidification processes, reducing the time required to complete the cycle. Different characteristics of fins, such as size, type, spacing, and the number of fins, affect the thermal performance of PPCM (Shehzad et al., 2021; Zayed et al., 2020). The different shapes and designs of the fins utilized for the PPCM TC improvement are shown in Figure. 11.

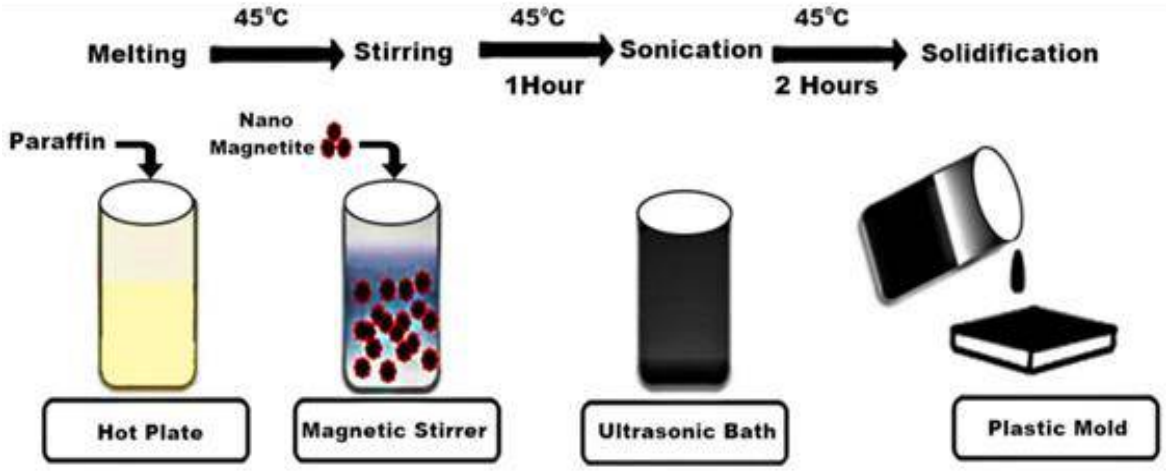

Figure 8. Preparation steps of PPCM-NPs (Mohammad et al., 2019).

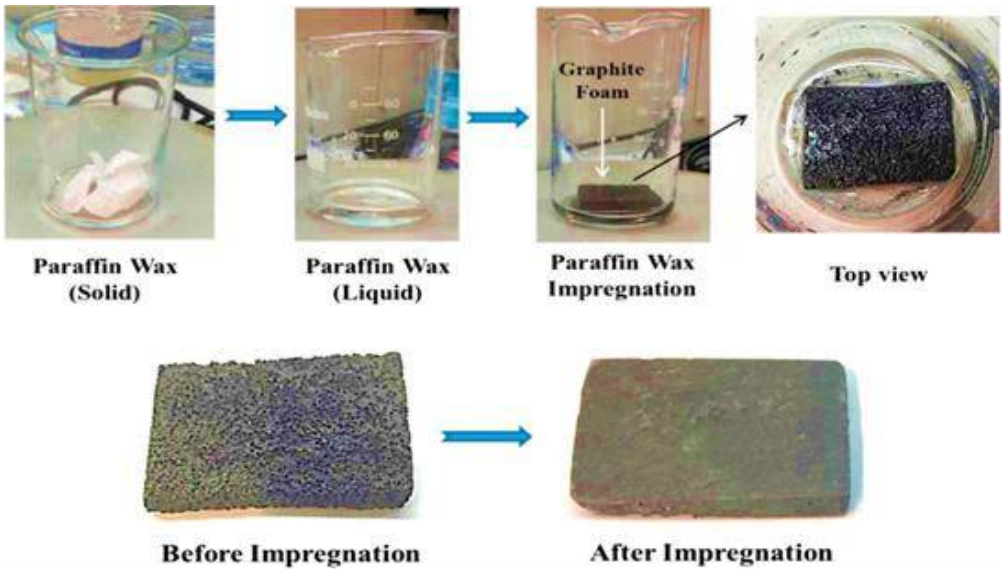

Figure 9. PPCM-EG preparation steps (Karthik et al., 2017).

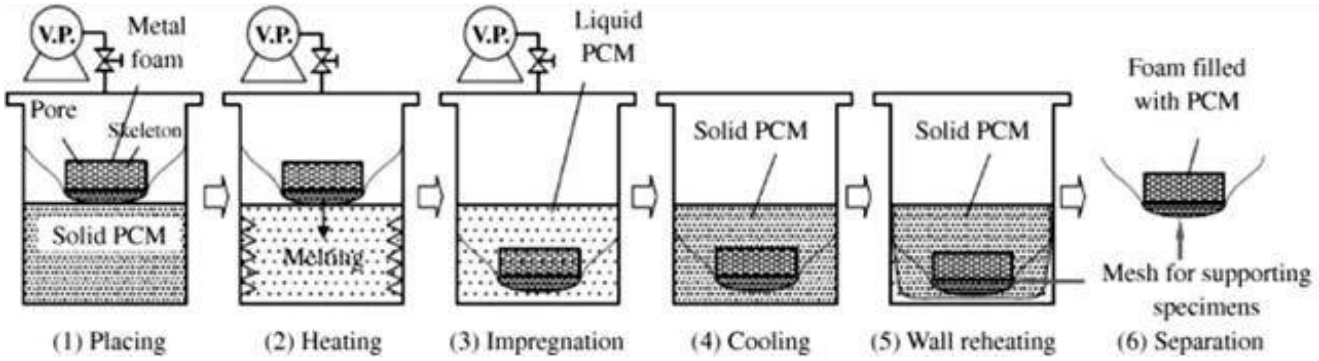

Figure 10. Preparation of PPCM-metal foam (Xiao et al., 2013).

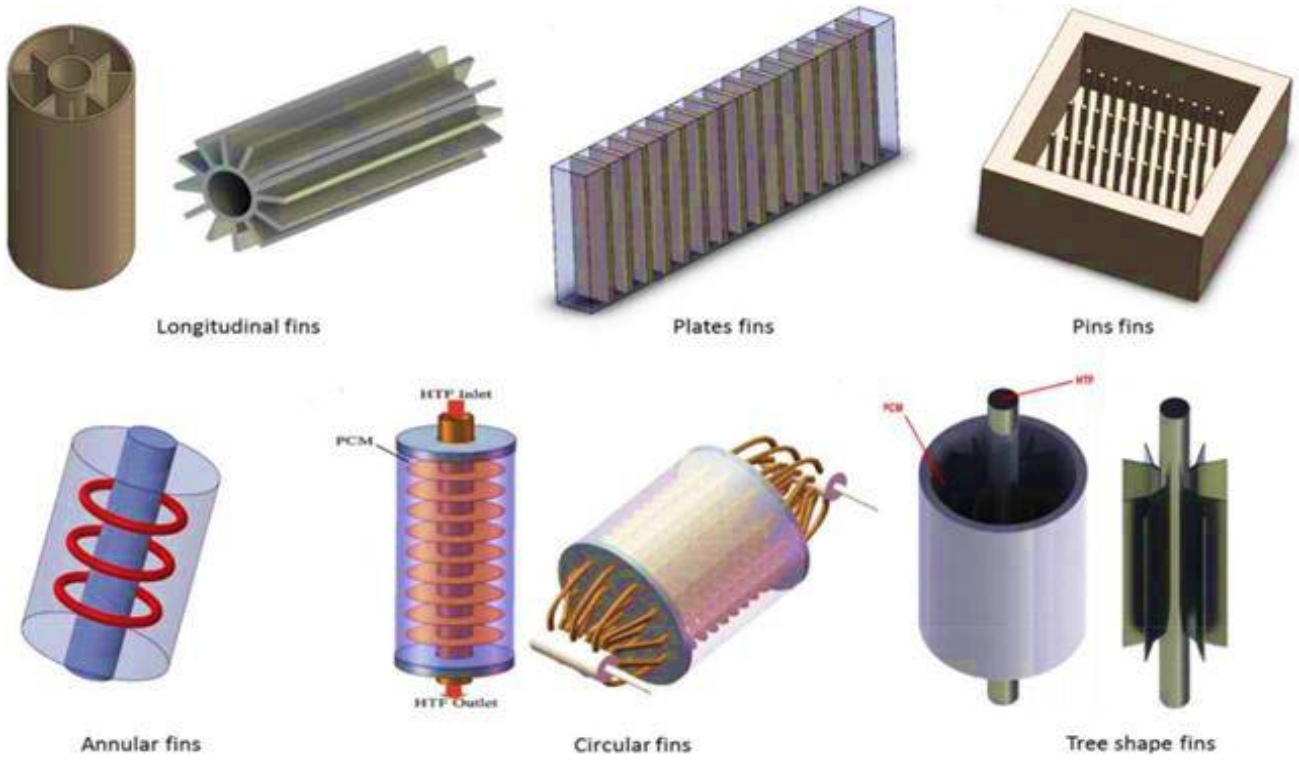

Figure 11. Various types of TEAs/containers encapsulated with external and internal fins (Al-yasiri, 2021; Wu et al., 2021).

3. RECENT RELEVANT STUDIES AND EXPERIMENTS

In connection with the topic of the current article, this section presents and discusses the reported investigations. Due to the large volume of published research on the use of TEAs with PCMs in drying systems, this review focuses on the relevant and strong works published in recent years. Hamad, 2021, were applied PCMs to solar air drying and air conditioning systems for energy saving. An experimental setup was developed to investigate two PCMs: paraffin wax and RT-42 in different locations. The findings showed a considerable increase in energy saving. For the first PCM1 (paraffin wax) and PCM2 (RT-42), complete melting occurred during the charging cycle at temperatures of 57-60°C as well as 38-43°C. When two PCMs were used, the overall energy saving was higher by around 29.5% and 46.7% than the application of PCM1 and PCM2, respectively. Poonia et al., 2022, investigated a solar dryer with and without PCMs to dry arid fruits. They employed an experimental approach to test the use of polyethylene glycol (PEG) 600 as a heat storage material during drying. The results revealed that the moisture content of the product decreased from 80% to 22% in seven days in the case of PCM and in 9 days without PCM. In date palm fruit, MC was reduced from 65 to 20% in 6 and 8 days with and without PCM, respectively. The thermal efficiency was 18% with PCM compared to 15% without PCM. Mahdavi Nejad, 2020, studied the drying process of paper with PCM. The drying efficiency was enhanced by about 45%. Bhardwaj et al., 2021, evaluated the thermal performance of the solar dryer using PCM. They used paraffin RT-42 as PCM during the experimental test. The outcome of study indicated that the products were dehydrated to a value of 9% from preliminary MC of 89% and it took 120 (216) hours with (without) use of PCM. The mean values of the exergy and energy efficiencies of the SAC without (with) PCM were calculated to be 0.14 (0.81%) and 9.8 (26.2%)%, respectively. Rodionov et al, 2020, integrated TEA-based PCMs to enhance the energy efficiency of a two-stage combined vacuum impulsive drying for plant materials. They introduced nano modified PPCM as a material to store the heat during their experimental studies. Utilized TEAs reduced electricity losses by 20%-25%. In this regard, they (Zorin et al, 2019), were awarded a patent.

4. CONCLUSION AND FUTURE PERSPECTIVE

This study investigated the application characteristics of TAs with PPCM and thermal conductivity improvement techniques to be used in the CVID unit. From the results of previously reported studies, the following conclusions can be derived.

1. The use of TEAs with PPCM is a successful method to reduce the time consumed in the drying process of materials in CVID system;
2. The design of TEAs based on PCMs is a complex issue when inserted in such systems;
3. Paraffin waxes are most commonly used as a heat storage material. Their main disadvantage lies in the low thermal conductivity;
4. Many techniques for improving the thermal conductivity of PPCM are reported in the literatures. A cost-effective method is encapsulating it in finned containers (internal and/or external fins).

Currently, work is underway to use TEAs based on paraffin waxes or modified paraffin as a heat storage material/cooler and temperature regulation in a CVID technology. Considering the characteristics of TEAs with PPCMs presented in this paper, it is recommended to design liquid ring vacuum pumps units with integration of TEAs with PPCMs to prevent the deformation of form of liquid ring (evaporation of liquid) in the working cavity during their use in heat and mass transfer devices/processes such as drying and evaporation. Studies such as suitable design of TEAs and the possibility of recirculation of stored heat are candidate.

5. ACKNOWLEDGEMENT

The author would like to thank the Department of Mechanics and Engineering Graphics of Tambov State Technical University, Russia for supporting us. The researcher would like to express great appreciation of Prof. Rodionov Yuriy Viktorovich for providing remarkable support for this study.

NOMENCLATURE

PCM/ PCMs	Phase change material/ materials
TEA/TEAs	Thermal energy accumulator/ accumulators
CVID	Convective-vacuum impulsive drying
TE	Thermal energy
TC	Thermal conductivity
NPs	Nanoparticles
PPCM	Paraffin phase change materials
EG	Expanded graphite
LRVP	liquid ring vacuum pump
TVID	Thermo-vacuum impulsive drying

REFERENCES

1. Abedin, A. H. (2011). A Critical Review of Thermochemical Energy Storage Systems. The Open Renewable Energy Journal, 4(1), 42–46. https://doi.org/10.2174/1876387101004010042.
2. Ahmadi Mezjani, M., Karimi, G. R., Medi, B., Babapoor, A., & Paar, M. (2022). Passive Thermal Management of a Lithium-Ion Battery Using Carbon Fiber Loaded Phase Change Material: Comparison and Optimization. Iranian Journal of Chemistry and Chemical Engineering, 41(1), 310–327. https://doi.org/10.30492/ijcce.2020.118203.3862.
3. Aktaş, M., Şevik, S., & Aktekeli, B. (2016). Development of heat pump and infrared-convective dryer and performance analysis for stale bread drying. Energy Conversion and Management, 113, 82–94. https://doi.org/10.1016/j.enconman.2016.01.028.
4. Al-yasiri, Q. (2021). Paraffin As a Phase Change Material to Improve Building Performance : An Overview of Applications and Thermal Conductivity Enhancement Techniques Paraf fi n As a Phase Change Material to Improve Building Performance : An Overview of Applications and Therm. Renewable Energy and Environmental Sustainability, 6(38), 12. https://doi.org/10.1051/rees/2021040.
5. Al-yasiri, Q., Szabó, M., & Arıcı, M. (2021). Single and Hybrid Nanofluids to Enhance Performance of Flat Plate Solar Collectors: Application and Obstacles. Periodica Polytechnica Mechanical Engineering, 65eriodica(1), 86–102. https://doi.org/10.3311/PPme.17312.
6. Azzouz, S., Hermassi, I., Chouikh, R., Guizani, A., & Belghith, A. (2018). The convective drying of grape seeds: Effect of shrinkage on heat and mass transfer. Journal of Food Process Engineering, 41(1), 1–8. https://doi.org/10.1111/jfpe.12614.
7. Babapoor, A., Azizi, M., & Karimi, G. (2015). Thermal management of a Li-ion battery using carbon fiber-PCM composites. Applied Thermal Engineering, 82, Vol. 41, (2022), 310-327. https://doi.org/10.1016/j.applthermaleng.2015.02.068
8. Babapoor, A., Haghighi, A. R., Jokar, S. M., & Ahmadi Mezjin, M. (2022). The Performance Enhancement of Paraffin as a PCM During the Solidification Process: Utilization of Graphene and Metal Oxide Nanoparticles. Iranian Journal of Chemistry and Chemical Engineering, 41(1), 37–48. https://doi.org/10.30492/ijcce.2020.127799.4135
9. Bahari, M., Najafi, B., & Babapoor, A. (2020). Evaluation of α-AL2O3-PW nanocomposites for thermal energy storage in the agro-products solar dryer. Journal of Energy Storage, 28(October 2019). https://doi.org/10.1016/j.est.2019.101181

10. Bhardwaj, A. K., Kumar, R., Kumar, S., Goel, B., & Chauhan, R. (2021). Energy and exergy analyses of drying medicinal herb in a novel forced convection solar dryer integrated with SHSM and PCM. Sustainable Energy Technologies and Assessments, 45(February), 101119. https://doi.org/10.1016/j.seta.2021.101119
11. Didone, M., & Tosello, G. (2016). Potential of impulse drying technology for molded pulp products manufacture. Progress in Paper Physics Seminar 2016, Darmstadt, 9–15. https://backend.orbit.dtu.dk/ws/portalfiles/portal/126860019/2016_C_08_Paper_Conference_Darmstadt_Article.pdf.
12. Du, K., Calautit, J., Wang, Z., Wu, Y., & Liu, H. (2018). A review of the applications of phase change materials in cooling, heating and power generation in different temperature ranges. Applied Energy, 220(February), 242–273. https://doi.org/10.1016/j.apenergy.2018.03.005.
13. Ghoneim, A. A. (1989). Comparison of theoretical models of phase-change and sensible heat storage for air and water-based solar heating systems. 42(3), 209–220. https://doi.org/10.1016/0038-092X(89)90013-3.
14. Hamad, A. J. (2021). Energy saving and charging discharging characteristics of multiple pcms subjected to internal air flow. Fluids, 6(8). https://doi.org/10.3390/fluids6080275.
15. Iqbal M, J., Akbar M, W., Aftab, R., Younas, I., & Jamil, U. (2019). Heat and mass transfer modeling for fruit drying: a review. MOJ Food Processing & Technology, 7(3), 69–73. https://doi.org/10.15406/mojfpt.2019.07.00222.
16. Karthik, M., Faik, A., & Aguanno, B. D. (2017). Solar Energy Materials and Solar Cells Graphite foam as interpenetrating matrices for phase change para ffi n wax : A candidate composite for low temperature thermal energy storage. Solar Energy Materials and Solar Cells, 172(April), 324–334. https://doi.org/10.1016/j.solmat.2017.08.004.
17. Kenisarin, M., Mahkamov, K., Kahwash, F., & Makhkamova, I. (2019). Solar Energy Materials and Solar Cells Enhancing thermal conductivity of para ffi n wax 53 – 57 ° C using expanded graphite. Solar Energy Materials and Solar Cells, 200(June), 110026. https://doi.org/10.1016/j.solmat.2019.110026.
18. Kumar, A., & Shukla, S. K. (2015). A Review on Thermal Energy Storage Unit for Solar Thermal Power Plant Application. Energy Procedia, 74, 462–469. https://doi.org/10.1016/j.egypro.2015.07.728.
19. Mahdavi Nejad, A. (2020). Enhancement of drying of paper with phase change material: A numerical study. International Journal of Heat and Mass Transfer, 149. https://doi.org/10.1016/j.ijheatmasstransfer.2019.119169.
20. Malakar, S., & Arora, V. K. (2022). Development of phase change material assisted evacuated tube solar dryer: Investigation of thermal profile, drying characteristics, and functional properties of pumpkin slices. Innovative Food Science and Emerging Technologies, 80(July), 103109. https://doi.org/10.1016/j.ifset.2022.103109.
21. Mohammad Reza Safaei, Hamid Reza Goshayeshi, I. C. (2019). Solar Still E ffi ciency Enhancement by Using Graphene Oxide / Paraffin Nano-PCM. 12(10), 1–13. https://doi.org/10.3390/en12102002
22. Mondal, S. (2008). Phase change materials for smart textiles – An overview. Applied Thermal Engineering, 28, 1536–1550. https://doi.org/10.1016/j.applthermaleng.2007.08.009
23. Morrison, D. J. (1978). Effects of phase change energy storage on the performance of air-based and liquid-based solar heating systems. Solar Energy, 20. https://doi.org/10.1016/0038-092X(78)90141-X.
24. Nikitin, D. V., Rodionov, Y. V., Makhmud, M. A. S., Skomorokhova, A. I., Pakhomov, A. N., & Zorin, A. S. (2021). Liquid Ring Vacuum Pumps for Heat and Mass Transfer Processes. Vestnik Tambovskogo Gosudarstvennogo Tehnicheskogo Universiteta, 27(3), 428–441. https://doi.org/10.17277/vestnik.2021.03.pp.428-441. (In Russian).
25. Pahamli, Y., & Valipour, M. S. (2021). Application of Phase Change Materials in Refrigerator and Freezer Appliances : A Comprehensive Review. Journal of Heat and Mass Transfer Research, 8, 87–104. https://doi.org/10.22075/jhmtr.2021.21860.1316.
26. Petrovna, I. E. (2016). Development of technology for the preparation of dry sourdough based on vegetable raw materials for the production of functional bakery products. Michurinsk State Agrarian University. http://intern.mgau.ru/. (In Russian).
27. Poonia, S., Singh, A. K., & Jain, D. (2022). Performance evaluation of phase change material (PCM) based hybrid photovoltaic/thermal solar dryer for drying arid fruits. Materials Today: Proceedings, 52, 1302–1308. https://doi.org/10.1016/j.matpr.2021.11.058
28. Rodionov Yury, Shchegolkov Alexander, Nikitin Dmitry, Zorin Alexande. (2020). Application of Nanomodified Heat-Accumulating Materials in Plant Drying Systems. 1(43), 43–50. https://doi.org/10.35887/2305-2538-2020-1-43-50
29. Qureshi, Z. A., Ali, H. M., & Khushnood, S. (2018). Recent advances on thermal conductivity enhancement of phase change materials for energy storage system: A review. International Journal of Heat and Mass Transfer, 127, 838–856. https://doi.org/10.1016/j.ijheatmasstransfer.2018.08.049
30. Sarbu, I., & Sebarchievici, C. (2018). A comprehensive review of thermal energy storage. Sustainability (Switzerland), 10(1). https://doi.org/10.3390/su10010191
31. Sharma, A., Tyagi, V. V, Chen, C. R., & Buddhi, D. (2009). Review on thermal energy storage with phase change materials and applications. Renewable and Sustainable Energy Reviews, 13, 318–345. https://doi.org/10.1016/j.rser.2007.10.005.
32. Shehzad, S. A., Alshuraiaan, B., Saad, M., & Izadi, M. (2021). Influence of fin orientation on the natural convection of aqueous-based nano-encapsulated PCMs in a heat exchanger equipped with wing-like fins. Chemical Engineering and Processing - Process Intensification, 160(December 2020), 108287. https://doi.org/10.1016/j.cep.2020.108287.
33. Socaciu, L. G. (2012). Thermal energy storage with phase change material. Leonardo Electronic Journal of Practices and Technologies, 11(20), 75–98. https://doi.org/10.1201/9780367567699
34. Srinivasan, G., Rabha, D. K., & Muthukumar, P. (2021a). A review on solar dryers integrated with thermal energy storage units for drying agricultural and food products. Solar Energy, 229(July), 22–38. https://doi.org/10.1016/j.solener.2021.07.075.
35. Sundar, L. S., Sharma, K. V, Singh, M. K., & Sousa, A. C. M. (2017). Hybrid nanofluids preparation, thermal properties, heat transfer and friction factor – A review. Renewable and Sustainable Energy Reviews, 68(March 2016), 185–198. https://doi.org/10.1016/j.rser.2016.09.108
36. Tauseef-ur- Rehman, H. M. A. (2018). Experimental investigation on para ffi n wax integrated with copper foam based heat sinks for electronic components thermal cooling. International Communications in Heat and Mass Transfer, 98(September), 155–162. https://doi.org/10.1016/j.icheatmasstransfer.2018.08.003
37. Wang, Q., Wei, W., Li, D., Qi, H., Wang, F., & Ar, M. (2019). Experimental investigation of thermal radiative properties of Al2O3-paraffin nanoflui. 177(May 2018), 420–426. https://doi.org/10.1016/j.solener.2018.11.034.
38. Wu, J., Chen, Q., Zhang, Y., & Sun, K. (2021). Phase change material heat transfer enhancement in latent heat thermal energy storage unit with single fin: Comprehensive effect of position and length. Journal of Energy Storage, 42(August), 103101. https://doi.org/10.1016/j.est.2021.103101.
39. Xiao, X., Zhang, P., & Li, M. (2013). Preparation and thermal characterization of paraffin / metal foam composite phase change material. Applied Energy, 112, 1357–1366. https://doi.org/10.1016/j.apenergy.2013.04.050.
40. Zayed, M. E., Zhao, J., Li, W., Elsheikh, A. H., Mohamed, A., Jing, L., & Geweda, A. E. (2020). Recent progress in phase change materials storage containers : Geometries , design considerations and heat transfer improvement methods. Journal of Energy Storage, 30(May), 101341. https://doi.org/10.1016/j.est.2020.101341
41. Zhang, G. (2020). Seasonal thermal performance analysis of glazed window filled with paraffin including various nanoparticles. Energy Research, 44(4), 1–12. https://doi.org/10.1002/er.5129
42. Zhang, M., Wang, C., Luo, A., Liu, Z., & Zhang, X. (2020). Molecular dynamics simulation on thermophysics of paraffin/EVA/graphene nanocomposites as phase change materials. Applied Thermal Engineering, 166(October 2019), 114639. https://doi.org/10.1016/j.applthermaleng.2019.114639
43. Zorin, A. S. (2019). Improvement of technology and technical means of combined vacuum drying of vegetable raw materials for the production of chips. Tambov State Technical University. https://www.tstu.ru/en/. (In Russian).
44. Zorin A.S. , Ivanova I.V. , Nikitin D.V. , Rodionov Y.V., S. A. V. (2019). Energy-efficient convective vacuum impulse dryer with heat accumulators. No. 2716056. Russian federation. https://patents.s3.yandex.net/RU2716056C1_20200306.pdf.
45. Zubov D.M., and Khamitova L.V. (2011). Grounds for the use of pulse-vacuum wood drying. 1–7. http://www.intermedia-publishing.ru/ENZhM/Zubov_Ground.pdf. (In Russian).

JREE: Vol. 10, No. 4, (Autumn 2023) 107-118

Journal of Renewable Energy and Environment

Journal Homepage: www.jree.ir

Materials and Energy Research Center

MERC

Research Article

Variability Assessment of Solar Irradiance for the Safe Grid Integration of Solar Photovoltaic Power Plants

Md. Rashedul Alam [a], Iftekhar Uddin Bhuiyan [b*], Nur Mohammad [c]

[a] *Sustainable and Renewable Energy Development Authority (SREDA), P. O. Box: 1000, Dhaka, Bangladesh.*
[b] *Institute of Appropriate Technology, Bangladesh University of Engineering and Technology, P. O. Box: 1000, Dhaka, Bangladesh.*
[c] *Department of Electrical and Electronic Engineering, Chittagong University of Engineering and Technology, P. O. Box: 4349, Chittagong, Bangladesh.*

PAPER INFO

Paper history:
Received: 21 December 2022
Revised: 02 April 2023
Accepted; 14 April 2023

Keywords:
Assessment of Solar Irradiance,
Short-term variation of Solar Irradiance,
Integration Challenges of Variable Renewable Energy,
Voltage-frequency aspects of Solar Photovoltaic grid integration

ABSTRACT

The output power of a Solar Photovoltaic (SPV) plant depends mainly on the solar irradiance on the photovoltaic (PV) modules. Therefore, short-term variations in solar irradiance cause variations in the output power of solar power plants, making solar photovoltaic grid integration unstable. Solar irradiance variations mainly occur due to the weather conditions of a given location, especially the movement of clouds and seasonal effects. Consequently, assessing the variability of solar irradiance over the course of a year is essential to identify the extent of these variations. Geographical dispersion and cloud enhancement are two important factors affecting output power variations in a PV plant. Geographical dispersion reduces such variations, while cloud enhancement increases them. This study utilizes two ground station-based solar Global Horizontal Irradiance (GHI) datasets to assess the viability of solar irradiance in the Chittagong division of Bangladesh. The analysis reveals a significant number of days with high short-term solar irradiance variation. In addition to solar irradiance, the frequency and voltage at the interconnection point are important for safe grid integration. It was observed that the grid frequency exceeded the range specified by the International Electrotechnical Commission (IEC), but remained within the grid code range of Bangladesh. Grid voltage variation at the interconnection substation was found to be within the standard range during the daytime, but low voltage was observed at the grid level during the rest period. Therefore, it is crucial to implement necessary preventive measures to reduce short-term variations for the safe grid integration of large-scale variable SPV plants.

https://doi.org/10.30501/jree.2023.377735.1522

1. INTRODUCTION

Global irradiance, a summation of direct irradiance and diffuse irradiance (including reflected irradiances), depends on the wind speed and cloud patterns that are the driving forces of variations of solar power (Blanc et al., 2014; Järvelä et al., 2020; Keeratimahat et al., 2019). Solar photovoltaic systems collect energy from the sun in a spatial dimension (Jazayeri et al., 2017). Therefore, it is important to understand the amount of variability of solar irradiance in the area with solar power systems. Variable Renewable Energy (VRE) adaptation capability of the electricity network depends on the amount of variability of the output power of the Solar Photovoltaic (SPV) plant. The movement of the cloud creates shadows on the Photovoltaic (PV) modules and changes the incidence of solar irradiance (Ahmed et al., 2020). The output of the PV system varies accordingly and provides a great effect on the integrated electric system (Tahir & Asim, 2018). For example, the Teknaf 20MW Solar plant, connected to a 33kV distribution substation of Cox's Bazar Palli Bidyut Somity of Bangladesh, faced unexpected shutdown due to protection sensitivity, long distribution line faults, and dynamic change of load flow. The maximum load of the Teknaf area was around 25MW and connected to the Cox's Bazar grid substation through a 33kV 80km long transmission line (Kainat et al., 2021).

Geographical dispersion and cloud enhancement are two important factors. The geographic dispersion of solar-photovoltaic panels reduces variability in energy production. In the study of geographic dispersion, Van Haaren et al characterized the variability in power output of six photovoltaic plants based on minute-averaged radiation data from each plant and the output from 390 inverters. They found maximum ramp rates of 0.7, 0.58, 0.53, and 0.43 times the plant's capacity for 5, 21, 48, and 80 MW AC plants, respectively, due to geographical dispersion. The study was conducted by simulating a step-by-step increase in the plant size at the same location (Van Haaren et al., 2014). On the other hand, the Cloud Enhancement (CE) or over-irradiance or irradiance enhancement can exceed the expected clear sky irradiance value during partly cloudy days. The CE phenomenon can be observed all around the world, but the amount may vary from place to place. Järvelä et al. (Järvelä et al., 2020) measured solar irradiance on such days that might be increased up to 1.5 times the clear weather days for some time. The output power fluctuation of the SPV power plant increases due to CE.

*Corresponding Author's Email: iftekhar@iat.buet.ac.bd (I. U. Bhuiyan)
URL: https://www.jree.ir/article_171371.html

Please cite this article as: Alam, M. R., Bhuiyan, I. U., Mohammad, N. (2023). Variability Assessment of Solar Irradiance for the Safe Grid Integration of Solar Photovoltaic Power Plants, *Journal of Renewable Energy and Environment (JREE)*, 10(4), 107-118. https://doi.org/10.30501/jree.2023.377735.1522.

Variation in the amount of solar irradiance depends on the location-specific weather status and cloud pattern of that place (Sengupta et al., 2018). Solar research focuses on understanding historical solar resource patterns and making future predictions, both of which are needed to support reliable power system operations (Sivaneasan et al., 2017). As solar technologies mature, more and increasingly larger solar energy systems are installed across the country (Shuvho et al., 2019). Financing these systems requires assurance that they will produce the energy predicted through performance models (Boopathi et al., 2021; Van Haaren et al., 2014). Failing to meet the minimum energy performance requirements can result in financial penalties, requiring expensive risk mitigation measures. Accurate solar irradiance data sets include the foundation of a successful performance model and are critical in reducing the expense associated with mitigating this performance risk (Denholm & Margolis, 2007; Karthikeyan & Janarthanan, 2017). Those data are available from Satellite and Ground station-based sources (Choi et al., 2019; Zhang et al., 2017). Ground station-based solar irradiation data is more reliable than Satellite source-based solar irradiation data (Carmona et al., 2018; Wei, 2017). Pyranometer, Pyrheliometer, and sun-tracker are used in ground station-based solar radiation measurement stations (Jamil & Akhtar, 2017).

This paper aims to highlight the challenges concerning the grid integration of the SPV plant, especially analyzing the variation of solar irradiance in Bangladesh. To this end, the following issues are to be addressed:

a) Grid reliability parameters like frequency variation and voltage variation in a nearest SPV plant have been assessed to identify the interconnection aspects;
b) Daily solar irradiance scenario has been assessed for a year for two case study sites to understand the seasonal effect and variation patterns in a day;
c) Basic comparative analysis of daily solar irradiance data between two sites is conducted.

Solar irradiance studies concerning the safe grid integration of solar photovoltaic power plants are very scarce in Bangladesh, although numerous SPV plants are established in different divisions of the country. In this regard, the paper is organized in the following manners: the first section describes the need for the research, objectives, and approach. The second section describes the case study site and data source; the third section describes the research methodology in detail; the fourth section presents the important findings and discussion according to the research methodology. Section 5 discusses the comparative scenario between the two case study sites. The sixth section discusses the research findings, recommendations, and further research opportunities.

2. DATA

2.1. Kaptai 7.4MW Solar Power Plant

The Kaptai 7.4MW Solar Power Plant is located beside the Kaptai hydroelectric dam at the Rangamati district of Chittagong division, Bangladesh. The plant achieved commercial operation on 28 May, 2019 and was the 4th utility-scale solar park installed in Bangladesh (*Annual Report 2019-2020 of SREDA*, 2020). It is operated by the Bangladesh Power Development Board (BPDB), a state-owned power generation and distribution utility in Bangladesh. The latitude and longitude of the site were 22.491945 and 92.227349, respectively. The solar irradiance data were recorded by a pyranometer and datalogger at the mentioned solar plant. Calibrated pyranometers were used at the site. The recorded Global Horizontal Irradiance (GHI) data were used for understanding the solar insolation status of that place. The data averaging frequency was 10 minutes and the unit was in W/m^2. Since the less precise time-scale solar irradiance data were not available in that solar power plant, the mentioned data were obtained for this variation analysis.

2.2. National Solar Radiation Resource Assessment Station, Chittagong

The Sustainable and Renewable Energy Development Authority (SREDA), the nodal agency of Bangladesh aiming to promote Renewable Energy and Energy Efficiency in the country, has installed eight solar radiation resource measurement stations in different locations of Bangladesh under a Global Environment Facility (GEF) funded project 'Sustainable Renewable Energy Power Generation (SREPGen)'. Locations of the solar resource monitoring sites are Rangpur (Begum Rokeya University, Rangpur), Rajshahi (Rajshahi University of Engineering and Technology), Mymensingh (Bangladesh Agricultural University), Sylhet (Shahjalal University of Science and Technology), Kushtia (Kushita Police Line), Khulna (Khulna University), Patuakhali (Patuakhali Science & Technology University), and Chittagong (Chittagong University of Engineering and Technology). The resource monitoring stations of Rajshahi and Patuakhali have advanced facilities including Pyrheliometer and sun tracker systems. Most of the stations are located at public universities in different regions of Bangladesh. Out of these eight solar radiation resource measurement stations, the Chittagong division's site is located at the Chittagong University of Engineering of Technology (CUET) campus, Raojan, Chittagong. The latitude and longitude of the site are 22.463998 and 91.973298, respectively. Global Horizontal Irradiance (GHI), Diffuse Horizontal Irradiance, and some weather data were recorded at a resource monitoring station. Only GHI data was used in this study to understand the variation analysis. This data was recorded by a Class-A calibrated pyranometer and its brand name was Kipp&Zonen. The data sampling frequency was 10 seconds and averaging frequency was 4 minutes. The maximum, minimum, and standard deviations of GHI data also were present with the average GHI data exhibiting a more precise scenario of solar irradiance variation. The locations of the selected sites are shown in Figure 1.

Figure 1. Location of the selected case study sites for irradiation assessment (*Customized Bangladesh Map - Google My Maps*, n.d.).

Figure 1 observes that the two sites are very close to each other, located in the Chittagong division of Bangladesh. According to the satellite-based solar irradiation data, developed by the Global Solar Atlas, a joint study of SOLARGIS, ESMAP, and the World Bank Group observed that the Chittagong division had the highest solar insolation among the other divisions' solar insolation in Bangladesh (*Global Solar Atlas*, n.d.). Most of the publicly published solar irradiation data are very good for expected energy calculation but not suitable for analysis of the VRE integration aspect due to the unavailability of less-than-minute time interval raw data on an open-source basis.

3. METHODOLOGY

The weather condition of any location varies from time to time due to seasonal changes, because the relative position between the sun and earth varies every day due to the change of declination angle and distance between them. There are summer solstice, winter solstice, and two equinoxes in a year. The weather conditions, especially clouds, and their patterns are different in different months due to several effects including the seasonal effect. Therefore, at least a whole year's data is needed to be taken under consideration for variability analysis of solar irradiance of any location.

The two nearest sites in Bangladesh have been selected for this analysis. The solar irradiance data (time series GHI data) of the Kaptai 7.4MW Solar Power Plant were recorded by a calibrated pyranometer and datalogger, as shown in Figure 2. The data averaging frequency was 10 minutes. Global Horizontal Irradiance (GHI) data of the CUET station were recorded by Class-A calibrated pyranometer (brand name: Kipp&Zonen). The data sampling frequency was 10 seconds and averaging frequency was 4 minutes. Collected daily time series solar GHI data were plotted to identify the daily irradiance status using MATLAB software, where the data unit is in W/m^2.

Figure 2. Data recording process.

The pyranometer mentioned in Figure 2 is a sensor device that senses solar irradiance and gives an output value in W/m^2 to the data logger through a digital communication protocol RS-485. Similarly, some other related sensors are connected with a datalogger to measure some related parameters like wind speed, wind direction, temperature, humidity, etc. A 4G-enabled sim card was connected to a data logger and the datalogger was sending the recorded data to the remote server through File Transfer Protocol (FTP). More than two power sources were connected to the datalogger to get interruption-free operation of solar irradiance data logging and transfer.

Voltage and frequency data were collected from Teknaf 20MW Solar Power Plant, located at Teknaf, Cox's Bazar, Bangladesh. Those data were recorded by an energy meter tested and installed by the power offtaker utility, Bangladesh Power Development Board (BPDB). Some voltage data of related 33/11kV substation and grid substation were collected from the respective utility recorded data. The distribution grid level data provider was Cox's Bazar Palli Bidyut Somity (PBS) and grid voltage level data were collected from the data published on the Power Grid Company of Bangladesh (PGCB) website.

Figure 3 represents the daily solar irradiance status of the National Solar Radiation Resource Assessment (NSRRA) Chittagong station of Bangladesh where the Y-axis represents the solar irradiance and the X-axis represents the number of records with 4-minute-interval averaging data. The data sampling was 10 seconds. The mean, max, min, and standard deviation data were plotted to understand the solar irradiance variation, whereas max, min, and standard deviation data gave more confidence about the variation of solar irradiance.

The daily solar irradiance data were plotted and their status was classified into four categories in the current study: Washout Days, High Variability Days, Low Variability Days, and Clear Days. The days on which maximum solar irradiance is limited to 300 W/m^2 were classified as Washout days in this study. The days on which maximum solar irradiance is greater than 800 W/m^2 but so many ramp-ups and ramp-down events occur in those days with high ramp level (more than 400 W/m^2) were defined as High Variability days. The more solar irradiance ramping gave more deep blue plots that help categorization, as mentioned above. If we expand a daily summary plot, then it will look like the following in Figure 3. If we compact this figure on X-axis, so many dark vertical lines will be observed.

The Low Variability days are similar, but the ramp level and the number of ramps per day are comparatively lower, at least one-third of the high variability days at the reference level. Clear weather days are defined, where daily short-term variations are negligible and non-cloudy days.

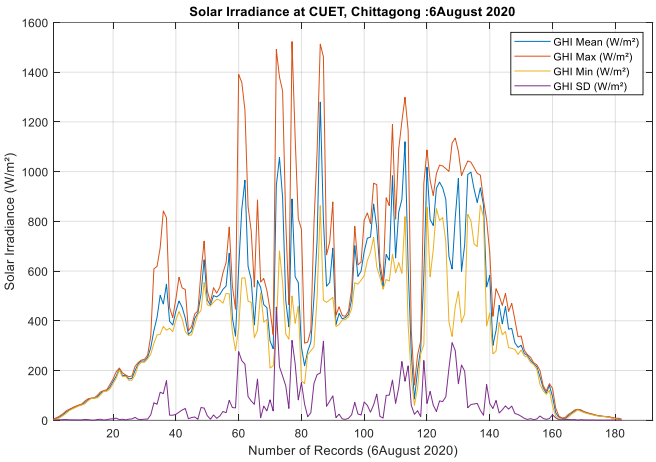

Figure 3. Daily solar irradiance with high solar ramping.

Given that we recognize the full-year solar ramping status, monthly summarized data are plotted in the result and discussion section to get the solar irradiance variation status using approximate daily classifications. Finally, monthly and yearly summary tables and bar charts are presented. This regional short-term variation analysis of solar irradiance is helpful to understand the requirement of ramp management support for safe integration of high VRE penetration into the grid.

4. RESULTS AND DISCUSSION

4.1. Voltage-frequency Status of an Interconnection Point

The variable renewable energy resources like solar irradiance are responsible for the variation of the output power of SPV plants, creating an effect in the interconnection area of the utility network. The utility network itself is subject to some variation due to its instantaneous demand-supply management. The voltage and frequency of the interconnection point have also a key role to play in this regard. Therefore, it is important to understand the real scenario of those parameters. Some of those data were collected from Teknaf 20MW Solar Power Plant, located at Teknaf, Cox's Bazar, Bangladesh.

4.1.1. Voltage records at Teknaf solar power plant

This 20-MW solar park is connected to a 33kV distribution substation operated by the Palli Bidyut Somity (PBS) of Cox's Bazar of the Bangladesh Rural Electrification Board (BREB). Data were collected from Teknaf Solartech Energy Limited (TSEL), the operating subsidiary of Joules Power Limited (JPL). The finding on the 33kV grid voltage on the plant side is given below.

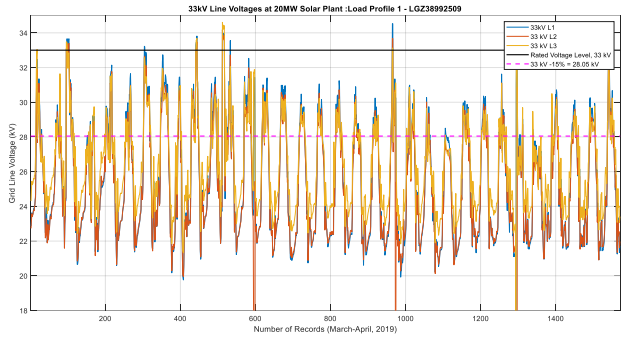

Figure 4. 33kV grid voltage at Teknaf 20MW Solar Plant; Data source: TSEL.

Figure 4 shows the 33kV grid voltage at Teknaf 20MW Solar Plant for 2 months, March-April 2019. These two months were selected as a sample among 12 months when electricity feeders were loaded with cooling loads. The grid voltage of the daytime was observed between 33kV and 28kV, which is within the -15% range. In the rest of the time of the month, the low voltage was observed at the grid level. The collected data were recorded at the energy meter of the Teknaf 20MW Solar Power plant. A sample of the daily voltage profile among these 2 months (4 April) at the plant level is shown in Figure 5 below.

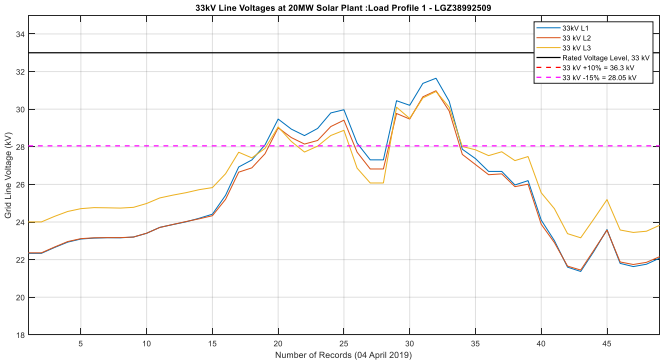

Figure 5. Grid voltage observed at Teknaf 20MW solar plant, 04 April 2019; Data source: TSEL.

According to Figure 5, grid voltage goes down beyond the standard level when the contribution of the Teknaf 20MW solar power plant is less or absent. The voltage fluctuates due to the amount of solar power generation and the load of the consumer in that area. Load change did not occur very quickly and frequently in a substation or feeder, but solar power generation changes very fast with the rapid change of solar irradiance with the time domain.

4.1.2 Frequency records at Teknaf solar power plant

After projecting the voltage data of the TSEL interconnection point, the recorded grid frequency data for the same period at Teknaf 20MW solar power plant is projected in Figure 6 below.

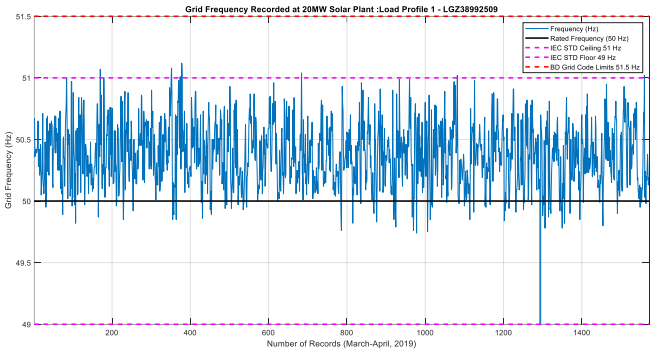

Figure 6. Grid frequency recorded at Teknaf 20MW solar power plant; Data source: TSEL.

According to the standard of the International Electrotechnical Commission IEC 61727, the utility frequency needs to be maintained within ±2% (1 Hz) for safe and continuous operation of the Solar Power Plant (*IEC 61727:2004 | IEC Webstore | Invertor, Smart City, LVDC*, n.d.). However, this limit ranges from 47.5 Hz to 51.5 Hz in the grid code of Bangladesh, which is wider than the IEC range (*Bangladesh Energy Regulatory Commission (Electricity Grid Code) Regulations, 2019*, 2020). According to Figure 6, the frequency variation remains often within the IEC range, but it crosses the IEC range, sometimes. The operating frequency range of the Bangladesh Grid Code is wider than the IEC range and this variation is always within the grid code range. Grid-tied solar inverters are capable to maintain this frequency variation. The plant operator informed us that Solar Plants frequency settings of the Teknaf 20 MW solar plant were modified after reviewing the interconnection problem (Kainat et al., 2021).

4.2 Solar Irradiance Data at Kaptai 7.4MW Solar Power Plant

According to the data recording procedure mentioned in the methodology, the time series solar irradiance data of the Kaptai 7.4MW Solar power plant were recorded into the data logger and remote server. The data quality was checked before using the collected solar irradiance data set. The solar GHI data of the Kaptai 7.4MW solar power plant were plotted on the monthly basis and observed in the daily condition as classified. Monthly plotted figures are given below:

4.2.1. *Solar irradiance observed in October 2019*

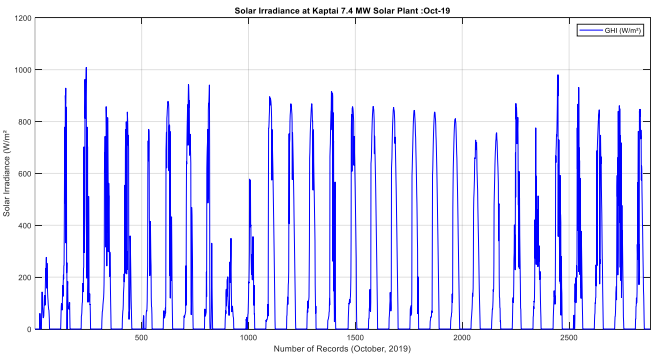

Figure 7. GHI Data of Kaptai, October 2019.

Solar irradiance observed in the Kaptai 7.4MW solar power plant for the entire month of October 2019 is represented by a single line in Figure 7. The figure reveals clear weather days when solar ramping was not present. Some days look deep blue with different levels on Y-axis. Those were partly cloudy days and solar irradiance variation was present. More deep blue represents more ramping on that day. A ramping level can be identified by the height of the deep blue lines. Some full cloudy days are also present where the peak irradiance of those days is less than 300 W/m^2. Therefore, according to the mentioned initial screening, around 50% of days are high solar resource variability, 3 days are washouts, and the rest are clear weather days. The highest solar irradiance level is around 1000 W/m^2, while the lowest is around 250 W/m^2.

4.2.2. *Solar irradiance observed in November 2019*

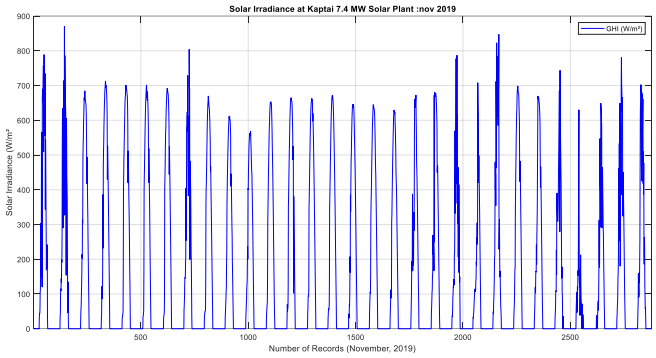

Figure 8: GHI Data of Kaptai, November 2019.

Figure 8 shows that most of the days of November 2019 are clear weather days except variability-containing days. The highest solar irradiance level is around 950 W/m^2, while the lowest is around 580 W/m^2.

4.2.3. *Solar irradiance observed in December 2019*

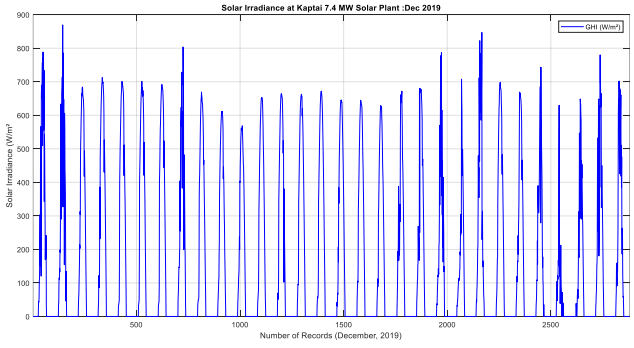

Figure 9: GHI Data of Kaptai, December 2019.

According to Figure 9, most of the days are clear weather days except for a few variability-containing days. The highest solar irradiance level is around 950 W/m^2, while the lowest is around 650 W/m^2.

4.2.4. *Solar irradiance observed in January 2020*

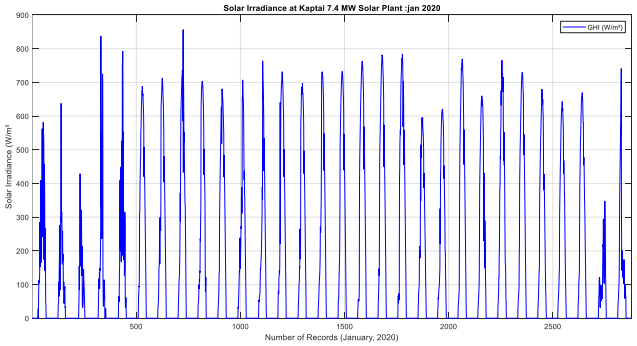

Figure 10. GHI Data of Kaptai, January 2020.

Figure 10 shows solar irradiance observed in January 2020. According to Figure 10, it is observed that most of the days are clear weather days except for a few variability-containing days and washout days. The highest solar irradiance level is around 850 W/m^2, while the lowest is around 350 W/m^2.

4.2.5. *Solar irradiance observed in February 2020*

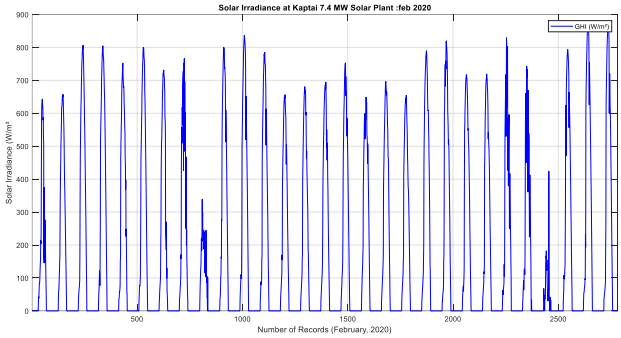

Figure 11. GHI Data of Kaptai, February 2020.

Figure 11 reveals that most of the days of February 2020 were clear weather days except few variability-containing days and washout days. Here the number of variability/washout days is lower than the previous figures. The highest solar irradiance level is around 830 W/m^2, while the lowest is around 300 W/m^2.

4.2.6. *Solar irradiance observed in March 2020*

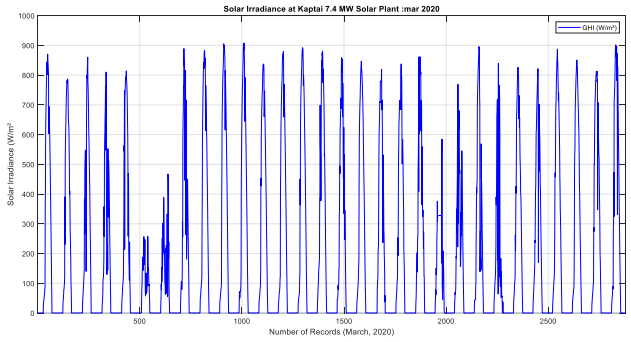

Figure 12. GHI Data of Kaptai, March 2020.

According to Figure 12, solar irradiance is observed to be clear weather days in March 2020 except few variability-containing days and washout days. The highest solar irradiance level is around 900 W/m^2, while the lowest is around 250 W/m^2.

4.2.7. *Solar irradiance observed in April 2020*

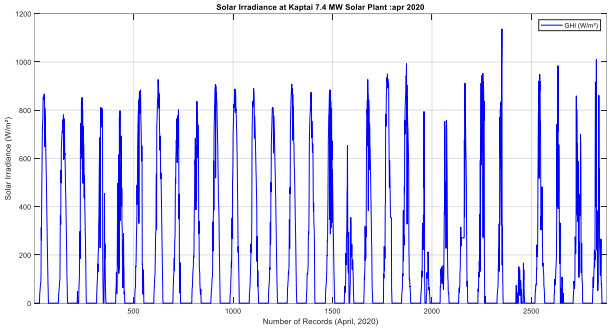

Figure 13. GHI Data of Kaptai, April 2020.

Figure 13 reveals that the number of high solar resource variable days is more than 50%, a few are washout days and the rest are clear weather days. It is observed that clear weather days are decreasing and variability days are increasing as compared to the previous months. The highest solar irradiance level is around 1150 W/m^2, while the lowest is around 150 W/m^2. The cloud enhancement is observed during the highest solar irradiance-containing day.

4.2.8. *Solar irradiance observed in May 2020*

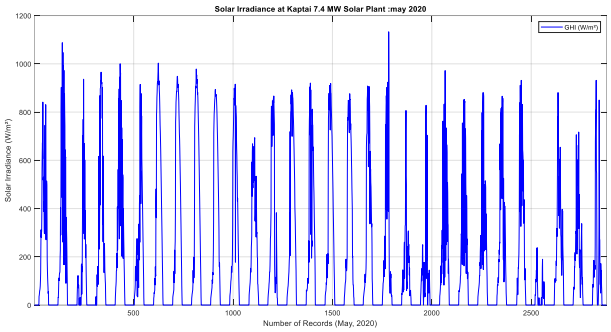

Figure 14. GHI Data of Kaptai, May 2020.

According to Figure 14, the number of clear weather days is quite small in May 2020. Most of the days are high solar resource variables, while few are washout days. The highest solar irradiance level is around 1100 W/m^2, while the lowest is around 200 W/m^2. The cloud enhancement is observed in a few days.

4.2.9. *Solar irradiance observed in June 2020*

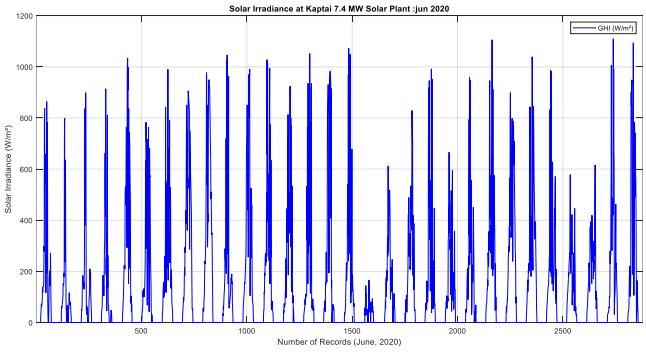

Figure 15. GHI Data of Kaptai, June 2020.

According to Figure 15, all days are high solar resource variables except a few washout days. There is no clear weather day. The highest solar irradiance level is around 1100 W/m^2, while the lowest is around 150 W/m^2. Cloud enhancement is observed on many days this month.

4.2.10. *Solar irradiance observed in July 2020*

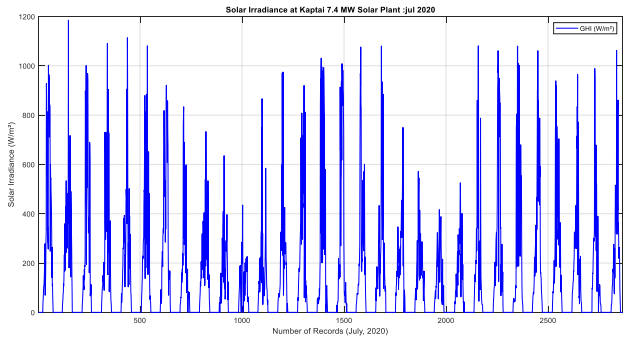

Figure 16. GHI Data of Kaptai, July 2020.

According to Figure 16, all days of July 2020 are high solar resource variables except a few washout days. There is no clear weather day. The highest solar irradiance level is around 1200 W/m^2, while the lowest is around 400 W/m^2. Cloud enhancement is observed on many days this month.

4.2.11. *Solar irradiance observed in August 2020*

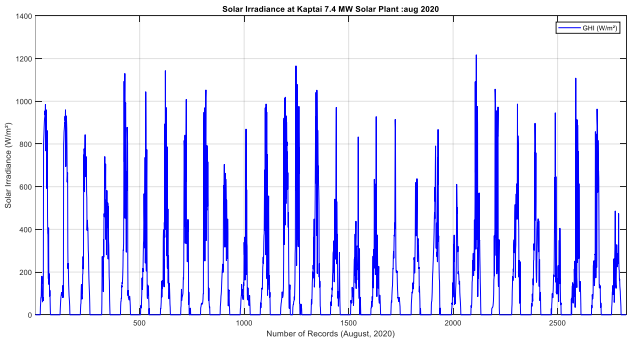

Figure 17. GHI Data of Kaptai, August 2020.

According to Figure 17, all days of August 2020 are high solar resource variables except a few washout days. There is no clear weather day. The highest solar irradiance level is around 1200 W/m^2, while the lowest is around 450 W/m^2. This month, cloud enhancement is observed on many days.

4.2.12. *Solar irradiance observed in September2020*

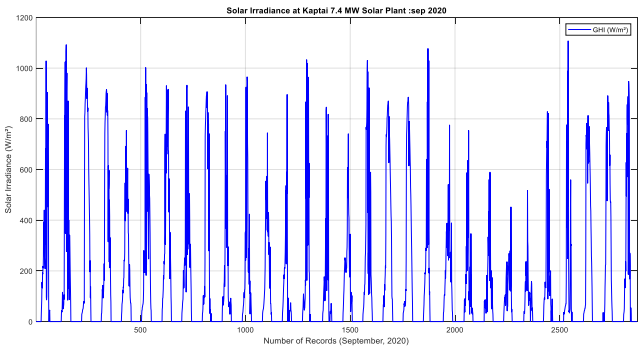

Figure 18. GHI Data of Kaptai, September 2020.

According to Figure 18, most of the days are high solar resource variable days; a few are washout days and the number of clear weather days is less than five. The highest solar irradiance level is around 1150 W/m^2, while the lowest is around 400 W/m^2. Cloud enhancement is observed on many days of this month, as well.

4.2.13. *Solar irradiance observed for a year*

The daily irradiance status summary is shown below in based on the above one-year solar irradiance data assessment of the Kaptai 7.5MW Solar Power Plant.

From, it is observed that only 105 days (29%) in a year are clear weather days, whereas 188 days (51%) are high solar resource variable days. Only 40 days (11%) are low variability days and 33 days (9%) are washout days. Given that the high solar resource variability days of a year are more than 50%, it is important to take necessary preventive measures to minimize the output power variation of solar power plants for safe grid integration and high PV penetration, because the output power of the SPV plant is proportional to the input solar irradiance. This output power variation needs to be addressed by the alternative support system connected to the grid and nearest to the interconnection areas. Washout days, high variability days, low variability days, and clear days for a year are shown in Figure **19** as a monthly bar chart.

Table 1. Yearly status of solar irradiance at Kaptai, Chittagong, Bangladesh.

Month	Total Days	Washout Days	High Variability Days	Low Variability Days	Clear Days
JAN 2020	31	3	4	4	20
FEB 2020	29	2	4	3	20
MAR 2020	31	3	9	8	11
APR 2020	30	2	17	8	3
MAY 2020	31	1	22	3	5
JUN 2020	30	3	27	0	0
JUL 2020	31	6	23	0	2
AUG 2020	31	6	22	3	0
SEP 2020	30	3	22	3	2
OCT 2019*	31	2	17	4	8
NOV 2019*	30	1	11	2	16
DEC 2019*	31	1	10	2	18
Total	366	33	188	40	105
Percentage		9%	51%	11%	29%

* Due to the unavailability of the data, the previous year's data has been considered for 3 months

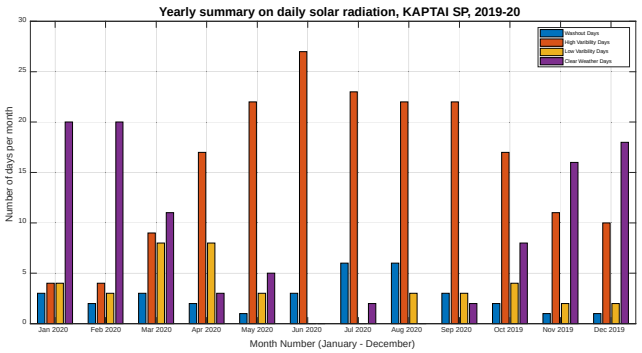

Figure 19. A yearly summary of daily solar irradiance, KAPTAI SP.

According to Figure **19** , November to February have more clear weather days, while October and March have some clear weather days. On the other hand, the months of April to October have more high solar irradiance variability days, whereas June has the peak conditions in terms of the number of days. Every month has 1-3 washout days, but it is high (6 days in each month) in July and August.

4.3 National Solar Radiation Resource Assessment Station, Chittagong

The solar GHI data of the National Solar Radiation Resource Assessment Station, Chittagong were plotted on the monthly basis and the daily condition, which is classified and mentioned in the methodology section, was observed. Monthly plotted figures are given below:

4.3.1. *Solar irradiance observed in January 2020*

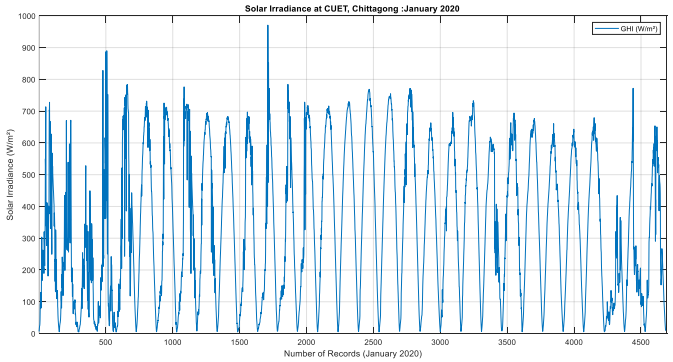

Figure 20. GHI Data of NSRRA CTG, January 2020.

According to Figure 20, in January 2020, most of the days are clear weather days with few high variability days and one washout day. The average peak solar irradiance is approximately 700 W/m^2, the highest solar irradiance level is around 1000 W/m^2, and the lowest is around 400 W/m^2. The cloud enhancement is observed in a few days of this month.

4.3.2. *Solar irradiance observed in February 2020*

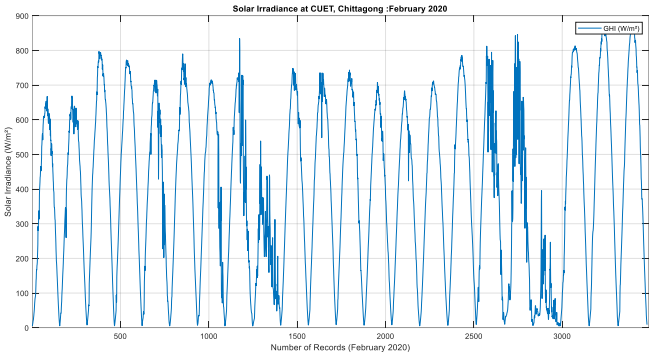

Figure 21. GHI Data of NSRRA CTG, February 2020.

In February 2020, as shown in Figure 21, most of the days are clear weather days with four high variability days and one washout day. The average peak solar irradiance is approximately 700 W/m^2, the highest solar irradiance level is around 950 W/m^2, and the lowest is around 400 W/m^2. Cloud enhancement is observed in a few days of this month.

4.3.3. *Solar irradiance observed in March 2020*

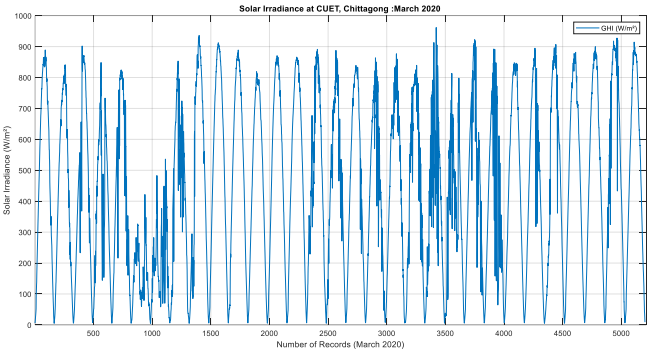

Figure 22. GHI Data of NSRRA CTG, March 2020.

According to Figure 22, in March, most of the days are clear weather days with 7 high variability days and 2 washout days. The average peak solar irradiance is approximately 850 W/m^2, the highest solar irradiance level is around 950 W/m^2, and the lowest is around 400 W/m^2.

4.3.4. *Solar irradiance observed in April 2020*

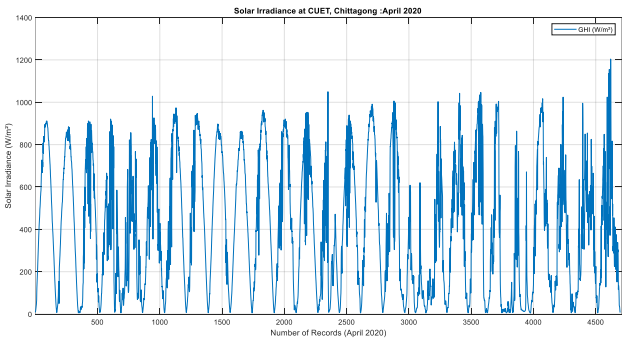

Figure 23. GHI Data of NSRRA CTG, April 2020.

In April 2020, as shown in Figure 23, only 7 days are clear weather days with one washout day and the rest of the days being high variability days. The average peak solar irradiance is approximately 900 W/m^2, the highest solar irradiance level is around 1200 W/m^2, and the lowest is around 400 W/m^2. The cloud enhancement is observed in a few days of this month.

4.3.5. *Solar irradiance observed in May 2020*

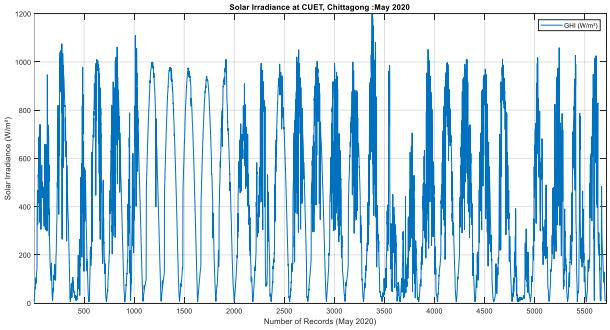

Figure 24. GHI Data of NSRRA CTG, May 2020.

According to Figure 24 (May 2020), only 5 days are clear weather days, while the rest of the days are high variability days including one washout day. The average peak solar irradiance is approximately 1000 W/m^2, the highest solar irradiance level is around 1200 W/m^2, and the lowest is around 400 W/m^2. The cloud enhancement is observed in a few days of this month.

4.3.6. *Solar irradiance observed in June 2020*

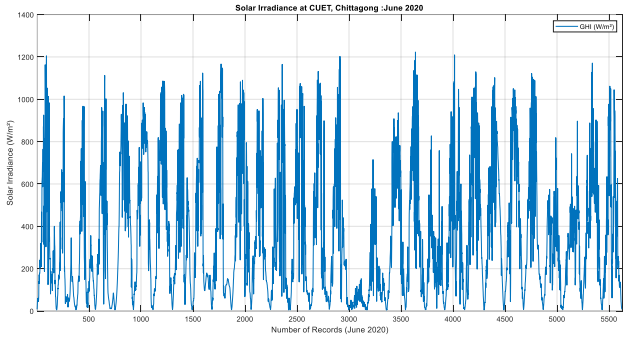

Figure 25. GHI Data of NSRRA CTG, June 2020.

According to Figure 25 (June 2020), there are no clear weather days. Most of the days are high variability days including a few washout days. The average peak solar irradiance is approximately 1000 W/m^2, the highest solar irradiance level is around 1200 W/m^2, and the lowest is around 150 W/m^2. The cloud enhancement is observed in a few days of this month.

4.3.7. *Solar irradiance observed in July 2020*

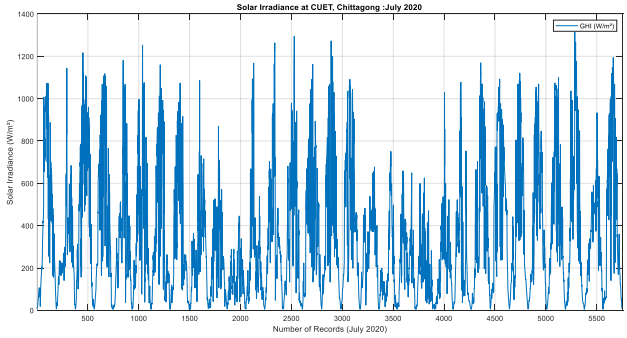

Figure 26. GHI Data of NSRRA CTG, July 2020.

According to Figure 26 (July 2020), there are no clear weather days. Most of the days are high variability days including a few washout days. The average peak solar irradiance is approximately 1000 W/m^2, the highest solar irradiance level is around 1250 W/m^2, and the lowest is around 400 W/m^2. Cloud enhancement is observed on many days this month.

4.3.8. *Solar irradiance observed in August 2020*

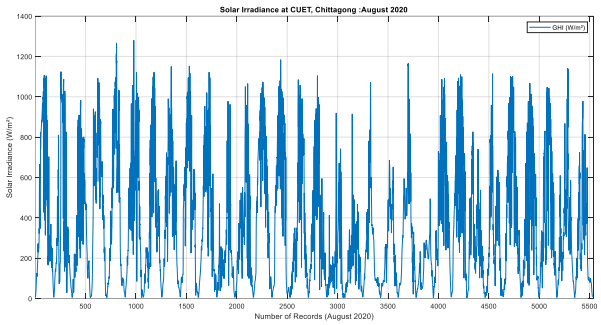

Figure 27. GHI Data of NSRRA CTG, August 2020.

According to Figure 27 (August 2020), there are no clear weather days. Most of the days are high variability days including a few washout days. The average peak solar irradiance is approximately 1050 W/m^2, the highest solar irradiance level is around 1300 W/m^2, and the lowest is around 400 W/m^2. Cloud enhancement is observed on many days this month.

4.3.9. *Solar irradiance observed in September 2020*

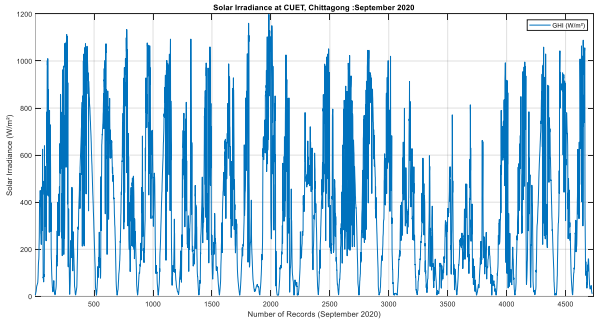

Figure 28. GHI Data of NSRRA CTG, September 2020.

According to Figure 28 (September 2020), there are no clear weather days. Most of the days are high variability days including 4-5 washout days. The average peak solar irradiance is approximately 1000 W/m^2, the highest solar irradiance level is around 1200 W/m^2, and the lowest is around 600 W/m^2. Cloud enhancement is observed on many days this month.

4.3.10. *Solar irradiance observed in October 2020*

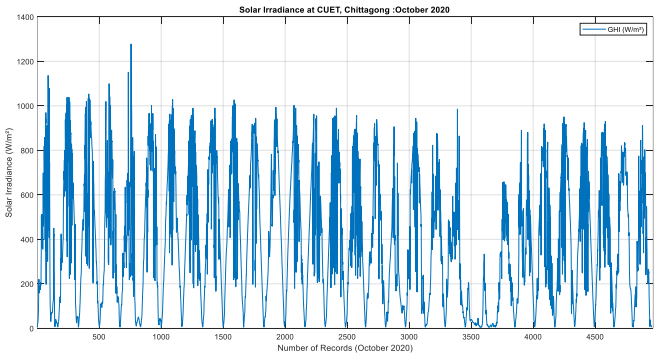

Figure 29. GHI Data of NSRRA CTG, October 2020.

According to Figure 29 (October 2020), there are no clear weather days. Most of the days are high variability days including 1-2 washout days. The average peak solar irradiance is approximately 950 W/m^2, the highest solar irradiance level is around 1300 W/m^2, and the lowest is around 350 W/m^2. Cloud enhancement is observed on many days this month.

4.3.11. *Solar irradiance observed in November 2020*

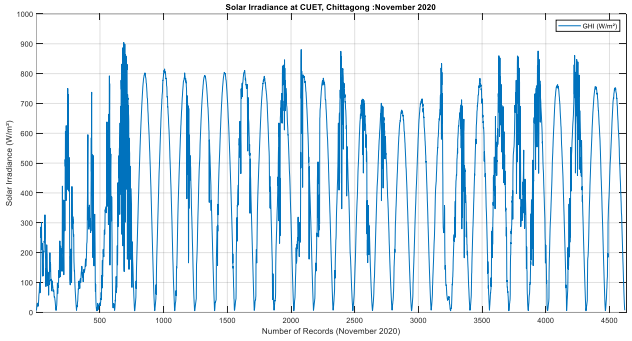

Figure 30. GHI Data of NSRRA CTG, November 2020.

According to Figure 30 (November 2020), most of the days are clear weather days and the rest of the days are high variability days including 1-2 washout days. The average peak solar irradiance is approximately 800 W/m^2, the highest solar irradiance level is around 900 W/m^2, and the lowest is around 300 W/m^2. The cloud enhancement is observed in a few days of this month.

4.3.12. *Solar irradiance observed in December 2020*

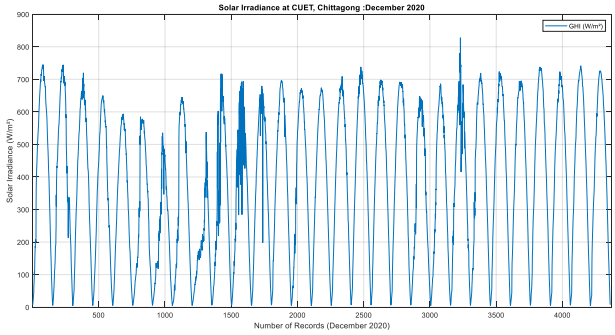

Figure 31. GHI Data of NSRRA CTG, December 2020.

According to Figure 31 (December 2020), most of the days are clear weather days and the rest 2-3 days involve a few variabilities. The average peak solar irradiance is approximately 700 W/m^2, the highest solar irradiance level is around 850 W/m^2, and the lowest is around 500 W/m^2. The cloud enhancement is observed in a few days of this month.

4.3.13. *Solar irradiance scenario for a year*

The daily solar irradiance status is given below in **Error! R eference source not found.** and Figure 32 based on the above one-year solar irradiance data assessment of the National Solar Radiation Resource Assessment (NSRRA) station, Chittagong.

Table 2. Yearly status of solar irradiance at CUET, Chittagong.

Month	Total Days	Washout Days	High Variability Days	Low Variability Days	Clear Days
JAN 2020	31	2	8	4	17
FEB 2020	29	2	3	5	19
MAR 2020	31	2	14	5	10
APR 2020	30	4	20	4	2
MAY 2020	31	4	22	2	3
JUN 2020	30	3	27	0	0
JUL 2020	31	5	26	0	0
AUG 2020	31	2	29	0	0
SEP 2020	30	0	30	0	0
OCT 2020	31	2	28	1	0
NOV 2020	30	1	13	5	11
DEC 2020	31	0	4	2	25
Total	**366**	**27**	**224**	**28**	**87**
Percentage		7%	61%	8%	24%

Table 2 shows that more than 50% of days in a year contain high solar variability. Approximately 10% contain washout days and another approximately 10% involve low variability days. Only approximately 25 – 30% of days are obtained as clear weather days.

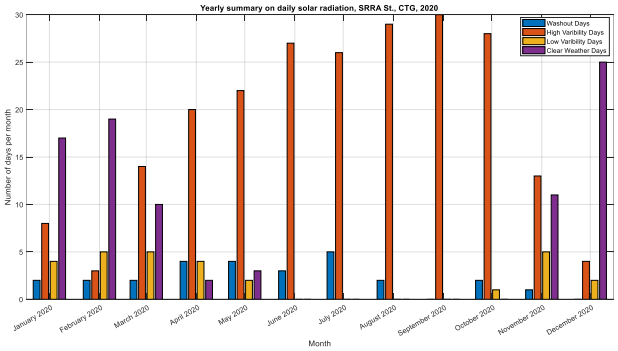

Figure 32. Yearly summary on daily solar irradiance, SRRA St., CTG.

Figure 32 shows that the months of December to February have a higher number of clear weather days, while November and March have around 10 days with clear weather. In contrast, the months from April to October have more days with high solar irradiance variability, with June to October having the highest number of such days. March and November have a similar percentage of high solar irradiance variability days, close to 50%. Each month has between 0 and 3 washout days, but April, May, and July have a higher number of washout days, around 4 to 5 days per month.

5. COMPARATIVE SCENARIO

As shown in **Error! Reference source not found.** and **Error! Re ference source not found.**, the first case study site has 51% high variability days while the second case study site has 61% high variability days in a year. Similarly, their low variability days in a year were 11% and 8%, respectively. The monthly comparative analysis is presented in Figure 33.

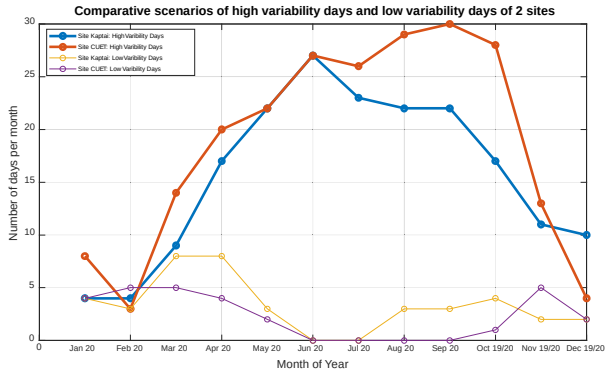

Figure 33. Comparative scenarios of the 2 case study sites on high variability days and low variability days.

According to Figure 33, the monthly high variability days of 2 case study sites are very close to each other although some significant differences are observed between August and November. In addition, monthly small variability days are very close to each other. Similarly, comparative scenarios of clear weather days and washout days are shown below in Figure 34.

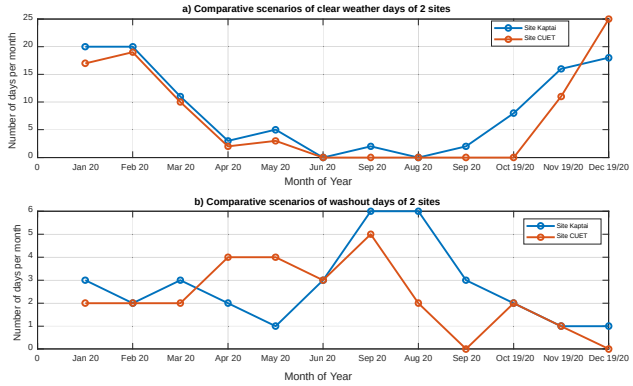

Figure 34. Comparative scenarios of clear weather days and washout days.

Figure 34(a) represents the comparative scenarios between two sites on monthly clear weather days. The monthly clear weather patterns of the two sites look almost similar with a negligible difference in January, May, June, and September and a significant difference from October to December. Figure 34(b) represents the comparative scenarios between two sites on monthly washout days. Some significant differences were observed between the two sites, although limited to monthly six days. This yearly analysis of solar irradiance gives us the scenario of variation of solar irradiance and its major variation time. The alternative support system to meet the output power variation of the SPV plant requires planning according to the variation of solar irradiance. This assessment of the two sites gives a scenario of this region.

Considering the minimum values, at least more than 50% of days in a year contain high solar irradiance variation. Around 8% of days of a year are washout days, 10% of days are low variability days, and only approximately 25–30% of days are obtained as clear weather days. As observed, since 50% of the days in a year have high solar irradiance variability, it is crucial to consider this factor in the grid integration study of any proposed large-capacity solar photovoltaic (SPV) plant, because the output power of the SPV plant is directly proportional to the input solar irradiance. Also, geographical dispersion can reduce some ramping effects and cloud enhancement increases the solar ramping effect which can change the resultant effect in a few amounts. More precision time interval data can provide more reliable solar ramp management results but still, an approximate scenario was identified.

This variable power output of the SPV plant creates a quick load flow change in the interconnection area of the utility network. Ramp rate and ramp level are important issues here. If the utility network is unable to manage such load flow in that area, then several adverse effects will be observed due to the integration of such variable renewable energy. Therefore, it is important to promote variable renewable energy like solar photovoltaic power plants in Bangladesh with safe grid integration including necessary correction measures.

6. CONCLUSIONS

Solar irradiance is variable in nature due to the weather conditions of that location. Yearly assessment is essential as seasonal variations are present in weather conditions. The important findings of this study are summarized below.

a) The variation of grid frequency at the interconnection point of the case study site was observed although higher than the IEC range, but still within the grid code range of Bangladesh. Available grid-tied solar PV inverters were capable to operate within the range.

b) Variation of grid voltage at the grid interconnection substation was found within the standard range in the daytime, but within the rest of the observed time period, the low voltage was witnessed at the grid level. However, the variation of grid voltage at the interconnection point of the case study site depended on the regional load, the generation capacity of the nearest power plant, the distance from the grid substation, the capacity of the grid transmission line, etc. It may vary based on the conditions of the interconnection points.

c) According to the information of selected two sites (Kaptai 7.4MW solar power plant and NSRRA, Chittagong), more than 50% of days in a year contain a high short-term variation of solar irradiance. Only 7% - 9% were annual washout days.

d) Only 24-29% of days in a year were clear weather days where short-term variations of solar irradiance were not present. Also, 8%-11% of days in a year contained a low short-term variation of solar irradiance.

e) Two case study sites were taken to get reliable results. The result of the two sites obtained from this study was very close to each other, which is acceptable.

Therefore, for safe grid integration of large-scale variable solar power plants into the grid with high VRE penetration, it is essential to take necessary preventive measures to reduce the solar ramping. This result is a site or region-specific scenario that can reflect the SPV integration picture of Bangladesh. This assessment was conducted using existing time series solar irradiance data. More precision solar irradiance data will give a more reliable result for further study.

7. ACKNOWLEDGEMENT

We thank the financial support from the Bangladesh University of Engineering and Technology (BUET) through Committee for Advanced Studies and Research (CASR). The editor-in-chief and reviewers of the JREE are greatly acknowledged for their comments and support.

NOMENCLATURE

BPDB	Bangladesh Power Development Board
BREB	Bangladesh Rural Electrification Board
BUET	Bangladesh University of Engineering and Technology
CASR	Committee for Advanced Studies and Research
CE	Cloud Enhancement
CUET	Chittagong University of Engineering of Technology
GEF	Global Environment Facility
GHI	Global Horizontal Irradiance
IEC	International Electrotechnical Commission
JPL	Joules Power Limited
NSRRA	National Solar Radiation Resource Assessment
PBS	PalliBidyutSomity
PGCB	Power Grid Company of Bangladesh
PV	Photovoltaic
SPV	Solar Photovoltaic
SREDA	Sustainable and Renewable Energy Development Authority
SREPGen	Sustainable Renewable Energy Power Generation
TSEL	Teknaf Solartech Energy Limited
VRE	Variable Renewable Energy

REFERENCES

1. Ahmed, R., Sreeram, V., Mishra, Y., & Arif, M. D. (2020). A review and evaluation of the state-of-the-art in PV solar power forecasting: Techniques and optimization. Renewable and Sustainable Energy Reviews, 124, 109792. https://doi.org/10.1016/j.rser.2020.109792
2. Annual Report 2019-2020 of SREDA. (2020). http://www.sreda.gov.bd
3. Bangladesh Energy Regulatory Commission (Electricity Grid Code) Regulations, 2019. (2020). http://www.berc.org.bd
4. Blanc, P., Espinar, B., Geuder, N., Gueymard, C., Meyer, R., Pitz-Paal, R., Reinhardt, B., Renné, D., Sengupta, M., Wald, L., & Wilbert, S. (2014). Direct normal irradiance related definitions and applications: The circumsolar issue. Solar Energy, 110, 561–577. https://doi.org/10.1016/j.solener.2014.10.001
5. Boopathi, K., Ramaswamy, S., Kirubakaran, V., Uma, K., Saravanan, G., Thyagaraj, S., & Balaraman, K. (2021). Economic investigation of repowering of the existing wind farms with hybrid wind and solar power plants: a case study. International Journal of Energy and Environmental Engineering, 12(4), 855–871. https://doi.org/10.1007/s40095-021-00391-3
6. Carmona, F., Orte, P. F., Rivas, R., Wolfram, E., & Kruse, E. (2018). Development and Analysis of a New Solar Radiation Atlas for Argentina from Ground-Based Measurements and CERES_SYN1deg data. The Egyptian Journal of Remote Sensing and Space Science, 21(3), 211–217. https://doi.org/10.1016/j.ejrs.2017.11.003
7. Choi, Y., Suh, J., & Kim, S.-M. (2019). GIS-Based Solar Radiation Mapping, Site Evaluation, and Potential Assessment: A Review. Applied Sciences, 9(9), 1960. https://doi.org/10.3390/app9091960
8. Customized Bangladesh Map - Google My Maps. (n.d.). Retrieved March 26, 2023, from https://www.google.com/maps/d/u/0/edit?hl=en&mid=1eKcsqjkBzI3jgVfOkJ6xpVPVU1guOtg&ll=23.608281830845563%2C92.008983247944439&z=7
9. Denholm, P., & Margolis, R. M. (2007). Evaluating the limits of solar photovoltaics (PV) in electric power systems utilizing energy storage and other enabling technologies. Energy Policy, 35(9), 4424–4433. https://doi.org/10.1016/j.enpol.2007.03.004
10. Global Solar Atlas. (n.d.). Retrieved March 27, 2023, from https://globalsolaratlas.info/download/bangladesh
11. IEC 61727:2004 | IEC Webstore | invertor, smart city, LVDC. (n.d.). Retrieved March 27, 2023, from https://webstore.iec.ch/publication/5736
12. Jamil, B., & Akhtar, N. (2017). Estimation of diffuse solar radiation in humid-subtropical climatic region of India: Comparison of diffuse fraction and diffusion coefficient models. Energy, 131, 149–164. https://doi.org/10.1016/j.energy.2017.05.018
13. Järvelä, M., Lappalainen, K., & Valkealahti, S. (2020). Characteristics of the cloud enhancement phenomenon and PV power plants. Solar Energy, 196, 137–145. https://doi.org/10.1016/j.solener.2019.11.090
14. Jazayeri, M., Jazayeri, K., & Uysal, S. (2017). Generation of spatially dispersed irradiance time-series based on real cloud patterns. Solar Energy, 158, 977–994. https://doi.org/10.1016/j.solener.2017.10.026
15. Kainat, Engr. M. G. S., Alam, Engr. Md. R., & Masud, Engr. Md. T. (2021). Towards a Sustainable Energy Future. Grid Integration of Solar Energy: A case study on 20 MW Solar Power Plant of Teknaf Solar Energy Ltd. In Towards Sustainable Energy Future (Vol. 1, Number 1). SREDA, Bangladesh. http://www.sreda.gov.bd/site/page/95b63d6e-aac2-46ae-a46d-37faae6f9e86
16. Karthikeyan, V., & Janarthanan, S. (2017). Yield factor of grid connected solar photovoltaic system-a case study. Journal of Advanced Research in Dynamical and Control Systems, 9, 206–213. https://www.academia.edu/download/62920747/635020200411-35167-11vvlag.pdf
17. Keeratimahat, K., Bruce, A., & MacGill, I. (2019). Partial curtailment to firm photovoltaic generation dispatch. 2019 IEEE PES Asia-Pacific Power and Energy Engineering Conference (APPEEC), 1–5. https://doi.org/10.1109/APPEEC45492.2019.8994464
18. Sengupta, M., Xie, Y., Lopez, A., Habte, A., Maclaurin, G., & Shelby, J. (2018). The National Solar Radiation Data Base (NSRDB). Renewable and Sustainable Energy Reviews, 89, 51–60. https://doi.org/10.1016/j.rser.2018.03.003
19. Shuvho, Md. B. A., Chowdhury, M. A., Ahmed, S., & Kashem, M. A. (2019). Prediction of solar irradiation and performance evaluation of grid connected solar 80KWp PV plant in Bangladesh. Energy Reports, 5, 714–722. https://doi.org/10.1016/j.egyr.2019.06.011
20. Sivaneasan, B., Yu, C. Y., & Goh, K. P. (2017). Solar Forecasting using ANN with Fuzzy Logic Pre-processing. Energy Procedia, 143, 727–732. https://doi.org/10.1016/j.egypro.2017.12.753
21. Tahir, Z. R., & Asim, M. (2018). Surface measured solar radiation data and solar energy resource assessment of Pakistan: A review. Renewable and Sustainable Energy Reviews, 81, 2839–2861. https://doi.org/10.1016/j.rser.2017.06.090
22. Van Haaren, R., Morjaria, M., & Fthenakis, V. (2014). Empirical assessment of short-term variability from utility-scale solar PV plants. Progress in Photovoltaics: Research and Applications, 22(5), 548–559. https://doi.org/10.1002/pip.2302
23. Wei, C.-C. (2017). Predictions of Surface Solar Radiation on Tilted Solar Panels using Machine Learning Models: A Case Study of Tainan City, Taiwan. Energies, 10(10), 1660. https://doi.org/10.3390/en10101660
24. Zhang, J., Zhao, L., Deng, S., Xu, W., & Zhang, Y. (2017). A critical review of the models used to estimate solar radiation. Renewable and Sustainable Energy Reviews, 70, 314–329. https://doi.org/10.1016/j.rser.2016.11.124

JREE: Vol. 10, No. 4, (Autumn 2023) 119-130

Journal of Renewable Energy and Environment

Journal Homepage: www.jree.ir

Materials and Energy Research Center

MERC

Research Article

Biofuel Commercialization in Developing Countries: Readiness and Prospects

Mosees Emetere [a,b], Wisdom O. Joel [c]

[a] *Department of Physics, Bowen University, Iwo, Nigeria.*
[b] *Department of Mechanical Engineering Science, University of Johannesburg, South Africa.*
[c] *Department of Biochemistry, Covenant University, Ota, Nigeria.*

PAPER INFO

Paper history:
Received: 6 January 2023
Revised: 23 June 2023
Accepted: 17 July 2023

Keywords:
Biofuel,
Energy,
Renewable Energy,
Prospects

ABSTRACT

Several researchers have reported the prospects of biofuel commercialization in several countries across the globe. With over 400 million tons of biomass and 150 million tons of agro-waste produced annually in most developing countries, the prospect of biofuel commercialization looks promising. However, it is crucial to adopt a forward-thinking approach and anticipate potential challenges that may arise, building upon the lessons learned from current obstacles. This paper review addresses the current issues that have discouraged some developing countries against embracing biofuels as an economical tool to mitigate poverty. Also, future challenges that may scuttle biofuel commercialization in developing countries was discussed to provide a workable blueprint towards wealth creation. This review identified policies and political unwillingness as fundamental challenges that must be overcome in developing countries to attract investors. Other identified salient challenges include mono-economy, poor technical know-how, poor technology, government hypocrisy, lack of funds, sustainable biomass resources, inadequate farmland, poor policies, and weak infrastructure. It is recommended that conscious short- and long-term planning be implemented to actualize biofuel commercialization in developing countries.

https://doi.org/10.30501/jree.2023.379263.1533

1. INTRODUCTION

Biofuel is a form of renewable source of energy that refers to liquid fuel (such as biodiesel, bioethanol, etc.) or gaseous fuel (such as biogas) produced from biomass which is mainly plant or animal waste or oil. Currently, the production of biofuel has attracted African countries on a global scale, indicating thoughtful interest in ambiguous and scale-large production. In some developed countries, biofuels are sold on a commercial scale, such that users visit a filing station to purchase whatever quantity of biofuel they desire. Economically, the cost of producing biofuel is relatively low because it does not require complex processes. Few countries (such as the United States of America, Japan, Brazil, and some parts of Europe) around the globe have taken biofuel to a commercial scale. Brazil produces an estimation of 21 billion liters of bioethanol every year, while Japan and China are aiming for a biofuel capacity of 6.3 billion liters (Zhou and Elspeth, 2009). The United States of America has proven that the biofuel project is lucrative and has created 70,000 direct jobs that generated $20 billion and 200,000 indirect and induced jobs that generated $23 billion (€21.1 billion) in 2019 (Biofuel, 2020). Before biofuel became commercial, individuals and local communities in some parts of the world engaged in various feedstocks for energy production (Kemausuor et al., 2013).

Feedstocks are categorized into three main classes: homogeneous (wood chips), quasi-homogeneous (agricultural and forest residues), and non-homogeneous (solid waste), with average economic values of around $110/ton, $62/ton, and $31/ton, respectively (Elegbede and Guerrero, 2016). In light of the raw materials (biomasses) used for biofuel production, it is clear that huge resources are wasted on a yearly basis. If half of the wasted resources are fully utilized, developing countries could potentially generate over 80 billion liters of biofuel. This possibility can be substantiated by considering factors such as population (e.g., human biogas production), arable land (biomasses, e.g., inedible seeds, dead tree trunks, and fallen leaves), and agricultural practices that incorporate agro-waste (Emetere et al., 2018; Emetere and Adesina, 2019).

The most common biofuels are bioethanol, biogas, and biodiesel. Bioethanol is synthesized from carbohydrates like cellulose biomass. Coarse grain and sugarcane are two of the most common ethanol feedstocks, but their prevalence may vary depending on the region. Biodiesel is generated from fats and oils. Vegetable oil is one of the most common feedstocks used in biodiesel production, while non-agricultural feedstocks like waste are becoming more relevant in regions like the United States and Europe. The biogas largely depends on agro-waste, human excreta, and a few biomasses as its feedstock. The above information further corroborates the importance of this review to address Items 1 and 7 in Sustainable Development Goals (SDG) in developing countries.

*Corresponding Author's Email: emetere@yahoo.com (M. Emetere)
URl: https://www.jree.ir/article_176462.html

Please cite this article as: Emetere, M. & Joel, W. O. (2023). Biofuel Commercialization in Developing Countries: Readiness and Prospects, *Journal of Renewable Energy and Environment (JREE)*, 10(4), 119-130. https://doi.org/10.30501/jree.2023.379263.1533.

The main hindrance to unlocking the business potential of biofuel commercialization is the sentiment toward fossil fuels. The use of fossil fuels in developing countries will continue for a long time because their main source of income and the lifestyle of their populace revolve around fossil fuels. For example, fossil-fuel generators have been given substantial credit in terms of powering organizations and houses in most developing countries. In other words, dissociating the mental attachments or sentiments of its population from fossil fuels is a difficult task. A broad spectrum of energy requirements in rural and urban settlements in Africa is presented in Figure 1. Over 80% of the energy usage in both rural and urban settlements comes from fossil-fuel generators or automobiles. This reality further corroborates the huge pollution from fossil fuels in its atmosphere. The commercialization of biofuel in developing countries will lead to a reduction in overdependence on fossil fuels and promote lower carbon emission into the atmosphere. Renewables have a lower carbon footprint and can lead to a reduction of over 90% of the carbon footprint (IRENA, 2019). Szetela et al. (2022) reported that the carbon footprint of more than forty-three countries, which had significantly invested in renewable energy projects, resulted in reduced carbon dioxide emissions during the period 2000–2015.

Some accruable benefits of biofuel commercialization to developing countries include poverty reduction, increase in employment rate, conversion of waste into wealth, a safer environment, diversification of the economy, and social emancipation. Recent biofuel projects in Africa are basically tailored towards automobiles or domestic cooking alone. However, its further applications include providing heat for homes, generation of energy, and removal of paint and adhesives, lubrication, etc.

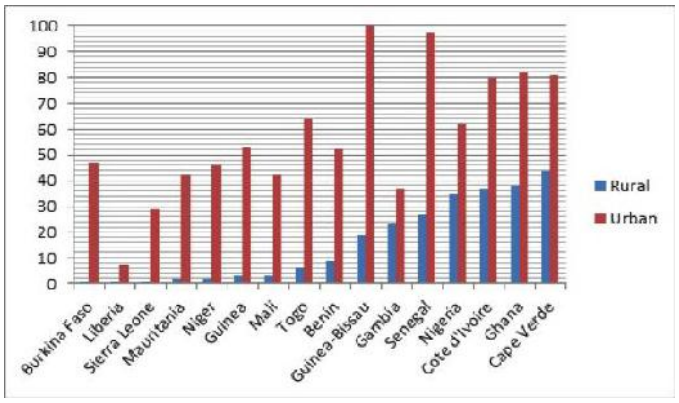

Figure 1. Energy consumption in rural and urban areas in Africa

In the past ten years, there has been a noticeable presence of biofuel companies in some developing countries. For example, in Nigeria, the Green Energy and Biofuels (Geb) Bio-Refinery Project was developed by Small and Medium Entrepreneurship Fundamentals (SMEFunds). Their product was bio-ethanol gel cooking fuel made from waste products such as sawdust and water hyacinth. Within the two-year pilot phase, the company produced 700,000 liters of biofuel (ADBG, 2021). Contec Global Energy is a biofuel company that produces ethanol from edible cassava tubers. In recent years, little has been heard from these companies. According to the Nigerian national newspaper titled 'Nigeria puts brakes on ambitious biorefinery plan', the bottlenecks facing the commercialization of biofuels are poor infrastructure, lack of funding for private companies, and government hypocrisy (Aduloju, 2021). Business_list (2022) flagged the fourteen best biomass fuel companies in Nigeria. Not much progress had been observed in their operations, except for the company's proposal to scale up production, which poses significant challenges due to the unique problems that exist in developing countries. Overcoming these challenges would require considerable effort.

Biofuel is an extremely important commodity for developing countries as it contributes to the following: combating climate change through its low-carbon content; addressing higher energy consumption due to an expected world population increase of 8 - 10.5 billion by 2050; securing energy supply by reducing reliance on fossil fuel sources; creating job opportunities for rural and urban women and youths; and making the most of scarce resources such as waste and residue. Canabarro et al. (2023) have extensively elaborated on the immense benefits of biofuels for developing countries, including Argentina, Brazil, Colombia, and Guatemala. As biofuel commercialization progresses, and countries identify bioresources, certain peculiar problems have emerged. These issues, observed in countries that have already commercialized biofuels, may be a source of concern for emerging economies. In this review, the common challenges against biofuel commercialization are discussed. Also, the observed challenges of countries with commercialized biofuel are examined in light of their political framework. This review serves as the blueprint for overcoming energy poverty in most developing countries.

2. GLOBAL VIEW ON BIOFUEL COMMERCIALIZATION AS A GAME CHANGER

Global adoption of biofuel as an economic and energy tool is unprecedented. Most developed countries have already overcome the bottlenecks of funding and consumer patronage. With the active participation of the industry, there are customized machinery, automobiles, or devices that work on biofuels. However, the challenge remains the sustainability of the biofuel project due to the limited feedstock. Agro-waste was used as feedstock in Europe and the United States of America (Guyomard et al., 2011); however, this type of feedstock cannot sustain a large consumer base. Cellulosic biomass, e.g., hemicellulose and lignin, became another potential source of feedstock for bioethanol production (GAIN, 2019). Some developing countries use rotten fruits from the market as feedstock (Tiwari et al., 2014). Also, sawdust was adopted for bioethanol production using fermentative bacteria to achieve accurate fermentation. Scientists have proffered ways of adopting other feedstocks so that food security would not be threatened. Algae became a novel feedstock as the global production rate of algae biomass was around 10,000 tons in 2007 (DOE, 2010). At the moment, China leads the world in algae biodiesel production. The USA and Australia are also recognized for their adoption of algae biodiesel.

At the moment, the United States of America (USA) has optimized bioethanol production using domestically grown maize to about 132.6 billion liters (Biofuel International, 2020). Like the USA, Brazil has a tremendous bioethanol production of over 21 billion liters on a yearly basis. The governments of nations are currently funding the biofuel project (GAIN, 2019). This funding development has made countries like the

Netherlands, the United Kingdom, Indonesia, Japan, Malaysia, the Philippines, Thailand, China, India, Argentina, and France large producers of biofuel (Guyomard et al., 2011). Wang (2019) reported the geographical distribution of world biofuel production in 2019. Most of the countries (e.g., the US, Brazil, China, etc.) that invested in the biofuel project are reaping huge proceeds. For example, in 2019, ABF Economics, on behalf of the Renewable Fuels Association (RFA), reported that the bioethanol industry supported almost 350,000 jobs and generated almost $43 billion (€39.6 billion) in gross domestic product. More so, 280,000 of the employees came from indirect and induced jobs that generated $23 billion (€21.1 billion) in income for American households (biofuels, 2020). Brazil's total 2019 ethanol production is estimated at 34.45 billion liters, an increase of four percent compared to the revised figure for 2018 (Biofuel International, 2020). The global market performance for biofuels is presented in Figure 2.

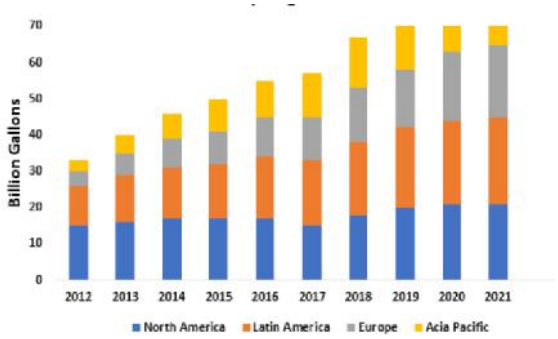

Figure 2. Biofuel production by region (IRENA, 2019)

Figure 2 shows that countries in Latin America, North America, Europe, and Asia have consistently invested into biofuel. What implications does this data hold for oil-dependent economies in developing countries? It means that crude oil prices will eventually crash beyond expected (Defterios, 2020), leading to inflation, poverty, loss of job, and criminality amongst other dangerous outcomes. With the importation of fossil-fuel ethanol of about $33 million in 2018, it is clear that the biofuel market in developing countries is huge, judging by its bioresources.

3. POTENTIALS AND PROSPECTS OF BIOFUEL IN DEVELOPING COUNTRIES

Developing countries have access to unquantifiable feedstock resources. For example, there are large-scale farmers scattered all over the countries due to their agrarian occupation. The database on small-medium farmers in developing countries is large and can be extrapolated to accurately estimate the quantity of agro-waste that can be obtained from larger and smaller farmers (Agricdemy, 2020). Lee (2017) claimed that there were about sixteen million small and medium farmers in some developing countries. In addition, there are a large number of local farmers whose names are not in the existing database. This fact can be substantiated by the diverse trainings and workshops on piggery, poultry, snail, and fishery farming organized for graduates, jobless, and retirees (Oji, 2020). The accumulation of agro-waste from these sources is enormous. The agro-wastes include post-harvest waste such as rice husk, Guinea corn husk, corn stalk, millet stalk, cassava peelings, coconut shell, tomato or pepper stalk, withered vegetables, feathers, cow dung, poultry droppings, pig dung, horse dung, rabbit dung, fish bones, bean peels, palm fruit waste, palm kernel, etc. Aside from the post-harvest wastes, there are abundant biomasses such as inedible seeds for biodiesel production, broken branches of trees for bioethanol production, seedpods for ethanol production, inedible leaves for biodiesel production, dried leaves for bioethanol, sawdust, etc. Energy sources and prospects in developing countries have been analyzed by the IEA (2012), with biomass accounting for over 84.9% of its total renewable resources. The biomass sources include wood fuel and charcoal, which accounted for 85% of total energy consumption. Garba and Umar (2015) reported that Nigeria had the potential to produce 434.6 million metric tons of rice straw and 0.9 million metric tons of rice husk. Ogbonna et al. (2015) reported that Nigeria's potential for large-scale microalgae cultivation was a good sign for biofuel commercialization. More so, the inedible seeds namely Jatropha, Cassia fistula, Abrus precatorius, etc. can serve as sources of oil, starch, and cellulose. Starch and cellulose can serve as feedstock for bioethanol, while oil can be used for biodiesel production (Biofuel, 2020).

There are tropical crops in developing countries that can be adopted for bioethanol production. A typical example of such a crop is sugarcane. Moses et al. (2017) reported that there were over 400,000 hectares of land in rural communities in sub-Saharan Africa that could enhance sugarcane cultivation. Another tropical crop is cassava. Cassava is high in starch and cellulose and can be cultivated easily. There are tropical weeds, such as tiger nuts (Cyperus esculentus), that grow with minimal supervision. It is a tough, erect, fibrous-rooted perennial plant that has found relevance in medicine and the food industry as a flavoring agent for ice cream and biscuits, etc. Oyedele et al. (2015) reported that tiger nut oil possessed a high level of commercial value. In other words, there are several tropical weeds and crops that can sustain the biofuel project in developing countries.

Sustainable agricultural production and utilization of resources are among the added values of the advancements in biofuel industries in most developed countries. In 2016, the value of arable land (hectares) in Nigeria was 34,000,000. At the moment, only 41% of the arable land is being cultivated. It is believed that cultivated lands are still underutilized. This is evident in the Nigerian agriculture sector's contribution to GDP between 2013 and 2016, which was between 22 and 25%. The Nigerian agriculture sector's contribution to GDP shows no significant improvement.

India's biofuel project already has a list of biomasses accruable for agriculture (Figure 3). With this estimate, both the government and investors can fund agricultural activities to empower biofuel distillers and plants. The starch and cellulose crops can serve as feedstock for bioethanol, while the oil-rich crops can be used for biodiesel production. Examples of starch and cellulose crops that can be found in sub-Saharan Africa include millet, sorghum, sugarcane, maize, guinea corn, cassava, cotton, paddy, rice, etc. According to the World Bank (2020 , maize production in Nigeria is about 9180270 metric tons; millet production is 1271100 metric tons; and sorghum production is 6897060 metric tons (World Bank, 2020). In 2018, farmers in four local government areas of Kebbi State (Zuru, Danko-Wasagu, Fakai, and Sakaba) in northern Nigeria were reported to have massive cultivation and production of millet, guinea corn, and maize.

In 2010, Nigeria produced approximately 45 million metric tons of cassava, which is almost 19% of the world's production (IITA, 1990). The average yield per hectare is 10.6 tons. Fortunately, the crop is produced in 24 of the country's 36 states (Kristen and Jerrod, 2015). Analysis proves that the present average national yield of cassava of about 15 tons per hectare is suitable to meet the demand for bioethanol plants.

The oil-rich crops or plants that are cultivated in Asia, Africa, and Latin America include palm trees, soy beans, groundnuts, coconuts, sunflowers, etc. AMREC (2017) reported that 13 out of the 36 states in Nigeria are the main producers of soy beans, i.e., Benue, Kaduna, Plateau, Niger, Nasarawa, Kebbi, Kwara, Oyo, Jigawa, Borno, Bauchi, Sokoto, Taraba, and the FCT. Ajeigbe et al. (2015) reported that China, India, Nigeria, the USA, and Myanmar are the leading groundnut-producing countries in the world. The chaff of the oil crop can also be used for bioethanol production. Aside from the known crops, there are other biomasses that are abundant, i.e., jatropha seeds, shrubs, and even wastes from agricultural activities.

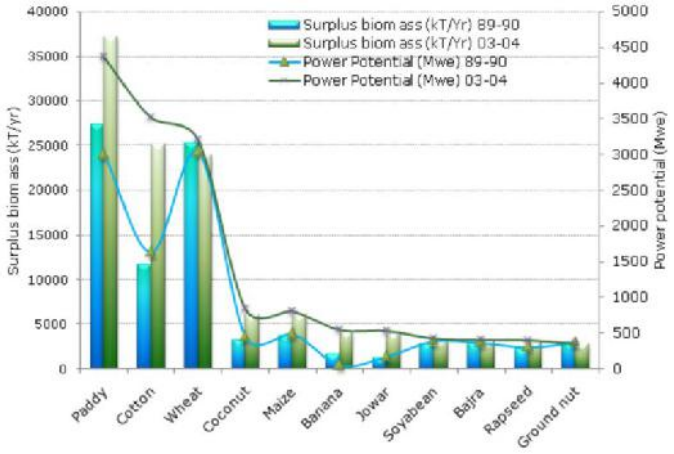

Figure 3. Biomass resources in India (Bikramjit and Indranil, 2008).

4. DRAWBACKS OF BIOFUEL PROSPECTS IN DEVELOPING COUNTRIES

Salient challenges may mitigate or stifle biofuel commercialization in developing countries. These challenges include poor technology, sustainable biomass resources, inadequate farmland, policies, and infrastructure. In addition, the main drawback of the economies of developing countries is their extensive mono-economies. In oil-dependent countries, the economy is heavily dependent on fossil fuels as the apex and most controversial source of energy. Some oil-dependent countries, such as Nigeria, rely on imports of finished fossil fuel products, thereby leading to paranoia about the escalation of the price of gasoline. Furthermore, the dependence on fossil fuel for energy demand, i.e., either for automobiles, generators, or industrial machines, has created new challenges such as the depletion of the total volume of the oil reserve and an increase in air pollution and emissions of pollutants (Emetere and Akinyemi, 2017). The diversion from fossil fuel to biofuel is expected to boost the economy by creating different classes of market among the small, medium, and major players in the economy. For example, if biofuel production in developing countries moves to the commercial stage, it will first create jobs for rural women and farmers, as they will be involved in going to the forest and farms to trade agro-waste and biomass. Medium players are the companies that will produce biofuel in commercial quantities. Major players are the consumers, i.e., the populace. In other words, the adoption of biofuel in developing countries would activate the economy and reduce poverty by 18%. However, this project cannot simply be achieved by the eradication of fossil fuels, but by the drive on the fossil-biodiesel ratios for the start. The conversion of natural gas into biogas products, as projected by big oil companies, may provide resources for biofuel commercialization. The inevitable eradication of fossil fuels, as seen in the investments of notable countries, is a clear reason why mental detachment from fossil fuels should be the next program for government officials and policymakers in various parts of the globe. Based on these proven biomass resources, the drawbacks of biofuel commercialization in developing countries are discussed in the next section.

Another notable drawback is the lack of public awareness of the aforementioned resources. This is deliberate, as government organs at all levels have not come to terms with the reality of fossil-fuel eradication or mitigation in the coming years. The records of health conditions due to land and air pollution are too numerous to jettison. Additionally, there has been an increase in oil spillage, resulting in the elimination of aquatic and terrestrial organisms and animals. Low access to potable water and an agrarian setting for rural dwellers are fast becoming a mirage. Moreover, some agro-waste is disposed of at the nearest dumpsite. Bioaerosols, which can contain fungi, bacteria, or viruses, are a cause for concern as their generation and proliferation are more prominent when there is a high volume of fossil-fuel pollution in the atmosphere. Therefore, apart from their potential to stimulate the economy, reducing air pollution from fossil fuels would significantly contribute to lowering the incidence of respiratory and cardiac illnesses or diseases in both infants and adults.

Another futuristic drawback to commercial biofuel production in most developing countries is the farmer's disposition to sell edible seeds to biofuel companies rather than the populace. This inevitable situation would lead to the use of edible seeds such as soya seed, palm fruit, moringa seed, maize, and olive seed for biodiesel production. This challenge will certainly have a significant impact on food prices and food security. For developing countries, food security is low, as seen in the high importation of rice from China, India, etc. Rice importation alone is about 6.3 million tons of milled rice, with an annual consumption per capita of 29 kg (FMARD, 2016). In other words, most developing countries are not ready for the commercialization of biofuel, judging by their population and low supply chain for biomass when consumption reaches its peak. So, the immediate solution is to have a proper takeoff platform, i.e., enhance the yield of feedstock and provide aiding infrastructure such as roads, electricity, and water to improve feedstock production.

One of the main challenges confronting most developing countries is policymaking. Most researchers have argued that policy implementation is the main challenge in developing countries. The best policy is judged by its performance. Biofuel commercialization becomes lucrative when policies are made to encourage the use and production of biofuels. This gesture has improved biofuel production globally (Guyomard et al., 2011) to 95.4 million metric tons of oil equivalent, thereby increasing its profit to over 59% yearly (Figure 4). Figure 5

presents the global renewable biofuel production over the years. Coincidentally, this chart also infers the slow pace of policy-making in developing countries and how it has impacted biofuel production. It is clear that this slow response is largely due to the vested interests of politicians in other spheres of business across countries.

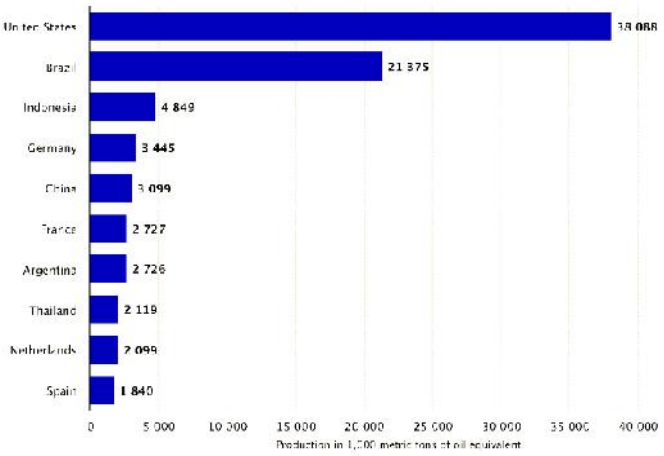

Figure 4. Global renewable biofuel production over the years (Biofuel, 2019)

There is no doubt that US policies to promote alternative and renewable energies should be among the best in the world. The focus of US policy on renewable energies is to improve the environment and the economy. For example, the Clean Air Act of 1970 created initiatives to reduce pollutants from mobile sources. Then, the Energy Policy Act of 1992 was enacted to reduce the nation's dependence on imported oil and improve air quality.

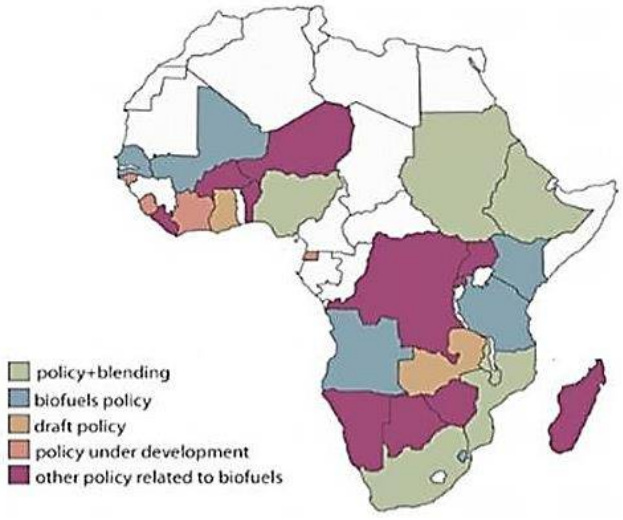

Figure 5. Overview of nation policy on biofuel in Africa (Kiggundu et al. 2017)

In the case of Nigeria, this would be the greatest hurdle the nation would endeavor to overcome because of its dependency on fossil fuel importation. Reliance on mono-economy may be tempting, as global influences can crash the economy. For example, oil prices are determined by a lot of factors, which include price wars (launched by key players), war, international politics, and pandemic outbreaks (Schnepf and Yacobucci, 2013). The willpower to diversify the economy does not lie in the hands of the government alone. The role of the investor is crucial to activating the biofuel project in various developing countries. For example, after the US Energy Policy Act of 1992, there was a need to bring in investors; this idea gave birth to the Energy Policy Act of 2005, which called for tax incentives for alternative fuels as well as other policy initiatives. When this supportive policy was properly executed, there was a need to diversify the biofuel project into renewable fuels (including corn-based ethanol), advanced biofuels, biomass-based diesel, and cellulosic biofuels. This feat was achieved via the Energy Independence and Security Act (EISA) of 2007. This initiative led to growth in the US ethanol industry. In 2012, the ethanol industry contributed approximately $43.4 billion to the gross domestic product (RFA, 2012; Urbanchuk, 2013). Also, the ethanol industry's influence on household income has grown from US$29.9 billion in 2012 to US$43 billion in 2019 (Hoekman, 2009). More so, this progress extends to both the agricultural and rural sectors (RFA, 2012).

On the other hand, in the context of policy-making in a developing country, the Nigerian Bio-fuel Policy of 2007 was implemented to facilitate the establishment of biofuel distilleries and plants, with the government providing over US$ 50 million as equity investment (OGNPBI, 2007). The objective of the policy is to have a significant impact on petroleum product quality. Unfortunately, the policy did not make room for the commercialization of the biofuel. The projection made for 2020 was 480 million liters. In comparison to the US, which produces 4.328 billion gallons per year, Brazil's 30.755 billion liters of ethanol in 2018, Argentina's 700 million liters per year, and China's 19,005 million liters per year (NS Energy, 2019), it is sad to note that the projection did not come to fruition. The policy had no form of tax rebate for investors. Rather, it made projections on tax revenue accruable to the project. Lastly, the policy did not foresee scarce biomass resources and how to make them sustainable. It is no surprise that this policy never saw the light of day. Hence, the way forward is to expunge all existing (i.e., faulty) policies and re-enact workable ones that would be of interest to investors.

Another notable challenge facing most developing countries is inadequate infrastructure, such as roads and electricity. Since biofuel commercialization would naturally affect both agricultural and rural sectors in the short and long term, the primary transport segment (between the farm and an all-season access road) is important, as it ensures crop movement from the farmer to the biofuel distilleries and plants. Also, good roads avoid post-harvest losses and crop deterioration (Oyatoye, 1994). Many agricultural scientists in Nigeria have reported poor infrastructure for two decades (Oyatoye, 1994; Akinola, 2003). The issues with electricity in some developing countries are worrisome, as investors would have to spend more on powering machines. Figure 6 gives a typical outlook on electricity generation in Africa and why it is considered a major challenge. For example, in 2015, the energy needs of Nigeria were 10.713 GWh/year; however, current power generation in the country is less than 3000 MW (World Bank, 2020). Based on all that has been discussed above, there is a need to examine the technical know-how of researchers in developing countries to prepare for the challenges. This leads us to the next section on past research work done on biofuels.

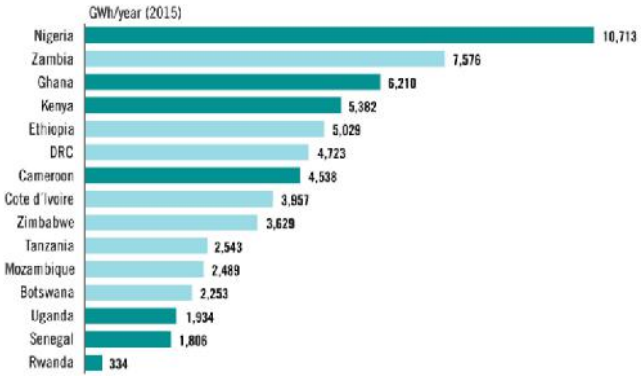

Figure 6. Energy demand of African countries in 2015 (Nordsid, 2019)

5. Technical Analysis Biofuel Production Feasibility in Developing countries

On the basis of their feedstock, biofuel production has been classified into three families: first, second, and third generations. Agricultural crops are used in the first-generation biofuels, where biogas, biodiesel, and bioethanol are the most common examples, whereas the second generation employed the digestion of sugars such as sugar beets, maize, and wheat, as well as starch, to yield biogas, otherwise known as biomethane. Bioethanol can also be made from sugar fermentation, such as that of corn, potatoes, or sugarcane used in the United States and Brazil, respectively (Lackner, 2017). Third-generation biofuels are obtained from photosynthetic microbes such as microalgae and cyanobacteria in order to manufacture higher alcohols and lipid-based products (Hammer et al., 2020). Due to the biochemical composition of these microbes, which includes carbohydrates, fats, and proteins, they have gained prominence over lignocellulosic biomass. Higher carbohydrate contents allow for the production of higher alcohols and bioethanols, whereas the lipid fraction facilitates the production of biodiesel, isoprenoids, and other lipid-based compounds. Two very illustrative examples are Spirulina maxima, with 60–71% w/w of proteins, and Schizochytrium spp., with 50–77%w/w of lipids (Razaghifard, 2013). Green diesel is a biodiesel that has been used as an alternative energy source for diesel fuel. Green diesel is a biofuel. It is produced from food sources that contain triglycerides and fatty acids, such as vegetable oil and crude palm oil. Green diesel has also been observed to be derived from algae, a third-generation feedstock that is considered livestock for next-generation biofuel production. They could be micro- or macroalgae, as both do not require pre-treatment since they are free lignin (Kumar et al., 2018). Microalgae store energy in their cells in the form of lipid droplets (Pragya & Pandey, 2015). They include green algae and cyanobacteria, which are both made of polyglucans, such as starch and glycogen, and sugar alcohols, like glucuronic acid and mannitol. Microalgae ensure the release of fermentable sugars through hydrolysis because of their cellulose and hemicellulose cell walls (Kumar et al., 2018). Algae generally yield more at a higher growth rate than energy crops. Microalgae have the ability to grow in both artificial and natural surroundings, their CO2 uptake rate is high, and they are environmentally friendly (Jutakridsada et al., 2019). However, due to cultivation, harvesting, and downstream processing limitations, commercial usage of third-generation feedstock is minimal (Tarafder et al., 2021). The fourth-generation biofuels come from bioengineered microorganisms such as algae, yeast, fungi, cyanobacteria, and crops to improve the efficiency of the process and the yield of the products.

Biofuel production involves a lot of processes, which include chemical, thermochemical, and biochemical conversions (Table 1). The biochemical conversion involves anaerobic digestion, alcoholic fermentation, and photobiological hydrogen gas production (Subramani et al., 2015). Biochemical processes employ enzymes (Table 2) to process raw materials into fuels. Lipase and phospholipase are the most important enzymes in biodiesel production (Hood & Bauer, 2016). Lipase transforms free fatty acids (FFA) and triacylglycerols into fatty acid methyl esters (FAME), which are the major components of biodiesel. Phospholipase converts phospholipids into diacylglycerols, which serve as substrates for lipase. Cellulase digests cellulose into reducing sugars, which are then fermented into ethanol by yeast or bacteria (Ashraf et al., 2021). Anaerobic digestion is employed for treating wet organic waste. It is a fermentation process that involves the conversion of biodegradable materials by bacteria in the absence of oxygen into biogas such as methane, carbon (IV) oxide, and other gases such as methane, CO2, and hydrogen sulfide. Fermentation takes place in two phases in an airtight digester vessel by bacteria (acid-forming bacteria and methane-forming bacteria) (Hashemi et al., 2019; Rajput & Visvanathan, 2018). The first is the liquefaction phase, where complex organic substances are hydrolyzed to simple organics such as fatty acids, alcohols, and sugars by the acid-forming bacteria. The second phase is the gasification phase, where the simple organics are converted into biogas by methane-forming bacteria. Biogas and digestate are the products of anaerobic digestion and can be processed to make secondary goods (Zang et al., 2016). Biogas can then be used to generate electricity, heat, and fuel for transportation. Digestate can indeed be transformed into fiber with reduced nutrient content, making it suitable for use as a soil conditioner. Additionally, the liquor produced during the process, which contains higher nutrients, can be utilized as a liquid fertilizer (Mohamed et al., 2022). Anaerobic digestion reduces toxic gas emission and odor below unprocessed waste odor levels.

Biomass materials comprising sugar, starch, or cellulose can be converted into alcohols through microorganisms such as yeast and bacteria. The table below shows examples of some biofuels and their production pathways, including the substrates and microorganisms that catalyze their production (Kim & Gadd, 2019).

In the third generation of biofuel production, the pathways are genetically modified to optimize the yield of biofuels. Such modifications include endogenous overexpression, heterologous overexpression, expression cassettes, and inactivated gene expression. For example, by genetically modifying Clostridium for an overexpression of the TER (trans-enoyl-coenzyme A reductase gene), butanol production increased (Wen et al., 2020). Overexpressed SFA1 (alcohol dehydrogenase) in genetically modified S. cerevisiae with lignocellulosic hydrolysate substrate gives a higher yield of ethanol (Zhu et al., 2020; Rajeswari et al. 2022). The acetone, butanol, and ethanol yields are far better when Clostridium with overexpressed sol-operon and EC cassette is applied (Wang et al., 2019). An activated Entner-Doudoroff pathway, enhanced by an engineered E. coli strain and a glucose-inducible system,

along with the deletion of side pathways, leads to a higher yield of 2,3-butanediol. This innovative approach offers the potential for increased efficiency in 2,3-butanediol production (Sathesh-Prabu et al., 2020). Likewise, iso-butanol production increases in P. putida when soluble transhydrogenase is inactivated with the overexpression of ILVC and ILVD and the introduction of feedback-resistant acetolactate synthase, aldehyde dehydrogenase, and ketoacid decarboxylase (Nitschel et al., 2020).

There are indeed numerous challenges associated with the biochemical processes involved in biofuel production. These obstacles have impeded the rapid and widespread production of sustainable biofuels. However, if these issues can be effectively addressed and resolved, the production of biofuels has the potential to become more consistent and widespread, leading to a more sustainable and reliable source of energy.

The table below (Table 3) highlights some challenges involved in the production of specific biofuels derived from alcohol, hydrocarbons, and fatty acids..

Based on the above report, it is reasonable to suggest that the industrial production of all types of biofuel is feasible in developing countries, considering the cost, availability of required feedstock, and technical expertise. Table 4 illustrates the CO2 emissions in renewable and non-renewable sources, highlighting the significant impact of renewable energy on the carbon footprint over a geographical area.

Table 1. Pathways involved in the biochemical production of biofuels

Pathway	Substrate	Microorganism	Biofuels
Butyrate/ Acetone-Butanol Ethanol (ABE) pathway	Sugar	Clostridium sp.	n-butanol acetone, ethanol, hydrogen gas
Ethanol/Entner-doudoroff pathway	Sugar	Saccharomyces cerevisiae, zymomonas mobilis	Ethanol
1,2-propanediol pathway	Deoxy sugars, glucose, 1,2-propanediol	Salmonella typhimurium	1,2-propanediol, propanol, propionate
Butanediol	Sugar	Klebsiella, Enterobacter	2,3 butanediol, hydrogen gas
Mixed acid fermentation	Glucose	Escherichia, Shigella	Ethanol, hydrogen gas

Table 2. Biochemical processes involved in some biofuel production

Feedstock	Decomposition	Intermediate	Products
Sugarcane	Hydrolysis	Sugars	Ethanol
Lignocellulosic	Biochemical/Gasification/pyrolysis/liquefaction	Sugars/Syngas/lipids/oil	Ethanol/Hydrogen/Methanol/hydrocarbon biofuels
Algae and oil-seeds	Lipid extraction	Lipids/oil	Biodiesel / Hydrocarbon biofuels

Table 3. Challenges involved in the production of specific biofuels

(a) Alcohols-based biofuels		
BIOFUEL	**MICROBE**	**CHALLENGES**
Butanol	Clostridium acetobutylicum Clostridium tyrobutyricum	The toxicity of butanol decreased growth rate and cell density.
Isobutanol	S. cerevisae P. pastoris	
2, 3 Butanediol	Z. mobilis Synechococcus elongatus	Cell growth inhibition with increased titres of butanol (Fu et al., 2021).
1,3-PD 2,3-BD	Klebsiella pneumoniae	Competition between Iso-butanol and other pathways to produce other metabolites might be a limiting factor for increased level of iso-butanol (Wess et al., 2019;Yang et al., 2016).
Isopentanol	S. cerevisiae	Overproduction of KIV mitigates the production of other alcohols (Siripong et al., 2018).
2,3-BDO	Pichia Pastoris	(Oliver et al., 2013; Park et al., 2017; Yang Zhang, 2018)

(b) Hydrocarbon-based biofuels		
BIOFUEL	**MICROBES**	**CHALLENGES**
Isobutyraldehyde	E. coli	Combined deletion of genes caused decreased iso-butanol production (Rodriguez & Atsumi, 2012).
Alkane	E. coli	Endogenic formation fatty alcohols thought to be competitive with alkane production
Heptadecane (10.2 mg/l) Pentadecane (2.7 mg/l)	A. carbonarius	An unknown, innate fatty aldehyde dehydrogenase networks diverted the fatty aldehydes back to the fatty acid metabolism (Sinha et al., 2017).
Alkenes	Cupriavidusnecator	The expression of aferredoxin ferredoxin-NADP + reductase system sharply lowered the C-flow towards fatty aldehydes (Crepin et al., 2018).
(**c**) Fatty-acid-derived biofuels		
BIOFUEL	**MICROBES**	**CHALLENGES**
FAEEs	Yarrowia lipolytica	Need to enhance production of FAEEs to reach commercially acceptable level (Yu et al., 2020).
Oleic acid	Rhodosporidium toruloides	Fatty acids produced showed promising potential to be blended with vegetable oils (Tsai et al., 2019).
FFAs	S. cerevisiae	Creating higher titers of FAs requires substantial amounts of acetyl-CoA, ATP, and NADPH, making it difficult to engineer (Ferreira et al., 2018).
Odd-chain FA	Y. lipolytica	Difficulty in assessing toxicity and understanding the role of propionic catabolism in odd FA production (Tai & Stephanopoulos, 2013).

Table 4. CO_2 emission from renewable and non-renewable sources

RENEWABLE ENERGY FUELS

S/N	Fuel	CO_2 Emission (C/Ti)	Reference
1	Gasohol E10	2.159	Nicha et al., 2014
2	Gasohol E20	2.159	Nicha et al., 2014
3	Gasohol E85	0.482	Nicha et al., 2014
4	Natural gas	15.3, 56.74	Khan et al. 2019; Geraldine et al., 2014
5	Biodiesel (B5)	2.284	Nicha et al., 2014
6	Liquefied petroleum gas (LPG or LP gas)	2.041, 17.2, 65	Nicha et al., 2014; Khan et al. 2019;
7	Biogas	0	Geraldine et al., 2014
8	Compressed natural gas (CNG)	1.737	Geraldine et al., 2014

NON- RENEWABLE ENERGY FUELS

1	Diesel Fuels (HSD)	2.395, 20.2	Nicha et al., 2014; Khan et al. 2019
2	Gasoline	18.9	Khan et al. 2019
3	Kerosene	19.6	Khan et al. 2019
4	Residual Fuel Oil	21.1	Khan et al. 2019
5	Naphtha	20.0	Khan et al. 2019
6	Refinery Gas	18.2, 56.9	Khan et al. 2019; Geraldine et al., 2014
7	Coking Coal	25.8, 80	Khan et al. 2019; Geraldine et al., 2014
8	Fuel Oil	78	Geraldine et al., 2014
9	Waste Oil	78	Geraldine et al., 2014
10	Gas Oil	74	Geraldine et al., 2014

6. POLITICAL WILLINGNESS TO COMMERCIALIZING BIOFUEL IN DEVELOPING COUNTRIES

Outcomes leading to political economy are simply the political decisions that have been reached through consultation with stakeholders (Anderson et al., 2013). In reality, policies are created and enhanced by politicians, not economists. For example, Statista (2021) reported that Nigeria imported petrol worth about 688 trillion naira between January and March 2021. This information could also be a game changer if the government provides 20% of the cost of gasoline or ethanol importation into the country as incentives to investors. In most developing countries, investors are discouraged by politicians who, at one end, consider the interests of stakeholders. In oil-rich developing countries, many stakeholders have become accustomed to the substantial income generated from fossil-fuel-associated businesses. Most stakeholders are politicians who would constantly disrupt biofuel commercialization through unstable or unreliable decision-making or policy formulation. Some of the stakeholders may be lobbyists that lobby governments into policy positions. Some of the stakeholders are ideologists who believe that biofuel would cause greater problems. Some of the stakeholders are the farmers who are expected to produce the biomass used for biofuels. In the US, the use of edible crops for biofuels has been criticized because an equivalent of 330 million people could have been fed with the grain grown by American farmers in 2009. In developing countries, some of the stakeholders constitute small and medium businesses that rely on fossil fuels. Hence, the weakness of the political class to negotiate with the various stakeholders in developing countries is one of the main challenges facing biofuel commercialization.

Zilberman et al. (2014) proposed that in such a case of conflicting interests, the political outcome of introducing incentives for biofuel operators to pay the price of externalities would be a soft-landing pad, especially in an environment with associated bottlenecks such as mono-economy, unreliable technical know-how, poor technology, government hypocrisy, lack of funds, sustainable biomass resources, inadequate farmland, policies, and infrastructure. Canada and Brazil prioritize some exporters operating in the Middle East. The US government provided subsidies worth at least US$43 billion to the renewable energy and biofuel industries in 2009 (Robbins, 2011). After the incentives given in 2009, the US still subsidies biofuels to the tune of US$7 billion a year, while China provides around US$2 billion in direct subsidies a year. These political decisions in the US were initiated by mid-western states, which led to the campaign on certain biofuel policies that have been adopted by US government agencies (Notaras, 2018). The dividend of the emerging policies was the production of 10 billion gallons of biofuels in 2010 and 15 billion gallons in 2015, with a projection of 36 billion gallons in 2022.

One of the misleading agitations by some ideologists against biofuel commercialization is land use, populace addictions to fossil fuels, and food prices. Some policymakers in developing countries are already leveraging on this idea to continue the fossil-fuel addictions that have brought about high importations of essential goods and services (Robbins, 2011). A significant growing human population is expected to impact land use and, by extension, food prices. For example, in most developing countries (as seen in Mozambique), corporations have preference over the government in land allocation. This action has led to food insecurity and resource deprivation. Another sect of ideologists sees the call for biofuel commercialization as a 'biofuel complex' ideology that has far-reaching political implications. They believe that the political economy of the 'biofuel complex' is indeed parochial as it may lead to 'land grabs' across the world (Monsalve et al., 2008; Cotula, 2009), political-economic-ecological instabilities, destabilization of existing agrarian structures, etc. Contrary to all these, another school of thought believes that biofuel commercialization is a new profitability frontier for the agribusiness and energy sectors (McMichael 2009). Policy debates by countries that have commercialized biofuels clearly show that conscious economic planning is vital in balancing political decisions across different stakeholders (Franco et al., 2010; Hollander, 2010; Gillon, 2010). In other words, the challenges of biofuel commercialization in developing countries can be overcome through conscious political decisions.

5. CONCLUSIONS

In a nutshell, this review established that despite the awareness of biofuel for the past two decades, developing countries are far from commercializing biofuel, judging from the points raised in the review. Aside from the immediate danger of environmental pollution from fossil fuels that has been reported in most developing countries, biofuel commercialization is a new profitability frontier for agribusiness and energy sectors with huge short-term gains. This development means that developing countries stimulate their economies to avoid inflation, poverty, loss of jobs, and criminality, among other dangerous outcomes, whenever crude oil prices crash.

The biomass resources in developing countries were wholly examined, with high prospects for the use of agro waste such as rice husk, guinea corn husk, corn stalk, millet stalk, cassava peelings, coconut shell, tomato or pepper stalk, withered vegetables, feathers, cow dung, poultry droppings, pig dung, horse dung, rabbit dung, fish bones, beans peels, palm fruit waste, palm kernel, etc. The main question in this abundant biomass resource is sustainability. It is noted that the future drawback of commercial biofuel production in developing countries is inadequate planning and policy formulation to prevent land grab, food insecurity, social imbalances, and political instabilities. .

The drawbacks of the biofuel project in developing countries were discussed. Salient challenges that may mitigate or straggle biofuel commercialization in developing countries include mono-economy, poor technology, sustainable biomass resources, inadequate farmland, policies, technical know-how, and infrastructure. The technical know-how was discussed in depth. It was clearly seen from the technical trends that researchers in developing countries have a lot to do in expanding the scope of affordable biofuel processing techniques.

In order to improve biofuel production yield, technological advancement and technical know-how are well needed to boost biofuel commercialization. Recommendations to enhance biofuel commercialization include fostering synergy between industry, academia, and government. Conscious political decisions, such as providing incentives and negotiating with stakeholders, are essential to create an enabling environment

for investors. Governments should formulate standardized policies that promote active participation from financial institutions. Public-awareness programs should be launched to educate the populace about the benefits of biofuels. Additionally, providing reliable infrastructure, such as good roads, proper water, and power supply, will boost feedstock production. Finally, the formulation of workable policies to attract investors is crucial for the successful development of the biofuel industry.

6. ACKNOWLEDGEMENT

The authors appreciate the host institutions.

REFERENCES

1. ADBG, (2021). Nigeria - Green Energy & Biofuels (Geb) Bio-Refinery Project - SEFA Project Summary Note. https://www.afdb.org/en/documents/nigeria-green-energy- biofuels-geb-bio-refinery-project-sefa-project-summary-note
2. Aduloju Bunmi, (2021). Nigeria puts brakes on ambitious biorefinery plan. https://africaoilgasreport.com/2021/04/energy-transition/nigeria-puts-the-brakes-on-ambitious-biofuels-refinery-plan/
3. Agricdemy, (2020), Nigeria agriculture data. https://agricdemy.com/post/nigeria-data (Accessed 02/04/2020)
4. Ajeigbe, Hakeem A., Farid, W., Ayuba, K., Babu, N. M., Candidus, A. E., Damilola E., & Abubakar, I., (2015). A Farmer's Guide to Profitable Groundnut Production in Nigeria. http://oar.icrisat.org/8856/1/2015-084%20Gnut%20Production%20in%20Nigeria.pdf (Accessed 4/4/2020)
5. Akinola, S. R. (2003). Coping with Infrastructural Deprivation through Collective Action among Rural People in Nigeria. *Nordic Journal of African Studies, 16(1),* 30–46. https://citeseerx.ist.psu.edu/document?repid=rep1&type=pdf&doi=6d98b88afc2c4d7b82c96738e5fdd6cd4558cc6c
6. AMREC (2007). Mapping of soybean production areas in Nigeria. http://www.propcommaikarfi.org/wp-content/uploads/2013/08/28-Mapping-of-soybean-production-areas-in-Nigeria-3-07-1.pdf (Accessed 4/4/2020)
7. Anderson, K., Rausser, G., & Swin- nen, J. (2013). Political economy of public policies: insights from distortions to agricultural and food markets. Journal of Economic Literature 51(2), 423-477. http://dx.doi.org/10.1257/jel.51.2.423
8. Ashraf, A., El-Desouky, M.G., & El-Afify, M.A., (2021).Thermal and Spectroscopic Studies of Some Prepared Metal Complexes and Investigation of their Potential Anticancer and Antiviral Drug Activity against SARS-CoV2 by Molecular Docking Simulation. *Biointerface Research in Applied Chemistry, 12*, 1053-1075, https://doi.org/10.33263/BRIAC121.10531075.
9. Biofuel (2019), Biofuels and Bioenergy. https://chemicalengineeringnob.com/biofuels-and-bioenergy-conference-2019-in-netherlands/ (Accessed 3/4/2020)
10. Biofuel International (2020), US ethanol industry generated $43 billion in 2019, despite policy challenges https://biofuels-news.com/news/us-ethanol-industry-generated-43-billion-in-2019-despite-policy-challenges/ (Accessed 3/4/2020)
11. Business_list (2022). Best Biomass Fuel Companies in Nigeria. https://www.businesslist.com.ng/category/biomass-fuel
12. Canabarro, N.I., Silva-Ortiz, P., Nogueira, L.A.H., Cantarella, H., Maciel-Filho, R., & Souza, G.M., (2023).Sustainability assessment of ethanol and biodiesel production in Argentina, Brazil, Colombia, and Guatemala, *Renewable and Sustainable Energy Reviews*, *171*, 113019, https://doi.org/10.1016/j.rser.2022.113019.
13. Cotula, L. (2009). Land grab or development opportunity?: Agricultural investment and international land deals in Africa. London: International Institute for Environment and Development (IIED) https://www.iied.org/12561iied
14. Crepin, L., Barthe, M., Leray, F., Guillouet, S.E., 2018. Alka(e)ne synthesis in Cupriavidus necator boosted by the expression of endogenous and heterologous ferredoxin–ferredoxin reductase systems. *Biotechnology and Bioengineering 115 (10),* 2576–2584. https://doi.org/10.1002/bit.26805.
15. Defterios John, (2020), Why oil prices are crashing and what it means, https://edition.cnn.com/2020/03/09/business/oil-price-crash-explainer/index.html (Accessed 04/04/2020)
16. DOE, U. S. National Algal Biofuels Technology Roadmap. Maryland, (2010). https://www.energy.gov/eere/bioenergy/articles/national-algal-biofuels-technology-roadmap
17. Elegbede, I., & Guerrero, C., (2016), Algae Biofuel in the Nigerian Energy Context, *Environmental and Climate Technologies, 2016/17*, 44-60 http://dx.doi.org/10.1515/rtuect-2016-0005
18. Emetere Moses Eterigho & Akinyemi M.L. (2017) Atmospheric Dynamics of Air Pollution Dispersion and Sustainable Environment in Nigeria, *Journal of Urban and Environmental Engineering, 11 (1)*, 51-57 https://core.ac.uk/download/pdf/143483494.pdf
19. Emetere Moses Eterigho, Solomon Jack-Quincy, Akolade Adejumo, Oluwatobi Dauda, Israel Osunlola, Damola Adelekan & Oladipupo Adeyemi (2018). Empirical Analysis of biodiesel effect on the automobile properties of diesel engine: A case study of Olive and Soya biomass, *Energy Science & Engineering, 6(6),* 693-705. http://dx.doi.org/10.1002/ese3.244
20. Emetere Moses Eterigho, & Adesina, T. A., (2019), Short review on the prospects of human biogas utilization in Nigeria, *IOP Conference Series: Earth and Environmental Science 331 (1),* 012051 http://dx.doi.org/10.1088/1755-1315/331/1/012051
21. Ferreira, R., Teixeira, P.G., Siewers, V., & Nielsen, J., 2018. Redirection of lipid flux toward phospholipids in yeast increases fatty acid turnover and secretion. *Proc Natl Acad Sci USA 115 (6),* 1262–1267. https://doi.org/10.1073/pnas.1715282115.
22. FMARD-Federal Ministry of Agriculture and Rural Development. (2016), The Agriculture Promotion Policy (2016-2020). Federal Ministry of Agriculture and Rural Development, Abuja, Nigeria. pp.1-59. https://www.fao.org/faolex/results/details/en/c/LEX-FAOC165890/#:~:text=The%20present%20Agriculture%20Promotion%20Policy%20is%20founded%20on%20the%20following,7)%20Factoring%20climate%20change%20and
23. Franco, J., Levidow, L., Fig, D., Goldfarb, L., Hönicke, M. & Mendonca, M. L. (2010). Assumptions in the European Union biofuels policy: frictions with experiences in Germany, Brazil and Mozambique. *The Journal of Peasant Studies, 37(4),* 661–98. http://dx.doi.org/10.1080/03066150.2010.512454
24. Fu, H., Hu, J., Guo, X., Feng, J., Yang, S.-T., & Wang, J., 2021. Butanol production from Saccharina japonica hydrolysate by engineered Clostridium tyrobutyricum: The effects of pretreatment method and heat shock protein overexpression. *Bioresource Technology 335*, 125290. http://dx.doi.org/10.1016/j.biortech.2021.125290
25. GAIN (2019), Brazil: Biofuels Annual, https://www.fas.usda.gov/data/brazil-biofuels-annual-5 (Accessed 3/4/2020)
26. Garba, N.A., & Umar Z. U., (2015) Rice straw and husk as potential sources for mini-grid rural electricity in Nigeria, *International Journal of Applied Sciences and Engineering Research, 4(4),* 523–530. https://www.semanticscholar.org/paper/Rice-straw-%26-husk-as-potential-sources-for-rural-in-Garba-Zangina/415bf204b298172eee2684078098e8f9b11cabcc
27. Geraldine Henningsen, Arne Henningsen, Sascha T. Schröder & Simon Bolwig, (2014). "The Development of Environmental Productivity: the Case of Danish Energy Plants," IFRO Working Paper 2014/04, University of Copenhagen, Department of Food and Resource Economics. http://okonomi.foi.dk/workingpapers/WPpdf/WP2014/IFRO_WP_2014_04.pdf
28. Gillon, S. (2010). Fields of dreams: negotiating an ethanol agenda in the Midwest United States. *The Journal of Peasant Studies, 37(4),* 723–48. http://dx.doi.org/10.1080/03066150.2010.512456

29. Guyomard Hervé, Forslund Agneta, & Dronne Yves (2011), Biofuels and World Agricultural Markets: Outlook for 2020 and 2050, https://www.intechopen.com/books/economic-effects-of-biofuel-production/biofuels-and-world-agricultural-markets-outlook-for-2020-and-2050 (Accessed 3/4/2020)

30. Hammer, S.K., Zhang, Y., & Avalos, J.L., (2020). Mitochondrial compartmentalization confers specificity to the 2-ketoacid recursive pathway: increasing isopentanol production in Saccharomyces cerevisiae. *ACS synthetic biology 9 (3),* 546–555. http://dx.doi.org/10.1021/acssynbio.9b00420

31. Hashemi, S.S., Karimi, K., & Karimi, A.M. (2019). Ethanolic ammonia pretreatment for efficient biogas production from sugarcane bagasse. *Fuel, 248,* 196-204, https://doi.org/10.1016/j.fuel.2019.03.080.

32. Hoekman, S. Kent. (2009): Biofuels in the US–challenges and opportunities. *Renewable energy 34,* 14-22. https://doi.org/10.1016/j.renene.2008.04.030

33. Hollander, G. (2010). Power is sweet: sugarcane in the global ethanol assemblage. *The Journal of Peasant Studies, 37(4),* 699–721. http://dx.doi.org/10.1080/03066150.2010.512455

34. Hood Elizabeth E., & Lorenz Bauer (2016). Catalysts and Enzymes in Biofuel Production. https://www.biofuelsdigest.com/bdigest/2016/06/06/catalysts-and-enzymes-in-biofuel-production/ 30th/01/2022.

35. IEA (2012). Energy balance for Nigeria . OECD/IEA . http://data.iea.org. Accessed 1st September 2012.

36. IITA (1990), Cassava in tropical Africa:A Reference Manual https://www.iita.org/wpcontent/uploads/2016/06/Cassava_in_tropical_Africa_a_reference_manual_1990.pdf (Accessed 4/4/2020)

37. IRENA (2019). Global energy transformation: A roadmap to 2050 (2019 edition), International Renewable Energy Agency, Abu Dhabi. https://www.irena.org/apps/DigitalArticles/-/media/652AE07BBAAC407ABD1D45F6BBA8494B.ashx (Accessed 11/5/2023)

38. Jutakridsada, P., Saengprachatanarug, K., Kasemsiri, P., Hiziroglu, S., Kamwilaisak, K., & Chindaprasirt, P., (2019). Bioconversion of Saccharum officinarum leaves for ethanol production using separate hydrolysis and fermentation processes. *Waste and Biomass Valorization, 10,* 817-825, https://doi.org/10.1007/s12649-017-0104-x.

39. Kemausuor, F., Akowuah, J.O., & Ofori, E., (2013). Assessment of feedstock options for biofuels production in Ghana. *J. Sust. Bioenergy Syst. 3,* 119–128. http://dx.doi.org/10.4236/jsbs.2013.32017

40. Khan, A., Jamil, F. & Khan, N.H. (2019). Decomposition analysis of carbon dioxide emissions in Pakistan. *SN Appl. Sci. 1,* 1012 . https://doi.org/10.1007/s42452-019-1017-z

41. Kiggundu Nicholas, Isa Kabenge, Samuel Gyebi Arhin, & Noble Banadda, (2017). Impacts of Biofuel Policies on Welfare and Food Security: Assessing the Socioeconomic and Environmental Tradeoffs in Sub-Saharan Africa, *International Journal of Renewable Energy Research, 7(4),* 2162-2171 https://doi.org/10.20508/ijrer.v7i4.6272.g7264

42. Kim, B., & Gadd, G. (2019). Anaerobic fermentation. In Prokaryotic Metabolism and Physiology (pp. 230-267). Cambridge: Cambridge University Press. https://doi.org/10.1017/9781316761625.008.

43. Kristen Schubert and Jerrod Mason, (2015), Cost-Benefit Analysis of USAID/Nigeria's MARKETS II Program. https://www.usaid.gov/sites/default/files/documents/1865/150305%20MARKETS%20CBA%20REPORT%20FINAL.pdf (Accessed 4/4/2020)

44. Kumar, V., Sindhu, R. K., & Kumar, S. (2018). Comparative analysis of green diesel versus petro-diesel in compression ignition engine. *Bioscience biotechnology research communications, 11(1),* 128-135. http://dx.doi.org/10.21786/bbrc/11.1/18

45. Lackner, M., Winter, F., & Palotas, A., (2013) Combustion: from basics to applications. Wiley-VCH, Weinheim. ISBN 978-3-527-33376-9. http://dx.doi.org/10.1002/9783527667185

46. Lee Justin (2017), Nigeria to register 16M farmers in biometric database. https://www.biometricupdate.com/201703/nigeria-to-register-16m-farmers-in-biometric-database (Accessed 02/04/2020)

47. McMichael, P. (2009). The agrofuels project at large. *Critical Sociology, 35(6),* 825–839 http://dx.doi.org/10.1177/0896920509343071

48. Mohamed G. El-Desouky, Muhammad A. Khalil, Ashraf A. El-Bindary, & Mohamed A. El-Bindary. (2022). Biological, Biochemical and Thermochemical Techniques for Biofuel Production: an Updated Review, *Biointerface Research in Applied Chemistry 12(3),* 3034 – 3054 https://doi.org/10.33263/BRIAC123.30343054.

49. Monsalve, S. Suárez, Monsalve Suárez, Ulrike Bickel, Frank Garbers, Lucia Goldfar, & Vilmar Schneider. (2008). Agrofuels in Brazil. https://fianat-live-7318544636224c40bb0b0af5b09-745b6a8.divio-media.net/filer_public/6a/3e/6a3ed02b-8513-4996-82d0-a70c75a81a45/agrofuelsinbrazil.pdf

50. Moses, N., Mohammed, S., Saidu, H., Galadima, A.I., Umar, D.M., Abubakar, K., Kefa, M., & Billah, C., (2017). Determination of physicochemical parameters and riparian land effect on kwadon stream. *J. Adv. Res. Design,36,* 13–24. https://www.akademiabaru.com/doc/ARDV36_N1_P13_24.pdf

51. Nicha Sritong, Kamphol Promjiraprawat, & Bundit Limmeechokchai, (2014). CO2 Mitigation in the Road Transport Sector in Thailand: Analysis of Energy Efficiency and Bio-energy, *Energy Procedia, 52,*131-141, https://doi.org/10.1016/j.egypro.2014.07.063.

52. Nitschel, R., Ankenbauer, A., Welsch, I., Wirth, N.T., Massner, C., Ahmad, N., McColm, S., Borges, F., Fotheringham, I., Takors, R., & Blombach, B., (2020). Engineering Pseudomonas putida KT2440 for the production of isobutanol. *Eng. Life Sci. 20 (5-6),* 148–159. https://doi.org/10.1002/elsc.201900151.

53. Nordsid, (2019), Price And Need For Reliable Electricity Are Spurring Solar Sales To Businesses. https://nordsip.com/2019/01/24/price-and-need-for-reliable-electricity-are-spurring-solar-sales-to-businesses-press-release (Acessed 4/4/2020)

54. Notaras M. (2018). All Biofuel Policies Are Political, https://ourworld.unu.edu/en/all-biofuel-policies-are-political

55. NS Energy, (2019). Top five countries for biofuel production across the globe, https://www.nsenergybusiness.com/features/top-biofuel-production-countries/ (Acessed 04/04/2020)

56. Ogbonna, I.O., Moheimani, N.R. &Ogbonna, J.C. (2015) Potentials of microalgae biodiesel production in Nigeria, *Nigerian Journal of Biotechnology, 29,* 44–55. http://dx.doi.org/10.4314/njb.v29i1.7

57. OGNPBI (2007), Official Gazette of the Nigerian Bio-fuel Policy and Incentives. http://www.lse.ac.uk/GranthamInstitute/wp-content/uploads/laws/1517.pdf (Accessed 04/04/2020)

58. Oji Chuka (2020), Snail Farming Business Plan In Nigeria, https://www.pinterest.ca/pin/25966135334283235/ (Accessed 02/04/2020)

59. Oliver, J.W.K., Machado, I.M.P., Yoneda, H., & Atsumi, S., (2013). Cyanobacterial conversion of carbon dioxide to 2,3-butanediol. *Proc Natl Acad Sci USA 110 (4),* 1249–1254. https://doi.org/10.1073/pnas.1213024110.

60. Oyatoye, E. T. O. (1994). The impact of Rural Roads on Agricultural Development in Nigeria: A case study of Kwara State. *Ife Journal of Agriculture, 16,* 114-122. https://ija.oauife.edu.ng/index.php/ija/article/view/574

61. Oyedele O. A., Oladipo I. O. & Adebayo A. O., (2015), Investigation into Edible and Non-edible Oil Potentials of Tiger Nut (Cyperus esculentus) Grown in Nigeria, *Global journal of Engineering, Design & Technl., 4(4),* 20-24 https://www.longdom.org/articles-pdfs/investigation-into-edible-and-nonedible-oil-potentials-of-tiger-nut-cyperus-esculentus-grown-in-nigeria.pdf

62. Park, J.M..,Rathnasingh, C.., & Song, H., (2017). Metabolic engineering of Klebsiella pneumoniae based on in silico analysis and its pilot-scale application for 1,3-propanediol and 2,3-butanediol co-production. *Journal of Industrial Microbiology and Biotechnology. 44(3),* 431-441. http://dx.doi.org/10.1007/s10295-016-1898-4

63. Pragya, N., & Pandey, K. K. (2016). Life cycle assessment of green diesel production from microalgae. *Renewable energy, 86,* 623-632. http://dx.doi.org/10.1016/j.renene.2015.08.064

64. Rajeswari Shanmugam, Divya Baskaran, Panchamoorthy Saravanan, Manivasagan Rajasimman, Natarajan Rajamohan, & Yasser Vasseghian,(2022). Production of ethanol from biomass – Recent research, scientometric review and future perspectives, *Fuel, 317,* 123448, https://doi.org/10.1016/j.fuel.2022.123448.

65. Rajput, A.A., &Visvanathan, C., (2018). Effect of thermal pretreatment on chemical composition, physical structure and biogas production kinetics of wheat straw. *Journal of environmental management, 221*, 45-52, https://doi.org/10.1016/j.jenvman.2018.05.011.

66. Razaghifard, R. (2013). Algal biofuels. *Photosynth Res;117*,207e19. http://dx.doi.org/10.1007/s11120-013-9828-z

67. Renewable Fuels Association (RFA). 2012. 2012 Ethanol Industry Outlook. Renewable Fuels Association, Washington, DC. https://www.renewableenergymagazine.com/noor-hal-cuellar/ethanol-industry-outlook-2012-the-challenge-is (Accessed 24/12/2023)

68. Robbins Martin, (2011). Policy: Fuelling politics, *Nature, 474,* S22–S24 http://dx.doi.org/10.1038/474S022a

69. Rodriguez, G.M., & Atsumi, S., (2014). Toward aldehyde and alkane production by removing aldehyde reductase activity in Escherichia coli. *Metabolic Engineering. 25*, 227–237. http://dx.doi.org/10.1016/j.ymben.2014.07.012

70. Sathesh-Prabu, C., Kim, D., & Lee, S.K., (2020). Metabolic engineering of Escherichia coli for 2, 3-butanediol production from cellulosic biomass by using glucose-inducible gene expression system. *Bioresource technology. 309*, 123361. http://dx.doi.org/10.1016/j.biortech.2020.123361

71. Schnepf, R., & B. D. Yacobucci. (2013). Renewable Fuel Standard (RFS): Overview and Issues. Congressional Research Service, Washington, DC. https://sgp.fas.org/crs/misc/R40155.pdf (Accessed 24/12/2023)

72. Sinha J., and Indranil Biswas, (2008). Rural Energy security in India: reality checks. https://nistads.res.in/all-html/Rural%20Energy%20security%20in%20India_%20reality%20checks.html (Accessed 4/4/2020)

73. Siripong W, Wolf P, Kusumoputri TP, Downes JJ, Kocharin K, Tanapongpipat S, & Runguphan W., (2018) Metabolic engineering of Pichia pastoris for produc-tion of isobutanol and isobutyl acetate. B*iotechnol Biofuels 11*,1 https://biotechnologyforbiofuels.biomedcentral.com/articles/10.1186/s13068-017-1003-x (Accessed 24/12/2023)

74. Statista (2021). Petrol import into Nigeria between the 1st quarter of 2018 and the 1st quarter of 2021. https://www.statista.com/statistics/1165962/petrol-import-in-nigeria/

75. Subramani Velu, Angelo Basile, & Nejat Veziroglu (2015). Compendium of Hydrogen Energy Hydrogen Production and Purification 1st Edition - May 23, 2015 eBook ISBN: 9781782423836. Hardcover ISBN: 9781782423614. https://doi.org/10.1016/C2014-0-02671-8

76. Szetela Beata, Bekhzod Djalilov, & Raufhon Salahodjaev (2022). Renewable Energy and CO2 Emissions in Top Natural Resource Rents Depending Countries: *The Role of Governance, Frontiers in Energy Research, 10,* 1-5. https://doi.org/10.3389/fenrg.2022.872941 .

77. Tai, M., & Stephanopoulos, G., (2013). Engineering the push and pull of lipid biosynthesis in oleaginous yeast Yarrowia lipolytica for biofuel production. *Metabolic Engineering. 15*, 1–9 http://dx.doi.org/10.1016/j.ymben.2012.08.007

78. Tarafdar, A., Sirohi, R., Gaur, V.K., Kumar, S., Sharma, P., Varjani, S., Pandey, H.O., Sindhu, R., Madhavan, A., & Rajasekharan, R., (2021). Engineering interventions in enzyme production: Lab to industrial scale. *Bioresource technology 361*, 124771. https://doi.org/10.1016/j.biortech.2022.127770

79. Tiwari, S., Jadhav, S.K., Sharma, M., & Tiwari, K.L., (2014). Fermentation of waste fruits for bioethanol production. *Asian J. Biol. Sci. 7*, 30–34. http://dx.doi.org/10.3923/ajbs.2014.30.34

80. Tsai, Y.-Y., Ohashi, T., Wu, C.-C., Bataa, D., Misaki, R., Limtong, S., & Fujiyama, K., (2019). Delta 9 fatty acid desaturase overexpression enhanced lipid production and oleic acid content in Rhodosporidium toruloides for preferable yeast lipid production. *Journal of Bioscience and Bioengineering. 127 (4)*, 430–440. http://dx.doi.org/10.1016/j.jbiosc.2018.09.005

81. Urbanchuk, J.M. (2013). Contribution of the Ethanol Industry to the Economy of the United States. http://ethanolrfa.3cdn.net/af18baea89e31dadbe_68m6bnto3.pdf. (Accessed 04/04/2020)

82. Wang T., (2019). Global biofuel production by select country 2018. https://www.statista.com/statistics/274168/biofuel-production-in-leading-countries-in-oil-equivalent/ (Accessed 4/4/2020)

83. Wang, P., Zhang, J., Feng, J., Wang, S., Guo, L., Wang, Y., Lee, Y.Y., Taylor, S., McDonald, T., & Wang, Y., (2019). Enhancement of acid re-assimilation and biosolvent production in Clostridium saccharoperbutylacetonicum through metabolic engineering for efficient biofuel production from lignocellulosic biomass. *Bioresource technology. 281*, 217–225. http://dx.doi.org/10.1016/j.biortech.2019.02.096

84. Wen, Z., Ledesma-Amaro, R., Lu, M., Jin, M., & Yang, S., (2020). Metabolic Engineering of Clostridium cellulovorans to improve butanol production by consolidated bioprocessing. *ACS Synthetic Biology. 9 (2),* 304–315. http://dx.doi.org/10.1021/acssynbio.9b00331

85. Wess, J., Brinek, M., & Boles, E., (2019). Improving isobutanol production with the yeast Saccharomyces cerevisiae by successively blocking competing metabolic pathways as well as ethanol and glycerol formation. *Biotechnology for Biofuels. 12 (1)*, 173. http://dx.doi.org/10.1186/s13068-019-1486-8

86. World Bank (2020). orld Bank Open Data Nigeria. https://data.worldbank.org/ (Accessed 4/4/2020)

87. Yang, S., Mohagheghi, A., Franden, M.A., Chou, Y.-C., Chen, X., Dowe, N., Himmel, M.E., & Zhang, M., (2016). Metabolic engineering of Zymomonas mobilis for 2,3-butanediol production from lignocellulosic biomass sugars. *Biotechnology for Biofuels. 9 (1)*, 189. http://dx.doi.org/10.1186/s13068-016-0606-y

88. Yang, Z.,& Zhang, Z., (2018). Production of (2R, 3R)-2,3-butanediol using engineered Pichia pastoris: strain construction, characterization and fermentation. *Biotechnology for Biofuels. 11 (1)*, 35. http://dx.doi.org/10.1186/s13068-018-1031-1

89. Yu, A., Zhao, Y., Li, J., Li, S., Pang, Y., Zhao, Y., Zhang, C., & Xiao, D., 2020. Sustainable production of FAEE biodiesel using the oleaginous yeast Yarrowia lipolytica. *Microbiology Open. 9 (7)*, e1051. http://dx.doi.org/10.1002/mbo3.1051

90. Zhang, Q., Hu, J., & Lee, D.-J., (2016). Biogas from anaerobic digestion processes: Research updates. *Renewable Energy, 98,* 108-119, https://doi.org/10.1016/j.renene.2016.02.029.

91. Zhou Adrian, & Elspeth Thomson. (2009), The development of biofuels in Asia, *Applied Energy, 86,* 11-20. http://dx.doi.org/10.1016/j.apenergy.2009.04.028

92. Zhu, L., Li, P., Sun, T., Kong, M., Li, X., Ali, S., Liu, W., Fan, S., Qiao, J., & Li, S., 2020. Overexpression of SFA1 in engineered Saccharomyces cerevisiae to increase xylose utilization and ethanol production from different lignocellulose hydrolysates. *Bioresource technology. 313*, 123724. http://dx.doi.org/10.1016/j.biortech.2020.123724

93. Zilberman David, Gal Hochman, Scott Kaplan, & Eunice Kim (2014). Political Economy of Biofuel, *Choices, 29(1),* 1–5 http://dx.doi.org/10.1007/978-1-4939-0518-8_11

JREE: Vol. 10, No. 4, (Autumn 2023) 131-145

Journal of Renewable Energy and Environment

Journal Homepage: www.jree.ir

Materials and Energy Research Center

MERC

Research Note

Predicting Solar Power Generation Based on the Combination of Meteorological Parameters in Iran: Neural Networks Approach

Abbas Ahmadi [a], Mahsa Zaman [b], Siab Mamipour [b*]

[a] *Department of Industrial Engineering & Management Systems, Amirkabir University of Technology (Tehran Polytechnic), Tehran, Iran.*
[b] *Department of Economics, Kharazmi University, Tehran, Iran.*

PAPER INFO

Paper History:
Received: 07 October 2022
Revised: 03 January 2023
Accepted: 17 January 2023

Keywords:
Solar Power Plants,
Metrological Parameters,
Artificial Neural Networks,
Iran

ABSTRACT

Clean solar energy is one of the best sources of energy. Solar power plants can generate electricity in Iran due to their large number of sunny days. This paper presents a short-term forecasting approach based on artificial neural networks (ANNs) for selected solar power plants in Iran and ranks the input variables of the neural network according to their importance. Two solar power plants in Hamadan province (Amirkabir and Khalij-Fars) were selected for the project. The output of solar power plants is dependent on weather conditions. Solar radiation on the horizontal plane, air temperature, air pressure, day length, number of sunny hours, cloudiness, and airborne dust particles are considered input variables in this study to predict solar power plant output. Forecasting model selection is based on considering zero and nonzero quantities of target variables. The results show that solar production forecasting based on meteorological parameters in the Khalij-Fars is more accurate than Amirkabir. The global solar radiation, air temperature, number of sunny hours, day length, airborne dust particles, cloudiness, air pressure, and dummy variables[1] are the order of the most important inputs to solar power generation. Results show simultaneous influences of radiation and temperature on solar power plant production.

https://doi.org/10.30501/jree.2023.363386.1461

[1]. The first half of the year is counted as one, and the second half is counted as zero.

1. INTRODUCTION

Energy production has long been accompanied by carbon emissions. Carbon emission is one of the most important environmental issues leading communities to use renewable energy sources. According to the EIA report of Country Analysis Executive summary, Iran was the fifth-largest oil producer in 2020 and the third-largest gas producer in 2019. Iran is ranked the third as the world's largest proved reserve holder of oil and second-largest proved reserve holder of natural gas. Easy access to fossil fuels means that 73 % of Iran's net electricity generation is from natural gas, 15 % from oil, 10 % from hydropower, 2 % from nuclear power plants, and just less than 1 % from coal and non-hydro renewable energies (EIA, 2021). There are several major oil and gas refineries in Iran, which have led to the country ranking seventh in carbon dioxide emissions worldwide indicating the importance of reducing them (Mamipour et al., 2019).

In spite of the cheaper cost of production of electricity from the combustion of fossil fuels and the lower amount of electricity produced by renewable power plants and fossil fuel power plants, the development of renewable energy is more pragmatic for environmental reasons. Since the establishment of new solar power plants in Iran is assigned to the private sector, the return of capital to investors is an important aspect and it is indicative that accurate predictions are critical to the establishment of new solar power plants. Some deficiencies might dampen investment enthusiasm for building new solar power plants. To maximize the amount of power generated in a given region, the meteorological variables affecting solar power output must be precisely calculated. A weather forecast can help investors select the optimal equipment and panels for a particular region. Due to Iran's vast size and wide range of climates, this factor is very important in choosing the best sites for establishing new power plants. An accurate assessment of the impact of weather variables on the output of solar power plants can greatly affect the optimum choice for their siting.

The general idea is that the high radiation points are the best regions for establishing solar power plants, but the temperature will rise as the sun rises, which will decrease the efficiency of the power plant (Bhavani et al., 2021). The main factors that affect the performance of power plants should be ranked empirically based on climate and region. In determining the output of solar power plants, only the factors

*Corresponding Author's Email: s.mamipoor@khu.ac.ir (S. Mamipour)
URL: https://www.jree.ir/article_166555.html

Please cite this article as: Ahmadi, A., Zaman, M. & Mamipour, S. (2023). Predicting solar power generation based on the combination of meteorological parameters in Iran: Neural networks approach. *Journal of Renewable Energy and Environment (JREE), 10*(4), 131-145. https://doi.org/10.30501/jree.2023.363386.1461.

that are most likely to affect solar power production should be taken into account.

As shown in Figure 1, solar power plants should be established in flat, wide areas that are near the main power grids. To ensure that the selected place is a suitable location concerning points in its immediate vicinity, one needs to examine and analyze the most important meteorological parameters of the selected region.

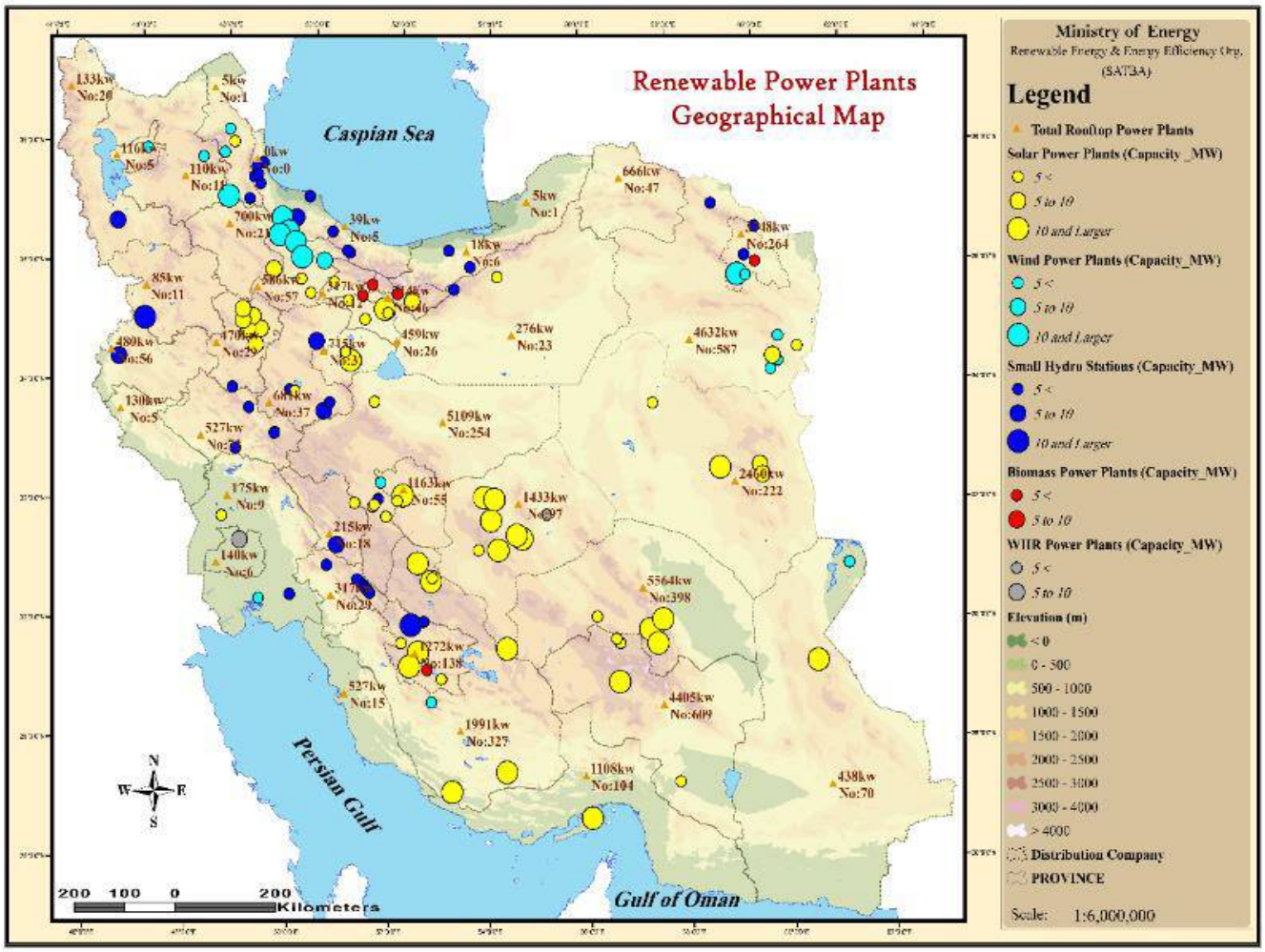

Figure 1. Overview of Iran's renewable power plants –end of year summary 2020

Figure 1 outlines the location and capacity of installed renewable power plants in Iran. The north of Iran has no solar power plants in operation because the weather condition is mild and there are more rainy days than sunny days.

As the sun shines for long periods in most regions of Iran, this clean energy may be used to generate electricity. As a result of intermittent fluctuations in PV[3] system output, production is also volatile during the day. Some particles in the atmosphere, such as water vapor and gases in the atmosphere, absorb some of the sun's rays, while others, such as dust particles in the atmosphere, disperse this energy into space (Carra et al., 2018). In general, about 340 watts per square meter of solar energy falls to the earth, but only 48 percent of it reaches the ground and can be used for solar energy production. 29 % of solar radiation is reflected in space by clouds, bright surfaces, and atmospheres. Gases in the atmosphere, dust, and other particles absorb 23 percent of this energy (NASA, 2009). Approximately, 48 % of this solar radiation can be used by photovoltaic panels to produce solar energy. Accordingly, the amount of sunlight reaching the earth's surface fluctuates with climate conditions, Thus, photovoltaic cells have variable output. Atmospheric fluctuations affect solar electricity production. There have been many studies attempting to model the output of solar energy production based on this fluctuation, which has led to numerous studies estimating the output of solar plants (Jung et al., 2020; Vaka & Talukdar, 2020; Zaaoumi et al., 2021; Zhao et al., 2021). The major categories for predicting solar energy are theoretical sunshine-based models, empirical meteorological parameters, and combinations of both meteorological models and sunshine-based models (Jahani et al., 2017). It has been reported that the amount of global solar radiation on the horizontal plane, air temperature, air pressure, number of sunny hours, cloudiness, dust particles in the air, and relative humidity can have an impact on the performance of solar power plants (Bugała et al., 2018; Khosravi et al., 2018; Loghmari et al., 2018; Rao et al., 2018).

In some cases, solar power plants are not located near meteorological stations. However, they need to measure meteorological parameters to accurately predict power plant output. Since establishing new meteorological stations is very expensive, this study investigates what can be done to make accurate predictions more reasonable.

2. LITERATURE REVIEW

[3] A photovoltaic (PV) system is made up of one or more solar panels with an inverter and other electrical and mechanical equipment that converts sunlight into electricity.

The following papers (Bugała et al., 2018; Ghritlahre & Prasad, 2018; Loghmari et al., 2018; Olden et al., 2004; Rao et al., 2018; Shireen et al., 2018) discuss the application of neural networks to solar system prediction. In previous research, neural networks have been used to estimate the following topics:

i. Solar energy prediction
ii. Solar radiation prediction
iii. Predicting the output of solar systems
iv. Meteorological ANN models for Iran's weather condition

Detailed in the topics below, it explains that the connection weight method is selected in the current research based on previous studies to analyze the importance of input variables.

i. Solar energy prediction

Shireen et al. (2018) developed a model based on repeated multi-purpose learning. Owners of solar power systems can benefit from modeling PV output time series because this allows them to understand how energy systems behave over time. An effective method of multifunctional learning is proposed for the MTL-GP-TS time series to predict PV output. By combining PV measurements from multiple solar panels with similar traits, measurements are improved. Learning the proposed MTL-GP-TS model iteratively uncovers hidden or missing values in a set of panel-related time series that are potentially useful in predicting PV trends. Furthermore, it improves the traditional multifunctional learning process and generalizes the Gaussian process of learning both global trends and irregular local components. Based on a real-world case study, the proposed approach can improve conventional approaches significantly.

ii. Solar radiation prediction

Halabi et al. (2018) evaluated the performance of hybrid models of adaptive neuro-fuzzy inference systems for predicting monthly solar radiation. The output of solar energy systems is highly dependent on solar radiation. Therefore, accurate forecasting of solar radiation is very important. Hence, a consistent independent fuzzy inference system and a hybrid model were developed to predict monthly solar radiation following various meteorological parameters such as irradiation time S(h) and air temperature. Their proposed hybrid models include particle swarm optimization, genetic algorithms, and differential evaluation. To evaluate the capability and efficiency of the proposed model, several statistical indicators such as mean squared error, correlation coefficient, and mean absolute error are used. Performance evaluation over various statistical indicators exhibited a high correlation for all of the developed modules. Hybrid particle swarm optimization has obtained the best statistical indicators in all of the models. An accurate comparison with other studies has been performed to validate the accuracy of the proposed prediction models and their appropriateness. The results showed that the developed hybrid models had the highest reliability, more accurate estimation, and the most efficient methods for global prediction.

Loghmari et al. (2018) compared the performance of two models of global solar radiation. They developed two global satellite models for solar radiation: an artificial neural network (ANN) and a reverse weighting model (IDW). The goal is to predict global solar radiation at a distance of more than 50 km. The ANN model uses meteorological data in the inventory target area, while the IDW model employs global solar radiation measured in neighboring areas. For the construction and validation of the models, for 5 consecutive years (2008-2012), the values of 5 different meteorological parameters were collected monthly from 10 meteorological stations located in the south and center of Tunisia. The evaluation results of the two models provide comparable results. For the developed ANN model, the average root of the mean square error is 6.4 %, while for the IDW model, it is 5.11 %. The IDW model is simpler and slightly more accurate than the ANN model. This study examined the behavior of two models for different climate conditions through two scenarios. The results show that the number of samples that ANN is trained to predict Global Horizontal Irradiance (GHI) is more important than the climatic conditions from which these samples are retrieved. However, providing input data from sites with similar weather conditions to the predicted area increases the accuracy of the IDW model. In the present study, data from meteorological stations are collected because, in real conditions, all countries cannot have free access to satellite meteorological data.

Rao et al. (2018) analyzed different combinations of meteorological parameters in predicting the amount of total horizontal solar energy radiation with a neural network approach. For the input variables of biennial data for the characteristics of total daily radiation, minimum temperature, maximum temperature, minimum and maximum temperature difference, sunny hours, sunny hours in theory, and extraterrestrial radiation are considered. Different combinations of input variables were considered to predict monthly solar radiation. Out of 32 possible modes, models with a combination of the theoretical sunny hours and extraterrestrial radiation had the best performance. These two parameters are available for any location and do not need to be measured. The best performance belonged to the case with the least number of inputs. In the present study, we try to eliminate unnecessary parameters and unreasonable combinations from the predicted models and with fewer computations try to get more accurate results.

iii. Predicting the output of solar systems

Short-term predictions of power generation in photovoltaic systems were made (Bugała et al., 2018). An in-depth analysis of the input data measured in Poland showed that the effect of some variables such as air pressure and day length was statistically insignificant. The values of skewness, elongation, and the results of experiments applied to investigate the distribution of the dependent variable for daily power generation indicated that the linear regression model should not be the only method in the forecasting process. The developed neural network was based on the RBF model with a quality test of approximately 93 % and an RMS error of 0.02 %. The input variables required for the proposed ANN model included the number of sunshine hours, day length, air pressure, maximum air temperature, amount of daily radiation, and cloudiness.

Ghritlahre & Prasad (2018) applied neural network techniques to predicting the performance of solar collectors. Solar collectors are designed for low- to medium-temperature ranges. Therefore, the optimal design of collector systems helps to increase solar energy efficiency. In this research, a neural network technique is proposed to estimate the thermal

performance of the multilateral flow of a porous solar air heating bed. This study further addresses the research gap in research conducted on solar collectors. The present study has confirmed that both temperature and global horizontal solar radiation in real case studies are simultaneously significant to the output of solar power plants.

iv. Meteorological ANN models for Iran's weather condition

Gorjian et al. (2015) modeled solar radiation potential in Iran based on the meteorological and geological data of 31 stations spreading all over the country. They considered solar radiation as the target variable and month of the year, latitude, longitude, altitude, sunshine duration, minimum air temperature, maximum air temperature, maximum daily earth temperature, atmospheric pressure, and precipitation as input variables.

Solar radiation reaching the Earth was modelled using ANFIS, NN-ARX (Piri & Kisi, 2015). It was a case study of two synoptic stations of Zahedan and Bojnurd. The data included sunshine hours, maximum and minimum temperatures, average relative humidity, and solar radiation. A comparison was made between artificial intelligence models and empirical models. It was found that ANFIS performed better than the empirical models in estimating daily solar radiation.

Khosravi et al. (2018) performed hourly predictions of solar radiation on Abu Musa Island using machine learning algorithms. This study proposed machine learning algorithms for predicting hourly solar radiation. Prediction models were developed based on two types of input data. The first model uses local time, temperature, pressure, wind speed, and relative humidity as input variables of the model (N1), and the second model predicted solar radiation (N2). Predictive models use only past solar radiation values to estimate future values. For this purpose, a multilayer feed-forward neural network (MLFFNN), radial basis function neural network (RBFNN), support vector regression (SVR), fuzzy inference system (FIS), and an adaptive fuzzy inference system (ANFIS) were used. The results showed that for N1 models, SVR and MLFFNN had the maximum predicted solar radiation performance with R = 0.9999 and 0.9957, respectively. For N2, SVR, MLFFNN, and ANFIS models reported a correlation coefficient more than 0.95 for the test data set.

Many empirical studies predict solar radiation depending on the weather conditions in Iran, but none of these studies has investigated the impact of meteorological parameters on the production of solar power plants, and their focus is only on prediction solar radiation. Obviously, to predict the production of solar power plants based on meteorological parameters, real and accurate data are required, which is followed in this research. Therefore, the main contribution of this paper is that it tries to predict the output of solar power plants by using meteorological parameters. In this study, eight meteorological parameters that affect the output of solar power plants are considered as input variables. In meteorological and hydrological research, the question always arises as to which one of the input variables of the neural network has a more important role in prediction. Although model sensitivity analysis in most studies is not common, there are methods to determine the importance of input variables. Garson methods, connection weights, partial derivatives, sensitivity analysis, adding a parameter to the model, and removing a parameter from the model are some of the methods for measuring the importance of parameters (Olden et al., 2004). Based on the research of Olden et al. (2004), the best method is the connection weights. In this study, the connection weights method is used to rank the importance of input variables.

3. METHODOLOGY

ANN models are the most common data mining models inspired by human brain functions and are used to model both linear and nonlinear systems. In the present study, data with three-hour and daily frequency for the meteorological parameters are considered from the IRIMO organization for the parameters of cloudiness, temperature, air pressure, and the number of sunny hours, but the purpose of the study includes hourly and daily prediction. Consequently, hourly and daily data sets were retrieved from the SODA website for temperature, air pressure, solar radiation, day length, and global horizontal irradiation. Since the website does not report cloudiness information and the number of sunny hours, data from the IRIMO organization was used. By assuming that the amount of cloudiness and the number of sunny hours during three hours are constant, these two variables are converted into hourly ones. One of the highly correlated variables of meteorological features is cloudiness. This variable is often reported at airport meteorological stations. In the city of Qahavand, cloudiness was not reported for 5 months; therefore, cloudiness data were retrieved from the nearest meteorological station, Hamadan airport station. ANNs were made of three layers. The first one is called the input layer which consists of input variables introduced in Table 1.

Table 1. Input and output parameters

Input Output	Symbols	Unit	Frequency	Source	Explanation
Input	GHI	Wh/m^2	Hourly & daily	SODA (Professionals, 2021)	Global solar radiation on a horizontal plane at the ground level
	Temp	Celsius degree[4]	Hourly & daily	SODA	Temperature at a height of 2 meters above the ground
	Press	hPa 5	Hourly & daily	SODA	Air pressure
	Dayl	Hour	Daily	SODA	Length of the day from sunrise to sunset
	Nsun	Hour	Daily	IRIMO (IRIMO, 2018)	Number of sunny hours
	C	Okta	Each 3-hours	IRIMO	Cloudiness
	Dust	Nanometer	Each 3-hours	SODA	Dust @ 550 nm
	Dummy	-	-	-	first half of the year = 1; second half of the

[4] Two data collections for temperature are acquired from IRIMO and SODA website.
[5] Hectopascal (100 x 1 pascal) - pressure units.

					year = 0.
Output	Target	kWh	Hourly & daily	IGMC (IGMC, 2017)	The amount of solar power generation per unit

The second one is called the hidden layer which is the center of all computations, weights, biases, activation functions, and calculation nodes located in this layer. Finally, the last layer is called the output layer which only shows the result of computations in the hidden layer. A brief diagram of ANN with input and output parameters is shown in Figure 2.

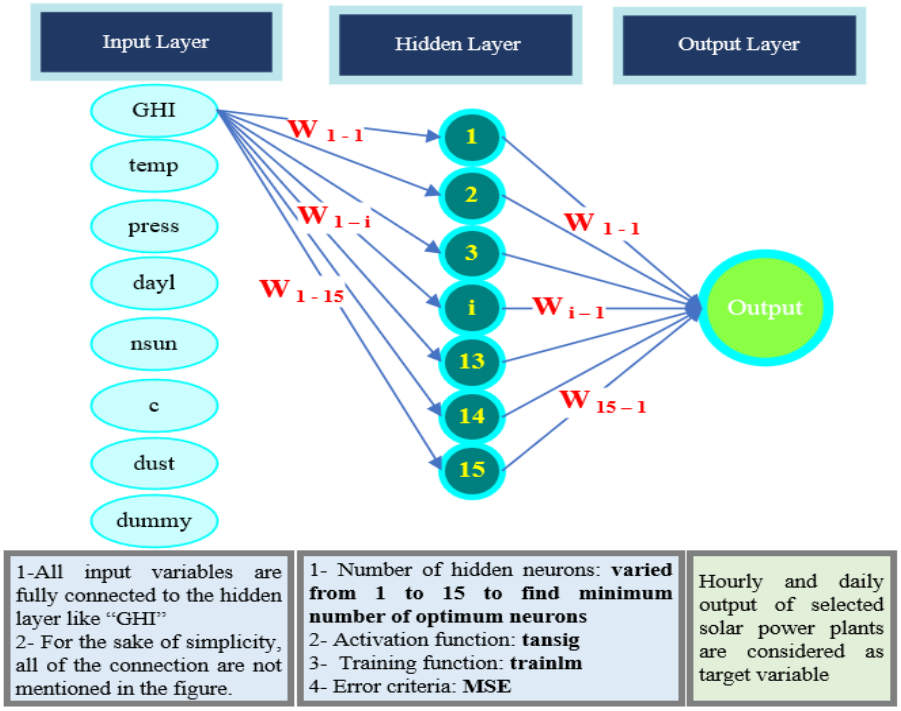

Figure 2. Schematic structure of neural networks

The purpose of the current study is to propose how to select input variables to estimate an accurate model for predicting the output of solar power plants with meteorological station data. The process of estimation of models in this paper is shown in Figure 3. After selecting the best estimation model, input variables are ranked based on the connection weight method. The proposed model can be used to select input variables to estimate the output of solar power plants. Indeed, the current study is done with real meteorological station data and it can be useful for medium to small power plants that do not have access to satellite meteorological data.

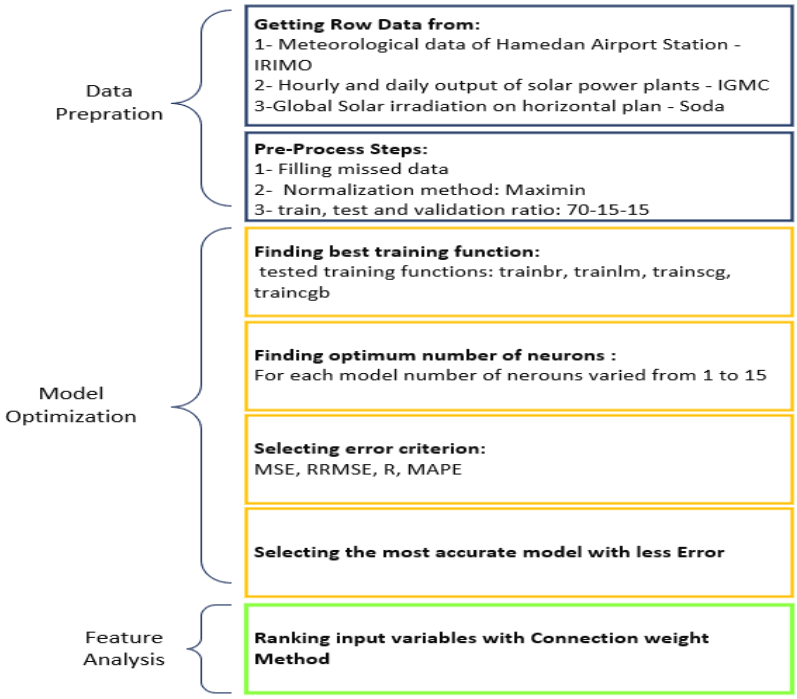

Figure 3. The process of modeling

3.1. Pre-processing steps

The algorithm of the proposed approach is given in Algorithm 1. For minimizing the estimation error, some steps are necessary for cleaning data before estimation. Preprocessing eliminates the negative effect of different input variable scales. The min-max method is used in the current study to normalize input variables and convert all input and target variables to ranges 0 and 1. In this method, the data is normalized based on the following formula:

$$x'_{ij} = \frac{x_{ij} - x_{mini\,j}}{x_{maxi\,j} - x_{mini\,j}}(x'_{maxi\,j} - x'_{mini\,j}) + x'_{mini\,j}$$

where $x_{maxi\,j} = \max x_{ij}$ indicates the maximum value of variable j and $x_{mini\,j} = \min x_{ij}$ indicates the minimum value of variable j. Moreover, $x'_{maxi\,j}$ and $x'_{mini\,j}$ are maximum and minimum values of variable j, respectively, in the new range. In the current study, $x'_{maxi\,j}$ and $x'_{mini\,j}$ are considered 1 and 0.1 to normalize data between (0.1,1).

3.2. Select the best training function

To choose the best training function, it is necessary to compare the performance of different training functions. Daily data from the Khalij-Fars power plant were used for this purpose. Each neuron is trained 30 times with a specific training function. As the weights and biases are assigned random values at every execution of the neural network, the error is sensitive to sampling and it was not satisfactory to rely on the results of one run of the model. Therefore, for each neuron i, the network is trained 30 times with each of these training functions. The function with the least mean squares error was selected as the optimum training function.

3.3. Find the optimal number of neurons

Data were randomly divided into three sets of training, validation, and test data with a ratio of 15-15-70. In each model, for one neuron up to 15 neurons, the model was repeated 100 times so that we could find the minimum optimal neuron. The average MSE error of 100 repetitions was calculated for each neuron. The model that was minimized in terms of the average MSE error of the validation dataset was selected as the optimal network.

3.4. Estimate model and rank input variables

In the present study, the logsig transfer function is used for the Multi-Layer Perceptron neural network (MLP). In the following, we turn to the selection of the optimal neural network model. The first step is to select the appropriate training function and the second step is to find the optimal number of neurons.

Algorithm1. Algorithm of the proposed approach

- **Input variables**: i = [GHI, Temp, Press, Dayl, Nsun, C, Dust, Dummy]
- **Target variable**: output of solar power plants
- **Final result**:

1-Predicting the output of solar power plants

2- Ranking the importance of each variable by the connection weight method

- **Data pre-process steps**:

Step1: Normalizing data with maximin method between (0.1,1) using the following equation:

$$x'_{ij} = \frac{x_{ij} - x_{mini\,j}}{x_{maxi\,j} - x_{mini\,j}}(x'_{maxi\,j} - x'_{mini\,j}) + x'_{mini\,j}$$

Step2: Find the best training function among Bayesian Regularization Backpropagation (trainbr), Levenberg-Marquardt (trainlm), Scaled Conjugate Gradient (trinscg), and Conjugate Gradient with Powel/Beale Restarts (traincgb).

Step3: Find the optimum number of neurons for each model

- **Model estimation**

Step4: Estimate the model with 8 input variables and evaluate the error criteria

Step5: Save the network weights:
1- Input to hidden layer weights: $W_{input(\,i\,)\,-\,hidden\ neuron(\,j\,)}$

2- Hidden layer to output layer weights: $W_{hidden\ neuron(\,j\,)\,-\,output}$

Step6: Eliminate one variable and estimate the model with 7 input variables and evaluate error criteria.

Step7: Save the network weights:
1- Input to hidden layer weights: $W_{input(\,i\,)\,-\,hidden\ neuron(\,j\,)}$

2- Hidden layer to output layer weights: $W_{hidden\ neuron(j\,)\,-\,output}$

- **Ranking parameters**

Step8: Connection weight method: The calculations of the method of connection weights are as follows:

1- Multiplication of the transpose of weights from the input layer to the hidden layer by the weights of the hidden layer to the output layer (Each row of this matrix represents an input).

$$W - Connectionweightmethod_{input(i)} = W_{input(i)-hiddenneuron(j)} * W_{hiddenneuron(j)-output}$$

2- Summarization of the numbers in each row of this matrix indicates the importance of its corresponding property.

$$\text{Total Rank of Input (i)} = \sum_{j=1}^{n}(W_{input(i)-hidden\ neuron(j)} \times W_{hidden\ neuron(j)-output})$$

3.5. Case study

The Iranian grid management company provided daily and hourly output data for all in-operation solar power plants. As shown in Figure 4, Hamedan is ranked the first in solar energy production. We selected two power plants with the most available data from the received data. In Hamadan province, the final outputs of two solar power plants, Amirkabir and Khalij-Fars, are considered since their establishmen.

The target variable for this study is the amount of electricity generated by selected solar power plants. In three formats, hourly, daily, and monthly, the Iran power grid management company has provided data related to the production of the Khalij-Fars power plant located in the city of Qahvand during the period of 2017/03/19 until 2018/03/20 and data related to Amirkabir, located in the city of Qerkhlar, from the date the power plant began operating, 2017/01/28, until 2018/03/20.

According to Google maps, the distance between Amirkabir solar power plant and Hamedan airport is 14.7 km (Map, 2023a) and the distance between Khalij-Fars solar power plant and Hamedan airport is 33.1 km (Map, 2023b).

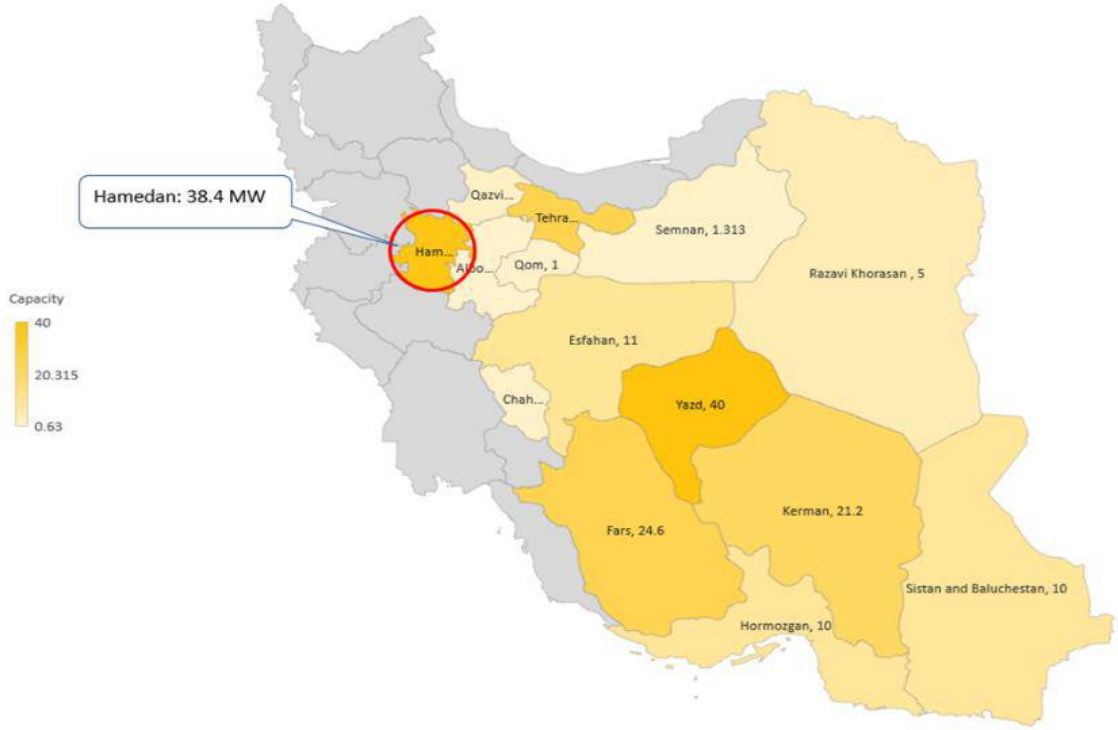

Figure 4. The total number of installed photovoltaic power plants in each province (MW) – Iran

Table 2. Description of data and the geographical location of selected solar power plants

Plant	City	Longitude	Latitude	Start date	End date	Number of daily data with zero production	Number of hourly data with non-zero production	Number of hourly data with zero production
Khalij-Fars	Qerkhlar	48.5550	34.9847	2017/03/21	2018/03/21	417	5367	10008
Amirkabir	Qahavand	48.9984	34.8586	2017/03/21	2018/03/21	426	5438	10224

In previous studies and as mentioned above, the temperature negatively affects solar collector performance (Ma et al., 2020). It is also shown in Figures 5 and 6. Although greater solar radiation occurs during warm days of the year when temperatures exceed 25 degrees Celsius, PV solar energy plants often produce the most when temperatures are below that level.

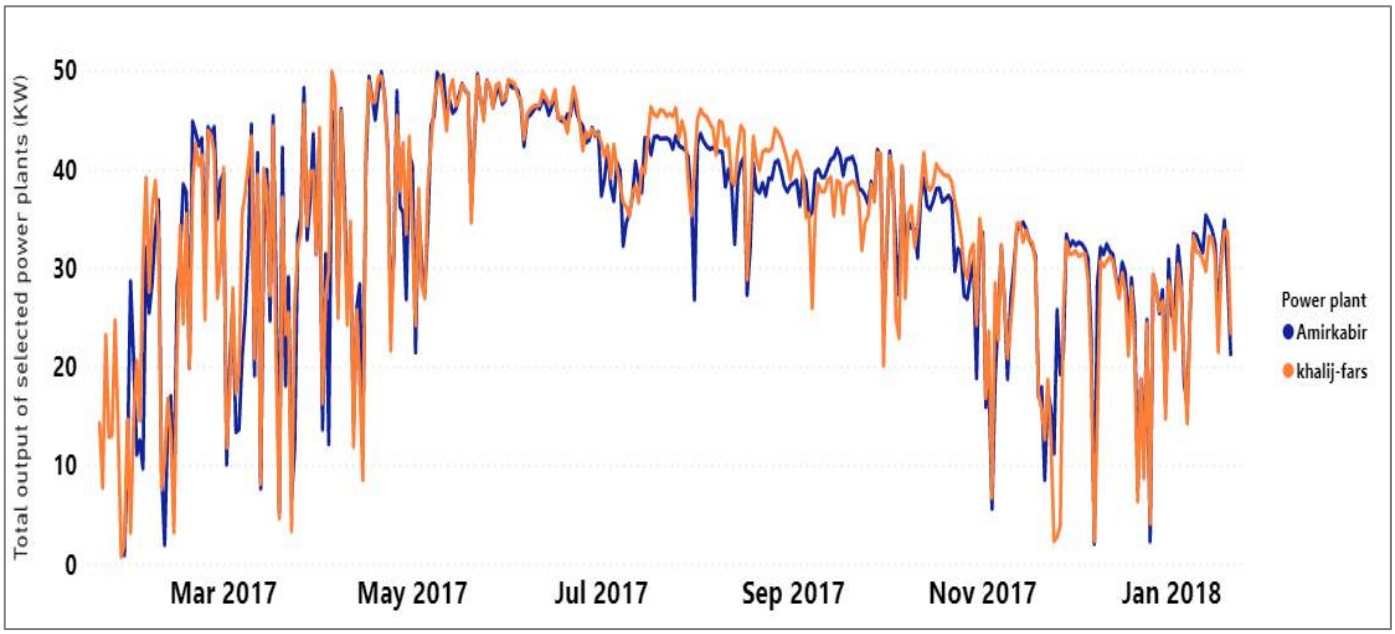

Figure 5. The daily total output of the selected solar power plants (IGMC, 2018)

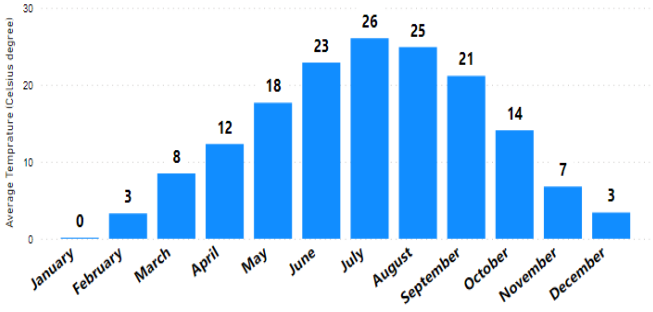

6(a) Average Temperature by Month – Hamedan airport station

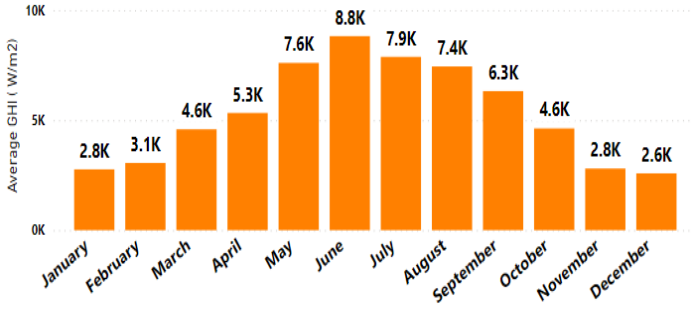

6(b) Average GHI by month – Hamedan airport station

Figure 6. Average Temperature & GHI by month – Hamedan airport station (IRIMO, 2018)

3.6. Assessment criteria

A prediction model's accuracy must be checked after evaluation. For the time series Y_t which contains k elements, the time series f_t is estimated. Table 3 presents the performance evaluation functions and a brief description of them.

Table 3. Assessment criteria and descriptions

The formula of the performance function	Description	Performance analysis
$MAPE = \frac{\sum_{t=1}^{k} \left\lvert \frac{y_t - f_t}{y_t} \right\rvert}{k}$	Mean absolute percentage error (MAPE) is used to differentiate between prediction models and to select the optimal model	• MAPE < 10 %: High predictive power • 10 % < MAPE < 20 %: Good predictive power • 20 % < MAPE < 50 %: Logical predictive power • MAPE > 50 %: Incorrect prediction
$MSE = \frac{\sum_{t=1}^{k}(y_t - f_t)^2}{k}$	Mean square error (MSE) is one of the most popular performance evaluation criteria. The most important drawback of this criterion is that it increases the effect of large errors.	Nearest to zero shows a more accurate forecast
$RRMSE = \frac{\sqrt{\frac{\sum_{t=1}^{k}(y_t - f_t)^2}{k}}}{\sum_{t=1}^{k} y_t} * 100$	This error is the root of RMSE and is called (RRMSE). In the present study, the model was selected with the highest accuracy by comparing the two criteria of MAPE and RRMSE.	• RRMSE < 10 %: High predictive power • 10 % < RRMSE < 20 %: Good predictive power • 20 % < RRMSE < 30 %: Logical predictive power • RRMSE > 30 %: Incorrect prediction
$R = \frac{\sum_{i=1}^{k}(f_i - \bar{f})(y_i - \bar{y})}{\sqrt{\sum_{i=1}^{k}(f_i - \bar{f})^2}\sqrt{\sum_{i=1}^{k}(y_i - \bar{y})}}$	The correlation coefficient called (R) represents the percentage of a total change of the dependent parameter, which can be explained by independent parameters. If the value of the correlation coefficient is exactly 1, it indicates that 100% of the dependent parameter changes are explained by independent parameters.	• R > 0.9 shows well-fitted models • 0.8 < R < 0.9 shows good accuracy • 0.5 < R < 0.8 shows weak fitted models

4. RESULTS AND DISCUSSION

4.1. Heatmap correlation of all variables in Khalij-Fars dataset

The heatmap correlation of all input and output variables for the Khalij-Fars power plant is shown in Figure 7. As is shown in Figures 7-a and 7-b, there are some differences between the correlation of parameters in daily and hourly inputs and target. In daily estimation, three more correlated factors are Nsun GHI and Dayl. In hourly estimation, 3 more correlated factors are GHI temperature and Nsun.

4.2. Heatmap correlation of all variables in the Amirkabir dataset

The heatmap correlation of all input and output variables of Amirkabir solar power plant is shown in Figure 8. Based on Figure 8-a, six input variables correlate more than 0.6, showing that our daily prediction will be more precise than the hourly forecast. In daily estimation, three more correlated factors are Nsun, GHI, and Dayl. In hourly estimation, three more correlated factors are GHI temperature and Nsun; however, as shown in Figure 8-b, just one input variable (GHI) has a correlation above 0.5 and it shows that hourly forecasts are highly dependent on the GHI data. This result shows that in both power plants, three more correlated factors in daily and hourly estimations are the same; therefore, it is confirmed that the most important factor should be selected based on the granularity of the model.

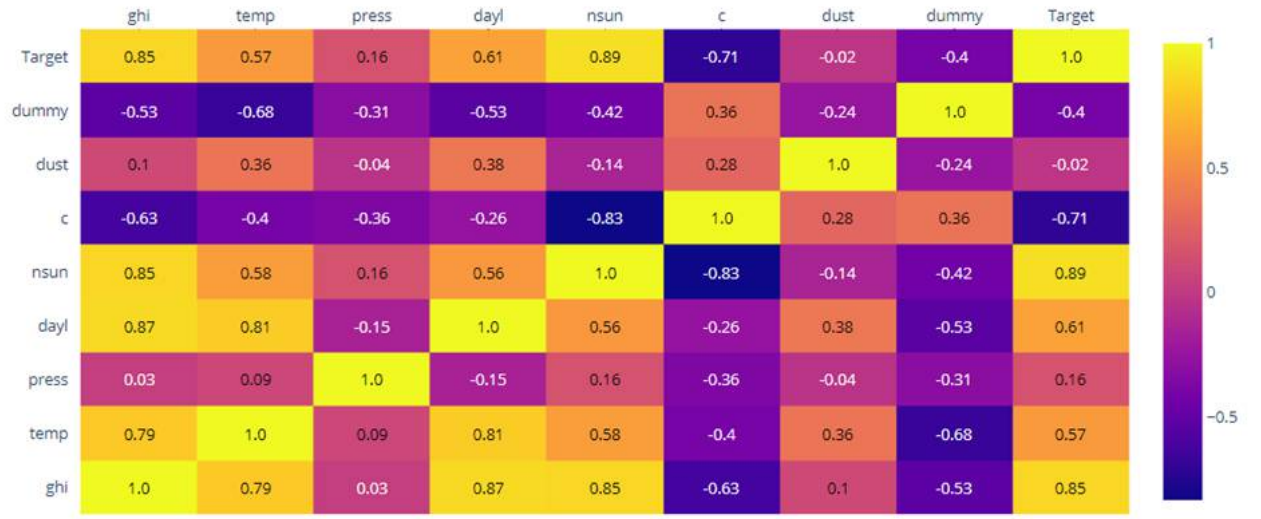

7(a) Heatmap correlation of daily inputs

7(b) Heatmap correlation of hourly inputs

Figure 7. Heatmap correlation of inputs and target - Khalij-Fars

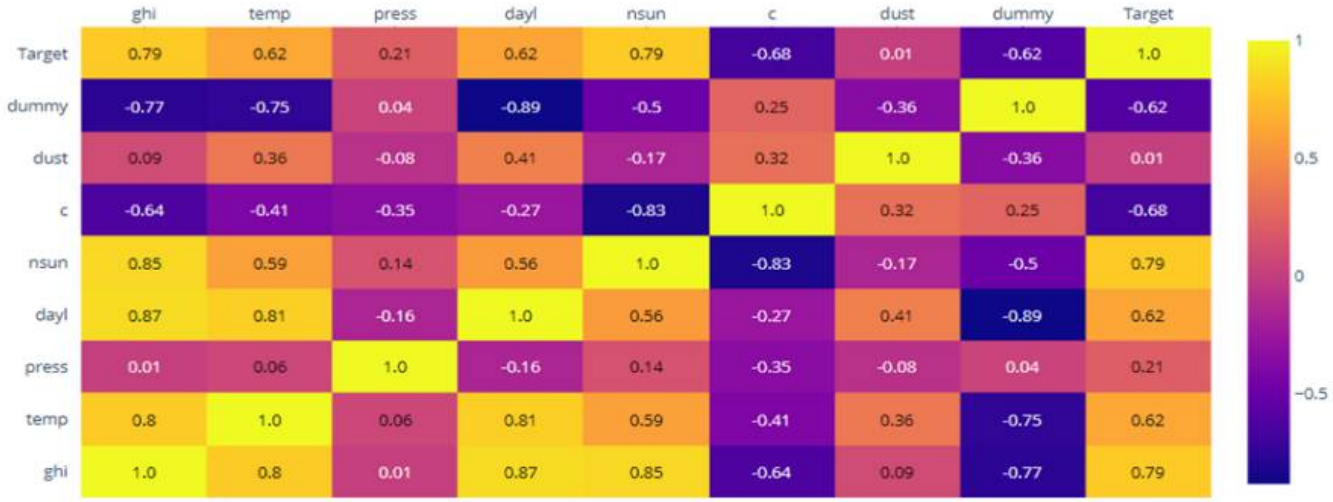

8(a) Heatmap correlation of daily inputs

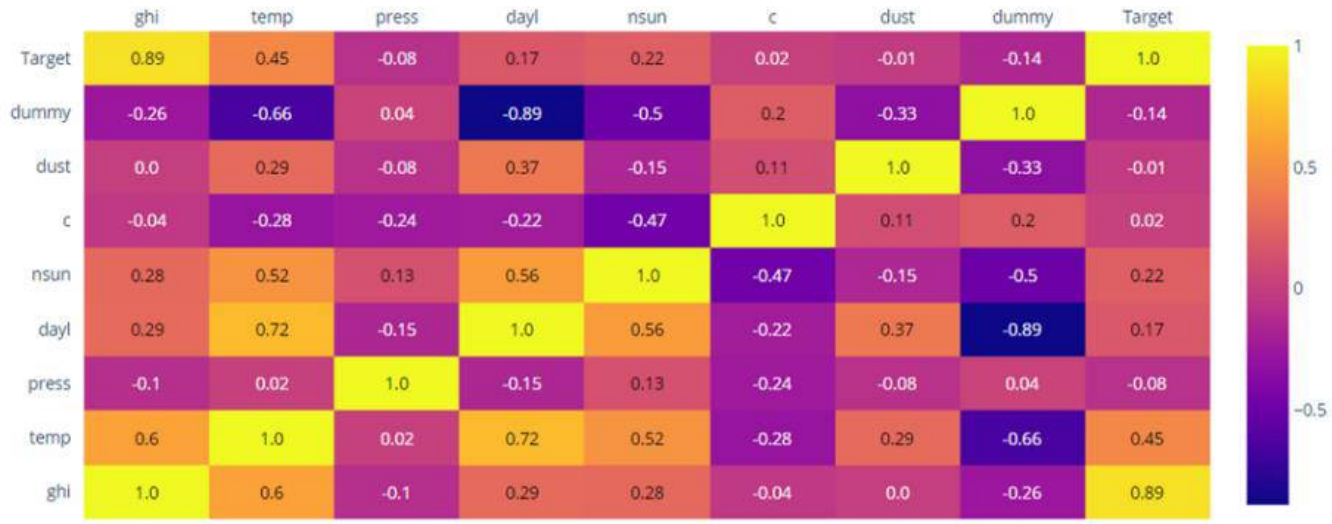

8(b) Heatmap correlation of hourly inputs

Figure 8. Heatmap correlation of inputs and target- Amirkabir

4.3. Selecting the best training function

As shown in Figure 9, the mean squared error of four training functions is compared to select the best function with minimum squared error. For each training function, the number of neurons varied from 1 to 10 to see the result of an increasing number of neurons on the performance of the train function. As shown in Figure 9, the network error with the trainlm and trainbr training functions is similarly lower than trinscg and traincgb. The model error with the trainlm training function and 7 neurons (i = 7) has the least error. As the selection of the optimal neuron and training function should be based on the selection of the neuron with the least average squared error in the validation data set, the Cumulative error distribution diagram is used to compare the four training functions.

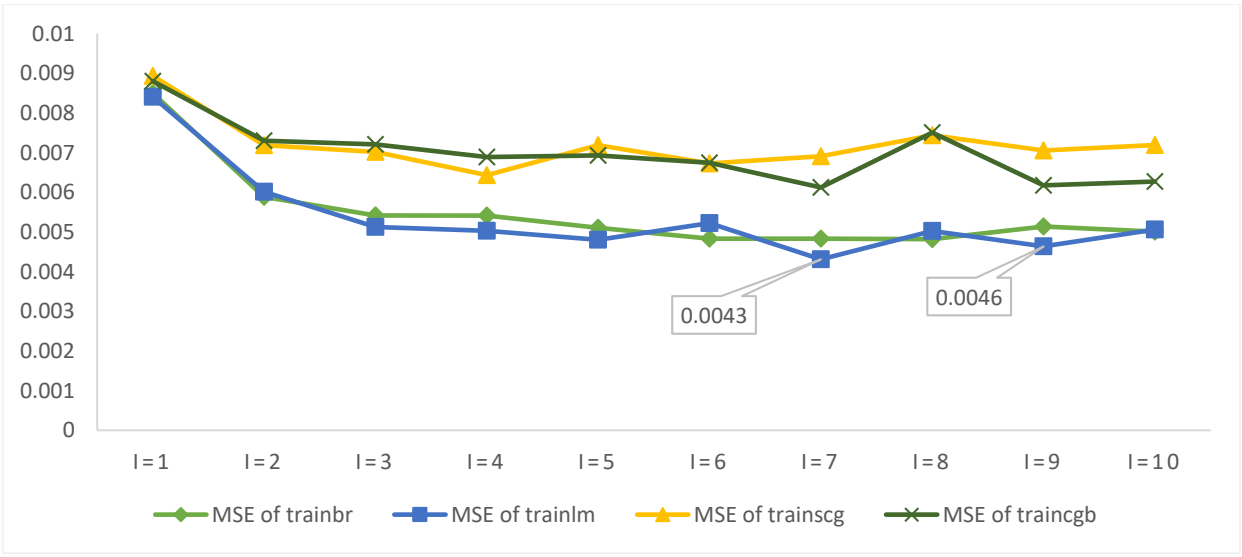

Figure 9. Selecting the best training function

4.4. Finding optimized network

The initial phase of our study will examine the network outputs of each solar power plant. First, a network with 8 parameters is estimated. Then, one of the features is removed from the model. A feature is omitted from every model, The optimal network structure (based on the least number of neurons and the best training function) is determined by the least amount of error in the validation data set. Errors are more likely to occur when a variable is highly correlated with a target variable. The optimal models are selected based on the MSE, RRMSE, R, and MAPE values. According to the correlation-weight method, the variables are then ranked based on their importance. Reported errors are calculated based on the average of 100 replicates.

4.4.1. MSE criterion

As shown in Figure 10, the hourly forecast with zero production in the Khalij-Fars power plant has the least error. If we increase the number of data, then MSE errors will decrease. Therefore, if we compare only MSE errors, we cannot determine the most accurate models between hourly forecast and daily forecast.

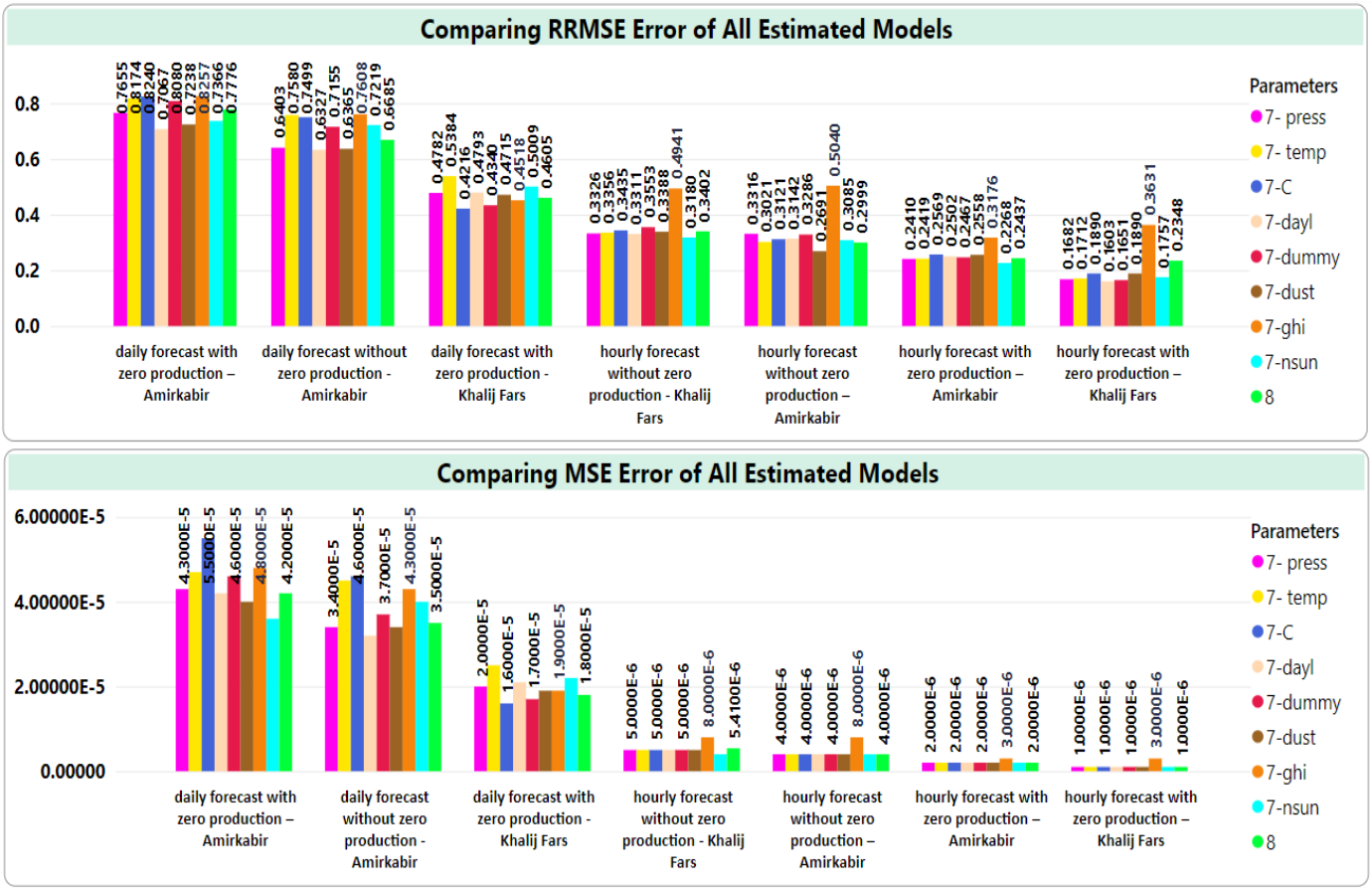

Figure 10. MSE and RRMSE error criteria of forecast models

4.4.2. RRMSE criterion

As shown in Figure 10, the hourly forecast with zero production in the Khalij-Fars power plant has the least RRMSE error**.**

4.4.3. R criterion

In Figure 11, hourly forecast with zero production in the Khalij-Fars power plant model with 7 input variables without the air pressure has the nearest value of 1. It means that the elimination of the pressure from the input variables will increase the R and decrease the MAPE and it shows that air pressure does not have a major impact on the output of solar power plants.

4.4.4. MAPE criterion

As shown in Figure 11, Khalij-Fars daily forecast with zero production without considering air pressure has the lowest MAPE error. In all the estimated models, elimination of GHI has the most negative effect on the performance of estimation and this shows the obvious high impact of GHI on the output of the solar power plant.

Compared to estimations of the Amirkabir power plant, the Khalij-Fars power plant has the least errors. To improve forecasting at Amirkabir, more accurate data is needed. In the absence of data on cloudiness parameters and the number of sunny hours, Hamadan airport data was used, which is approximately 15 kilometers away from the power plant. Note that the number of sunny hours was only reported once during the day and this variable was reported only at airport meteorological stations. It was expected that the number of sunny hours would be highly correlated with the amount of energy produced; however, the frequency of this variable did not line up with the hourly forecast (it was reported every 3 hours in the IRIMO dataset). As a result, removing this variable improves model performance in most of the hourly forecast models.

4.5. Importance analysis of input variables by connection weight method

In all the forecasting models, the connection weight method is run and the most important input parameters are ranked. The most important factor in all of the models is global horizontal irradiance, as illustrated in Figures 12. The second important parameter for the Khalij-Fars solar power plant (which is the more accurate forecast) is the temperature, and the third is the number of sunny hours. According to the connection weights method, the number of sunny hours appears to be an important variable in the model. Recent studies have supported this finding (Bugała et al., 2018; Loghmari et al., 2018; Rao et al., 2018). The number of sunny hours has been reported as an important and influential variable in the amount of solar energy production. This demonstrates the importance of measuring the number of sunny hours at meteorological stations on an hourly basis. As mentioned above, the best prediction model for the Amirkabir power plant was introduced the daily forecast mode with zero production and without air pressure.

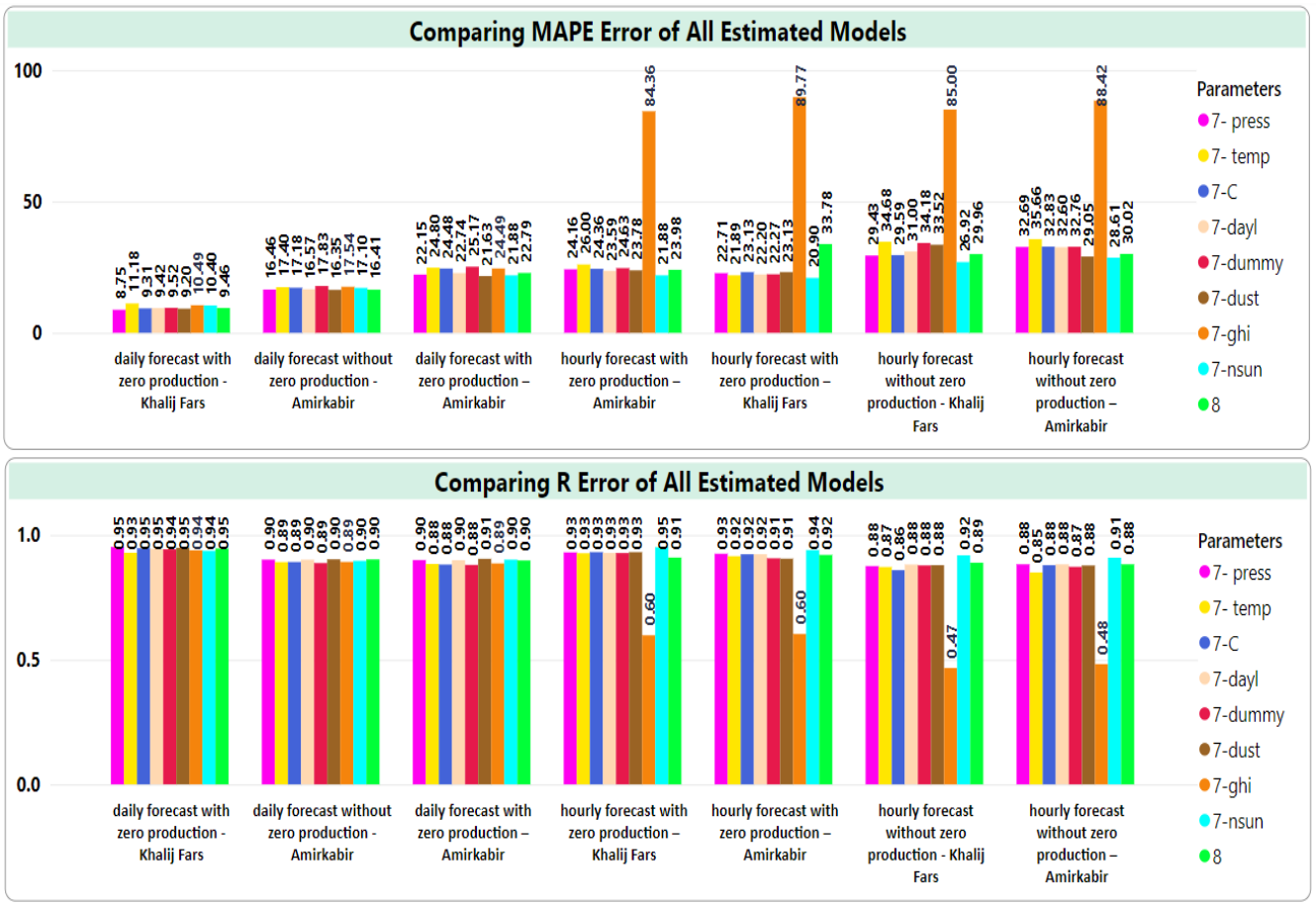

Figure 11. R and MAPE error criteria of the forecast models

Table 4. Finding minimum error in all the estimated models

Model	MSE	RRMSE	MAPE	R
Hourly forecast with zero production Khalij-Fars power plant	*	*		
Daily forecast with zero production Khalij-Fars power plant			*	*

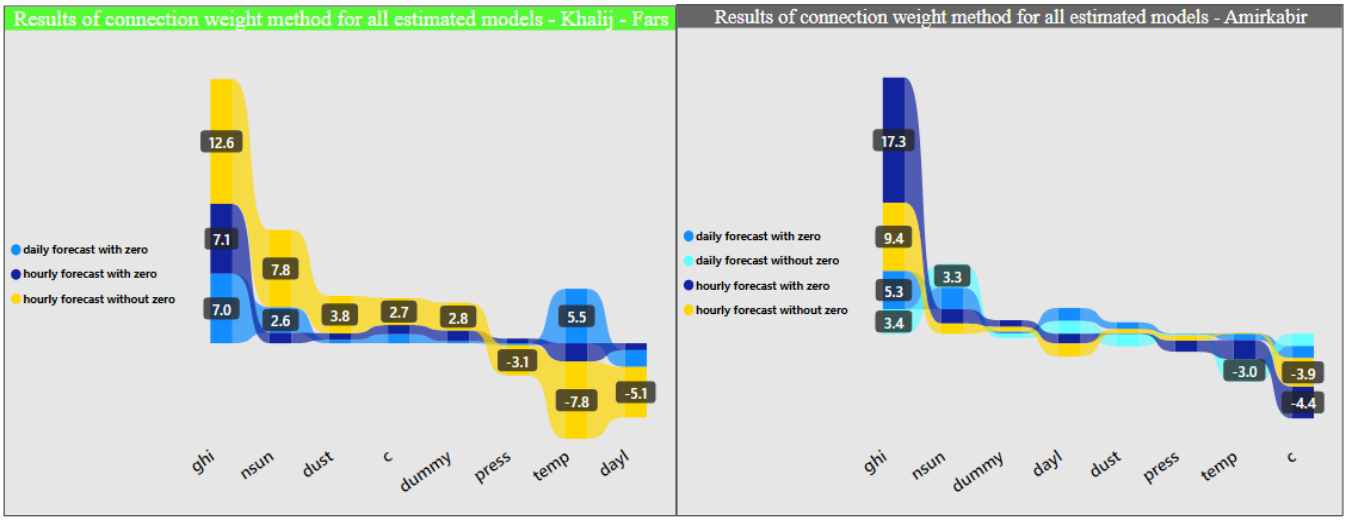

Figure 12. Result of the connection weight method

Consequently, this mode should be used to analyze the importance of input variables since it is the most accurate. In the case of daily forecast mode without zero production with seven variables without dust, the most important variable is global horizontal irradiance; the second one is the number of sunny hours; and the third one is temperature.

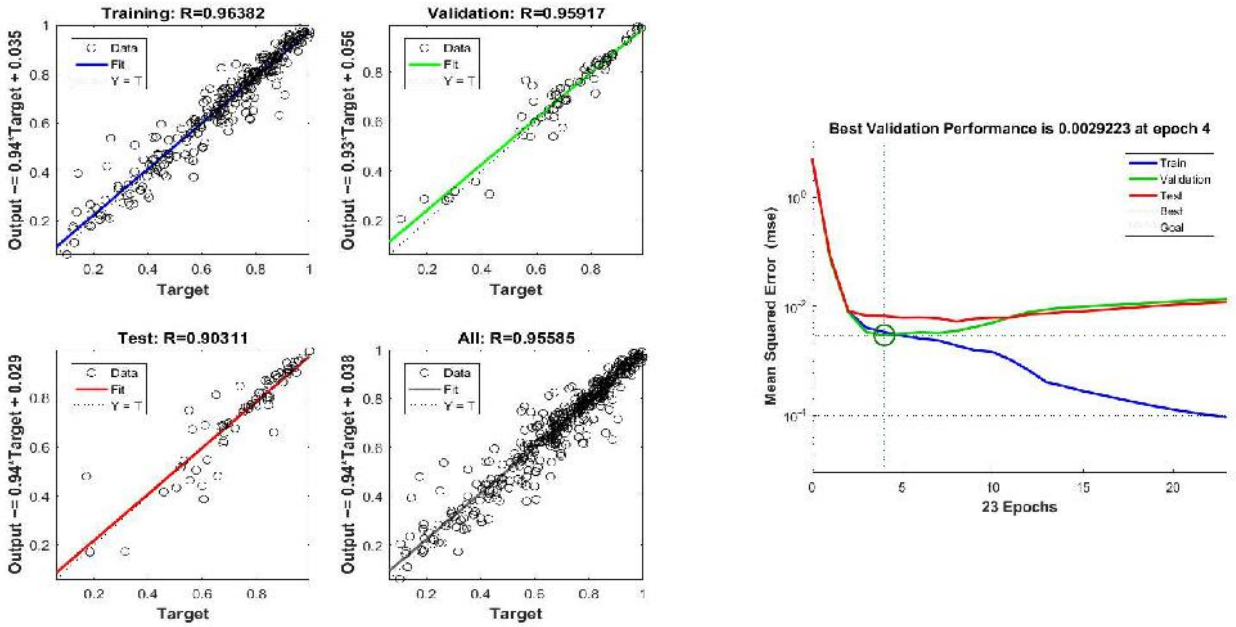

Figure 13. Performance plot of the best-estimated model Khalij-Fars daily forecast without considering air pressure

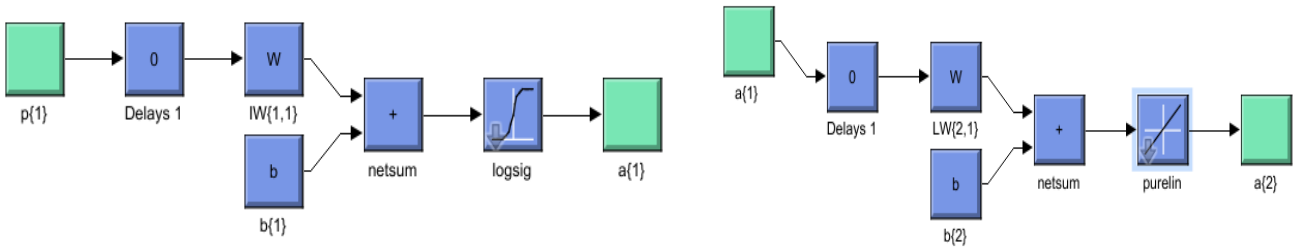

Structure of input layers to the hidden layer Structure of the hidden layers to output

Figure 14. Structure of the estimated neural network

According to the results in Figure 13, all datasets show that the value of R is greater than 0.90; thus, the results of the connection weight method for Khalij-Fars daily forecast without considering air pressure with 6 neuron is considered the best-estimated model. Figure 14 shows the structure of the estimated network.

The equation of best-estimated model (Khalij-Fars daily forecast) without considering air pressure with 6 neurons is reported below:

$$W_{\text{input(i)-hidden neuron(j)}} * \text{input(i)} = \alpha_j$$

$$O_1 = f(\alpha_1) = f((-2.27 * \text{ghi}) + (1.74 * \text{temp}) + (2.50 * \text{dayl}) + (0.64 * \text{nsunh}) + (2.71 * \text{c}) + (-0.73 * \text{dust}) + (-1.21 * \text{dummy}) - \phi_1) = \frac{1}{1 + e^{-\alpha_1}}$$

$$O_2 = f(\alpha_2) = f((1.32 * \text{ghi}) + (-0.30 * \text{temp}) + (0.01 * \text{dayl}) + (1.82 * \text{nsunh}) + (1.99 * \text{c}) + (-0.62 * \text{dust}) + (0.02 * \text{dummy}) - \phi_2) = \frac{1}{1 + e^{-\alpha_2}}$$

$$O_3 = f(\alpha_3) = f((0.76 * \text{ghi}) + (2.52 * \text{temp}) + (1.11 * \text{dayl}) + (0.80 * \text{nsunh}) + (0.90 * \text{c}) + (-0.27 * \text{dust}) + (0.99 * \text{dummy}) - \phi_3) = \frac{1}{1 + e^{-\alpha_3}}$$

$$O_4 = f(\alpha_4) = f((-1.56 * \text{ghi}) + (1.28 * \text{temp}) + (-0.34 * \text{dayl}) + (-0.17 * \text{nsunh}) + (-2.82 * \text{c}) + (1.05 * \text{dust}) + (-2.98 * \text{dummy}) - \phi_4) = \frac{1}{1 + e^{-\alpha_4}}$$

$$O_5 = f(\alpha_5) = f((0.29 * \text{ghi}) + (1.71 * \text{temp}) + (-1.29 * \text{dayl}) + (0.83 * \text{nsunh}) + (-1.51 * \text{c}) + (1.57 * \text{dust}) + (-2.06 * \text{dummy}) - \phi_5) = \frac{1}{1 + e^{-\alpha_5}}$$

$$O_6 = f(\alpha_6) = f((1.36 * \text{ghi}) + (-2.18 * \text{temp}) + (-1.44 * \text{dayl}) + (0.19 * \text{nsunh}) + (-1.78 * \text{c}) + (1.45 * \text{dust}) + (0.93 * \text{dummy}) - \phi_6) = \frac{1}{1 + e^{-\alpha_6}}$$

$$O_{\text{Final}} = f((-0.98 * O_1) + (0.94 * O_2) + (1.20 * O_3) + (1.19 * O_4) + (-0.45 * O_5) + (0.72 * O_6)) = (-0.98 * O_1) + (0.94 * O_2) + (1.20 * O_3) + (1.19 * O_4) + (-0.45 * O_5) + (0.72 * O_6)$$

5. CONCLUSIONS

By considering meteorological factors and ranking their importance on solar power plant output, this research attempted to provide an optimal model to predict solar energy production more accurately. This study examined the effects of eight variables on solar power plant output. Due to the increase in the number of dusty days in the country and the negative effect of the dust parameter on the amount of solar energy production, the objective was to determine the most effective input variable for solar energy production using a connection weight method. Out of the eight variables studied in this paper, air pressure had the least effect on solar energy production. Solar global irradiance on the horizontal plane, air temperature, and the number of sunny hours were the most significant variables in the present study. The amount of global radiation on the horizontal plane was retrieved from the SODA website and is not currently reported by meteorological stations across the received data from IRIMO. Besides, calculating this variable using radiation data is not difficult. Air temperature is the second most important variable affecting the amount of solar energy production. The third place in the Khalij-Fars power plant was the number of sunny hours. Day length and the number of sunny hours were two other important variables that we encountered in the hourly forecasts because they were reported once a day. In total, for both power plants, four parameters of solar radiation, number of sunny hours, temperature, and cloudiness were introduced as the most effective parameters in the amount of solar energy production. Because the frequency measurement parameter was the number of hours of daily sunshine, this parameter was only effective in daily forecasting. The Meteorological Organization must make arrangements for monitoring and measuring these parameters on an hourly basis.

The country currently has solar power plants connected to the electricity distribution network in 18 provinces. The provinces of Kermanshah, Markazi, Ilam, and Lorestan are among those with good potential for establishing solar power plants, but have yet to do so. In addition to helping the country become self-sufficient in electricity generation with the development of solar power plants in temperate regions and border launches, with proper planning, surplus production can be exported to neighboring countries. In the present study, much time was wasted trying to format meteorological data correctly. Several hours were spent cleaning the data because the data was not recorded correctly at non-airport stations. Due to the lack of data on some days, the data of some variables were replaced with the data of the SODA site. Since the development of renewable power plants is a good alternative to fossil fuel power plants, it is necessary for the national meteorological organization to review the structure of the collected data and to be as sensitive as possible in recording the data. Given the location of Hamedan province and its proximity to Iraq, the study of the effect of dust storms on the reduction of solar energy production is one of the challenging issues in predicting the amount of solar power generation. It is practically unprofitable to set up a meteorological station near each solar power plant. Predicting production based on calculating the factors of radiation angle, radiation intensity, and temperature is one of the useful solutions that does not require the establishment of a meteorological station in the solar power plant and is done only based on theoretical calculations and temperature data. It shows the importance of conducting more research to develop precise prediction models in future studies.

6. ACKNOWLEDGEMENT

The authors thank the editor and the reviewers of the Journal of Renewable Energy and Environment for their very helpful suggestions and constructive comments with significantly improved quality of the manuscript. The authors would like to acknowledge Kharazmi University (Iran) for all the support provided.

REFERENCES

1. Bhavani, M., Vijaybhaskar Reddy, K., Mahesh, K., & Saravanan, S. (2021). Impact of variation of solar irradiance and temperature on the inverter output for grid connected photo voltaic (PV) system at different climate conditions. *Materials Today: Proceedings*. https://doi.org/https://doi.org/10.1016/j.matpr.2021.06.120
2. Bugała, A., Zaborowicz, M., Boniecki, P., Janczak, D., Koszela, K., Czekała, W., & Lewicki, A. (2018). Short-term forecast of generation of electric energy in photovoltaic systems. *Renewable and Sustainable Energy Reviews*, *81*, 306-312. https://doi.org/https://doi.org/10.1016/j.rser.2017.07.032
3. Carra, E., Ballestrín, J., Polo, J., Barbero, J., & Fernández-Reche, J. (2018). Atmospheric extinction levels of solar radiation at Plataforma Solar de Almería. Application to solar thermal electric plants. *Energy*, *145*, 400-407. https://doi.org/https://doi.org/10.1016/j.energy.2017.12.111
4. EIA. (2021). *Country analysis executive summary: Iran*. T. U. S. E. I. Administration. https://www.eia.gov/international/content/analysis/countries_long/Iran/pdf/iran_exe.pdf
5. Ghritlahre, H.K., & Prasad, R.K. (2018). Application of ANN technique to predict the performance of solar collector systems - A review. *Renewable and Sustainable Energy Reviews*, *84*, 75-88. https://doi.org/https://doi.org/10.1016/j.rser.2018.01.001
6. Gorjian, S., Ghobadian, B., & Tavakkoli Hashjin, T. (2015). Modeling of solar radiation potential in Iran using artificial neural networks. *Journal of Agricultural Science and Technology (JAST)*, *17*(7), 1707-1723. http://jast.modares.ac.ir/article-23-7341-en.html
7. Halabi, L.M., Mekhilef, S., & Hossain, M. (2018). Performance evaluation of hybrid adaptive neuro-fuzzy inference system models for predicting monthly global solar radiation. *Applied Energy*, *213*, 247-261. https://doi.org/https://doi.org/10.1016/j.apenergy.2018.01.035
8. IGMC. (2017). *Statistics and information request system*. Retrieved 2018-07-01 from https://www.igmc.ir/statistical-center
9. IGMC. (2018, 2018/07/01). *Statistical center - IGMC*. https://www.igmc.ir/statistical-center
10. IRIMO. (2018). *I.R. Of IRAN Meteorological Organization*. Retrieved 2018/09/01 from https://data.irimo.ir/
11. Jahani, B., Dinpashoh, Y., & Raisi Nafchi, A. (2017). Evaluation and development of empirical models for estimating daily solar radiation. *Renewable and Sustainable Energy Reviews*, *73*, 878-891. https://doi.org/https://doi.org/10.1016/j.rser.2017.01.124
12. Jung, Y., Jung, J., Kim, B., & Han, S. (2020). Long short-term memory recurrent neural network for modeling temporal patterns in long-term power forecasting for solar PV facilities: Case study of South Korea. *Journal of Cleaner Production*, *250*, 119476. https://doi.org/https://doi.org/10.1016/j.jclepro.2019.119476
13. Khosravi, A., Koury, R.N.N., Machado, L., & Pabon, J.J.G. (2018). Prediction of hourly solar radiation in Abu Musa Island using machine learning algorithms. *Journal of Cleaner Production*, *176*, 63-75. https://doi.org/https://doi.org/10.1016/j.jclepro.2017.12.065
14. Loghmari, I., Timoumi, Y., & Messadi, A. (2018). Performance comparison of two global solar radiation models for spatial interpolation purposes. *Renewable and Sustainable Energy Reviews*, *82*, 837-844. https://doi.org/https://doi.org/10.1016/j.rser.2017.09.092
15. Ma, T., Li, M., & Kazemian, A. (2020). Photovoltaic thermal module and solar thermal collector connected in series to produce electricity and high-grade heat simultaneously. *Applied Energy*, *261*, 114380. https://doi.org/https://doi.org/10.1016/j.apenergy.2019.114380

16. Mamipour, S., Beheshtipour, H., Feshari, M., & Amiri, H. (2019). Factors influencing carbon dioxide emissions in Iran's provinces with emphasis on spatial linkages. *Environmental Science and Pollution Research*, *26*(18), 18365-18378. https://doi.org/https://doi.org/10.1007/s11356-019-05192-0

17. Map, G. (2023a). *Distance of Hamedan airport to Amirkabir solar power plant*. https://www.google.com/maps/dir/Hamadan+Airport,+Hamadan+Province,+Hamedan,+Sardar+Hamedani+Square,+Iran/Amir+Kabir+Solar+Power+Plant,+Hamadan+Province,+Iran/@34.9217361,48.4903413,12z/data=!3m1!4b1!4m14!4m13!1m5!1m1!1s0x3ff19279257e16c5:0x5fb78c39f38ea2dc!2m2!1d48.5378564!2d34.8673!1m5!1m1!1s0x3ff18fe4d74317c7:0xdaf5af4141bb3d0e!2m2!1d48.5660117!2d34.9669339!3e2

18. Map, G. (2023b). *Distance of Hamedan airport to Khalij Fars solar power plant*. https://www.google.com/maps/dir/Hamadan+Airport,+Hamadan+Province,+Hamedan,+Sardar+Hamedani+Square,+Iran/Persian+Gulf+Solar+Power+Plant,+Hamadan+Province/@34.9586888,48.5793117,11z/data=!4m14!4m13!1m5!1m1!1s0x3ff19279257e16c5:0x5fb78c39f38ea2dc!2m2!1d48.5378564!2d34.8673!1m5!1m1!1s0x3ff227025e5464e9:0x3af582d0f3d87ab2!2m2!1d48.7579169!2d35.0126439!3e0).

19. NASA. (2009). Retrieved 23-06-2019 from https://earthobservatory.nasa.gov/features/EnergyBalance/page4.php

20. Olden, J.D., Joy, M.K., & Death, R.G. (2004). An accurate comparison of methods for quantifying variable importance in artificial neural networks using simulated data. *Ecological Modelling*, *178*(3), 389-397. https://doi.org/https://doi.org/10.1016/j.ecolmodel.2004.03.013

21. Piri, J., & Kisi, O. (2015). Modelling solar radiation reached to the Earth using ANFIS, NN-ARX, and empirical models (Case studies: Zahedan and Bojnurd stations). *Journal of Atmospheric and Solar-Terrestrial Physics*, *123*, 39-47. https://doi.org/https://doi.org/10.1016/j.jastp.2014.12.006

22. Professionals, S.E.S.F. (2021). *MERRA-2 METEOROLOGICAL RE-ANALYSIS*. Retrieved 05/17/2018 from http://www.soda-pro.com/web-services/meteo-data/merra

23. Siva Krishna Rao K., D.V., Premalatha, M., & Naveen, C. (2018). Analysis of different combinations of meteorological parameters in predicting the horizontal global solar radiation with ANN approach: A case study. *Renewable and Sustainable Energy Reviews*, *91*, 248-258. https://doi.org/https://doi.org/10.1016/j.rser.2018.03.096

24. SATBA. (2021). *Renewable power plants geographical map*. Retrieved 08/05/2021 from http://www.satba.gov.ir/suna_content/media/image/2020/03/8144_orig.png

25. Shireen, T., Shao, C., Wang, H., Li, J., Zhang, X., & Li, M. (2018). Iterative multi-task learning for time-series modeling of solar panel PV outputs. *Applied Energy*, *212*, 654-662. https://doi.org/https://doi.org/10.1016/j.apenergy.2017.12.058

26. Vaka, A.S., & Talukdar, P. (2020). Novel inverse heat transfer technique for estimation of properties and location-specific process parameters of roof-mounted solar PV plants. *Thermal Science and Engineering Progress*, *19*, 100657. https://doi.org/https://doi.org/10.1016/j.tsep.2020.100657

27. Zaaoumi, A., Bah, A., Ciocan, M., Sebastian, P., Balan, M. C., Mechaqrane, A., & Alaoui, M. (2021). Estimation of the energy production of a parabolic trough solar thermal power plant using analytical and artificial neural networks models. *Renewable Energy*, *170*, 620-638. https://doi.org/https://doi.org/10.1016/j.renene.2021.01.129

28. Zhao, W., Zhang, H., Zheng, J., Dai, Y., Huang, L., Shang, W., & Liang, Y. (2021). A point prediction method based automatic machine learning for day-ahead power output of multi-region photovoltaic plants. *Energy*, *223*, 120026. https://doi.org/https://doi.org/10.1016/j.energy.2021.120026

JREE: Vol. 10, No. 4, (Autumn 2023) 146-155

Journal of Renewable Energy and Environment

Journal Homepage: www.jree.ir

Materials and Energy Research Center

MERC

Review Article

Thermal Performance and Efficiency Enhancement in Evacuated Tube Solar Collectors Using Various Nanofluids

Mohamed Ramadan Gomaa*, Njoud Hussein Alhabahbh, Mohammed Abbas Al-Nawafleh

Department of Mechanical Engineering, Faculty of Engineering, Al-Hussein Bin Talal University, Maan, Jordan.

PAPER INFO

Paper history:
Received: 20 January 2023
Revised: 28 July 2023
Accepted: 30 August 2023

Keywords:
Evacuated Tube Collector,
Energy Enhancement,
Thermal Efficiency,
Nanofluid

ABSTRACT

This research reviews various studies on the effect of using nanofluids in evacuated tube solar collectors (ETSC). The initial segment of this study elaborates on the importance of using the ETSCs and categorizes these collectors in terms of classification and application. The second segment evaluates the physical properties of nanofluids incorporated in the solar system collector and presents some applications of nanofluids. The last segment of the research reviews the works of a group of researchers who have already applied nanofluids to evacuated tube solar collectors for various purposes, including increasing the heat transfer coefficient and improving efficiency. Among the prevalent nanofluids employed in solar applications, Al_2O_3, CuO, and TiO_2 feature prominently, whereas Ag, WO_3, and CeO_2 find limited application in the solar context. Furthermore, nanofluids within the size range of 1–25 nm, 25–50 nm, and 50–100 nm constitutes 54%, 25%, and 11% of the applications, respectively. Particularly noteworthy, the single-walled carbon nanotubes/water (SWCNT/water) heat pipe showcases the most remarkable efficiency enhancement, achieving an impressive 93.43% improvement.

https://doi.org/10.30501/jree.2023.374760.1507

1. INTRODUCTION

In conjunction with the increase in the population and the increase in demand for energy, fossil fuels threaten the environment, which is the main cause of emissions that cause pollution and climate change. For this reason, it was and is necessary to seek alternative sources of energy that are less harmful, clean, and inexpensive (Al-Bawwat et al., 2023; Al-Bawwat et al., 2023; Marmoush et al., 2018; Rezk et al., 2019; Zambolin & Del Col, 2010). Renewable energy sources such as solar energy are among the most widely used. Solar energy is clean, safe for the environment, less harmful than fossil fuels, and relatively cheap because the main source of its provision is the sun, which is free (Gomaa, et al., 2020; Gomaa et al., 2020). However, there are still limitations with respect to the use of solar energy, including the relatively low energy density compared to other renewable energy sources; and the difficulty exploiting it during evening and night times or in unsuitable weather conditions. With this said, a new trend attempts to improve the efficiency of solar collectors with highly effective technologies that improve the use of collectors in inappropriate conditions (Ayompe & Duffy, 2013; Selvakumar et al., 2014). There are several types of solar collectors, such as flat-plate collectors (FPC), evacuated tube collectors (ETC), parabolic collectors, etc. and they are used based on several factors, including the required temperature and the purpose of use (Morrison et al., 1984).

The ETSC has a strong heat derivation capability due to vacuum insulation and selective surface coating of absorber components, making them suitable for foggy or severely cold circumstances. Additionally, the working fluid is a component that must receive the highest amount of heat from the collector, and changing it into nanofluid from pure fluids is one of the most common ways to accelerate heat transfer in the collectors under study (Elsheikh et al., 2018). A fluid that contains a small amount of uniformly distributed, suspended nanometer-sized particles, with an average size of under 100 nm in the base fluid, is referred to as a nanofluid (Estellé et al., 2017; Kolsi et al., 2017; Selimefendigil & Öztop, 2019). The ability to completely understand the heat fluid transfer mechanism of conduction in nanofluids and to identify possible enhancements is presently a major difficulty in the field of nanofluids. To fully understand the dynamic and static nature of these systems, future research on nanofluids is about to achieve its primary objective (Das, 2008). Recently, numerous researchers have presented multiple strategies for employing nanofluids as the working fluid in solar collectors. The current work offers a thorough overview of the most recent advances in the use of a nanofluid in evacuated tube solar collectors. This study aims to evaluate how efficiently they contribute to the overall efficiency of an evacuated tube solar collector system. Numerous researchers have also noted improvements in the thermo physical characteristics and heat transfer coefficient of nanofluids in comparison to basic fluids. This research conducted a review-based investigation into the significance of nanofluids in the performance of evacuated tube solar collector systems.

*Corresponding Author's Email: *Behiri@bhit.bu.edu.eg* (M. R. Gomaa)
URL: https://www.jree.ir/article_178754.html

Please cite this article as: Gomaa, M. R., Alhabahbh, N. H., & Nawafleh, M. A. (2023). Thermal Performance and Efficiency Enhancement in Evacuated Tube Solar Collector using Various Nanofluids, *Journal of Renewable Energy and Environment (JREE)*, 10(4), 146-155. https://doi.org/10.30501/jree.2023.374760.1507.

1.1. Solar collector types

Sunlight is collected by solar collectors and converted into heat which is, in turn, transferred to the working fluid (usually water or air). Solar collectors are characterized by a variety of forms and one's choice depends on the temperature that the collectors are expected to reach, their main purpose, and the working temperature specific to each type in a specific range (low, medium, and high) (Muhammad et al., 2016; Sayed et al., 2022). The FPC is generally recommended and suitable for application within the temperature range of 20–80 ºC and is applicable to domestic water heating. The outlet temperature of this collector type (FPC) is considered low, given the losses resulting from the glass cover and its lack of a sun tracking system. Therefore, the efficiency is considered to be lower than other types (Tang et al., 2010). Evacuated tube solar collectors are mostly used for medium-operating temperatures between 50-200 ºC. The ETSC is often used in domestic water heating and this type is more suitable than FPC in case of cold weather conditions (the presence of clouds) (Papadimitratos et al., 2016).

Parabolic Trough collectors represent moving or tracking collectors that track the sun throughout the day and they are mostly used in power plants. This type is considered a viable option due to its commercial and technological advantages as well as its ability to couple with fossil fuel systems to facilitate higher outlet system temperatures at night. The temperature of the Parabolic Trough collector system ranges between 400 and 500 ºC (Gomaa et al., 2020; Gomaa et al., 2020; X. Li et al., 2019). The Compound Parabolic Collectors (CPC), generally fixed, do not have a sun tracking system. The CPC is effective in collecting and focusing the sun's rays at a certain angle of incidence with a temperature range of 60–240 ºC (Arunkumar et al., 2016). Parabolic Dish Reflectors (PDR) are used at high temperatures and can achieve an excess of 1500 ºC. This collector type is similar to an electric generator upon exploiting solar energy and converting it into electricity. The parabolic dish reflector collector fully tracks the sun rays (L. Li & Dubowsky, 2011).

1.2. An overview of evacuated tube solar collectors

There are three ETSC categories namely Thermo-syphon, U-pipe, and Heat pipe and the mechanism of each one has been studied.

1.2.1. Thermo-syphon

The collector consists of about 15 to 40 tubes and it is connected to a horizontal tank directly. Heat is transmitted in the Thermo-syphon collector through the convection of water. As the sun's radiation targets the tubes at the top of the tank, the temperature of the water inside the tubes increases and is replaced by cold water due to the density difference (Budihardjo et al., 2007). Figure 1 represents the actual thermosyphon solar water heater (Tang & Yang, 2014).

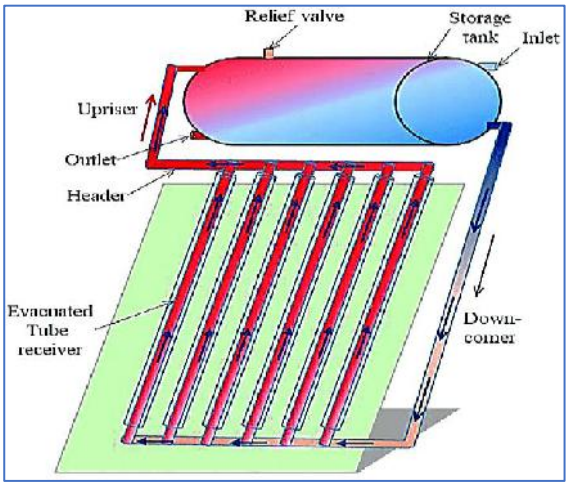

Figure 1. Thermo-syphon solar collectors.

1.2.2. U-pipe evacuated tubular solar collector

The U-pipe ETSC is considered the most common type used for several reasons including its simple geometric shape and high thermal efficiency. This type consists of tubes in the shape of a U made of copper. The liquid inside these tubes is heated as a result of solar radiation, and the heat energy is transmitted to a storage tank through a heat exchanger (Nie et al., 2017). Figure 2 represents three sections: the evaporator, the adiabatic, and the condenser. The evaporator's working fluid boils because of the external heat source, as shown in Figure 2(a). Heat is released to the cooling medium when vapor passes through the adiabatic portion, as illustrated in Figure 2(b), and into the condenser section (Figure 2(c)), which is above it. Due to the gravity, the condensed liquid flows back to the evaporator part (Nie et al., 2017).

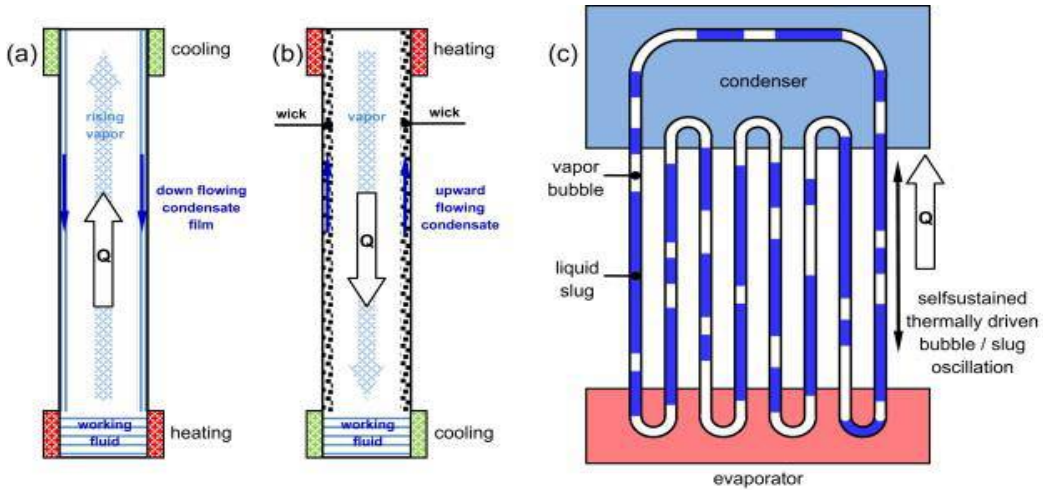

Figure 2. U-pipe ETSC (a) heating (evaporator), (b) cooling (adiabatic), and (c) condenser processes.

1.2.3. Heat pipe

This type is characterized by very high thermal conductivity and a low level of vaporizable fluid. The mechanism of this type is released to the evaporation condensation cycle. In the evaporation mechanism, the sun radiation is released to the collector and fluid to make the phase of evaporation. The condensation mechanism, which ensures the flow of heat, is transferred to the heat sink (Daghigh & Shafieian, 2016; Hayek et al., 2011). The design of a typical direct solar thermal absorption collector using a nanofluid as the working fluid is shown in Figure 3(a). Figure 3(b) shows a typical direct solar thermal absorption system with a separate freshwater circuit and a closed-loop nanofluid circuit. Figure 3 represents the heat pipe solar water heater (Daghigh & Shafieian, 2016).

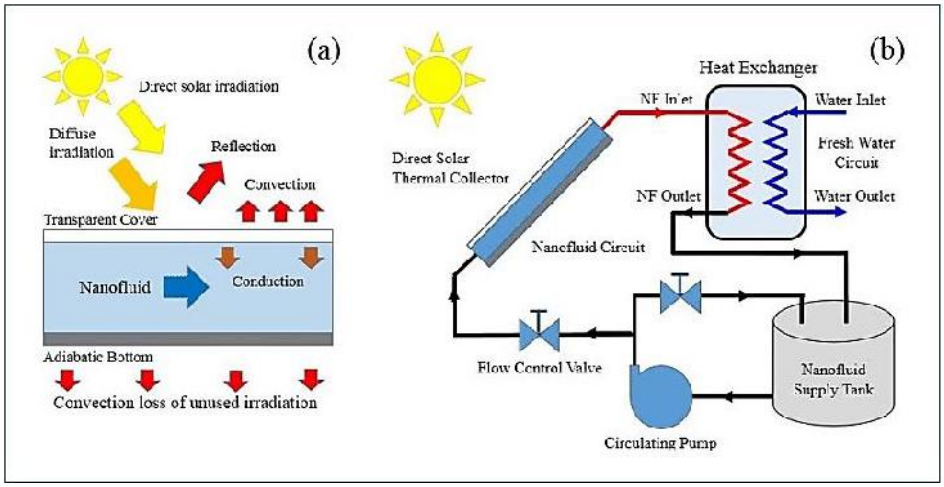

Figure 3. Heat Pipe solar collectors.

2. THERMOPHYSICAL PROPERTIES OF NANOFLUIDS

Nanofluid is a liquid or suspension mixture that is prepared by mixing certain fluids such as water, oil, and glycol with metallic (Cu, Al, Zn, Ni, Si, Fe, Ti, Au, Ag) or non-metallic (Al_2O_3, CuO, SiC, ZnO, TiO_2) nanoparticles ranging in size from 1–100 nm in diameter.

Several previous studies have made attempts to improve the thermal-physical properties of the nanoparticle, including thermal conductivity, specific heat, and viscosity. The nanoparticle is then mixed with a fluid. Nanoparticles are used to improve the thermal properties of fluids and the enhancement of the properties of nanofluid depends on several factors, e.g., the concentration of nanoparticles, the shape and size of nanoparticles, and the temperature of the working fluid (Lee et al., 2008).

Nanofluids exhibit several properties, including the thermal conductivity of nanoparticles, which is one of their most significant properties, nanofluid dispersion rate, nanofluid concentration, and nanoparticle size. Al_2O_3 thermal conductivity and nanofluid concentration were found to be linearly related (Hong et al., 2005). For copper to have a higher thermal conductivity value, it is essential to increase the surface area of nanoparticles (Alsboul et al., 2022a, 2022b; M. S. Liu et al., 2006).

Nanoparticles have different specific heats depending on their type and concentration. Specific heat (C) is defined as the amount of heat needed to increase a unit mass by one degree Celsius. According to the results, the specific heat decreased as the volume fraction of Al_2O_3 increased (Sajadi & Kazemi, 2011).

A critical characteristic of any heat transfer system is the convective transfer of heat. Heat transfer coefficient values must be determined in terms of how nano properties and volume fractions change over time. The value of the heat transfer coefficient increases by 47% when the nanoparticle size of Al_2O_3 is 27–56 nm in diameter and volume fractions of 0.6–1.6% (Wen & Ding, 2004). Water enhanced by TiO_2 nanoparticles delivers a 22% higher heat transfer coefficient than pure water when TiO_2 nanoparticles are added (Zhou & Ni, 2008).

2.1. Potential of nanofluids

In recent years, nanofluids have attracted much more attention. Improving thermal properties is the main goal of using metallic and non-metallic nanoparticles in various applications**.** Nanofluids are used in many applications including heat transfer applications such as the extraction of geothermal power, heating building, and nuclear system cooling; biomedical applications such as sensing and imaging and nano drug delivery; and energy applications such as Energy Storage and Solar Absorption (Al-Rawashdeh et al., 2021; Chand, 2017; Gomaa et al., 2022; Marashli et al., 2022).

There are many advantages of applying nanofluids in the solar system. As a result of their small size and large surface area, nanoparticles possess many characteristics, which increase the absorption of solar energy. In addition, nanofluids are characterized by their high density, high heat transfer coefficient, and high conductivity, enhancing the effectiveness of thermal properties (Elsheikh et al., 2018). Nanofluids have disadvantages including restricted use and high costs, the latter being the most important. In addition, they require certain chemicals and manufacturing conditions as well as advanced equipment (Wang et al., 2022).

2.2. Nanofluid-based performance of an evacuated tube solar collector

In the same operating conditions, ETSC enjoys higher efficiency, which is defined as the proportion of heat energy that a solar thermal collector produces to the total solar energy it receives, than FPC (Tong & Cho, 2015), and it is important

to note that the efficiency of ETSC varies from type with type. It was found that the heat pipe type was more efficient than the U-pipe type by approximately 8% on sunny days, whereas the U-pipe type performed better on cloudy days (Zambolin & Del Col, 2010). Many studies have investigated the incorporation of nanofluid in different types of ETSC extensively. These research studies pursued the objective of identifying the impact of nanofluid on the performance and efficiency of the ETSC.

The thermosyphon ETSC efficiency increased when TiO_2 was used as a nanofluid with a 30-50 nm diameter at a flow rate of 2.7 liters per minute, approximately 16.7% more efficient than water (Mahendran et al., 2012). The enhancement of maximum thermal performance and energy efficiency of the U-shaped pipe ETSC can be achieved at 12.2% and 5.4%, respectively, by incorporating TiO_2 as a heat transfer fluid (Muhammad, 2016). The thermal conductivity of the nanofluid increases as the TiO_2 volume fraction increases in thermosyphon ETSC (Hosseini & Shafiey Dehaj, 2021). The use of CuO nanoparticles improves the efficiency of the U-tube ETSC. The highest efficiency of ETSC was determined to be 69.1% when 400 nm of CuO was added as a nanoparticle (Hussein, 2016). The addition of CuO to the thermo-syphon ETSC increases the temperature of the outside air used in heating operations and this method improves the efficiency by as much as 14 percent, compared to the water-based method (Sharafeldin & Gróf, 2019).

The maximum efficiency of the thermosyphon ETSC was achieved at 57.63% with a 40 nm diameter by incorporating Al2O3 as a nanoparticle (Kim et al., 2017). Adding Al_2O_3 to the U-tube ETSC yielded a maximum efficiency of 72.4% at a diameter of 20 nm (Ghaderian & Sidik, 2017). The addition of WO3 as a nanoparticle to the thermosyphon ETSC resulted in a 21% increase in the nanofluid temperature difference (Z. H. Liu et al., 2013). Generally, the utilization of WO_3 nanoparticles in ETSCs is restricted (Kang et al., 2019). Moreover, the inclusion of CeO_2 as a nanoparticle in the thermosyphon ETSC elevated the temperature difference for nanofluids by up to 37.3% compared to pure water (Sharafeldin & Gróf, 2018). Introducing Ag nanoparticles into the thermosyphon ETSC raised energy efficiency from 20.7% to 40% compared to pure water (Ozsoy & Corumlu, 2018). In the U-tube ETSC, ZnO/Ethylene-glycol nanoparticles achieved a maximum efficiency of 62.87%, and increasing nanoparticle volume concentration enhanced the thermal conductivity of ZnO/Ethylene-glycol with water nanofluids (Kaya & Arslan, 2019). Implementing nanofluids in heat pipe ETSCs reduced fuel consumption by approximately 67.7%, with CuO nanoparticles and TiO_2 nanoparticles increasing system performance by 12% and 5%, respectively (Daghigh & Zandi, 2019). A mixture of Ag nanoparticles (30 nm), ZrO_2 nanoparticles (50 nm), and water as a base fluid in the thermosyphon ETSC improved thermal performance compared to pure water due to the high thermal conductivity of Ag and ZrO_2 (Hussain et al., 2015). The use of MgO/water nanofluid exhibited superior thermal performance in heat pipe ETSCs compared to pure water (Dehaj & Mohiabadi, 2019).

To enhance the heat transfer rate, hybrid nanofluids with high thermal conductivity are employed. The addition of $ZnFe_2O_4$ and water as a hybrid nanofluid led to a 42.99% increase in the convective heat transfer coefficient (Gupta et al., 2020). Assessing different concentrations of Al_2O_3 and CuO nanoparticles on the thermal performance of ETSC heat pipes revealed optimal conditions resulting in thermal performance enhancement of 20-54% and energy efficiency improvement of 15-38% (Eidan et al., 2018). For U-tube ETSCs, Ag, ZnO, and MgO nanoparticles were tested in various concentrations alongside ethylene glycol-pure water (EG-PW). The highest collector efficiency, 68.7%, was achieved with Ag/EG-PW as a heat transfer fluid, while pure water yielded an efficiency of 26.7%. Additionally, reductions of 855.5 kg and 7.2 kg per year in CO_2 and SO_2 generation were observed (Kaya & Arslan, 2019).

Increasing nanoparticle concentration improved thermal conductivity, leading to a more efficient solar collector. Among MWCNT, CuO, Al_2O_3, TiO_2, and SiO_2 nanofluids, the greatest efficiency enhancement of 62.8% compared to pure water was attained with MWCNT nanofluid in U-tube ETSCs (Kim et al., 2016). Heat pipe ETSCs with varying volumes of Al_2O_3 and CuO nanoparticles demonstrated better heat transfer with CuO/H_2O as the nanoparticle volume to water ratio increased, showing a 6.70% improvement over Al_2O_3/H_2O under the same conditions (Mercan & Yurddaş, 2019). In thermo-syphon ETSCs, the addition of

SiO2/water nanofluids enhanced heat transfer and heat flux, with the increased mass fraction of SiO_2 resulting in higher thermal conductivity (Yan et al., 2017). Utilizing TiO_2/water as a nanofluid enhanced the performance of thermosyphon ETSCs, where higher mass flow rates led to increased thermal efficiency and reduced entropy generation (Gan et al., 2018). For U-tube ETSCs, MWCNT combined with water improved efficiency by 4%, and CO_2 and SO_2 emissions were reduced by 1600 kg and 5.3 kg, respectively (Tong et al., 2015). The utilization of SWCNT with water as a nanofluid in heat pipe ETSCs led to enhanced collector efficiency, with a maximum efficiency of 93.43% (Sabiha et al., 2015). The addition of MWCNT/water nanofluid to thermosyphon ETSCs improved thermal efficiency by over 20% (Shanbedi et al., 2014). Heat transfer was enhanced by approximately 1.23% with CuO/water nanofluid in thermo-syphon ETSCs (Z. H. Liu et al., 2007). Similarly, the use of Fe_2O_3/Water nanofluid in thermo-syphon ETSCs led to a heat transfer coefficient increase of about 1.15% (Huminic & Huminic, 2013). The application of GNP-COOH/Water nanofluid in thermo-syphon ETSCs increased heat transfer coefficients by over 66%, and CuO/water nanofluid led to a more than 160% increase (Amiri et al., 2015; Yang & Liu, 2012).

When Iron oxide/water, TiO_2/water, Graphene/Acetone, and SiC/water nanofluid are used in thermosyphon ETSC, the thermal resistance will be reduced by about 35% (Huminic & Huminic, 2011), 24% (Buschmann & Franzke, 2014), 70.3% (Asirvatham et al., 2015), and 6.1% (H. jie Li et al., 2018), respectively.

3. RESULTS AND DISCUSSION

3.1. Comparison of Nanofluids Used In The Evacuated Tube Solar Collector

In the initial stages, prior research undertook a comparison of the performance of distinct ETSC designs across various

liquids and nanofluids, a depiction of which can be observed in Figure 4.

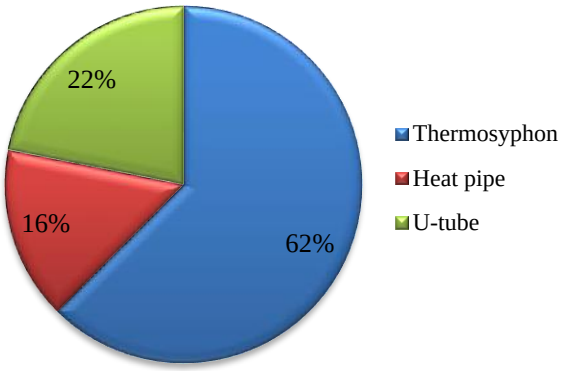

Figure 4. Prior studies have used nanofluids in a variety of ETSCs.

Based on the insights presented in Figure 4, it becomes evident that the Thermo-syphon ETSC design holds the dominant position, while the U-tube configuration is preferable when compared to the heat pipe design. This analysis has yielded the following distribution: approximately 62% of the previous research centered around the implementation of thermo-syphon ETSCs, 22% focused on U-tube variations, and the remaining 16% explored heat pipe configurations, each coupled with diverse nanofluid formulations in an endeavor to enhance thermal efficiency. Further investigation into previous research reveals the utilization of a diverse array of nanofluids, some of which have been employed repeatedly, as shown in Figure 5.

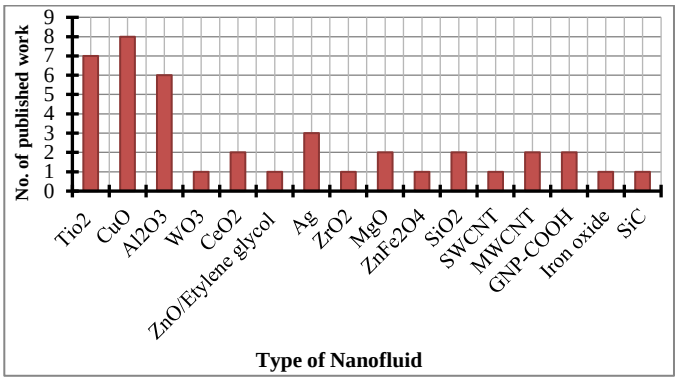

Figure 5. Nanofluids were used in previous ETSC studies.

Figure 5 visually presents the distinct contributions of various nanofluid types within prior research endeavors. Among these, TiO_2, CuO, and Al_2O_3 emerge as the most prevalent choices for integration into ETSC designs. Conversely, nanofluids like WO_3, ZrO_2, SWCNT, and SiC were utilized less frequently. As reported by Ref. (Sabiha et al., 2015). A noteworthy achievement was noted in Ref. (Sabiha et al., 2015), attesting to a maximum efficiency improvement of 93.43% in heat pipe ETSCs through the utilization of SWCNT/water nanofluids.
For a comprehensive comparison of the outcomes stemming from Nanofluid application in ETSCs aimed at enhancing thermal performance through various approaches, refer to Table 1.

Table 1. Analyses of past studies of the effects of nanofluids on ETSCs.

Type of ETSC	Nanofluid	Size (nm)	Thermal Enhancement	Ref.
Thermosyphon	Tio_2/Water	30–50	The efficiency increased by about 16.7% compared to water, which equals 73%.	(Mahendran et al., 2012)
U-tube	Tio_2/Water	40-60	Thermal conductivity and maximum efficiency were achieved at up to 5.4% and 12.2%, respectively.	(Muhammad, 2016)
Thermosyphon	TiO_2/Water	30-50	The thermal conductivity of a nanofluid increases with increasing TiO_2 volume fractions.	(Hosseini & Shafiey Dehaj, 2021)
U-tube	CuO/Water	400	The efficiency at a maximum of about 69.1% was achieved.	(Hussein, 2016)
Thermosyphon	CuO/Water	50	The temperature of the outside air used in heating operations increased and the efficiency was improved by up to 14% when compared to water.	(Sharafeldin & Gróf, 2019)
Thermosyphon	Al_2O_3/Water	40	Maximum efficiency reached 57.63% when the Al_2O_3 nanoparticle was added to water as a nanofluid.	(Kim et al., 2017)
U-tube	Al_2O_3/Water	20	Maximum efficiency reached 72.4% when the Al_2O_3 nanoparticle was added to water as a nanofluid.	(Ghaderian & Sidik, 2017)
Thermosyphon	WO_3/Water	90	The temperature difference between nanofluids and pure water was improved by as much as 21%.	(Z. H. Liu et al., 2013)
Thermosyphon	CeO_2/Water	25	The temperature difference was improved for a nanofluid maximally by 37.3% compared to pure water.	(Sharafeldin & Gróf, 2018)
Thermosyphon	Ag/Water	-	The ratio of enhancement in temperature between nanofluids and pure water reached 37.3%.	(Ozsoy & Corumlu, 2018)
U-tube	ZnO/Ethylene-glycol	30	The maximum efficiency of ZnO/Ethylene-glycol was 62.87%, and an increase in nanoparticle volume concentration was associated with an increase in thermal conductivity.	(Kaya & Arslan, 2019)

Type of ETSC	Nanofluid	Size (nm)	Thermal Enhancement	Ref.
Heat pipe	CuO/Water TiO_2/Water	-	The thermal performance of the system increased by about 12% by using CuO and by using TiO_2, it increased by 5%.	(Daghigh & Zandi, 2019)
Thermosyphon	Ag/water ZrO_2/water	30 50	The high thermal conductivity of Ag and ZrO_2 improved the thermal performance of the system in comparison with pure water.	(Hussain et al., 2015)
Heat pipe	MgO/water	20	As compared with pure water, MgO/water nanofluid enhanced the thermal performance of heat pipe ETSCs.	(Dehaj & Mohiabadi, 2019)
Thermosyphon	$ZnFe_2O_4$/water	-	There was a 42.99% increase in the convective heat transfer coefficient.	(Gupta et al., 2020)
Heat pipe	Al_2O_3/water CuO/water	25 50	The thermal performance and efficiency were enhanced by 20–54 and 15–38 percent, respectively.	(Eidan et al., 2018)
U-tube	Ag/ EG-PW ZnO/EG-PW MgO/ EG-PW	-	According to the results, the highest collector efficiency was achieved with Ag/EG-PW, which was higher than 26.7% than pure water and EG-PW. As a result, the maximum value of reducing CO_2 and SO_2 generation was 855.5 kg and 7.2 kg per year, respectively.	(Kaya & Arslan, 2019)
U-tube	MWCNT/water	-	The maximum efficiency reached 62.8 %, in comparison to 20 % with pure water.	(Kim et al., 2016)
Heat pipe	Al_2O_3/water CuO/water	-	Better results were obtained for CuO/H_2O, and increasing the nanoparticle volume ratio increased heat transfer. In contrast, Al_2O_3/H_2O demonstrated a 4.13% increase in heat transfer.	(Mercan & Yurddaş, 2019)
Thermosyphon	Sio_2/water	50	The thermal conductivity of SiO_2/water nanofluids increased with an increase in the mass fraction of SiO_2.	(Yan et al., 2017)
Thermosyphon	TiO_2 /water	21	In general, the higher the mass flow rate, the greater the thermal efficiency and the lower the generation of entropy.	(Gan et al., 2018)
U-tube	MWCNT/water	10-20	This increase in efficiency was accompanied by a reduction in CO_2 and SO_2 emissions of 1600 kg and 5.3 kg, respectively.	(Tong et al., 2015)
Heat pipe	SWCNT/water	-	The maximum efficiency of the collector was found to be 93.43 %.	(Sabiha et al., 2015)
Thermosyphon	MWCNT/water	10-20	The thermal efficiency was enhanced by more than 20%.	(Shanbedi et al., 2014)
Thermosyphon	CuO/water	50	Heat transfer was enhanced by about 1.23%.	(Z. H. Liu et al., 2007)
Thermosyphon	Fe_2O/Water	4-5	Heat transfer was enhanced by about 1.15%.	(Huminic & Huminic, 2013)
Thermosyphon	GNP-COOH/Water	-	This led to a more than 66% increase in the heat transfer coefficient.	(Yang & Liu, 2012)
Thermosyphon	CuO/water	30	This led to a more than 160% increase in the heat transfer coefficient.	(Amiri et al., 2015)
Thermosyphon	Iron oxide/water	4-5	The thermal resistance was reduced by about 35%.	(Huminic & Huminic, 2011)
Thermosyphon	TiO_2/water	42	The thermal resistance was reduced by about 24%.	(Buschmann & Franzke, 2014)
Thermosyphon	Graphene/Acetone	-	The thermal resistance was reduced by about 24%.	(Asirvatham et al., 2015)
Thermosyphon	SiC/water	30-50	The thermal resistance was reduced by about 6.1%.	(H. jie Li et al., 2018)

Table 1 illustrates a comparative analysis of the impact of employing distinct nanofluid variants in ETSC applications. The utilization of nanofluids leads to a notable enhancement in both efficiency and overall performance. This phenomenon is attributed to the diverse selection of nanofluids integrated into different ETSC protocols. While certain nanofluid types contribute to efficiency improvement, others augment thermal conductivity or refine temperature differentials. Some nanofluids result in reduced fuel consumption across varying degrees, whereas others engender escalated heat transfer coefficients or decreased thermal resistances.

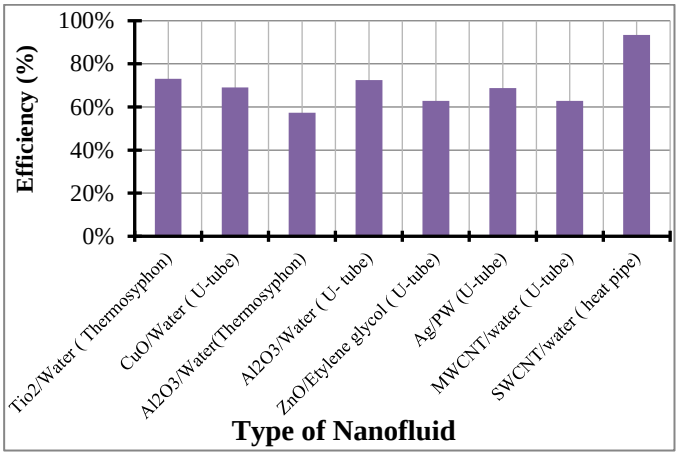

Figure 6. Efficiency of ETSC under various types of Nanofluid.

Figure 6 showcases the varied impact of nanofluids on the efficiency values of ETSCs. The highest alleged efficiency enhancement of 93.43% originated from SWCNT/water (Sabiha et al., 2015), followed by 72.4% achieved by Al_2O_3 in U-tube ETSCs (Kim et al., 2017), and subsequently 62.87% for ZnO/Ethylene-glycol nanofluids (Ozsoy & Corumlu, 2018). In contrast, the lowest efficiency, noted as 57.63%, was recorded in previous research using Al_2O_3 in Thermosyphon ETSCs (Ghaderian & Sidik, 2017). It's evident from Figure 6 that the use of Al_2O_3/water in U-tube ETSCs achieves greater effectiveness compared to its application in Thermosyphon ETSCs.

Enhancing the heat transfer coefficient stands as a paramount objective in employing nanofluid materials within ETSCs. Table 1 exhibits diverse nanofluid types with varying concentrations and sizes, each contributing to the improvement of the heat transfer coefficient. Notably, CuO/water with a size of 30 nm led to a remarkable increase of over 160% in the heat transfer coefficient, as depicted in Table 1 (Amiri et al., 2015). Furthermore, when utilizing the same nanofluid (CuO/water) but with a size of 50 nm, heat transfer is enhanced by approximately 1.23% (Yang & Liu, 2012). The reduction of thermal resistance was also a key target of nanofluid implementation in ETSCs. Employing TiO_2/water with a size of 42 nm led to a reduction in thermal resistance by around 24% (Buschmann & Franzke, 2014). Conversely, using SiC/water with a nearly identical volume size contributed to a reduction in thermal resistance by 6.1% (H. jie Li et al., 2018).

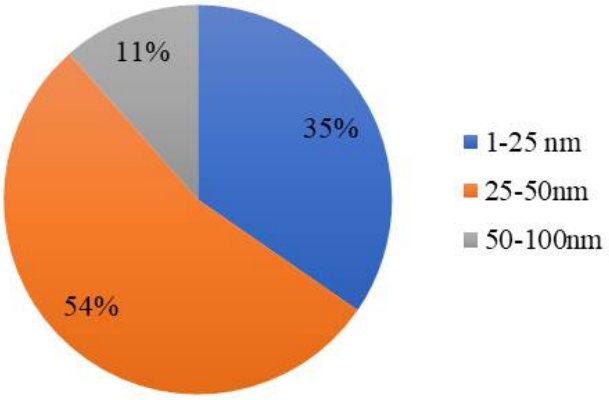

Figure 7. Used of different sizes of Nano Particle.

One of the most formidable challenges confronting researchers while engaging with nanofluids pertains to the size of nanoparticles. Consequently, the judicious selection of nanofluid sizes holds paramount significance for this study. Illustrated in Figure 7 is the application of nanoparticles of varying sizes in ETSCs. Within the spectrum of sizes studied, the range spanning 25-50 nm emerges as the most frequently employed. Throughout the research experiments, it was discerned that approximately 35% and 54% of nanofluids, characterized by sizes within the intervals of 1-25 nm and 25-50 nm respectively, were subjected to investigation. Furthermore, 11% of the selected nanofluids possessed sizes within the 50-100 nm range.

4. CONCLUSION

The research encompasses a collection of papers delving into the applications of nanofluids in ETSCs. These studies encompass a variety of nanofluid types, each characterized by a diverse range of sizes, and employed across different ETSC configurations. Each distinct nanofluid type has successfully achieved its designated objective within a particular context - the enhancement of thermal performance and system efficiency.

- ETSCs exhibit superior thermal efficiency compared to FPCs due to their operation at elevated temperatures.
- Three classifications of ETSCs were investigated, with Thermo-syphon emerging as the most prominent, accounting for 62% of the total research, followed by U-tube at 22%, and heat pipe at 16%.
- Prevalent nanofluids employed in ETSCs consist of Al_2O_3, CuO, and TiO_2, whereas Ag, WO_3, and CeO_2 are less commonly utilized.
- Nanoparticle size significantly influences the efficiency of various solar collectors. Research indicates that 54% of the studied nanofluids maintained an average size ranging from 25 to 50 nm, 25% fell within the 1 to 25 nm range, and 11% had sizes between 50 and 100 nm.
- Prior research identified the highest efficiency enhancement as 93.43% achieved by SWCNT/water in a heat pipe configuration, followed by 72.4% through the utilization of Al_2O_3 in U-tube ETSCs.

Nanofluids exhibit considerable potential in enhancing heat transmission, attributed in part to the heightened heat conductivity stemming from the inclusion of suspended

ultrafine particles. Enhancing the heat transfer coefficient stands as a pivotal objective in adopting nanofluid materials within ETSCs. Previous endeavors demonstrated a 160% increase in the heat transfer coefficient using water/CuO (30 nm).

Conflict of interest

The authors declare that they have no conflict of interest in relation to this research, whether financial, personal, authorship or otherwise, that could affect the research and its results presented in this paper.

Funding: This research was funded by the Deanship of Scientific Research, Al-Hussein Bin Talal University, Maan, Jordan, grant number 268/2023.

Data Availability Statement: The manuscript has no associated data.

6. ACKNOWLEDGEMENT

We would like to thank the reviewers and the editor-in-charge for spending their valuable time on the article and we are grateful to all the foundations that supported us.

REFERENCES

1. Al-Bawwat, A. K., Cano, A., Gomaa, M. R. & Jurado, F. (2023). Availability of Biomass and Potential of Nanotechnologies for Bioenergy Production in Jordan. In *Processes* (Vol. 11, Issue 4, p. 992). Multidisciplinary Digital Publishing Institute. https://doi.org/10.3390/pr11040992

2. Al-Bawwat, A. K., Jurado, F., Gomaa, M. R. & Cano, A. (2023). Availability and the Possibility of Employing Wastes and Biomass Materials Energy in Jordan. In *Sustainability (Switzerland)* (Vol. 15, Issue 7, p. 5879). Multidisciplinary Digital Publishing Institute. https://doi.org/10.3390/su15075879

3. Al-Rawashdeh, H., Hasan, A. O., Al-Shakhanbeh, H. A., Al-Dhaifallah, M., Gomaa, M. R. & Rezk, H. (2021). Investigation of the effect of solar ventilation on the cabin temperature of vehicles parked under the sun. *Sustainability (Switzerland)*, *13*(24), 13963. https://doi.org/10.3390/su132413963

4. Alsboul, M., Ghazali, M. S. M., Gomaa, M. R. & Albani, A. (2022a). Experimental and Theoretical Investigation of the Thermophysical Properties of Cobalt Oxide (Co3O4) in Distilled Water (DW), Ethylene Glycol (EG), and DW–EG Mixture Nanofluids. *Nanomaterials*, *12*(16), 2779. https://doi.org/10.3390/nano12162779

5. Alsboul, M., Ghazali, M. S. M., Gomaa, M. R. & Albani, A. (2022b). Experimental and Theoretical Investigations of the Thermal Conductivity of Erbium Oxide/Ethylene Glycol Nanofluids for Thermal Energy Applications. *Chemical Engineering and Technology*, *45*(12), 2139–2149. https://doi.org/10.1002/ceat.202200159

6. Amiri, A., Sadri, R., Shanbedi, M., Ahmadi, G., Chew, B. T., Kazi, S. N. & Dahari, M. (2015). Performance dependence of thermosyphon on the functionalization approaches: An experimental study on thermo-physical properties of graphene nanoplatelet-based water nanofluids. *Energy Conversion and Management*, *92*, 322–330. https://doi.org/10.1016/j.enconman.2014.12.051

7. Arunkumar, T., Velraj, R., Denkenberger, D. C., Sathyamurthy, R., Kumar, K. V. & Ahsan, A. (2016). Productivity enhancements of compound parabolic concentrator tubular solar stills. *Renewable Energy*, *88*, 391–400. https://doi.org/10.1016/j.renene.2015.11.051

8. Asirvatham, L. G., Wongwises, S. & Babu, J. (2015). Heat transfer performance of a glass thermosyphon using graphene-acetone nanofluid. *Journal of Heat Transfer*, *137*(11). https://doi.org/10.1115/1.4030479

9. Ayompe, L. M. & Duffy, A. (2013). Thermal performance analysis of a solar water heating system with heat pipe evacuated tube collector using data from a field trial. *Solar Energy*, *90*, 17–28. https://doi.org/10.1016/j.solener.2013.01.001

10. Budihardjo, I., Morrison, G. L. & Behnia, M. (2007). Natural circulation flow through water-in-glass evacuated tube solar collectors. *Solar Energy*, *81*(12), 1460–1472. https://doi.org/10.1016/j.solener.2007.03.002

11. Buschmann, M. H. & Franzke, U. (2014). Improvement of thermosyphon performance by employing nanofluid. *International Journal of Refrigeration*, *40*, 416–428. https://doi.org/10.1016/j.ijrefrig.2013.11.022

12. Chand, R. (2017). Nanofluid technologies and thermal convection techniques. In *Nanofluid Technologies and Thermal Convection Techniques*. IGI Global. https://doi.org/10.4018/978-1-68318-006-7

13. Daghigh, R. & Shafieian, A. (2016). An experimental study of a heat pipe evacuated tube solar dryer with heat recovery system. *Renewable Energy*, *96*, 872–880. https://doi.org/10.1016/j.renene.2016.05.025

14. Daghigh, R. & Zandi, P. (2019). Improving the performance of heat pipe embedded evacuated tube collector with nanofluids and auxiliary gas system. *Renewable Energy*, *134*, 888–901. https://doi.org/10.1016/j.renene.2018.11.090

15. Das, S. K. (2008). *Nanofluids : science and technology*. 397. https://www.wiley.com/en-sg/Nanofluids%3A+Science+and+Technology-p-9780470074732

16. Dehaj, M. S. & Mohiabadi, M. Z. (2019). Experimental investigation of heat pipe solar collector using MgO nanofluids. *Solar Energy Materials and Solar Cells*, *191*, 91–99. https://doi.org/10.1016/j.solmat.2018.10.025

17. Eidan, A. A., AlSahlani, A., Ahmed, A. Q., Al-fahham, M. & Jalil, J. M. (2018). Improving the performance of heat pipe-evacuated tube solar collector experimentally by using Al2O3 and CuO/acetone nanofluids. *Solar Energy*, *173*, 780–788. https://doi.org/10.1016/j.solener.2018.08.013

18. Elsheikh, A. H., Sharshir, S. W., Mostafa, M. E., Essa, F. A. & Ahmed Ali, M. K. (2018). Applications of nanofluids in solar energy: A review of recent advances. In *Renewable and Sustainable Energy Reviews* (Vol. 82, pp. 3483–3502). Pergamon. https://doi.org/10.1016/j.rser.2017.10.108

19. Estellé, P., Mahian, O., Maré, T. & Öztop, H. F. (2017). Natural convection of CNT water-based nanofluids in a differentially heated square cavity. *Journal of Thermal Analysis and Calorimetry*, *128*(3), 1765–1770. https://doi.org/10.1007/s10973-017-6102-1

20. Gan, Y. Y., Ong, H. C., Ling, T. C., Zulkifli, N. W. M., Wang, C. T. & Yang, Y. C. (2018). Thermal conductivity optimization and entropy generation analysis of titanium dioxide nanofluid in evacuated tube solar collector. *Applied Thermal Engineering*, *145*, 155–164. https://doi.org/10.1016/j.applthermaleng.2018.09.012

21. Ghaderian, J. & Sidik, N. A. C. (2017). An experimental investigation on the effect of Al2O3/distilled water nanofluid on the energy efficiency of evacuated tube solar collector. *International Journal of Heat and Mass Transfer*, *108*, 972–987. https://doi.org/10.1016/j.ijheatmasstransfer.2016.12.101

22. Gomaa, Mohamed R., Al-Dhaifallah, M., Alahmer, A. & Rezk, H. (2020). Design, modeling, and experimental investigation of activewater cooling concentrating photovoltaic system. *Sustainability (Switzerland)*, *12*(13), 5392. https://doi.org/10.3390/su12135392

23. Gomaa, Mohamed R., Al-Dmour, N., AL-Rawashdeh, H. A. & Shalby, M. (2020). Theoretical model of a fluidized bed solar reactor design with the aid of MCRT method and synthesis gas production. *Renewable Energy*, *148*, 91–102. https://doi.org/10.1016/j.renene.2019.12.010

24. Gomaa, Mohamed R., Murtadha, T. K., Abu-jrai, A., Rezk, H., Altarawneh, M. A. & Marashli, A. (2022). Experimental Investigation on Waste Heat Recovery from a Cement Factory to Enhance Thermoelectric Generation. *Sustainability (Switzerland)*, *14*(16), 10146. https://doi.org/10.3390/su141610146

25. Gomaa, Mohamed R., Mustafa, R. J., Al-Dhaifallah, M. & Rezk, H. (2020). A low-grade heat Organic Rankine Cycle driven by hybrid solar collectors and a waste heat recovery system. *Energy Reports*, *6*, 3425–3445. https://doi.org/10.1016/j.egyr.2020.12.011

26. Gomaa, Mohamed Ramadan, Matarneh, G. A., Shalby, M. & AL-Rawashdeh, H. A. (2020). A State of the art Review on a Thermochemical Conversion of Carbonaceous Materials: Production of Synthesis Gas by Co-Gasification Process-Part I. *Current Alternative Energy*, *4*(1), 26–46. https://doi.org/10.2174/2405463104999200904115100

27. Gupta, M., Singh, V. & Said, Z. (2020). Heat transfer analysis using zinc Ferrite/water (Hybrid) nanofluids in a circular tube: An experimental investigation and development of new correlations for thermophysical and heat transfer properties. *Sustainable Energy Technologies and Assessments*, *39*, 100720. https://doi.org/10.1016/j.seta.2020.100720

28. Hayek, M., Assaf, J. & Lteif, W. (2011). Experimental investigation of the performance of evacuated-tube solar collectors under eastern mediterranean climatic conditions. *Energy Procedia*, *6*, 618–626. https://doi.org/10.1016/j.egypro.2011.05.071

29. Hong, T. K., Yang, H. S. & Choi, C. J. (2005). Study of the enhanced thermal conductivity of Fe nanofluids. *Journal of Applied Physics*, *97*(6). https://doi.org/10.1063/1.1861145

30. Hosseini, S. M. S. & Shafiey Dehaj, M. (2021). Assessment of TiO2 water-based nanofluids with two distinct morphologies in a U type evacuated tube solar collector. *Applied Thermal Engineering*, *182*, 116086. https://doi.org/10.1016/j.applthermaleng.2020.116086

31. Huminic, G. & Huminic, A. (2011). Heat transfer characteristics of a two-phase closed thermosyphons using nanofluids. *Experimental Thermal and Fluid Science*, *35*(3), 550–557. https://doi.org/10.1016/j.expthermflusci.2010.12.009

32. Huminic, G. & Huminic, A. (2013). Numerical study on heat transfer characteristics of thermosyphon heat pipes using nanofluids. *Energy Conversion and Management*, *76*, 393–399. https://doi.org/10.1016/j.enconman.2013.07.026

33. Hussain, A. H., Jawad, Q. & Sultan, K. F. (2015). Experimental analysis on thermal efficiency of evacuated tube solar collector by using nanofluids 2 . Preparation of Silver and Zirconium. *Internatonal Journal of Sustainable and Green Energy*, *4*(3–1), 19–28. https://doi.org/10.11648/J.IJRSE.S.2015040301.14

34. Hussein, A. K. (2016). Applications of nanotechnology to improve the performance of solar collectors - Recent advances and overview. In *Renewable and Sustainable Energy Reviews* (Vol. 62, pp. 767–792). Pergamon. https://doi.org/10.1016/j.rser.2016.04.050

35. Kang, W., Shin, Y. & Cho, H. (2019). Experimental investigation on the heat transfer performance of evacuated tube solar collector using CuO nanofluid and water. *Journal of Mechanical Science and Technology*, *33*(3), 1477–1485. https://doi.org/10.1007/s12206-019-0249-6

36. Kaya, H. & Arslan, K. (2019). Numerical investigation of efficiency and economic analysis of an evacuated U-tube solar collector with different nanofluids. *Heat and Mass Transfer/Waerme- Und Stoffuebertragung*, *55*(3), 581–593. https://doi.org/10.1007/s00231-018-2442-z

37. Kim, H., Ham, J., Park, C. & Cho, H. (2016). Theoretical investigation of the efficiency of a U-tube solar collector using various nanofluids. *Energy*, *94*, 497–507. https://doi.org/10.1016/j.energy.2015.11.021

38. Kim, H., Kim, J. & Cho, H. (2017). Experimental study on performance improvement of U-tube solar collector depending on nanoparticle size and concentration of Al2O3 nanofluid. *Energy*, *118*, 1304–1312. https://doi.org/10.1016/j.energy.2016.11.009

39. Kolsi, L., Alrashed, A. A. A. A., Al-Salem, K., Oztop, H. F. & Borjini, M. N. (2017). Control of natural convection via inclined plate of CNT-water nanofluid in an open sided cubical enclosure under magnetic field. *International Journal of Heat and Mass Transfer*, *111*, 1007–1018. https://doi.org/10.1016/j.ijheatmasstransfer.2017.04.069

40. Lee, J. H., Hwang, K. S., Jang, S. P., Lee, B. H., Kim, J. H., Choi, S. U. S. & Choi, C. J. (2008). Effective viscosities and thermal conductivities of aqueous nanofluids containing low volume concentrations of Al2O3 nanoparticles. *International Journal of Heat and Mass Transfer*, *51*(11–12), 2651–2656. https://doi.org/10.1016/j.ijheatmasstransfer.2007.10.026

41. Li, H. jie, Jiang, F., Qi, G. peng, Zhao, P. li, Jiang, T., Li, N., Chen, X. ling & Li, X. lun. (2018). Effect of particle size and solid holdup on heat transfer performance of a SiC/water three-phase closed thermosyphon. *Applied Thermal Engineering*, *132*, 808–816. https://doi.org/10.1016/j.applthermaleng.2017.12.114

42. Li, L. & Dubowsky, S. (2011). A new design approach for solar concentrating parabolic dish based on optimized flexible petals. *Mechanism and Machine Theory*, *46*(10), 1536–1548. https://doi.org/10.1016/j.mechmachtheory.2011.04.012

43. Li, X., Xu, E., Ma, L., Song, S. & Xu, L. (2019). Modeling and dynamic simulation of a steam generation system for a parabolic trough solar power plant. *Renewable Energy*, *132*, 998–1017. https://doi.org/10.1016/j.renene.2018.06.094

44. Liu, M. S., Lin, M. C. C., Tsai, C. Y. & Wang, C. C. (2006). Enhancement of thermal conductivity with Cu for nanofluids using chemical reduction method. *International Journal of Heat and Mass Transfer*, *49*(17–18), 3028–3033. https://doi.org/10.1016/j.ijheatmasstransfer.2006.02.012

45. Liu, Z. H., Hu, R. L., Lu, L., Zhao, F. & Xiao, H. S. (2013). Thermal performance of an open thermosyphon using nanofluid for evacuated tubular high temperature air solar collector. *Energy Conversion and Management*, *73*, 135–143. https://doi.org/10.1016/j.enconman.2013.04.010

46. Liu, Z. H., Yang, X. F. & Guo, G. L. (2007). Effect of nanoparticles in nanofluid on thermal performance in a miniature thermosyphon. *Journal of Applied Physics*, *102*(1). https://doi.org/10.1063/1.2748348

47. Mahendran, M., Lee, G. C., Sharma, K. V. & Shahrani, A. (2012). Performance of Evacuated Tube Solar Collector using Water-Based Titanium Oxide Nanofluid. *JOURNAL OF MECHANICAL ENGINEERING AND SCIENCES*, *3*, 301–310. https://doi.org/10.15282/jmes.3.2012.6.0028

48. Marashli, A., Alfanatseh, E., Shalby, M. & Gomaa, M. R. (2022). Modelling single-effect of Lithium Bromide-Water (LiBr-H2O) driven by an evacuated solar tube collector in Ma'an city (Jordan) case study. *Case Studies in Thermal Engineering*, *37*, 102239. https://doi.org/10.1016/j.csite.2022.102239

49. Marmoush, M. M., Rezk, H., Shehata, N., Henry, J. & Gomaa, M. R. (2018). A novel merging Tubular Daylight Device with Solar Water Heater – Experimental study. *Renewable Energy*, *125*, 947–961. https://doi.org/10.1016/j.renene.2018.03.031

50. Mercan, M. & Yurddaş, A. (2019). Numerical analysis of evacuated tube solar collectors using nanofluids. *Solar Energy*, *191*, 167–179. https://doi.org/10.1016/j.solener.2019.08.074

51. Morrison, G. L., Tran, N. H., McKenzie, D. R., Onley, I. C., Harding, G. L. & Collins, R. E. (1984). Long term performance of evacuated tubular solar water heaters in Sydney, Australia. *Solar Energy*, *32*(6), 785–791. https://doi.org/10.1016/0038-092X(84)90253-6

52. Muhammad, M. J. (2016). Thermal Performance of Thermosyphon Evacuated Tube Solar Collector using TiO2/Water Nanofluid Thermal Rating of underground Power Cables View project CFD simulation of SARS-CoV-2 airborne transmission View project. In *Journal of Advanced Research in Fluid Mechanics and Thermal Sciences* (Vol. 20, Issue 1). https://www.akademiabaru.com/submit/index.php/arfmts/article/view/2067

53. Muhammad, M. J., Muhammad, I. A., Sidik, N. A. C., Yazid, M. N. A. W. M., Mamat, R. & Najafi, G. (2016). The use of nanofluids for enhancing the thermal performance of stationary solar collectors: A review. In *Renewable and Sustainable Energy Reviews* (Vol. 63, pp. 226–236). Pergamon. https://doi.org/10.1016/j.rser.2016.05.063

54. Nie, X., Zhao, L., Deng, S. & Lin, X. (2017). Experimental study on thermal performance of U-type evacuated glass tubular solar collector with low inlet temperature. *Solar Energy*, *150*, 192–201. https://doi.org/10.1016/j.solener.2017.04.030

55. Ozsoy, A. & Corumlu, V. (2018). Thermal performance of a thermosyphon heat pipe evacuated tube solar collector using silver-water nanofluid for commercial applications. *Renewable Energy*, *122*, 26–34. https://doi.org/10.1016/j.renene.2018.01.031

56. Papadimitratos, A., Sobhansarbandi, S., Pozdin, V., Zakhidov, A. & Hassanipour, F. (2016). Evacuated tube solar collectors integrated with phase change materials. *Solar Energy*, *129*, 10–19. https://doi.org/10.1016/j.solener.2015.12.040

57. Rezk, H., Gomaa, M. R., Marmoush, M. M., Shehata, N. & Henry, J. (2019). Theoretical and experimental performance investigation of a newly combined TDD and SWH system. *Applied Thermal Engineering*, *161*, 114156. https://doi.org/10.1016/j.applthermaleng.2019.114156

58. Sabiha, M. A., Saidur, R., Hassani, S., Said, Z. & Mekhilef, S. (2015). Energy performance of an evacuated tube solar collector using single walled carbon nanotubes nanofluids. *Energy Conversion and Management*, *105*, 1377–1388. https://doi.org/10.1016/j.enconman.2015.09.009

59. Sajadi, A. R. & Kazemi, M. H. (2011). Investigation of turbulent convective heat transfer and pressure drop of TiO2/water nanofluid in circular tube. *International Communications in Heat and Mass Transfer*, *38*(10), 1474–1478. https://doi.org/10.1016/j.icheatmasstransfer.2011.07.007

60. Sayed, E. T., Rezk, H., Olabi, A. G., Gomaa, M. R., Hassan, Y. B., Rahman, S. M. A., Shah, S. K. & Abdelkareem, M. A. (2022). Application of Artificial Intelligence to Improve the Thermal Energy and Exergy of Nanofluid-Based PV Thermal/Nano-Enhanced Phase Change Material. *Energies*, *15*(22), 8494. https://doi.org/10.3390/en15228494

61. Selimefendigil, F. & Öztop, H. F. (2019). Corrugated conductive partition effects on MHD free convection of CNT-water nanofluid in a cavity. *International Journal of Heat and Mass Transfer*, *129*, 265–277. https://doi.org/10.1016/j.ijheatmasstransfer.2018.09.101

62. Selvakumar, P., Somasundaram, P. & Thangavel, P. (2014). Performance study on evacuated tube solar collector using therminol D-12 as heat transfer fluid coupled with parabolic trough. *Energy Conversion and Management*, *85*, 505–510. https://doi.org/10.1016/j.enconman.2014.05.069

63. Shanbedi, M., Heris, S. Z., Amiri, A. & Baniadam, M. (2014). Improvement in Heat Transfer of a Two-Phased Closed Thermosyphon Using Silver-Decorated MWCNT/Water. *Journal of Dispersion Science and Technology*, *35*(8), 1086–1096. https://doi.org/10.1080/01932691.2013.833101

64. Sharafeldin, M. A. & Gróf, G. (2018). Evacuated tube solar collector performance using CeO2/water nanofluid. *Journal of Cleaner Production*, *185*, 347–356. https://doi.org/10.1016/j.jclepro.2018.03.054

65. Sharafeldin, M. A. & Gróf, G. (2019). Efficiency of evacuated tube solar collector using WO3/Water nanofluid. *Renewable Energy*, *134*, 453–460. https://doi.org/10.1016/j.renene.2018.11.010

66. Tang, R., Cheng, Y., Wu, M., Li, Z. & Yu, Y. (2010). Experimental and modeling studies on thermosiphon domestic solar water heaters with flat-plate collectors at clear nights. *Energy Conversion and Management*, *51*(12), 2548–2556. https://doi.org/10.1016/j.enconman.2010.04.015

67. Tang, R. & Yang, Y. (2014). Nocturnal reverse flow in water-in-glass evacuated tube solar water heaters. *Energy Conversion and Management*, *80*, 173–177. https://doi.org/10.1016/j.enconman.2014.01.025

68. Tong, Y. & Cho, H. (2015). Comparative study on the thermal performance of evacuated solar collectors with U-Tubes and heat pipes. *International Journal of Air-Conditioning and Refrigeration*, *23*(3). https://doi.org/10.1142/S2010132515500194

69. Tong, Y., Kim, J. & Cho, H. (2015). Effects of thermal performance of enclosed-type evacuated U-tube solar collector with multi-walled carbon nanotube/water nanofluid. *Renewable Energy*, *83*, 463–473. https://doi.org/10.1016/j.renene.2015.04.042

70. Wang, X., Huang, K., Yuying, Y. & Cen, H. (2022). Heat transfer enhancement with nanofluids in automotive. In *Advances in Nanofluid Heat Transfer* (pp. 229–263). https://doi.org/10.1016/B978-0-323-88656-7.00016-7

71. Wen, D. & Ding, Y. (2004). Experimental investigation into convective heat transfer of nanofluids at the entrance region under laminar flow conditions. *International Journal of Heat and Mass Transfer*, *47*(24), 5181–5188. https://doi.org/10.1016/j.ijheatmasstransfer.2004.07.012

72. Yan, S., Wang, F., Shi, Z. G. & Tian, R. (2017). Heat transfer property of SiO2/water nanofluid flow inside solar collector vacuum tubes. *Applied Thermal Engineering*, *118*, 385–391. https://doi.org/10.1016/j.applthermaleng.2017.02.108

73. Yang, X. F. & Liu, Z. H. (2012). Flow boiling heat transfer in the evaporator of a loop thermosyphon operating with CuO based aqueous nanofluid. *International Journal of Heat and Mass Transfer*, *55*(25–26), 7375–7384. https://doi.org/10.1016/j.ijheatmasstransfer.2012.07.026

74. Zambolin, E. & Del Col, D. (2010). Experimental analysis of thermal performance of flat plate and evacuated tube solar collectors in stationary standard and daily conditions. *Solar Energy*, *84*(8), 1382–1396. https://doi.org/10.1016/j.solener.2010.04.020

75. Zhou, S. Q. & Ni, R. (2008). Measurement of the specific heat capacity of water-based Al2 O3 nanofluid. *Applied Physics Letters*, *92*(9). https://doi.org/10.1063/1.2890431

JREE: Vol. 10, No. 4, (Autumn 2023) 156-162

Journal of Renewable Energy and Environment

Journal Homepage: www.jree.ir

Materials and Energy Research Center

MERC

Technical Note Article

Thermal Investigation of Single Slope Solar Still by Using Energy Storage Material

Subramanian Kumaravel [a], Nagaraj Meenakshi Sunadaram [b*], Govindarajan Bharathiraja [a]

[a] Department of Mechanical Engineering, Saveetha School of Engineering, Saveetha Institute of Medical and Technical Sciences, P. O. Box: 602 105, Chennai, India.
[b] Department of Agricultural Engineering ,Saveetha School of Engineering, Saveetha Institute of Medical and Technical Sciences, P. O. Box: 602 105, Chennai , India.

PAPER INFO

Paper history:
Received: 21 December 2022
Revised: 12 May 2023
Accepted: 13 May 2023

Keywords:
Solar Still,
Copper Scrap,
Brass Scrap,
Temperature,
Productivity,
Water,
Salt Water

ABSTRACT

In this research, a piece of copper scrap was placed in the 1m × 1m base of a single-slope solar still. An automated system steadily dripped salt water into the basin of the solar still. The experiment utilized dripping salt water and energy storage materials such as copper and brass scrap. Research has shown that the presence of copper scrap in the basin, combined with a shallow layer of salt water, has a significant impact on the distillate output. However, the high thermal capacity of the salt water in the basin can lead to reduced production. As more salt water is added to the basin, the temperature difference between the water inside and the glass cover increases. Based on the experimental results, the calculated yield is satisfactory, and the overall thermal efficiency remains at 71.3%. The production rate is also influenced by the diffusion process on the south-facing condensing cover. The temperatures of water, glass, and air, as well as their combined effects, are measured and analyzed.

https://doi.org/10.30501/jree.2023.376724.1518

1. INTRODUCTION

Contamination of natural and artificial water supplies is a major contributor to the global fresh water crisis (Zhang et al., 2022). The use of solar distillation as a radical, forward-thinking approach is recommended as part of the overall solution. A basin can be built by using only readily available materials Still, many scientists have attempted and failed to find a way to boost distillation output. Researchers (Beemkumar et al., 2017) (Dhaidan & Khodadadi, 2017) (Lamnatou et al., 2019) (Liu et al., 2020) (Rasheed, 2020)found that decreasing the amount of water used in the still increased the yield. In addition to boosting distillate yield and solar energy absorption, adding dye to the basin water has other advantages (P. M. Cuce et al., 2021). There are a few strategies to improve the distillate production process, and one of them is the use of salt water and other absorbent materials. Researchers (Dhivagar et al., 2021) maximized the solar energy absorption of charcoal by using it in conjunction with other materials, while other authors (Xiao et al., 2019) relied on rubber mates to do the same. In an effort to increase output, scientists (E. Cuce et al., 2020) (Nagaraj et al., 2020;) (Panchal et al., 2017) performed experiments that involved adding "brass" components like glass, rubber, and brass gravel. It is crucial that water be distributed uniformly across the basin. Researchers in a recent study (Bhardwaj et al., 2020) soaked their printed materials in water before mailing them. The authors (Imran et al., 2020) proposed using a method to store daytime energy surplus for night time evaporation in a conventional still. This article identifies an evaporation zone and a heat storage zone within the basin water. About 35% of the solar heat is absorbed by water each day, according to their estimates. The researchers utilized a basin made of brass granite gravel, measuring 1 m long, 0.5 m wide, and 6 mm thick.

Storing the heat generated during the day in the blue metal scraps of solar stills, as described by author (Duan et al., 2020), allows the process to be repeated at night. Testing has shown that adding a layer of water in between red brick pieces, quartzite rock, cleaned scraps, cement concrete parts, and ferrous scraps significantly increases productivity. In recent studies, the authors (Bhardwaj et al., 2019) distilled liquid using a shallow basin of water and various wick materials.

The impact of combining beach sand with paraffin wax as a composite heat energy storage material is studied. Experiments are conducted in a solar still equipped with a composite heat storage material (SSCHSM), and the results are compared to those obtained in a solar still using a sensible heat storage material (SSSHSM), a solar still using a latent heat storage material (SLHSM), and a conventional solar still (CSS) (Sampathkumar et al., 2023)**.** The most practical solution to the global water issue is the use of desalination techniques driven by renewable energy sources since they do not deplete current energy sources, which causes ecological imbalance. Coupling solar stills with photovoltaic systems is becoming increasingly popular as a means of solar desalination (Suraparaju, Sampathkumar, et al., 2022)**.** Theoretically, the system was only around 31.58% efficient, although both the traditional and modified desalination systems achieved experimental

*Corresponding Author's Email: nagarajm.sse@saveetha.com (N. Meenakshi Sunadaram)
URL: https://www.jree.ir/article_171878.html

Please cite this article as: Kumaravel, S., Meenakshi Sunadaram, N., & Bharathiraj, G. (2023). Thermal Investigation of Single Slope Solar Still by Using Energy Storage Material, *Journal of Renewable Energy and Environment (JREE)*, 10(4), 156-162. https://doi.org/10.30501/jree.2023.376724.1518.

efficiencies of about 36.28 and 78.86%, respectively. Changing the absorber material to copper, which is very thermally conductive, significantly increased system temperatures and, in turn, the system efficiency and yield (Suraparaju, Jha, et al., 2022).

By increasing the condensation rate using natural fibres on the glass cover, this study aims to assess the long-term viability of solar stills. Banana fibres (BF) and jute fibres (JF) are used to cover the solar still glass, both of which are readily available and eco-friendly (SS). The absorbency, retention, and porosity of natural fibres are crucial factors in increasing the condensation rate (Suraparaju & Natarajan, 2022c). Energy use to convert salt or brackish water into potable water might be one solution to this issue. In order to achieve long-term sustainability, the global community is moving away from traditional energy consumption patterns. When compared to other renewable energy sources, solar energy has higher efficiency and greater availability (Suraparaju et al., 2023). The solar still is one of several solar energy-driven desalination methods that may desalinate accessible saltwater or brackish water at low costs and with fewer infrastructure requirements. However, solar stills have a low freshwater yield, and many methods are being studied to prove their efficiency (Suraparaju & Natarajan, 2022b).

Incorporating a corncob filtration system improved scaling prevention over simply recirculating water through the hoses. In addition to producing more pure water per unit of energy expended, combined SPDC and LTTD systems are more cost-effective than solar stills (Suraparaju, Arjun Singh, et al., 2022). The results show that the RT-58 PCM can provide a higher yield than the traditional solar still (CSS) that did not use PCM. The efficiency of a solar still equipped with PCM is 46% higher than that with CSS. In addition, the cost per liter of freshwater produced and the payback period were shown to be lower for the solar still with PCM than they were for CSS (Sahu et al., 2022). The efficiency of SSGC is higher than that of CSS by roughly 19.1%. The Payback Time (PT) for obtaining one liter of clean water from SSGCF is 3.9 months, whereas the PTs for obtaining one liter of clean water from SSGC and CSS are 5.5 and 7.1 months, respectively (Suraparaju & Natarajan, 2022a).

This research presents the theoretical design and testing of a thermal storage component-based single-slope solar still. Copper and brass scrap is immersed in saline water one at a time to determine the technique efficacy.

2. DESIGN OF THE SYSTEM

The outer and inner plywood casings of the still are identically sized at 1 square meters. Air gaps in enclosures can be filled with glass wool, which has a heat conductivity rate of 0.0042 W/mK. Splitting the difference of 0.10 m between the front and back walls is done. Considering the latitude of the site, a glass dome with a condensing surface slope of 11° makes the most sense. According to Figure. 1, the experiment made use of a solar still setup in a single-slope configuration. Through a j-shaped tube linked to the front wall, distillate pours into a measuring jar (Manente et al., 2016) (Wu & Lin, 2015). It consists of galvanized iron sheets, coated brass for maximum solar absorption, and thin copper sheets bonded together (Qu et al., 2015). By controlling the rate at which seawater is passed into the basin, its floor has been brought to its lowest point. (Jamel et al., 2013) The gate valve in the saltwater tanks delivers water to the drip system, which consists of horizontal heat transmission pipes with drip buttons at a depth of 0.10 m within the basin (Baral et.,2015)

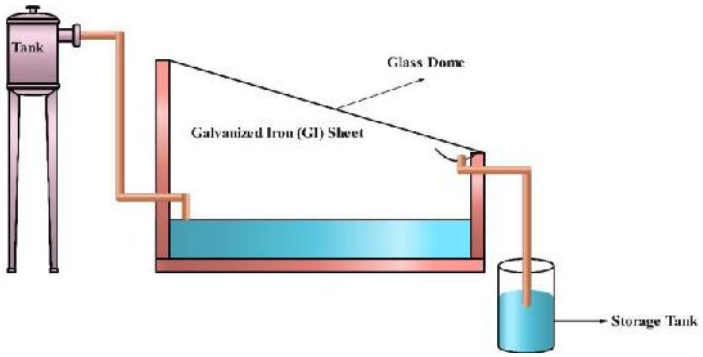

Figure 1. Schematic view of a solar still.

Copper-constantan thermocouples are used for accurate temperature readings in the basin, salt water, and condensation lid. Air temperature and solar radiation can be evaluated with the help of digital thermometers and radiation monitors, respectively. Table 1 summarizes key properties of common energy storage material.

Table 1. Properties of Energy-Storage Materials

Constituents	Density	Thermal conduction	Latent heat capacity
	g/cm³	(W/mK)	(kJ/kg)
Copper scrap	8.6	386.00	206
Brass scrap	3076	2.07 – 2.91	754

3. TEMPERATURE ANALYSIS

3.1. Transmission on Glass top

The condensing glass was covered with light from a wide range of directions and at variable intensity, all of which depended on the Earth's latitude (Jaafar & Hameed, 2021). If researchers want to determine the amount of energy absorbed by the water in the basin, they need to consider both the radiation energy received by the cover glass and the temporal variation in the transmittance of the cover glass. A theoretical evaluation is conducted, taking into account factors such as the radiant energy from the horizontal surface and the consistent transmission of the cover glass. The liquid within the still is heated by the solar energy that enters through the south-facing glass top (Sampathkumar & Natarajan, 2021).

$$Q_i = Q_s \quad (1)$$

where $Q_s = A_s I_S$.

Using this formula, which assumes all south-facing coverings are open at all times (Elsheikh et al., 2021) (Khairat Dawood et al., 2021)the authors can estimate the total solar radiation entering the still from the south:

$$Q\tau = Q\tau_S \quad (2)$$

where $Q\tau_S = \tau_S A_g I_S$

Based on the incidence angle (θ) of solar radiation, the percentage of diffused radiation (Kd), and the breadth of the glass cover (d), the authors (Labied et al., 2020) derived an equation to forecast the glass transmittance.

3.2. Energy balancing equation

When solar rays enter the basin through the glass top, they heat up the surface of the salt water, causing it to evaporate. Convection, radiation, and evaporation all play roles in transferring heat from the water surface to the base of the glass. Since the water and glass have different partial pressures, heat and mass are transferred from the water surface to the covering via evaporation. Some of the latent heat caused by the water vapor during evaporation is transmitted to the exterior of the container when the vapor condenses on the bottom of a glass container. Bottom and side walls are responsible for some of the heat loss to the environment through conduction and convection. With drip irrigation, salt water can gradually enter the basin and the basin's fresh and saltwater masses can achieve thermal equilibrium through sensible heat transfer.

The energy balance equations have been formulated under the following assumptions:

(i) Glass surface temperature is uniform across its entire area.

(ii) In order to prevent any vapor from escaping the still, the mechanism is hermetically sealed.

(iii) The small slope of the cover ensures that the glass top and the water surface are at right angles to one another.

Glass cover

$$I_g\alpha_g A_g + h_1 A_W(T_W - T_g) = h_2 A_g(T_g - T_a) \quad (3)$$

Basin water

$$(m_w C_w + m_{em} C_{cm})\ \frac{dT_w}{dt} = Q_\tau \alpha_{bw} - h_1 A_w(T_w - T_g) - h_3 A_{bs}(T_w - T_a) - h_{fw}(T_a - T_w) \quad (4)$$

The expression for T_g., obtained by solving Eq. (3), is as follows (Nazari et al., 2019a)

$$T_g = \frac{I_g\alpha_g A_g + h_1 A_w T_w + h_2 A_g T_a}{h_2 A_g + h_1 A_w} \quad (5)$$

wher

$h_1 = h_{cwg} + h_{rwg} + h_{ewg}$

$h_2 = h_{rga} + h_{cga}$

$h_3 = h_{ta} + h_{sa}$

$T_{sky} = (T_a - 6)$ is the apparent sky temperature

The following form (Nazari et al., 2019b) (Arunkumar et al., 2019) is obtained by making the necessary changes to Eq. (4):

$$\frac{dT_w}{dt} + PT_w = Q \quad (6)$$

where

$$P = \frac{h_1^2 A_w^2}{(m_w C_w + m_{em} C_{cm})(h_2 A_g + h_1 A_w)} - \left(\frac{h_1 A_w + h_3 A_{bs} - h_{fw}}{m_w C_w + m_{em} C_{cm}}\right)$$

$$Q = \frac{Q_\tau \alpha_{bw}}{m_w C_w + m_{em} C_{em}} + \frac{h_1 A_w I_g \alpha_g A_g + h_1 h_2 A_w A_g T_a}{(m_w C_w + m_{em} C_{em})(h_2 A_g + h_1 A_w)} + \frac{(h_3 A_{bs} - h_{fw}) T_a}{m_w C_w + m_{em} C_{cmm}}$$

The generic form of the solution to Eq. (6) is as follows (Shoeibi et al., 2022):

$$y \cdot e^{\int p \cdot dt} = \int Q \cdot e^{\int p dt} \cdot dt + c \quad (7)$$

An expression for T_w is

$$T_w = \frac{Q}{p} + c \cdot e^{-pt} \quad (8)$$

Under the initial conditions, Eq. (8) holds when t=0, $T_w = T_{wi}$

$$c = T_{wi} - \frac{Q}{p} \quad (9)$$

By adjusting c in Eq. (8), it was obtained that

$$T_w = \frac{Q}{p}(1 - e^{-pt}) + T_{wi}\ .e^{-pt} \quad (10)$$

The water temperatures in the basin and glass can be determined with great precision using Eqs. (5) and (10), respectively.

Distillation yield per still basin is calculated using

$$m_e = \left(\frac{h_{ewg}(T_w - T_g}{L}\right) \times 3600 \quad (11)$$

The still efficiency is determined by (Abdelgaied et al., 2021)

$$\eta\% = \frac{M_e L}{A_b \int I_s \Delta t} \times 100 \quad (12)$$

where Δt is the duration of time in which solar radiation is quantified.

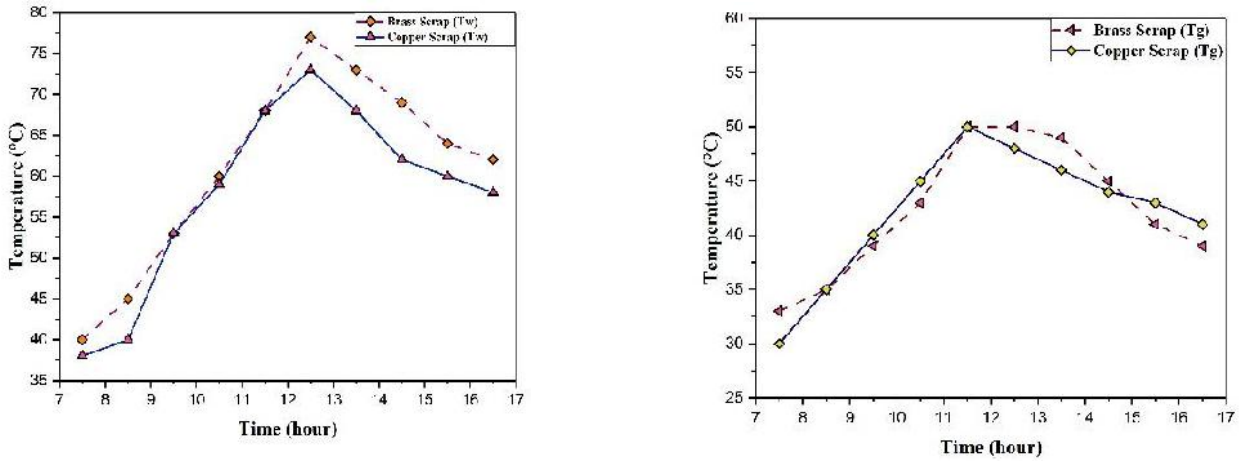

(a) (b)

Figure 2. Evaluation of Temperature for (a) water and (b) glass cover.

4. RESULTS AND DISCUSSION

The analytical response is derived by solving the energy balance equations to analyze the numerical findings obtained with the following design variables:

$A_g = 1.72\ m^2;\ A_w = A_b = 1.6215\ m^2;\ C_w = 4287\ J/kg^{\circ}C^{-1};$

$m_w = 14\ kg;\ m_{em} = 32\ kg;\ A_{bs} = 0.15\ m^2;$

$\alpha_{bw} = 0.91; \alpha_g = 0.06;$ L = 2386000 j/kg

$V = 1.8\ m/s, K = 0.042\ W/mk.$

$\sigma = 6.19 \times 10^{-8}\ W/m^2k^4$

The sun radiation and room temperature data are used as inputs in the numerical calculations. Between noon and two in the afternoon, as illustrated in Figure 2, the temperature difference between the evaporation surface of the liquid and the face of the condensing glass cover reaches its peak. Subsequently, it gradually diminishes throughout the day.

It is also worth noting the important temperature variation between the liquid and the surface of the glass cover in the basin containing the Copper scrap. Therefore, there is a linear relationship between the temperature difference midday and Productivity. Even during the peak solar light of the day, the water level in the basin remained low due to the slow dripping of salt water into it. Given that the water in the basin has a low thermal capacity, it increases production. Independent of the dripping setup, the energy storage materials are put through their paces. For 24 hours, the basin drip system continues to deliver 12 liters of salt water.

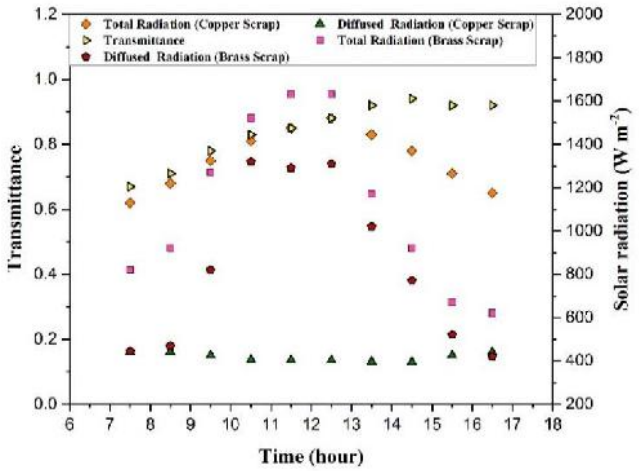

Figure 3. Difference of Solar Radiation and time with respect to time.

The transmission and diffuse radiation fraction are modified when glass is oriented toward the south (see Figure. 3). After analyzing the transmittance correlation reported by the authors (Bahiraei et al., 2021), it was concluded that the cover allowed for sufficient transmittance at all incident angles of solar energy. Glass covers facilitate the passage of a significant amount of light even when the solar angle is low, such as during the mornings and evenings.

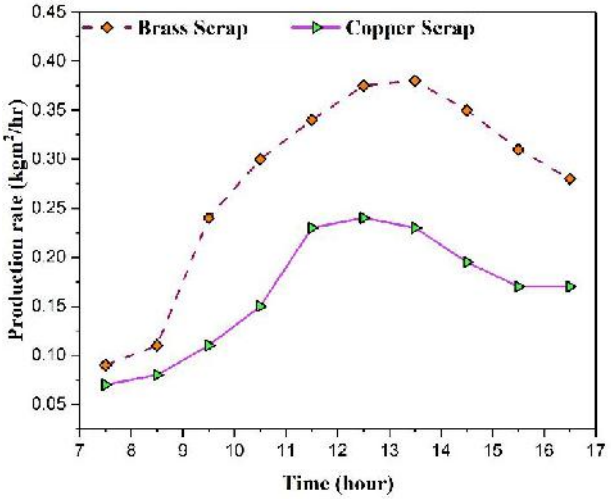

Figure 4. The production rate for energy storage materials.

Figure 4 displays the daily production rates of copper and brass scrap. Small, effective thermal storage materials were used thanks to a drip system that maintained a 1-cm water level in the basin, facilitating the collection of the required data. The findings indicate that employing Copper scrap as a storage medium enables the highest output rate to be maintained continuously throughout the day.

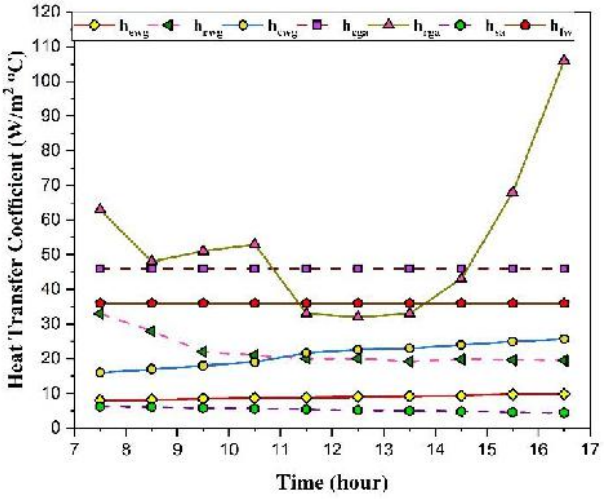

Figure 5. Difference in the average heat transfer coefficient

The internal and exterior heat transmission coefficients of solar still change throughout the day, as shown in Figure 5. Convection and thermal radiation exchange between the glass cover and the atmosphere have larger coefficients than other heat transfer processes inside the building throughout the day. Consequently, the saltwater used in the still exhibits a higher heat transfer coefficient than the still itself. This difference arises because, unlike the interior of the still, the exterior casing is always exposed to the elements.

Figure 6 displays the sum of output from a wide variety of plausible heat storage materials during the hours of 7:30 am and 4:30 pm. As can be seen from the graph, between 7:30 AM and 4:30 PM, the copper scrap in the basin generates more heat than any other sensible thermal storage material. After 24 hours of distillation, copper scrap is expected to yield 5.16 kg/m^2 of distillate. The nighttime production rate of 3.2 kg/m^2 can be attributed to the copper scrap in the basin.

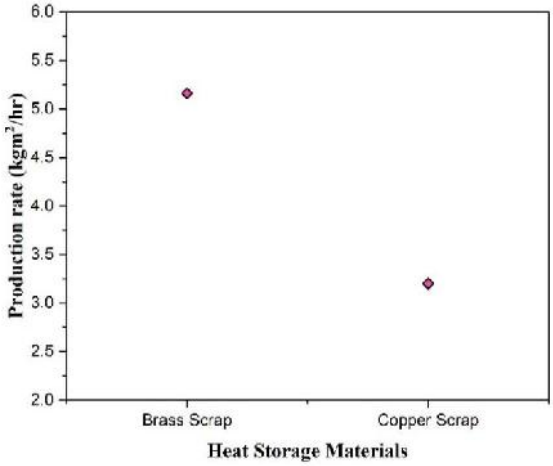

Figure 6. Comparison of Energy storage materials with Production rate.

Copper scrap has a higher heat capacity than any other material. The enhanced thermal conductivity of the scrap facilitates absorbing much solar heat during the day, thus increasing the distillate yield in the evening. The salt water is retained by the porous Copper scrap, and the energy in the water is utilized throughout the distillation process, even when the sun is not out or at night.

Based on the information provided, it appears that during May and June of 2022, tests were conducted on different sensible heat storage materials at consistent solar radiation levels. The consistent radiation levels observed across all days suggest that the tests were likely carried out under controlled conditions. This controlled environment enables accurate and reliable comparisons between the different materials being tested. When such days occur, it is reasonable to assume that the weather will be consistent with the usual conditions. Midday consistently exhibits the highest levels of solar energy, and this pattern repeats on a daily basis. Figure 7 illustrates the monitoring of daily changes in solar radiation and ambient temperature using different thermal storage materials.

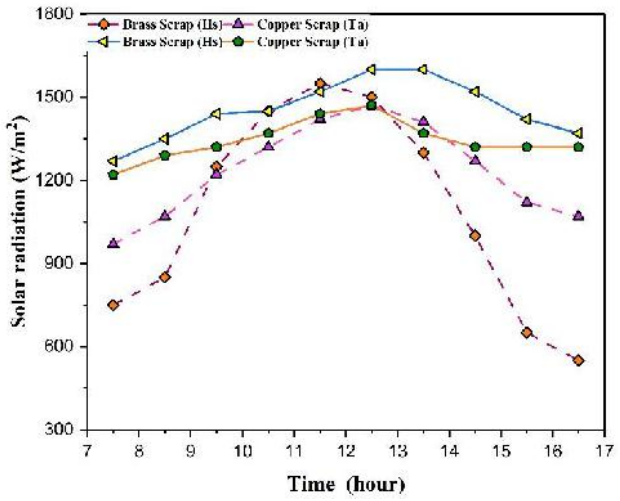

Figure 7. Difference between ambient temperature and solar radiation intensity.

A drop-free experiment with 1.8 cm salt water and Copper scrap was conducted. Figure 8 displays that adding a salty water basin with a dripper changes the output, water, and glass cover temperatures. As indicated by the graph, there is a significant temperature gradient between the water and the glass cover, which causes the evaporation rate to rise when a drop of salt water is generated using Copper scrap. Evaporation slows down because glass has a high thermal capacity, decreasing the temperature difference among the water and the surface. After 24 hours of dripping with copper scrap, distillate production increases by 36% compared to a saline basin.

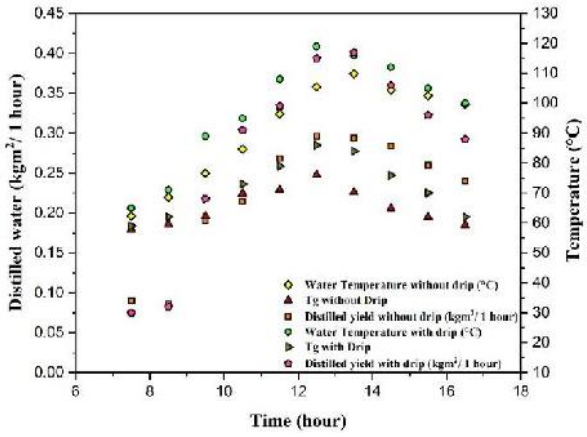

Figure 8. Variation of drip and drip-free factors

The basin cover glass temperature, water temperature, and copper scrap production rate are all depicted in Figure. 9 after a thorough examination. The experimental outcomes are in reasonable agreement with the theoretical predictions. Some experimental observations may deviate from the norm at specific points due to the projection of the basin's back and side walls, but these conditions are beyond the researchers' control.

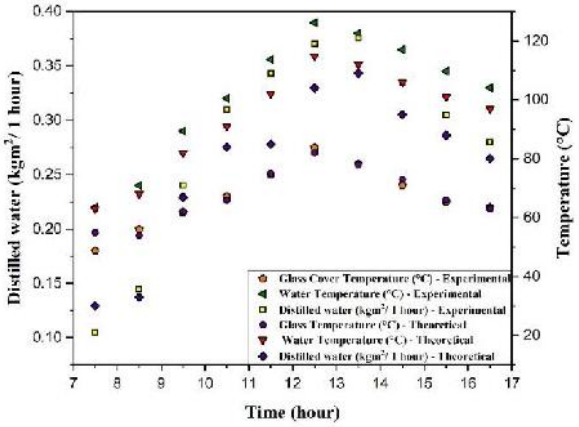

Figure 9. Comparison of theoretical and experimental data on water and glass cover.

The research paper refers to the diffusion process, which involves the movement of water molecules from areas of high concentration to regions of lower concentration, leading to the even dispersion of these molecules. In the context of a solar still, diffusion plays a crucial role in controlling the production of distilled water.

A typical solar still comprises a structure that captures sunlight, a basin that holds the water intended for distillation, and a sloping or angled condensing surface, often a transparent lid. When sunlight enters the still, it warms the water, causing it to vaporize. The resulting water vapor rises and meets the cooler condensing surface, which is usually cooler due to its position and thermal characteristics. As it touches the cooler surface, the

water vapor transforms back into liquid droplets through the process of condensation.

In the case of the south-facing condensed cover mentioned in the research paper, the diffusion process is affected by several factors:

1. The production of distilled water is influenced by the temperature gradient that exists between the water vapor and the cooler condensing surface. A larger temperature difference results in a faster diffusion process, thereby increasing the rate of production of distilled water.
2. Surface properties of the south-facing condensing cover can have an impact on the diffusion process. Hydrophilic surfaces, which attract water, can accelerate the condensation process, while hydrophobic surfaces, which repel water, slow it down. Furthermore, the cover's transparency and thermal properties can affect the temperature gradient inside the solar still.
3. The rate of diffusion is influenced by the inclination angle of the south-facing condensing cover. A steeper angle can accelerate the process of condensation and runoff, thereby increasing the rate of production of distilled water. Conversely, a shallower angle may result in slower condensation and runoff, leading to a decrease in the production rate.

External factors such as air temperature, humidity, and wind speed can affect the diffusion process. For instance, higher air temperatures can augment the rate of water evaporation, while elevated humidity and wind speed have an adverse effect on the condensation process occurring on the cover.

Understanding the diffusion process in a solar still is essential to optimizing its performance. By carefully selecting materials, design, and operating conditions, it is possible to improve the efficiency of the solar still and increase the production rate of distilled water

5. CONCLUSION

(i) The theoretical modeling of the transfer and absorption of solar radiation through south-facing windows is explained, as well as the thermal efficiency of single-slope solar stills under typical conditions.

(ii) Copper scrap, with its high thermal mass and excellent heat retention properties, can be used to increase evaporation rates throughout the day and night.

(iii) In the presence of a copper scrap-containing basin, the thermal efficiency of the solar still is substantially increased due to the release of stored heat energy during periods of reduced solar radiation. Nonetheless, the high thermal capacity of the basin can adversely affect the overall production of the still when salt water is used. As salt water accumulates in the basin, the temperature difference between the condensing glass cover and the water beneath it increases due to the lower thermal capacity of salt water compared to fresh water.

The calculations indicate that the still has a total thermal efficiency of 71.3% and the results of the experiments support this finding. Additionally, the production rate is influenced by the diffusion process on the south-facing condensing cover, which in turn affects the temperature differential between the water, glass, and surrounding air.

6. ACKNOWLEDGEMENT

The authors would like to express their heartfelt gratitude to the Research Department of Simats School of Engineering for their invaluable support. A special thanks goes to Dr. G. Venkatesh, Scientist F, National Institute of Ocean Technology, for his valuable contributions.

NOMENCLATURE

PCM	Phase change material
SSSHSM	solar still using sensible heat storage material
CSS	Conventional solar Still
SSGC	Solar Still with only water dripping arrangemnt without
SSGCF	Solar still using glass cooling with water dripping and sisal fibers

REFERENCES

1. Abdelgaied, M., Zakaria, Y., Kabeel, A. E., & Essa, F. A. (2021). Improving the tubular solar still performance using square and circular hollow fins with phase change materials. *Journal of Energy Storage*, *38*. https://doi.org/10.1016/j.est.2021.102564
2. Arunkumar, T., Murugesan, D., Raj, K., Denkenberger, D., Viswanathan, C., Rufuss, D. D. W., & Velraj, R. (2019). Effect of nano-coated CuO absorbers with PVA sponges in solar water desalting system. *Applied Thermal Engineering*, *148*, 1416–1424. https://doi.org/10.1016/j.applthermaleng.2018.10.129
3. Bahiraei, M., Nazari, S., & Safarzadeh, H. (2021). Modeling of energy efficiency for a solar still fitted with thermoelectric modules by ANFIS and PSO-enhanced neural network: A nanofluid application. *Powder Technology*, *385*, 185–198. https://doi.org/10.1016/j.powtec.2021.03.001
4. Baral, S., Kim, D., Yun, E., & Kim, K. C. (2015). Energy, exergy and performance analysis of small-scale organic rankine cycle systems for electrical power generation applicable in rural areas of developing countries. *Energies*, *8*(2), 684–713. https://doi.org/10.3390/en8020684
5. Beemkumar, N., Karthikeyan, A., Keshava Reddy, K. S., Rajesh, K., & Anderson, A. (2017). Analysis of Thermal Energy Storage Tank by ANSYS and Comparison with Experimental Results to Improve its Thermal Efficiency. *IOP Conference Series: Materials Science and Engineering*, *197*(1). https://doi.org/10.1088/1757-899X/197/1/012039
6. Bhardwaj, A. K., Kumar, R., & Chauhan, R. (2019). Experimental investigation of the performance of a novel solar dryer for drying medicinal plants in Western Himalayan region. *Solar Energy*, *177*, 395–407. https://doi.org/10.1016/j.solener.2018.11.007
7. Bhardwaj, A. K., Kumar, R., Chauhan, R., & Kumar, S. (2020). Experimental investigation and performance evaluation of a novel solar dryer integrated with a combination of SHS and PCM for drying chilli in the Himalayan region. *Thermal Science and Engineering Progress*, *20*. https://doi.org/10.1016/j.tsep.2020.100713
8. Cuce, E., Cuce, P. M., Saxena, A., Guclu, T., & Besir, A. B. (2020). Performance analysis of a novel solar desalination system – Part 1: The unit with sensible energy storage and booster reflector without thermal insulation and cooling system. *Sustainable Energy Technologies and Assessments*, *37*. https://doi.org/10.1016/j.seta.2019.100566
9. Cuce, P. M., Cuce, E., & Tonyali, A. (2021). Performance analysis of a novel solar desalination system – Part 2: The unit with sensible energy storage with thermal insulation and cooling system. *Sustainable Energy Technologies and Assessments*, *48*. https://doi.org/10.1016/j.seta.2021.101674
10. Dhaidan, N. S., & Khodadadi, J. M. (2017). Improved performance of latent heat energy storage systems utilizing high thermal conductivity fins: A review. *Journal of Renewable and Sustainable Energy*, *9*(3). https://doi.org/10.1063/1.4989738
11. Dhivagar, R., Mohanraj, M., & Belyayev, Y. (2021). Performance analysis of crushed gravel sand heat storage and biomass evaporator-assisted single slope solar still. *Environmental Science and Pollution Research*, *28*(46), 65610–65620. https://doi.org/10.1007/s11356-021-15487-w

12. Duan, L., Wang, Z., Liu, Y., & Pang, L. (2020). Comparison study of two different integrated solar combined cycle systems. *American Society of Mechanical Engineers, Power Division (Publication) POWER*, *2020-Augus*. https://doi.org/10.1115/POWER2020-16695

13. Elsheikh, A. H., Katekar, V. P., Muskens, O. L., Deshmukh, S. S., Elaziz, M. A., & Dabour, S. M. (2021). Utilization of LSTM neural network for water production forecasting of a stepped solar still with a corrugated absorber plate. *Process Safety and Environmental Protection*, *148*, 273–282. https://doi.org/10.1016/j.psep.2020.09.068

14. Imran, M., Pili, R., Usman, M., & Haglind, F. (2020). Dynamic modeling and control strategies of organic Rankine cycle systems: Methods and challenges. *Applied Energy*, *276*. https://doi.org/10.1016/j.apenergy.2020.115537

15. Jaafar, Z. A., & Hameed, H. G. (2021). Experimental Investigation of a Single Slope Solar Still Performance-Evaporation Process Enhancement Using Evacuated Pipes. *IOP Conference Series: Earth and Environmental Science*, *877*(1). https://doi.org/10.1088/1755-1315/877/1/012041

16. Jamel, M. S., Abd Rahman, A., & Shamsuddin, A. H. (2013). Advances in the integration of solar thermal energy with conventional and non-conventional power plants. *Renewable and Sustainable Energy Reviews*, *20*, 71–81. https://doi.org/10.1016/j.rser.2012.10.027

17. Khairat Dawood, M. M., Shehata, A. I., Kabeel, A. E., Elharidi, A. M., Abdelsalam Taha, A., Bayoumi, S., & Abdalla, A. M. (2021). Increasing the freshwater productivity of a solar still loaded with CuO nanofluids using vibration motion and cover cooling techniques. *International Journal of Energy Research*, *45*(6), 9099–9115. https://doi.org/10.1002/er.6440

18. Labied, A., Hassen Sellami, M., & Cherraye, R. (2020). Experimental study to improve the performance of a conventional single-slope solar still using the photo-catalytic effect of three different metal oxides. *Desalination and Water Treatment*, *208*, 9–16. https://doi.org/10.5004/dwt.2020.26467

19. Lamnatou, C., Smyth, M., & Chemisana, D. (2019). Building-Integrated Photovoltaic/Thermal (BIPVT): LCA of a façade-integrated prototype and issues about human health, ecosystems, resources. *Science of the Total Environment*, *660*, 1576–1592. https://doi.org/10.1016/j.scitotenv.2018.12.461

20. Liu, K., Lang, J., Yang, M., Xu, J., Sun, B., Wu, Y., Wang, K., Zheng, Z., Huang, Z., Wang, C.-A., Wu, H., Jin, Y., & Cui, Y. (2020). Molten Lithium-Brass/Zinc Chloride System as High-Performance and Low-Cost Battery. *Matter*, *3*(5), 1714–1724. https://doi.org/10.1016/j.matt.2020.08.022

21. Manente, G., Rech, S., & Lazzaretto, A. (2016). Optimum choice and placement of concentrating solar power technologies in integrated solar combined cycle systems. *Renewable Energy*, *96*, 172–189. https://doi.org/10.1016/j.renene.2016.04.066

22. Nagaraj, S. K., Nagarajan, B. M., & Ponnusamy, P. (2020). Performance analysis of solar still with Quartzite rock as a sensible storage medium. *Materials Today: Proceedings*, *37*(Part 2), 2214–2218. https://doi.org/10.1016/j.matpr.2020.07.655

23. Nazari, S., Safarzadeh, H., & Bahiraei, M. (2019a). Experimental and analytical investigations of productivity, energy and exergy efficiency of a single slope solar still enhanced with thermoelectric channel and nanofluid. *Renewable Energy*, *135*, 729–744. https://doi.org/10.1016/j.renene.2018.12.059

24. Nazari, S., Safarzadeh, H., & Bahiraei, M. (2019b). Performance improvement of a single slope solar still by employing thermoelectric cooling channel and copper oxide nanofluid: An experimental study. *Journal of Cleaner Production*, *208*, 1041–1052. https://doi.org/10.1016/j.jclepro.2018.10.194

25. Panchal, H., Patel, P., Patel, N., & Thakkar, H. (2017). Performance analysis of solar still with different energy-absorbing materials. *International Journal of Ambient Energy*, *38*(3), 224–228. https://doi.org/10.1080/01430750.2015.1086683

26. Qu, J., Feng, Y., Zhang, Q., Cong, Q., Luo, C., & Yuan, X. (2015). A new insight of recycling of spent Zn-Mn alkaline batteries: Synthesis of ZnxMn1-xO nanoparticles and solar light driven photocatalytic degradation of bisphenol A using them. *Journal of Alloys and Compounds*, *622*, 703–707. https://doi.org/10.1016/j.jallcom.2014.10.166

27. Rasheed, M. H. (2020). Performance enhancement of solar air heater using different phase change materials (PCMs). *Journal of Advanced Research in Fluid Mechanics and Thermal Sciences*, *66*(1), 64–75. https://www.akademiabaru.com/submit/index.php/arfmts/article/view/2807

28. Sahu, S. K., Natarajan, S. K., Arjun Singh, K., & Suraparaju, S. K. (2022). Experimental investigation of a solar still combined with phase change material (RT58) in southern India climatic conditions. *Proceedings of the Institution of Mechanical Engineers, Part C: Journal of Mechanical Engineering Science*. https://doi.org/10.1177/09544062221139986

29. Sampathkumar, A., & Natarajan, S. K. (2021). Experimental investigation on productivity enhancement in single slope solar still using Borassus Flabellifer micro-sized particles. *Materials Letters*, *299*. https://doi.org/10.1016/j.matlet.2021.130097

30. Sampathkumar, A., Suraparaju, S. K., & Natarajan, S. K. (2023). Enhancement of Yield in Single Slope Solar Still by Composite Heat Storage Material—Experimental and Thermo-Economic Assessment. *Journal of Solar Energy Engineering, Transactions of the ASME*, *145*(2). https://doi.org/10.1115/1.4055100

31. Shoeibi, S., Kargarsharifabad, H., Rahbar, N., Khosravi, G., & Sharifpur, M. (2022). An integrated solar desalination with evacuated tube heat pipe solar collector and new wind ventilator external condenser. *Sustainable Energy Technologies and Assessments*, *50*. https://doi.org/10.1016/j.seta.2021.101857

32. Suraparaju, S. K., Arjun Singh, K., Jayan, V., & Natarajan, S. K. (2022). Performance analysis of a novel solar cogeneration system for generating potable water and electricity. *World Journal of Engineering*. https://doi.org/10.1108/WJE-05-2022-0185

33. Suraparaju, S. K., Jha, N., Manoj, S., & Natarajan, S. K. (2022). Mathematical Modelling and Performance Analysis of Single Slope Solar Desalination System. *Lecture Notes in Mechanical Engineering*, 17–33. https://doi.org/10.1007/978-981-16-2794-1_2

34. Suraparaju, S. K., & Natarajan, S. K. (2022a). Effect of natural sisal fibre on enhancing the condensation rate of solar still for sustainable clean water production. *Thermal Science and Engineering Progress*, *36*. https://doi.org/10.1016/j.tsep.2022.101527

35. Suraparaju, S. K., & Natarajan, S. K. (2022b). Review on productivity enhancement of passive solar stills. In *Renewable Energy Technologies: Advances and Emerging Trends for Sustainability* (pp. 165–216). https://doi.org/10.1002/9781119827634.ch6

36. Suraparaju, S. K., & Natarajan, S. K. (2022c). Sustainability assessment of single slope solar still with glass cover cooling using naturally available fibers. *Environmental Progress and Sustainable Energy*, *41*(4). https://doi.org/10.1002/ep.13840

37. Suraparaju, S. K., Natarajan, S. K., Mamilla, V. R., Pappala, S. M. T., Kurada, A., & Lakamsani, M. S. V. P. (2023). Energy, exergy, economic and environmental (4E) analyses of solar still with paraffin wax as phase change energy storage material. *Materials Today: Proceedings*. https://doi.org/10.1016/j.matpr.2023.03.345

38. Suraparaju, S. K., Sampathkumar, A., & Natarajan, S. K. (2022). A Mini State of Art Survey on Photovoltaic/Thermal Desalination Systems. *Lecture Notes in Mechanical Engineering*, 1–15. https://doi.org/10.1007/978-981-16-2794-1_1

39. Wu, J., & Lin, J. (2015). Thermodynamic analysis of a novel heat pump water heater with two-stage heating for a great rise of water temperature. *Energy and Buildings*, *91*, 97–104. https://doi.org/10.1016/j.enbuild.2015.01.042

40. Xiao, G., Chen, J., Yang, T., Ni, M., Cen, K., & Liu, S. (2019). Experiment and simulation study of tubular solar air receiver using a solar dish. *Taiyangneng Xuebao/Acta Energiae Solaris Sinica*, *40*(12), 3355–3363. https://scholar.google.com/scholar?hl=en&as_sdt=0%2C5&q=Experiment+and+simulation+study+of+tubular+solar+air+receiver+using+a+solar+dish+&btnG=

41. Zhang, Y., Lu, B., Wang, Z., Zhu, J., Zhang, J., & Wang, C. (2022). Experimental investigation on the charging and discharging performance enhancement of a vertical latent heat thermal energy storage unit via snowflake fin design. *International Journal of Heat and Mass Transfer*, *199*. https://doi.org/10.1016/j.ijheatmasstransfer.2022.123455

Analysis and Evaluation of Effective Environmental Indicators in the Heat Island of District 1 of Tehran using (RS)

Ali Sayyadi, Mohammad Javad Amiri *

Faculty of Environment, College of Engineering, University of Tehran, Tehran, Iran.

PAPER INFO

Paper History:
Received: 30 August 2022
Revised: 10 November 2022
Accepted: 30 November 2022

Keywords:
Heat Island,
NDVI,
LST,
SPSS

ABSTRACT

One of the environmental problems today is the rising land surface temperature and the formation of heat islands in metropolitan areas, which have arisen due to the unplanned expansion of these cities. Satellite imagery is widely used in urban environmental studies to provide an integrated view and reduce costs and time. In this study, Landsat satellite imagery in TM, ETM+, and OLI sensors from 1984 to 2020, remote sensing techniques, and GIS is used to analyze the data, and SPSS software is employed to examine the correlation between the data. The results indicate that the land surface temperature in District 1 of Tehran has increased during the last 38 years. Moreover, land use in District 1 has changed significantly over this period, and urban land use increased from 16 % (1984) to 35 % (2020) while vegetation declined from 32 % to 14 %. The results of linear regression analysis show a significant correlation between satellite images and weather station data. The significance coefficient (Sig) in all stations is less than 0.05 with a 95 % confidence interval. Besides, the coefficient of variation (R) for all stations is above 80 %, and the coefficient R2 has a desirable value. The findings suggest that the trend of rising temperatures in District 1 of Tehran has become an environmental problem and the changes in land use such as declining vegetation and increasing the acceleration of urbanization are among the factors that affect it.

https://doi.org/10.30501/jree.2022.355387.1438

چکیده:

یکی از مشکلات زیست‌محیطی امروزه افزایش دمای سطح زمین و تشکیل جزایر گرمایی در کلان شهرها است که به دلیل گسترش بی رویه این شهرها به وجود آمده است. تصاویر ماهواره ای به طور گسترده در مطالعات محیطی شهری برای ارائه یک نمای یکپارچه و کاهش هزینه ها و زمان استفاده می‌شود. در این مطالعه، از تصاویر ماهواره‌ای لندست در سنسورهای TM، ETM+ و OLI از سال ۱۹۸۴ تا ۲۰۲۰، تکنیک‌های سنجش از دور و GIS برای تجزیه و تحلیل داده‌ها و نرم‌افزار SPSS برای بررسی همبستگی بین داده‌ها استفاده شده است. نتایج حاکی از آن است که دمای سطح زمین در منطقه ۱ تهران طی ۳۸ سال گذشته افزایش یافته است. علاوه بر این، کاربری زمین در منطقه ۱ به طور قابل توجهی در این دوره تغییر کرده است و کاربری اراضی شهری از ۱۶ ٪ (۱۹۸۴) به ۳۵ ٪ (۲۰۲۰) افزایش یافته است در حالی که پوشش گیاهی از ۳۲ ٪ به ۱۴ ٪ کاهش یافته است. نتایج تحلیل رگرسیون خطی، همبستگی معنی داری را بین تصاویر ماهواره‌ای و داده‌های ایستگاه هواشناسی نشان می‌دهد. ضریب معنی داری (Sig) در تمامی ایستگاه ها کمتر از ۰/۰۵ با فاصله اطمینان ۹۵ درصد است. علاوه بر این، ضریب تغییرات (R) برای همه ایستگاه‌ها بالای ۸۰ درصد است و ضریب R2 مقدار مطلوبی دارد. یافته‌ها حاکی از آن است که روند افزایش دما در منطقه یک تهران به یک معضل زیست‌محیطی تبدیل شده است و تغییرات کاربری اراضی مانند کاهش پوشش گیاهی و افزایش شتاب شهرنشینی از جمله عوامل مؤثر بر آن است.

JREE: Vol. 10, No. 4, (Autumn 2023) 14-21

Thermal Characterization of Eicosane/Graphite Nano-Composite-Based Phase Change Material

Ala Moradi [a], Hajar Es-haghi [b], Seyed Hasan Hashemabadi [a*], Majid Haghgoo [b], Zahra Emami [c]

[a] *Computational Fluid Dynamics (CFD) Research Laboratory, School of Chemical, Petroleum and Gas Engineering, Iran University of Science and Technology (IUST), Tehran, Iran.*
[b] *Iran Space Institute, P. O. Box: 13455/754, Tehran, Iran.*
[c] *Department of Material Science and Engineering, Sharif University of Technology, P. O. Box: 14588 89694, Tehran, Iran.*

PAPER INFO

Paper History:
Received: 19 September 2022
Revised: 21 December 2022
Accepted: 30 December 2022

Keywords:
Thermal Conductivity,
Phase Change Materials,
Graphite Nanoparticles,
Morphological Characterization

ABSTRACT

Phase Change Materials (PCMs) have received much consideration as thermal energy storage systems due to their high storage capacity. However, their heat transfer rate is limited because of the low thermal conductivity. Incorporating of carbon-based nanoparticles into the matrix of PCMs with good dispersion can be an efficient way to solve their deficiency. In this research, graphite nanoparticles were homogeneously dispersed within the Eicosane PCM matrix to prepare a Nano-Enhanced PCM (NEPCM). The main objective is to determine the optimum amount of graphite to maximize the thermal properties of NEPCM composites. The Scanning Electron Microscopy (SEM) images of the prepared nanocomposites confirmed the excellent dispersion of graphite nanoparticles within the Eicosane layers through an ultrasonic bath-assisted homogenization procedure followed by solidification. In addition, Differential Scanning Calorimetry (DSC) and Thermal Conductivity Evaluation (TC) of the samples were conducted to determine their heat capacity and thermal diffusivity. The results illustrated that the more the number of graphite nanoparticles, the larger the number of collisions between graphite and Eicosane. As the nanoparticle content increased, the thermal conductivity and diffusivity were enhanced, as well. Numerically, the maximum thermal conductivity was 4.1 W/m K for the composite containing 10 wt% graphite, 15.66 times that of the pure Eicosane. Furthermore, increasing crystal growth and reducing heat capacity for the large number of nanoparticles in the composite were discussed. The significantly improved thermal properties of the prepared NEPCMs with an optimal nanoparticle content could make them applicable for different thermal management applications.

https://doi.org/10.30501/jree.2023.362050.1454

چکیده:

مواد تغییر فاز دهنده (PCM) به دلیل ظرفیت ذخیره‌سازی انرژی بالا، به عنوان سیستم‌های ذخیره‌سازی انرژی حرارتی مورد توجه قرار گرفته‌اند. با این حال، سرعت انتقال حرارت آنها به دلیل رسانایی حرارتی کم، محدود است. ترکیب نانوذرات در ماتریس PCM با پراکندگی مناسب می‌تواند راهی کارآمد برای رفع این مشکل باشد. در تحقیق حاضر، نانوذرات گرافیت به طور همگن در ماتریس ایکوزان پراکنده شدند تا یک PCM نانو تقویت شده (NEPCM) تهیه شود. هدف ا صلی یافتن مقدار بهینه گرافیت جهت به حداکثر ر ساندن خواص حرارتی کامپوزیت های NEPCM بود. میکروگراف های SEM نانوکامپوزیت های تهیه شده، پراکندگی عالی نانوذرات گرافیت در لایه های ایکوزان را از طریق یک روش همگن سازی به کمک حمام اولتراسونیک و سپس انجماد تأیید کرد. علاوه بر این، کالریمتری روبشی افتراقی (DSC) و ارزیابی هدایت حرارتی (TC) نمونه‌ها برای تعیین ظرفیت گرمایی، نفوذ حرارتی و هدایت حرارتی آنها انجام شد. نتایج نشان داد که هر چه نانوذرات گرافیت بیشتر باشد، تعداد برخورد بین گرافیت و ایکوزان بیشتر است. با افزایش محتوای نانوذرات، رسانایی و انتشار حرارتی افزایش یافت. از نظر عددی، حداکثر رسانایی حرارتی ۴/۱ W/m K برای کامپوزیت حاوی ۱۰ ٪ وزنی گرافیت، ۱۵/۶۶ برابر بیشتر از ایکوزان خالص بود. همچنین، افزایش رشد کریستال و کاهش ظرفیت گرمایی برای مقدار بالای نانوذرات در کامپوزیت مورد بحث قرار گرفت. بهبود قابل توجه خواص حرارتی NEPCM های تهیه شده با محتوای نانوذرات بهینه می‌تواند آنها را برای کاربردهای مختلف مدیریت حرارتی قابل استفاده کند.

JREE: Vol. 10, No. 4, (Autumn 2023) 22-34

An Improved Hottel-Whiller-Bliss Equation for the Nth Photo-Voltaic Thermal-Thermo-Electric Cooler Air Collectors Connected in Series: Exergy Analysis

Gopal Nath Tiwari [a], Prashant Bhardwaj [b*], Sujata Nayak [c]

[a] *BERS Pubic School, Margupur, P. O. Box: 221701, Chilkhar, Ballia (UP), India.*
[b] *Department of Mechanical Engineering, Manav Rachna University, P. O. Box: 121004, Faridabad, Haryana, India.*
[c] *Legato Health Technologies, P. O. Box: 560045, Bengaluru, Karnataka, India.*

PAPER INFO

Paper history:
Received: 26 December 2022
Revised: 10 March 2023
Accepted: 11 March 2023

Keywords:
Photovoltaic Thermal (PVT),
Solar Energy,
Thermo-Electric Cooler (TEC)

ABSTRACT

This study considers N-photovoltaic thermal-thermo electric cooler (PVT-TEC) air collectors connected in series for thermal and electrical performance. An improved Hottel-Whiller-Bliss (HWB) equation and mass flow rate factor were derived for the nth PVT-TEC air collectors. The derivation is based on energy balance equation for each component of N-photovoltaic thermal-thermo electric cooler (PVT-TEC) air collectors connected in series. Further, thermal energy and electrical energy from PV module and TEC were analyzed based on a given design and climatic parameters along with the overall exergy of the proposed system on the hourly and daily bases. Numerical computations were conducted using MATLAB under Indian climatic conditions. The proposed thermal model is valid for all climatic and weather conditions. Based on the numerical computations carried out, the following conclusions were made:

i. The electrical power of PV module decreased with increase in the number of the n^th PVT-TEC air collectors as the electrical power of TEC increased.

ii. The overall instantaneous exergy efficiency decreased with increase in the number of the n^th PVT-TEC air collectors.

iii. Packing factor of TEC was found to be a very sensitive parameter for optimizing the number of PVT-TEC air collectors to ensure maximum overall exergy, and it was found to be β_tec=0.5. for N=7

https://doi.org/10.30501/jree.2023.376480.1516

چکیده:

این مطالعه عملکرد حرارتی و الکتریکی-N مجمع‌های هواشناسی نوری-گرمایی-ترموتریک (PVT-TEC) را در نظر می‌گیرد که در سری به هم متصل شده‌اند. یک معادله Hottel-Whiller-Bliss (HWB) بهبود یافته و عامل جریان جرم برای-n امین مجمع‌های هواشناسی PVT-TEC استخراج شد. این استخراج بر اساس معادله توازن انرژی برای هر جزء از-N مجمع‌های نوری-گرمایی-ترموتریک (PVT-TEC) که در سری به هم متصل شده‌اند، استوار است .علاوه بر این، انرژی حرارتی و الکتریکی از ماژول PV و TEC بر اساس یک طراحی و پارامترهای اقلیمی همراه با کل انرژی خروجی این سیستم در پایه‌های ساعتی و روزانه تجزیه و تحلیل شد .محاسبات عددی با استفاده از MATLAB تحت شرایط اقلیمی هند انجام شد .مدل حرارتی پیشنهادی برای همه شرایط اقلیمی و آب و هوایی معتبر است .بر اساس محاسبات عددی انجام شده، نتیجه‌های زیر حاصل شد:

۱. توان الکتریکی ماژول PV با افزایش تعداد مجمع‌های هواشناسی PVT-TEC n^th با افزایش توان الکتریکی TEC کاهش می‌یابد.
۲. کارایی برون‌یابی آنی کل با افزایش تعداد مجمع‌های هواشناسی PVT-TEC n^th کاهش می‌یابد.
۳. عامل بسته‌بندی TEC به عنوان یک پارامتر بسیار حساس برای بهینه‌سازی تعداد مجمع‌های هواشناسی PVT-TEC برای تضمین حداکثر انرژی برون‌یابی شناخته شد و β_tec=0.5 برای N=7 یافت شد.

JREE: Vol. 10, No. 4, (Autumn 2023) 35-43

Design, Fabrication, and Experimental Study of a Low-cost and Accurate Weather Station Using a Microcontroller System

Mahdi Pourbafrani [a], Hossein Ghadamian [a*], Meisam Moghadasi [a], Masoud Mardani [a]

[a] *Department of Energy, Materials and Energy Research Center, Karaj, Iran.*

PAPER INFO

Paper history:
Received: 31 January 2023
Revised: 13 March 2023
Accepted: 16 March 2023

Keywords:
Weather Station,
Anemometer,
Pyranometer,
Humidity Sensor,
Thermometer,
Microcontroller System

ABSTRACT

In this research study, a cost-effective and reliable weather station using a microcontroller system containing instruments and sensors for measuring and recording ambient variables was designed, fabricated, and tested. The dataset recorded and stored in the meteorological system can be applied to conduct various research in the field of energy and environment, especially in solar systems. Employing a microcontroller system reduces costs and provides special features such as accessing data on the web-based spreadsheets and adding control devices. In this system, meteorological information including solar radiation, air temperature, wind velocity, and air relative humidity is measured and saved in user-defined time intervals such as 30 seconds. The total cost for measuring equipment, sensors, and microcontroller along with a data logger is about 110 USD. To demonstrate the importance of using local meteorological data, in the vicinity of the case studies, the dataset provided by the local weather station was compared with the meteorological data of two nearby national stations for one month. The results revealed that the values reported by the national stations were different from the actual values measured by the local weather station. The deviations for solar radiation, wind velocity, air temperature and humidity values were at least 5, 9, 7%, and more than 100%, respectively.

https://doi.org/ 10.30501/JREE.2023.383796.1551

چکیده:

در این تحقیق یک سامانه هواشناسی مقرون به صرفه و قابل اعتماد طراحی، ساخته و آزمایش شده است. در این سامانه از یک سیستم ریزپردازنده شامل تجهیزات و سنسورها برای پایش متغیرهای هواشناسی استفاده شده است. داده‌های ثبت شده از این پایانه هواشناسی را می توان در انجام تحقیقات مختلفی در زمینه انرژی و محیط زیست بخصوص در سیستم های خورشیدی استفاده کرد. بکارگیری سیستم ریزپردازنده باعث کاهش هزینه شده و امکانات ویژه مانند دسترسی به داده ها در بستر اینترنت یا اضافه کردن تجهیزات کنترلی را فراهم می آورد. در این سیستم، اطلاعات هواشناسی شامل شدت تابش خورشید، دمای هوا، سرعت باد و رطوبت نسبی هوا در بازه‌ی زمانی مورد نظر کاربر (در اینجا بازه ۳۰ ثانیه ای) اندازه گیری و ذخیره می شود. هزینه تمام شده برای تجهیزات اندازه گیری، ریزپردازنده و سنسورها به همراه ثبت کننده داده‌ها ۱۱۰ دلار آمریکا شد. به منظور اثبات اهمیت استفاده از داده‌های ایستگاه هواشناسی در مجاورت سیستم مورد بررسی، داده‌های ثبت شده طی یک ماه با داده‌های ۲ ایستگاه هواشناسی دولتی نزدیک مقایسه شد. نتایج نشان داد که داده‌های دمای ایستگاه های هواشناسی حداقل ۵ درصد، رطوبت نسبی ۹ درصد، تابش ۷ درصد و سرعت باد بیش از ۱۰۰ درصد با شرایط واقعی موجود در محل داده برداری اختلاف دارند.

JREE: Vol. 10, No. 4, (Autumn 2023) 44-58

A Novel Approach to Fast Determining the Maximum Power Point Based on Photovoltaic Panel's Datasheet

Sameer Khader[a]*, Abdel-Karim Khalid Daud[a]

[a] *Department of Electrical Engineering, Faculty of Engineering, Palestine Polytechnic University, P. O. Box: 198, Hebron, Palestine.*

PAPER INFO

Paper history:
Received: 13 September 2022
Revised: 18 January 2023
Accepted: 31 January 2023

Keywords:
Buck-Boost Converter,
Traditional SEPIC Converter,
Modified SEPIC Converter,
MPPT

ABSTRACT

This study proposes a novel approach to fast and direct determination of the Maximum Power Point (MPP) at any value of solar irradiation and cell temperature, without applying further mathematical processing to operate at that point. The current approach aims to reduce algorithm complexity, time consumption during the iteration, and oscillation to reach the point at which the panel generates maximum possible power. For avoiding or eliminating these drawbacks, the chopper duty cycle (D) at which the panel-generated power should be the maximum is determined using the panel datasheet with respect to voltage and power at different irradiation rates (G). Mathematical equations are derived for MPP voltage and power at any value of solar irradiation using the manufacturer Photovoltaic (PV) specification. The simulation results obtained by MATLAB/SIMULINK platform showed that the power had a linear change, while the voltage had a nonlinear one with narrow variations. The yield duty cycle controls the Modified Single Ended Primary Converter (MSEPIC) that regulates the load voltage through a wide range below and above the rated panel voltage. The simulation results showed the fast response of chopper operation with a negligible starting time required by the MPPT algorithm, no duty cycle oscillation, and shorter iteration time. Furthermore, the conducted approach is validated based on the data published in a reputed journal, and the obtained results gave rise to new aspects that helped reduce dependency on conventional MPPT algorithms and, consequently, enhance the system response, efficiency and cost reduction.

https://doi.org/10.30501/jree.2023.361697.1450

چکیده:

این مطالعه رویکردی نوین برای تعیین سریع و مستقیم نقطه توان حداکثر (MPP) در هر مقدار تابش خورشیدی و دمای سلول ارائه می دهد، بدون اینکه پردازش ریاضی بیشتری برای کار در آن نقطه اعمال شود. رویکرد فعلی در نظر دارد تا پیچیدگی الگوریتم، مصرف زمان در طول تکرار و نوسان را برای رسیدن به نقطه ای که پانل بیشترین توان ممکن را تولید می کند، کاهش دهد. برای جلوگیری یا از بین بردن این کاستی ها، ضریب duty cycle شاپرون (D) که در آن توان تولید شده پانل باید حداکثر باشد، با استفاده از برگه داده پانل در رابطه با ولتاژ و توان در نرخ های تابش مختلف (G) تعیین می شود. معادلات ریاضی برای ولتاژ و توان MPPدر هر مقدار تابش خورشیدی با استفاده از مشخصات فتوولتائک (PV) تولید کننده مشتق می شوند. نتایج شبیه سازی حاصل از پلتفرم MATLAB/SIMULINKنشان داد که قدرت تغییر خطی داشت، در حالی که ولتاژ تغییر غیرخطی با تغییرات محدود داشت. duty cycle کنترل کننده مبدل اولیه تک طرفه اصلاح شده (MSEPIC) است که ولتاژ بار را در محدوده وسیعی زیر و بالای ولتاژ نامی پانل تنظیم می کند. نتایج شبیه سازی نشان داد که پاسخ سریع شاپرون با زمان شروع قابل توجهی مورد نیاز توسط الگوریتمMPPT ، عدم نوسان duty cycle و زمان تکرار کوتاهتر. علاوه بر این، رویکرد انجام شده بر اساس داده های منتشر شده در یک نشریه معتبر مورد اعتبارسنجی قرار گرفت و نتایج حاصله به جنبه های جدیدی کمک کرد که به کاهش وابستگی به الگوریتم های MPPT متداول و در نتیجه بهبود پاسخ سیستم، کارایی و کاهش هزینه منجر شد.

JREE: Vol. 10, No. 4, (Autumn 2023) 59-65

Experimental Study of Phase Change Process of the Paraffin as a PCM with Copper Foam and Iron Wool

Mohammad Saleh Barghi Jahromi[a], Vali Kalantar[a,*], Mohammad Sefid[a], Masoud Iranmanesh[b,*] Hadi Samimi Akhijahani[c]

[a] *Department of Mechanical Engineering, Faculty of Mechanical Engineering, Yazd University, Yazd, Iran.*
[b] *Department of Energy, Institute of Science and High Technology and Environmental Sciences, Graduate University of Advanced Technology, Kerman, Iran.*
[c] *Department of BioSystems Engineering, Faculty of Agriculture, University of Kurdistan, Sanandaj, Iran.*

PAPER INFO

Paper history:
Received: 22 October 2022
Revised: 26 November 2022
Accepted: 8 January 2023

Keywords:
Copper Foam and Iron Wool,
Copper Absorber Plate,
Energy Storage,
Phase Change Material

ABSTRACT

Paraffin waxes are widely used as commercial organic heat storage phase changes (PCM) for many applications due to their suitable properties. Significant heat from fusion, nonpoisonous and stable properties, no phase separation, and the phase process result in a small volume change. Meanwhile, they are subject to low thermal conductivity. The thermal conductivity of PCMs can be increased by different techniques such as the use of dispersion of particles or nanomaterials with high conductivity in PCM and the use of metal foams. The use of nanoparticles has such disadvantages as high cost and particle deposition after various cycles. Hence, in this study, some experiments were carried out to investigate the effect of porous media like copper foam and iron wool as the filler instead of nanomaterials on improving the heat conductivity of PCM. The results show that the porous foam increases the heat transfer and during the charging operation, the temperature of the porous plate wall increases continuously at the same rate as the paraffin. At 2400 s, the temperature of pure PCM, iron wool, and copper foam reaches 67.3, 72.5, and 73.27□, respectively. The optimal mode is the one in which the copper absorber plate is connected to the copper foam, thus reducing the charging time by 600 s compared to pure PCM and saving 75% of energy. Connecting the copper absorber plate to the iron wool has a good thermal performance and stores 70.83% of energy. Thus, iron wool has an acceptable performance and is suitable for storage systems.

https://doi.org/10.30501/jree.2023.365995.1483

چکیده:

موم‌های پارافین به دلیل خواص مناسب به طور گسترده به عنوان تغییر فاز ذخیره حرارت آلی تجاری (PCM) برای بسیاری از کاربردها استفاده می شود. گرمای زیاد همجوشی، خواص غیر سمی، پایدار، عدم جداسازی فاز، و فرآیند فاز تنها منجر به تغییر حجم کمی می‌شود. در ضمن از رسانایی حرارتی پایین رنج می‌برد. تکنیک‌های مختلف را می‌توان با استفاده از پراکندگی ذرات یا نانومواد با رسانایی بالا در خود PCM و استفاده از فوم‌های فلزی، هدایت حرارتی PCM ها را افزایش داد. استفاده از نانوذرات دارای معایب هزینه گران و رسوب ذرات پس از چرخه‌های مختلف است. از این رو، در این مطالعه، آزمایش‌هایی برای بررسی اثر محیط‌های متخلخل مانند فوم مس و پشم آهن به‌عنوان پرکننده به‌جای نانومواد برای بهبود هدایت حرارتی PCM انجام شد. نتایج نشان می‌دهد که فوم متخلخل باعث افزایش انتقال حرارت می‌شود و در طول عملیات شارژ، دمای دیواره صفحه متخلخل به طور مداوم با همان سرعت پارافین افزایش می‌یابد. در ۲۴۰۰ ثانیه دمای PCM خالص، پشم آهن و فوم مس به ترتیب به ۶۷/۳، ۷۲/۵ و ۷۳/۲۷ درجه سانتیگراد می‌رسد. حالت بهینه حالتی است که صفحه جاذب مس به فوم مس متصل می‌شود و در مقایسه با PCM خالص ۶۰۰ ثانیه زمان شارژ را کاهش می‌دهد و ۷۵ درصد در انرژی صرفه جویی می‌کند. اتصال صفحه جاذب مس به پشم آهن عملکرد حرارتی خوبی دارد و ۷۰/۸۳ درصد انرژی را ذخیره می‌کند، بنابراین پشم آهن عملکرد قابل قبولی دارد و برای سیستم‌های ذخیره سازی مناسب است.

JREE: Vol. 10, No. 4, (Autumn 2023) 66-77

Techno-Environmental Analysis of Hybrid Energy System for Offshore Oil Rig Black Start

Abraham Olatide Amole[a*], Adebimpe Oluwaseun Adeyeye[a], Daniel Oluwaseun Akinyele[b], Kehinde Adeleye Makinde[c], Stephen Oladipo[d]

[a] *Department of Electrical, Electronics, and Telecommunication Engineering, College of Engineering, Bells University of Technology, Ota, Nigeria.*
[b] *Department of Electrical and Electronics Engineering, Olabisi Onabanjo University, Ago-Iwoye, Nigeria.*
[c] *School of Computing, Design and Digital Technologies, Teesside University, Middlesbrough, UK.*
[d] *Department of Electrical and Electronics Engineering, University of Johannesburg, Johannesburg, 2006, South Africa.*

PAPER INFO

Paper history:
Received: 13 July 2022
Revised: 30 October 2022
Accepted: 07 November 2022

Keywords:
Oil Rig,
Black Start,
Energy Systems,
Technical,
Environmental,
Analysis

ABSTRACT

The use of Diesel Generators (DGs) and gas turbines to power oil rigs is characterized by pollution due to the emission of harmful gases like carbon dioxide, very high noise levels, high maintenance costs, and the inability to start the platform if the DG fails. Offshore wind energy generation system provides a viable alternative means of powering the oil rig and can also be integrated to operate in parallel with gas turbines. However, offshore wind energy might fail if not properly designed due to the high variability of wind resources. Hence, the objective of this work is to design offshore Wind Turbine Generator (WTG) energy generation system, DG, and hybrid DG-WTG for the black start of an offshore oil rig. The designed energy systems are simulated using HOMER Pro. Furthermore, the performance of the simulated systems was evaluated using the electrical production, unmet load, and emission profile as the performance metrics. The results of the hybrid DG-WTG powered black start revealed that 150kW DG generated 322,071kWh/yr representing 6.77% of the total generation and 1.5MW WTG generated 4,434,632kWh/yr representing 93.2% of the total generation. The comparison of the emissions from DG and DG-WTG revealed that 294,058kg/yr, 1,945kg/yr, 80.9kg/yr, 9.02kg/yr, 720kg/yr, and 688kg/yr of CO_2, CO, UH, PM, SO_2, and NO, respectively, were released into the atmosphere by DG-WTG which is very low compared to 969,129kg/yr, 6,109kg/yr, 267kg/yr, 37kg/yr, 2373kg/yr, and 5739kg/yr of CO_2, CO, UH, PM, SO_2, and NO, respectively, released into the atmosphere by DG. The sensitivity analysis revealed that while the electrical production of 100kW and 50kW DGs decreased with an increase in WTG height, the electrical production of 1.5MW WTG increased with an increase in WTG height. It was further revealed that the higher the WTG height the smaller the quantity of the emission released into the atmosphere.

https://doi.org/10.30501/jree.2022.350408.1402

چکیده:

استفاده از ژنراتورهای دیزلی (DGs) و توربین های گازی برای تامین انرژی سکوی نفتی همراه با آلودگی به دلیل انتشار گازهای مضر مانند دی اکسید کربن، سر و صدای بسیار زیاد، هزینه های نگهداری بالا و عدم توانایی راه اندازی سکوی نفتی در صورت خرابی DG می باشد. سیستم تولید انرژی باد دریایی راه حل جایگزین وموثری جهت تامین انرژی سکوی نفتی است و همچنین می تواند جهت عملیات در راستای توربین های گازی ادغام شود. با این حال، انرژی باد دریایی ممکن است در صورت عدم طراحی صحیح به دلیل عدم ثبات قابل توجه منابع بادی موثر واقع نشود. بنابراین، هدف از این کار طراحی سیستمی جهت تولید انرژی ژنراتور توربین بادی دریایی (WTG) ; سیستم تولید انرژی دیزلی DG و سیستم هیبریدی DG-WTG برای راه اندازی مجدد یک سکوی نفتی دریایی است. سیستم های انرژی طراحی شده با استفاده از HOMER Pro شبیه سازی شدند. علاوه بر این، عملکرد سیستم های شبیه سازی شده بر مبنای معیارهای از قبیل تولید برق، بار برآورده نشده و میزان انتشار آلایندگی ارزیابی شدند. نتایج به دست آمده از DG-WTG هیبریدی نشان داد که ژنراتور ۱۵۰ کیلوواتی توانست 322.07 کیلووات در سال تولید داشته باشد که بیانگر ۶,۷۷٪ از کل تولید را می باشد و ژنراتور ۱,۵ مگاوات WTG 4 موفق به تولید 434,632 کیلووات ساعت در سال شد، که ۹۳,۲٪ از کل تولید را نشان می دهد. مقایسه میزان انتشارات آلایندگی توسط DG و DG-WTG نشان داد که مقادیر ۲۹۴۰۵۸، ۱۹۴۵، ۸۰,۹، ۹,۰۲، ۷۲۰ و ۶۸۸ کیلوگرم در سال از CO_2، CO، UH، PM، SO_2، و NO به ترتیب توسط DG-WTG وارد جو زمین شد، در حالی که مقادیر ۹۶۹۱۲۹ کیلوگرم در سال، ۶۱۰۹ کیلوگرم در سال، ۲۶۷ کیلوگرم در سال، ۳۷ کیلوگرم در سال، ۲۳۷۳ کیلوگرم در سال، و ۵۷۳۹ کیلوگرم در سال از آلاینده های مذکور تولید شده توسط DG بسیار بیشتر می باشند. تحلیل حساسیت نشان داد که در حالی که تولید برق ۱۰۰ کیلووات و ۵۰ کیلووات DG با افزایش ارتفاع WTG کاهش می یابد، تولید برق ۱,۵ مگاوات WTG با افزایش ارتفاع آن افزایش می یابد. علاوه بر این، مشخص شد که هر چه ارتفاع WTG بیشتر باشد، مقدار انتشار آلایندگی وارد شده به جو کمتر است.

JREE: Vol. 10, No. 4, (Autumn 2023) 78-88

Impact of Dust and Degradation on the Electrical Properties of PV Panels

Samir Tabet[a,b], Razika Ihaddadene[a,c*], Belhi Guerira[d], Nabila Ihaddadene[a,c]

[a] *Department of Mechanical Engineering, Faculty of Technology, University of Med Boudiaf, M'sila, Algeria.*
[b] *Laboratory of Materials and Mechanics of Structure L.M.MS, University of Med Boudiaf, M'sila, Algeria.*
[c] *Laboratory of Renewable Energy and Sustainable Development L.R.E.S.E, University of Mentouri Brothers, Constantine, Algeria.*
[d] *Laboratory of Mechanical Engineering L.M.G, University Mohamed Khider , Biskra, Algeria.*

PAPER INFO

Paper history:
Received: 05 November 2022
Revised: 01 November 2022
Accepted: 11 December 2022

Keywords:
Dust Accumulation,
Solar PV Performance,
Degradation Rate,
Degradation Mechanisms,
Electrical Characteristics

ABSTRACT

Dust accumulation on PV surface panels is a crucial factor affecting their performance. It is more frequently noted in the desert zones. The effect of dust on the electrical behavior of damaged PV panels was investigated in this study. Three panels are used: the degraded panels (with and without dust) and the reference panels; they are located in an industrial zone with a continental climate (Bordj Bou Arréridj, Algeria). The I-V and P-V characterization and degradation mechanism visualization are used. Also, a numerical simulation was conducted to calculate the five parameters of the three modeled PV panels (diode ideality factor (a), series resistance (Rs), Shunt resistance (Rp), photocurrent (Ipv), and diode saturation current (I0)). These parameters were utilized for the first time to study the impact of dust on their degradation rate and the PV panel behavior. The degradation rate and the annual degradation rate of each parameter are affected by dust differently. The power degradation rate is increased by 5.45%. The Isc and Imax degradation rates are climbed by 6.97% and 6.0%, respectively. Vmax and Voc degradation rates decrease by 1.20% and 0.35%, respectively. Dust increased the rate of degradation for a, Iph, and I0 by 4.12%, 6.99%, and 68.17%, respectively. For Rs and Rp, the degradation rate was reduced by 4.51% and 20.01%, respectively. An appropriate netoiling approach must be considered because dust, even in non-desert areas and industrial zones, has a significant impact on the electrical characteristics degradation of a PV panel.

https://doi.org/10.30501/jree.2023.367573.1491

چکیده:

تجمع گرد و غبار روی پانل های سطحی PV عامل مهمی است که بر عملکرد آنها تأثیر می گذارد. این امر بیشتر در مناطق بیابانی مشاهده می شود. در این مطالعه تأثیر گرد و غبار بر رفتار الکتریکی پانل های PV آسیب دیده مورد بررسی قرار گرفت. از سه پنل استفاده شده است: پانل های خراب (با گرد و غبار و بدون گرد و غبار) و پانل های مرجع. آنها در یک منطقه صنعتی با آب و هوای قاره ای (Bordj Bou Arréridj ، الجزایر) قرار دارند. از مشخصات I-V و P-V و تجسم مکانیزم تخریب استفاده می شود. همچنین، یک شبیه سازی عددی انجام شد تا پنج پارامتر سه پنل مدل شده PV ضریب ایدئال دیود(a) ، مقاومت سری(Rs) ، مقاومت شانت(Rp) ، جریان فوتو (Ipv) و جریان اشباع دیود ((I0) محاسبه شود. این پارامترها برای اولین بار برای مطالعه تأثیر گرد و غبار بر نرخ تخریب آنها و رفتار پانل PV استفاده شد. نرخ تخریب و نرخ تخریب سالانه هر پارامتر به طور متفاوتی تحت تأثیر گرد و غبار قرار می گیرد. نرخ تخریب قدرت ۵,۴۵٪ افزایش یافته است. نرخ تخریب Isc و Imax به ترتیب ۶,۹۷٪ و ۶,۰٪ افزایش یافت. نرخ تخریب Vmax و Voc به ترتیب ۱,۲۰٪ و ۰,۳۵٪ کاهش یافت. گرد و غبار سرعت تخریب a ، Iph و I0 را به ترتیب ۴,۱۲٪ ، ۶,۹۹٪ و ۶۸,۱۷٪ افزایش داد. برای Rs و Rp نرخ تخریب به ترتیب ۴,۵۱٪ و ۲۰,۰۱٪ کاهش یافت. باید یک روش تمیز کردن مناسب سطوح در نظر گرفته شود زیرا گرد و غبار ، حتی در مناطق غیر بیابانی و مناطق صنعتی ، تأثیر قابل توجهی بر تخریب مشخصات الکتریکی یک پانل PV دارد.

JREE: Vol. 10, No. 4, (Autumn 2023) 89-98

Phenolic Compound Removal Technique For Efficient Biobutanol Production Using Oil Palm Fronds Hydrolysate

Abdurrahman Abubakar[a&b], Madihah Binti MD Salleh*[a], Adibah Yahya[a], Chong Chun Shiong[a], Shaza Eva Mohamad[a], Suraini Binti Abd-Aziz[c], Huszalina Hussin[a]

[a] *Department of Biosciences, Faculty of Sciences, Universiti Teknologi Malaysia, P. O. Box: 81310, Skudai, Johor, Malaysia.*
[b] *Department of Biological Sciences, Faculty of Science, Federal University of Kashere, P. O. Box: 0182, Gombe, Gombe State, Nigeria.*
[c] Department of Bioprocess Technology, Faculty of Biotechnology and Biomolecular Sciences, Universiti Putra Malaysia, *P. O. Box:* 43400 Seri Kembangan, Selangor, Malaysia.

P A P E R I N F O

Paper history:
Received: 07 December 2022
Revised: 01 March 2023
Accepted: 09 April 2023

Keywords:
ABEFermentation,
Biobutanol,
Detoxification,
Phenolic Compounds,
Oil Palm Frond Hydrolysate

A B S T R A C T

Oil Palm Frond (OPF) juice has been the focus of Malaysian bioenergy producers through acetone-butanol-ethanol (ABE) fermentation. However, due to the high concentration of phenolic compounds in the hydrolysate, usually gallicacid and ferulic acids, the fermentation medium turns acidic which hinders the growth of most microorganisms. A suitable method of phenolic compound removal with a minimal effect on the sugar stability of OPF juice has been employed using Amberlite XAD-4 resin. During the detoxification process, the effects of temperature and pH on the removal of phenolic compounds and sugar stability were also assessed. The Amberlite XAD-4 resin managed to adsorb about 32% of phenolic compound from the OPF hydrolysate at an optimum temperature of 50 °C and hydrogen ion concentration (pH) of 6. In addition, it maintained as much as 93.7 % of the sugar in the OPF juice. The effect of detoxifying OPF hydrolysate was further tested for biobutanol production in batch culture using strain *Clostridium acetobutylicum* SR1, L2, and A1. Strain L2 gave the highest improvement in biobutanol and total solvent production by 22.7% and 14.41%, respectively, in medium with detoxified OPF juice. Meanwhile, compared to non-detoxified OPF juice, the acid production of strain L2 significantly decreased by 2.99-fold when using detoxified OPF juice, despite a 1.2-fold increase in sugar consumption. Conclusively, using Amberlite XAD-4 resin to detoxify OPF hydrolysate at pH 6 and 50 °C removed the phenolic compound while increasing the strain L2 capability to improve biobutanol and total solvent production.

https://doi.org/10.30501/jree.2023.374488.1512

چکیده:

روغن نخل خرما (OPF) به عنوان منبعی از انرژی زیستی مورد توجه تولیدکنندگان زیست انرژی مالزی از طریق تخمیر استون-بوتانول-اتانول (ABE) قرار گرفته است. با این حال، به دلیل غلظت بالای ترکیبات فنلی در هیدرولیزات، معمولاً اسید گالیک و اسید فرولیک محیط تخمیر اسیدی می شود که مانع رشد اکثر میکروارگانیسم ها می شود. یک روش مناسب برای حذف ترکیبات فنلی با تأثیر کم بر پایداری قند آب OPF با استفاده از رزین Amberlite XAD-4 به کار گرفته شده است. در طی فرآیند سم زدایی، تأثیر دما و pH بر حذف ترکیبات فنلی و پایداری قند نیز مورد ارزیابی قرار گرفت. رزین Amberlite XAD-4 توانست حدود ۳۲ درصد ترکیبات فنلی را از هیدرولیزات OPF در دمای بهینه ۵۰ درجه سانتیگراد و غلظت یون هیدروژن 6 (pH) جذب کند. علاوه بر این، تا ۹۳,۷ درصد قند موجود در آب OPF را حفظ کرد. اثر سم زدایی هیدرولیزات OPF برای تولید بوتانول زیستی در کشت دسته ای با استفاده از سویه های *Clostridium acetobutylicum* SR1، L2 و A1 نیز آزمایش شد. سویه L2 بیشترین بهبود را در تولید بوتانول و حلال کل به ترتیب ۲۲,۷ و ۱۴,۴۱ درصد در محیط با آب OPF سم زدایی شده نشان داد. در همین حال، در مقایسه با آب OPF غیر سم زدایی شده، تولید اسید سویه L2 به طور قابل توجهی با ۲,۹۹ برابر کاهش یافت، اگرچه مصرف قند ۱,۲ برابر افزایش یافت. در نتیجه، استفاده از رزین Amberlite XAD-4 برای سم زدایی هیدرولیزات OPF در pH 6 و ۵۰ درجه سانتیگراد ترکیبات فنلی را حذف کرد و در عین حال توانایی سویه L2 برای بهبود تولید بوتانول و حلال کل را افزایش داد.

JREE: Vol. 10, No. 4, (Autumn 2023) 99-106

Application of Thermal Energy Accumulators Based on Paraffin Phase Change Materials in Convective-Vacuum Impulsive Drying Units: A Brief-Focused Overview of Characteristics and Thermal Conductivity Enhancement Techniques

Mohammed Ali Sami Mahmood[a,b*], Rodionov Yuriy Viktorovich[a], Shchegolkov Alexandr Viktorovich[c]

[a] *Department of Mechanics and Engineering Graphics, Tambov State Technical University, Tambov, Russia.*
[b] *Department of Machines and Equipment Engineering Techniques, Al-Mussaib Technical College, Al-Furat Al-Awsat Technical University, Babil, Iraq.*
[c] *Department of Technology and Methods of Nanoproducts Manufacturing, Tambov State Technical University, Tambov, Russia.*

PAPER INFO

Paper history:
Received: 19 November 2022
Revised: 06 January 2023
Accepted: 17 January 2023

Keywords:
Thermal Energy Accumulator,
Paraffin,
Phase Change Material,
Convective Drying,
Convective-vacuum Impulsive Drying,
Energetic Efficiency

ABSTRACT

Researchers worldwide are studying thermal energy storage with phase change materials because of their substantial benefits in the enhancement of energy efficiency of thermal drying systems. A two-stage convective-vacuum impulsive drying plant is a technology for the manufacturing of chemical and food products with high quality and low energy costs. Energy consumption during the drying process is the main indicator in terms of economy. In this paper, a brief and focused review of the peculiarities of TEAs with PPCMs and opportunities of their application in such drying systems is done and discussed. The paper described the mentioned manufacturing system. The advantages of paraffin wax and thermal conductivity improvement techniques were demonstrated for their use as heat storage materials in CVID drying units. The results of similar previous studies were presented. The results of the experimental studies conducted by the researchers proved that the use of heat accumulators with PCMs increased the overall energy efficiency of drying systems. Finally, integration of TEAs based on modified PPCMs in the CVID system was recommended to intensify thermal energy, reduce thermal influence on the main indicators of the vacuum pump during the evacuation process, and decrease production costs.

https://doi.org/10.30501/jree.2023.370842.1501

چکیده:

محققان در سراسر جهان به دلیل مزایای قابل توجه آنها در بهبود بهره وری انرژی سیستم های خشک شدن حرارتی، در حال مطالعه ذخیره انرژی حرارتی با مواد تغییر فاز هستند. یک کارخانه خشک کردن ضربه ای دو مرحله ای جابجایی-خلاء یک فناوری برای تولید محصولات شیمیایی و غذایی با کیفیت بالا و هزینه انرژی کم است. مصرف انرژی در طول فرآیند خشک کردن اصلی ترین شاخص در زمینه اقتصاد است. در این مقاله، مروری مختصر و متمرکز بر ویژگی های خاص TEA ها با PPCM ها و فرصت های کاربرد آنها در چنین سیستم های خشک کردن انجام شده و مورد بحث قرار گرفته است. مزایای موم پارافین و تکنیک های بهبود هدایت حرارتی برای استفاده به عنوان مواد ذخیره سازی گرما در واحدهای خشک کردن CVID نشان داده شد. نتایج مطالعات مشابه قبلی ارائه شد. نتایج مطالعات تجربی انجام شده توسط محققان نشان داد که استفاده از انباشت گرما با PCM ها بهره وری انرژی کلی سیستم های خشک کردن را افزایش داده است. در نهایت، توصیه می شود که TEA های مبتنی بر PPCM های اصلاح شده را در سیستم CVID ادغام شوند تا انرژی حرارتی تقویت شوند، تأثیر حرارتی را بر شاخص های اصلی پمپ خلاء در طول فرآیند تخلیه کاهش و هزینه های تولید کاهش داده شود.

JREE: Vol. 10, No. 4, (Autumn 2023) 107-118

Variability Assessment of Solar Irradiance for the Safe Grid Integration of Solar Photovoltaic Power Plants

Md. Rashedul Alam [a], Iftekhar Uddin Bhuiyan [b*], Nur Mohammad [c]

[a] *Sustainable and Renewable Energy Development Authority (SREDA), P. O. Box: 1000, Dhaka, Bangladesh.*
[b] *Institute of Appropriate Technology, Bangladesh University of Engineering and Technology, P. O. Box: 1000, Dhaka, Bangladesh.*
[c] *Department of Electrical and Electronic Engineering, Chittagong University of Engineering and Technology, P. O. Box: 4349, Chittagong, Bangladesh.*

PAPER INFO

Paper history:
Received: 21 December 2022
Revised: 02 April 2023
Accepted; 14 April 2023

Keywords:
Assessment of Solar Irradiance,
Short-term variation of Solar Irradiance,
Integration Challenges of Variable Renewable Energy,
Voltage-frequency aspects of Solar Photovoltaic grid integration

ABSTRACT

The output power of a Solar Photovoltaic (SPV) plant depends mainly on the solar irradiance on the photovoltaic (PV) modules. Therefore, short-term variations in solar irradiance cause variations in the output power of solar power plants, making solar photovoltaic grid integration unstable. Solar irradiance variations mainly occur due to the weather conditions of a given location, especially the movement of clouds and seasonal effects. Consequently, assessing the variability of solar irradiance over the course of a year is essential to identify the extent of these variations. Geographical dispersion and cloud enhancement are two important factors affecting output power variations in a PV plant. Geographical dispersion reduces such variations, while cloud enhancement increases them. This study utilizes two ground station-based solar Global Horizontal Irradiance (GHI) datasets to assess the viability of solar irradiance in the Chittagong division of Bangladesh. The analysis reveals a significant number of days with high short-term solar irradiance variation. In addition to solar irradiance, the frequency and voltage at the interconnection point are important for safe grid integration. It was observed that the grid frequency exceeded the range specified by the International Electrotechnical Commission (IEC), but remained within the grid code range of Bangladesh. Grid voltage variation at the interconnection substation was found to be within the standard range during the daytime, but low voltage was observed at the grid level during the rest period. Therefore, it is crucial to implement necessary preventive measures to reduce short-term variations for the safe grid integration of large-scale variable SPV plants.

https://doi.org/10.30501/jree.2023.377735.1522

چکیده:

خروجی توان یک نیروگاه خورشیدی فتوولتائیک (SPV) عمدتاً به تابش خورشیدی بر روی صفحات فتوولتائیک (PV) بستگی دارد. بنابراین، تغییرات کوتاه مدت در تابش خورشیدی باعث تغییراتی در خروجی توان نیروگاه های خورشیدی می شود و باعث بی ثباتی ادغام شبکه خورشیدی فتوولتائیک می شود. تغییرات تابش خورشیدی عمدتاً به دلیل شرایط آب و هوایی یک مکان خاص، به ویژه حرکت ابرها و اثرات فصلی رخ می دهد. در نتیجه، ارزیابی واریانس تابش خورشیدی در طول یک سال برای شناسایی میزان این تغییرات ضروری است. پراکندگی جغرافیایی و تقویت ابر دو عامل مهمی هستند که بر تغییرات خروجی توان در یک نیروگاه PV تأثیر می گذارند. پراکندگی جغرافیایی چنین تغییراتی را کاهش می دهد، در حالی که تقویت ابرها آنها را افزایش می دهد. این مطالعه از دو مجموعه داده خورشیدی Global Horizontal Irradiance (GHI) مبتنی بر ایستگاه زمینی برای ارزیابی امکان سنجی تابش خورشیدی در منطقه چیتگانگ بنگلادش استفاده می کند. تجزیه و تحلیل نشان می دهد که تعداد قابل توجهی از روزهای با تنوع زیاد کوتاه مدت تابش خورشیدی وجود دارد. علاوه بر تابش خورشیدی، فرکانس و ولتاژ در نقطه اتصال نیز برای ادغام ایمن شبکه مهم هستند. مشاهده شد که فرکانس شبکه از محدوده مشخص شده توسط کمیسیون بین المللی الکتروتکنیک (IEC) تجاوز کرده است، اما در محدوده کد شبکه بنگلادش باقی مانده است. مشخص شد که واریانس ولتاژ شبکه در ایستگاه زیرمجموعه اتصال در طی روز در محدوده استاندارد است، اما در طی دوره استراحت ولتاژ پایین در سطح شبکه مشاهده شد. بنابراین، لازم است اقدامات پیشگیرانه لازم برای کاهش تغییرات کوتاه مدت برای ادغام ایمن شبکه بزرگ مقیاس SPV متغیر انجام شود.

JREE: Vol. 10, No. 4, (Autumn 2023) 119-130

Biofuel Commercialization in Developing Countries: Readiness and Prospects

Mosees Emetere [a,b], Wisdom O. Joel [c]

[a] *Department of Physics, Bowen University, Iwo, Nigeria.*
[b] *Department of Mechanical Engineering Science, University of Johannesburg, South Africa.*
[c] *Department of Biochemistry, Covenant University, Ota, Nigeria.*

PAPER INFO

Paper history:
Received: 6 January 2023
Revised: 23 June 2023
Accepted: 17 July 2023

Keywords:
Biofuel,
Energy,
Renewable Energy,
Prospects

ABSTRACT

Several researchers have reported the prospects of biofuel commercialization in several countries across the globe. With over 400 million tons of biomass and 150 million tons of agro-waste produced annually in most developing countries, the prospect of biofuel commercialization looks promising. However, it is crucial to adopt a forward-thinking approach and anticipate potential challenges that may arise, building upon the lessons learned from current obstacles. This paper review addresses the current issues that have discouraged some developing countries against embracing biofuels as an economical tool to mitigate poverty. Also, future challenges that may scuttle biofuel commercialization in developing countries was discussed to provide a workable blueprint towards wealth creation. This review identified policies and political unwillingness as fundamental challenges that must be overcome in developing countries to attract investors. Other identified salient challenges include mono-economy, poor technical know-how, poor technology, government hypocrisy, lack of funds, sustainable biomass resources, inadequate farmland, poor policies, and weak infrastructure. It is recommended that conscious short- and long-term planning be implemented to actualize biofuel commercialization in developing countries.

https://doi.org/10.30501/jree.2023.379263.1533

چکیده:

چندین محقق گزارش دادند که پتانسیل تجاری سازی زیست سوخت در چندین کشور جهان وجود دارد. با تولید بیش از ۴۰۰ میلیون تن زیست توده و ۱۵۰ میلیون تن پسماند کشاورزی در هر سال در بیشتر کشورهای در حال توسعه، چشم انداز تجاری سازی زیست سوخت امیدوار کننده است. با این حال، مهم است که یک رویکرد آینده نگر را اتخاذ کرده و چالش های بالقوه ای را که ممکن است بوجود آید، پیش بینی کنیم، و بر اساس درس هایی که از موانع فعلی آموخته شده است، عمل کنیم. این بررسی به مسائل جاری که برخی از کشورهای در حال توسعه را از پذیرفتن زیست سوخت ها به عنوان ابزاری اقتصادی برای کاهش فقر دلسرد کرده است، می پردازد. همچنین، چالش های آینده ای که ممکن است تجاری سازی بیو سوخت ها در کشورهای در حال توسعه را مختل کند، مورد بحث قرار گرفت تا یک نقشه راه قابل اجرا برای ایجاد ثروت ارائه دهد. این بررسی سیاست ها و عدم تمایل سیاسی را به عنوان چالش های اساسی شناسایی کرد که باید در کشورهای در حال توسعه برای جذب سرمایه گذاران برطرف شود. سایر چالش های برجسته شناسایی شده عبارتند از: اقتصاد تک محوری، دانش فنی ضعیف، فناوری ضعیف، ریاکاری دولت، کمبود بودجه، منابع زیست توده پایدار، زمین کشاورزی ناکافی، سیاست های نامناسب و زیرساخت های ضعیف. پیشنهاد می شود برنامه ریزی آگاهانه کوتاه مدت و بلند مدت برای تحقق تجاری سازی زیست سوخت در کشورهای در حال توسعه اجرا شود.

JREE: Vol. 10, No. 4, (Autumn 2023) 131-145

Predicting Solar Power Generation Based on the Combination of Meteorological Parameters in Iran: Neural Networks Approach

Abbas Ahmadi [a], Mahsa Zaman [b], Siab Mamipour [b*]

[a] *Department of Industrial Engineering & Management Systems, Amirkabir University of Technology (Tehran Polytechnic), Tehran, Iran.*
[b] *Department of Economics, Kharazmi University, Tehran, Iran.*

PAPER INFO

Paper History:
Received: 07 October 2022
Revised: 03 January 2023
Accepted: 17 January 2023

Keywords:
Solar Power Plants,
Metrological Parameters,
Artificial Neural Networks,
Iran

ABSTRACT

Clean solar energy is one of the best sources of energy. Solar power plants can generate electricity in Iran due to their large number of sunny days. This paper presents a short-term forecasting approach based on artificial neural networks (ANNs) for selected solar power plants in Iran and ranks the input variables of the neural network according to their importance. Two solar power plants in Hamadan province (Amirkabir and Khalij-Fars) were selected for the project. The output of solar power plants is dependent on weather conditions. Solar radiation on the horizontal plane, air temperature, air pressure, day length, number of sunny hours, cloudiness, and airborne dust particles are considered input variables in this study to predict solar power plant output. Forecasting model selection is based on considering zero and nonzero quantities of target variables. The results show that solar production forecasting based on meteorological parameters in the Khalij-Fars is more accurate than Amirkabir. The global solar radiation, air temperature, number of sunny hours, day length, airborne dust particles, cloudiness, air pressure, and dummy variables[1] are the order of the most important inputs to solar power generation. Results show simultaneous influences of radiation and temperature on solar power plant production.

https://doi.org/10.30501/jree.2023.363386.1461

چکیده:

انرژی خور شیدی پاک یکی از بهترین منابع انرژی ا ست. نیروگاه‌های خور شیدی در ایران به دلیل روزهای آفتابی زیاد می‌توانند برق تولید کنند. این مقاله یک رویکرد پیش‌بینی کوتاه‌مدت مبتنی بر شبکه‌های عصبی مصنوعی برای نیروگاه‌های خور شیدی منتخب در ایران ارائه می‌کند و متغیرهای ورودی شبکه عصبی را با توجه به اهمیت آنها رتبه‌بندی می‌کند. دو نیروگاه خور شیدی در ا ستان همدان (امیرکبیر و خلیج فارس) برای اجرای این طرح انتخاب شده اند. تولید نیروگاه های خور شیدی به شرایط آب و هوایی بستگی دارد. تابش خور شید در صفحه افقی، دمای هوا، فشار هوا، طول روز، تعداد ساعات آفتابی، ابری و ذرات گرد و غبار موجود در هوا به عنوان متغیرهای ورودی در این مطالعه برای پیش‌بینی تولید این نیروگاههای خور شیدی در نظر گرفته شده‌اند. انتخاب مدل پیش‌بینی بر اساس در نظر گرفتن مقادیر صفر و غیر صفر متغیرهای هدف است. نتایج نشان می‌دهد پیش‌بینی تولید برق برا ساس پارامترهای هوا شنا سی در نیروگاه خور شیدی خلیج فارس دقیق‌تر از نیروگاه امیرکبیر ا ست. تابش خور شیدی جهانی، دمای هوا، تعداد ساعات آفتابی، طول روز، ذرات گرد و غبار موجود در هوا، ابری بودن، فشار هوا و متغیرهای مجازی[۲] مهم‌ترین ورودی‌های تولید انرژی خورشیدی هستند. نتایج، نشان‌دهنده تأثیرات همزمان تابش دما بر تولید نیروگاه خورشیدی است.

[1]. The first half of the year is counted as one, and the second half is counted as zero.

[۲]. نیمه اول سال، یک و نیمه دوم سال برابر صفر درنظر گرفته شده است.

JREE: Vol. 10, No. 4, (Autumn 2023) 146-155

Thermal Performance and Efficiency Enhancement in Evacuated Tube Solar Collectors Using Various Nanofluids

Mohamed Ramadan Gomaa*, Njoud Hussein Alhabahbh, Mohammed Abbas Al-Nawafleh

Department of Mechanical Engineering, Faculty of Engineering, Al-Hussein Bin Talal University, Maan, Jordan.

PAPER INFO

Paper history:
Received: 20 January 2023
Revised: 28 July 2023
Accepted: 30 August 2023

Keywords:
Evacuated Tube Collector,
Energy Enhancement,
Thermal Efficiency,
Nanofluid

ABSTRACT

This research reviews various studies on the effect of using nanofluids in evacuated tube solar collectors (ETSC). The initial segment of this study elaborates on the importance of using the ETSCs and categorizes these collectors in terms of classification and application. The second segment evaluates the physical properties of nanofluids incorporated in the solar system collector and presents some applications of nanofluids. The last segment of the research reviews the works of a group of researchers who have already applied nanofluids to evacuated tube solar collectors for various purposes, including increasing the heat transfer coefficient and improving efficiency. Among the prevalent nanofluids employed in solar applications, Al_2O_3, CuO, and TiO_2 feature prominently, whereas Ag, WO_3, and CeO_2 find limited application in the solar context. Furthermore, nanofluids within the size range of 1–25 nm, 25–50 nm, and 50–100 nm constitutes 54%, 25%, and 11% of the applications, respectively. Particularly noteworthy, the single-walled carbon nanotubes/water (SWCNT/water) heat pipe showcases the most remarkable efficiency enhancement, achieving an impressive 93.43% improvement.

https://doi.org/10.30501/jree.2023.374760.1507

چکیده:

این تحقیق به بررسی مطالعات مختلف در مورد تأثیر استفاده از نانو سوسپانسیون های نانوذرات در جمع کننده های خورشیدی لوله خلاء (ETSC) می پردازد. بخش اولیه این مطالعه بر اهمیت استفاده از ETSC ها و دسته بندی بندی این جمع کننده ها از نظر طبقه بندی و کاربرد، تاکید دارد. بخش دوم ویژگی های فیزیکی نانو سوسپانسیون های ادغام شده در جمع کننده سیستم خورشیدی را ارزیابی می کند و برخی از کاربردهای نانو سوسپانسیون ها را ارائه می دهد. بخش آخر تحقیق کارهای یک گروه از محققان را بررسی می کند که قبلاً از نانو سوسپانسیون ها برای جمع کننده های خورشیدی لوله خلاء برای مقاصد مختلف، از جمله افزایش ضریب انتقال حرارت و بهبود بهره وری استفاده کرده اند. در میان نانو سوسپانسیونی که در کاربردهای خورشیدی مورد استفاده قرار می گیرند، Al_2O_3، CuO و TiO_2 به طور برجسته ای ظاهر می شوند، در حالی که Ag ، WO_3 و CeO_2 کاربرد محدودی در زمینه خورشید دارند. علاوه بر این، نانو سوسپانسیون ها در محدوده اندازه ۱-۲۵ نانومتر، ۲۵-۵۰ نانومتر و ۵۰-۱۰۰ نانومتر به ترتیب ۵۴ درصد، ۲۵ درصد و ۱۱ درصد از کاربردها را تشکیل می دهند. از جمله موارد قابل توجه، لوله گرمایشی تک جداره کربن نانوتیوب/آب (SWCNT/water) بهترین افزایش بهره وری را نشان می دهد و بهبود قابل توجه ۹۳,۴۳ درصدی را به دست می‌آورد.

JREE: Vol. 10, No. 4, (Autumn 2023) 156-162

Thermal Investigation of Single Slope Solar Still by Using Energy Storage Material

Subramanian Kumaravel [a], Meenakshi Sunadaram Nagaraj [b*], Govindarajan Bharathiraja [a]

[a] *Department of Mechanical Engineering, Saveetha School of Engineering, Saveetha Institute of Medical and Technical Sciences, P. O. Box: 602 105, Chennai, India.*
[b] *Department of Agricultural Engineering ,Saveetha School of Engineering, Saveetha Institute of Medical and Technical Sciences, P. O. Box: 602 105, Chennai , India.*

PAPER INFO

Paper history:
Received: 21 December 2022
Revised: 12 May 2023
Accepted: 13 May 2023

Keywords:
Solar Still,
Copper Scrap,
Brass Scrap,
Temperature,
Productivity,
Water,
Salt Water

ABSTRACT

In this research, a piece of copper scrap was placed in the 1m × 1m base of a single-slope solar still. An automated system steadily dripped salt water into the basin of the solar still. The experiment utilized dripping salt water and energy storage materials such as copper and brass scrap. Research has shown that the presence of copper scrap in the basin, combined with a shallow layer of salt water, has a significant impact on the distillate output. However, the high thermal capacity of the salt water in the basin can lead to reduced production. As more salt water is added to the basin, the temperature difference between the water inside and the glass cover increases. Based on the experimental results, the calculated yield is satisfactory, and the overall thermal efficiency remains at 71.3%. The production rate is also influenced by the diffusion process on the south-facing condensing cover. The temperatures of water, glass, and air, as well as their combined effects, are measured and analyzed.

https://doi.org/10.30501/jree.2023.376724.1518

چکیده:

در این تحقیق، یک قطعه قراضه مس در پایه ۱ متر × ۱ متر یک دستگاه تقطیر خورشیدی تک شیب قرار داده شد. یک سیستم خودکار به طور پیوسته آب شور را به دهانه دستگاه تقطیر خورشیدی می چکاند. برای آزمایش از آب شور چکه ای و مواد ذخیره انرژی مانند قراضه مس و برنج استفاده شد. تحقیقات نشان داده است که وجود قراضه مس در حوضچه همراه با یک لایه کم آب شور تأثیر قابل توجهی بر تولید تقطیر دارد. با این حال، ظرفیت حرارتی بالای آب شور در حوضچه می تواند منجر به کاهش تولید شود. با افزودن آب شور بیشتر به حوضچه، اختلاف دما بین آب داخل و پوشش شیشه ای افزایش می یابد. بر اساس نتایج تجربی، بازده محاسبه شده رضایت بخش است و بازده حرارتی کلی در ۷۱,۳ درصد باقی می ماند. نرخ تولید همچنین تحت تأثیر فرآیند انتشار در پوشش متراکم کننده رو به جنوب قرار دارد. دمای آب، شیشه و هوا، همراه با اثرات ترکیبی آنها اندازه گیری و تجزیه و تحلیل می شوند.

CONTENTS

Journal Homepage: www.jree.ir